Akira Furusawa and Peter van Loock
Quantum Teleportation and Entanglement

Related Titles

Huang, K.

Quantum Field Theory
From Operators to Path Integrals

2010
ISBN 978-3-527-40846-7

Morsch, O.

Quantum Bits and Quantum Secrets
How Quantum Physics is Revolutionizing Codes and Computers

2008
ISBN 978-3-527-40710-1

Audretsch, J.

Entangled Systems
New Directions in Quantum Physics

2007
ISBN 978-3-527-40684-5

Vogel, W., Welsch, D.-G.

Quantum Optics

2006
ISBN 978-3-527-40507-7

Audretsch, J. (ed.)

Entangled World
The Fascination of Quantum Information and Computation

2006
ISBN 978-3-527-40470-4

Leuchs, G., Beth, T. (eds.)

Quantum Information Processing

2003
ISBN 978-3-527-40371-4

Schleich, W. P.

Quantum Optics in Phase Space

2001
ISBN 978-3-527-29435-0

Akira Furusawa and Peter van Loock

Quantum Teleportation and Entanglement

A Hybrid Approach to Optical Quantum Information Processing

WILEY-VCH Verlag GmbH & Co. KGaA

The Authors

Prof. Akira Furusawa
The University of Tokyo
Department of Applied Physics
Tokyo, Japan
akiraf@ap.t.u-tokyo.ac.jp

Dr. Peter van Loock
Physik Institut LS für Optik
Institut Theorie I
Universität Erlangen-Nürnberg
Max-Planck-Institut (MPL)
Erlangen, Germany
peter.vanloock@mpl.mpg.de

All books published by Wiley-VCH are carefully produced. Nevertheless, authors, editors, and publisher do not warrant the information contained in these books, including this book, to be free of errors. Readers are advised to keep in mind that statements, data, illustrations, procedural details or other items may inadvertently be inaccurate.

Library of Congress Card No.: applied for

British Library Cataloguing-in-Publication Data:
A catalogue record for this book is available from the British Library.

Bibliographic information published by the Deutsche Nationalbibliothek
The Deutsche Nationalbibliothek lists this publication in the Deutsche Nationalbibliografie; detailed bibliographic data are available on the Internet at http://dnb.d-nb.de.

© 2011 WILEY-VCH Verlag GmbH & Co. KGaA, Boschstr. 12, 69469 Weinheim, Germany

All rights reserved (including those of translation into other languages). No part of this book may be reproduced in any form – by photoprinting, microfilm, or any other means – nor transmitted or translated into a machine language without written permission from the publishers. Registered names, trademarks, etc. used in this book, even when not specifically marked as such, are not to be considered unprotected by law.

Typesetting le-tex publishing services GmbH, Leipzig
Printing and Binding Fabulous Printers Pte Ltd, Singapore
Cover Design Adam Design, Weinheim

Printed in Singapore
Printed on acid-free paper

ISBN 978-3-527-40930-3

Contents

Preface *IX*

Part One Introductions and Basics *1*

1 Introduction to Quantum Information Processing *3*
1.1 Why Quantum Information? *5*
1.2 States and Observables *10*
1.2.1 Qubit *12*
1.2.2 Qumode *13*
1.3 Unitaries *18*
1.3.1 Qubit *19*
1.3.2 Qumode *20*
1.4 Non-unitaries *23*
1.4.1 Channels *23*
1.4.2 Measurements *27*
1.4.2.1 POVM *27*
1.4.2.2 Naimark Extension *29*
1.5 Entanglement *31*
1.5.1 Pure States *31*
1.5.1.1 Qubits *33*
1.5.1.2 Qumodes *33*
1.5.2 Mixed States and Inseparability Criteria *34*
1.5.3 Entanglement Witnesses and Measures *35*
1.6 Quantum Teleportation *38*
1.6.1 Discrete Variables *39*
1.6.2 Continuous Variables *40*
1.7 Quantum Communication *41*
1.7.1 Key Distribution *42*
1.7.2 Repeaters and Relays *45*
1.7.3 Shannon Theory *47*
1.8 Quantum Computation *49*
1.8.1 Models *52*
1.8.2 Universality *54*
1.8.2.1 Qubits *54*

Quantum Teleportation and Entanglement. Akira Furusawa, Peter van Loock
Copyright © 2011 WILEY-VCH Verlag GmbH & Co. KGaA, Weinheim
ISBN: 978-3-527-40930-3

1.8.2.2 Qumodes *57*
1.9 Quantum Error Correction *62*
1.9.1 Discretization *63*
1.9.2 Stabilizer Codes *67*
1.10 Experiment: Non-optical Implementations *70*

2 Introduction to Optical Quantum Information Processing *79*
2.1 Why Optics? *80*
2.2 Quantum Optical States and Encodings *82*
2.2.1 Field Quantization *83*
2.2.1.1 Discrete Modes *84*
2.2.1.2 Continuous Modes *87*
2.2.2 Quadratures *88*
2.2.3 Coherent States *89*
2.2.4 Squeezed States *90*
2.2.5 Phase-Space Representations *94*
2.2.6 Photonic Qubits *98*
2.2.7 Experiment: Polarization Qubits *99*
2.2.8 Photonic Qumodes *100*
2.2.8.1 Stabilizer States *101*
2.2.8.2 Gaussian States *102*
2.2.9 Experiment: Broadband Qumodes *107*
2.3 Quantum Optical Unitaries *109*
2.4 Gaussian Unitaries *113*
2.5 Quantum Optical Non-unitaries *114*
2.5.1 Channels *114*
2.5.2 Measurements *116*
2.6 Gaussian Non-unitaries *117*
2.7 Linear Optics: Possibilities and Impossibilities *120*
2.8 Optical Quantum Computation *121*

Part Two Fundamental Resources and Protocols *125*

3 Entanglement *127*
3.1 Qubit Entanglement *128*
3.1.1 Characterization and Witnesses *128*
3.1.1.1 Two Parties *128*
3.1.1.2 Three or More Parties *129*
3.1.2 Cluster and Graph States *131*
3.1.3 Experiment: Entangled Photonic Qubits *132*
3.1.3.1 EPR/Bell State *132*
3.1.3.2 GHZ State *135*
3.1.3.3 Cluster States *138*
3.2 Qumode Entanglement *142*
3.2.1 Characterization and Witnesses *142*
3.2.1.1 Two Parties *142*

3.2.1.2 Three or More Parties *149*
3.2.2 Cluster and Graph States *154*
3.2.3 Experiment: Entangled Photonic Qumodes *160*
3.2.3.1 Frequency-Domain EPR-Type State *160*
3.2.3.2 Time-Domain EPR-Type State *161*
3.2.3.3 GHZ-Type State *167*
3.2.3.4 Cluster-Type States *172*

4 Quantum Teleportation *179*
4.1 Qubit Quantum Teleportation *180*
4.1.1 Experiment: Qubit Quantum Teleportation *180*
4.1.2 Experiment: Qubit Telecloning *183*
4.1.3 Experiment: Qubit Entanglement Swapping *185*
4.2 Qumode Quantum Teleportation *188*
4.2.1 Experiment: Qumode Quantum Teleportation *189*
4.2.2 Experiment: Qumode Telecloning *196*
4.2.3 Experiment: Qumode Teleportation Network *203*
4.2.4 Experiment: Qumode Entanglement Swapping *210*

5 Quantum Error Correction *217*
5.1 The Nine-Qubit Code *218*
5.2 The Nine-Qumode Code *219*
5.3 Experiment: Quantum Error Correction *220*
5.3.1 Qubits *220*
5.3.2 Qumodes *223*
5.4 Entanglement Distillation *231*
5.5 Experiment: Entanglement Distillation *233*
5.5.1 Qubits *233*
5.5.2 Qumodes *236*

Part Three Measurement-Based and Hybrid Approaches *243*

6 Quantum Teleportation of Gates *245*
6.1 Teleporting Qubit Gates *246*
6.1.1 KLM *246*
6.1.2 Experiment: Qubit Gates *248*
6.2 Teleporting Qumode Gates *252*
6.2.1 Experiment: Gaussian Qumode Gates *252*
6.2.1.1 Universal Squeezer *252*
6.2.1.2 Quantum Non-demolition (QND) Sum Gate *259*
6.2.2 Universal Qumode Gates *266*

7 Cluster-Based Quantum Information Processing *271*
7.1 Qubits *272*
7.1.1 Elementary Qubit Teleportations *272*
7.1.2 Experiment: Qubit Cluster Computation *273*
7.2 Qumodes *280*

7.2.1 Elementary Qumode Teleportations *281*
7.2.2 Gaussian Computation *282*
7.2.3 Experiment: Gaussian Qumode Cluster Computation *283*
7.2.3.1 Quadratic Phase Gate *283*
7.2.3.2 Fourier and Squeezing Gates *291*

8 Hybrid Quantum Information Processing *299*
8.1 How to Create Non-Gaussian States, Cat States *300*
8.2 Experiment: Creation of Non-Gaussian States, Cat States *303*
8.3 Hybrid Entanglement *310*
8.4 Hybrid Quantum Teleportation *312*
8.4.1 Experiment: Broadband Qumode Teleportation of a Non-Gaussian Wavepacket *313*
8.4.2 Experiment: Broadband Qumode Teleportation of a Polarization Qubit *314*
8.5 Hybrid Quantum Computing *315*
8.5.1 Hybrid Hamiltonians *315*
8.5.2 Encoding Qubits into Qumodes *317*
8.5.3 GKP *318*

References *323*

Index *333*

Preface

The field of quantum information processing has reached a remarkable maturity in recent years with regard to experimental demonstrations. In particular, towards an extension of optical communications from the classical into the quantum realm, many proof-of-principle experiments were performed including the generation and distribution of photonic entangled states over free-space or fiber channels. As an application, unconditionally secure quantum key distribution systems have emerged and even developed into a commercially available technology.

Light systems, apart from their obvious usefulness for communication, have now as well turned out to be a serious contender for approaches to quantum computation. A breakthrough in this context was the theoretical discovery of so-called measurement-based models: quantum algorithms no longer depend on sequences of reversible quantum gates, each enacted through well controlled interactions between, for instance, two or more qubits; instead, sequences of measurements on parts of an entangled resource state prepared prior to the computation will do the trick. In other words, quantum entanglement, already known to be a universal resource for quantum communication in conjunction with quantum teleportation, represents a universal resource for quantum computation too – and again the exploitation of the entangled resource relies upon quantum teleportation which, in its ultimate form, achieves arbitrary quantum state manipulations.

The aim of this book is to give a fairly general introduction to two complementary approaches to quantum information processing: those based upon discrete-variable "qubit" systems and those utilizing quantum oscillator systems ("qumodes") most naturally represented by continuous quantum variables such as amplitude and phase. In quantum optics, the corresponding photonic systems would consist of just a few photons or they would correspond to fields with extremely high mean photon numbers, respectively. The qubit may then be represented by the polarization of a single photon, while a qumode state is encoded into an infinite-dimensional phase space. Entangled states can be defined, formulated, and experimentally realized in either dimension, including their use for quantum teleportation. Since either approach encounters somewhat different complications when it comes to more sophisticated quantum information protocols, a recent trend in optical quantum information is to combine the two approaches and to exploit at the same time discrete and continuous degrees of freedom in a so-called

Quantum Teleportation and Entanglement. Akira Furusawa, Peter van Loock
Copyright © 2011 WILEY-VCH Verlag GmbH & Co. KGaA, Weinheim
ISBN: 978-3-527-40930-3

hybrid fashion. From a more physical point of view, one could say that in an optical hybrid protocol both the wave and the particle properties of light are exploited simultaneously. Sometimes people would use a more general definition for "hybrid systems", namely any combined light-matter systems. In our quantum optical context, the two definitions would coincide when the matter system consists of atomic spin particles and the light system is described by continuous quantum variables –- a fairly natural scenario.

In the first part of the book, an introduction to the basics of quantum information processing is given independent of any specific realization, but with an emphasis on the two complementary qubit and qumode descriptions. The second chapter of part I then specifically refers to optical implementations. While this first part of the book is mainly theoretical, parts II and III contain detailed descriptions of various experiments. Those specific sections on experiments are each indicated by "experiment:" throughout. One can easily infer from the table of contents that the frequency of experimental sections increases with each chapter of the book. The in some sense unifying formalism for the qubit and qumode approaches is the so-called stabilizer formalism which is therefore used in various sections throughout the book starting from the introductory sections. Summary boxes of the most important formulas and definitions have been included throughout the first three chapters of the book in order to make the introductory parts more comprehensible to the reader.

We hope this book will convey some of the excitement triggered by recent quantum information experiments and encourage both students and researchers to (further) participate in the joint efforts of the quantum optics and quantum information community.

November 2010

Akira Furusawa and
Peter van Loock

Part One Introductions and Basics

1
Introduction to Quantum Information Processing

Quantum information is a relatively young area of interdisciplinary research. One of its main goals is, from a more conceptual point of view, to combine the principles of quantum physics with those of information theory. Information is physical is one of the key messages, and, on a fundamental level, it is quantum physical. Apart from its conceptual importance, however, quantum information may also lead to real-world applications for communication (quantum communication) and computation (quantum computation) by exploiting quantum properties such as the superposition principle and entanglement. In recent years, especially entanglement turned out to play the most prominent role, representing a universal resource for both quantum computation and quantum communication. More precisely, multipartite entangled, so-called cluster states are a sufficient resource for universal, measurement-based quantum computation [1]. Further, the sequential distribution of many copies of entangled states in a quantum repeater allow for extending quantum communication to large distances, even when the physical quantum channel is imperfect such as a lossy, optical fiber [2, 3].

In this introductory chapter, we shall give a brief, certainly incomplete, and in some sense biased overview of quantum information. It will be incomplete, as the focus of this book is on optical quantum information protocols, and their experimental realizations, including many experiment-oriented details otherwise missing in textbooks on quantum information. Regarding the more abstract, mathematical foundations of quantum information, there are various excellent sources already existing [4–8].

Nonetheless, we do attempt to introduce some selected topics of quantum information theory, which then serve as the conceptual footing for our detailed descriptions of the most recent quantum information experiments. In this sense, on the one hand, we are biased concerning the chosen topics. On the other hand, as our goal is to advertise a rather new concept for the realization of quantum information protocols, namely, the combination of notions and techniques from two complementary approaches, our presentation of the basics of quantum information should also provide a new perspective on quantum information. The two complementary approaches are the two most commonly used encodings of quantum information: the one based upon discrete two-level systems (so-called qubits), certainly by far the most popular and well-known approach, in analogy to classi-

Quantum Teleportation and Entanglement. Akira Furusawa, Peter van Loock
Copyright © 2011 WILEY-VCH Verlag GmbH & Co. KGaA, Weinheim
ISBN: 978-3-527-40930-3

cal digital encodings; the other approach relies on infinite-dimensional quantum systems, especially quantized harmonic oscillators (so-called qumodes), more reminiscent of classical analog encodings.

There are also approaches in between based on elementary systems that live in more than two, but still finite dimensions. Such discrete multi-level systems share many of their most distinct features with those of simple qubit systems. In fact, we may simulate any d-level system (so-called qudit) by a set of $\log_2 d$ qubits. Therefore, one may expect to obtain qualitatively new features only when the limit $d \to \infty$ is taken. Schemes based on qubit and qudit encodings are commonly referred to as discrete-variable (DV) approaches, whereas those exploiting infinite-dimensional systems and the possibility of preparing and measuring quantum information in terms of variables with a continuous spectrum are called continuous-variable (CV) schemes. Many fundamental results of quantum information theory, however, would not even depend on a particular encoding or dimensionality. These results based on fundamental elements of quantum theory such as linearity stay solid even when the infinite-dimensional limit is taken.

Similar to a classical, digital/analog hybrid computer, one may also consider utilizing discrete and continuous degrees of freedom at the same time for encoding, logic gates, or measurements. Later, when we start discussing optical implementations of quantum information protocols in Chapter 2, we can give the motivation as to why such a hybrid approach would be useful for processing quantum information. The purpose of the present chapter is solely conceptual and independent of potential implementations. We shall introduce some basic results and notions of quantum information theory, and, in particular, apply these to both DV qubit and CV qumode systems.

Starting with a short motivation for the interest in quantum information theory in Section 1.1, we discuss the preparation and representation of quantum information in the form of quantum states and observables (Section 1.2), its manipulation using unitary gates and evolution (Section 1.3), and its behavior under non-unitary evolution in the form of quantum channels and measurements (Section 1.4). The latter scenario is very important, as an initialized quantum information carrier would typically be subject to unwanted interactions with its environment, and such a pure-into-mixed-state evolution is described by a channel map (Section 1.4.1). Whenever the environment is replaced by an auxiliary system that can be measured, information about the original quantum system may be obtained, as we discuss in Section 1.4.2.

Before concluding this chapter in Section 1.10 with a discussion of some non-optical experimental realizations of quantum information processing, we briefly introduce some basic notions, resources, subroutines, and full-scale applications such as entanglement (Section 1.5), quantum teleportation (Section 1.6), quantum communication (Section 1.7), quantum computation (Section 1.8), and quantum error correction (Section 1.9). Since the remainder of this book is intended to describe and illustrate many of these protocols and applications, we shall postpone such more detailed discussions until the respective chapters regarding optical implementations.

1.1
Why Quantum Information?

Quantum computers are designed to process information units which are no longer just abstract mathematical entities according to Shannon's theory, but rather truly physical objects, adequately described by one of the two[1] most fundamental physical theories – quantum mechanics.

Classical information is typically encoded in digital form. A single basic information unit, a bit, contains the information whether a "zero" or a "one" has been chosen between only those two options, for example, depending on the electric current in a computer wire exceeding a certain value or not. Quantum information is encoded in quantum mechanical superpositions, most prominently, an arbitrary superposition of "zero" and "one", called a "qubit".[2] Because there is an infinite number of possible superposition states, each giving the "zero" and the "one" particular weights within a continuous range, even just a single qubit requires, in principle, an infinite amount of information to describe it.

We also know that classical information is not necessarily encoded in bits. Bits may be tailor-made for handling by a computer. However, when we perform calculations ourselves, we prefer the decimal to the binary system. In the decimal system, a single digit informs us about a particular choice between ten discrete options, not just two as in the binary system. Similarly, quantum information may also be encoded into higher-dimensional systems instead of those qubit states defined in a two-dimensional Hilbert space. By pushing the limits and extending classical analog encoding to the quantum realm, quantum observables with a continuous spectrum may also serve as an infinite-dimensional basis for encoding and processing quantum information. In this book, we shall attempt to use both the discrete and the continuous approaches in order to formulate quantum information protocols, to conceptually understand their meaning and significance, and to recast them into a form most accessible to experimental implementations. We will try to convey some answers as to why quantum information is such a fascinating field that stimulates interdisciplinary research among physicists, mathematicians, computer scientists, and others.

There is one answer we can offer in this introductory chapter straight away. In most research areas of physics, normally a physicist has to make a choice. If she or he is most interested in basic concepts and the most fundamental theories, she or he may acquire sufficient skills in abstract mathematical formalisms and become part of the joint effort of the physics community to fill some of the gaps in the basic physical theories. Typically, this kind of research, though of undoubted importance for the whole field of physics as such, is arbitrarily far from any real-world applications. Often, these research lines even remain completely disconnected from any potential experimental realizations which could support or falsify the corresponding theory. On the other hand, those physicists who are eager to contribute to the

1) The other, complementary, fundamental physical theory is well known to be general relativity.
2) The term qubit was coined by Schumacher [9].

real world by using their knowledge of fundamental physical theories would typically have to sacrifice (at least to some extent)[3] their deeper interest into those theories and concepts, as day and life times are finite.

Thus, here is one of the most attractive features of the field of quantum information: it is oriented towards both directions, namely, one that aims at a deeper understanding of fundamental concepts and theories, and, at the same time, one that may lead to new forms of communication and computation for real-world applications.[4] Obviously, as quantum information has been an interdisciplinary field from the beginning, the large diversity of quantum information scientists naturally means that some of them would be mainly devoted to abstract, mathematical models, whereas others would spend most of their time attempting to bridge the gaps between theoretical proposals, experimental proof-of-principle demonstrations, and, possibly, real-world applications. However, and this is maybe one of the most remarkable aspects of quantum information, new fundamental concepts and insights may even emerge when the actual research effort is less ambitious and mostly oriented towards potential applications. In fact, even without sophisticated extensions of the existing mathematical formalisms, within the standard framework of quantum mechanics, deep insights may be gained. A nice example of this is the famous no-cloning theorem [14, 15] which is, historically, probably the first fundamental law of quantum information.[5]

The no-cloning theorem states that quantum information encoded in an arbitrary, potentially unknown quantum state cannot be copied with perfect accuracy. This theorem has no classical counterpart because no fundamental principle prevents us from making arbitrarily many copies of classical information. The no-cloning theorem was one of the first results on the more general concepts of quantum theory that had the flavor of today's quantum information theory (see Figure 1.1). Though only based upon the linearity of quantum mechanics, no-cloning is of fundamental importance because it is a necessary precondition for physical laws as fundamental as no-signaling (i.e., the impossibility of superluminal communication) and the Heisenberg uncertainty relation.

3) A famous exception, of course, is Albert Einstein who dealt with fridges during his working hours in a patent office and discovered general relativity during his spare time.

4) Very recent examples for these two complementary directions are, on the one hand, the emerging subfield of relativistic quantum information that is intended to provide new insights into more complete theories connecting quantum mechanics with relativity [10, 11]; and, on the other hand, the recent demonstration of a quantum key distribution network in Vienna [12, 13].

5) There is a fascinating anecdote related to the discovery of no-cloning in 1982. The theorem was inspired by a proposal for a "superluminal communicator", the so-called FLASH (an acronym for First Laser-Amplified Superluminal Hookup) [16]. The flaw in this proposal and the non-existence of such a device was realized by both referees: Asher Peres, who nonetheless accepted the paper in order to stimulate further research into this matter, and GianCarlo Ghirardi, who even gave a no-cloning-based proof for the incorrectness of the scheme in his report. Eventually, the issue was settled through the published works by Dieks, Wootters, and Zurek [14, 15], proving that *any* such device would be unphysical.

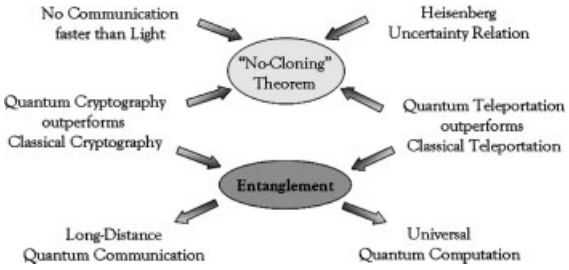

Figure 1.1 A summary of concepts and applications linked to or originating from quantum information. The upper part is devoted to fundamental physical laws, while the middle and lower parts refer to elementary quantum protocols and the ultimate full-scale quantum applications, respectively.

At the center of quantum information is the notion of entanglement, a necessary resource for elementary quantum protocols such as quantum teleportation [17] (the reliable transfer of quantum information using shared entanglement and classical communication) and quantum key distribution [18] (the secure transmission of classical information using quantum communication);[6] entanglement has also been shown to be a sufficient resource for the ultimate applications, long-distance quantum communication [2] and universal quantum computation [1]. Missing in Figure 1.1 are important subroutines for quantum error correction [5, 21] in order to distribute or reliably store entanglement; in quantum communication, such a quantum error correction may be probabilistic (so-called entanglement distillation [22]), while for quantum computation, we need to measure and manipulate entangled states fault-tolerantly in a deterministic fashion [5].

Without no-cloning, the following scenario appears to be possible [16]. Two parties, "Alice" (subscript A) and "Bob" (subscript B), sharing a maximally entangled two-qubit state,[7]

$$\frac{1}{\sqrt{2}}\left(|0\rangle_A \otimes |0\rangle_B + |1\rangle_A \otimes |1\rangle_B\right) = \frac{1}{\sqrt{2}}\left(|+\rangle_A \otimes |+\rangle_B + |-\rangle_A \otimes |-\rangle_B\right) , \tag{1.1}$$

may use their resource to communicate faster than the speed of light. The essential element for this to work would be the Einstein, Podolsky, and Rosen (EPR) [23]

6) The importance of entanglement as a necessary precondition for secure key distribution was shown by Curty *et al.* [19]. Even though entanglement may not be physically distributed between the sender and the receiver (as in [18], as opposed to, for example, the Ekert protocol [20]), for secure communication, the measured correlations must not be consistent with classical correlations described by an unentangled state. Note that a possible eavesdropper attack is always given by approximate cloning of the quantum signals such that perfect cloning would definitely prevent secure quantum key distribution (Figure 1.1), and, in a realistic scenario, approximate cloning may as well.

7) The following discussion requires some familiarity with basic quantum mechanical notions such as state vectors, density operators, and partial trace operations, a brief introduction of which will be given in the succeeding section.

correlations of the entangled state which are stronger than classical correlations as they are present at the same time in different, conjugate bases, $\{|0\rangle, |1\rangle\}$ and $\{|+\rangle, |-\rangle\}$ with $|\pm\rangle \equiv (|0\rangle \pm |1\rangle)/\sqrt{2}$, corresponding to different, non-commuting observables Z and X, respectively, where $Z|k\rangle = (-1)^k|k\rangle$ and $X|\pm\rangle = \pm|\pm\rangle$ with $k = 0, 1$. Physically, each of the two bases could correspond to two orthogonal polarizations of a single photon; one basis for linear polarization and the other one for circular polarization.

Alice could now choose to measure her half of the entangled state in the basis $\{|0\rangle, |1\rangle\}$. Alternatively, she may as well project onto $\{|+\rangle, |-\rangle\}$. In the former case, Bob's half ends up in the corresponding eigenstate $|0\rangle$ or $|1\rangle$ and so would all copies that he could generate from his half. In the latter case, copies of Bob's half would all be in the corresponding state $|+\rangle$ or $|-\rangle$, and measurements in the basis $\{|0\rangle, |1\rangle\}$ would yield, on average, half of the copies in the state $|0\rangle$ and likewise half of them in the state $|1\rangle$. Therefore, the statistics of measurements on copies of Bob's half would enable him to find out which measurement basis Alice has chosen. Such a scheme could be exploited for a deterministic, superluminal transfer of binary information from Alice to Bob. However, the other crucial element here would be Bob's capability of producing many copies of the states $\{|0\rangle, |1\rangle\}$ or $\{|+\rangle, |-\rangle\}$ without knowing what the actual states are. This is forbidden by the no-cloning theorem.

Physically, no-cloning would become manifest in an optical implementation of the above scheme through the impossibility of amplifying Bob's photons in a noiseless fashion; spontaneous emissions would add random photons and destroy the supposed correlations. From a mathematical, more fundamental point of view, the linearity of quantum mechanics alone suffices to negate the possibility of superluminal communication using shared entanglement.

The crucial ingredient of the entanglement-assisted superluminal communication scenario above is the copying device that may be represented by an (initial) state $|\mathrm{A}\rangle$. It must be capable of copying *arbitrary* quantum states $|\psi\rangle$ as

$$|\psi\rangle|\mathrm{A}\rangle \longrightarrow |\psi\rangle|\psi\rangle|\mathrm{A}'\rangle \,. \tag{1.2}$$

The final state of the copying apparatus is described by $|\mathrm{A}'\rangle$. More accurately, the transformation should read

$$|\psi\rangle_\mathrm{a}|0\rangle_\mathrm{b}|\mathrm{A}\rangle_\mathrm{c} \longrightarrow |\psi\rangle_\mathrm{a}|\psi\rangle_\mathrm{b}|\mathrm{A}'\rangle_\mathrm{c} \,, \tag{1.3}$$

where the original input a to be cloned is described by $|\psi\rangle_\mathrm{a}$ and a second qubit b is initially in the "blank" state $|0\rangle_\mathrm{b}$. After the copying process, both qubits end up in the original quantum state $|\psi\rangle$.

Wootters and Zurek [15] (and similarly Dieks for his "multiplier" [14]) considered a device that does clone the basis states $\{|0\rangle, |1\rangle\}$ in the appropriate way according to Eq. (1.2),

$$\begin{aligned} |0\rangle|\mathrm{A}\rangle &\longrightarrow |0\rangle|0\rangle|\mathrm{A}_0\rangle \,, \\ |1\rangle|\mathrm{A}\rangle &\longrightarrow |1\rangle|1\rangle|\mathrm{A}_1\rangle \,. \end{aligned} \tag{1.4}$$

Since this transformation must be unitary[8] and linear, its application to an input in the superposition state $|\psi\rangle = \alpha|0\rangle + \beta|1\rangle$ leads to

$$|\psi\rangle|\mathrm{A}\rangle \longrightarrow \alpha|0\rangle|0\rangle|\mathrm{A}_0\rangle + \beta|1\rangle|1\rangle|\mathrm{A}_1\rangle \; . \tag{1.5}$$

For identical output states of the copying apparatus, $|\mathrm{A}_0\rangle = |\mathrm{A}_1\rangle$, a and b are in the pure state $\alpha|0\rangle|0\rangle + \beta|1\rangle|1\rangle$ which is not the desired output state $|\psi\rangle|\psi\rangle$. With a distinction between the apparatus states, that is, taking them to be orthonormal, $\langle \mathrm{A}_0|\mathrm{A}_0\rangle = \langle \mathrm{A}_1|\mathrm{A}_1\rangle = 1$, $\langle \mathrm{A}_0|\mathrm{A}_1\rangle = 0$, we obtain from the density operator of the whole output system (for simplicity, assuming real α and β),

$$\begin{aligned}\hat{\rho}_{\mathrm{abc}} = {} & \alpha^2|00\mathrm{A}_0\rangle_{\mathrm{abc}}\langle 00\mathrm{A}_0| + \beta^2|11\mathrm{A}_1\rangle_{\mathrm{abc}}\langle 11\mathrm{A}_1| \\ & + \alpha\beta|00\mathrm{A}_0\rangle_{\mathrm{abc}}\langle 11\mathrm{A}_1| + \alpha\beta|11\mathrm{A}_1\rangle_{\mathrm{abc}}\langle 00\mathrm{A}_0| \; ,\end{aligned} \tag{1.6}$$

the density operator of the original-copy system ab by tracing out the apparatus,

$$\mathrm{Tr}_{\mathrm{c}}\hat{\rho}_{\mathrm{abc}} = \alpha^2|00\rangle_{\mathrm{ab}}\langle 00| + \beta^2|11\rangle_{\mathrm{ab}}\langle 11| \equiv \hat{\rho}_{\mathrm{ab}} \; . \tag{1.7}$$

Finally, we can calculate the individual density operators of a and b,

$$\begin{aligned}\mathrm{Tr}_{\mathrm{b}}\hat{\rho}_{\mathrm{ab}} &= \alpha^2|0\rangle_{\mathrm{a}}\langle 0| + \beta^2|1\rangle_{\mathrm{a}}\langle 1| \equiv \hat{\rho}_{\mathrm{a}} \; , \\ \mathrm{Tr}_{\mathrm{a}}\hat{\rho}_{\mathrm{ab}} &= \alpha^2|0\rangle_{\mathrm{b}}\langle 0| + \beta^2|1\rangle_{\mathrm{b}}\langle 1| \equiv \hat{\rho}_{\mathrm{b}} \; .\end{aligned} \tag{1.8}$$

The two outgoing states are identical, but significantly different from the desired original density operator,

$$|\psi\rangle_{\mathrm{a}}\langle\psi| = \alpha^2|0\rangle_{\mathrm{a}}\langle 0| + \alpha\beta|0\rangle_{\mathrm{a}}\langle 1| + \alpha\beta|1\rangle_{\mathrm{a}}\langle 0| + \beta^2|1\rangle_{\mathrm{a}}\langle 1| \; . \tag{1.9}$$

In fact, any information about quantum coherence encoded in the off-diagonal terms of $|\psi\rangle$ is eliminated in the output states of Eq. (1.8). The degree of similarity between the actual output states and the original state, expressed by their overlap, the so-called fidelity [9],

$$F = {}_{\mathrm{a}}\langle\psi|\hat{\rho}_{\mathrm{a}}|\psi\rangle_{\mathrm{a}} = {}_{\mathrm{b}}\langle\psi|\hat{\rho}_{\mathrm{b}}|\psi\rangle_{\mathrm{b}} = \alpha^4 + \beta^4 = \alpha^4 + (1-\alpha^2)^2 \; , \tag{1.10}$$

depends on the original input state. The basis states $|0\rangle$ or $|1\rangle$ are perfectly copied with unit fidelity ($\alpha = 1$ or $\alpha = 0$), as we know from Eq. (1.4). However, coherent superpositions are copied with non-unit fidelity, where the worst result is obtained for the symmetric superposition $\alpha = 1/\sqrt{2}$ with $F = 1/2$.

Is it inevitable to obtain such a bad result when copying a symmetric superposition? Of course, only when we insist on perfectly copying certain basis states such

8) It was pointed out by Werner [24] that the "constructive" approach here, i.e, coupling the input system with an apparatus or "ancilla" through a unitary transformation and then tracing out the ancilla, is equivalent to a general quantum cloner described by linear, completely positive trace-preserving (CPTP) maps. General quantum operations, channels, and CPTP maps as well as states represented by density operators instead of vectors in Hilbert space will be discussed in more detail in the following sections.

as $\{|0\rangle, |1\rangle\}$. A universal copying machine that "treats all input states equally well" could be considered instead. For any input state $|s\rangle = \alpha|0\rangle + \beta|1\rangle$, it would always yield the same optimal non-unit fidelity independent of α, namely, $F = 5/6$ [25]. This would correspond to the optimal, approximate, universal cloning of an unknown qubit.

Since no-cloning only depends on the linearity of quantum theory, it applies to quantum states of any dimensionality, not only to qubits. Optimal, approximate, universal cloning may then be considered for all kinds of quantum states, from DV d-level systems [24] to CV infinite-dimensional systems [26, 27], including extensions with certain given numbers of input and output copies.

1.2 States and Observables

A *pure* quantum state is given by a vector in Hilbert space $|\psi\rangle$, and the vector may be expanded in an arbitrary basis,

$$|\psi\rangle = \sum_m \langle m|\psi\rangle |m\rangle \ . \tag{1.11}$$

The basis is complete and orthonormal,

$$\sum_m |m\rangle\langle m| = \mathbb{1} \ , \langle m|m'\rangle = \delta_{mm'} \ . \tag{1.12}$$

The complex numbers $\langle m|\psi\rangle$ are the components of the Hilbert space vector $|\psi\rangle$. When measuring an observable $\hat{M}$, the probability for obtaining the measurement result m (a *real* eigenvalue of $\hat{M}$ with eigenstate $|m\rangle$) is determined by the size of the component of $|\psi\rangle$ in direction of $|m\rangle$,

$$p_m = \frac{|\langle m|\psi\rangle|^2}{\langle\psi|\psi\rangle} \ . \tag{1.13}$$

Here,

$$\langle\psi|\psi\rangle = \sum_m \sum_{m'} \langle\psi|m\rangle\langle m|\langle m'|\psi\rangle|m'\rangle = \sum_m |\langle m|\psi\rangle|^2 \tag{1.14}$$

ensures the proper normalization, with $\langle m|\psi\rangle^* = \langle\psi|m\rangle$. Once the measurement result m is obtained, the state vector $|\psi\rangle$ is reduced ("collapses") onto the corresponding eigenstate $|m\rangle$. The overlap $\langle\psi|\psi'\rangle$ is the scalar product of the vector space, which is obviously independent of the basis choice in Eq. (1.11). The expectation value of the observable $\hat{M}$ in the state $|\psi\rangle$ is given by (with $\langle\psi|\psi\rangle = 1$)

$$\begin{aligned} \langle\hat{M}\rangle &= \sum_m p_m m = \sum_m m\langle\psi|m\rangle\langle m|\psi\rangle \\ &= \langle\psi| \sum_m m|m\rangle\langle m|\psi\rangle = \langle\psi|\hat{M}|\psi\rangle \ . \end{aligned} \tag{1.15}$$

This equation reveals the *spectral decomposition* of the observable $\hat{M}$,

$$\hat{M} = \sum_m m|m\rangle\langle m| \,, \tag{1.16}$$

which is a Hermitian operator and so the eigenvalues m are real. Thus far, we have considered observables with a *discrete, countable* spectrum, regardless of whether the Hilbert space is finite or infinite-dimensional. In the infinite-dimensional case, an observable $\hat{X}$ may have a *continuous* spectrum. Its spectral decomposition becomes

$$\hat{X} = \int \mathrm{d}x\, x|x\rangle\langle x| \,, \tag{1.17}$$

with the continuous eigenbasis $\{|x\rangle\}$ and the real, continuous eigenvalues x.

In contrast to pure states, *mixed* states cannot be described by Hilbert space vectors, taking into account the case of incomplete knowledge about the state preparation. A mixed state is a statistical mixture of pure states given by the density operator (with $\rho_k > 0$ and $\sum_k \rho_k = 1$)

$$\hat{\rho} = \sum_k \rho_k |\psi_k\rangle\langle\psi_k| \,. \tag{1.18}$$

As opposed to the coherent superposition in Eq. (1.11), a mixed state is sometimes called an incoherent superposition. According to this definition, we find for the overall expectation value of the observable $\hat{M}$,

$$\begin{aligned}\langle\hat{M}\rangle &= \sum_k \rho_k \langle\psi_k|\hat{M}|\psi_k\rangle = \sum_m \sum_k \rho_k \langle\psi_k|\hat{M}|m\rangle\langle m|\psi_k\rangle \\ &= \sum_m \langle m| \sum_k \rho_k |\psi_k\rangle\langle\psi_k|\hat{M}|m\rangle = \mathrm{Tr}(\hat{\rho}\hat{M}) \,,\end{aligned} \tag{1.19}$$

where we have introduced the trace operation $\mathrm{Tr}(\cdots) = \sum_m \langle m|\cdots|m\rangle$ with an arbitrary basis $\{|m\rangle\}$. The density operator is a normalized Hermitian operator, so $\mathrm{Tr}(\hat{\rho}) = 1$, and it is non-negative (i.e., it has only non-negative eigenvalues) because

$$\langle\phi|\hat{\rho}|\phi\rangle = \sum_k \rho_k |\langle\phi|\psi_k\rangle|^2 \geq 0 \tag{1.20}$$

for any $|\phi\rangle$. Note that the states $|\psi_k\rangle$ in the mixture $\hat{\rho}$ need not be orthogonal to each other. Further, the mixed-state decomposition is not unique. However, when the density operator of Eq. (1.18) is written in its eigenbasis, we find

$$\mathrm{Tr}(\hat{\rho}^2) = \sum_k \rho_k^2 \leq \sum_k \rho_k = 1 \,, \tag{1.21}$$

with ρ_k now being the eigenvalues of $\hat{\rho}$. Equality, $\mathrm{Tr}(\hat{\rho}^2) = 1$, only holds for pure states. Therefore, any state with $\mathrm{Tr}(\hat{\rho}^2) < 1$ is mixed. Alternatively, this becomes

manifest in the von Neumann entropy of a state,

$$S(\hat{\rho}) \equiv -\mathrm{Tr}\hat{\rho}\log\hat{\rho} = -\mathrm{Tr}\left[\sum_k \rho_k|\psi_k\rangle\langle\psi_k|\sum_l(\log\rho_l)|\psi_l\rangle\langle\psi_l|\right] = -\sum_k \rho_k\log\rho_k \ . \tag{1.22}$$

It becomes nonzero for any mixed state and vanishes for pure states.

1.2.1 Qubit

We shall now consider specific quantum states as they are typically used in quantum information. In a two-dimensional Hilbert space, a general pure qubit state can be written as

$$|\psi_{\theta,\phi}\rangle = \cos(\theta/2)|0\rangle + \sin(\theta/2)\mathrm{e}^{\mathrm{i}\phi}|1\rangle \ . \tag{1.23}$$

This state can also be represented in terms of the Bloch vector representation,

$$\begin{aligned}\hat{\rho} &= |\psi_{\theta,\phi}\rangle\langle\psi_{\theta,\phi}| \\ &= \frac{1}{2}\mathbb{1} + \frac{1}{2}\begin{pmatrix}\cos\theta & \sin\theta\,\mathrm{e}^{-\mathrm{i}\phi}\\ \sin\theta\,\mathrm{e}^{+\mathrm{i}\phi} & -\cos\theta\end{pmatrix} \\ &= \frac{1}{2}\begin{pmatrix}1+s_3 & s_1-\mathrm{i}s_2\\ s_1+\mathrm{i}s_2 & 1-s_3\end{pmatrix} = \frac{1}{2}(\mathbb{1}+\boldsymbol{s}\cdot\boldsymbol{\sigma}) \ ,\end{aligned} \tag{1.24}$$

with $\boldsymbol{\sigma} = (\sigma_1, \sigma_2, \sigma_3)^{\mathrm{T}}$, the Pauli matrices

$$\sigma_1 = \begin{pmatrix}0 & 1\\ 1 & 0\end{pmatrix}, \quad \sigma_2 = \begin{pmatrix}0 & -\mathrm{i}\\ \mathrm{i} & 0\end{pmatrix}, \quad \sigma_3 = \begin{pmatrix}1 & 0\\ 0 & -1\end{pmatrix}, \tag{1.25}$$

and

$$\boldsymbol{s} = (s_1, s_2, s_3) = (\sin\theta\cos\phi, \sin\theta\sin\phi, \cos\theta) \ . \tag{1.26}$$

The Bloch vector $\boldsymbol{s}$ fully describes the qubit state. It points in the direction specified by the spherical coordinates θ and ϕ. The vector's tip lies on the surface of the Bloch sphere, representing a pure state with $|\boldsymbol{s}| = 1$. For mixed states, we would have $|\boldsymbol{s}| < 1$. Throughout, we will interchangeably use $\{\sigma_1, \sigma_2, \sigma_3\}$, $\{\sigma_x, \sigma_y, \sigma_z\}$, and $\{X, Y, Z\}$, respectively, to express the Pauli matrices and operators (where $Y = \mathrm{i}XZ$).

A particularly important set of pure qubit states are the six $+1$ eigenstates of $\{\pm X, \pm Y, \pm Z\}$, according to[9]

$$\pm X|\pm\rangle = |\pm\rangle \ , \quad (-1)^k Z|k\rangle = |k\rangle \ , \tag{1.27}$$

9) For a definition of stabilizers, see the discussion and the box in Section 1.9.

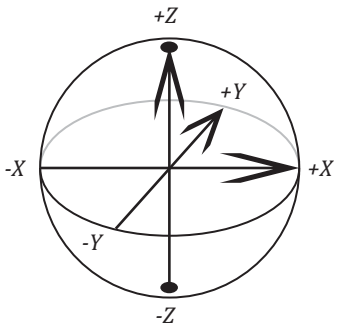

Figure 1.2 The qubit Bloch sphere. There are six $+1$ eigenstates of the Pauli operators $\{\pm X, \pm Y, \pm Z\}$ corresponding to three pairs of basis vectors on opposite sides of the Bloch sphere.

and $\pm Y(|0\rangle \pm \mathrm{i}|1\rangle)/\sqrt{2} = (|0\rangle \pm \mathrm{i}|1\rangle)/\sqrt{2}$, with $k = 0, 1$ and $|\pm\rangle \equiv (|0\rangle \pm |1\rangle)/\sqrt{2}$. These are the so-called *stabilizer* states for one qubit, where each pair represents a basis situated on opposite sides of the Bloch sphere (see Figure 1.2). Typically, the Z eigenstates are chosen to be the computational basis, while the X eigenstates are then obtained through Hadamard transformation, $H|k\rangle = (|0\rangle + (-1)^k|1\rangle)/\sqrt{2}$.

1.2.2 Qumode

A natural way to encode quantum information is in terms of quantized harmonic oscillators. In general, we shall refer to these quantum objects as qumodes. In this case, the Hilbert space vectors live in an infinite-dimensional Hilbert space. The observables are Hermitian operators with a discrete, countable or a continuous spectrum such as occupation number or amplitude and phase of the oscillator, respectively. These mathematical notions have their physical interpretation in the complementary particle and wave properties of a quantum oscillator.

The well-known Hamiltonian of a single qumode is $\hbar\omega(\hat{n}+1/2)$, with the Hermitian occupation number operator $\hat{n} \equiv \hat{a}^\dagger\hat{a}$. The eigenstates of the number operator are the number states $|n\rangle$,

$$\hat{n}|n\rangle = n|n\rangle \ , \tag{1.28}$$

where $n = 0, 1, 2, \ldots, \infty$ is the occupation or excitation number of the oscillator. The ground state of the oscillator is defined by

$$\hat{a}|0\rangle = 0 \ . \tag{1.29}$$

The energy $\hbar\omega/2$ corresponds to the ground-state or zero-point energy which is still present when the qumode has an excitation number zero.

The non-Hermitian operators $\hat{a}$ and $\hat{a}^\dagger$ are the lowering and raising operators, respectively,

$$\hat{a}|n\rangle = \sqrt{n}|n-1\rangle \ , \qquad \hat{a}^\dagger|n\rangle = \sqrt{n+1}|n+1\rangle \ . \tag{1.30}$$

By successive application of the raising operator, all number states can be obtained from the ground state,

$$|n\rangle = \frac{\left(\hat{a}^\dagger\right)^n}{\sqrt{n!}}|0\rangle \ . \tag{1.31}$$

The number states form an orthonormal,[10)]

$$\langle n|m\rangle = \delta_{nm} \ , \tag{1.32}$$

and complete basis,

$$\sum_{n=0}^{\infty} |n\rangle\langle n| = \mathbb{1} \ . \tag{1.33}$$

The Hamiltonian of a single qumode, $\hat{H} = \hbar\omega(\hat{a}^\dagger\hat{a} + 1/2)$, may be rewritten as,

$$\hat{H} = \frac{1}{2}\left(\hat{p}^2 + \omega^2\hat{x}^2\right), \tag{1.34}$$

with

$$\hat{a} = \frac{1}{\sqrt{2\hbar\omega}}\left(\omega\hat{x} + \mathrm{i}\hat{p}\right), \quad \hat{a}^\dagger = \frac{1}{\sqrt{2\hbar\omega}}\left(\omega\hat{x} - \mathrm{i}\hat{p}\right) \ , \tag{1.35}$$

or, conversely,

$$\hat{x} = \sqrt{\frac{\hbar}{2\omega}}\left(\hat{a} + \hat{a}^\dagger\right), \quad \hat{p} = -\mathrm{i}\sqrt{\frac{\hbar\omega}{2}}\left(\hat{a} - \hat{a}^\dagger\right) \ , \tag{1.36}$$

using the well-known commutation relation for "position" and "momentum",

$$[\hat{x}, \hat{p}] = \mathrm{i}\hbar \ . \tag{1.37}$$

These Hermitian operators are the position and momentum operators of an oscillator with unit mass. The lowering and raising operators satisfy the commutator $[\hat{a}, \hat{a}^\dagger] = 1$. In Eq. (1.35), we see that up to some dimensional factors, the position and momentum operators are the Hermitian real and imaginary parts of the lowering operator. It is then convenient to define the *dimensionless* pair of conjugate quantum variables,

$$\hat{X} \equiv \sqrt{\frac{\omega}{2\hbar}}\hat{x} = \mathrm{Re}\hat{a} \ , \qquad \hat{P} \equiv \frac{1}{\sqrt{2\hbar\omega}}\hat{p} = \mathrm{Im}\hat{a} \ . \tag{1.38}$$

Their commutation relation is given by

$$[\hat{X}, \hat{P}] = \frac{\mathrm{i}}{2} \ . \tag{1.39}$$

10) The proper normalization is ensured by the prefactors in Eq. (1.30).

In other words, the dimensionless "position" and "momentum" operators, $\hat{X}$ and $\hat{P}$, are defined as if we set $\hbar = 1/2$. Considering a classical oscillator, they would correspond to the real and imaginary parts of the oscillator's complex amplitude. Throughout the text, we use $\hat{x} \equiv \hat{X}$ and $\hat{p} \equiv \hat{P}$ to express the dimensionless position and momentum operators so that $\hat{a} = \hat{x} + \mathrm{i}\hat{p}$.

The Heisenberg uncertainty relation for the variances of two non-commuting observables $\hat{A}$ and $\hat{B}$ in a given quantum state,

$$\begin{aligned} \langle(\Delta\hat{A})^2\rangle &\equiv \langle(\hat{A} - \langle\hat{A}\rangle)^2\rangle = \langle\hat{A}^2\rangle - \langle\hat{A}\rangle^2 \,, \\ \langle(\Delta\hat{B})^2\rangle &\equiv \langle(\hat{B} - \langle\hat{B}\rangle)^2\rangle = \langle\hat{B}^2\rangle - \langle\hat{B}\rangle^2 \,, \end{aligned} \tag{1.40}$$

becomes

$$\langle(\Delta\hat{A})^2\rangle\langle(\Delta\hat{B})^2\rangle \geq \frac{1}{4}|\langle[\hat{A}, \hat{B}]\rangle|^2 \,. \tag{1.41}$$

Inserting Eq. (1.39) into Eq. (1.41) gives the uncertainty relation for a pair of conjugate phase-space variables of a single qumode,

$$\hat{x} = (\hat{a} + \hat{a}^\dagger)/2 \,, \qquad \hat{p} = (\hat{a} - \hat{a}^\dagger)/2\mathrm{i} \,, \tag{1.42}$$

namely,

$$\langle(\Delta\hat{x})^2\rangle\langle(\Delta\hat{p})^2\rangle \geq \frac{1}{4}|\langle[\hat{x}, \hat{p}]\rangle|^2 = \frac{1}{16} \,. \tag{1.43}$$

A single qumode has position and momentum eigenstates,

$$\hat{x}|x\rangle = x|x\rangle \,, \qquad \hat{p}|p\rangle = p|p\rangle \,. \tag{1.44}$$

These are orthogonal,

$$\langle x|x'\rangle = \delta(x - x') \,, \qquad \langle p|p'\rangle = \delta(p - p') \,, \tag{1.45}$$

and complete,

$$\int_{-\infty}^{\infty} |x\rangle\langle x|\mathrm{d}x = \mathbb{1} \,, \qquad \int_{-\infty}^{\infty} |p\rangle\langle p|\mathrm{d}p = \mathbb{1} \,, \tag{1.46}$$

and they would correspond to lines in phase space, as shown in Figure 1.3.

As it is well-known from quantum mechanics, the position and momentum eigenstates are related to each other by the Fourier transformation,

$$|x\rangle = \frac{1}{\sqrt{\pi}} \int_{-\infty}^{\infty} \mathrm{e}^{-2\mathrm{i}xp}|p\rangle\mathrm{d}p \,, \qquad |p\rangle = \frac{1}{\sqrt{\pi}} \int_{-\infty}^{\infty} \mathrm{e}^{+2\mathrm{i}xp}|x\rangle\mathrm{d}x \,. \tag{1.47}$$

The Fourier transformation of a qumode is the analogue of the discrete Hadamard gate for a qubit mentioned in the preceding section (see Figure 1.4). Similarly, $|x\rangle$

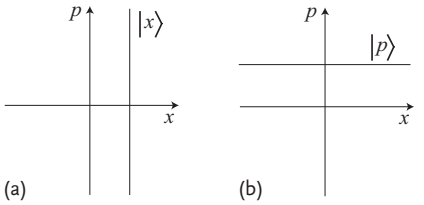

Figure 1.3 *Z* and *X* stabilizer states of a qumode in phase space. (a) Computational position basis, (b) conjugate momentum basis.

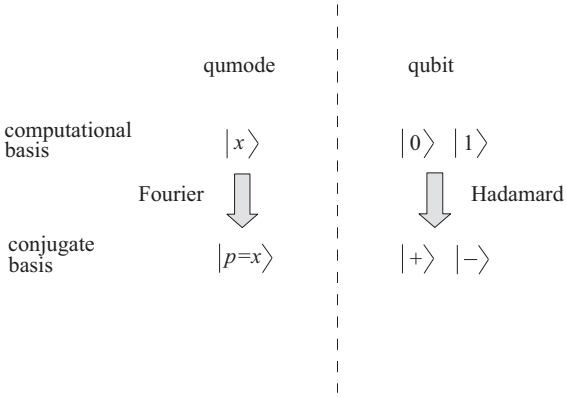

Figure 1.4 Basis state transformations for a qumode and a qubit. $|\pm\rangle = (|0\rangle \pm |1\rangle)/\sqrt{2}$.

and $|p\rangle$ play the roles of the computational and the conjugate basis, respectively, like $\{|0\rangle, |1\rangle\}$ and $\{|+\rangle, |-\rangle\}$ in the qubit case. They are the eigenstates of the Weyl–Heisenberg (WH) operators,

$$X(s) \equiv \mathrm{e}^{-2\mathrm{i}s\hat{p}}\,, \qquad Z(s) \equiv \mathrm{e}^{+2\mathrm{i}s\hat{x}}\,, \tag{1.48}$$

with

$$\mathrm{e}^{+2\mathrm{i}sp}\,X(s)|p\rangle = |p\rangle\,, \qquad \mathrm{e}^{-2\mathrm{i}sx}\,Z(s)|x\rangle = |x\rangle\,, \tag{1.49}$$

similar to Eq. (1.27) for a single qubit. The position and momentum states, being the above $+1$ WH eigenstates, are among the stabilizer states[11] for a single qumode. A more general set of stabilizer states would include rotated position or momentum eigenstates. For instance, the rotated p-momentum states are $+1$ eigenstates of

$$\mathrm{e}^{+2\mathrm{i}sp-\mathrm{i}s^2\cos\theta\,\sin\theta}\,X(s\cos\theta)Z(-s\sin\theta) \equiv g_p^{(\theta)}(s)\,, \tag{1.50}$$

with a "clockwise" rotation angle θ. In particular, by using our convention, for $\theta = -\pi/2$, we recover the stabilizer of the position states (here with eigenvalue

11) For a definition of stabilizers, see the discussion and the box in Section 1.9.

$-p$) corresponding to a Fourier transformation of the p-momentum states. We shall get back to these qumode stabilizers later in various contexts such as unitaries on qumodes and optical Gaussian states of one or more qumodes.

A general pure qumode state $|\psi\rangle$ can be expanded in the position basis,

$$|\psi\rangle = \int \mathrm{d}x |x\rangle\langle x|\psi\rangle = \int \mathrm{d}x\, \psi(x)|x\rangle \,, \tag{1.51}$$

where $\langle x|\psi\rangle = \psi(x)$ is the position wave function. Any mixed state may be written as

$$\hat{\rho} = \int f(s,t)\, X(s) Z(t) \mathrm{d}s\, \mathrm{d}t \,, \tag{1.52}$$

with a complex function $f(s,t)$. In quantum optics, this would correspond to a phase-space expansion in terms of the quantum optical displacement operator.

Encoding quantum information

⊙ **Qubit:**
arbitrary pure states:

$$|\psi_{\theta,\phi}\rangle = \cos(\theta/2)|0\rangle + \sin(\theta/2)\mathrm{e}^{\mathrm{i}\phi}|1\rangle$$

arbitrary mixed states:

$$\hat{\rho} = \frac{1}{2}(\mathbb{1} + \boldsymbol{s}\cdot\boldsymbol{\sigma}) \,, \quad \boldsymbol{\sigma} = (\sigma_1, \sigma_2, \sigma_3)^{\mathrm{T}} \,, \quad |\boldsymbol{s}| \leq 1$$

stabilizer states as $+1$ eigenstates of $\{\pm X \equiv \pm\sigma_1, \pm Y \equiv \pm\sigma_2, \pm Z \equiv \pm\sigma_3\}$:

$$\begin{aligned} \pm X(|0\rangle \pm |1\rangle)/\sqrt{2} &= (|0\rangle \pm |1\rangle)/\sqrt{2} \\ \pm Y(|0\rangle \pm \mathrm{i}|1\rangle)/\sqrt{2} &= (|0\rangle \pm \mathrm{i}|1\rangle)/\sqrt{2} \\ +Z|0\rangle = |0\rangle \,, &\quad -Z|1\rangle = |1\rangle \end{aligned}$$

with qubit Pauli operators X, Y, Z

〰 **Qumode:**
arbitrary pure states:

$$|\psi\rangle = \int \mathrm{d}x\, \psi(x)|x\rangle$$

arbitrary mixed states:

$$\hat{\rho} = \int \mathrm{d}s\, \mathrm{d}t\, f(s,t) X(s) Z(t)$$

stabilizer states as $+1$ eigenstates of $\{\mathrm{e}^{+2\mathrm{i}sp} X(s), \mathrm{e}^{-2\mathrm{i}sx} Z(s)\}$:

$$\begin{aligned} \mathrm{e}^{+2\mathrm{i}sp} X(s)|p\rangle &= |p\rangle \\ \mathrm{e}^{-2\mathrm{i}sx} Z(s)|x\rangle &= |x\rangle \end{aligned}$$

with qumode Weyl–Heisenberg operators $X(s) = \mathrm{e}^{-2\mathrm{i}s\hat{p}}$ and $Z(s) = \mathrm{e}^{+2\mathrm{i}s\hat{x}}$

A general physical operation on a density operator can be non-unitary, including irreversible channels and measurements. However, reversibly mapping a normalized density operator onto another normalized density operator is described by unitaries which we briefly discuss in the following section.

1.3 Unitaries

Unitary transformations (unitaries) represented by unitary operators $\hat{U}$, with $\hat{U}^\dagger \hat{U} = \hat{U}\hat{U}^\dagger = \mathbb{1}$, preserve the norms and overlaps of states. However, this trace-preserving property is not the most distinct feature of unitaries. Rather, it is reversibility.[12] By acting on Hilbert space vectors, unitaries are used in order to access any other vector in the same Hilbert space; an important tool for quantum computation.[13]

As it is well-known from standard quantum mechanics, the unitary evolution of a quantum system can be described in the Schrödinger as well as the Heisenberg representation. Assume the pure state $|\psi(t_0)\rangle$ is prepared at time t_0. The unitarily evolved state at time $t > t_0$ can then be written in the Schrödinger representation as

$$|\psi(t)\rangle = \hat{U}(t, t_0)|\psi(t_0)\rangle \; . \tag{1.53}$$

For a closed system where the Hamiltonian is time independent, $\partial \hat{H}/\partial t = 0$, the unitary operator $\hat{U}(t, t_0)$ takes on the simple form

$$\hat{U}(t, t_0) = \exp\left[-\frac{\mathrm{i}}{\hbar}\hat{H}(t - t_0)\right] \; . \tag{1.54}$$

The unitary evolution of a mixed state is easily found to be

$$\hat{\rho}(t) = \hat{U}(t, t_0)\hat{\rho}(t_0)\,\hat{U}^\dagger(t, t_0) \; , \tag{1.55}$$

using Eq. (1.18).

In the Heisenberg representation, the initial states remain unchanged during the evolution, $|\psi_{\mathrm{H}}(t)\rangle \equiv |\psi_{\mathrm{H}}\rangle = |\psi(t_0)\rangle$. It follows $|\psi_{\mathrm{H}}\rangle = \hat{U}^\dagger(t, t_0)|\psi(t)\rangle$. Equivalence of the expectation values in both representations means

$$\begin{aligned} \langle\psi_{\mathrm{H}}|\hat{M}_{\mathrm{H}}(t)|\psi_{\mathrm{H}}\rangle &= \langle\psi(t)|\,\hat{U}(t, t_0)\,\hat{U}^\dagger(t, t_0)\,\hat{M}\,\hat{U}(t, t_0)\,\hat{U}^\dagger(t, t_0)|\psi(t)\rangle \\ &= \langle\psi(t)|\hat{M}|\psi(t)\rangle \; , \end{aligned} \tag{1.56}$$

for arbitrary $|\psi_{\mathrm{H}}\rangle$. Thus, we obtain

$$\hat{M}_{\mathrm{H}}(t) = \hat{U}^\dagger(t, t_0)\,\hat{M}\,\hat{U}(t, t_0) \; . \tag{1.57}$$

12) Which refers to physical reversibility; a notion stronger than just mathematical invertibility.

13) Later, however, we shall describe the one-way model of quantum computation which achieves this universal accessibility of quantum states in an irreversible fashion through measurements on an entangled resource state.

This corresponds to the equation of motion

$$\frac{\mathrm{d}}{\mathrm{d}t}\hat{M}_{\mathrm{H}}(t) = \frac{1}{\mathrm{i}\hbar}\,\hat{U}^{\dagger}[\hat{M},\hat{H}]\,\hat{U} + \hat{U}^{\dagger}\frac{\partial\hat{M}}{\partial t}\,\hat{U}\,, \tag{1.58}$$

or

$$\mathrm{i}\hbar\frac{\mathrm{d}}{\mathrm{d}t}\hat{M}_{\mathrm{H}}(t) = \left[\hat{M}_{\mathrm{H}},\hat{H}_{\mathrm{H}}\right] + \mathrm{i}\hbar\frac{\partial\hat{M}_{\mathrm{H}}}{\partial t}\,. \tag{1.59}$$

Therefore, the action of an arbitrary unitary operator $\hat{U}$ is described by either $\hat{M} \to \hat{U}^{\dagger}\hat{M}\,\hat{U}$ (Heisenberg) or $\hat{\rho} \to \hat{U}\hat{\rho}\,\hat{U}^{\dagger}$ (Schrödinger). Here, we dropped the time dependence, focusing on an input–output relation between states or observables.

1.3.1 Qubit

Consider a single qubit. According to the Bloch sphere representation in Figure 1.2, it is convenient to think of single-qubit unitaries as rotations. In particular, finite rotations around the coordinate axes are expressed by

$$\hat{R}_{\boldsymbol{s}}(\theta) = \mathrm{e}^{-\mathrm{i}\theta\,\boldsymbol{s}\cdot\boldsymbol{\sigma}/2} = \cos(\theta/2)\mathbb{1} - \mathrm{i}\sin(\theta/2)\boldsymbol{s}\cdot\boldsymbol{\sigma}\,, \tag{1.60}$$

again with $\boldsymbol{\sigma} = (\sigma_1,\sigma_2,\sigma_3)^{\mathrm{T}}$ for the Pauli operators $\{\sigma_1,\sigma_2,\sigma_3\} \equiv \{X,Y,Z\}$ and the real unit vector $\boldsymbol{s}$ (thus, strictly $|\boldsymbol{s}| = 1$), using $(\boldsymbol{s}\cdot\boldsymbol{\sigma})^2 = \mathbb{1}$. For example, a rotation around the Z-axis corresponds to $\hat{R}_{(0,0,1)}(\theta) \equiv \hat{R}_Z(\theta) = \mathrm{e}^{-\mathrm{i}\theta Z/2} \equiv Z_\theta$. In the Heisenberg representation, it becomes clear that the rotation takes place in the XY-plane,

$$\begin{aligned} Z_\theta^{\dagger}\,X\,Z_\theta &= Z_{-\theta}\,X\,Z_\theta = X\cos\theta - Y\sin\theta\,,\\ Z_\theta^{\dagger}\,Y\,Z_\theta &= Z_{-\theta}\,Y\,Z_\theta = X\sin\theta + Y\cos\theta\,,\\ Z_\theta^{\dagger}\,Z\,Z_\theta &= Z_{-\theta}\,Z\,Z_\theta = Z\,. \end{aligned} \tag{1.61}$$

Another thing becomes apparent here. Two different, though discrete choices of the rotation angle, for instance, $\theta = \pi/2$ and $\theta = \pi/4$, lead to very distinct output operators: while $\theta = \pi/2$ transforms the Pauli operators into Pauli operators, the choice of $\theta = \pi/4$ results in linear combinations of Pauli operators.

The set of single-qubit unitaries that transform Pauli operators into Pauli operators,

$$\left\{\hat{U}\,|\,\hat{U}^{\dagger}\sigma_k\,\hat{U} = \pm\sigma_l\right\}, \tag{1.62}$$

forms a group, the so-called *Clifford* group. Clifford group elements map stabilizer states $|S\rangle$ onto stabilizer states $|S'\rangle$.[14] Assume $g, g' \in \{\pm X, \pm Y, \pm Z\}$ such that

14) The corresponding stabilizer group S is an abelian subgroup of the one-qubit Pauli group, $\{\pm\mathbb{1}, \pm i\mathbb{1}, \pm X, \pm iX, \pm Y, \pm iY, \pm Z, \pm iZ\}$. The prefactors $(\pm i)$ which ensure that the Pauli group is closed under multiplication are not important for our purposes and will be omitted throughout. For a detailed definition of stabilizers see Section 1.9.

$g|S\rangle = |S\rangle$ and $g'|S'\rangle = |S'\rangle$. Then, we obtain the Clifford transformed state

$$\hat{U}|S\rangle = \hat{U}g|S\rangle = \hat{U}g\hat{U}^\dagger\hat{U}|S\rangle = \hat{U}g\hat{U}^\dagger|S'\rangle = g'|S'\rangle \,. \tag{1.63}$$

Thus, the inverse Heisenberg evolution of the corresponding single-qubit stabilizer, $g \in \{\pm X, \pm Y, \pm Z\} \to g' = \hat{U}g\hat{U}^\dagger \in \{\pm X, \pm Y, \pm Z\}$, completely determines the resulting state $|S'\rangle$. For example,

$$Z_{\pi/2}|+\rangle = \left(\mathrm{e}^{-\mathrm{i}\pi/4}|0\rangle + \mathrm{e}^{+\mathrm{i}\pi/4}|1\rangle\right)/\sqrt{2} = \mathrm{e}^{-\mathrm{i}\pi/4}(|0\rangle + \mathrm{i}|1\rangle)/\sqrt{2} \,, \tag{1.64}$$

corresponds to

$$X \to Z_{\pi/2} X Z_{-\pi/2} = Y \,, \tag{1.65}$$

up to an irrelevant phase factor. The distinction between Clifford unitaries and non-Clifford unitaries will be important regarding universality and nonclassical speed-up in quantum computation (see Section 1.8).

1.3.2 Qumode

Now, consider a single qumode. In this case, the free evolution of the oscillator is a rotation in phase space. Using the input–output formalism, such a phase rotation of a single qumode with annihilation operator $\hat{a}$ can be expressed by

$$\hat{a} \to \hat{R}^\dagger(\theta)\hat{a}\hat{R}(\theta) = \hat{a}\mathrm{e}^{-\mathrm{i}\theta} \,, \tag{1.66}$$

with

$$\hat{R}(\theta) = \exp\left(-\mathrm{i}\theta\,\hat{a}^\dagger\hat{a}\right). \tag{1.67}$$

In terms of the position and momentum operators (recall that $\hat{a} = \hat{x} + \mathrm{i}\hat{p}$), we obtain

$$\begin{aligned} \hat{R}^\dagger(\theta)\hat{x}\hat{R}(\theta) &= \hat{x}\cos\theta + \hat{p}\sin\theta \,, \\ \hat{R}^\dagger(\theta)\hat{p}\hat{R}(\theta) &= -\hat{x}\sin\theta + \hat{p}\cos\theta \,. \end{aligned} \tag{1.68}$$

In this case, the resulting operators are always linear combinations of the input operators for any choice of θ. The phase-rotation unitary is an element of the Clifford group which, for qumodes, may be defined similar to the qubit case as

$$\left\{\hat{U}\,|\,\hat{U}^\dagger X_k(s)\,\hat{U} \propto X_l(s)\right\}. \tag{1.69}$$

In this case, $X_k(s)$ and $X_l(s)$ stand for products of WH operators, that is, products of elements of the WH group. Thus, the Clifford single-qumode unitaries transform WH operators into products of WH operators. In terms of the WH group generators, that is, the momentum and position operators, Clifford transformations

always lead to linear combinations of the generators. Non-Clifford transformations result in nonlinear combinations of $\hat{x}$ and $\hat{p}$.

We observe that general single-qubit rotations on the Bloch sphere do contain non-Clifford elements, whereas single-qumode rotations in phase space do not.[15] In the qubit case, the rotation angle determines whether a unitary is Clifford or not. For qumodes, the Clifford or non-Clifford character of a unitary $\hat{U}$ depends on the order of the Hamiltonian that generates $\hat{U}$. We shall return to this discussion later.

The above discussion on transforming stabilizer states through Clifford unitaries applies as well to qumodes. Stabilizer states $|S\rangle$ are then mapped onto stabilizer states $|S'\rangle$. The stabilizers this time, represented by $g(s)$ and $g'(s)$, are products of WH operators. Again, the inverse Heisenberg evolution of the corresponding single-qumode stabilizer, $g(s) \to g'(s) = \hat{U} g(s) \hat{U}^\dagger$, completely determines the resulting state $|S'\rangle$. For example, the Fourier transform of a p-momentum eigenstate, with $\hat{F} \equiv \hat{R}(-\pi/2)$ in our convention, leads to an x-position eigenstate with eigenvalue $-p$, $\hat{F}|p\rangle = |x = -p\rangle$. This corresponds to

$$\mathrm{e}^{+2\mathrm{i}sp} X(s) \to \mathrm{e}^{+2\mathrm{i}sp} \hat{F} X(s) \hat{F}^\dagger = \mathrm{e}^{+2\mathrm{i}sp} Z(s) \,, \tag{1.70}$$

using $\hat{F} \hat{p} \hat{F}^\dagger = -\hat{x}$. More generally, an arbitrary rotation $\hat{R}(\theta)$ acting, for instance, on a p-momentum eigenstate, gives the state $\hat{R}(\theta)|p\rangle$ which is stabilized by

$$\begin{aligned} \hat{R}(\theta) \mathrm{e}^{+2\mathrm{i}sp} X(s) \hat{R}^\dagger(\theta) &= \mathrm{e}^{+2\mathrm{i}sp} \mathrm{e}^{-2\mathrm{i}s\left(\hat{p}\cos\theta + \hat{x}\sin\theta\right)} \\ &= \mathrm{e}^{+2\mathrm{i}sp} \mathrm{e}^{-2\mathrm{i}s\hat{p}\cos\theta} \mathrm{e}^{-2\mathrm{i}s\hat{x}\sin\theta} \mathrm{e}^{-2[\mathrm{i}s\hat{p}\cos\theta, \mathrm{i}s\hat{x}\sin\theta]} \\ &= g_p^{(\theta)}(s) \,, \end{aligned} \tag{1.71}$$

as defined earlier in Eq. (1.50). Here, we used the well-known Baker–Campbell–Hausdorff formula, $\mathrm{e}^{\hat{A}+\hat{B}} = \mathrm{e}^{\hat{A}} \mathrm{e}^{\hat{B}} \mathrm{e}^{-[\hat{A},\hat{B}]/2}$ for $[\hat{A}, [\hat{A}, \hat{B}]] = 0$, and so on, and the input–output relations in Eq. (1.68). General single-qumode Clifford unitaries also include squeezers beside the phase rotations. Squeezing applied to an unphysical, qumode stabilizer state corresponds to a rescaling of the eigenvalue. For instance, for a squeezing operation $\hat{S}(-r)$ acting on a p-momentum eigenstate, we obtain the new stabilizer

$$\hat{S}(-r) \mathrm{e}^{+2\mathrm{i}sp} X(s) \hat{S}^\dagger(-r) = \mathrm{e}^{+2\mathrm{i}sp} X(s\mathrm{e}^{+r}) \,, \tag{1.72}$$

using $\hat{S}(-r) \hat{p} \hat{S}^\dagger(-r) = \mathrm{e}^{+r} \hat{p}$ [see Eq. (2.52) through Eq. (2.56)]. Therefore, the new stabilizer state is $|\mathrm{e}^{-r} p\rangle$ since we have $\mathrm{e}^{+2\mathrm{i}sp} X(s\mathrm{e}^{+r}) |\mathrm{e}^{-r} p\rangle = |\mathrm{e}^{-r} p\rangle$.

15) This is a first hint that single-qubit non-Clifford unitaries might be optically easy to implement, while those for a single qumode are hard to realize. This is, however, compensated by the complication of making two photons interact for a two-qubit entangling gate, whereas entangling two qumodes is relatively easy. The next chapter will provide additional details on this issue.

Reversible quantum operations

state $\hat{\rho} \to \hat{U}\hat{\rho}\hat{U}^\dagger$ (Schrödinger), observable $\hat{M} \to \hat{U}^\dagger \hat{M}\,\hat{U}$ (Heisenberg)

$$\langle \hat{M} \rangle = \mathrm{Tr}(\hat{\rho}\hat{M}) \to \mathrm{Tr}[(\hat{U}\hat{\rho}\hat{U}^\dagger)\hat{M}] = \mathrm{Tr}[\hat{\rho}(\hat{U}^\dagger \hat{M}\,\hat{U})] \quad \text{and}$$
$$\hat{U}\hat{U}^\dagger = \hat{U}^\dagger\hat{U} = \mathbb{1}$$

⊙ **Qubit:** arbitrary unitaries:

$$\mathrm{e}^{\mathrm{i}\phi}\,\hat{R}_s(\theta) = \mathrm{e}^{\mathrm{i}\phi}\mathrm{e}^{-\mathrm{i}\theta\, \boldsymbol{s}\cdot\boldsymbol{\sigma}/2} = \mathrm{e}^{\mathrm{i}\phi}\left[\cos(\theta/2)\mathbb{1} - \mathrm{i}\sin(\theta/2)\boldsymbol{s}\cdot\boldsymbol{\sigma}\right], \quad |\boldsymbol{s}| = 1$$

with $\boldsymbol{\sigma} = (\sigma_1, \sigma_2, \sigma_3)^{\mathrm{T}}$ and the Pauli operators $\{X \equiv \sigma_1, Y \equiv \sigma_2, Z \equiv \sigma_3\}$

Clifford unitaries:

$$g \in \{\pm X, \pm Y, \pm Z\} \to g' = \hat{U} g \hat{U}^\dagger \in \{\pm X, \pm Y, \pm Z\}$$

with $g|S\rangle = |S\rangle$ and $g'|S'\rangle = |S'\rangle$ for qubit stabilizer states $|S\rangle$, $|S'\rangle = \hat{U}|S\rangle$

∼∼∼ **Qumode:** arbitrary unitaries:

$$\hat{U} = \mathrm{e}^{-\mathrm{i}t\,H(\hat{a},\hat{a}^\dagger)},\ H(\hat{a},\hat{a}^\dagger) \quad \text{is arbitrary Hamiltonian ,}$$
$$\hat{a} \to \hat{U}^\dagger \hat{a}\,\hat{U} \quad \text{is nonlinear transformation}$$

Clifford unitaries:

$$\left\{\hat{U}\,|\,\hat{U}^\dagger X_k(s)\,\hat{U} \propto X_l(s)\right\}$$

with $X_k(s)$ and $X_l(s)$ products of WH operators and

$$\hat{U} = \mathrm{e}^{-\mathrm{i}t\,H(\hat{a},\hat{a}^\dagger)},\ H(\hat{a},\hat{a}^\dagger) \quad \text{is quadratic Hamiltonian ,}$$
$$\hat{a} \to \hat{U}^\dagger \hat{a}\,\hat{U} \quad \text{is linear transformation}$$

The qumode Clifford unitaries, combining squeezing, rotations, and displacements, are useful for defining a universal gate set (see later in Section 1.8).

Squeezing itself will become an important tool when we discuss physical qumode stabilizer states, that is, Gaussian states, in the next chapter. While any qumode Clifford unitary can be generated by a Hamiltonian which is a quadratic polynomial of $\hat{x}$, $\hat{p}$ or $\hat{a}$, $\hat{a}^\dagger$, a general qumode unitary requires a Hamiltonian of sufficiently high order. An at least cubic Hamiltonian suffices to realize arbitrary qumode unitaries asymptotically (see Section 1.8).

In the next section, we will discuss quantum operations which do not belong to the class of unitaries. These are the irreversible channels and measurements.

1.4 Non-unitaries

A physical, generally non-unitary quantum operation corresponds to a linear map between density operators, $\hat{\rho} \to \hat{\rho}' = \mathcal{E}(\hat{\rho})$.

For this linear map to be physical, it must satisfy the mathematical notion of *complete positivity*. Such a completely positive (CP) map can always be written in the form of an operator sum,

$$\mathcal{E}(\hat{\rho}) = \sum_k \hat{A}_k \hat{\rho} \hat{A}_k^\dagger \,. \tag{1.73}$$

The sum may be finite or go to infinity and the summation over k may also be replaced by an integral. The operators $\hat{A}_k$ are usually referred to as Kraus operators. When the corresponding set of positive operators $\hat{A}_k^\dagger \hat{A}_k$ sums up to the identity, $\sum_k \hat{A}_k^\dagger \hat{A}_k = \mathbb{1}$, we have a CP trace-preserving (CPTP) map. Otherwise, when $\sum_k \hat{A}_k^\dagger \hat{A}_k < \mathbb{1}$, the CP map is trace-decreasing (CPTD).

This distinction leads to an output density operator which is either normalized or not. In the former case, the corresponding CPTP map describes an, in general, irreversible channel. The case of an unnormalized output after a CPTD map represents situations where information is gained through measurements and hence a certain output state is only obtained with non-unit probability. The following two sections are devoted to this distinction of channels and measurements. In the next section, we will also explain the important difference between positivity and complete positivity.

1.4.1 Channels

Consider a signal system A in a state $\hat{\rho}_\mathrm{A}$. Now, suppose the signal interacts with an ancilla system B in a state $\hat{\rho}_\mathrm{B}$ through a global unitary $\hat{U}_\mathrm{AB}$ (see Figure 1.5). When the ancilla is traced over, the effect of this transformation on the signal is described by

$$\begin{aligned}
\hat{\rho}_\mathrm{A} \to \hat{\rho}'_\mathrm{A} &= \mathrm{Tr}_\mathrm{B}\left[\hat{U}_\mathrm{AB}\,(\hat{\rho}_\mathrm{A} \otimes \hat{\rho}_\mathrm{B})\,\hat{U}_\mathrm{AB}^\dagger\right] \\
&= \sum_k {}_\mathrm{B}\langle k|\,\hat{U}_\mathrm{AB}\left[\hat{\rho}_\mathrm{A} \otimes \left(\sum_l \rho_l |l\rangle_\mathrm{B}\langle l|\right)\right]\hat{U}_\mathrm{AB}^\dagger |k\rangle_\mathrm{B} \\
&= \sum_{k,l} \left({}_\mathrm{B}\langle k|\sqrt{\rho_l}\,\hat{U}_\mathrm{AB}|l\rangle_\mathrm{B}\right)\hat{\rho}_\mathrm{A}\left({}_\mathrm{B}\langle l|\sqrt{\rho_l}\,\hat{U}_\mathrm{AB}^\dagger|k\rangle_\mathrm{B}\right) \\
&\equiv \sum_{k,l} \hat{A}_{kl}\hat{\rho}_\mathrm{A}\hat{A}_{kl}^\dagger = \mathcal{E}(\hat{\rho}_\mathrm{A})\,,
\end{aligned} \tag{1.74}$$

where we used a diagonal basis $\{|l\rangle_\mathrm{B}\}$ to express $\hat{\rho}_\mathrm{B}$ and to trace over B. Note that $\hat{A}_{kl}$ is an operator in the Hilbert space of the signal A. For the simple case of an

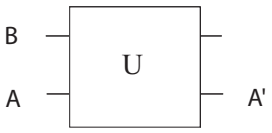

Figure 1.5 A signal system A in an initial state labeled by A interacts with an ancilla system B in an initial state labeled by B through a global unitary U. The resulting signal state is labeled by A′ after tracing over system B.

ancilla starting in the state $\hat{\rho}_{\rm B} = |0\rangle_{\rm B}\langle 0|$, that is, $\rho_k = \delta_{k0}$, we obtain the operator sum in Eq. (1.73) with $\hat{A}_k \equiv {}_{\rm B}\langle k|\hat{U}_{\rm AB}|0\rangle_{\rm B}$ and the signal density operators $\hat{\rho} \equiv \hat{\rho}_{\rm A}$.[16)]

The *operator sum* or Kraus representation in Eq. (1.73) represents a CPTP map. The TP property is easily confirmed through

$$\begin{aligned} {\rm Tr}\mathcal{E}(\hat{\rho}) &= {\rm Tr}\left(\sum_k \hat{A}_k\hat{\rho}\hat{A}_k^\dagger\right) = \sum_k {\rm Tr}\left(\hat{A}_k^\dagger\hat{A}_k\hat{\rho}\right) \\ &= {\rm Tr}\left[\left(\sum_k \hat{A}_k^\dagger\hat{A}_k\right)\hat{\rho}\right] = 1\,, \end{aligned} \tag{1.75}$$

provided that $\sum_k \hat{A}_k^\dagger\hat{A}_k = \mathbb{1}$ holds. In the first line of Eq. (1.75), we used the invariance property of the trace operation under cyclic permutations. In order to see that $\sum_k \hat{A}_k^\dagger\hat{A}_k = \mathbb{1}$ is not only sufficient, but also necessary for the TP property of $\mathcal{E}$, note that the last line in Eq. (1.75) must be satisfied for *any* normalized state $\hat{\rho}$.

Let us now explain the CP property of the map $\mathcal{E}$. Clearly, for the output density operator to represent a physical state we need $\mathcal{E}(\hat{\rho}) \geq 0$. However, there are operations that do satisfy this positivity constraint, but nonetheless are unphysical.[17)] Hence, a stricter condition is required, assuming that the signal A is part of a larger composite system A and B. In this case, the condition is $\$_\mathcal{E}\,\hat{\rho}_{\rm A} = \hat{\rho}'_{\rm A} \geq 0$ *and* $(\$_\mathcal{E}\otimes\mathbb{1}_{\rm B})\hat{\rho}_{\rm AB} = \hat{\rho}'_{\rm AB} \geq 0$, where $\$_\mathcal{E}$ stands for the (super)operator that affects the map $\mathcal{E}$ on system A.

In conclusion, a map $\mathcal{E}$ that describes a physical operation is CP and linear. Linearity means that $\mathcal{E}[\lambda\hat{\rho}_1 + (1-\lambda)\hat{\rho}_2] = \lambda\mathcal{E}(\hat{\rho}_1) + (1-\lambda)\mathcal{E}(\hat{\rho}_2)$. Whenever the ancilla system B in Figure 1.5 is assumed to be inaccessible such that no information can be gained from it (for instance, when it represents the uncontrollable environment of the signal A), the trace over B gives a new normalized density operator for A; thus, $\mathcal{E}$ is TP. The situation of an accessible ancilla system B that can be measured and acts as a probe to the signal will be considered in the next section.

We introduced CPTP maps in the Schrödinger representation. Similar to the unitary case, we may also describe the reduced dynamics of the signal system in

16) Note that the operators $\hat{A}_k$ are not unique and can always be transformed into new operators $\hat{A}'_l = \sum_k u_{lk}\hat{A}_k$ with a unitary matrix u such that $\sum_l \hat{A}'_l\hat{\rho}\hat{A}'^\dagger_l = \sum_{lkm} u_{lk}u^*_{lm}\hat{A}_k\hat{\rho}\hat{A}^\dagger_m = \sum_k \hat{A}_k\hat{\rho}\hat{A}^\dagger_k$ since $\sum_l u^*_{lm}u_{lk} = \delta_{mk}$.

17) An example for such an unphysical operation is transposition. It is a positive, but not completely positive TP map. This property turns out to be useful for inseparability checks of bipartite density matrices (see Section 1.5).

the Heisenberg representation,

$$\mathcal{E}^*(\hat{M}) = \sum_k \hat{A}_k^\dagger \hat{M} \hat{A}_k \ , \tag{1.76}$$

where now the *dual map* $\mathcal{E}^*$ is a completely positive unity-preserving (CPUP) map, $\mathcal{E}^*(\mathbb{1}) = \mathbb{1}$, when $\sum_k \hat{A}_k^\dagger \hat{A}_k = \mathbb{1}$, and $\hat{M}$ is an observable. This map is uniquely defined by requiring that the expectation values are independent of the representation, $\langle \hat{M} \rangle = \mathrm{Tr}(\hat{\rho}\hat{M}) \to \mathrm{Tr}[\mathcal{E}(\hat{\rho})\hat{M}] = \mathrm{Tr}[\hat{\rho}\mathcal{E}^*(\hat{M})]$.

In general, the dual map will change the commutators, that is, the algebra is not preserved; a sign for non-unitary evolution. Only for reversible channels, that is, unitaries, the algebra is invariant. For instance, for a single qumode, we have $[\hat{x}, \hat{p}] \to \hat{U}^\dagger[\hat{x}, \hat{p}]\hat{U} = [\hat{U}^\dagger \hat{x} \hat{U}, U^\dagger \hat{p} \hat{U}]$, whereas, in general, $[\hat{x}, \hat{p}] \to \mathcal{E}^*([\hat{x}, \hat{p}]) \neq [\mathcal{E}^*(\hat{x}), \mathcal{E}^*(\hat{p})]$. Similarly, only for unitaries do we have $f(\hat{x}, \hat{p}) \to f(\hat{U}^\dagger \hat{x} \hat{U}, \hat{U}^\dagger \hat{p} \hat{U})$ for arbitrary polynomials $f(\hat{x}, \hat{p})$ (in fact, we used this earlier on). However, under a non-unitary map $\mathcal{E}^*$, in general, $f(\hat{x}, \hat{p})$ evolves into $\mathcal{E}^*(f(\hat{x}, \hat{p})) \neq f(\mathcal{E}^*(\hat{x}), \mathcal{E}^*(\hat{p}))$.[18)]

For a general qubit channel expressed by an operator sum, Eq. (1.73), the Kraus operators can be expanded in terms of the Pauli basis. Thus, we have [5]

$$\hat{A}_k = \alpha_k \mathbb{1} + \beta_k X + \gamma_k Y + \delta_k Z \ . \tag{1.77}$$

Similarly, for a general qumode channel, we can use the WH operators as a complete basis such that [28]

$$\mathcal{E}(\hat{\rho}) = \int \mathrm{d}s\mathrm{d}t\mathrm{d}s'\mathrm{d}t' \, f(s, t, s', t') X(s) Z(t) \hat{\rho} X(-s') Z(-t') \ . \tag{1.78}$$

Finally, we note that also for non-unitary dynamics, similar to the case of reversible, unitary dynamics, we may keep track of the continuous time evolution of the states or observables. Such continuous, non-unitary, mixed-state evolutions are given by the well-known master and Langevin equations, respectively [29].[19)]

18) We should at least mention that those dual maps that map the generators $\hat{x}$ and $\hat{p}$ to linear combinations of $\hat{x}$ and $\hat{p}$ (and WH operators to products of WH operators) correspond to the important Gaussian channels in the Schrödinger representation. These will be discussed later in Chapter 2. This particular case of non-unitary reduced dynamics is a kind of mixed-state extension of the Clifford unitaries that transform stabilizer states into stabilizer states, as presented in the preceding section. A mathematically more rigorous discussion of channels, Schrödinger CPTP maps, and Heisenberg CPUP dual maps and other examples can be found in Chapter II.5 of [6].

19) However, the operator sum representation is in some sense more general, as it even allows one to describe non-Markovian dynamics [5]. The continuous time evolution of the master equation corresponds to the quantum version of a continuous Markov chain while the operator sum is the quantum analogue of a probability map. In particular, for the master equation, the signal A and the ancilla/environment B must not be entangled initially (so-called Markovian approximation). The solution of the master equation can always be written as well as $\hat{\rho}(t) = \sum_k \hat{A}_k(t)\hat{\rho}(0)\hat{A}_k^\dagger(t)$.

Irreversible quantum operations, channels

state $\hat{\rho} \to \mathcal{E}(\hat{\rho}) = \sum_k \hat{A}_k \hat{\rho} \hat{A}_k^\dagger$ (Schrödinger CPTP),
observable $\hat{M} \to \mathcal{E}^*(\hat{M}) = \sum_k \hat{A}_k^\dagger \hat{M} \hat{A}_k$ (Heisenberg CPUP)

$$\langle \hat{M} \rangle = \mathrm{Tr}(\hat{\rho}\hat{M}) \to \mathrm{Tr}\left[\left(\sum_k \hat{A}_k \hat{\rho} \hat{A}_k^\dagger\right)\hat{M}\right] = \mathrm{Tr}\left[\hat{\rho}\left(\sum_k \hat{A}_k^\dagger \hat{M} \hat{A}_k\right)\right]$$

and $\sum_k \hat{A}_k^\dagger \hat{A}_k = \mathbb{1}$

⊙ **Qubit:** arbitrary channels:

$$\hat{A}_k = \alpha_k \mathbb{1} + \beta_k X + \gamma_k Y + \delta_k Z$$

Pauli channels:

$$\hat{A}_k \propto \mathbb{1}, X, Y, Z\ , \quad \forall k\ ,$$

amplitude damping channel:

$$\hat{A}_0 = \begin{pmatrix} 1 & 0 \\ 0 & \sqrt{1-\gamma} \end{pmatrix}, \quad \hat{A}_1 = \begin{pmatrix} 0 & \sqrt{\gamma} \\ 0 & 0 \end{pmatrix}$$

~~~~ **Qumode:** arbitrary channels:

$$\mathcal{E}(\hat{\rho}) = \int \mathrm{d}s\mathrm{d}t\mathrm{d}s'\mathrm{d}t'\, f(s,t,s',t') X(s) Z(t) \hat{\rho} X(-s') Z(-t')$$

WH channels:

$$\mathcal{E}(\hat{\rho}) = \int \mathrm{d}s\mathrm{d}t\, f(s,t) X(s) Z(t) \hat{\rho} X(-s) Z(-t)$$

amplitude damping channel:

$$\mathcal{E}(\hat{\rho}) = \sum_{k=0}^{\infty} \hat{A}_k \hat{\rho} \hat{A}_k^\dagger\ , \quad \hat{A}_k = \sum_{n=k}^{\infty} \left[\binom{n}{k}(1-\gamma)^{n-k}\gamma^k\right]^{1/2} |n-k\rangle\langle n|$$

Channel maps of density operators are trace-preserving and hence deterministic. They are non-selective in the sense that none of the terms in the operator sum are discarded. In the next section, we shall consider the nondeterministic, selective case of trace-decreasing CP maps corresponding to situations that include measurements.
~~~~

1.4.2 Measurements

A reversible channel map as written in the form of the operator sum in Eq. (1.73) only has one term left in the sum and the one remaining Kraus operator becomes a unitary operator, $\sum_k \hat{A}_k \hat{\rho} \hat{A}_k^\dagger = \hat{U}\hat{\rho}\hat{U}^\dagger$ with $\sum_k \hat{A}_k^\dagger \hat{A}_k = \hat{U}^\dagger \hat{U} = \mathbb{1}$.

Are there also irreversible, non-unitary operations that are described by a map with only one term such that $\hat{\rho} \to \mathcal{E}(\hat{\rho}) = \hat{A}_0 \hat{\rho} \hat{A}_0^\dagger$? Since such a non-unitary map must have $\hat{A}_0^\dagger \hat{A}_0 \neq \mathbb{1}$, we would obtain an output density operator with non-unit trace, $\mathrm{Tr}\mathcal{E}(\hat{\rho}) \neq 1$ [see Eq. (1.75)], and the map, in general, would not be trace-preserving. Indeed, the corresponding probabilistic operation could describe, for example, a measurement and the measurement-induced "state reduction" would leave the signal system in a pure, conditional state depending on the measurement result,

$$\frac{\mathcal{E}(\hat{\rho})}{\mathrm{Tr}\mathcal{E}(\hat{\rho})} = \frac{\hat{A}_0 \hat{\rho} \hat{A}_0^\dagger}{\mathrm{Tr}(\hat{A}_0^\dagger \hat{A}_0 \hat{\rho})} \,. \tag{1.79}$$

Here, the measurement result is labeled by the subscript "0". The state after the measurement is renormalized to unit trace with the unnormalized conditional state divided by the probability for the measurement outcome, $p(k = 0) = \mathrm{Tr}(\hat{A}_0^\dagger \hat{A}_0 \hat{\rho}) < 1$. Let us make this probabilistic interpretation in terms of measurement-induced state evolution more plausible.

For this purpose, first we introduce a very useful and well-known extension of the standard von Neumann, projection measurement to a generalized measurement, a so-called *positive-operator valued measure* (POVM). Recall that the measurement of an observable, that is, a Hermitian operator with real eigenvalues, leads to an eigenstate from the observable's orthogonal eigenbasis and the corresponding eigenvalue is the measurement result. This is a projection measurement.

1.4.2.1 POVM

Let us now define the positive operator

$$\hat{E}_k \equiv \hat{A}_k^\dagger \hat{A}_k \,. \tag{1.80}$$

The set of positive operators $\{\hat{E}_k\}$ is referred to as POVM. It determines a set of probabilities given by $p(k) = \mathrm{Tr}(\hat{E}_k \hat{\rho})$. This probability distribution of measurement outcomes should be normalized such that $\sum_k p(k) = \sum_k \mathrm{Tr}(\hat{A}_k^\dagger \hat{A}_k \hat{\rho}) = 1$. This holds for $\sum_k \hat{A}_k^\dagger \hat{A}_k = \mathbb{1}$ and $\mathrm{Tr}\hat{\rho} = 1$. In other words, *any* complete set of positive operators $\{\hat{E}_k\}$ with $\sum_k \hat{E}_k = \mathbb{1}$ defines a generalized measurement. The POVM elements and the Kraus operators coincide if and only if the measurement is a projection measurement so that $\hat{E}_k \equiv \hat{A}_k$, $\hat{A}_k^\dagger = \hat{A}_k$, and $\hat{A}_k \hat{A}_l = \delta_{kl} \hat{A}_k$.

Note that the POVM formalism itself is only about probabilities and not about state evolution. However, we can make statements about non-unitary state evolution as follows.

Consider again the scheme in Figure 1.5. This time, we assume that a projective POVM is applied to the output state of the ancilla after the unitary. This POVM is given by the set of projectors $\{\hat{E}_k\} \equiv \{|k\rangle\langle k|\}$ with an orthonormal basis $\{|k\rangle\}$ for the ancilla system. Similar to what we did before, we can write down the total unitary state evolution of the composite system of signal A and ancilla B, where we assume the ancilla starts in the state $\hat{\rho}_\mathrm{B} = |0\rangle_\mathrm{B}\langle 0|$. However, this time, we do not simply trace over the ancilla system. Instead, we calculate the probabilities for obtaining the measurement outcome k,

$$\begin{aligned} p(k) &= \mathrm{Tr}_{\mathrm{AB}}\left[\hat{U}_{\mathrm{AB}}\left(\hat{\rho}_\mathrm{A}\otimes|0\rangle_\mathrm{B}\langle 0|\right)\hat{U}_{\mathrm{AB}}^\dagger\left(\mathbb{1}_\mathrm{A}\otimes\hat{E}_k\right)\right] \\ &= \mathrm{Tr}_\mathrm{A}\left[\sum_l {}_\mathrm{B}\langle l|\,\hat{U}_{\mathrm{AB}}\left(\hat{\rho}_\mathrm{A}\otimes|0\rangle_\mathrm{B}\langle 0|\right)\hat{U}_{\mathrm{AB}}^\dagger\left(\mathbb{1}_\mathrm{A}\otimes|k\rangle_\mathrm{B}\langle k|\right)|l\rangle_\mathrm{B}\right] \\ &= \mathrm{Tr}_\mathrm{A}\left(\hat{A}_k\hat{\rho}_\mathrm{A}\hat{A}_k^\dagger\right) = \mathrm{Tr}_\mathrm{A}\left(\hat{A}_k^\dagger\hat{A}_k\hat{\rho}_\mathrm{A}\right)\,, \end{aligned} \tag{1.81}$$

using $\hat{A}_k \equiv {}_\mathrm{B}\langle k|\hat{U}_{\mathrm{AB}}|0\rangle_\mathrm{B}$ as before and ${}_\mathrm{B}\langle k|l\rangle_\mathrm{B} = \delta_{kl}$. This defines the POVM $\{\hat{A}_k^\dagger\hat{A}_k\}$ on the signal system $\hat{\rho}_\mathrm{A}$. An additional new POVM, $\{\hat{F}_l\}$, acting upon the signal output state would result in the joint probabilities

$$\begin{aligned} p(k,l) &= \mathrm{Tr}_{\mathrm{AB}}\left[\hat{U}_{\mathrm{AB}}\left(\hat{\rho}_\mathrm{A}\otimes|0\rangle_\mathrm{B}\langle 0|\right)\hat{U}_{\mathrm{AB}}^\dagger\left(\hat{F}_l\otimes\hat{E}_k\right)\right] \\ &= \mathrm{Tr}_\mathrm{A}\left(\hat{A}_k\hat{\rho}_\mathrm{A}\hat{A}_k^\dagger\hat{F}_l\right). \end{aligned} \tag{1.82}$$

From this, we can immediately infer the probabilities for obtaining the POVM element $\hat{F}_l$ when the initial state prior to the second POVM is $\hat{\rho}_\mathrm{A}^{(k)}$, namely, $\mathrm{Tr}_\mathrm{A}[\hat{\rho}_\mathrm{A}^{(k)}\hat{F}_l] = p(l|k) = p(k,l)/p(k) = \mathrm{Tr}_\mathrm{A}\{[\hat{A}_k\hat{\rho}_\mathrm{A}\hat{A}_k^\dagger/p(k)]\hat{F}_l\}$. Thus, we must have the conditional state of the first POVM,

$$\hat{\rho}_\mathrm{A}^{(k)} = \frac{\hat{A}_k\hat{\rho}_\mathrm{A}\hat{A}_k^\dagger}{p(k)} = \frac{\hat{A}_k\hat{\rho}_\mathrm{A}\hat{A}_k^\dagger}{\mathrm{Tr}_\mathrm{A}\left(\hat{A}_k^\dagger\hat{A}_k\hat{\rho}_\mathrm{A}\right)} \equiv \frac{\mathcal{E}(\hat{\rho}_\mathrm{A})}{\mathrm{Tr}_\mathrm{A}\mathcal{E}(\hat{\rho}_\mathrm{A})}\,. \tag{1.83}$$

Thus, the a-priori-state of the second POVM gives us the a-posteriori-state of the first POVM and hence the state evolution consistent with the first measurement. Here, the a-posteriori-state is pure (provided $\hat{\rho}_\mathrm{A}$ is pure), as we have assumed perfect knowledge about the outcome k. More generally, a CP trace-decreasing (CPTD) map can be written in the same way as Eq. (1.73), but with $\sum_k \hat{A}_k^\dagger\hat{A}_k < \mathbb{1}$. This may lead to an unpure output state, but the trace is strictly decreasing, provided some information is gained through the measurement. In the special case when no information is gained or, equivalently, when the average is taken over all possible outcomes k, we obtain the ensemble output state,

$$\begin{aligned} \hat{\rho}'_\mathrm{A} &= \sum_k p(k)\hat{\rho}_\mathrm{A}^{(k)} = \sum_k p(k)\hat{A}_k\hat{\rho}_\mathrm{A}\hat{A}_k^\dagger/p(k) \\ &= \sum_k \hat{A}_k\hat{\rho}_\mathrm{A}\hat{A}_k^\dagger = \mathcal{E}(\hat{\rho}_\mathrm{A})\,. \end{aligned} \tag{1.84}$$

This is again a CPTP map and we see that there is a physical interpretation of such a CPTP map. We can think of a channel as an ancilla system like the signal's environment which is monitoring the signal system with random outcomes k. As long as we do not have access to these outcomes, we cannot use them for processing. Therefore, effectively, the input state $\hat{\rho}_{\mathrm{A}}$ is randomly replaced by $\hat{\rho}_{\mathrm{A}}^{(k)}$ with probability $p(k)$. The ensemble state is then the same as before when we traced over the environment using a complete, orthonormal basis.

To summarize, a channel is a CPTP map that *non-selectively* and *deterministically* transforms density operators. It will always map pure states to mixed states, unless it is a unitary channel. A CPTD map is then expressed by a *selective* and hence *nondeterministic* Kraus evolution. It can map pure states to either pure or mixed states, depending, for example, on the resolution of a measurement.

Finally, we shall discuss that there is an alternate way to formulate a generalized measurement besides attaching an ancilla and considering measurements in the product Hilbert space of signal and ancilla, as depicted in Figure 1.5.

1.4.2.2 **Naimark Extension**

Though maybe less physically motivated, but mathematically more systematic, the alternate approach uses an extended Hilbert space from the original signal space corresponding to the total Hilbert space $\mathcal{H} = \mathcal{K} \oplus \mathcal{K}^{\perp}$. Through this direct-sum structure, the POVM is then described by a projection measurement onto the orthogonal set of vectors in the total space,

$$|w_\mu\rangle = |u_\mu\rangle + |N_\mu\rangle \ , \tag{1.85}$$

with $\langle w_\mu | w_\nu \rangle = \delta_{\mu\nu}$. The vectors $\{|u_\mu\rangle\}$ are unnormalized, possibly non-orthogonal state vectors in the Hilbert space $\mathcal{K}$. We may write

$$\hat{E}_\mu = |u_\mu\rangle\langle u_\mu| \ . \tag{1.86}$$

These are the POVM operators of an N-valued POVM with $\sum_{\mu=1}^{N} \hat{E}_\mu = \mathbb{1}$. The vectors $\{|N_\mu\rangle\}$ are defined in the complementary space $\mathcal{K}^{\perp}$ orthogonal to $\mathcal{K}$, with the total Hilbert space $\mathcal{H} = \mathcal{K} \oplus \mathcal{K}^{\perp}$. If the dimension of the signal space is n, with $|u_\mu\rangle = \sum_{i=1}^{n} b_{\mu i}|v_i\rangle$, some complex coefficients $b_{\mu i}$, and $\{|v_i\rangle\}_{i=1}^{n}$ as a basis in $\mathcal{K}$, we have $|N_\mu\rangle = \sum_{i=n+1}^{N} b_{\mu i}|v_i\rangle$ with some complex coefficients $b_{\mu i}$, and $\{|v_i\rangle\}_{i=n+1}^{N}$ as a basis in $\mathcal{K}^{\perp}$. The vectors $\{|N_\mu\rangle\}$ are referred to as a *Naimark extension*.

Let us give an example for a POVM on a single qubit, $n = 2$. Consider a pair of pure and non-orthogonal qubit states,[20)]

$$|\chi_\pm\rangle = \alpha|\bar{0}\rangle \pm \beta|\bar{1}\rangle \ , \tag{1.87}$$

where $\alpha > \beta$ are assumed to be real and $\{|\bar{0}\rangle, |\bar{1}\rangle\}$ are two basis states. When we are given a single copy of this qubit without knowing whether it is in the $+$ or the $-$

20) Actually, any pair of pure states can be written this way up to a global phase. We use the notation $|\bar{0}\rangle$ and so on in order to indicate that the basis states here are logical basis states. Later, in the optical context, a logical basis state may be encoded into photonic states of several optical modes.

state, there are various restrictions. We cannot perfectly discriminate the two states and so we cannot unambiguously *and* deterministically decide in which quantum state the qubit exists. In fact, if we were able to achieve perfect state discrimination, we could also create more copies from a single copy of the unknown quantum state, thus violating the no-cloning theorem; as a result, we could even communicate at a speed faster than light (recall Section 1.1). The fundamental inability of perfect state discrimination for non-orthogonal states is also the essence of quantum key distribution (see Section 1.7).

However, there are measurement schemes that do achieve state discrimination to some extent in an imperfect fashion, either unambiguously *or* deterministically, or somewhere in between. The two extreme cases are the deterministic discrimination with an ideally minimal error (so-called minimum error discrimination, MED) and the error-free discrimination with an ideally minimal probability for obtaining an inconclusive result (so-called unambiguous state discrimination, USD). In either case, the optimal performance can be derived from the laws of quantum theory.

Now let us consider the USD for the two states in Eq. (1.87). The POVM for this USD may have three elements, $N = 3$, two of which correspond to an error-free identification of the $+$ and $-$ states. The third POVM element would express an additional inconclusive measurement outcome. Thus, we have $\sum_{\mu=1}^{3} \hat{E}_\mu = \mathbb{1}$ with $\hat{E}_\mu$ from Eq. (1.86). The elements $\hat{E}_1$ and $\hat{E}_2$ are conclusive, while $\hat{E}_3$ is inconclusive. Now, in order to make the first two POVM elements unambiguous, that is, error-free, we must satisfy $p(1|-) = \mathrm{Tr}(\hat{E}_1|\chi_-\rangle\langle\chi_-|) = p(2|+) = \mathrm{Tr}(\hat{E}_2|\chi_+\rangle\langle\chi_+|) = 0$, where $p(1|-)$ and $p(2|+)$ are the probabilities for obtaining the 1 outcome for the $-$ state and the 2 outcome for the $+$ state, respectively. Using the ansatz in Eq. (1.85), a projection onto a three-dimensional basis $\{|w_\mu\rangle\}$ can be constructed that satisfies the above constraints. More precisely, the choice of

$$
\begin{aligned}
|u_{1/2}\rangle &= \frac{1}{\sqrt{2}}\left(\frac{\beta}{\alpha}|\bar{0}\rangle \pm |\bar{1}\rangle\right), \qquad |N_{1/2}\rangle = \frac{1}{\sqrt{2}}\sqrt{1-\frac{\beta^2}{\alpha^2}}|\bar{2}\rangle\,, \\
|u_3\rangle &= \sqrt{1-\frac{\beta^2}{\alpha^2}}|\bar{0}\rangle\,, \qquad |N_3\rangle = -\frac{\beta}{\alpha}|\bar{2}\rangle\,,
\end{aligned}
\tag{1.88}
$$

with $\langle\bar{2}|\bar{0}\rangle = \langle\bar{2}|\bar{1}\rangle = 0$, would even achieve the optimal USD with minimal failure probability, that is, minimal probability for obtaining an inconclusive result, $\mathrm{Prob}_{\mathrm{fail}} = |\langle\chi_+|\chi_-\rangle|$ for equal a priori probabilities [30–32]. The optimality is easily confirmed through

$$
\begin{aligned}
\mathrm{Prob}_{\mathrm{succ}} &= \mathrm{Tr}\left(\hat{E}_1|\chi_+\rangle\langle\chi_+|\right)/2 + \mathrm{Tr}\left(\hat{E}_2|\chi_-\rangle\langle\chi_-|\right)/2 \\
&= 1 - \mathrm{Prob}_{\mathrm{fail}} \\
&= 1 - \mathrm{Tr}\left(\hat{E}_3|\chi_+\rangle\langle\chi_+|\right)/2 - \mathrm{Tr}\left(\hat{E}_3|\chi_-\rangle\langle\chi_-|\right)/2 \\
&= 1 - (\alpha^2 - \beta^2) = 1 - |\langle\chi_+|\chi_-\rangle| = 2\beta^2\,.
\end{aligned}
\tag{1.89}
$$

The factors $1/2$ in lines one and three are the a priori probabilities. Examples of projection measurements, POVMs, and USD on optically encoded quantum states,

both in the DV qubit and the CV qumode regime, will be presented in Chapter 2. Such quantum measurements are highly relevant for many applications in optical quantum information, especially quantum communication.

Irreversible quantum operations, measurements

generalized measurement, positive-operator valued measure (POVM):

$$\hat{E}_k = \hat{A}_k^\dagger \hat{A}_k \quad \text{with} \quad \sum_k \hat{E}_k = \mathbb{1} \quad \text{and} \quad \text{probabilities } p(k) = \mathrm{Tr}\left(\hat{E}_k \hat{\rho}\right)$$

non-unitary state evolution, completely positive trace-decreasing (CPTD):

$$\hat{\rho} \to \frac{\mathcal{E}(\hat{\rho})}{\mathrm{Tr}\mathcal{E}(\hat{\rho})} = \frac{\sum_k \hat{A}_k \hat{\rho} \hat{A}_k^\dagger}{\mathrm{Tr}\left(\sum_k \hat{A}_k^\dagger \hat{A}_k \hat{\rho}\right)} \quad \text{with} \quad \sum_k \hat{A}_k^\dagger \hat{A}_k < \mathbb{1}$$

Besides those POVMs on a single qubit or qumode, an important extension are collective, joint POVMs on many qubits or qumodes. An example is the projection onto an entangled-state basis as needed for quantum teleportation. We shall now proceed with an introduction to the notion of entanglement.

1.5 Entanglement

In this section, we will first introduce pure entangled states, focusing on qubit and qumode states. Further, extending the discussion on quantum states for a single qubit and a single qumode in Section 1.2, we shall now look at bipartite qubit and qumode states from a point of view that is based on stabilizers (see the discussion and the box in Section 1.9). For the case of qumodes, the stabilizer states introduced in this section are idealized, unphysical states. We will briefly introduce inseparability criteria for mixed states and entanglement witnesses as well as a few entanglement measures.

1.5.1 Pure States

For any *pure state of two parties*, for instance, a pure state of two qubits or two qumodes, there is always an orthonormal basis for each subsystem, $\{|u_n\rangle\}$ and $\{|v_n\rangle\}$, such that the total state vector can be written in the "Schmidt decomposition" [33] as

$$|\psi\rangle = \sum_n c_n |u_n\rangle |v_n\rangle \,. \tag{1.90}$$

The summation goes over the smaller of the dimensionalities of the two subsystems and would go to infinity for two qumodes. Therefore, for two qubits, there are, in general, two terms. In order to write a bipartite pure state of a qubit and a qumode, two terms are enough as well (see the notion of hybrid entanglement introduced in Chapter 8).

The Schmidt coefficients c_n are real and non-negative, and satisfy $\sum_n c_n^2 = 1$. The Schmidt decomposition may be obtained by writing an arbitrary pure bipartite state as

$$\begin{aligned} |\psi\rangle &= \sum_{mk} a_{mk}|m\rangle|k\rangle = \sum_{nmk} u_{mn}c_{nn}v_{kn}|m\rangle|k\rangle \\ &= \sum_n c_n|u_n\rangle|v_n\rangle \ , \end{aligned} \tag{1.91}$$

with $c_{nn} \equiv c_n$. In the first step, the matrix a with complex elements a_{mk} is diagonalized using singular-value decomposition, $a = ucv^{\mathrm{T}}$, where u and v are unitary matrices and c is a diagonal matrix with real, non-negative elements. In the second step, we defined $|u_n\rangle \equiv \sum_m u_{mn}|m\rangle$ and $|v_n\rangle \equiv \sum_k v_{kn}|k\rangle$ which form orthonormal sets due to the unitarity of u and v, and the orthonormality of $|m\rangle$ and $|k\rangle$.

A pure state of two finite-dimensional, d-level systems is maximally entangled when the Schmidt coefficients of the total state vector are all equal. Since the eigenvalues of the reduced density operator after tracing out one half of a bipartite state are the Schmidt coefficients squared,

$$\hat{\rho}_1 = \mathrm{Tr}_2\hat{\rho}_{12} = \mathrm{Tr}_2|\psi\rangle_{12}\langle\psi| = \sum_n c_n^2|u_n\rangle_1\langle u_n| \ , \tag{1.92}$$

tracing out either subsystem of a maximally entangled state leaves the other half in the maximally mixed state $\mathbb{1}/d$. In other words, if one party is discarded, the remaining party is in a maximally noisy state with maximum entropy. Conversely, a pure bipartite state is factorizable (not entangled) if and only if the number of nonzero Schmidt coefficients, the so-called *Schmidt rank*, is one. In this case, the reduced states are pure and have zero entropy.

A unique measure of bipartite entanglement for pure states is given by the partial von Neumann entropy, that is, the von Neumann entropy as defined in Eq. (1.22) for the remaining system after tracing out either subsystem [34], $-\mathrm{Tr}\hat{\rho}_1 \log_d \hat{\rho}_1 = -\mathrm{Tr}\hat{\rho}_2 \log_d \hat{\rho}_2 = -\sum_n c_n^2 \log_d c_n^2$, with $\mathrm{Tr}_2\hat{\rho}_{12} = \hat{\rho}_1$, $\mathrm{Tr}_1\hat{\rho}_{12} = \hat{\rho}_2$. This measure ranges between zero and one, and for qubits ($d = 2$) its units are "ebits". It can be understood as the amount of maximum entanglement contained in a given pure state.[21] For example, an entropy of 0.4 means that asymptotically 1000 copies of the state can be transformed into 400 maximally entangled states through deterministic state transformations using local operations and classical communication [5].

21) For general bipartite qumode states, there are some complications of this entanglement entropy. The entropy fails to be continuous in the sense that there are (rather artificial) states that have arbitrarily large entanglement, though being arbitrarily close to a pure product state. However, through restriction on bounded mean energies continuity of the entanglement can be recovered [35].

1.5.1.1 Qubits

For two qubits, a maximally entangled basis is given by the four "Bell states",[22]

$$|\Phi^{\pm}\rangle = \frac{1}{\sqrt{2}}(|00\rangle \pm |11\rangle) , \qquad |\Psi^{\pm}\rangle = \frac{1}{\sqrt{2}}(|01\rangle \pm |10\rangle) . \tag{1.93}$$

These are stabilizer states with nonlocal stabilizer generators.[23] For instance, the $|\Phi^{+}\rangle$ state has stabilizer generators $\langle X \otimes X, Z \otimes Z\rangle$ corresponding to a stabilizer group $\{\mathbb{1} \otimes \mathbb{1}, X \otimes X, -Y \otimes Y, Z \otimes Z\}$. Any of these Pauli products has eigenvalue $+1$ when applied upon $|\Phi^{+}\rangle$. The set of generators is sufficient to represent every stabilizer since the products $(X \otimes X)(Z \otimes Z) = XZ \otimes XZ = -Y \otimes Y$ and $(X \otimes X)(X \otimes X) = \mathbb{1} \otimes \mathbb{1}$ must have $+1$ eigenvalue as well.

Recall that a one-qubit stabilizer state has a single stabilizer generator, namely, ± 1 times one of the Pauli operators. The stabilizer group has two elements after adding the unity operator. Two qubits require two stabilizer generators as a minimal set to give a stabilizer group of four elements. For instance, a product state of two qubits, $|0\rangle \otimes |0\rangle$, is a stabilizer state with stabilizer group $\{\mathbb{1} \otimes \mathbb{1}, \mathbb{1} \otimes Z, Z \otimes \mathbb{1}, Z \otimes Z\}$ and, in this case, local stabilizer generators[24] $\langle \mathbb{1} \otimes Z, Z \otimes \mathbb{1}\rangle$. The *nonlocal* stabilizer generators of the four Bell states in Eq. (1.93) are easily found to be

$$\begin{aligned} &\langle X \otimes X, Z \otimes Z\rangle , \qquad \langle X \otimes X, -Z \otimes Z\rangle , \\ &\langle -X \otimes X, Z \otimes Z\rangle , \qquad \langle -X \otimes X, -Z \otimes Z\rangle , \end{aligned} \tag{1.94}$$

respectively. The two-qubit stabilizer states are either product states or maximally entangled states. The two-qubit non-stabilizer states are the non-maximally (partially) entangled states (or products of non-stabilizer states).

1.5.1.2 Qumodes

Now, consider the case of two qumodes. The "CV Bell states" for two qumodes may be written as

$$|\Psi(u, v)\rangle = \frac{1}{\sqrt{\pi}} \int \mathrm{d}x \mathrm{e}^{2\mathrm{i}xv} |x\rangle |x - u\rangle . \tag{1.95}$$

Although these states obey the completeness and orthogonality relations

$$\begin{aligned} \int \mathrm{d}u\mathrm{d}v |\Psi(u, v)\rangle\langle\Psi(u, v)| &= \mathbb{1} \otimes \mathbb{1} , \\ \langle\Psi(u, v)|\Psi(u', v')\rangle &= \delta(u - u')\delta(v - v') , \end{aligned} \tag{1.96}$$

they are nonetheless unphysical since they exhibit an infinite degree of quantum correlations. This is similar to the position and momentum eigenstates of a single qumode with infinitely precise position and momentum eigenvalues as depicted in Figure 1.3. Each of the CV Bell states is similarly determined through infinitely

22) We shall use the notations $|\Phi^{\pm}\rangle$ and $|\Phi^{(\pm)}\rangle$, and so on, interchangeably throughout.

23) For a definition of stabilizers, see the discussion and the box in Section 1.9.

24) Where, more precisely, "local" refers to the local subgroup into which the total stabilizer group of the state can be split together with a nonlocal subgroup. The local subgroup then contains stabilizer operators that act exclusively upon either subsystem [36]. For the product state $|0\rangle \otimes |0\rangle$, the whole stabilizer is given by the local subgroup $\{\mathbb{1}, Z\} \cdot \{\mathbb{1}, Z\}$.

precise, continuous eigenvalues. However, for two qumodes, we need two such eigenvalues, corresponding to two *nonlocal* observables with $(\hat{x}_1 - \hat{x}_2)|\Psi(u,v)\rangle = u|\Psi(u,v)\rangle$ and $(\hat{p}_1 + \hat{p}_2)|\Psi(u,v)\rangle = v|\Psi(u,v)\rangle$.

Expressed in terms of the WH shift operators, we can equivalently write for all t, s,

$$\begin{aligned} \mathrm{e}^{-2\mathrm{i}tu}\mathrm{e}^{+2\mathrm{i}t(\hat{x}_1-\hat{x}_2)}|\Psi(u,v)\rangle &= \mathrm{e}^{-2\mathrm{i}tu}Z(t)\otimes Z^{\dagger}(t)|\Psi(u,v)\rangle \\ &= |\Psi(u,v)\rangle \ , \\ \mathrm{e}^{+2\mathrm{i}sv}\mathrm{e}^{-2\mathrm{i}s(\hat{p}_1+\hat{p}_2)}|\Psi(u,v)\rangle &= \mathrm{e}^{+2\mathrm{i}sv}X(s)\otimes X(s)|\Psi(u,v)\rangle \\ &= |\Psi(u,v)\rangle \ . \end{aligned} \tag{1.97}$$

In other words, for the unphysical, infinitely correlated CV Bell states, we obtain the nonlocal stabilizer generators

$$\langle \mathrm{e}^{+2\mathrm{i}sv}X(s)\otimes X(s), \mathrm{e}^{-2\mathrm{i}tu}Z(t)\otimes Z^{\dagger}(t)\rangle \ . \tag{1.98}$$

Note that for $v = 0$, this would be a unique representation for the famous two-particle state presented by Einstein, Podolsky, and Rosen (EPR) which is quantum mechanically correlated in the positions $(x_1 - x_2 = u)$ and the momenta $(p_1 + p_2 = 0)$ [23]. In the optical context, a physical version of the EPR state corresponds to a Gaussian two-mode squeezed state in the limit of large squeezing (see Chapter 3). Moreover, similar to the two-qubit stabilizers, the two-qumode stabilizers here are useful to construct so-called entanglement witnesses. These witnesses would enable one to detect the entanglement of the physical, finitely correlated, and possibly even noisy mixed-state approximations of the EPR state. How to find such witnesses for qubits and qumodes will be discussed in Chapter 3. At this point, we shall proceed by looking at the entanglement of mixed states, inseparability criteria, and the definition of entanglement witnesses.

Given an arbitrary two-party (e.g., two-qubit or two-qumode) density operator, how can we find out whether the bipartite state is entangled or not? For this purpose, first of all, a definition of entanglement is needed which goes beyond that of pure-state entanglement expressed by the Schmidt rank and so is applicable to mixed states as well.

1.5.2 Mixed States and Inseparability Criteria

A *mixed state of two parties* is separable if its total density operator can be written as a mixture (a convex sum) of product states,[25)]

$$\hat{\rho}_{12} = \sum_i \eta_i \hat{\rho}_{i,1}\otimes\hat{\rho}_{i,2} \ . \tag{1.99}$$

25) Corresponding to a *classically correlated* state [37]. For instance, for the qubit or the qumode Bell states, the nonclassical character of entanglement is reflected by the nonlocal stabilizer generators simultaneously in terms of X and Z. However, note that this notion of nonlocality is weaker than the historically well-known notion of nonlocality that refers to the inapplicability of local realistic models. In fact, Werner's [37] original intention was to demonstrate that quantum states exist which are inseparable according to the convex-sum definition and yet admit a local realistic description.

Otherwise, it is inseparable and hence entangled. In general, it is a highly nontrivial question whether a given density operator is separable or inseparable.

A very powerful method to test for inseparability is Peres' *partial transpose* criterion [38]. For a separable state as in Eq. (1.99), transposition of either density matrix yields again a legitimate non-negative density operator with unit trace,

$$\hat{\rho}'_{12} = \sum_i \eta_i (\hat{\rho}_{i,1})^{\mathrm{T}} \otimes \hat{\rho}_{i,2} \tag{1.100}$$

since $(\hat{\rho}_{i,1})^{\mathrm{T}} = (\hat{\rho}_{i,1})^*$ corresponds to a legitimate density matrix. This is a necessary condition for a separable state, and hence a single negative eigenvalue of the partially transposed density matrix is a sufficient condition for inseparability. Applied to one party entangled with another party, transposition may indeed lead to an unphysical state because it is a positive but not a CP map. For inseparable states of two qubits and of one qubit and one qutrit, partial transposition always leads to an unphysical state [39]. The same holds true for any bipartite Gaussian state of one qumode entangled with arbitrarily many other qumodes (see Chapter 3).

1.5.3
Entanglement Witnesses and Measures

Independent of partial transposition, an *entanglement witness* $\hat{W}$ is an observable whose expectation value is non-negative for all separable states $\hat{\rho}_{\mathrm{sep}}$, $\mathrm{Tr}(\hat{W}\hat{\rho}_{\mathrm{sep}}) \geq 0$, and negative for some inseparable state $\hat{\rho}$, $\mathrm{Tr}(\hat{W}\hat{\rho}) < 0$ (see Figure 1.6).

A very important class of entanglement witnesses is given by the Bell-type inequalities imposed by local realistic theories [41]. For both qubits and qumodes, we shall discuss the canonical and most commonly used entanglement witnesses in Chapter 3. These witnesses are independent of local realism. Since the inseparability criteria expressed in terms of expectation values of observables are directly measurable, entanglement witnesses are of great significance for the experimental verification of the presence of entanglement.

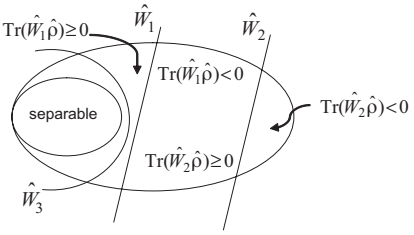

Figure 1.6 Entanglement witnesses are Hermitian operators that define hyperplanes in the space of density operators (states), separating some inseparable states from all separable states. The plane closer to the set of separable states represents a "better" witness $\hat{W}_1$ than the other plane corresponding to $\hat{W}_2$, as the former detects more inseparable states. An optimal linear witness would correspond to a plane tangent on the set of separable states. However, there are even better witnesses like $\hat{W}_3$ which are nonlinear and can detect even more inseparable states [40].

Besides those qualitative inseparability criteria, which we may call entanglement *qualifiers*, a more ambitious task is to provide entanglement measures and to obtain entanglement *quantifiers* for a given density operator, both theoretically and experimentally. In general, the known measures for mixed-state entanglement are not unique. In the summary box 'Entanglement', we included some of the most commonly used and most convenient entanglement measures.

In the case of pure states, (most of) these measures would coincide. The naive approach for extending pure-state quantifiers to mixed states would be to simply apply a pure-state measure such as the reduced von Neumann entropy to every term in a density operator decomposition. However, in general, a given decomposition $\sum_k \rho_k |\psi_k\rangle_{12}\langle\psi_k|$ may then give a completely wrong result,

$$\sum_k \rho_k \, S\left[\mathrm{Tr}_2\left(|\psi_k\rangle_{12}\langle\psi_k|\right)\right] \ . \tag{1.101}$$

For instance, the maximally mixed state of two qubits, $\hat{\rho}_{12} = \mathbb{1}_{12}/4$, can be decomposed as

$$\hat{\rho}_{12} = (|\Phi^+\rangle_{12}\langle\Phi^+| + |\Phi^-\rangle_{12}\langle\Phi^-| + |\Psi^+\rangle_{12}\langle\Psi^+| + |\Psi^-\rangle_{12}\langle\Psi^-|)/4 \tag{1.102}$$

using the two-qubit Bell basis in Eq. (1.93). In this case, every term corresponds to a maximally entangled state with unit reduced entropy. So the average reduced entropy as calculated by Eq. (1.101) also gives one ebit instead of the correct result of zero ebits for a separable density operator written as

$$\begin{aligned}\hat{\rho}_{12} = {} & (|0\rangle_1\langle 0| \otimes |0\rangle_2\langle 0| + |0\rangle_1\langle 0| \otimes |1\rangle_2\langle 1| \\ & + |1\rangle_1\langle 1| \otimes |0\rangle_2\langle 0| + |1\rangle_1\langle 1| \otimes |1\rangle_2\langle 1|)/4 \ .\end{aligned} \tag{1.103}$$

Therefore, for a globally mixed state, we only obtain sensible results if we *minimize* the average reduced entropy over *all possible ensemble decompositions*,

$$E_{\mathrm{F}}(\hat{\rho}_{12}) \equiv \inf_{\rho_k, \psi_k} \sum_k \rho_k \, S\left[\mathrm{Tr}_2\left(|\psi_k\rangle_{12}\langle\psi_k|\right)\right] \ . \tag{1.104}$$

This is the so-called entanglement of formation. In general, the minimization over all decompositions is hard to compute. However, for two qubits, the entanglement of formation can be obtained through the concurrence [42]. Another important and more practical (i.e., relatively easily computable) mixed-state entanglement quantifier is the logarithmic negativity which is based upon the negativity after partial transposition [43–45].

The logarithmic negativity is defined as follows,

$$E_{\mathrm{N}}(\hat{\rho}_{12}) \equiv \log_2 \left|\left|\hat{\rho}_{12}^{\mathrm{T}_2}\right|\right| \ , \tag{1.105}$$

where $||\hat{A}|| \equiv \mathrm{Tr}\sqrt{\hat{A}^\dagger \hat{A}}$ is the so-called trace norm and $\hat{\rho}_{12}^{\mathrm{T}_2}$ is the partial transpose of a given bipartite state $\hat{\rho}_{12}$ with respect to subsystem 2. This measure is

an entanglement monotone (i.e., it does not increase under local operations and classical communication) and, in addition, it is additive.[26] The trace norm of the partial transpose corresponds to the sum of the modulus of its eigenvalues. For instance, for a two-qubit Bell state $\hat{\rho}_{12}$, we have $||\hat{\rho}_{12}^{\mathrm{T}_2}|| = 2$, as the eigenvalues of $\hat{\rho}_{12}^{\mathrm{T}_2}$ are $\{-1/2, 1/2, 1/2, 1/2\}$. Conversely, for a separable state $\hat{\rho}_{12}$, we always obtain $||\hat{\rho}_{12}^{\mathrm{T}_2}|| = 1$. Thus, the Bell state gives $E_{\mathrm{N}}(\hat{\rho}_{12}) = 1$, whereas a separable state has $E_{\mathrm{N}}(\hat{\rho}_{12}) = 0$. In general, any entanglement measure should be an entanglement monotone and should vanish for separable states.

Entanglement

bipartite pure states: separable iff Schmidt rank is one in Schmidt decomposition $|\psi\rangle_{12} = \sum_n c_n |u_n\rangle_1 |v_n\rangle_2$

bipartite mixed states: separable iff $\hat{\rho}_{12} = \sum_i \eta_i \hat{\rho}_{i,1} \otimes \hat{\rho}_{i,2}$

qualifiers, witnesses: $\forall \hat{\rho}_{\mathrm{sep}} \mathrm{Tr}(\hat{W}\hat{\rho}_{\mathrm{sep}}) \geq 0$ and $\exists \hat{\rho}$ such that $\mathrm{Tr}(\hat{W}\hat{\rho}) < 0$
quantifiers: reduced entropy for pure states: $E(|\psi\rangle_{12}) \equiv S[\mathrm{Tr}_2(|\psi\rangle_{12}\langle\psi|)]$
entanglement of formation: $E_{\mathrm{F}}(\hat{\rho}_{12}) \equiv \inf_{\rho_k, \psi_k} \sum_k \rho_k S[\mathrm{Tr}_2(|\psi_k\rangle_{12}\langle\psi_k|)]$
logarithmic negativity: $E_{\mathrm{N}}(\hat{\rho}_{12}) \equiv \log_2 ||\hat{\rho}_{12}^{\mathrm{T}_2}||$

⊙ **Qubits:** maximally entangled two-qubit Bell states:

$$|\Phi^{\pm}\rangle = (|00\rangle \pm |11\rangle)/\sqrt{2}, \quad |\Psi^{\pm}\rangle = (|01\rangle \pm |10\rangle)/\sqrt{2}$$

stabilized by

$$\langle X\otimes X, Z\otimes Z\rangle \,, \langle X\otimes X, -Z\otimes Z\rangle \,, \langle -X\otimes X, Z\otimes Z\rangle \,, \langle -X\otimes X, -Z\otimes Z\rangle$$

~~~~ **Qumodes:** maximally entangled two-qumode Bell states:

$$|\Psi(u,v)\rangle = \int \mathrm{d}x \mathrm{e}^{2\mathrm{i}xv} |x\rangle |x-u\rangle/\sqrt{\pi}$$

stabilized by

$$\langle \mathrm{e}^{+2\mathrm{i}sv} X(s)\otimes X(s), \mathrm{e}^{-2\mathrm{i}tu} Z(t)\otimes Z^{\dagger}(t)\rangle$$

Since the trace norm of the partial transpose effectively expresses to what extent $\hat{\rho}_{12}^{\mathrm{T}_2}$ fails to represent a physical state, it can be considered a quantitative version of the above qualitative partial transpose criterion.

This connection is easier to understand by looking at the so-called negativity, defined as $N(\hat{\rho}_{12}) \equiv (||\hat{\rho}_{12}^{\mathrm{T}_2}|| - 1)/2$. This quantity corresponds to the modulus of the sum of the *negative* eigenvalues of $\hat{\rho}_{12}^{\mathrm{T}_2}$, and becomes $N(\hat{\rho}_{12}) = 1/2$ for a two-qubit Bell state and $N(\hat{\rho}_{12}) = 0$ for any separable state. In this sense, $N(\hat{\rho}_{12})$ is the

26) However, it is not convex, and, as an exception to what we said before, it does not reduce to the entanglement entropy for all pure states.
~~~~

actual measure of negativity. However, though also being an entanglement monotone, $N(\hat{\rho}_{12})$ fails to be additive. Therefore, usually, the logarithmic negativity is preferred.

A discussion of *multipartite* entangled states of many qubits or qumodes will be postponed until Chapter 3. Such a generalization is important in order to define and investigate qubit/qumode cluster and graph states.

1.6 Quantum Teleportation

Quantum teleportation [17] is the reliable transfer of quantum information through a classical communication channel using shared entanglement. It works as follows (see Figure 1.7). After an entangled state is generated and distributed between two parties, an external system in an arbitrary, even completely unknown quantum state is jointly measured together with one half of the entangled state. Finally, when the measurement result is received at the other half of the entangled state, this half is transformed by a basic operation (such as a bit or phase flip for qubits or a phase-space displacement for qumodes) conditioned upon the measurement outcome.

When we think of entanglement as the universal resource for quantum information processing, we may refer to quantum teleportation as the fundamental quantum information protocol or subroutine. Quantum teleportation of *states* (as introduced here and discussed in more detail in Chapter 4) has applications in quantum communication (see the following section) as well as quantum computation. In the latter case, it would enable one, in principle, to connect different quantum computers when every quantum computer performs only a part of the whole computation.

Besides transferring quantum information between quantum computers and propagating it through quantum computers, there is an extended version of quantum teleportation which incorporates a controlled unitary evolution of quantum information into the teleportation protocol. This is quantum teleportation of *gates* and using such gate teleportations for computation corresponds to a certain realization of measurement-based quantum computation (see Chapter 6). The measurements in this case are projections onto an entangled basis and so they are not always easy to implement, for example, in an optical approach. Complete state transfer or evolution is also possible by performing the corresponding entangling operations offline with only local projection measurements performed online (see Chapter 7).

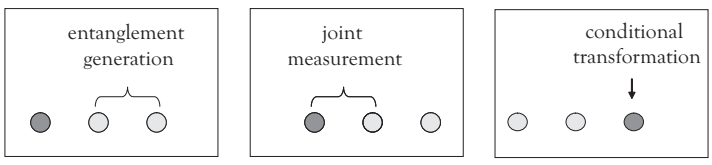

Figure 1.7 The fundamental protocol of quantum teleportation.

1.6.1 Discrete Variables

Let us consider quantum teleportation in finite dimensions. How the original DV quantum teleportation protocol [17] works can be understood from the following decomposition,

$$|\phi\rangle_{\text{in}} \otimes |\Psi_{0,0}\rangle_{12} = \frac{1}{d} \sum_{\alpha,\beta=0}^{d-1} |\Psi_{\alpha,\beta}\rangle_{\text{in},1} \hat{U}_2^{\dagger}(\alpha,\beta)|\phi\rangle_2 \ . \tag{1.106}$$

Here, we use α and β as discrete indices. The initial total state vector is a product of an arbitrary quantum state $|\phi\rangle_{\text{in}}$ for the input qudit (d-level system) and a particular maximally entangled state $|\Psi_{0,0}\rangle_{12}$ for qudits 1 and 2 (see below). A projection measurement of the input qudit and qudit one onto the maximally entangled basis of "qudit Bell states",

$$|\Psi_{\alpha,\beta}\rangle = \frac{1}{\sqrt{d}} \sum_{k=0}^{d-1} \exp(2\pi \mathrm{i} k\beta/d)|k\rangle|k \oplus \alpha\rangle \ , \tag{1.107}$$

reduces the above decomposition according to the measurement result (α_0, β_0). The qudit Bell states are complete and orthonormal,

$$\sum_{\alpha,\beta=0}^{d-1} |\Psi_{\alpha,\beta}\rangle\langle\Psi_{\alpha,\beta}| = \mathbb{1} \otimes \mathbb{1} \ , \quad \langle\Psi_{\alpha,\beta}|\Psi_{\alpha',\beta'}\rangle = \delta_{\alpha\alpha'}\delta_{\beta\beta'} \ . \tag{1.108}$$

Finally, applying to qudit two the unitary transformation that corresponds to the Bell measurement result (α_0, β_0) will correct the remaining $\hat{U}_2^{\dagger}(\alpha_0, \beta_0)$ operation in Eq. (1.106) and transform qudit two to the input state (the initial state of qudit "in"). The unitary transformations are defined as

$$\hat{U}(\alpha,\beta) = \sum_{k=0}^{d-1} \exp(2\pi \mathrm{i} k\beta/d)|k\rangle\langle k \oplus \alpha| \ , \tag{1.109}$$

and $\oplus$ means addition modulo d.

Quantum teleportation of an arbitrary quantum state from qudit "in" to qudit two is, in principle, independent of any spatial limitations. Suppose the two parties Alice and Bob initially share the maximally entangled state of qudits one and two. Alice is then capable of transferring an arbitrary quantum state from her location to Bob's. All she has to do is jointly measure the qudits "in" and one ("Bell measurement") and convey the measurement result to Bob through a classical communication channel. Finally, Bob has to apply the corresponding unitary transformation to qudit two. There are now three aspects of quantum teleportation that are particularly worth pointing out:

1. An unknown input state remains unknown to both Alice and Bob throughout the entire teleportation process. If Alice did gain some information through her

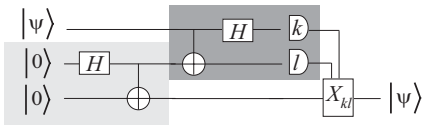

Figure 1.8 A quantum circuit description of qubit quantum teleportation. The part of the circuit in the light gray box is for entanglement generation between the two ancilla qubits. The part in the dark gray box is the circuit for the Bell measurement of the signal state and one half of the entangled pair.

Bell measurement, Bob would no longer obtain a perfect replica of the input state.
2. The input system does not remain in its initial state because of the Bell measurement. This fact ensures that no-cloning is not violated.
3. A contradiction to special relativity is avoided because the classical communication required between Alice and Bob is restricted by the speed of light.

For qubits ($d = 2$), the maximally entangled states $|\Psi_{\alpha,\beta}\rangle$ become the four Bell states from Eq. (1.93). The unitary transformations in this case correspond to the identity operator, $\hat{U}(0,0) = |0\rangle\langle 0| + |1\rangle\langle 1| = \mathbb{1}$, and the three Pauli operators

$$\begin{aligned}\hat{U}(1,0) &= |0\rangle\langle 1| + |1\rangle\langle 0| = X\ ,\\ \hat{U}(1,1) &= |0\rangle\langle 1| - |1\rangle\langle 0| = \mathrm{i}\,Y\ ,\\ \hat{U}(0,1) &= |0\rangle\langle 0| - |1\rangle\langle 1| = Z\ .\end{aligned} \tag{1.110}$$

Therefore, Bob will accomplish quantum teleporation of the input qubit by either flipping his qubit (X), flipping its phase (Z), doing both (Y), or doing nothing ($\mathbb{1}$). A quantum circuit description of qubit quantum teleportation is shown in Figure 1.8. The Bell measurement circuit is the inverse of the entanglement generation circuit, each consisting of Hadamard and CNOT gates (both belonging to the Clifford group of qubit unitaries, see Sections 1.3 and 1.8).

1.6.2 Continuous Variables

The translation of the quantum circuit for quantum teleportation from qubits to qumodes is straightforward. For this purpose, we need to replace the qubit gates by their qumode analogues, that is, the Hadamard gate by the Fourier gate and the two-qubit CNOT gate by a corresponding two-qumode entangling gate. We postpone the details about such gate sets until Section 1.8. However, we should mention that the two-qumode entangling gate can be effectively achieved through a linear beam splitter transformation (see Chapters 2 and 4). As a consequence, both the entanglement generation and the Bell measurement circuit become highly accessible to optical implementations when one-qumode stabilizer states and one-qumode projection measurements onto stabilizer states are available (and these are available in the form of squeezed states and homodyne detections, see Chapters 2

and 4). In this sense, quantum teleportation also serves as the prime example to reveal the practical significance of the CV approaches.

In order to illustrate the analogy between the above protocol for finite-dimensional, DV quantum teleportation and that for infinite-dimensional, CV quantum teleportation, we may write the following decomposition for the CV case,

$$|\phi\rangle_{\text{in}} \otimes |\Psi(0,0)\rangle_{12} = \frac{1}{\pi} \int \mathrm{d}u\mathrm{d}v |\Psi(u,v)\rangle_{\text{in},1} \hat{U}_2^{\dagger}(u,v)|\phi\rangle_2 \ , \tag{1.111}$$

with the CV Bell states of Eq. (1.95) and the unitary transformations,

$$\hat{U}(u,v) = \int \mathrm{d}x \mathrm{e}^{2\mathrm{i}xv} |x\rangle\langle x-u| \ . \tag{1.112}$$

These unitaries are equivalent to WH shifts expressed by $X(u)$ and $Z(v)$. The CV protocol is then completely analogous to the DV case, except that the entangled state used in the CV case is an unphysical, unnormalizable state. Only with this idealization do we obtain perfect quantum state transfer similar to the qubit case, with no information gain by Alice through her Bell measurement.

In a physical qumode quantum teleportation protocol using properly normalized, finite-energy states, Alice does gain partial information and the quantum state transfer to Bob becomes imperfect. This will be one of the subjects of Chapter 4, including the discussion of several variations of optical CV quantum teleportation experiments.

1.7 Quantum Communication

The goal of quantum communication is the reliable transfer of arbitrary quantum states (drawn from an alphabet of states) between a sender, usually named Alice, and a receiver, Bob. More colloquially, we can say that quantum communication is "the art to transfer quantum states" [46]. This may then lead to various applications, some of which are already emerging as an existing technology such as the secure distribution of a classical key through quantum key distribution (QKD) [47–49]. Other applications appear farther away from realization such as the connection of spatially separated quantum computers for distributed quantum computing and a kind of quantum internet [50].

Related with the above concepts and applications are the following important lines of current research efforts:

- search for practical QKD protocols,
- security proofs for unconditionally secure QKD,
- long-distance quantum communication beyond 200 km.

Another, more traditional branch of quantum communication deals with the fundamental limits that quantum theory imposes on classical communication. We

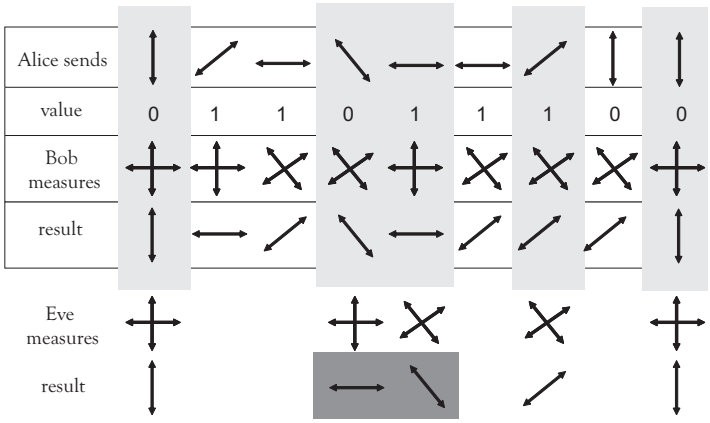

Figure 1.9 The concept of quantum key distribution [18]. Alice randomly prepares states from two non-orthogonal bases, for instance, corresponding to the qubit stabilizer states $\pm Z$ and $\pm X$, where the sign denotes the bit value 0 or 1. Bob, after receiving the states from Alice, randomly performs measurements in either basis. By postselecting those events where the bases coincide, correlated data between Alice and Bob will be obtained. In the presence of Eve, on average 25% of those otherwise correlated data would contain errors which can be detected by Alice and Bob on a subsample of their data.

shall get back to this quantum extension of classical information theory at the end of this section. The more recent approaches to quantum communication aim at the exploitation of nonclassical quantum features such as non-orthogonality and entanglement for quantum-enhanced communication. Let us briefly discuss the concepts behind QKD as an example.

1.7.1 Key Distribution

Quantum key distribution (QKD) [18, 20, 51] allows, in principle, for unconditionally secure communication. It relies upon the inability of a potential eavesdropper ("Eve") to discriminate non-orthogonal quantum states. Recall that Eve would be able to perfectly distinguish non-orthogonal states if she was able to produce copies of such states (Section 1.1). So no-cloning is a necessary requirement for quantum cryptography, and while perfect quantum cloning would prevent secure QKD, an approximate cloning attack performed by Eve may still be a threat to the security of a realistic QKD protocol, including imperfect channel transmissions.

In the BB84 protocol [18], Alice randomly prepares states from two non-orthogonal bases, for instance, corresponding to the qubit stabilizer states $\pm Z$ and $\pm X$ where the sign denotes the bit value zero or one (see Figure 1.9). Bob, after receiving the states from Alice, randomly performs measurements in either basis. By postselecting only those events where the bases coincide, correlated data between Alice and Bob will be obtained.

Now, Eve may, prior to Bob's measurements, intercept the communication between Alice and Bob and randomly pick her own basis in order to retrieve Alice's key values. However, only in half of the cases would Eve's basis coincide with that of Alice. As a consequence for those events where Eve's basis choice is wrong, she would have to pass on a state to Bob for which he obtains a bit value differing from Alice's bit value in half of the cases. Therefore, in this scenario, 25% of those otherwise correlated data would become contaminated with errors. Whenever Alice and Bob detect such a high error rate for a subsample of their data, they would abandon their protocol and start from scratch. More generally, the tolerable error rate depends on the quality of the quantum channel between Alice and Bob, and on the most general quantum operations that are available to Eve.

Note that in order to prevent Eve from pretending to be Bob and so from eventually sharing the key herself with Alice, Alice and Bob need to start with an initially shared key in order to utilize classical authentication techniques. The QKD protocol will then enable them to grow a larger key. Finally, they can use a sufficiently large key to exchange a message employing the well-known one-time pad.

The BB84 protocol as described so far is a so-called *prepare-and-measure* scheme. It does not directly depend on the physical distribution of entangled states; it relies upon preparing and measuring non-orthogonal quantum states. In fact, just any two non-orthogonal quantum states would suffice to do QKD [51]. As a consequence, instead of qubit states, qumode states may serve as well as a carrier for QKD. Especially, coherent states of light (see Chapter 2), forming an overcomplete, non-orthogonal set represent a convenient choice with regards to practical implementations. A scheme based on coherent states was already implemented experimentally [52].

In an *entanglement-based* QKD protocol [20], Alice and Bob would attempt to generate correlated data by distributing and measuring entangled pairs. In this case, one has to assume that Eve has total control over the whole three-party system – effectively an arbitrarily powerful Eve may distribute any tripartite state (see Chapter 3) among Alice, Bob, and herself. Now, whenever tracing over Eve's system (mimicking the situation where Eve corresponds to an untrusted, noncooperating third part or the inaccessible environmental degrees of freedom of an imperfect channel) leads to a separable state between Alice and Bob, they can no longer establish a secure key [19]. The reason for this is that the so-called intrinsic information (see later Section 1.7.3 for some words on classical information measures) for Alice and Bob provides an upper bound on the secure key rate [53] and it would strictly vanish for a separable, reduced state of Alice and Bob.

A conceptually very important observation now is that any prepare-and-measure scheme can also be rephrased such that the measured data for Alice and Bob (given by a joint probability distribution for their POVMs) can be used as a secure key provided that these data are inconsistent with a separable state for Alice and Bob [19]. The additional step for proving this is that in this case, the reduced density operator for Alice alone is known and controlled by Alice. It is basically given by the trace

over a bipartite source state of the form,

$$|\chi\rangle_{AB} = \sum_i \sqrt{p_i}|u_i\rangle_A \otimes |\psi_i\rangle_B \,, \tag{1.113}$$

with an orthonormal basis $\{|u_i\rangle\}$ and a non-orthogonal set of states $\{|\psi_i\rangle\}$ [54]. By measuring in the basis $\{|u_i\rangle\}$, Alice effectively prepares the non-orthogonal signal states $\{|\psi_i\rangle\}$, for instance, the BB84 states stabilized by $\pm Z$ and $\pm X$. However, still, when Eve has access to Bob's system, a reduced state for Alice and Bob which is separable leads to a vanishing intrinsic information and so no secure key is available.

The bottom line is that in any secure QKD protocol, Alice and Bob must share data that cannot be interpreted as coming from a separable state – the data have to come from an *effectively entangled* state.

When a certain alphabet of qumode states is used for QKD, for instance, the two non-orthogonal qumode states $|\psi_0\rangle$ and $|\psi_1\rangle$, the interpretation of the corresponding prepare-and-measure scheme in terms of effective entanglement leads to a very special manifestation of entanglement, namely, that between a qubit and a qumode in a kind of hybrid entangled state, $(|u_0\rangle_A \otimes |\psi_0\rangle_B + |u_1\rangle_A \otimes |\psi_1\rangle_B)/\sqrt{2}$. We shall get back to this notion of hybrid entanglement in Chapter 8. Further, it is useful to realize that the necessary precondition for secure QKD according to the theorem of [19], namely, the presence of (effective) entanglement, can be satisfied in the CV setting, in principle, for any channel losses: CV qumode entangled states always remain entangled, although their entanglement decays exponentially in the channel (see Chapters 2 and 3).

The preceding discussion highlights that entanglement (Section 1.5 and Chapter 3) is the *fundamental resource* for quantum communication, even when it is not directly used as a physical resource. Theoretical security proofs for unconditionally secure QKD, both for qubits [55] and for qumodes [56], are also most conveniently constructed with the help of entanglement distillation or quantum error correction (Chapter 5).

There are, of course, many quantum communication protocols where physical entangled states are used, the most prominent example of which is quantum teleportation (Section 1.6 and Chapter 4). In fact, quantum teleportation can be seen as the *fundamental protocol* for quantum communication. This becomes particularly clear when one attempts to extend quantum communication, including the QKD schemes described above, to large distances, where, for instance, a physical prepare-and-measure scheme over the entire channel distance would no longer be feasible. In this case, physical entangled states should be distributed over smaller channel segments and connected through teleportation. Eventually, quantum information can be teleported over the whole distance using the final, long-distance entangled pair (see Figure 1.10). Such an approach to long-distance quantum communication leads to the so-called quantum repeater which we shall discuss now.

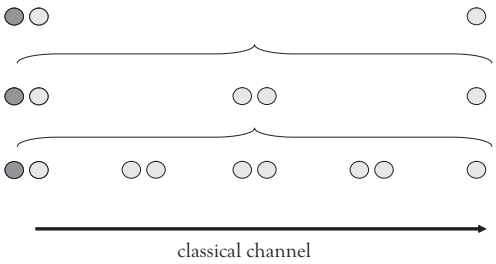

Figure 1.10 Transferring quantum information over large distances combining short-distance entanglement distribution, entanglement distillation, entanglement swapping, and quantum teleportation.

1.7.2 Repeaters and Relays

Light is an optimal information carrier for communication, and one may send quantum states encoded into a stream of single photons or a multi-photon pulse through an optical channel. However, quantum information encoded into fragile superposition states, for example, using photonic qubits or qumodes (Chapter 2), is very vulnerable against losses and other sources of excess noise along the channel such that the fidelity of the state transfer will exponentially decay with the length of the channel.

In long-distance, classical communication networks, signals that are gradually distorted during their propagation in a channel are repeatedly recreated through a chain of intermediate stations along the transmission line. For instance, optical pulses traveling through a glass fiber and being subject to photon loss can be reamplified at each repeater station. Such an amplification is impossible, when the signal carries quantum information. If a quantum bit is encoded into a single photon, its *unknown* quantum state cannot be copied along the line due to no-cloning; the photon must travel the entire distance with an exponentially decreasing probability to reach the end of the channel.

The solution to the problem of long-distance quantum communication is provided by the so-called quantum repeater [2, 3] (Figure 1.10). In this case, prior to the actual quantum-state communication, a supply of *known* quantum states, namely, standard entangled states, is generated and distributed among not too distant nodes of the channel. If a sufficient number of these imperfect entangled states are shared between the repeater stations, a combination of entanglement purification and swapping extends this shared entanglement over the entire channel. Through entanglement swapping [57] (Chapter 4), the entanglement of neighboring pairs is connected, gradually increasing the distance of the shared entanglement. The entanglement purification [22] (Chapter 5) enables one to distill (through local operations) a high-fidelity entangled pair from a larger number of low-fidelity entangled pairs, as they would emerge after a few rounds of entanglement swapping with imperfect entangled states and at the very beginning after the initial, imper-

fect entanglement generation and distribution between two neighboring repeater stations.

The essence of long-distance quantum communication as realized through the quantum repeater model [2, 3] can be summarized as follows: provided *sufficient local quantum memories* are available and *some form of quantum error detection* is applied, quantum communication over arbitrary distances is possible with an increase of (spatial or temporal) resources scaling only subexponentially with distance.

Note that the naive approach of dividing the total channel into several segments that are connected through quantum teleportation without incorporating any form of quantum error detection and without using quantum memories is not enough to render quantum communication efficient with regard to resource scaling. In this case, for instance, the probabilistic distribution of entangled pairs over the individual segments of the channel (Figure 1.10) must succeed at once. The number of pairs created over a total channel of length L per unit time interval (basically given by L_0/c with c, the speed of light in the channel and L_0, the length of each segment) is then proportional to

$$P_{\text{distr}}^{L/L_0} \times P_{\text{swap}}^{(L/L_0)-1}, \tag{1.114}$$

where P_{distr} is the success probability for obtaining an entangled pair in one segment, P_{swap} is the probability for a successful entanglement connection (swapping), L/L_0 is the number of segments, and so $(L/L_0)-1$ is the number of necessary swapping events. When either the distribution or the swapping is probabilistic,[27] $P_{\text{distr}} < 1$ or $P_{\text{swap}} < 1$, the pair creation rates will exponentially decay with the total distance L; even when, quite unrealistically, the initially generated pairs are perfectly entangled. Thus, in principle, if perfect local operations were available, the final pairs would have unit fidelities too with no need for any quantum error detection. This is the so-called *quantum relay*.[28]

Once perfect quantum memories are available, the exponential decay of the pair creation rate can be circumvented. For example, consider two neighboring segments. The time it takes in one segment to distribute a single pair is on average $(L_0/c)/P_{\text{distr}} \equiv T_0$. Now, a simultaneous distribution attempt in two segments will be successful in either one segment after approximately half that time period. The pair that is created first can then be stored in a quantum memory until the other segment has an entangled pair as well, after another waiting time of about T_0. Thus, after a time of roughly $3T_0/2$, two pairs will be present next to each other in the two neighboring segments [47] and one can proceed with the entanglement

27) Which is usually unavoidable, see the discussions on the postselected generation and swapping schemes for polarization-encoded DV photonic qubits (Chapters 3 and 4). However, using CV qumode entangled states, entanglement generation and distribution (Chapter 3) as well as entanglement swapping (Chapter 4) are deterministic. In this case, the problem is an exponentially decaying fidelity requiring efficient quantum error detection techniques, which are hard to obtain in the CV setting (Chapter 5).

28) Which, in the optical context (Chapter 2), may still help to enhance practicality of a scheme, for instance, in order to resolve single-photon signals against detector dark counts [47, 58–60].

swapping, with a total time of $(3T_0/2)/P_{\text{swap}} \equiv T_1$ to obtain one pair over double the elementary distance, $2L_0$.

In order to obtain two already swapped pairs (so each distributed over a distance of $2L_0$) next two each other, it will then take roughly a time of $3T_1/2$, and the corresponding next swapping step will lead to an entangled pair over distance $4L_0$ after a total average time of about $(3T_1/2)/P_{\text{swap}}$. Therefore, recursively, we end up having an average time of $(3/2)^n T_0/P_{\text{swap}}^n$, with $L/L_0 = 2^n$, for obtaining one pair over the total distance L. Compared with Eq. (1.114), this translates into a rate (number or pairs per time unit) proportional to

$$P_{\text{distr}}\left(\frac{2}{3}P_{\text{swap}}\right)^n = P_{\text{distr}}\left(\frac{2}{3}P_{\text{swap}}\right)^{\log_2(L/L_0)} \propto (L/L_0)^{\log_2\left(\frac{2}{3}P_{\text{swap}}\right)} . \tag{1.115}$$

This is the *quantum repeater* in its simplest manifestation (using ideal memories and without purification), achieving a rate that scales only polynomially with the total distance L. The above approximation on the rates is good for small probabilities P_{distr} and P_{swap}. In the limit of unit P_{distr} and P_{swap}, of course, there is no need for memories and the relay performs as well as the repeater.

1.7.3 Shannon Theory

Prior to those proposals for the above-mentioned applications through which Alice and Bob take advantage of using quantum resources, earlier treatments of quantum communication aimed at deriving the fundamental limits imposed by quantum theory on the classical communication by means of quantum signals. A very famous result in this context is that from Holevo [61], sometimes referred to as the fundamental law of quantum communication [62]. It places an upper bound, the so-called *Holevo bound*, on the mutual information of Alice and Bob,

$$I(\text{A}:\text{B}) \leq S(\hat{\rho}) - \sum_a p_a S(\hat{\rho}_a) \leq S(\hat{\rho}) , \tag{1.116}$$

where $S(\hat{\rho})$ is the von Neumann entropy from Eq. (1.22), $\hat{\rho}$ is the mean channel state, and $\hat{\rho}_a$ are the signal states with a priori probabilities p_a. In this relation, equality is attained when Alice sends pure orthogonal signal states.[29)]

29) In classical information theory [63], the information content of a message depends on the probabilities p_a for the occurrence of a letter drawn from an alphabet A. The less frequent a letter occurs, the more information it carries. The average information content per letter is then $I(\text{A}) = -\sum_a p_a \log_2 p_a$ in units of bits. For two parties, a sender and a receiver corresponding to two alphabets A and B, the information in the communication channel is quantified by the so-called mutual information $I(\text{A}:\text{B}) = I(\text{A}) + I(\text{B}) - I(\text{A},\text{B})$. Here, the sum $I(\text{A}) + I(\text{B})$ contains joint information in both alphabets, double counting the part which is mutual to both alphabets. By subtracting the actual expression for the joint information $I(\text{A},\text{B}) = -\sum_{ab} p_{ab} \log_2 p_{ab}$, where the joint alphabet AB has letters with probabilities p_{ab}, the mutual information is obtained.

Even assuming an ideal (noiseless) channel, any attempt by Bob to retrieve the classical information sent from Alice introduces noise when the signal states are non-orthogonal. In fact, there is an optimal, *accessible information*, depending on the measurement strategy that Bob employs. The most general measurement strategy is described by a POVM $\{\hat{E}_b\}$ with $\sum_b \hat{E}_b = \mathbb{1}$. The accessible information is typically hard to compute.

When Bob is presented with a state $\hat{\rho}_a$ representing letter a from Alice's alphabet, he will instead find letter b from his own alphabet with a conditional probability given by $p_{b|a} = p_{ab}/p_a = \mathrm{Tr}(\hat{E}_b\hat{\rho}_a)$. From this, one may usually compute the mutual information $I(\mathrm{A}:\mathrm{B}) = I(\mathrm{A}) + I(\mathrm{B}) - I(\mathrm{A},\mathrm{B}) = \sum_{ab} p_{ab}\log_2(p_{ab}/(p_a p_b))$.

Now, the information-theoretic condition for secure communication, that is, for enabling extraction of a secure key using privacy amplification [64] and error correction techniques [65], is given by the following relation for the mutual information between the three participants, Alice, Bob, and Eve,

$$I(\mathrm{A}:\mathrm{B}) > \max\{I(\mathrm{A}:\mathrm{E}),\, I(\mathrm{E}:\mathrm{B})\}\,. \tag{1.117}$$

In other words, the mutual information between Alice and Bob, $I(\mathrm{A}:\mathrm{B})$, must exceed the information that either of them shares with Eve.[30)]

Finally, there is another entanglement-based quantum communication scheme which is kind of complementary to quantum teleportation. In this so-called *superdense coding* [67], the roles of the classical and quantum channels are interchanged relative to those in quantum teleportation. Instead of reliably transferring quantum information through a classical channel using entanglement as in quantum teleportation, in a superdense coding scheme, the amount of classical information transmitted from Alice to Bob is increased when Alice sends quantum information, namely, her half of an entangled state shared with Bob through a quantum channel to Bob.

For instance, two bits of classical information can be conveyed by sending just one qubit. Superdense coding relies upon the remarkable feature that, for instance, all four two-qubit Bell states in Eq. (1.93) can be transformed into each other through local Pauli operations. Thus, Alice, similar to what Bob does in quantum teleportation, applies one of four possible operations to her half of a shared Bell pair, thereby encoding two classical bits. Finally, Bob, similar to what Alice does in quantum teleportation, performs a Bell measurement on his half of the entangled pair together with Alice's half to retrieve the bit values. Therefore, Alice has to send her half through a quantum channel to Bob. In general, superdense coding aims at increasing the capacity (the maximal mutual information) of a communication channel using entanglement.

30) In a CV QKD scheme based upon coherent-state signals, initially, for losses in the channel greater than 3 dB, the condition $I(\mathrm{A}:\mathrm{B}) > I(\mathrm{A}:\mathrm{E})$ is always violated using the classical standard techniques. However, there are various methods to beat the 3 dB loss limit. One method is using, in addition to the classical techniques, entanglement distillation and quantum memories, which are both rather demanding in a realistic implementation (see Chapter 5). Alternative approaches include a "reverse reconciliation" protocol [52] with Alice guessing what was received by Bob instead of Bob guessing what was sent by Alice, and another method based upon postselection [66].

Like quantum teleportation, superdense coding relies on preshared entanglement. Thus, superdense coding is still in agreement with Holevo's rule that, at most, one classical bit can be transmitted by sending one qubit because, taking into account Bob's half of the entangled state transmitted to him prior to the actual communication ("offline"), in total, two qubits must be sent to Bob. This entanglement-based superdense coding must not be confused with other "quantum coding" schemes such as those introduced by Schumacher [68]. The Schumacher protocols enable Alice and Bob to approach the Holevo bound even for non-orthogonal or mixed signal states through appropriate encoding of the classical information into these states. This type of quantum coding, including the results of Holevo, may be considered as part of an extension of Shannon's classical information theory [69] to the quantum realm [4, 5].

Superdense coding, like quantum teleportation, can be similarly translated from qubits to qumodes in a CV superdense coding protocol [70, 71].[31)]

Entanglement as a resource and quantum teleportation as a protocol are naturally associated with quantum communication, as we attempted to illustrate in this section. However, both are just as fundamental for quantum computation. This subject is discussed in the next section and in more detail in Chapters 6 and 7.

1.8 Quantum Computation

The ultimate real-world application of quantum theory would be the quantum computer. By processing quantum information encoded in a superposition of all possible classical inputs, a quantum computer is capable of simultaneously computing each output value for every possible input – a notion called quantum parallelism.

This field of quantum computation was initiated through Deutsch's work on universal quantum computation from 1985 [72], based on earlier ideas of Feynman [73]. Today, this field is divided into various subfields associated with complementary research efforts such as

- the search for quantum algorithms,
- proof-of-principle demonstrations of small-scale quantum circuits, and
- proofs of universality, fault-tolerance, and scalability.

Initially, quantum algorithms were only of interest to specialists in the field. However, when Shor discovered in 1994 how to factorize numbers into prime numbers significantly faster than classically (in polynomial rather than exponential time) by using a quantum algorithm [74], the possibility of realizing a quantum computer became a security issue. Codes such as the famous RSA encryption, considered ef-

31) By utilizing the idealized, unphysical two-qumode entangled states of Eq. (1.95), similar to the qubit case, CV superdense coding would approach, in this idealized limit, a capacity twice as big as that theoretically attainable in the absence of entanglement [71].

fectively secure based upon a mathematically unproven complexity assumption,[32] became suddenly vulnerable; no longer due to the nonexistence of a mathematical proof, but rather because of a new type of computer whose existence is permitted by the laws of physics.

Ironically, the solution to the problem of unconditional security was also offered by quantum theory in form of quantum key distribution, as discussed in the preceding section. Even a quantum computer cannot render quantum cryptography insecure.

The probably most well-known quantum algorithms, besides Shor's, are Grover's algorithm of 1996 for searching a database [75] and the Deutsch–Jozsa algorithm of 1992 [76] which inspired the works of Shor and Grover. All these ideas have in common that they illustrate the potential of quantum information processing to provide solutions for problems that are defined in purely classical terms and (most likely) cannot be solved efficiently through classical information processing. Similar to what quantum cryptography achieves for classical communication, quantum algorithmic offers potentially better ways to perform certain classical computations; even though at intermediate stages, both the communications and computations would rely upon quantum resources and processing.

There are basically two main categories of quantum algorithms, namely, those based upon the quantum Fourier transform corresponding to general implementations of the so-called hidden subgroup problem and quantum search algorithms [5, 77]. The Shor and Deutsch–Josza algorithms belong to the former category, while the latter one consists of variations of the Grover algorithm. An example of a class of algorithms that fit in neither of these two categories is quantum simulation. In this case, the quantum computation is used to simulate a quantum system, as it was originally envisaged by Feynman [73]. The notion of simulating a Hamiltonian is the most convenient starting point for defining quantum computation over continuous quantum variables on qumodes. This will be discussed in Section 1.8.2.

Typically, however, a model of quantum computation or a specific algorithm will be implemented on qubits. In this case, an algorithm for N qubits, computed in a 2^N-dimensional Hilbert space, will convert initially unentangled qubit product states at some stages of the computation into a multi-party entangled state of many qubits. It was already mentioned in Section 1.1 that entanglement can be a *sufficient* resource for quantum computation, and the engineering and exploitation or consumption of (multi-party) entangled states for quantum information processing will be the central topic of the remainder of this book. However, we may as well ask: is entanglement also a *necessary* resource for quantum computation?

Indeed, the answer to this question is neither a clear yes nor a clear no. First of all, we may simply redefine the total physical system and replace the tensor-product Hilbert space of the N qubits, $\otimes^N \mathcal{H}_2$ (where $\mathcal{H}_k$ denotes a Hilbert space of dimension k), by an equivalent (isomorphic) Hilbert space for a single $d = 2^N$-level qudit system, $\mathcal{H}_{2^N}$. Eventually, we may argue that it is not some form

32) That is, assuming that these codes are too hard to break by a classical computer. For instance, there is no classical algorithm known to factorize numbers in an efficient amount of time to break the RSA encryption.

of multi-party (multi-particle) entanglement, but rather the interference effect in complicated superposition states of a single qudit (particle) which is responsible for a quantum computational speed-up [78, 79]. However, should we always refer to a single-particle state such as

$$\frac{1}{\sqrt{2}}\left(|10\rangle + |01\rangle\right) \equiv \frac{1}{\sqrt{2}}\left(|\bar{0}\rangle + |\bar{1}\rangle\right) \tag{1.118}$$

as an unentangled state? More specifically, one physical manifestation of this kind of state would be a path-entangled state of two single-rail qubits, obtainable by splitting a single-photon wave-packet at a beam splitter (see Chapters 2 and 3; Figure 3.2), where $|10\rangle \equiv |1\rangle_1 \otimes |0\rangle_2$ represents a possible state of the two spatial modes one and two at the two output ports of the beam splitter. Alternatively, this state may as well be interpreted as a simple one-qubit $+X$-stabilizer state in polarization encoding (see Chapter 2), where this time, $|10\rangle \equiv |1\rangle_H \otimes |0\rangle_V \equiv |H\rangle \equiv |\bar{0}\rangle$ stands for a possible state of two orthogonal polarization modes; in this case, the horizontally polarized mode H is excited by a photon, while the vertically polarized mode V is in the vacuum state. In either case, the single-photon system lives in a (sub)space of two optical modes.

Regardless of whether the state in Eq. (1.118) is considered entangled or not,[33] extending the basis from two levels to 2^N levels would clearly provide enough (Hilbert) space to do quantum computation; either on a single 2^N-level system or on N two-level systems.[34] However, there is a crucial difference in terms of physical resources needed for realizing the quantum computations. For the N-qubit tensor-product-based quantum computer, N physical qubits (for instance, N polarization-encoded photons) will be needed, so that the physical resources scale linearly with the number of qubits. In contrast, a 2^N-level quantum computation in which, by definition, the multi-*party* entangled states are disguised as single-particle superposition states will always be at the expense of some exponential overhead in terms of physical resources (for instance, exponentially many optical elements for transforming 2^N optical modes or an exponentially increasing measurement precision). One may then argue that it is actually the multi-*particle* entanglement in

33) For a nice discussion on this issue, see [80–82]. In [80], a simple argument explains why a single-particle two-mode state like that in Eq. (1.118) should be considered entangled, provided the two modes are spatially separated, which is the case for path-encoding, but not for polarization encoding. The two modes of the path-entangled state may then be distributed among two spatially separated two-level atoms and map the two atoms onto the clearly entangled two-particle state $\left(|eg\rangle + |ge\rangle\right)/\sqrt{2}$ through *local* atom-light interactions (here, the initial atomic ground states $|g\rangle$ would only become excited, $|e\rangle$, provided a photon is in the optical mode that interacts with the respective atom). Most importantly, in an optical state like that in Eq. (1.118), the two field modes are entangled and not the photon with the vacuum. Similarly, a low-squeezing two-mode squeezed state, $|00\rangle + r|11\rangle$ with $r \ll 1$, has a small amount of entanglement which is not between the two photons and the vacuum, but rather between the two qumodes (see Chapters 2 and 3). Multi-party entanglement between many qumodes will be introduced in Chapter 3.

34) An example for the former type of quantum computation will be presented in Section 2.8 using 2^N optical modes for a single photon and linear optical elements.

the multi-qubit tensor-product approach that enables one to avoid the exponential overhead [78, 79].[35)]

Compared to discrete qubit encodings, qumodes naturally offer any desirable amount of space to process quantum information. However, it is not obvious whether and how such analog quantum information can be exploited. Unphysical qumode stabilizer states such as the position eigenstates $|x\rangle$ are not available as a computational basis. Instead, Gaussian states such as squeezed states (see Chapter 2) would have to be employed. These physical states, though producible in highly efficient ways, can then only be measured at a finite resolution or in a probabilistic fashion. For example, in order to implement a CV version of the Deutsch–Josza algorithm, there would be an uncertainty-based trade-off between a position x-encoding and a p-measurement resolution; thus, preventing a computational speed-up [83]. In this case, the exponential overhead can be thought of as the requirement of an infinite measurement precision or the preparation of a quantum state with infinite energy. In many cases, it is not even clear how to recast a given computational problem and the corresponding quantum algorithm in the CV setting.

Besides quantum algorithmic, as listed at the beginning of this section, the two other main directions of current research on quantum computation are experimental demonstrations of small-scale quantum circuits, and theoretical proofs of universal (potentially scalable and fault-tolerant) models and approaches for quantum computation. The former topic will be addressed to a great extent in the remainder of this book. Universality, in the context of both qubit and qumode encodings and processing, shall be considered in the section after next. Now, we briefly introduce two equivalent, but conceptually very different models for quantum computation.

1.8.1 Models

There are various models to describe quantum computations of which the most common one is the *circuit* model [5]. It uses sequences of reversible, unitary gates in order to transform an input quantum state into any desired output quantum state. Although, finally, the output state must be measured for read-out, the largest part of the computation is conducted in a measurement-free fashion. The circuit model provides a natural language to describe quantum algorithms. Important notions such as universality can be conveniently expressed in the circuit model, as we will discuss in the next section.

A conceptually very different model for quantum computation is that of *measurement-based* quantum computing. As opposed to the standard circuit model, in measurement-based quantum computation, the quantum gates are embedded into an entangled state prior to the actual computation – the gates are performed "offline" on the entangled-state resource. This turns out to be of great importance

35) However, there are specific examples of quantum algorithms which neither require multi-particle entanglement nor depend on an exponential overhead of spatial or temporal resources [79].

for experimental realizations because even highly probabilistic gate implementations can be useful, provided they are applied to the off-line state and a successfully transformed resource state is kept intact until its consumption during the online computation. In order to render measurement-based quantum computation (near-)deterministic despite the randomness induced by the measurements, typically, some form of measurement-dependent feedforward operations will be needed. Since an online, measurement-based computation is no longer reversible, such approaches to quantum computation are sometimes referred to as one-way models.

There are various specifications to measurement-based quantum computing. One approach is based upon a generalization of standard quantum teleportation [84]. In the qubit case, a single-qubit (multi-qubit) state is then teleported through a modified, unitarily transformed two-qubit Bell (multi-qubit entangled) state such that the desired gate operation is affected on the output state. This extension of the usual communication scenario for quantum teleportation with an ideally exact state transfer from Alice to Bob to gate teleportations for computation with a teleported state unitarily transformed depending on the modified resource state illustrates the general importance of quantum teleportation. Gate teleportation will be further discussed in Chapter 6.

In the standard version of gate teleportation, a *nonlocal* two-party Bell measurement projecting onto an entangled-state basis is still needed, which can be a severe complication for experimental implementations. However, there is an ultimate realization of measurement-based quantum computing in which all entangling operations are performed offline and for the actual computation, only *local* measurements are needed. In such a cluster-based one-way quantum computation [1], a multi-party entangled state is first prepared offline and the actual computation is then conducted solely through single-party projection measurements on the individual nodes of that resource state – the *cluster state*. By choosing appropriate measurement bases in each step, possibly depending on earlier measurement outcomes, any unitary gate can be applied to an input state which typically becomes part of the cluster at the beginning of the computation, see Figure 1.11.

The essence of cluster computation can be summarized as follows: the cluster state is *independent of the computation*; universality is achieved through *choice of*

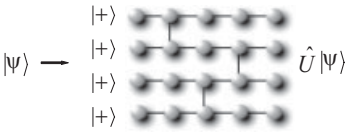

Figure 1.11 One-way cluster computation for qubits. Certain single-qubit stabilizer states become pairwise entangled to form a multi-qubit cluster state (see Section 3.1). Local projection measurements on the individual qubits, potentially including feedforward with a measurement order going from left to right, are then enough to realize (universal) quantum computation. A multi-qubit input state $|\psi\rangle$ attached to the left end of the cluster could, in principle, be (universally) processed with the output state occurring at the right end of the cluster. The vertical edges allow for two-qubit gates (more details can be found in Section 7.1).

measurement bases. A more detailed discussion of cluster computations on qubits and qumodes can be found in Chapter 7. Next, we turn to the notion of universality.

1.8.2 Universality

The two models of quantum computation as introduced in the preceding section, the circuit and the one-way model, are both known to be universal and in this sense, they can be considered equivalent models. So what does universality mean? Usually, universality is associated with the ability to apply an arbitrary unitary operator or matrix upon a given signal state, for instance, to an initial multi-qubit product state. Under certain circumstances, in particular, in realistic situations including experimental imperfections and errors, an exact implementation of a unitary matrix is not achievable and hence the notion of approximate, asymptotic universality becomes important. In this case, a universal set of elementary gates is considered that allows for approaching any given unitary gate at any desired precision through elementary-gate concatenations.

From a slightly different point of view, one may also think of universality as the ability to simulate any given Hamiltonian. This Hamiltonian approach to universality turns out to be particularly useful for qumode systems where the available transformations are naturally given in terms of interaction Hamiltonians which are polynomials of the bosonic mode operators. One possible way to understand this approach is to consider the following decomposition,[36)]

$$\mathrm{e}^{\mathrm{i}H_2 t}\mathrm{e}^{\mathrm{i}H_1 t}\mathrm{e}^{-\mathrm{i}H_2 t}\mathrm{e}^{-\mathrm{i}H_1 t} = \mathrm{e}^{[H_1,H_2]t^2} + \mathrm{O}(t^3)\,. \tag{1.119}$$

Thus, by applying the Hamiltonians H_1 and H_2 for some short time, we can also approximately implement the Hamiltonian $-\mathrm{i}[H_1, H_2]$, provided the interaction times are sufficiently short. Once the simplest commutator can be simulated, higher-order (nested) commutators are also available through further concatenation. Provided nested commutation of a set of elementary Hamiltonians allows one to generate an arbitrary Hamiltonian, the elementary set can be referred to as a universal set. This type of asymptotic, approximate model for universal quantum computation is applicable to both DV qubit [85] and CV qumode [86] systems on their own as well as to hybrid systems combining qubits and qumodes (see Chapter 8).

1.8.2.1 Qubits

Consider a single qubit and recall the discussion on single-qubit unitaries in Section 1.3.1. In the box at the end of Section 1.3.2, it is shown that an arbitrary single-qubit unitary can be expressed as $\mathrm{e}^{\mathrm{i}\phi}\,\hat{R}_s(\theta)$, depending on four real parameters

36) Using $\mathrm{e}^{\mathrm{A}}\mathrm{e}^{\mathrm{B}} = \mathrm{e}^{\mathrm{A}+\mathrm{B}}\mathrm{e}^{[\mathrm{A},\mathrm{B}]/2} + \mathrm{O}([\mathrm{A},[\mathrm{A},\mathrm{B}]],[[\mathrm{A},\mathrm{B}],\mathrm{B}])$ and so $\mathrm{e}^{\pm\mathrm{i}H_2 t}\mathrm{e}^{\pm\mathrm{i}H_1 t} = \mathrm{e}^{\pm\mathrm{i}(H_1+H_2)t}\mathrm{e}^{-[H_2,H_1]t^2/2} + \mathrm{O}(t^3)$, which is one of the well-known Baker–Campbell–Hausdorff (BCH) formulas, also commonly used in quantum optics (see Chapter 2). Here and in Eq. (1.119), we omitted the operator hats on the Hamiltonians.

determining ϕ, θ, and the real three-dimensional unit vector $\boldsymbol{s}$. Now, we can decompose this arbitrary rotation into a sequence of rotations around two fixed axes, for instance, the Z and Y axes,

$$e^{i\phi}\,\hat{R}_Z(\alpha)\,\hat{R}_Y(\beta)\,\hat{R}_Z(\gamma) = e^{i\phi}\,Z_\alpha\,Y_\beta\,Z_\gamma\ , \tag{1.120}$$

using the definitions given after Eq. (1.60), with real parameters ϕ, α, β, and γ. This can be easily seen by parameterizing an arbitrary, unitary 2×2 matrix with orthonormal rows and columns and decomposing it into a product of matrices [5].

From the preceding discussion, we learn that the set $\{Z_\theta, Y_{\theta'}\}$ represents a universal set for single-qubit unitaries; any single-qubit unitary can be constructed from a small sequence of Z and Y rotations. Moreover, the ability to perform these rotations precisely with angles α, β, and γ would mean that the set $\{Z_\theta, Y_{\theta'}\}$ allows for realizing any single-qubit unitary *exactly*. It can then be shown [5] that arbitrary unitaries in a multi-qubit space can be exactly realized through this universal set for single-qubit unitaries, together with one fixed two-qubit entangling gate such as the CNOT gate (see below). Hence, the set $\{Z_\theta, Y_{\theta'}\}$ supplemented by, for instance, the CNOT gate is universal for quantum computation in finite dimensions.

So why would we have to consider asymptotic, approximate realizations of unitaries or Hamiltonians as, for example, described by Eq. (1.119)? The problem with the set $\{Z_\theta, Y_{\theta'}\}$ is that it is continuous and so an arbitrary single-qubit rotation requires infinite precision for every rotation. This is hard to realize, especially in an error-resistant fashion. Therefore, it is useful to define a discrete, *finite* set of fixed elementary rotations which then can no longer achieve any multi-qubit unitary exactly as the whole set of unitary gates is continuous, but instead in an approximate fashion at arbitrary precision. In order to be efficient, a sufficiently good approximation must not require an exponential number of elementary gate applications.[37)]

A convenient universal set of gates is given by [5]

$$\{H, Z_{\pi/2}, Z_{\pi/4}, C_Z\}\ . \tag{1.121}$$

Here, H is the Hadamard gate, $H|k\rangle = (|0\rangle + (-1)^k|1\rangle)/\sqrt{2}$, needed in order to switch from gates diagonal in Z to gates diagonal in X. The two-qubit gate C_Z acts as an entangling gate, with

$$|k\rangle \otimes |l\rangle \to (-1)^{kl}|k\rangle \otimes |l\rangle\ , \quad k, l = 0, 1\ . \tag{1.122}$$

For convenience, we repeat the definition $Z_\theta \equiv e^{-i\theta Z/2}$ for a single-qubit rotation about the Z-axis by an angle θ with the computational Pauli operator Z acting as $Z|k\rangle = (-1)^k|k\rangle$; the conjugate Pauli operator X obtainable from Z through Hadamard describes bit flip operations, $X|k\rangle = |k \oplus 1\rangle$. Note that removing the

37) Indeed, there is the important issue here as to whether the number of elementary gate operations for simulating a given multi-qubit unitary scales subexponentially with the size of the exact circuit for any desired accuracy. Many multi-qubit unitaries cannot be efficiently simulated [5].

38) However, removing $Z_{\pi/2}$ from the elementary gate set would give the smaller set $\{H, Z_{\pi/4}, C_Z\}$ which is still universal, as we have $Z_{\pi/4}Z_{\pi/4} = Z_{\pi/2}$.

gate $Z_{\pi/4}$ from the elementary gate set means that only the Clifford unitaries (Section 1.3.1) can be realized, which are known to be insufficient for a quantum computational speed-up over classical computation.[38] For both universality and speed-up when computing with stabilizer states such as $|+\rangle^{\otimes N}$, the non-Clifford phase gate $Z_{\pi/4}$ must be included; otherwise, if only using the Clifford set $\{H, Z_{\pi/2}, C_Z\}$, the stabilizer states remain stabilizer states at all times since Pauli operators are only mapped back onto Pauli operators, see Eqs. (1.64) and (1.65). Obviously, this no longer allows for universality including universal state preparations. However, why does it also prevent a speed-up compared to classical computations?

We know that a single-qubit Pauli operator is Clifford-transformed into another Pauli operator. Hence, the evolution of the ith N-qubit stabilizer generator[39] corresponding to an N-party tensor product of Pauli operators, $g_i = X_{i1} \otimes X_{i2} \otimes \ldots X_{iN}$, is specified through $\sim N$ parameters. Here, X_{ik} can be any one of the single-qubit Pauli operators or the unity operator for the corresponding slot, including a sign choice $\pm$, with $k = 1, 2, \ldots, N$. Therefore, one can keep track of the evolution of the whole state by calculating the new stabilizer generators for every $i = 1, 2, \ldots, N$. As a result, $\sim N^2$ parameters have to be calculated at every step of the evolution, which can be done efficiently using a classical computer. The crucial element here is that during the entire Clifford evolution, every N-qubit stabilizer state is uniquely determined through N stabilizer generators $\langle g_1, g_2, \ldots, g_N\rangle$, even though the state's stabilizer group has 2^N elements.

In general, any quantum computation solely using Pauli and Clifford gates (which include the Hadamard and the C_Z gates) on stabilizer states, measurements in a Pauli basis, and classical feedforward can be efficiently simulated by a classical computer. This is the so-called *Gottesmann–Knill theorem*.

Before we turn our attention to universal sets for qumodes, we give a few additions to the preceding discussion. A more commonly used two-qubit entangling gate is the CNOT gate acting on two computational basis ($\pm Z$ stabilizer) states as

$$|k\rangle \otimes |l\rangle \rightarrow |k\rangle \otimes |l \oplus k\rangle \,, \tag{1.123}$$

where, here again, $\oplus$ denotes addition modulo 2. The CNOT gate can be obtained from the C_Z gate through local Hadamards,

$$(\mathbb{1} \otimes H) C_Z (\mathbb{1} \otimes H) = \mathrm{CNOT} \,. \tag{1.124}$$

We have used the CNOT gate already in the circuit of qubit quantum teleportation of Figure 1.8, illustrating the usual convention for drawing this particular two-qubit entangling gate.

While the Clifford gate $Z_{\pi/2}$ maps stabilizer states back onto stabilizer states, for the non-Clifford gate $Z_{\pi/4}$, we obtain non-stabilizer states. In this case, for instance, instead of Eq. (1.64), we have now

$$\begin{aligned} Z_{\pi/4}|+\rangle &= \left(\mathrm{e}^{-\mathrm{i}\pi/8}|0\rangle + \mathrm{e}^{+\mathrm{i}\pi/8}|1\rangle\right)/\sqrt{2} \\ &= \mathrm{e}^{-\mathrm{i}\pi/8}\left(|0\rangle + \mathrm{e}^{+\mathrm{i}\pi/4}|1\rangle\right)/\sqrt{2} \,. \end{aligned} \tag{1.125}$$

39) For a definition of stabilizers, see the discussion and the box in Section 1.9.

The resulting non-stabilizer state $(|0\rangle + e^{+i\pi/4}|1\rangle)/\sqrt{2}$ is sometimes referred to as the "magic state" [87]. Here, the Heisenberg evolution of the stabilizer X under the non-Clifford $\pi/8$-phase gate $Z_{\pi/4}$, $Z_{\pi/4}^{\dagger} X Z_{\pi/4} = 1/\sqrt{2}(X - Y)$, using Eq. (1.61), no longer gives a Pauli operator.

1.8.2.2 **Qumodes**

Consider now a single qumode and recall the discussion on single-qumode unitaries in Section 1.3.2. An arbitrary single-qumode unitary can be written as $\hat{U} = e^{-it\,H(\hat{a},\hat{a}^{\dagger})}$, with a general Hamiltonian $H(\hat{a}, \hat{a}^{\dagger})$ which is an arbitrary polynomial of the mode operators. Decomposing such a general Hamiltonian evolution into a set of elementary evolutions is a difficult task. In fact, for polynomials of arbitrary order in the mode operators, when the unitary on the qumode becomes a non-Clifford unitary, the Hamiltonian simulation will be, in general, only approximate and asymptotic, as expressed, for instance, by Eq. (1.119).

However, in the case of a single-qumode quadratic Hamiltonian corresponding to a Clifford unitary on the qumode, an *exact* decomposition similar to that in Eq. (1.120) is possible,[40] consisting of single-mode position-squeezers $\hat{S}(r)$ and phase rotations $\hat{R}(\theta)$ [recall the definitions in Section 1.3.2 and see Eq. (2.52) through Eq. (2.56)],

$$\hat{R}(\phi)\,\hat{S}(r)\,\hat{R}(\phi') \,. \tag{1.126}$$

More precisely, this decomposition only represents an arbitrary Clifford transformation up to displacements in phase space.[41] Therefore, the set $\{X(s), \hat{R}(\theta), \hat{S}(r)\}$, with the real parameters s, θ, and r, where we added the position-shift WH operator $X(s)$, is universal for arbitrary single-qumode Clifford unitaries (or, equivalently, Gaussian unitaries, see Chapter 2).

The three real parameters in Eq. (1.126) correspond to the three degrees of freedom needed for an arbitrary symplectic transformation on a single qumode. This decomposition can be obtained through Bloch–Messiah reduction [89] and generalized to an arbitrary number of qumodes (see Chapter 2). Note that the single-qumode Clifford set $\{X(s), \hat{R}(\theta), \hat{S}(r)\}$, though consisting of a finite number of elementary gates, is continuous, similar to the universal single-qubit set $\{Z_{\theta}, Y_{\theta'}\}$. Therefore, again, an *exact* realization of a single-qumode Clifford unitary would require infinite precision for implementing the parameters s, θ, and r, which correspond to effective interaction and free evolution times in the quantum optical

40) Note that there are also exceptions of cubic or higher-order Hamiltonians which are exactly decomposable into lower-order Hamiltonians. For instance, $e^{-i\kappa\hat{x}^3} e^{it\hat{p}^2} e^{i\kappa\hat{x}^3} = e^{it(\hat{p}+3\kappa\hat{x}^2/2)^2}$, where the right-hand side has a fourth-order Hamiltonian, while the left-hand side only has second and cubic orders [88].

41) The qumode Clifford group is a group whose generators are polynomials up to quadratic order in position $\hat{x}$ and momentum $\hat{p}$. Its group elements correspond to the unitary Gaussian transformations (see Chapter 2). For the general case of N qumodes, the Clifford group $\mathrm{Cl}(N)$ is a semidirect product of the symplectic group and the WH group, $\mathrm{Cl}(N) = \mathrm{Sp}(2N, \mathbb{R}) \ltimes \mathrm{WH}(N)$. According to our definition of the Clifford group in Eq. (1.69), the group $\mathrm{WH}(N)$ is a homogeneous space under the adjoint action of $\mathrm{Cl}(N)$, and one can construct a group representation of $\mathrm{Cl}(N)$ on the vector space of the Lie algebra $\mathrm{wh}(N)$.

context. Rather than attempting to get rid of this type of infiniteness, the purpose of constructing a *universal* single-qumode set (including non-Clifford unitaries) is primarily to simulate Hamiltonians of *arbitrary* order while still using a *finite* set of gates. As opposed to an exact Clifford simulation expressed by the symplectic transformation in Eq. (1.126) plus an additional complex phase-space displacement,[42] where each elementary gate may have arbitrary strength, the universal simulation is no longer possible without asymptotic concatenations like those in Eq. (1.119), requiring near-unity gates for each individual step.

Once arbitrary single-qumode Hamiltonians are available (in the asymptotic sense), it can be shown that, similar to the qubit case, arbitrary multi-qumode unitaries can be realized through the corresponding universal set for single-qumode unitaries, together with one fixed two-qumode Clifford gate [86, 90]. A two-qumode gate serving this purpose is the Clifford C_Z gate used below. Since the C_Z gate itself can be decomposed into a circuit of two two-qumode beam splitters and two single-qumode squeezers [89], the only entangling interactions needed for universal multi-qumode processing are provided by passive beam splitting transformations (see Chapter 2 for more details).

As a finite, elementary gate set for asymptotic simulations of arbitrary multi-qumode Hamiltonians, one may choose [90]

$$\{F, Z(s), D_2(t), D_3(\kappa), C_Z\}\,, \tag{1.127}$$

with $s, t, \kappa \in \mathbb{R}$. Now, F represents the Fourier transform operator that maps between the position and momentum basis states, $F|x\rangle_x = |x\rangle_p$. It is needed in order to switch from gates diagonal in $\hat{x}$ to gates diagonal in $\hat{p}$ since all the remaining gates are chosen to be diagonal in $\hat{x}$. The entangling gate C_Z is an x-controlled p-displacement, $C_Z = \exp(2\mathrm{i}\hat{x}_1 \otimes \hat{x}_2) = Z_1(\hat{x}_2) = Z_2(\hat{x}_1)$, with

$$C_Z|x\rangle_x|p\rangle_p = |x\rangle_x|p + x\rangle_p\,, \tag{1.128}$$

or, $C_Z^\dagger \hat{x}_{1,2} C_Z = \hat{x}_{1,2}$, $C_Z^\dagger \hat{p}_{1,2} C_Z = \hat{p}_{1,2} + \hat{x}_{2,1}$. The other $\hat{x}$-diagonal gates are the WH momentum shift operator, $Z(s) = \exp(2\mathrm{i}s\hat{x})$ with $Z(s)|p\rangle_p = |p + s\rangle_p$, and the phase gates $D_k(t) = \exp(\mathrm{i}t\hat{x}^k)$. The quadratic phase gate ($k = 2$) incorporates single-qumode squeezing (together with a rotation) and is sufficient in order to exactly simulate any multi-qumode Clifford (Gaussian) transformation (together with F, $Z(s)$, and C_Z). In order to asymptotically achieve universal multi-qumode processing including non-Clifford (non-Gaussian) unitaries, the additional cubic phase gate ($k = 3$) is needed.[43] in an efficient way.

42) Obtainable from $X(s)$ through Fourier rotations $\hat{R}(-\pi/2)$.

43) Similar to the qubit case, while removing the non-Clifford phase gate $D_3(t)$ renders the remaining Clifford set non-universal, removing the Clifford phase gate $D_2(t)$ gives a smaller, but still universal set. For example, in Eq. (1.131), the right-hand side contains a quadratic squeezing gate; thus, we can still obtain arbitrary Clifford gates [88]. From a practical point of view, however, it is better to implement Clifford unitaries whenever needed through Clifford gates (see Chapter 2).

Similar to the qubit stabilizer evolution under the qubit Clifford phase gate in Eq. (1.65), here, we obtain the qumode stabilizer evolution,[44)]

$$X(s) \to D_2(t)\,X(s)\,D_2^\dagger(t) = \mathrm{e}^{\mathrm{i}t\hat{x}^2}\,X(s)\mathrm{e}^{-\mathrm{i}t\hat{x}^2} = \mathrm{e}^{\mathrm{i}ts^2}\,X(s)\,Z(ts)\;. \tag{1.129}$$

The conjugate stabilizer is invariant, $Z(s) \to D_2(t)\,Z(s)\,D_2^\dagger(t) = Z(s)$. These equations correspond to the following *linear* Heisenberg evolution equations for the position and momentum of a single qumode,

$$\begin{aligned}\hat{x} &\to D_2^\dagger(t)\,\hat{x}\,D_2(t) = \hat{x}\;,\\ \hat{p} &\to D_2^\dagger(t)\,\hat{p}\,D_2(t) = \hat{p} + t\hat{x}\;.\end{aligned} \tag{1.130}$$

In contrast, the non-Clifford, cubic phase gate transforms the X stabilizer as[45)]

$$\begin{aligned}X(s) \to D_3(t)\,X(s)\,D_3^\dagger(t) &= \mathrm{e}^{\mathrm{i}t\hat{x}^3}\,X(s)\mathrm{e}^{-\mathrm{i}t\hat{x}^3}\\ &= X(s)\,Z(3ts^2/2)\mathrm{e}^{3\mathrm{i}st\hat{x}^2}\\ &= X(s)\,Z(3ts^2/2)\,D_2(3ts)\;.\end{aligned} \tag{1.131}$$

Instead of a multiple of WH operators, a product of quadratic and linear gates is obtained. The stabilizer $Z(s)$ remains unchanged. This is similar to what we found for qubits after performing the $\pi/8$-phase gate $Z_{\pi/4}$ on the Pauli X operator, which no longer gave a Pauli product. On the level of the WH generators, that is, in the Heisenberg evolution of the position and momentum operators, the momentum is no longer mapped onto a linear combination of the generators,

$$\begin{aligned}\hat{x} &\to D_3^\dagger(t)\,\hat{x}\,D_3(t) = \hat{x}\;,\\ \hat{p} &\to D_3^\dagger(t)\,\hat{p}\,D_3(t) = \hat{p} + \frac{3}{2}t\hat{x}^2\;.\end{aligned} \tag{1.132}$$

The momentum transformation becomes *nonlinear*.[46)]

The Gottesmann–Knill theorem that we had introduced in the preceding section for qubits applies to qumodes too [90]. In this case, the Clifford evolution of the stabilizers is most conveniently expressed in terms of the linear evolution of the WH generators $\hat{x}$ and $\hat{p}$. Similar to the discussion for qubits, the ith N-qumode stabilizer generator is determined through $\sim N$ parameters. For instance, the N positions of an initial product state of N position eigenstates are each transformed into position-momentum linear combinations with $2N$ real coefficients. Hence, the to-

44) Which corresponds to the inverse Heisenberg evolution, while the actual Heisenberg evolution is $D_2^\dagger(t)X(s)D_2(t) = D_2^\dagger(t)\mathrm{e}^{-2\mathrm{i}s\hat{p}}D_2(t) = \mathrm{e}^{-2\mathrm{i}s(\hat{p}+t\hat{x})} = \mathrm{e}^{-\mathrm{i}ts^2}X(s)Z(-ts)$ using Eq. (1.130) and one of the BCH formulas.

45) While the actual Heisenberg evolution is $D_3^\dagger(t)X(s)D_3(t) = \mathrm{e}^{-\mathrm{i}t\hat{x}^3}\mathrm{e}^{-2\mathrm{i}s\hat{p}}\mathrm{e}^{\mathrm{i}t\hat{x}^3} = \mathrm{e}^{-2\mathrm{i}s(\hat{p}+3t\hat{x}^2/2)} = X(s)Z(-3ts^2/2)\mathrm{e}^{-3\mathrm{i}ts\hat{x}^2}$ using one of the BCH formulas.

46) In these Heisenberg equations, we use our usual convention of $\hbar = 1/2$. In general, using the commutator $[\hat{x},\hat{p}] = \mathrm{i}\hbar$, and so $[\hat{x}^2,\hat{p}] = 2\mathrm{i}\hbar\hat{x}$ and $[\hat{x}^3,\hat{p}] = 3\mathrm{i}\hbar\hat{x}^2$, we obtain $D_2^\dagger(t)\hat{p}\,D_2(t) = \hat{p}+[\hat{p},\mathrm{i}t\hat{x}^2] = \hat{p}+2\hbar t\hat{x}$ and $D_3^\dagger(t)\hat{p}\,D_3(t) = \hat{p}+[\hat{p},\mathrm{i}t\hat{x}^3] = \hat{p}+3\hbar t\hat{x}^2$, using the BCH formula $\mathrm{e}^{-\mathrm{B}}\mathrm{A}\mathrm{e}^{\mathrm{B}} = \mathrm{A} + [\mathrm{A},\mathrm{B}]+1/2![[\mathrm{A},\mathrm{B}],\mathrm{B}]+1/3![[[\mathrm{A},\mathrm{B}],\mathrm{B}],\mathrm{B}]+\ldots$

tal evolution is completely specified through $2N^2$ real parameters. For the more interesting case of physical stabilizer states corresponding to Gaussian states (see Chapters 2 and 3), instead of the $2N^2$ real coefficients, $2N^2$ complex coefficients are needed, corresponding to $4N^2$ real parameters. The formalism of complex-valued stabilizers for physical qumode stabilizer states and their Clifford evolution will be discussed in Chapters 2 and 3. The Gottesmann–Knill theorem for qumodes then states that Gaussian operations on Gaussian states can be efficiently simulated classically [90].

Similar to the qubit case, one may also consider a CNOT gate for qumodes. This is defined as $\mathrm{CNOT} = \exp(-2\mathrm{i}\hat{x}_1 \otimes \hat{p}_2) = X_2(\hat{x}_1) = Z_1(-\hat{p}_2)$, corresponding to an x-controlled x-displacement of mode 2 and a p-controlled p-displacement of mode 1: $\hat{x}_2 \to \hat{x}_1 + \hat{x}_2$, $\hat{p}_1 \to \hat{p}_1 - \hat{p}_2$, $\hat{x}_1 \to \hat{x}_1$, and $\hat{p}_2 \to \hat{p}_2$. As opposed to the C_Z gate, CNOT is no longer symmetric under exchange of the two modes. The CNOT gate can be obtained from the C_Z gate through local Fourier transforms,

$$(\mathbb{1} \otimes F^\dagger) \exp(2\mathrm{i}\hat{x}_1 \otimes \hat{x}_2)(\mathbb{1} \otimes F) = \exp(-2\mathrm{i}\hat{x}_1 \otimes \hat{p}_2) \,. \tag{1.133}$$

Universal sets

⊙ **Qubits**

$\{H, Z_{\pi/2}, Z_{\pi/4}, C_Z\}$

single-qubit gates: Z-Pauli (phase flip):

$$Z|\pm\rangle = |\mp\rangle \,, \quad Z|k\rangle = (-1)^k|k\rangle$$

general Z-rotation:

$$Z_\theta = \exp(-\mathrm{i}\theta\, Z/2)$$

$\pi/4$-phase gate:

$$Z_{\pi/2}^\dagger Z Z_{\pi/2} = Z \,, \quad Z_{\pi/2}^\dagger X Z_{\pi/2} = -Y \quad \text{(Clifford)}$$

$\pi/8$-phase gate:

$$Z_{\pi/4}^\dagger Z Z_{\pi/4} = Z \,, \quad Z_{\pi/4}^\dagger X Z_{\pi/4} = \frac{1}{\sqrt{2}}(X - Y) \quad \text{(non-Clifford)}$$

Hadamard:

$$H|k\rangle = \frac{|0\rangle + (-1)^k|1\rangle}{\sqrt{2}} \,, \quad HXH = Z \,, \quad HZH = X \quad \text{(Clifford)}$$

X-Pauli (bit flip):

$$X|k\rangle = |k \oplus 1\rangle \,, \quad X|\pm\rangle = \pm|\pm\rangle$$

two-qubit gate:

$$C_Z|k\rangle \otimes |l\rangle = (-1)^{kl}|k\rangle \otimes |l\rangle \quad \text{(Clifford)}$$

Qumodes

$$\{F,\, Z(s),\, D_2(t),\, D_3(\kappa),\, C_Z\}$$

single-mode gates: WH-momentum shift:

$$Z(s)|p\rangle = |p+s\rangle\,, \quad Z(s)|x\rangle = \mathrm{e}^{2\mathrm{i}sx}|x\rangle$$

general phase (momentum) gate:

$$D = \exp[\mathrm{i}\, f(\hat{x})]\,, \quad \text{for example} \quad D_k(t) = \exp(\mathrm{i}t\hat{x}^k)$$

quadratic gate:

$$D_2^\dagger(t)\hat{x}\,D_2(t) = \hat{x}\,, \quad D_2^\dagger(t)\hat{p}\,D_2(t) = \hat{p} + t\hat{x} \quad \text{(Clifford)}$$

cubic gate:

$$D_3^\dagger(t)\hat{x}\,D_3(t) = \hat{x}\,, \quad D_3^\dagger(t)\hat{p}\,D_3(t) = \hat{p} + \frac{3}{2}t\hat{x}^2 \quad \text{(non-Clifford)}$$

Fourier:

$$F|x\rangle_{\mathrm{pos}} = \int \mathrm{d}y\mathrm{e}^{2\mathrm{i}xy}|y\rangle_{\mathrm{pos}} = |x\rangle_{\mathrm{mom}}\,,$$
$$F^\dagger \hat{p}\,F = \hat{x}\,, \quad F^\dagger \hat{x}\,F = -\hat{p} \quad \text{(Clifford)}$$

WH-position shift:

$$X(s)|x\rangle = |x+s\rangle\,, \quad X(s)|p\rangle = \mathrm{e}^{-2\mathrm{i}sp}|p\rangle$$

two-mode gate:

$$C_Z = \exp(2\mathrm{i}\hat{x}\otimes\hat{x}) : C_Z|x\rangle_{\mathrm{pos}}|p\rangle_{\mathrm{mom}} = |x\rangle_{\mathrm{pos}}|p+x\rangle_{\mathrm{mom}}\,,$$
$$C_Z^\dagger \hat{x}_{1,2}\,C_Z = \hat{x}_{1,2}\,, \quad C_Z^\dagger \hat{p}_{1,2}\,C_Z = \hat{p}_{1,2} + \hat{x}_{2,1} \quad \text{(Clifford)}$$

Again, similar to the qubit case, the "magic state" for qumodes is obtained by applying the non-Clifford, cubic phase gate upon a zero-momentum eigenstate,

$$D_3(t)|p=0\rangle = \mathrm{e}^{\mathrm{i}t\hat{x}^3}\frac{1}{\sqrt{\pi}}\int \mathrm{d}x|x\rangle = \frac{1}{\sqrt{\pi}}\int \mathrm{d}x\mathrm{e}^{\mathrm{i}tx^3}|x\rangle\,. \tag{1.134}$$

This is the so-called cubic phase state [28].

In the current section, we attempted to give an overview of various important notions in quantum computation including those of universality and scalability in the context of both qubit and qumode approaches. Universality in either approach will require some form of nonlinearity which may only be indirectly incorporated into a quantum computation through measurements or directly through some effectively enhanced weak nonlinear interaction. In the former scenario, a measurement-based model of quantum computation is applied, as we shall discuss in the context of experimental implementations in Chapters 6 and 7. The idea of weak nonlinear interactions is most intuitively realized in hybrid protocols in which both qubit and qumode systems participate (see Chapter 8). Once universality is achieved, including non-Clifford gates, in principle, a quantum computation can no longer be simulated classically in an efficient way.

Even when universality can be attained in principle, scalability remains a subtle issue. This issue will be part of the subsequent discussions on optical approaches to quantum computation.

Another topic of great importance is fault tolerance. Without some form of (concatenated) quantum error correction, a quantum computer will remain a theoretical construct. As we discussed before, quantum communication too must rely upon some form of quantum error detection when it is to be extended over larger distances. A complete treatment of fault tolerance for quantum information processing and computation is beyond the scope of this introductory chapter on quantum information. Nonetheless, in the next section, we shall at least mention the basic concepts of quantum error correction.

1.9 Quantum Error Correction

Quantum information processing and computation became an area of practical interest with potential real-world applications only after the discovery of quantum error correction (QEC) codes [5, 21, 91, 92]. Shor's code [21] was proposed at a time when people believed that QEC unlike classical error correction would be impossible. These initial doubts originated mainly from two supposed obstacles.

First, in classical error correction, the most natural way for protecting information against errors is to use *redundancy*. However, to create redundancy in the quantum case (by encoding qubits into multiple copies of the same qubits) appeared to be forbidden even in principle by the quantum mechanical no-cloning theorem (recall Section 1.1). Further, a second complication seemed to exist, following from the fundamental nature of quantum information: encoded into complex-amplitude superposition states, as opposed to classical digital information, quantum information is inherently *continuous*. This even holds for just a single qubit.

Despite these initial doubts, Shor's discovery and the many subsequent results on QEC demonstrated that there are two specific solutions to the two main problems mentioned in the preceding paragraph. A kind of redundancy can be obtained in the quantum case by encoding quantum information globally into *entangled*

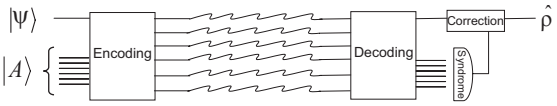

Figure 1.12 Basic elements of quantum error correction. Most commonly, the signal state $|\psi\rangle$ and a set of ancillae in some standard initial state $|A\rangle$ are unitarily transformed into an encoded state. After the effect of the errors, typically assumed to occur individually and independently on every subsystem, a unitary decoding circuit and a subsequent syndrome measurement of the ancillae reveal the type and location (and, for example, for qumodes, also the size) of the error. A final correction operation on the signal system will then recover the original state with a fidelity greater than that for an unprotected signal state, depending on the correctable set of errors for the specific code and on the actual error model.

states that are defined in a larger Hilbert space than the original signal space. These encoded states do not correspond to multiple copies of the original state and so do not violate no-cloning. For example, an arbitrary qubit state, $|\psi\rangle = a|0\rangle + b|1\rangle$, may be encoded into an entangled state of three physical qubits as[47)]

$$|\psi\rangle \otimes |0\rangle \otimes |0\rangle \rightarrow a|000\rangle + b|111\rangle \neq |\psi\rangle \otimes |\psi\rangle \otimes |\psi\rangle \,. \tag{1.135}$$

This encoding can be achieved by pairwise applying two CNOT gates upon the signal qubit together with the first ancilla qubit as well as with the second one. Eventually, local bit-flip errors occurring on exactly one of the three qubits can be detected and corrected, as we shall discuss in more detail shortly. The detection of the error will depend on some form of measurement, and it is this so-called syndrome measurement step which enables one to correct arbitrary, even continuous errors. This effect is called *discretization* of errors because a continuous error is reduced to a finite, discrete set of Pauli errors. We will illuminate this essential feature of QEC in the following section. Figure 1.12 shows the basic elements of QEC as applicable to both qubits and qumodes.

1.9.1 Discretization

In the preceding section, we wrote universal sets for qubits and qumodes in terms of single-variable gates, that is, gates diagonal in the computational variables Pauli Z and position $\hat{x}$, respectively. For universality, at least one diagonal gate needed to have a rotation angle $\neq k\pi/2$ on the Bloch sphere for qubits and a Hamiltonian of $>$ quadratic order for qumodes. In addition, the Hadamard and the Fourier gates were required in order to affect multi-variable gates.

The simplest manifestation of a QEC code also works with single-variable gates. However, quite remarkably, universality, that is, universal protection against *arbitrary* single-variable errors (including non-Clifford-type errors) follows directly

47) Recall the discussion of the preceding section. The state in Eq. (1.135) may as well be interpreted as a certain superposition state of an eight-level particle. However, in this case, encoding, occurrence of local errors, and syndrome identification lack the nice physical and operational meaning of the multi-particle scenario.

from the ability of a code to correct the simplest single-variable errors, for instance, Pauli X bit-flip errors for qubits and WH $X(s)$ position shift errors for qumodes. Let us see how this works.

Consider a single qubit in an arbitrary state, $|\psi\rangle = a|0\rangle + b|1\rangle$. First, the error model shall be described by a simple one-qubit bit flip Pauli channel, with $\mathcal{E}(\hat{\rho}) = (1-p)\hat{\rho} + p\,X\hat{\rho}X$ (see Section 1.4.1): with probability p a bit flip occurs; otherwise, the state remains unchanged. So the error set is discrete and finite, consisting only of Pauli X errors. Hence, the correctable error set should contain at least one-qubit X errors. Using the encoded state in Eq. (1.135) and applying the channel map upon every physical qubit independently gives the output density operator,

$$(1-p)^3\hat{\rho}_{\text{enc}} + p(1-p)^2\sum_{k=1}^{3} X_k\hat{\rho}_{\text{enc}}X_k + p^2(1-p)\sum_{l<k=2}^{3}(X_l\otimes X_k)\hat{\rho}_{\text{enc}}(X_l\otimes X_k) + p^3X^{\otimes 3}\hat{\rho}_{\text{enc}}X^{\otimes 3}\,, \quad (1.136)$$

with $\hat{\rho}_{\text{enc}} \equiv (a|000\rangle + b|111\rangle)(a^*\langle 000| + b^*\langle 111|)$. Now, if we were able to discriminate the orthogonal subspaces spanned by $\{|000\rangle, |111\rangle\}$ and $\{X_k|000\rangle, X_k|111\rangle\}$ with $k = 1, 2, 3$, without changing the original amplitudes of the corresponding terms, we could at least identify the errors up to $\mathrm{O}(p^2)$. In fact, the three-qubit code achieves exactly this. It uses four orthogonal subspaces, each two-dimensional with enough space to preserve the original qubit, which correspond to the four cases of no error at all and a bit-flip error occurring on any one of the three qubits. As a result, through the three-qubit repetition code, the effective error probability is reduced from p to p^2. Higher repetitions may lead to even better error suppression.

From this, it also becomes clear why two physical qubits are not enough for such a bit-flip code: in the four-dimensional physical Hilbert space of two qubits, there are only two possible orthogonal, two-dimensional subspaces; not enough for obtaining and discriminating all the three cases of an error occurring on either qubit ($\{X_k|00\rangle, X_k|11\rangle\}$), with $k = 1, 2$, and no error happening at all ($\{|00\rangle, |11\rangle\}$), which would require six physical dimensions. However, if we are satisfied with only detecting whether an error occurred (without correcting it), two qubits would be enough since the no-error subspace $\{|00\rangle, |11\rangle\}$ can still be discriminated from the error subspaces $\{X_k|00\rangle, X_k|11\rangle\}$. In general, this dimensional argument tells us how many physical qubits will be needed for a given error model and a desired correctable error set.

Now, let us consider a channel which is more general than the bit-flip channel and allow for an arbitrary X-error, that is, an arbitrary X-rotation $X_\theta = \mathrm{e}^{-\mathrm{i}\theta X/2} = \cos(\theta/2)\mathbb{1} - \mathrm{i}\sin(\theta/2)X$. In this case, using again the three-qubit code, we would still be able to correct the dominating errors by discriminating the orthogonal subspaces $\{|000\rangle, |111\rangle\}$ and $\{X_k|000\rangle, X_k|111\rangle\}$ with $k = 1, 2, 3$. In fact, the syndrome measurements that achieve this discrimination will reduce the total density operator again to terms which have no error at all or a bit flip on exactly one qubit in the leading order. More precisely, only terms like $p(1-p)^2\cos^2(\theta/2)\hat{\rho}_{\text{enc}}$ and $p(1-$

$p)^2 \sin^2(\theta/2) X_k \hat{\rho}_{\text{enc}} X_k$ with $k = 1, 2, 3$ will remain after the syndrome detection, and the off-diagonal terms like, for instance, $p(1-p)^2 \mathrm{i} \cos(\theta/2) \sin(\theta/2) \mathbb{1} \hat{\rho}_{\text{enc}} X_k$ vanish. In other words, even though the original error is a continuous X-rotation, due to the syndrome measurement, this error *will become* a simple Pauli X error or result in no error at all. The final correction operation then works as before by just unflipping the corrupted qubit.

Now, consider a single qumode in an arbitrary state, $|\psi\rangle = \int \mathrm{d}x \psi(x)|x\rangle$. A (perfectly) repetition-encoded three-qumode state in this case becomes

$$\int \mathrm{d}x \psi(x)|x\rangle \otimes |x\rangle \otimes |x\rangle \,. \tag{1.137}$$

Now, whenever exactly one qumode is subject to an arbitrary $\hat{x}$-error, acting as $\mathrm{e}^{\mathrm{i}f(\hat{p})}$, the syndrome detection discriminating between the subspaces $\{X_k(s)|xxx\rangle | \forall x \in \mathbb{R}\}$ with $k = 1, 2, 3$ and $s \in \mathbb{R}$ would result in a state where exactly one qumode is corrupted by a simple position shift. Since the location and the size of this position shift will be known from the syndrome measurement, the original, uncorrupted state can be recovered through a simple displacement operation on the corresponding qumode. For example, $\mathrm{e}^{\mathrm{i}f(\hat{p})}$ acting upon qumode 1 leads to

$$\begin{aligned}
\mathrm{e}^{\mathrm{i}f(\hat{p}_1)} \int \mathrm{d}x \psi(x)|xxx\rangle &= \mathrm{e}^{\mathrm{i}f(\hat{p}_1)} \int \mathrm{d}x \psi(x) \frac{1}{\sqrt{\pi}} \int \mathrm{d}p \mathrm{e}^{-2\mathrm{i}xp}|pxx\rangle \\
&= \frac{1}{\sqrt{\pi}} \int \mathrm{d}x \mathrm{d}p \psi(x) \mathrm{e}^{-2\mathrm{i}xp} \mathrm{e}^{\mathrm{i}f(p)}|pxx\rangle \\
&= \frac{1}{\pi} \int \mathrm{d}x \mathrm{d}y \mathrm{d}p \psi(x) \mathrm{e}^{2\mathrm{i}(y-x)p} \mathrm{e}^{\mathrm{i}f(p)}|yxx\rangle \,.
\end{aligned} \tag{1.138}$$

The syndrome identification amounts to projecting qumodes 1 and 2 as well as qumodes 2 and 3 onto the two-qumode projectors $\int \mathrm{d}z |z, z-u_k\rangle\langle z, z-u_k|$ with syndromes u_1 and u_2. In terms of the position operators, this corresponds to measurements of the relative positions $\hat{x}_1 - \hat{x}_2$ and $\hat{x}_2 - \hat{x}_3$ with outcomes u_1 and u_2, respectively. When the error $\mathrm{e}^{\mathrm{i}f(\hat{p})}$ occurred on qumode 1, we will always obtain $u_2 = 0$, whereas the other projector gives

$$\begin{aligned}
&\int \mathrm{d}z |z, z-u_1\rangle\langle z, z-u_1| \frac{1}{\pi} \int \mathrm{d}x \mathrm{d}y \mathrm{d}p \psi(x) \mathrm{e}^{2\mathrm{i}(y-x)p} \mathrm{e}^{\mathrm{i}f(p)}|yxx\rangle \\
&= \frac{1}{\pi} \int \mathrm{d}x \mathrm{d}y \mathrm{d}p \psi(x) \mathrm{e}^{2\mathrm{i}(y-x)p} \mathrm{e}^{\mathrm{i}f(p)} \delta(y-u_1-x)|y, y-u_1, x\rangle \\
&= \frac{1}{\pi} \int \mathrm{d}x \mathrm{d}p \psi(x) \mathrm{e}^{2\mathrm{i}u_1 p} \mathrm{e}^{\mathrm{i}f(p)}|x+u_1, x, x\rangle \\
&= g(u_1) \int \mathrm{d}x \psi(x)|x+u_1, x, x\rangle \,.
\end{aligned} \tag{1.139}$$

Though the function $g(u_1) \equiv (1/\pi \int \mathrm{d}p \mathrm{e}^{2\mathrm{i}u_1 p} \mathrm{e}^{\mathrm{i}f(p)})$ is a measurement-dependent prefactor, the conditional state for every syndrome u_1 becomes $\int \mathrm{d}x \psi(x)|x + u_1, x, x\rangle$ which can be corrected as described above. Note that for simplicity, we have used unnormalized states here and syndrome detections with infinite

resolution. In the realistic case, the encoded state would correspond to a three-mode Gaussian state[48] producible with two squeezed-state ancillary qumodes using beam splitters (see Chapters 2 and 5). The infinitely precise measurement should be more realistically described by a finite syndrome window with projectors $\int_{\Delta} \mathrm{d}u_k \int \mathrm{d}z |z, z-u_k\rangle\langle z, z-u_k|$. So when, for instance, $g(u_1) = \delta(u_1)$ for the no-error case with $\mathrm{e}^{\mathrm{i}f(p)} \equiv 1$, we would obtain $\int_{-\Delta/2}^{\Delta/2} \mathrm{d}u_1 g(u_1) \int \mathrm{d}x \psi(x)|x + u_1, x, x\rangle = \int \mathrm{d}x \psi(x)|x, x, x\rangle$ as the final state.

To summarize, the mechanism for correcting arbitrary single-variable errors is very similar for qubits and for qumodes. In either case, even when an arbitrary error diagonal in, for example, X (qubits) and $\hat{p}$ (qumodes) may disturb a quantum state in infinitely many ways, the syndrome detection will map the original error onto a simpler error from a smaller error set: for qubits, this would be a flip in the Z basis; for qumodes, a shift in the $\hat{x}$ basis. Although this guarantees that even non-Clifford-type *single-variable* errors can be corrected by simple means, it does not yet allow for the correction of *multi-variable* errors including two or more non-commuting variables such as X and Z for qubits, and $\hat{x}$ and $\hat{p}$ for qumodes. Such full QEC codes, however, can be constructed by concatenating a single-variable code using Hadamard and Fourier gates. The first and certainly most famous full QEC code is Shor's nine-qubit code [21]. A qumode version of this code and its experimental realization will be discussed in Chapter 5.

On the level of arbitrary channel (CPTP) maps, the effect of discretization in a QEC protocol can be understood by expanding an arbitrary qubit Kraus operator in the Pauli matrix basis as in Eq. (1.77). Similarly, the WH shift operators serve as a complete basis for arbitrary qumode CPTP maps, see Eq. (1.78). In either case, syndrome detections of Pauli and WH errors will then always remove the offdiagonal terms of the channel output matrix and the remaining terms can be easily corrected. In the qumode case, the reduced error set is, of course, not really discrete. It is, nonetheless, smaller and simpler, containing only phase-space shift errors.

Although universal QEC of *arbitrary, multi-variable* errors occurring on a subset of the physical qubits or qumodes is possible, a subtlety remains when comparing qubit and qumode QEC. This complication arises for the realistic scenario of *multi-channel* errors. Typically, not only a single qubit or qumode will be subject to an error. Usually, every subsystem will be corrupted, and so a hierarchy of errors in terms of the frequency of their occurrence or their size will become important. For instance, as we have seen for qubits, multiple-qubit bit-flip errors may simply be neglected when their probability scales as p^2 compared to the single-qubit error probability p. Similarly, an amplitude damping error may be corrected up to an order $\mathrm{O}(\gamma^2)$ in the damping parameter (see Section 1.4.1 and Chapter 2) [5]. However, for qumodes, amplitude damping becomes a Gaussian channel (see Chapter 2) and, as such, it may simply no longer be correctable when the damping occurs on every encoded qumode in every channel [93]. Nonetheless, whenever a stochastic channel leads to a hierarchy of errors, arbitrary multi-variable, multi-channel

48) When the signal state $|\psi\rangle = \int \mathrm{d}x \psi(x)|x\rangle$ is a Gaussian state, which is *not* a requirement here.

errors can be suppressed through the standard QEC codes, both for qubits and qumodes [94]. In either case, whether a QEC code is useful at all and whether it is efficient depends on the correctable error set (for instance, the set of arbitrary single-channel errors) and the given channel error model. The only basic assumption typically is that the errors act independently on the individual subsystems.

1.9.2 Stabilizer Codes

A particularly important class of QEC codes is that of so-called stabilizer codes [95, 96], the quantum analogue of classical additive codes. Stabilizer codes are generalizations of stabilizer states. This shall become clear in the present section.

In the DV setting, through an $[N, k]$ stabilizer code, k logical qubits are encoded into N physical qubits. The stabilizer group S, an abelian subgroup of the N-qubit Pauli group[49] with $(N-k)$ stabilizer generators $\langle g_1, g_2, \ldots, g_{N-k}\rangle$, defines the codespace which is spanned by the set of simultaneous $+1$ eigenvectors of S. Measuring the $N-k$ stabilizer generators, yielding 2^{N-k} classical syndrome bit values, reveals which orthogonal error subspace an encoded input state is mapped onto. Signal recovery is then achieved by mapping the state back into the codespace with stabilizer eigenvalues $+1$.

Let us illustrate these definitions and notions for the three-qubit code of the preceding section. This code represents a very simple example of a stabilizer code. In this case, $k = 1$ logical qubit is encoded into $N = 3$ physical qubits. The corresponding $[3, 1]$ code is defined through the minimal set of $N - k = 2$ independent stabilizer generators $\langle g_1 \equiv Z \otimes Z \otimes \mathbb{1}, g_2 \equiv \mathbb{1} \otimes Z \otimes Z\rangle$. This set uniquely defines the stabilizer group S for the corresponding stabilizer code with a two-dimensional codespace spanned by $\{|000\rangle, |111\rangle\}$. Since S is abelian, and we have $[g_1, g_2] = 0$, the basis vectors $|000\rangle$ and $|111\rangle$ can be simultaneous eigenvectors of g_1 and g_2 with eigenvalue $+1$.

The effect of the bit-flip channel on the three physical qubits of the repetition code, as described in the preceding section, can now be equivalently expressed in terms of the stabilizers. Up to order $O(p^2)$, including only linear terms in p, we obtain the following stochastic transformations of the stabilizer generators,

$$\begin{aligned}
&\langle Z_1Z_2, Z_2Z_3\rangle \to \langle Z_1Z_2, Z_2Z_3\rangle\ ; \quad \text{with probability} \quad (1-p)^3\ ,\\
&\langle Z_1Z_2, Z_2Z_3\rangle \to \langle -Z_1Z_2, Z_2Z_3\rangle\ ; \qquad\qquad\quad p(1-p)^2\ ,\\
&\langle Z_1Z_2, Z_2Z_3\rangle \to \langle -Z_1Z_2, -Z_2Z_3\rangle\ ; \qquad\qquad\quad p(1-p)^2\ ,\\
&\langle Z_1Z_2, Z_2Z_3\rangle \to \langle Z_1Z_2, -Z_2Z_3\rangle\ ; \qquad\qquad\quad p(1-p)^2\ . \qquad (1.140)
\end{aligned}$$

The first case in the top row corresponds to the no-error case; the encoded state remains in the original codespace. In the other three cases, the encoded state is subject to a bit flip on any one of the three qubits; hence, the encoded state is

49) Which itself is formed by a tensor product of the one-qubit Pauli group. Recall from footnote 14 on page 19 that we omit all unnecessary prefactors of Pauli operators such as $(\pm i)$.

mapped into one of the orthogonal subspaces $\{X_k|000\rangle, X_k|111\rangle\}$ with $k = 1, 2, 3$. These three error subspaces are each uniquely determined through the new stabilizer generators, as shown in Eq. (1.140), and are each spanned by a new two-dimensional set of simultaneous $+1$ eigenvectors. The syndrome measurement will then reveal the change of the eigenvalues with respect to the original stabilizers, that is, those of the codespace, g_1 and g_2. There are four syndrome outcomes corresponding to the four cases of no error at all ($g_1 = +1, g_2 = +1$), a bit flip on qubit 1 ($g_1 = -1, g_2 = +1$), a bit flip on qubit 2 ($g_1 = -1, g_2 = -1$), and a bit flip on qubit 3 ($g_1 = +1, g_2 = -1$). Thus, measuring the $N - k = 2$ stabilizers of the code uniquely determines the error. Mapping the state from one of the orthogonal error subspaces back into the original codespace enables one to recover an uncorrupted version of the encoded state. This is a general feature of stabilizer codes.

The three-qumode repetition code can be similarly expressed in terms of stabilizers. In this case, we need $N - k = 2$ products of WH operators, $\langle g_1(s) \equiv Z(s) \otimes Z(-s) \otimes \mathbb{1}, g_2(s) \equiv \mathbb{1} \otimes Z(s) \otimes Z(-s)\rangle$, in order to represent the stabilizer group and uniquely define a one-qumode codespace as a subspace of the whole three-qumode space. This infinite-dimensional subspace is spanned by the basis vectors $\{|xxx\rangle|\forall x \in \mathbb{R}\}$, which are simultaneous $+1$ eigenvectors of the stabilizers $g_1(s)$ and $g_2(s)$. More conveniently expressed in terms of the WH generators $\hat{x}$ and $\hat{p}$, we have $N-k = 2$ so-called nullifier conditions, $\hat{x}_1-\hat{x}_2 = 0$ and $\hat{x}_2-\hat{x}_3 = 0$ since these combinations must have $\{|xxx\rangle\,|\forall x \in \mathbb{R}\}$ as their simultaneous zero-eigenvectors. The syndrome information now becomes continuous, corresponding to the eigenvalues of $\hat{x}_1 - \hat{x}_2 = u_1$ and $\hat{x}_2 - \hat{x}_3 = u_2$ after an error occurred on any one of the three qumodes. Every pair of these eigenvalues uniquely determines one of the orthogonal error subspaces, $\{X_k(s)|xxx\rangle|\forall x \in \mathbb{R}\}$ with $k = 1, 2, 3$ and $s \in \mathbb{R}$, into which the encoded state is mapped by the channel. Compared with the qubit case in Eq. (1.140), the stabilizer map now becomes

$$\begin{aligned}&\langle Z_1(s)Z_2(-s), Z_2(s)Z_3(-s)\rangle\\ &\to \left\langle \mathrm{e}^{-2\mathrm{i}su_1} Z_1(s)Z_2(-s), \mathrm{e}^{-2\mathrm{i}su_2} Z_2(s)Z_3(-s)\right\rangle,\end{aligned} \tag{1.141}$$

with the syndrome information contained in the phase factors $\mathrm{e}^{-2\mathrm{i}su_1}$ and $\mathrm{e}^{-2\mathrm{i}su_2}$. Though the syndrome is now continuous, the QEC mechanism is very similar to the qubit case; however, the stochastic nature of the qubit channels, as illustrated by Eq. (1.140), will be missing in the most important examples of qumode channels (see Chapter 2).

We have used the notion of stabilizers and stabilizer states already at various times. A stabilizer is a (not necessarily unitary) operator M that, for some vector $|\psi\rangle$, has the property $M|\psi\rangle = |\psi\rangle$. If there is a commuting set of such stabilizers $\{M_i\}$ such that $M_i|\psi\rangle = |\psi\rangle$, $\forall i$, $|\psi\rangle$ may be a unique state vector or an arbitrary vector in a uniquely defined subspace. In fact, the former case is a special case of the latter one.

For instance, for N qubits, $N - k$ Pauli generators will define a 2^k-dimensional subspace $\mathcal{C}$ of the 2^N-dimensional N-qubit space. This subspace $\mathcal{C}$ represents a

stabilizer code, and the stabilizer condition becomes $M_i|\psi\rangle = |\psi\rangle$, $\forall i$ and $\forall|\psi\rangle \in \mathcal{C}$. Now, the special case with $k = 0$ means that $\mathcal{C}$ is specified through N Pauli generators. In this case, $\mathcal{C}$ has a dimension such that $M_i|\psi\rangle = |\psi\rangle$, $\forall i$ uniquely defines the rank-1 projector $|\psi\rangle\langle\psi|$ corresponding to a pure N-qubit state. These definitions are similar for qumodes. Later, we shall use full sets of N Pauli and WH stabilizers in order to define multi-party entangled N-qubit and N-qumode graph states, respectively.

Stabilizers and stabilizer codes

stabilizer: any operator M such that $M|\psi\rangle = |\psi\rangle$
stabilizer code: any subspace defined by a commuting stabilizer set $\{M_i\}$
stabilizer state: any such 1-dimensional subspace (pure-state projector)

⊙ **Qubits**

stabilizer codes:
any 2^k-dimensional subspace $\mathcal{C}$ of the 2^N-dimensional N-qubit space defined through $N - k$ Pauli stabilizer generators $\langle g_1, g_2, \ldots, g_{N-k}\rangle$ such that $[g_i, g_j] = 0$ and $g_i|\psi\rangle = |\psi\rangle$, $\forall i, j$ and $\forall|\psi\rangle \in \mathcal{C}$

stabilizer states:
any $2^0 = 1$-dimensional subspace $|\psi\rangle\langle\psi|$ of the 2^N-dimensional N-qubit space defined through N Pauli stabilizer generators $\langle g_1, g_2, \ldots, g_N\rangle$ such that $[g_i, g_j] = 0$ and $g_i|\psi\rangle = |\psi\rangle$, $\forall i, j$

〰 **Qumodes**

stabilizer codes:
any k-qumode subspace $\mathcal{C}$ of the infinite-dimensional N-qumode space defined through $N - k$ WH stabilizers $\langle g_1(s), g_2(s), \ldots, g_{N-k}(s)\rangle$ such that $[g_i(s), g_j(s)] = 0$ and $g_i(s)|\psi\rangle = |\psi\rangle$, $\forall i, j; s \in \mathbb{R}$, and $\forall|\psi\rangle \in \mathcal{C}$

stabilizer states:
any 1-dimensional subspace $|\psi\rangle\langle\psi|$ of the infinite-dimensional N-qumode space defined through N WH stabilizers $\langle g_1(s), g_2(s), \ldots, g_N(s)\rangle$ such that $[g_i(s), g_j(s)] = 0$ and $g_i(s)|\psi\rangle = |\psi\rangle$, $\forall i, j; s \in \mathbb{R}$

A great advantage of QEC schemes is that they are deterministic which makes them directly applicable to quantum computation. However, this comes at a price. Encoding logical quantum information into a sufficiently large physical system will require expensive resources. Alternatively, probabilistic quantum error detection and, in particular, entanglement purification schemes [22] may be employed in order to reduce the (spatial) resource consumption and the complexity of the quantum circuits for implementing the protocol. This would then be more useful for quantum communication applications, as described in Section 1.7.2. We shall

discuss some experimental realizations of QEC and entanglement distillation in Chapter 5.

1.10 Experiment: Non-optical Implementations

Quantum teleportation and quantum information processing were demonstrated in various non-optical implementations. Among these, probably the most prominent and fundamental concept was introduced by Cirac and Zoller for trapped ions [97]. This concept was later extended to other physical systems such as neutral trapped atoms [98] and quantum dots in electromagnetic cavities [99].

The approach by Cirac and Zoller is conceptually related to some of those hybrid protocols which we will discuss in the final chapter of this book. More specifically, the entangling gates between two electronic spin qubits (each defined on two internal energy levels of the ion) are not accomplished through direct interaction, but they are rather mediated by a third "system". In the Cirac–Zoller scheme, this third system is a phononic qubit (defined on two vibrational energy levels of the ion) and it acts as a kind of quantum bus – a so-called *qubus*.

Later, in the quantum optical context, we shall present the notion of optical, hybrid qubus computation, where the qubus is represented by the continuous phase-space variables of a photonic qumode instead of the qubit-subspace of a phononic qumode. An introduction to quantum optical encodings in terms of photonic qubits and qumodes shall be postponed until the following chapter. The motivation of the current section is to at least mention that many of the concepts and protocols discussed so far and applied to quantum optical implementations in the remainder of this book have their counterparts and analogues in implementations that employ non-optically encoded qubit, qumode, and qubus systems using, for instance, nuclear magnetic resonance, superconducting materials, or ion traps.

In this section, we will first explain how to implement a CNOT gate using the Cirac–Zoller scheme, for which we take Schmidt–Kaler's experiment [100] as an example. Then, we shall describe a teleportation experiment by Riebe *et al.* [101] as an example for a possible application.

In Schmidt–Kaler's CNOT-gate experiment, they used $^{40}Ca^{+}$ ions in a linear Paul trap [100]. The quantum mechanical energy levels are shown in Figure 1.13 [100, 102]. The essence of this scheme is a conditional sign flip operation R_{phase} of the single-ion "computational bases" $(|D,0\rangle, |D,1\rangle, |S,0\rangle, |S,1\rangle)$. More precisely, we have

$$\begin{aligned} R_{\text{phase}}|D,0\rangle &= |D,0\rangle\ , \\ R_{\text{phase}}|D,1\rangle &= -|D,1\rangle\ , \\ R_{\text{phase}}|S,0\rangle &= -|S,0\rangle\ , \\ R_{\text{phase}}|S,1\rangle &= -|S,1\rangle\ , \end{aligned} \tag{1.142}$$

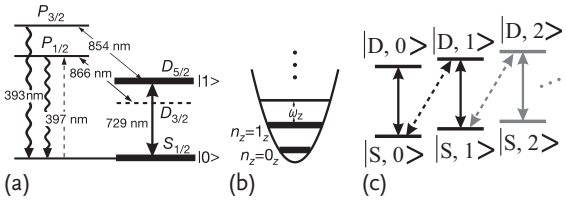

Figure 1.13 Quantum mechanical energy levels of a $^{40}Ca^{+}$ ion for quantum information processing [100, 102]. (a) The lower and upper electronic states $S_{1/2}$ ($m = -1/2$) and $D_{5/2}$ ($m = -1/2$) of the narrow quadrupole transition at 729 nm provide the two levels to implement a qubit. (b) The lowest two number states, $n_z = 0_z, 1_z$, of the axial vibrational motion in the trap. (c) The combination of electronic states. The notation is |electronic level, vibrational motion number).

where D and S denote the upper and lower electronic levels of a $^{40}Ca^{+}$ ion, and 0,1 denotes the quantized number (phonon number) of the vibrational motion of the trapped ions. This is the main trick for realizing the Cirac–Zoller scheme in this system.

The operation R_{phase} can be realized with an effective 2π-pulse on the two-level systems ($|S,0\rangle \leftrightarrow |D,1\rangle$) and ($|S,1\rangle \leftrightarrow |D,2\rangle$), changing the sign of all "computational basis" states except for $|D,0\rangle$. Since the Rabi frequency depends on the number of phonons of the trapped ions, we have to use a composite-pulse sequence [103] instead of a single 2π-pulse. More precisely, the operation R_{phase} can be realized through irradiation of four sequential pulses as follows:

$$R_{\text{phase}} = R^{+}(\pi,0)\,R^{+}\left(\frac{\pi}{\sqrt{2}},\frac{\pi}{2}\right)R^{+}(\pi,0)\,R^{+}\left(\frac{\pi}{\sqrt{2}},\frac{\pi}{2}\right), \tag{1.143}$$

where

$$R^{+}(\theta,\phi) = \exp\left[\mathrm{i}\frac{\theta}{2}\left(\mathrm{e}^{\mathrm{i}\phi}\sigma^{+}\hat{b}^{\dagger} + \mathrm{e}^{-\mathrm{i}\phi}\sigma^{-}\hat{b}\right)\right]. \tag{1.144}$$

The operator $\sigma^{+} = |D\rangle\langle S|$ represents the transition from $|S\rangle$ to $|D\rangle$, and, similarly, $\sigma^{-} = |S\rangle\langle D|$ that from $|D\rangle$ to $|S\rangle$. The annihilation and creation operators $\hat{b}$ and $\hat{b}^{\dagger}$, respectively, refer to the phonons in the ion trap and the parameter θ corresponds to the strength and duration of the applied pulse. Finally, ϕ is the relative phase between the optical field and the atomic polarization [102]. Here, the frequency of the optical field for R^{+} is blue-shifted from the $|S\rangle - |D\rangle$ transition by a single phonon energy.

One can now verify Eq. (1.142) by using Eqs. (1.143) and (1.144). For example,

$$\begin{aligned} R_{\text{phase}}|S,0\rangle &= R^{+}(\pi,0)\,R^{+}\left(\frac{\pi}{\sqrt{2}},\frac{\pi}{2}\right)R^{+}(\pi,0)\,R^{+}\left(\frac{\pi}{\sqrt{2}},\frac{\pi}{2}\right)|S,0\rangle \\ &= R^{+}(\pi,0)\,R^{+}\left(\frac{\pi}{\sqrt{2}},\frac{\pi}{2}\right)R^{+}(\pi,0) \\ &\quad\times\left(\cos\frac{\pi}{2\sqrt{2}}|S,0\rangle - \sin\frac{\pi}{2\sqrt{2}}|D,1\rangle\right) \end{aligned}$$

$$
\begin{aligned}
&= R^{+}(\pi,0)R^{+}\left(\frac{\pi}{\sqrt{2}},\frac{\pi}{2}\right)\\
&\quad\times\left(\mathrm{i}\cos\frac{\pi}{2\sqrt{2}}|D,1\rangle-\mathrm{i}\sin\frac{\pi}{2\sqrt{2}}|S,0\rangle\right)\\
&= R^{+}(\pi,0)\left[\mathrm{i}\cos\frac{\pi}{2\sqrt{2}}\left(\cos\frac{\pi}{2\sqrt{2}}|D,1\rangle+\sin\frac{\pi}{2\sqrt{2}}|S,0\rangle\right)\right.\\
&\quad\left.-\mathrm{i}\sin\frac{\pi}{2\sqrt{2}}\left(\cos\frac{\pi}{2\sqrt{2}}|S,0\rangle-\sin\frac{\pi}{2\sqrt{2}}|D,1\rangle\right)\right]\\
&= \mathrm{i}R^{+}(\pi,0)|D,1\rangle\\
&= -|S,0\rangle. \qquad (1.145)
\end{aligned}
$$

By using the R_{phase}, we can build a CNOT gate R_{CNOT} for the single-ion "computational bases", that is,

$$
R_{\text{CNOT}} = R\left(\frac{\pi}{2},-\frac{\pi}{2}\right)R_{\text{phase}}R\left(\frac{\pi}{2},\frac{\pi}{2}\right), \qquad (1.146)
$$

where

$$
R(\theta,\phi) = \exp\left[\mathrm{i}\frac{\theta}{2}\left(\mathrm{e}^{\mathrm{i}\phi}\sigma^{+}+\mathrm{e}^{-\mathrm{i}\phi}\sigma^{-}\right)\right], \qquad (1.147)
$$

and the $R(\theta,\phi)$ transformation can be realized with a pulse irradiation on resonance with the $|S\rangle-|D\rangle$ transition. The CNOT gate transforms the single-ion "computational bases" as follows:

$$
\begin{aligned}
R_{\text{CNOT}}|S,0\rangle &= -|D,0\rangle\ ,\\
R_{\text{CNOT}}|S,1\rangle &= -|S,1\rangle\ ,\\
R_{\text{CNOT}}|D,0\rangle &= -|S,0\rangle\ ,\\
R_{\text{CNOT}}|D,1\rangle &= -|D,1\rangle\ , \qquad (1.148)
\end{aligned}
$$

where the phonon numbers $n=0$ and $n=1$ correspond to a logical bit of one and zero, respectively. These relations can be checked using Eq. (1.147). For example,

$$
\begin{aligned}
R_{\text{CNOT}}|S,0\rangle &= R\left(\frac{\pi}{2},-\frac{\pi}{2}\right)R_{\text{phase}}R\left(\frac{\pi}{2},\frac{\pi}{2}\right)|S,0\rangle\\
&= R\left(\frac{\pi}{2},-\frac{\pi}{2}\right)R_{\text{phase}}\left(\cos\frac{\pi}{4}|S,0\rangle+\sin\frac{\pi}{4}|D,0\rangle\right)\\
&= R\left(\frac{\pi}{2},-\frac{\pi}{2}\right)\left(-\cos\frac{\pi}{4}|S,0\rangle-\sin\frac{\pi}{4}|D,0\rangle\right)\\
&= -\cos\frac{\pi}{4}\left(\cos\frac{\pi}{4}|S,0\rangle+\sin\frac{\pi}{4}|D,0\rangle\right)\\
&\quad-\sin\frac{\pi}{4}\left(\cos\frac{\pi}{4}|D,0\rangle-\sin\frac{\pi}{4}|S,0\rangle\right)\\
&= -|D,0\rangle\ . \qquad (1.149)
\end{aligned}
$$

Finally, we can construct a CNOT gate for two ions $|\text{ion1, ion2}\rangle = |\text{control, target}\rangle$, where the logical zero and one are encoded into the S and D levels of the ions, respectively. First, quantum information encoded into the electronic levels of the

control ion is transferred onto the phonon levels (i.e., the vibrational qubit encoded into the qubus mode) through the $R_c^+(\pi, 0)$ operation[50] (pulse irradiation) as follows:

$$\begin{aligned} R_c^+(\pi,0)(\alpha|S,0\rangle + \beta|D,0\rangle) &= \mathrm{i}\alpha|D,1\rangle + \beta|D,0\rangle \\ &= |D\rangle \otimes (\mathrm{i}\alpha|1\rangle + \beta|0\rangle) \,, \end{aligned} \tag{1.150}$$

where the phonon number is initially zero and we use the definition of R^+ in Eq. (1.144). Then, the single-ion CNOT operation R_{CNOT} is performed on the *target* ion. When the target ion is in the $|S\rangle$ state, the CNOT operation transforms the state as follows:

$$R_{\mathrm{CNOT}}(\mathrm{i}\alpha|S,1\rangle + \beta|S,0\rangle) = -\mathrm{i}\alpha|S,1\rangle - \beta|D,0\rangle \,, \tag{1.151}$$

using Eq. (1.148). As a final step, the $R_c^+(\pi, 0)$ operation is applied to the *control* ion again. With this operation, the state of the control ion, whose electronic state is $|D\rangle$ as in Eq. (1.150), is transformed as follows:

$$\begin{aligned} R_c^+(\pi,0)(-\mathrm{i}\alpha|D,S,1\rangle - \beta|D,D,0\rangle) &= -\mathrm{i}\alpha(-\mathrm{i}|S,S,0\rangle) - \beta|D,D,0\rangle \\ &= -(\alpha|S,S\rangle + \beta|D,D\rangle) \otimes |0\rangle \,, \end{aligned} \tag{1.152}$$

with the notation |control, target, phonon number⟩. Similarly, we obtain the result for the case with $|D\rangle$ as the initial target-ion's state. Overall we have the following input-output relation for the CNOT gate acting on a two-ion state |control, target⟩:

$$\begin{aligned} |S,S\rangle &\to -|S,S\rangle \,, \\ |S,D\rangle &\to -|S,D\rangle \,, \\ |D,S\rangle &\to -|D,D\rangle \,, \\ |D,D\rangle &\to -|D,S\rangle \,, \end{aligned} \tag{1.153}$$

corresponding to a CNOT operation for the logical states $|S\rangle = |0\rangle$ and $|D\rangle = |1\rangle$. Moreover, the result of Eq. (1.152) means that one can create an entangled state of two ions using this CNOT operation.

Figure 1.14 shows the experimental results of the CNOT gate performed by Schmidt–Kaler *et al.* [100]. From the results, one can see that Eq. (1.153) is very well experimentally verified. Schmidt–Kaler *et al.* also performed the CNOT experiment for a $|S + D, S\rangle$ input. Figure 1.15 shows the corresponding results. In this case, only the states $|S, S\rangle$ and $|D, D\rangle$ are observed with a probability of about 0.5. Phase coherence was also verified by applying an additional $\pi/2$ pulse on the $|S,0\rangle - |D,0\rangle$ transition followed by a projective measurement [100].

Now, we will turn to a discussion of the experiments for quantum teleportation between trapped ions performed by Riebe *et al.* [101].

50) The subscript c denotes the operation on the control ion.

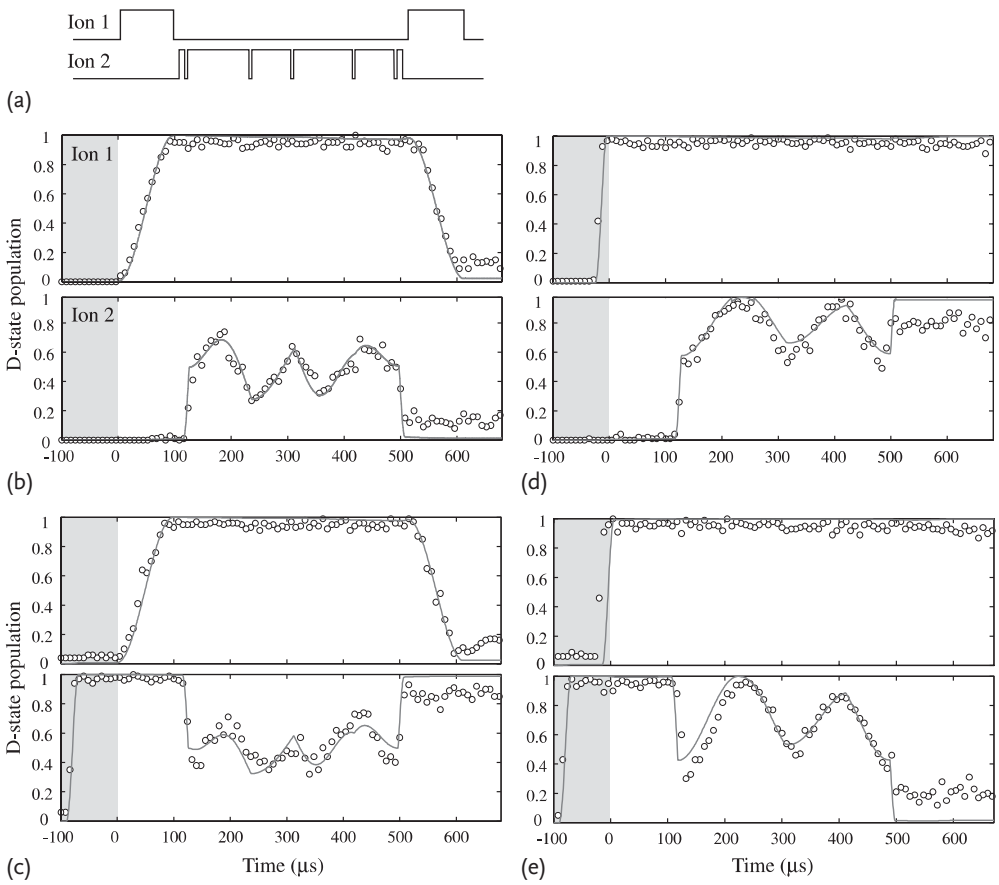

Figure 1.14 State evolution of $|\text{control}, \text{target}\rangle = |\text{ion1}, \text{ion2}\rangle$ under the CNOT operation [100]. First, the ions are initialized in the states (b) $|S, S\rangle$, (c) $|S, D\rangle$, (d) $|D, S\rangle$, or (e) $|D, D\rangle$ (shaded area, $t \leq 0$). Then, the quantum-gate pulse sequence (a) is applied: (i) quantum information encoded in the electronic levels of the *control* ion is transferred to the phonon levels (qubus mode) through $R_c^+(\pi, 0)$, (ii) the single-ion CNOT operation R_{CNOT} is applied to the *target* ion, (iii) the $R_c^+(\pi, 0)$ operation is performed on the *control* ion again.

Figure 1.16 shows the quantum circuit for teleportation from ion 1 to ion 3 [101]. This circuit is realized using the same system ($^{40}Ca^+$) and techniques (pulse irradiation) explained above for the CNOT gate. The pulse sequence for teleportation is summarized in Table 1.1 [101]. First, ion 2 and ion 3 are prepared in the Bell state $|\Psi^+\rangle_{23} = (|0\rangle_2|1\rangle_3 + |1\rangle_2|0\rangle_3)/\sqrt{2}$, the lifetime of which exceeds 100 ms.

Then, at any time within this lifetime, the actual teleportation step can be carried out: ion 1 is prepared in an arbitrary input state through local rotations. In Riebe's experiment, the input state $|\psi_{\text{in}}\rangle$ was drawn from a set of four non-orthogonal test states, $\{|1\rangle, |0\rangle, (|0\rangle + |1\rangle)/\sqrt{2}, (i|0\rangle + |1\rangle)/\sqrt{2}\}$. The Bell measurement is per-

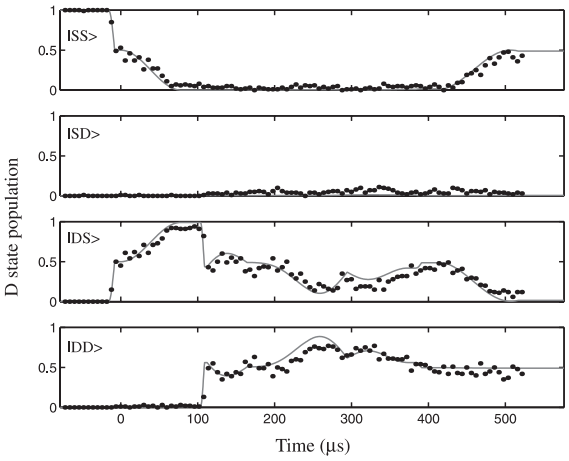

Figure 1.15 The CNOT operation for a $|S + D, S\rangle$ input [100].

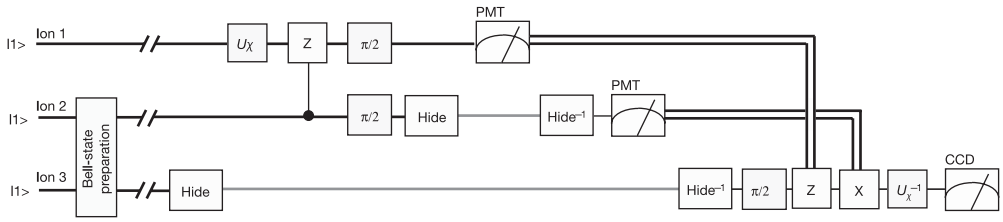

Figure 1.16 Quantum circuit for teleportation from ion 1 to ion 3 [101]. The state to be teleported (input state) is encoded in ion 1 by the operation U_x. The Bell measurement is performed through a controlled Z-gate (phase gate) followed by $\pi/2$ rotations and state detections of ions 1 and 2. This implementation uses a Bell basis rotated by $\pi/4$ with respect to the standard convention. Therefore, a $\pi/2$ rotation on ion 3 is required before the final reconstruction operations Z and X. Grey lines indicate qubits that are protected against light scattering. Ions 1 and 2 are detected by observing their fluorescence on a photomultiplier tube (PMT). For the fidelity analysis, U_x^{-1} is applied to ion 3 and its quantum state is measured by resonance fluorescence using a CCD camera. Here, the initial state is $|1\rangle = |S\rangle$ (different from the CNOT-gate experiment where the initial state is $|0\rangle$).

formed by means of a controlled Z-gate (phase gate) followed by $\pi/2$ rotations and state detections of ions 1 and 2, where the state detection is achieved by fluorescence detection from the $S_{1/2}$ state (logical $|1\rangle$) with a photomultiplier tube (PMT). Conditioned upon the measurement results, if necessary, an appropriate unitary qubit rotation, $-i\sigma_y, -i\sigma_z, i\sigma_x$, is applied in order to recreate the input state in ion 3.

Figure 1.17 shows the results of the teleportation experiment. Here, the fidelities between the input and the output $\langle\psi_{in}|\hat{\rho}_{out}|\psi_{in}\rangle$ are shown. Whenever the fidelity exceeds the classical boundary of 2/3, quantum teleportation is successful. The fidelities of Figure 1.17 are clearly higher than 2/3 for any inputs, thus confirming successful quantum teleportation. The fidelities for the output state without the

Table 1.1 Pulse sequence for teleportation from ion 1 to ion 3 [101]. Here, the superscript C denotes the carrier transition with no change of the motional states (phonon numbers). The corresponding operations are the same as before without the superscript for the CNOT gate. The superscript H denotes the carrier transition from the $S_{1/2}$ ($m = -1/2$) to the $D_{5/2}$ ($m = -5/2$) level in the Zeeman manifold.

	Action	Comment
1	Light at 397 nm	Doppler preparation
2	Light at 729 nm	Sideband cooling
3	Light at 397 nm	Optical pumping
		Entangle
4	$R_3^+(\pi/2, 3\pi/2)$	Entangle ion 3 with motional qubit
5	$R_2^C(\pi, 3\pi/2)$	Prepare ion 2 for entanglement
6	$R_2^+(\pi, \pi/2)$	Entangle ion 2 with ion 3
7	Wait for 1 μS–10 000 μS	Standby for teleportation
8	$R_3^H(\pi, 0)$	Hide target ion
9	$R_1^C(\vartheta_x, \varphi_x)$	Prepare source ion 1 in state x
		Rotate into Bell basis
10	$R_2^+(\pi, 3\pi/2)$	Get motional qubit from ion 2
11	$R_1^+(\pi/\sqrt{2}, \pi/2)$	Composite pulse for phase gate
12	$R_1^+(\pi, 0)$	Composite pulse for phase gate
13	$R_1^+(\pi/\sqrt{2}, \pi/2)$	Composite pulse for phase gate
14	$R_1^+(\pi, 0)$	Composite pulse for phase gate
15	$R_1^C(\pi, \pi/2)$	Spin echo on ion 1
16	$R_3^H(\pi, \pi)$	Unhide ion 3 for spin echo
17	$R_3^C(\pi, \pi/2)$	Spin echo on ion 3
18	$R_3^H(\pi, 0)$	Hide ion 3 again
19	$R_2^+(\pi, \pi/2)$	Write motional qubit back to ion 2
20	$R_1^C(\pi/2, 3\pi/2)$	Part of rotation into Bell basis
21	$R_2^C(\pi/2, \pi/2)$	Finalize rotation into Bell basis
		Read out
22	$R_2^H(\pi, 0)$	Hide ion 2
23	PM Detection for 250 μs	Read out of ion 1 with photomultiplier
24	$R_1^H(\pi, 0)$	Hide ion 1
25	$R_2^H(\pi, \pi)$	Unhide ion 2
26	PM Detection for 250 μs	Read out of ion 2 with photomultiplier
27	$R_2^H(\pi, 0)$	Hide ion 2
28	Wait 300 μs	Let system rephase; part of spin echo
29	$R_3^H(\pi, \pi)$	Unhide ion 3
30	$R_3^C(\pi/2, 3\pi/2 + \phi)$	Change basis
		Reconstruction
31	$R_3^C(\pi, \phi)$	$i\sigma_x = -i\sigma_z$ conditioned on PM detection 1
32	$R_3^C(\pi, \pi/2 + \phi)$	$-i\sigma_y = -i\sigma_z$ conditioned on PM detection 1
33	$R_3^C(\pi, \phi)$	$i\sigma_x$ conditioned on PM detection 2
34	$R_3^C(\vartheta_x, \varphi_x + \pi + \phi)$	Inverse of preparation of x with offset ϕ
35	Light at 397 nm	Read out of ion 3 with camera

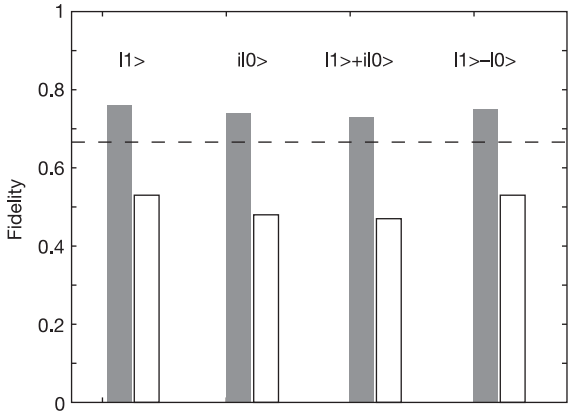

Figure 1.17 Results of the teleportation experiment [100]. The classical boundary of the teleportation fidelity (2/3) is shown by the dashed line. The gray bars correspond to the results obtained in quantum teleportation and the white bars are the results when the reconstruction operations are omitted.

final reconstruction operations are also shown in Figure 1.17. In this case, no more than 1/2 should be obtained for the fidelity and indeed the experimental value was 49.6%.

In the following chapter, an introduction to optical quantum information processing is presented. Most of those concepts, tools, and protocols presented thus far will turn out to have their specific manifestation in the language of quantum optics.

2
Introduction to Optical Quantum Information Processing

Many, if not most experiments related to quantum information are conducted with quantum optical systems. This includes the preparation, manipulation, and measurement of interesting and useful quantum optical states, in particular, entangled states; possibly supplemented by additional atomic systems for storing and processing quantum states.

Why is quantum optics the preferred approach to quantum information demonstrations? Based on mature techniques from nonlinear optics for state preparation such as parametric down conversion, together with the most accessible means for manipulating optical states with linear elements such as beam splitters, there is a long list of optical proof-of-principle demonstrations of various quantum information processing tasks. Some of these experiments are performed with single-photon states, leading to a discrete-variable (DV) encoding of quantum information where, for instance, a qubit space is spanned by two orthogonal polarizations ("photonic qubits"). In other experiments, continuous-variable (CV) states defined in an infinite-dimensional Hilbert space are utilized, for example, expressed in terms of the quadrature amplitudes of an optical, bosonic mode ("photonic qumodes").

Typically, the DV experiments involve some heralding mechanism, rendering them conditional, and hence less efficient; nonetheless, fidelities in the DV schemes are fairly high [104]. Conversely, in the CV regime, unconditional operations and high efficiencies are at the expense of lower fidelities [105]. These two complementary ways of measuring quantized optical fields correspond to the two complementary manifestations of light – in terms of photons that, in a kind of *particle*-like behavior, trigger discrete detection events; and in terms of light *waves* whose continuous amplitude and phase properties are measured similar to the standard detection techniques of classical coherent optics.

In the current chapter, after giving a brief motivation for employing optical schemes in quantum information (Section 2.1), we shall give an introduction to some basic elements and notions of quantum optics in Section 2.2, including the most important quantum optical states, their representations, and their exploitation for photonic qubit and qumode encodings. In the qumode case, Gaussian states, being the most readily available sources in the laboratory, play an exceptional and important role. We shall identify pure Gaussian states as the physical

Quantum Teleportation and Entanglement. Akira Furusawa, Peter van Loock
Copyright © 2011 WILEY-VCH Verlag GmbH & Co. KGaA, Weinheim
ISBN: 978-3-527-40930-3

versions of the CV qumode stabilizer states, as they were introduced in the preceding chapter.

Sections 2.3 and 2.4 are devoted to general quantum optical unitaries and the special case of Gaussian unitary transformations, respectively. Similarly, in Sections 2.5 and 2.6, respectively, we shall discuss non-unitary maps within a general quantum optical framework and in the Gaussian regime, including the important Gaussian channels. Finally, we conclude this chapter with a few remarks on the possibilities of linear optical schemes for quantum information (Section 2.7) and general optical approaches to quantum computation (Section 2.8).

2.1 Why Optics?

For communication, it is obvious that light is the ideal carrier of information at a maximum speed for any signal transfer. However, is there also an advantage of using light for computation? Before talking about quantum information processing, let us start with ordinary electronics. As a typical example, consider AM and FM radio. It is well-known that a signal is encoded as amplitude modulation of a carrier wave in AM radio, as shown in Figure 2.1. Similarly, in FM radio, the signal is encoded as frequency (phase) modulation of a carrier wave, as shown in Figure 2.2.

We can then extract or demodulate the encoded signal through homodyning. This means essentially multiplication between the received modulated wave and an output of a local oscillator with the same frequency as the carrier wave at the receiver. More precisely, when the received wave is $A(t)\sin\omega t$ ($A(t)$: amplitude modulation, AM signal, ω: carrier-wave frequency) and the local oscillator output is $B\sin\omega t$, we obtain

$$A(t)\sin\omega t \times B\sin\omega t = A(t)B \times \frac{1-\cos 2\omega t}{2}\,, \tag{2.1}$$

after the mixing (multiplication) with a mixing circuit. This signal then passes through a low-pass filter, and we get $A(t)B/2$ for the homodyne output. By means of this homodyning, we can tune the frequency (channel) and have the gain B by using the local oscillator. Similarly, we can demodulate the FM signal by changing the local oscillator phase.

The regime discussed here is classical because the frequencies of the carrier waves of AM and FM radio are at most 100 MHz and so we can neglect the photon energy $h\nu$, which is much smaller than the thermal energy $k_{\mathrm{B}}T$. However, the situation totally changes for optical frequencies. These are around 100 THz and the photon energy $h\nu$ is much higher than the thermal energy $k_{\mathrm{B}}T$.

Therefore, in the regime of optical frequencies, we can no longer neglect the occurrence of photons in a quantum mechanical description. In particular, there will be an uncertainty relation between the AM and FM signals of the carrier light and as a result, *we cannot determine the AM and FM signals of the carrier light simultaneously*. Here, in the quantum mechanical description, the AM and FM signals

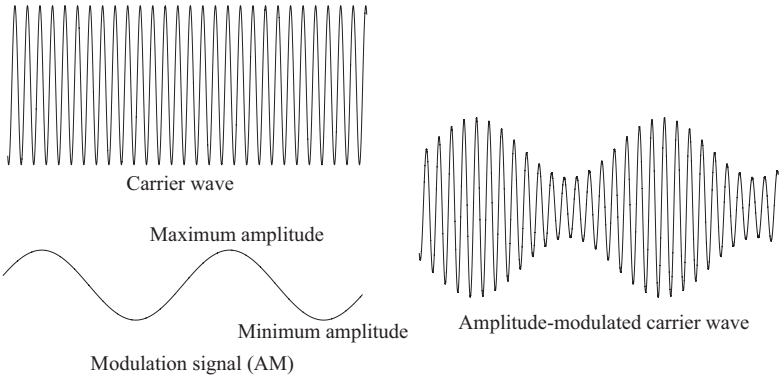

Figure 2.1 Amplitude modulation for AM radio.

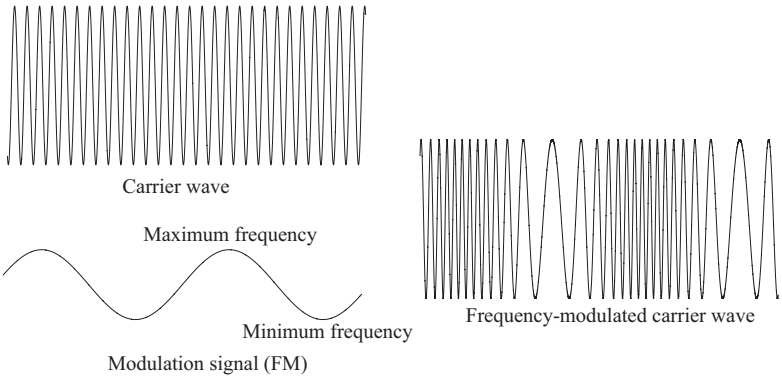

Figure 2.2 Frequency (phase) modulation for FM radio.

would correspond to the quadrature components $\hat{x}$ and $\hat{p}$ defined for a qumode (see Sections 1.2 and 2.2).

We can now perform homodyne detection for optical frequencies. In this case, the laser corresponds to a local oscillator and the beam splitter corresponds to a mixing circuit for optical frequencies. We may then demodulate the AM and FM signals of the carrier light through homodyne detection by changing the phase of the optical local-oscillator beam. Eventually, in this type of measurement, quantum mechanics and the presence of photons becomes manifest as a *shot noise*.

Although the shot noise or quantum fluctuations of the AM and FM signals is inevitable, the signals can become correlated on a nonclassical level for the multi-beam case. For example, with two optical beams A and B, it is possible to have

$$\begin{aligned} \hat{x}_{\mathrm{A}} - \hat{x}_{\mathrm{B}} &\to 0 \,, \\ \hat{p}_{\mathrm{A}} + \hat{p}_{\mathrm{B}} &\to 0 \,, \end{aligned} \tag{2.2}$$

where $\hat{x}_A$ and $\hat{x}_B$ are the AM signals for the optical beams A and B, while $\hat{p}_A$ and $\hat{p}_B$ are the corresponding FM signals. Most importantly, $\hat{x}_A$ and $\hat{p}_A$ cannot simultaneously take on certain values according to the uncertainty relation, and the same applies to $\hat{x}_B$ and $\hat{p}_B$. However, for combinations of the AM and FM signals, simultaneous values such as zero in Eq. (2.2) are possible because the uncertainty relation only prohibits the occurrence of a simultaneous eigenstate of two noncommuting observables of one optical beam, but not for two commuting observables of two optical beams. This type of nonclassical correlation is a manifestation of *entanglement* (see Chapter 3).

To conclude this section, we state that optics is a natural extension of electronics from the classical to the quantum domain and therefore well suited for quantum information processing.

2.2 Quantum Optical States and Encodings

The distinct quantum features of light have been known much longer than the relatively new ideas of quantum information theory. The famous papers by Glauber from 1963 [106–108] based on a rigorous quantum formulation of optical coherence represent milestones of a quantum theory of light. Thanks to the invention of the laser, a lot of progress has been made in experimental quantum optics as well.

What are the consequences of a quantum description of light? Put in simple terms, not only must the position and momentum of massive particles such as electrons obey the Heisenberg uncertainty relation, but also electromagnetic field observables such as the "quadrature amplitudes". In its simplest form, this becomes manifest in an uncertainty relation for a single qumode, as expressed by Eq. (1.43). Effectively, the quantized field represents a collection of quantum oscillators, that is, in our terminology, a collection of qumodes. As a consequence, light fields emitted from a laser source not only exhibit thermal fluctuations that in principle might be entirely suppressed, but also intrinsic unavoidable quantum fluctuations. The quantum state of the electromagnetic field closest to a well determined classical state is the so-called coherent state, with minimum uncertainty symmetrically distributed in phase space. Any decrease of, for example, the amplitude uncertainty ("amplitude squeezing") must be accompanied by an increase of the phase uncertainty ("phase antisqueezing") because otherwise the Heisenberg uncertainty relation is violated.

Originally, squeezing was considered as a means to enhance the sensitivity of optical measurements near the standard quantum limit (for example, in the interferometric detection of gravitational radiation [109] or for low-noise communications [110]). Later, we shall see that squeezed light represents a readily available resource to produce entanglement (Chapter 3). Let us now start by describing the quantization of the free electromagnetic field.

2.2.1 Field Quantization

In quantum optics textbooks, the electromagnetic field is usually quantized without a rigorous quantum field theoretical approach based on a more heuristic substitution of operators for c numbers. This approach is sufficient to identify modes of the electromagnetic field as quantum mechanical harmonic oscillators. It ultimately reveals that the number of photons in a mode corresponds to the degree of excitation of a quantum oscillator. Thus, in this sense, photons have a much more abstract and mathematical meaning than the "light particles" that Einstein's 1905 papers referred to for interpreting the photoelectric effect.

The starting point now shall be the Maxwell equations of classical electrodynamics,

$$\nabla \times \boldsymbol{E} = -\frac{\partial \boldsymbol{B}}{\partial t} \,, \tag{2.3}$$

$$\nabla \times \boldsymbol{H} = \boldsymbol{j} + \frac{\partial \boldsymbol{D}}{\partial t} \,, \tag{2.4}$$

$$\nabla \cdot \boldsymbol{D} = \rho \,, \tag{2.5}$$

$$\nabla \cdot \boldsymbol{B} = 0 \,, \tag{2.6}$$

with $\boldsymbol{D} = \varepsilon_0 \boldsymbol{E} + \boldsymbol{P}$ and $\boldsymbol{B} = \mu_0 \boldsymbol{H} + \boldsymbol{M}$. Here, ε_0 is the electric permittivity of free space and μ_0 is the magnetic permeability (with $\varepsilon_0 \mu_0 = c^{-2}$, c the vacuum speed of light). Considering the free electromagnetic field allows us to remove all charges and currents ($\rho = 0$, $\boldsymbol{j} = 0$), and also any electric polarization and magnetization ($\boldsymbol{P} = 0$, $\boldsymbol{M} = 0$).

By inserting Eq. (2.4) with $\boldsymbol{H} = \boldsymbol{B}/\mu_0$ into Eq. (2.3), with $\boldsymbol{D} = \varepsilon_0 \boldsymbol{E}$, and with $\nabla \times \nabla \times \boldsymbol{E} = \nabla(\nabla \cdot \boldsymbol{E}) - \nabla^2 \boldsymbol{E}$ and Eq. (2.5), one obtains the wave equation for the electric field

$$\nabla^2 \boldsymbol{E} - \frac{1}{c^2} \frac{\partial^2 \boldsymbol{E}}{\partial t^2} = 0 \,, \tag{2.7}$$

and likewise for the magnetic field.

In his quantum treatment of optical coherence, Glauber regarded the electric and magnetic field as a pair of Hermitian operators, $\hat{\boldsymbol{E}}(\boldsymbol{r}, t)$ and $\hat{\boldsymbol{B}}(\boldsymbol{r}, t)$, both obeying the wave equation [107]. Written as a Fourier integral, Hermiticity of the electric field operator,

$$\hat{\boldsymbol{E}}(\boldsymbol{r}, t) = \frac{1}{\sqrt{2\pi}} \int_{-\infty}^{\infty} \mathrm{d}\omega \hat{\boldsymbol{\mathcal{E}}}(\boldsymbol{r}, \omega) \mathrm{e}^{-\mathrm{i}\omega t} \,, \tag{2.8}$$

is ensured through $\hat{\boldsymbol{\mathcal{E}}}(\boldsymbol{r}, -\omega) = \hat{\boldsymbol{\mathcal{E}}}^{\dagger}(\boldsymbol{r}, \omega)$. The positive-frequency part,

$$\hat{\boldsymbol{E}}^{(+)}(\boldsymbol{r}, t) = \frac{1}{\sqrt{2\pi}} \int_{0}^{\infty} \mathrm{d}\omega \hat{\boldsymbol{\mathcal{E}}}(\boldsymbol{r}, \omega) \mathrm{e}^{-\mathrm{i}\omega t} \,, \tag{2.9}$$

and the negative-frequency part,

$$\hat{\boldsymbol{E}}^{(-)}(\boldsymbol{r},t) = \frac{1}{\sqrt{2\pi}}\int_{-\infty}^{0} \mathrm{d}\omega\,\hat{\boldsymbol{\mathcal{E}}}(\boldsymbol{r},\omega)\mathrm{e}^{-\mathrm{i}\omega t} = \frac{1}{\sqrt{2\pi}}\int_{0}^{\infty} \mathrm{d}\omega\,\hat{\boldsymbol{\mathcal{E}}}^{\dagger}(\boldsymbol{r},\omega)\mathrm{e}^{+\mathrm{i}\omega t}\,, \tag{2.10}$$

regarded separately, are non-Hermitian operators with $\hat{\boldsymbol{E}}(\boldsymbol{r},t) = \hat{\boldsymbol{E}}^{(+)}(\boldsymbol{r},t) + \hat{\boldsymbol{E}}^{(-)}(\boldsymbol{r},t)$. They are mutually adjoint, that is, $\hat{\boldsymbol{E}}^{(-)}(\boldsymbol{r},t) = \hat{\boldsymbol{E}}^{(+)\dagger}(\boldsymbol{r},t)$. In fact, Glauber realized that $\hat{\boldsymbol{E}}^{(-)}(\boldsymbol{r},t)$ and $\hat{\boldsymbol{E}}^{(+)}(\boldsymbol{r},t)$ must represent photon creation and annihilation operators, respectively [107].

However, we will find it more convenient to describe the electromagnetic field by a discrete set of "mode variables" rather than the whole continuum of frequencies. We will now deal with this discretization according to Walls and Milburn [29] whose approach is based on Glauber [108].

2.2.1.1 Discrete Modes

The free electromagnetic field vectors may both be determined from a vector potential $\boldsymbol{A}(\boldsymbol{r},t)$ as

$$\boldsymbol{B} = \nabla\times\boldsymbol{A}\,, \qquad \boldsymbol{E} = -\frac{\partial\boldsymbol{A}}{\partial t}\,, \tag{2.11}$$

where we have taken the Coulomb gauge condition $\nabla\cdot\boldsymbol{A} = 0$. Using these equations for the vector potential and the free Maxwell equations, we can also derive the wave equation for $\boldsymbol{A}(\boldsymbol{r},t)$,

$$\nabla^2\boldsymbol{A} - \frac{1}{c^2}\frac{\partial^2\boldsymbol{A}}{\partial t^2} = 0\,. \tag{2.12}$$

The vector potential can also be written as $\boldsymbol{A}(\boldsymbol{r},t) = \boldsymbol{A}^{(+)}(\boldsymbol{r},t) + \boldsymbol{A}^{(-)}(\boldsymbol{r},t)$, where again $\boldsymbol{A}^{(+)}(\boldsymbol{r},t)$ contains all amplitudes which vary as $\mathrm{e}^{-\mathrm{i}\omega t}$ for $\omega > 0$ and $\boldsymbol{A}^{(-)}(\boldsymbol{r},t)$ contains all amplitudes which vary as $\mathrm{e}^{+\mathrm{i}\omega t}$ [the positive and negative frequency parts here are still c numbers, $\boldsymbol{A}^{(-)} = (\boldsymbol{A}^{(+)})^*$]. In order to discretize the field variables, we assume that the field is confined within a spatial volume of finite size. Now, we can expand the vector potential in terms of a discrete set of orthogonal mode functions,

$$\boldsymbol{A}^{(+)}(\boldsymbol{r},t) = \sum_k c_k\,\boldsymbol{u}_k(\boldsymbol{r})\mathrm{e}^{-\mathrm{i}\omega_k t}\,. \tag{2.13}$$

The Fourier coefficients c_k are constant because the field is free. If the volume contains no refracting materials, every vector mode function $\boldsymbol{u}_k(\boldsymbol{r})$ corresponding to the frequency ω_k satisfies the wave equation [as the mode functions must independently satisfy Eq. (2.12)]

$$\left(\nabla^2 + \frac{\omega_k^2}{c^2}\right)\boldsymbol{u}_k(\boldsymbol{r}) = 0\,. \tag{2.14}$$

More generally, the mode functions are required to obey the transversality condition,

$$\nabla \cdot \boldsymbol{u}_k(\boldsymbol{r}) = 0 \,, \tag{2.15}$$

and they shall form a complete orthonormal set,

$$\int \boldsymbol{u}_k^*(\boldsymbol{r})\boldsymbol{u}_{k'}(\boldsymbol{r})\mathrm{d}^3 r = \delta_{kk'} \,. \tag{2.16}$$

The plane wave mode functions appropriate to a cubical volume of side L may now be written as

$$\boldsymbol{u}_k(\boldsymbol{r}) = L^{-3/2}\boldsymbol{e}^{(\lambda)}\mathrm{e}^{\mathrm{i}\boldsymbol{k}\cdot\boldsymbol{r}} \,, \tag{2.17}$$

with $\boldsymbol{e}^{(\lambda)}$ being a unit polarization vector [perpendicular to $\boldsymbol{k}$ due to transversality Eq. (2.15)]. We can verify that this choice leads with the wave equation (Eq. (2.14)) to the correct linear dispersion relation $|\boldsymbol{k}| = \omega_k/c$. The polarization index ($\lambda = 1, 2$) and the three components of the wave vector $\boldsymbol{k}$ are all labeled by the mode index k. The permissible values of the components of $\boldsymbol{k}$ are determined in a familiar way by means of periodic boundary conditions,

$$\begin{aligned} &k_x = \frac{2\pi n_x}{L} \,, \qquad k_y = \frac{2\pi n_y}{L} \,, \qquad k_z = \frac{2\pi n_z}{L} \,, \\ &n_x, n_y, n_z = 0, \pm 1, \pm 2, \ldots \end{aligned} \tag{2.18}$$

The vector potential then takes the quantized form [29, 108, 111]

$$\begin{aligned} \hat{\boldsymbol{A}}(\boldsymbol{r}, t) &= \sum_k \left(\frac{\hbar}{2\omega_k \varepsilon_0}\right)^{1/2} \left[\hat{a}_k \boldsymbol{u}_k(\boldsymbol{r})\mathrm{e}^{-\mathrm{i}\omega_k t} + \hat{a}_k^\dagger \boldsymbol{u}_k^*(\boldsymbol{r})\mathrm{e}^{+\mathrm{i}\omega_k t}\right] \\ &= \sum_k \left(\frac{\hbar}{2\omega_k \varepsilon_0 L^3}\right)^{1/2} \boldsymbol{e}^{(\lambda)} \left[\hat{a}_k \mathrm{e}^{\mathrm{i}(\boldsymbol{k}\cdot\boldsymbol{r}-\omega_k t)} + \hat{a}_k^\dagger \mathrm{e}^{-\mathrm{i}(\boldsymbol{k}\cdot\boldsymbol{r}-\omega_k t)}\right], \end{aligned} \tag{2.19}$$

where now the Fourier amplitudes c_k from Eq. (2.13) (complex numbers in the classical theory) are replaced by the operators $\hat{a}_k$ times a normalization factor. Quantization of the electromagnetic field is accomplished by choosing $\hat{a}_k$ and $\hat{a}_k^\dagger$ to be mutually adjoint operators. The normalization factor renders the pair of operators $\hat{a}_k$ and $\hat{a}_k^\dagger$ dimensionless. According to Eq. (2.11), the electric field operator becomes

$$\hat{\boldsymbol{E}}(\boldsymbol{r}, t) = \mathrm{i}\sum_k \left(\frac{\hbar\omega_k}{2\varepsilon_0}\right)^{1/2} \left[\hat{a}_k \boldsymbol{u}_k(\boldsymbol{r})\mathrm{e}^{-\mathrm{i}\omega_k t} - \hat{a}_k^\dagger \boldsymbol{u}_k^*(\boldsymbol{r})\mathrm{e}^{+\mathrm{i}\omega_k t}\right] \,, \tag{2.20}$$

and, likewise, the magnetic field operator,

$$\hat{\boldsymbol{B}}(\boldsymbol{r}, t) = \mathrm{i}\sum_k \left(\frac{\hbar}{2\omega_k \varepsilon_0}\right)^{1/2} \left[\hat{a}_k \boldsymbol{k} \times \boldsymbol{u}_k(\boldsymbol{r})\mathrm{e}^{-\mathrm{i}\omega_k t} - \hat{a}_k^\dagger \boldsymbol{k} \times \boldsymbol{u}_k^*(\boldsymbol{r})\mathrm{e}^{+\mathrm{i}\omega_k t}\right] \,. \tag{2.21}$$

Inserting these field operators into the Hamiltonian of the electromagnetic field,

$$\hat{H} = \frac{1}{2}\int \left(\varepsilon_0\,\hat{\boldsymbol{E}}^2 + \mu_0^{-1}\hat{\boldsymbol{B}}^2\right) \mathrm{d}^3 r\,, \tag{2.22}$$

using Eqs. (2.15) and (2.16), the Hamiltonian may be reduced to

$$\hat{H} = \frac{1}{2}\sum_k \hbar\omega_k \left(\hat{a}_k^\dagger \hat{a}_k + \hat{a}_k \hat{a}_k^\dagger\right)\,. \tag{2.23}$$

With the appropriate commutation relations for the operators $\hat{a}_k$ and $\hat{a}_k^\dagger$, the bosonic commutation relations

$$[\hat{a}_k, \hat{a}_{k'}] = \left[\hat{a}_k^\dagger, \hat{a}_{k'}^\dagger\right] = 0\,, \qquad \left[\hat{a}_k, \hat{a}_{k'}^\dagger\right] = \delta_{kk'}\,, \tag{2.24}$$

we recognize the Hamiltonian of an ensemble of independent quantum harmonic oscillators,

$$\hat{H} = \sum_k \hbar\omega_k \left(\hat{a}_k^\dagger \hat{a}_k + \frac{1}{2}\right)\,. \tag{2.25}$$

The entire electromagnetic field therefore may be described by the tensor product state of all these quantum harmonic oscillators of which each represents a *single electromagnetic mode*. The operator $\hat{a}_k^\dagger \hat{a}_k$ stands for the excitation number (photon number) of mode k, $\hat{a}_k$ itself is a photon annihilation, $\hat{a}_k^\dagger$ a photon creation operator of mode k. For most quantum optical calculations, in particular with regard to a compact description of protocols in quantum information theory, it is very convenient to use this discrete single-mode picture. However, we will also encounter the situation where we are explicitly interested in the continuous frequency spectrum of "modes" that are distinct from each other in a discrete sense only with respect to spatial separation and/or polarization. Let us briefly consider such a decomposition of the electromagnetic field into a continuous set of frequency "modes".

Quantized electromagnetic field

electric field:

$$\hat{\boldsymbol{E}}(\boldsymbol{r}, t) = \mathrm{i}\sum_k \left(\frac{\hbar\omega_k}{2\varepsilon_0}\right)^{1/2} \left[\hat{a}_k \boldsymbol{u}_k(\boldsymbol{r})\mathrm{e}^{-\mathrm{i}\omega_k t} - \hat{a}_k^\dagger \boldsymbol{u}_k^*(\boldsymbol{r})\mathrm{e}^{+\mathrm{i}\omega_k t}\right]$$

magnetic field:

$$\hat{\boldsymbol{B}}(\boldsymbol{r}, t) = \mathrm{i}\sum_k \left(\frac{\hbar}{2\omega_k\varepsilon_0}\right)^{1/2} \left[\hat{a}_k \boldsymbol{k}\times\boldsymbol{u}_k(\boldsymbol{r})\mathrm{e}^{-\mathrm{i}\omega_k t} - \hat{a}_k^\dagger \boldsymbol{k}\times\boldsymbol{u}_k^*(\boldsymbol{r})\mathrm{e}^{+\mathrm{i}\omega_k t}\right]$$

Hamiltonian:

$$\hat{H} = \frac{1}{2}\int \left(\varepsilon_0\hat{\boldsymbol{E}}^2 + \mu_0^{-1}\hat{\boldsymbol{B}}^2\right)\mathrm{d}^3 r = \sum_k \hbar\omega_k \left(\hat{a}_k^\dagger \hat{a}_k + \frac{1}{2}\right)$$

bosonic commutators:

$$[\hat{a}_k, \hat{a}_{k'}] = \left[\hat{a}_k^\dagger, \hat{a}_{k'}^\dagger\right] = 0\,, \qquad \left[\hat{a}_k, \hat{a}_{k'}^\dagger\right] = \delta_{kk'}$$

2.2.1.2 Continuous Modes

It seems in some ways more natural to describe the electromagnetic field vectors by Fourier integrals rather than by Fourier series, although the continuous formalism is less compact. The discrete mode expansion of the electric field in Eq. (2.20) becomes, in the continuous limit [111],

$$\hat{\boldsymbol{E}}(\boldsymbol{r}, t) = \frac{\mathrm{i}}{(2\pi)^{3/2}} \sum_\lambda \int \mathrm{d}^3 k \left(\frac{\hbar\omega}{2\varepsilon_0}\right)^{1/2} \boldsymbol{e}^{(\lambda)} \times \left[\hat{a}(\boldsymbol{k}, \lambda)\mathrm{e}^{\mathrm{i}(\boldsymbol{k}\cdot\boldsymbol{r}-\omega t)} - \hat{a}^\dagger(\boldsymbol{k}, \lambda)\mathrm{e}^{-\mathrm{i}(\boldsymbol{k}\cdot\boldsymbol{r}-\omega t)}\right]\,, \tag{2.26}$$

where the mode index k has been replaced by the discrete polarization index λ and the three continuous wave vector components. This corresponds to the limit of a very large cube of size $L \to \infty$. The discrete expansion of the magnetic field from Eq. (2.21) now becomes [111]

$$\hat{\boldsymbol{B}}(\boldsymbol{r}, t) = \frac{\mathrm{i}}{(2\pi)^{3/2}} \sum_\lambda \int \mathrm{d}^3 k \left(\frac{\hbar}{2\omega\varepsilon_0}\right)^{1/2} \boldsymbol{k} \times \boldsymbol{e}^{(\lambda)} \times \left[\hat{a}(\boldsymbol{k}, \lambda)\mathrm{e}^{\mathrm{i}(\boldsymbol{k}\cdot\boldsymbol{r}-\omega t)} - \hat{a}^\dagger(\boldsymbol{k}, \lambda)\mathrm{e}^{-\mathrm{i}(\boldsymbol{k}\cdot\boldsymbol{r}-\omega t)}\right]\,. \tag{2.27}$$

The commutation relations in this continuous representation take the form

$$[\hat{a}(\boldsymbol{k}, \lambda), \hat{a}(\boldsymbol{k}', \lambda')] = [\hat{a}^\dagger(\boldsymbol{k}, \lambda), \hat{a}^\dagger(\boldsymbol{k}', \lambda')] = 0\,, \tag{2.28}$$

$$[\hat{a}(\boldsymbol{k}, \lambda), \hat{a}^\dagger(\boldsymbol{k}', \lambda')] = \delta^3(\boldsymbol{k} - \boldsymbol{k}')\,\delta_{\lambda\lambda'}\,. \tag{2.29}$$

Note that now the photon number operator must be defined within a finite wave vector range, $\hat{a}^\dagger(\boldsymbol{k})\hat{a}(\boldsymbol{k})d^3k$, which means the operator $\hat{a}(\boldsymbol{k})$ has the dimension of $L^{3/2}$.

Finally, in terms of Glauber's continuous Fourier integral representation from Eq. (2.9), we can also write, for example, the electric field as

$$\hat{E}^{(+)}(z, t) = [\hat{E}^{(-)}(z, t)]^\dagger = \frac{1}{\sqrt{2\pi}} \int_0^\infty \mathrm{d}\omega \left(\frac{u\hbar\omega}{2cA_{\mathrm{tr}}}\right)^{1/2} \hat{a}(\omega)\mathrm{e}^{-\mathrm{i}\omega(t-z/c)}\,, \tag{2.30}$$

with $\hat{E}(z, t) = \hat{E}^{(+)}(z, t) + \hat{E}^{(-)}(z, t)$, traveling in the positive-z direction ($|\boldsymbol{k}| = \omega/c$) and describing a single unspecified polarization. The parameter A_{tr} represents the transverse structure of the field (dimension of L^2) and u is a units-dependent constant [for the units we have used in the Maxwell equations (SI

units), $u = \varepsilon_0^{-1}$, for Gaussian units, $u = 4\pi$]. Here, the photon number operator must be defined within a finite frequency range, $\hat{a}^\dagger(\omega)\hat{a}(\omega)\mathrm{d}\omega$, which means the operator $\hat{a}(\omega)$ has the dimension of time$^{1/2}$. Compared to the discrete expansion, a phase shift of $\exp(\mathrm{i}\pi/2)$ has been absorbed by the amplitude operator $\hat{a}(\omega)$. The correct commutation relations are now

$$[\hat{a}(\omega), \hat{a}(\omega')] = [\hat{a}^\dagger(\omega), \hat{a}^\dagger(\omega')] = 0 \ , \quad [\hat{a}(\omega), \hat{a}^\dagger(\omega')] = \delta(\omega - \omega') \ . \quad (2.31)$$

2.2.2 Quadratures

Let us introduce the so-called *quadratures* by looking at a single mode taken from the electric field in Eq. (2.20) for a single polarization [the phase shift of $\exp(\mathrm{i}\pi/2)$ is absorbed into $\hat{a}_k$],

$$\hat{E}_k(\boldsymbol{r}, t) = E_0 \left[\hat{a}_k \mathrm{e}^{\mathrm{i}(\boldsymbol{k}\cdot\boldsymbol{r} - \omega_k t)} + \hat{a}_k^\dagger \mathrm{e}^{-\mathrm{i}(\boldsymbol{k}\cdot\boldsymbol{r} - \omega_k t)} \right] . \quad (2.32)$$

The constant E_0 contains all the dimensional prefactors. By using Eq. (1.42), we can rewrite the mode as

$$\hat{E}_k(\boldsymbol{r}, t) = 2E_0 \left[\hat{x}_k \cos(\omega_k t - \boldsymbol{k}\cdot\boldsymbol{r}) + \hat{p}_k \sin(\omega_k t - \boldsymbol{k}\cdot\boldsymbol{r}) \right] . \quad (2.33)$$

Apparently, the "position" and "momentum" operators $\hat{x}_k$ and $\hat{p}_k$ represent the in-phase and the out-of-phase components of the electric field amplitude of the qumode k with respect to a (classical) reference wave $\propto \cos(\omega_k t - \boldsymbol{k}\cdot\boldsymbol{r})$. The choice of the phase of this wave is arbitrary, of course, and a more general reference wave would lead us to the single-mode description,

$$\hat{E}_k(\boldsymbol{r}, t) = 2E_0 \left[\hat{x}_k^{(\Theta)} \cos(\omega_k t - \boldsymbol{k}\cdot\boldsymbol{r} - \Theta) + \hat{p}_k^{(\Theta)} \sin(\omega_k t - \boldsymbol{k}\cdot\boldsymbol{r} - \Theta) \right] , \quad (2.34)$$

with the "more general" quadratures

$$\hat{x}_k^{(\Theta)} = \left(\hat{a}_k \mathrm{e}^{-\mathrm{i}\Theta} + \hat{a}_k^\dagger \mathrm{e}^{+\mathrm{i}\Theta} \right) /2 \ , \qquad \hat{p}_k^{(\Theta)} = \left(\hat{a}_k \mathrm{e}^{-\mathrm{i}\Theta} - \hat{a}_k^\dagger \mathrm{e}^{+\mathrm{i}\Theta} \right) /2\mathrm{i} \ . \quad (2.35)$$

These "new" quadratures can be obtained from $\hat{x}_k$ and $\hat{p}_k$ through the rotation

$$\begin{pmatrix} \hat{x}_k^{(\Theta)} \\ \hat{p}_k^{(\Theta)} \end{pmatrix} = \begin{pmatrix} \cos\Theta & \sin\Theta \\ -\sin\Theta & \cos\Theta \end{pmatrix} \begin{pmatrix} \hat{x}_k \\ \hat{p}_k \end{pmatrix} . \quad (2.36)$$

Since this is a unitary transformation, we again end up with a pair of conjugate observables fulfilling the commutation relation in Eq. (1.39). Furthermore, because $\hat{p}_k^{(\Theta)} = \hat{x}_k^{(\Theta+\pi/2)}$, the whole continuum of quadratures is covered by $\hat{x}_k^{(\Theta)}$ with $\Theta \in [0, \pi)$. This continuum of observables can be directly measured by homodyne

detection, where the phase of the so-called local-oscillator field enables one to tune between the rotated quadrature bases (see Section 2.6). The corresponding quadrature eigenstates are the (unphysical) CV qumode stabilizer states, as introduced in Section 1.3.2. A continuous set of rotated stabilizers is given by Eq. (1.71).

We shall mostly refer to the conjugate pair of quadratures $\hat{x}_k$ and $\hat{p}_k$ as the position and momentum of qumode k, corresponding to $\Theta = 0$ and $\Theta = \pi/2$. In terms of these quadratures, the number operator becomes

$$\hat{n}_k = \hat{a}_k^\dagger \hat{a}_k = \hat{x}_k^2 + \hat{p}_k^2 - \frac{1}{2} , \tag{2.37}$$

using Eq. (1.39).

2.2.3 Coherent States

We have seen that the qumode states of the electromagnetic field can be expressed in terms of the Fock basis, describing the photon or excitation number of the corresponding quantum harmonic oscillator. Another useful basis for representing optical fields are the coherent states. As opposed to the Fock states, the coherent states' photon number and phase exhibit equal, minimal Heisenberg uncertainties. In this sense, coherent states are the quantum states closest to a classical description of the field. They also correspond to the output states that are ideally produced from a laser source.

Coherent states are the eigenstates of the annihilation operator $\hat{a}$,

$$\hat{a}|\alpha\rangle = \alpha|\alpha\rangle , \tag{2.38}$$

with complex eigenvalues α since $\hat{a}$ is a non-Hermitian operator. Their mean photon number is given by

$$\langle\alpha|\hat{n}|\alpha\rangle = \langle\alpha|\hat{a}^\dagger\hat{a}|\alpha\rangle = |\alpha|^2 . \tag{2.39}$$

The quantum optical displacement operator is given by

$$\hat{D}(\alpha) = \exp(\alpha\hat{a}^\dagger - \alpha^*\hat{a}) = \exp(2\mathrm{i}p_\alpha\hat{x} - 2\mathrm{i}x_\alpha\hat{p}) , \tag{2.40}$$

with $\alpha = x_\alpha + \mathrm{i}p_\alpha$ and again $\hat{a} = \hat{x} + \mathrm{i}\hat{p}$. The displacement operator acting on $\hat{a}$ in the Heisenberg picture yields a displacement by the complex number α,

$$\hat{D}^\dagger(\alpha)\hat{a}\hat{D}(\alpha) = \hat{a} + \alpha . \tag{2.41}$$

Coherent states are now displaced vacuum states,

$$|\alpha\rangle = \hat{D}(\alpha)|0\rangle . \tag{2.42}$$

The Fock basis expansion for coherent states is

$$|\alpha\rangle = \exp\left(-\frac{|\alpha|^2}{2}\right)\sum_{n=0}^{\infty}\frac{\alpha^n}{\sqrt{n!}}|n\rangle , \tag{2.43}$$

using the polynomial expansion of $\exp(\alpha\hat{a}^\dagger)$ with Eq. (1.31) and the fact that $\exp(-\alpha^*\hat{a})$ leaves the vacuum state $|0\rangle$ unchanged. Apparently, the photon statistics of coherent states obeys a Poissonian distribution with mean photon number $|\alpha|^2$,

$$|\langle n|\alpha\rangle|^2 = \frac{|\alpha|^{2n}}{n!}\exp(-|\alpha|^2)\,. \tag{2.44}$$

Though being non-orthogonal, coherent states represent a very useful basis for representing optical fields with the completeness relation, [where the integration is over the whole complex plane with $\mathrm{d}^2\alpha \equiv \mathrm{d}(\mathrm{Re}\alpha)\mathrm{d}(\mathrm{Im}\alpha) \equiv \mathrm{d}x_\alpha \mathrm{d}p_\alpha$],

$$\frac{1}{\pi}\int |\alpha\rangle\langle\alpha|\mathrm{d}^2\alpha = \mathbb{1}\,, \tag{2.45}$$

which can be proven using Eq. (2.43) and polar coordinates in the complex plane [29].

In fact, coherent states are actually overcomplete (a consequence of their lack of orthogonality) because any coherent state can be expanded in terms of the others,

$$|\alpha\rangle = \frac{1}{\pi}\int \mathrm{d}^2\beta|\beta\rangle\langle\beta|\alpha\rangle = \frac{1}{\pi}\int \mathrm{d}^2\beta|\beta\rangle\exp(-|\alpha|^2/2 - |\beta|^2/2 + \alpha\beta^*)\,. \tag{2.46}$$

Always, when we consider a coherent state of the electromagnetic field as a whole (e.g., for a broadband field), what we mean is a tensor product of coherent states for the individual modes $|\alpha_1\rangle \otimes |\alpha_2\rangle \otimes \cdots$.

2.2.4 Squeezed States

In general, squeezing refers to the reduction of quantum fluctuations in one variable below the standard quantum limit (the minimal noise level of the vacuum state) at the expense of an increased uncertainty of the conjugate variable. Nonlinear optical interactions enable one to achieve this experimentally. There are various schemes for generating squeezed states of light, differing, especially, in the optical nonlinearity they use. The most common approach is to use a so-called $\chi^{(2)}$ nonlinearity,[1)] where in an optical parametric amplifier (OPA), a pump beam produces signal and idler beams. Depending on the pump strength, one obtains multiphoton states with high squeezing or a state with very small numbers of photons

1) Describing the relation between the polarization $\boldsymbol{P}$, i.e., the response of a nonmagnetic medium to an external light field, and the external light field, $P_i(\boldsymbol{r},t) = P_i^{(0)} + \sum_j \chi_{ij}^{(1)} E_j(\boldsymbol{r},t) + \sum_{jk}\chi_{ijk}^{(2)} E_j(\boldsymbol{r},t)E_k(\boldsymbol{r},t) + \sum_{jkl}\chi_{ijkl}^{(3)} E_j(\boldsymbol{r},t)E_k(\boldsymbol{r},t)E_l(\boldsymbol{r},t) + \cdots$. The nth order susceptibilities $\chi^{(n)}$ are then given by tensors of rank $n+1$. Typically, the linear susceptibility $\chi^{(1)}$ is the dominant contribution, assuming $P_i^{(0)} = 0$. If the electric field is linearly polarized and the induced polarization of the medium has only one nonzero component, say P_1, the susceptibility tensors can be replaced by scalars, $\chi_{11}^{(1)} \equiv \chi^{(1)}$, $\chi_{111}^{(2)} \equiv \chi^{(2)}$, etc.

in the low-squeezing regime. Higher nonlinearities such as $\chi^{(3)}$ are typically rather weak and hence require larger field intensities for their effective enhancement.

The output state of degenerate parametric amplification where the signal and idler frequencies each are half the pump frequency corresponds to a single-mode squeezed state. This single-mode squeezing can be calculated with an interaction Hamiltonian quadratic in the creation and annihilation operators,

$$\hat{H}_{\text{int}} = \mathrm{i}\hbar\frac{\kappa}{2}\left(\hat{a}^{\dagger 2}\mathrm{e}^{\mathrm{i}\Theta} - \hat{a}^{2}\mathrm{e}^{-\mathrm{i}\Theta}\right) . \tag{2.47}$$

It describes the amplification of the signal mode $\hat{a}$ at half the pump frequency in an interaction picture. The coherent pump mode is assumed to be classical (the so-called parametric approximation), its real amplitude $|\alpha_{\text{pump}}|$ is absorbed in κ, and the pump phase is Θ. The parameter κ also contains the susceptibility, $\kappa \propto \chi^{(2)}|\alpha_{\text{pump}}|$.[2)]

In the interaction picture, we can insert $\hat{H}_{\text{int}}$ into the Heisenberg equation of motion Eq. (1.59) for the annihilation operator, and obtain (taking zero pump phase $\Theta = 0$)

$$\frac{\mathrm{d}}{\mathrm{d}t}\hat{a}(t) = \frac{1}{\mathrm{i}\hbar}\left[\hat{a}(t), \hat{H}_{\text{int}}\right] = \kappa\,\hat{a}^{\dagger}(t) . \tag{2.48}$$

This equation is solved by

$$\hat{a}(t) = \hat{a}(0)\cosh(\kappa t) + \hat{a}^{\dagger}(0)\sinh(\kappa t) . \tag{2.49}$$

The quadrature operators evolve correspondingly into

$$\hat{x}(t) = \mathrm{e}^{+\kappa t}\hat{x}(0) , \qquad \hat{p}(t) = \mathrm{e}^{-\kappa t}\hat{p}(0) . \tag{2.50}$$

The uncertainty of the p quadrature decreases, whereas that of the x quadrature grows,

$$\left\langle\left[\Delta\hat{x}(t)\right]^2\right\rangle = \mathrm{e}^{+2\kappa t}\left\langle\left[\Delta\hat{x}^{(0)}\right]^2\right\rangle, \qquad \left\langle\left[\Delta\hat{p}(t)\right]^2\right\rangle = \mathrm{e}^{-2\kappa t}\left\langle\left[\Delta\hat{p}^{(0)}\right]^2\right\rangle . \tag{2.51}$$

For initial quadratures corresponding to a coherent-state or vacuum-state input labeled by a superscript "(0)", the evolved states remain minimum uncertainty states with p fluctuations below and x fluctuations above the vacuum uncertainty. They have become *quadrature squeezed states*.

According to Eq. (1.54) with the Hamiltonian from Eq. (2.47) and $t_0 = 0$, we may introduce the unitary squeezing or squeeze operator $\hat{S}(\zeta)$ by defining $\zeta \equiv r\exp(\mathrm{i}\Theta)$ with the squeezing parameter $r \equiv -\kappa t$ (a dimensionless effective interaction time; the minus sign is the usual phase convention),

$$\hat{U}(t,0) = \exp\left[\frac{\kappa}{2}\left(\hat{a}^{\dagger 2}\mathrm{e}^{\mathrm{i}\Theta} - \hat{a}^{2}\mathrm{e}^{-\mathrm{i}\Theta}\right)t\right] \equiv \hat{S}(\zeta) = \exp\left(\frac{\zeta^*}{2}\hat{a}^{2} - \frac{\zeta}{2}\hat{a}^{\dagger 2}\right) . \tag{2.52}$$

2) The fully quantum mechanical Hamiltonian is $\hat{H}_{\text{int}} \propto \hat{a}^{\dagger 2}\hat{a}_{\text{pump}} - \hat{a}^{2}\hat{a}^{\dagger}_{\text{pump}}$, and with the parametric approximation we assume $\hat{a}_{\text{pump}} \to \alpha_{\text{pump}} = |\alpha_{\text{pump}}|\mathrm{e}^{\mathrm{i}\Theta}$.

The squeezing operator obviously satisfies $\hat{S}^{\dagger}(\zeta) = \hat{S}^{-1}(\zeta) = \hat{S}(-\zeta)$. Applying it to an arbitrary initial operator $\hat{a}(0) \equiv \hat{a}$ yields the transformation [Eq. (1.57)]

$$\hat{S}^{\dagger}(\zeta)\hat{a}\,\hat{S}(\zeta) = \hat{a}\cosh r - \hat{a}^{\dagger}\mathrm{e}^{\mathrm{i}\Theta}\sinh r\ . \tag{2.53}$$

For the rotated mode

$$\hat{x}^{(\Theta/2)} + \mathrm{i}\hat{p}^{(\Theta/2)} = (\hat{x} + \mathrm{i}\hat{p})\mathrm{e}^{-\mathrm{i}\Theta/2} = \hat{a}\mathrm{e}^{-\mathrm{i}\Theta/2}\ , \tag{2.54}$$

the squeezing transformation results in

$$\begin{aligned}\hat{S}^{\dagger}(\zeta)\left[\hat{x}^{(\Theta/2)} + \mathrm{i}\hat{p}^{(\Theta/2)}\right]\hat{S}(\zeta) &= \hat{a}\mathrm{e}^{-\mathrm{i}\Theta/2}\cosh r - \hat{a}^{\dagger}\mathrm{e}^{+\mathrm{i}\Theta/2}\sinh r \\ &= \mathrm{e}^{-r}\hat{x}^{(\Theta/2)} + \mathrm{i}\mathrm{e}^{+r}\hat{p}^{(\Theta/2)}\ .\end{aligned} \tag{2.55}$$

Thus, the effect of the squeezing operator on an arbitrary pair of quadratures, as generally defined in Eq. (2.35), is the attenuation of one quadrature and the amplification of the other. We have seen that the squeezing operator effectively represents the unitary evolution due to the OPA Hamiltonian. The corresponding expressions for the resulting Heisenberg quadrature operators (with $\Theta = 0$ and vacuum inputs) are[3)]

$$\hat{x}(r) = \mathrm{e}^{-r}\hat{x}^{(0)}\ , \qquad \hat{p}(r) = \mathrm{e}^{+r}\hat{p}^{(0)}\ . \tag{2.56}$$

The Heisenberg equations in Eq. (2.56) lead to a squeezed vacuum state (see Figures 2.3 and 2.4) in the Schrödinger picture given by the vector $\hat{S}(\zeta)|0\rangle = \hat{S}(r, \Theta = 0)|0\rangle \equiv \hat{S}(r)|0\rangle$. More generally, all single-qumode minimum uncertainty states are displaced squeezed vacua (see Figures 2.5 and 2.6),

$$|\alpha, \zeta\rangle = \hat{D}(\alpha)\hat{S}(\zeta)|0\rangle\ , \tag{2.57}$$

for which the position wave function becomes (with $\Theta = 0$)

$$\psi(x) = \left(\frac{2}{\pi}\right)^{1/4}\mathrm{e}^{r/2}\exp\left[-\mathrm{e}^{2r}(x - x_{\alpha})^2 + 2\mathrm{i}p_{\alpha}x - \mathrm{i}x_{\alpha}p_{\alpha}\right]. \tag{2.58}$$

The corresponding Wigner function[4)] is (with $\Theta = 0$)

$$W(x, p) = \frac{2}{\pi}\exp\left[-2\mathrm{e}^{+2r}(x - x_{\alpha})^2 - 2\mathrm{e}^{-2r}(p - p_{\alpha})^2\right]. \tag{2.59}$$

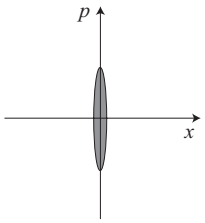

Figure 2.3 A position-squeezed vacuum state in phase space.

3) Comparing Eq. (2.50) with Eq. (2.56), note that the time reversal due to the sign convention in $r \equiv -\kappa t$ just swaps the squeezed and the antisqueezed quadrature.

4) The Wigner function together with other quasi-probability distributions will be introduced in the next section.

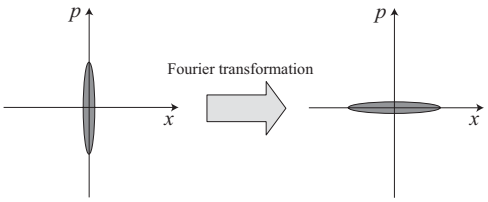

Figure 2.4 A momentum-squeezed vacuum state obtained by Fourier-transforming the position-squeezed vacuum state.

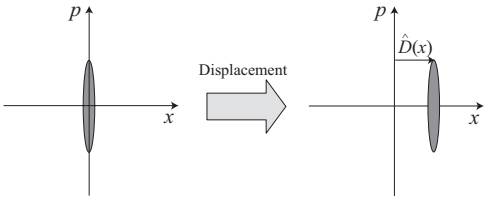

Figure 2.5 A position-displaced position-squeezed vacuum in phase space.

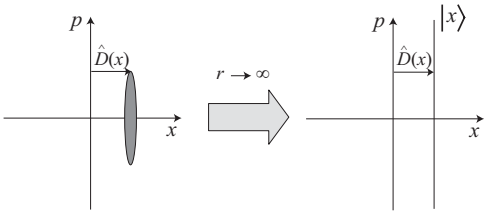

Figure 2.6 Position-displaced position-squeezed vacuum, $\exp(-2ix\hat{p})\hat{S}(r)|0\rangle$, approaching the CV position stabilizer state $|x\rangle_x$ for $r \to \infty$. Note that the squeezing operation and the position shift do not commute such that $\hat{S}(r)\exp(-2ix\hat{p})|0\rangle = \hat{S}(r)\exp(-2ix\hat{p})\hat{S}(-r)\hat{S}(r)|0\rangle = \exp(-2ixe^{-r}\hat{p})\hat{S}(r)|0\rangle$ will result in the zero-position stabilizer state $|0\rangle_x$ for $r \to \infty$.

The quadrature variances here are $\sigma_x = e^{-2r}/4$ and $\sigma_p = e^{+2r}/4$. In the limit of infinite squeezing $r \to \infty$, the position probability density, $|\psi(x)|^2 = \sqrt{2/\pi}e^r \times \exp[-2e^{2r}(x - x_\alpha)^2]$ becomes a delta function $\lim_{\epsilon\to 0}\exp[-(x - x_\alpha)^2/\epsilon^2]/\epsilon\sqrt{\pi} = \delta(x - x_\alpha)$ with $\epsilon = e^{-r}/\sqrt{2}$. The squeezed-vacuum wave function in that limit, $\psi(x) \propto \delta(x)$, describes a zero-position eigenstate, $\int dx\,\psi(x)|x\rangle_x \propto |0\rangle_x$, not to be confused with the vacuum state $|0\rangle$, for which the wave function is that of Eq. (2.58) with $r = x_\alpha = p_\alpha = 0$.

The mean photon number of an infinitely squeezed state becomes infinite because for the displaced squeezed vacuum, we have

$$\langle\hat{n}\rangle = \langle\hat{x}^2\rangle + \langle\hat{p}^2\rangle - \frac{1}{2} = |\alpha|^2 + \sinh^2 r\,, \tag{2.60}$$

using Eq. (2.37).

In the following section, we shall now briefly discuss an alternative way to represent quantum states, complementary to the Heisenberg and Schrödinger representations. Among these so-called quasi-probability distributions, the Wigner representation turns out to be particularly convenient in order to describe qumode states and to compute expectation values of phase-space variables.

Quantum optical states

coherent states:

- as eigenstates of the annihilation operator:

$$\hat{a}|\alpha\rangle = \alpha|\alpha\rangle$$

- as displaced vacuum states:

$$|\alpha\rangle = \hat{D}(\alpha)|0\rangle$$

with displacement operator $\hat{D}(\alpha) = \exp(\alpha\hat{a}^\dagger - \alpha^*\hat{a}) = \mathrm{e}^{-\mathrm{i}x_\alpha p_\alpha} Z(p_\alpha) X(x_\alpha)$

- as number superposition states:

$$|\alpha\rangle = \mathrm{e}^{-|\alpha|^2/2} \sum_{n=0}^{\infty} \frac{\alpha^n}{\sqrt{n!}} |n\rangle$$

squeezed states: position-squeezed:

$$\hat{S}^\dagger(r)\hat{x}\hat{S}(r) = \mathrm{e}^{-r}\hat{x}\,, \quad \hat{S}^\dagger(r)\hat{p}\hat{S}(r) = \mathrm{e}^{+r}\hat{p}$$

with squeezing operator

$$\hat{S}(\zeta) = \exp\left(\frac{\zeta^*}{2}\hat{a}^2 - \frac{\zeta}{2}\hat{a}^{\dagger 2}\right)$$

and

$$\zeta \equiv r\exp(\mathrm{i}\Theta)\,, \quad \hat{S}(r) \equiv \hat{S}(r, \Theta = 0) = \mathrm{e}^{r(\hat{a}^2 - \hat{a}^{\dagger 2})/2} = \mathrm{e}^{\mathrm{i}r(\hat{x}\hat{p} + \hat{p}\hat{x})}$$

displaced squeezed vacuum states:

$$|\alpha, \zeta\rangle = \hat{D}(\alpha)\hat{S}(\zeta)|0\rangle$$

2.2.5 Phase-Space Representations

The Wigner function was originally proposed by Wigner in his 1932 paper "On the quantum correction for thermodynamic equilibrium" [112]. Wigner introduced the

following expression,[5)]

$$W(x,p) = \frac{2}{\pi}\int \mathrm{d}y \mathrm{e}^{+4\mathrm{i}yp}\langle x-y|\hat{\rho}|x+y\rangle \ . \tag{2.61}$$

This is the Wigner function for one qumode. Wigner's original formula applies to many particles or, in our case, qumodes. However, this extension to an N-mode Wigner function is straightforward.

The function $W(x,p)$ is normalized,

$$\int W(\alpha)\mathrm{d}^2\alpha = 1 \ , \tag{2.62}$$

and it gives the correct marginal distributions,

$$\int W(x,p)\mathrm{d}x = \langle p|\hat{\rho}|p\rangle \ , \quad \int W(x,p)\mathrm{d}p = \langle x|\hat{\rho}|x\rangle \ . \tag{2.63}$$

It resembles a classical probability distribution in the sense that expectation values of a certain class of operators $\hat{A}$ in a given quantum state $\hat{\rho}$ can be calculated as,

$$\langle\hat{A}\rangle = \mathrm{Tr}(\hat{\rho}\hat{A}) = \int W(\alpha)A(\alpha)\mathrm{d}^2\alpha \ , \tag{2.64}$$

with a function $A(\alpha)$ related to the operator $\hat{A}$. Here, $\mathrm{d}^2\alpha = \mathrm{d}(\mathrm{Re}\alpha)\mathrm{d}(\mathrm{Im}\alpha) = \mathrm{d}x\mathrm{d}p$ with $W(\alpha = x+\mathrm{i}p) \equiv W(x,p)$, and we may use $\mathrm{d}^2\alpha$ and $\mathrm{d}x\mathrm{d}p$ interchangeably. The operator $\hat{A}$ represents a particular class of functions of $\hat{a}$ and $\hat{a}^\dagger$ or $\hat{x}$ and $\hat{p}$. The marginal distribution for p, $\langle p|\hat{\rho}|p\rangle$, is obtained by changing the integration variables ($x-y=u$, $x+y=v$) and using (1.47), that for x, $\langle x|\hat{\rho}|x\rangle$, by using $\int \exp(+4\mathrm{i}yp)\mathrm{d}p = (\pi/2)\delta(y)$. The normalization of the Wigner function then follows from $\mathrm{Tr}(\hat{\rho}) = 1$.

In order to derive an equation of the form of Eq. (2.64), we can write the Wigner function from Eq. (2.61) as

$$\begin{aligned} W(x,p) &= \frac{2}{\pi}\int \mathrm{d}y\mathrm{d}x'\mathrm{e}^{+4\mathrm{i}yp}\delta(x-x')\langle x'-y|\hat{\rho}|x'+y\rangle \\ &= \frac{1}{\pi^2}\int \mathrm{d}x'\mathrm{d}u\mathrm{d}v\mathrm{e}^{+2\mathrm{i}u(x-x')+2\mathrm{i}vp}\left\langle x'-\frac{v}{2}\middle|\,\hat{\rho}\,\middle|x'+\frac{v}{2}\right\rangle \\ &= \frac{1}{\pi^2}\int \chi_W(u,v)\mathrm{e}^{+2\mathrm{i}ux+2\mathrm{i}vp}\mathrm{d}u\mathrm{d}v \ , \end{aligned} \tag{2.65}$$

with the Fourier transform of the Wigner function, called the characteristic function,

$$\chi_W(u,v) = \int W(x,p)\mathrm{e}^{-2\mathrm{i}ux-2\mathrm{i}vp}\mathrm{d}x\mathrm{d}p \tag{2.66}$$

$$= \int \mathrm{e}^{-2\mathrm{i}ux'}\left\langle x'-\frac{v}{2}\middle|\,\hat{\rho}\,\middle|x'+\frac{v}{2}\right\rangle\mathrm{d}x' \ . \tag{2.67}$$

5) As throughout, without specified integration limits, the integration goes from $-\infty$ to ∞.

With the substitution $x = x' - v/2$ in Eq. (2.67), we now obtain

$$\begin{aligned}\chi_W(u,v) &= \exp(-\mathrm{i}uv)\int \exp(-2\mathrm{i}ux)\langle x|\hat{\rho}|x+v\rangle \mathrm{d}x \\ &= \int \langle x|\hat{\rho}\exp(-2\mathrm{i}u\hat{x} - 2\mathrm{i}v\hat{p})|x\rangle \mathrm{d}x \ , \end{aligned} \tag{2.68}$$

where in the last line we have used a Baker–Campbell–Hausdorff (BCH) formula, and $\exp(-2\mathrm{i}v\hat{p})|x\rangle = |x+v\rangle$, and $\exp(-2\mathrm{i}u\hat{x})|x+v\rangle = \exp[-2\mathrm{i}u(x+v)]|x+v\rangle$. With Eq. (2.68), we have found a compact formula for the characteristic function,

$$\chi_W(u,v) = \mathrm{Tr}[\hat{\rho}\exp(-2\mathrm{i}u\hat{x} - 2\mathrm{i}v\hat{p})] \ . \tag{2.69}$$

Let us now calculate the expectation value [113],

$$\begin{aligned}\mathrm{Tr}\left[\hat{\rho}(\lambda\hat{x} + \mu\hat{p})^k\right] &= \left(\frac{\mathrm{i}}{2}\right)^k \frac{\partial^k}{\partial\xi^k}\chi_W(\lambda\xi, \mu\xi)\bigg|_{\xi=0} \\ &= \int W(x,p)(\lambda x + \mu p)^k \mathrm{d}x\mathrm{d}p \ , \end{aligned} \tag{2.70}$$

according to Eqs. (2.69) (in the first line) and (2.66) (in the second line). By comparison of the powers of λ and μ, we find [113]

$$\mathrm{Tr}[\hat{\rho}\mathcal{S}(\hat{x}^n\hat{p}^m)] = \int W(x,p)x^n p^m \mathrm{d}x\mathrm{d}p \ , \tag{2.71}$$

where $\mathcal{S}(\hat{x}^n\hat{p}^m)$ denotes symmetrization. For example, $\mathcal{S}(\hat{x}^2\hat{p}) = (\hat{x}^2\hat{p} + \hat{x}\hat{p}\hat{x} + \hat{p}\hat{x}^2)/3$ corresponds to x^2p [113]. This is the so-called *Weyl correspondence* [114]. It provides a rule as how to calculate quantum mechanical expectation values in a classical-like fashion as in Eq. (2.64). Apparently, any symmetrized operator belongs to the particular class of operators $\hat{A}$ in Eq. (2.64) for which the classical-like averaging procedure works. In terms of creation and annihilation operators, we have

$$\mathrm{Tr}[\hat{\rho}\mathcal{S}(\hat{a}^{\dagger n}\hat{a}^m)] = \int W(\alpha)\alpha^{*n}\alpha^m \mathrm{d}^2\alpha \ . \tag{2.72}$$

This correspondence can be similarly derived as above through Fourier transform, expressing the characteristic function in terms of complex variables,

$$\begin{aligned}\chi_W(\beta) &= \int W(\alpha)\exp(-\mathrm{i}\beta\alpha^* - \mathrm{i}\beta^*\alpha)\mathrm{d}^2\alpha \equiv \mathcal{F}\{W\} \\ &= \mathrm{Tr}\left[\hat{\rho}\exp(-\mathrm{i}\beta\hat{a}^\dagger - \mathrm{i}\beta^*\hat{a})\right], \end{aligned} \tag{2.73}$$

with $\beta = u + \mathrm{i}v$.

Such a classical-like formulation of quantum optics in terms of quasi-probability distributions is not unique. In fact, there is a whole family of distributions $P(\alpha, s)$ of which each member corresponds to a particular value of a real parameter s,

$$P(\alpha,s) = \frac{1}{\pi^2}\int \chi(\beta,s)\exp(\mathrm{i}\beta\alpha^* + \mathrm{i}\beta^*\alpha)\mathrm{d}^2\beta \ , \tag{2.74}$$

with the s-parameterized characteristic functions

$$\chi(\beta, s) = \mathrm{Tr}\left[\hat{\rho}\exp\left(-\mathrm{i}\beta\hat{a}^\dagger - \mathrm{i}\beta^*\hat{a}\right)\right]\exp(s|\beta|^2/2)\ . \tag{2.75}$$

The expectation values of operators *normally* and *antinormally* ordered in $\hat{a}$ and $\hat{a}^\dagger$ may then be calculated through the so-called P function ($s = 1$) and Q function ($s = -1$), respectively, as can be seen using a BCH formula in Eq. (2.75). The corresponding characteristic functions are $\chi_P(\beta) \equiv \chi(\beta, 1)$ and $\chi_Q(\beta) \equiv \chi(\beta, -1)$, respectively.

The Wigner function ($s = 0$) and its characteristic function $\chi_W(\beta) \equiv \chi(\beta, 0)$ directly provide expectation values of quantities *symmetric* in $\hat{a}$ and $\hat{a}^\dagger$ such as the position $\hat{x} = (\hat{a} + \hat{a}^\dagger)/2$ and the momentum $\hat{p} = (\hat{a} - \hat{a}^\dagger)/2\mathrm{i}$. Note that the Wigner function is not always positive definite,[6] and neither is the P function. The Q function is an exception, being always non-negative. Though negativity of the Wigner function is clearly a sign of nonclassicality (see Chapter 8), it is not a necessary requirement to obtain nonclassical states. Pure states with a positive Wigner function, including those being entangled, are always Gaussian states (see Section 2.2.8.2 and Chapter 3).

Quantum optical phase-space representations

P function:

$$\hat{\rho} = \int P(\alpha)|\alpha\rangle\langle\alpha|\mathrm{d}^2\alpha\ , \quad \mathrm{Tr}(\hat{\rho}\hat{a}^{\dagger n}\hat{a}^m) = \int P(\alpha)\alpha^{*n}\alpha^m\mathrm{d}^2\alpha$$
$$\chi_P(\beta) = \mathcal{F}\{P\} = \mathrm{Tr}\left[\hat{\rho}\exp(-\mathrm{i}\beta\hat{a}^\dagger)\exp(-\mathrm{i}\beta^*\hat{a})\right]$$

Wigner function:

$$W(\alpha) = \frac{2}{\pi}\int \mathrm{d}^2\beta\, P(\beta)\mathrm{e}^{-2|\alpha-\beta|^2}$$
$$= W(x,p) = \frac{2}{\pi}\int \mathrm{d}y\mathrm{e}^{+4\mathrm{i}yp}\langle x - y|\hat{\rho}|x + y\rangle$$
$$\mathrm{Tr}\left[\hat{\rho}\mathcal{S}\left(\hat{a}^{\dagger n}\hat{a}^m\right)\right] = \int W(\alpha)\alpha^{*n}\alpha^m\mathrm{d}^2\alpha$$
$$\mathrm{Tr}\left[\hat{\rho}\mathcal{S}\left(\hat{x}^n\hat{p}^m\right)\right] = \int W(x,p)x^n p^m\mathrm{d}x\mathrm{d}p \quad \text{(Weyl correspondence)}$$
$$\chi_W(\beta) = \mathcal{F}\{W\} = \mathrm{Tr}\left(\hat{\rho}\mathrm{e}^{-\mathrm{i}\beta\hat{a}^\dagger - \mathrm{i}\beta^*\hat{a}}\right) = \chi_W(u,v) = \mathrm{Tr}\left(\hat{\rho}\mathrm{e}^{-2\mathrm{i}u\hat{x} - 2\mathrm{i}v\hat{p}}\right)$$

6) Wigner called $W(x, p)$ "the probability function of the simultaneous values of x and p" [112]. Since position and momentum cannot simultaneously take on precise values, $W(x, p)$ must exhibit some odd properties compared with classical probability distributions. In fact, the overlap formula [113], $|\langle\psi_1|\psi_2\rangle|^2 = \pi\int W_1(x,p)\,W_2(x,p)\mathrm{d}x\mathrm{d}p$, shows that either $W_1(x, p)$ or $W_2(x, p)$ must become negative for orthogonal states $\langle\psi_1|\psi_2\rangle = 0$.

Q function:

$$Q(\alpha) = \frac{2}{\pi}\int \mathrm{d}^2\beta\, W(\beta)\mathrm{e}^{-2|\alpha-\beta|^2} = \frac{1}{\pi}\int \mathrm{d}^2\beta\, P(\beta)\mathrm{e}^{-|\alpha-\beta|^2} = \frac{1}{\pi}\langle\alpha|\hat{\rho}|\alpha\rangle$$

$$\mathrm{Tr}\left(\hat{\rho}\hat{a}^n\hat{a}^{\dagger m}\right) = \int Q(\alpha)\alpha^n\alpha^{*m}\mathrm{d}^2\alpha$$

$$\chi_Q(\beta) = \mathcal{F}\{Q\} = \mathrm{Tr}\left[\hat{\rho}\exp(-\mathrm{i}\beta^*\hat{a})\exp(-\mathrm{i}\beta\hat{a}^\dagger)\right]$$

P function: can be negative and singular
Wigner function: can be negative but always regular
Q function: always non-negative

Finally, we note that any mixed quantum state $\hat{\rho}$, for which $\mathrm{Tr}(\hat{\rho}^2) < 1$, satisfies the following condition for the Wigner function,

$$\mathrm{Tr}(\hat{\rho}^2) = \pi\int[W(x,p)]^2\mathrm{d}x\mathrm{d}p < 1\,. \tag{2.76}$$

Here, $W(x,p)$ is the Wigner function corresponding to a single-qumode state $\hat{\rho}$. Next, we shall now start discussing photonic encodings for quantum information processing.

2.2.6 Photonic Qubits

Using the photon number Fock basis, there are various ways to encode an optical qubit. One possible encoding is called "single-rail" (or "occupation number") encoding, as it is based upon just a single optical mode,

$$\cos(\theta/2)|0\rangle + \mathrm{e}^{\mathrm{i}\phi}\sin(\theta/2)|1\rangle\,. \tag{2.77}$$

This encoding, however, is rather inconvenient because even simple single-qubit rotations would require nonlinear interactions. For example, the Hadamard gate, acting as $|k\rangle \to (|0\rangle + (-1)^k|1\rangle)/\sqrt{2}$, transforms a Gaussian state (the vacuum) into a non-Gaussian state (a superposition of vacuum and one-photon Fock state) which cannot be achieved through Gaussian unitaries (see Sections 2.2.8.2 and 2.4).

In contrast, for the so-called "dual-rail" encoding,

$$\cos(\theta/2)|10\rangle + \mathrm{e}^{\mathrm{i}\phi}\sin(\theta/2)|01\rangle\,, \tag{2.78}$$

single-qubit rotations become an easy task (see Figure 2.7). A 50 : 50 beam splitter, for instance, would turn $|10\rangle = \hat{a}_1^\dagger|00\rangle$ into $(1/\sqrt{2})(\hat{a}_1^\dagger + \hat{a}_2^\dagger)|00\rangle = (1/\sqrt{2})(|10\rangle + |01\rangle)$, and similarly for the other basis state. The two modes in this case are spatial modes. The linear beam-splitter transformation here is a simple, special case of a general passive (number-preserving) linear transformation introduced later in Eq. (2.105).

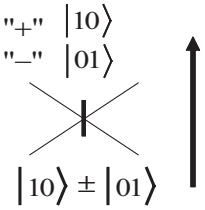

Figure 2.7 Using a beam splitter to switch between the computational and the Hadamard transformed, conjugate basis. Here, measuring the photons at the output of the beam splitter would project the input state onto the conjugate basis.

The most common dual-rail encoded, photonic qubit is a polarization encoded qubit,

$$\cos(\theta/2)|H\rangle + e^{i\phi}\sin(\theta/2)|V\rangle\ , \tag{2.79}$$

for two polarization modes, where one is horizontally polarized while the other is vertically polarized. Hence, polarization encoding is a specific manifestation of dual-rail encoding. Single-qubit rotations are then particularly simple, corresponding to polarization rotations.

The drawback of the dual-rail encoding is that for realizing two-qubit entangling gates, it is necessary to make two photons (each representing a dual-rail qubit) "talk" to each other. This kind of interaction between two photons would require some form of nonlinearity. In Chapters 6–8, we shall discuss various possibilities for realizing such two-photon entangling gates. Already in Section 2.8, we will discuss an extension of dual-rail to multiple-rail encoding, where every logical basis state is represented by a single photon that can occupy any one of sufficiently many, different modes (not just two as for dual-rail encoding).

Despite the difficulty for realizing a two-photon entangling gate, there is a clear advantage of the single-photon encoding. Single photons are fairly robust against noise. Therefore, typically, processing single-photon states can be achieved with high fidelity, though, in most cases, only conditional operations are possible at very low success probabilities. As additional resources for processing DV quantum information in a hybrid light-matter system, the atomic counterpart of the photonic polarization (spin) states are the electronic spin states (see Chapter 8).

2.2.7
Experiment: Polarization Qubits

A qubit can be conveniently encoded into the polarization of a single photon wavepacket. This polarization encoding is referred to as a polarization qubit. It corresponds to a specific manifestation of the dual-rail encoding introduced in the preceding section. In this case, the two spatial modes that may be originally used to obtain a dual-rail qubit are replaced by two orthogonal polarization modes.

Figure 2.8 shows the schematic for encoding and manipulating a polarization qubit $\alpha|H\rangle + \beta|V\rangle \equiv \alpha|\leftrightarrow\rangle + \beta|\updownarrow\rangle$. An arbitrary qubit state can be represented on the Bloch sphere (see Figure 1.2) known as the Poincaré sphere in optics (Figure 2.8b). A half-waveplate ($\lambda/2$) can be used to perform a Hadamard gate (Figure 2.8c). Moreover, a polarization qubit can be converted into a spatial (path-

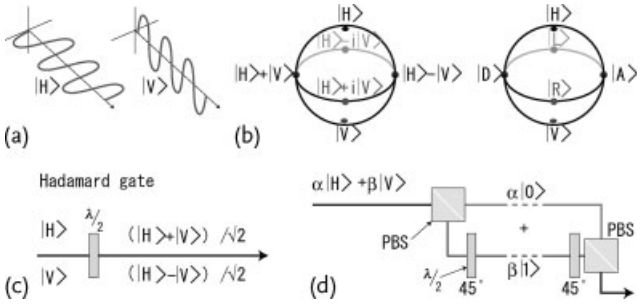

Figure 2.8 Representing and manipulating a polarization qubit encoded in a single photon wavepacket [115]. (a) *H* and *V* denote horizontal and vertical polarization, respectively. (b) An arbitrary qubit state can be represented on the Bloch sphere (known as the Poincaré sphere in optics). Examples of diagonal (D), anti-diagonal (A), right circular (R), and left circular (L) polarization states are shown. (c) A half-waveplate ($\lambda/2$) can be used to perform a Hadamard transformation. (d) A polarization qubit can be converted into a spatial (path-encoded) qubit by means of a polarization beam splitter (PBS).

encoded) qubit $\alpha|0,1\rangle + \beta|1,0\rangle$ (|upper photon number, lower photon number⟩) through a polarization beam splitter (PBS) (Figure 2.8d).

Typically, in the language of quantum information, H and V are chosen as the computational basis, corresponding to the ± 1 eigenstates of the Pauli Z operator. In this case, the other two bases on the equatorial circle which are superposition states of H and V correspond to the ± 1 eigenstates of the Pauli X and Y operators. These are the one-qubit stabilizer states (Section 1.2) in polarization encoding.

2.2.8 Photonic Qumodes

Apart from discrete photon numbers, an optical state may be described by its amplitude and phase. The corresponding quantum phase-space variables could be considered the quantum analogues of classical, analog encoding. Such qumode encoding, that is, CV quantum information encoded into optical modes, leads to states which are rather sensitive to noise, but can be processed in an unconditional fashion; even entangling gates can be accomplished through deterministic, linear optics (see Chapter 3).

In the linear, CV Gaussian regime, the optical encoding into qumodes is achieved either through approximate x/p-eigenstates (largely squeezed states), for which projection measurements are well approximated by homodyne detections (see Section 2.6); alternatively, the overcomplete and non-orthogonal set of coherent states may serve as a basis for qumodes. Perfectly projecting onto this basis is only possible for sufficiently large amplitudes $|\alpha|$, for which the coherent states become near-orthogonal. Nonetheless, two coherent states can also be unambiguously discriminated in the regime of small amplitudes using a beam splitter, an ancilla coherent

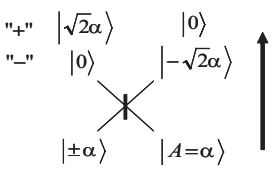

Figure 2.9 Optimal unambiguous state discrimination of equally occurring, binary coherent states $\{|\pm\alpha\rangle\}$ using a beam splitter, an ancilla coherent state, and on/off detectors. The inconclusive event here corresponds to the detection of the two-mode vacuum $e^{-\alpha^2}|00\rangle$ for the two output modes with probability $e^{-2\alpha^2}$ ($\alpha \in \mathbb{R}$). Another discussion related with this measurement is presented in Section 2.5.2.

state, and on/off detectors (see Figure 2.9 and Section 2.5.2). This unambiguous state discrimination (USD) is probabilistic, but, in principle, error free.

In the following two sections, we shall start establishing a connection between properly normalized qumode stabilizer states, that is, the physical CV analogues of the DV stabilizer states, and CV Gaussian pure states.

2.2.8.1 Stabilizer States

Consider a single qumode. In Section 1.2, we found that the stabilizers[7] in Eq. (1.50) represent an infinite set of rotated quadrature eigenstates obtained by phase-rotating an unphysical momentum eigenstate, $\hat{R}(\theta)|p\rangle$. Now, we wish to generalize the CV qumode stabilizer states to properly normalized, physical states. It will turn out that the Gaussian pure states play this role, and hence for a single qumode, the stabilizer must uniquely represent a displaced squeezed vacuum state, $|\alpha, \zeta\rangle = \hat{D}(\alpha)\hat{S}(\zeta)|0\rangle$.[8]

Let us start by introducing the stabilizer operator of the vacuum state of a single qumode with mode operator $\hat{a}$. We obtain

$$\exp(\alpha\hat{a})|0\rangle = \exp[\alpha(\hat{x} + i\hat{p})]|0\rangle = |0\rangle \ . \tag{2.80}$$

Note that, although the mode operator $\hat{a}$ is non-Hermitian and $\exp(\alpha\hat{a})$ non-unitary, the exponentiated $\hat{a}$ operator does behave like a stabilizer, uniquely representing the vacuum state as the only eigenstate with +1 eigenvalue. From this, we get the stabilizer for a single-mode squeezed vacuum state, with squeezing parameter $r > 0$ for an x-squeezing operation $\hat{S}(r) = \exp[ir(\hat{x}\hat{p} + \hat{p}\hat{x})]$, through inverse Heisenberg evolution,

$$\hat{S}(r)\exp[\alpha(\hat{x} + i\hat{p})]\hat{S}^\dagger(r) = \exp\left[\alpha(e^{+r}\hat{x} + ie^{-r}\hat{p})\right]. \tag{2.81}$$

In the case of momentum squeezing, with $\hat{S}(-r)$, we have

$$\hat{S}(-r)\exp[\alpha(\hat{x} + i\hat{p})]\hat{S}^\dagger(-r) = \exp\left[\alpha(e^{-r}\hat{x} + ie^{+r}\hat{p})\right]. \tag{2.82}$$

Let us rewrite this as[9]

$$\exp\left(-\alpha^2/4\right) X(-\alpha e^{+r}/2) Z[\alpha e^{-r}/(2i)]. \tag{2.83}$$

7) For a definition and a discussion of stabilizers, see Section 1.9.
8) The standard formalism to describe Gaussian states will be introduced in the following section.
9) All of these expressions are convention-dependent; recall that our convention is $\hbar = 1/2$.

Now, we define $\alpha \equiv -2\mathrm{e}^{-r}s$ such that the momentum-squeezed stabilizer becomes

$$\exp\left(-\mathrm{e}^{-2r}s^2\right) X(s) Z\left(\mathrm{i}\mathrm{e}^{-2r}s\right) . \tag{2.84}$$

In the limit of infinite p-squeezing $r \to \infty$, this operator approaches $X(s)$, which stabilizes the zero-eigenstate $|p=0\rangle$, $X(s)|p=0\rangle = |p=0\rangle$, $\forall s \in \mathbb{R}$, as expected.

In order to represent not only squeezed states like $\hat{S}(r)|0\rangle$, but also the rotated states $\hat{S}(\zeta)|0\rangle$, we use the rotated momentum-squeezed-vacuum stabilizer,

$$\begin{aligned}
&\mathrm{e}^{-\mathrm{e}^{-2r}s^2} \hat{R}(\theta) X(s) \hat{R}^\dagger(\theta) \hat{R}(\theta) Z\left(\mathrm{i}\mathrm{e}^{-2r}s\right) \hat{R}^\dagger(\theta) \\
&= \mathrm{e}^{-\mathrm{e}^{-2r}s^2(1-\mathrm{i}\mathrm{e}^{-2r}\cos\theta\sin\theta)} g^{(\theta)}_{p=0}(s) Z\left(\mathrm{i}\mathrm{e}^{-2r}s\cos\theta\right) X\left(\mathrm{i}\mathrm{e}^{-2r}s\sin\theta\right) \\
&\equiv g^{(\theta)}_{p=0}(s,r) ,
\end{aligned} \tag{2.85}$$

which becomes the rotated-zero-momentum stabilizer in the limit $r \to \infty$, with $g^{(\theta)}_p(s)$ from Eq. (1.50) and Eq. (1.71). Finally, we only have to express a complex phase-space displacement affected by $\hat{D}(\alpha)$ through stabilizers (which we implicitly did already for defining the unphysical qumode stabilizer x and p eigenstates in Section 1.2). While the stabilizer for a displaced vacuum state, $\hat{D}(\alpha)|0\rangle$, is simply

$$\hat{D}(\alpha)\mathrm{e}^{-s^2} X(s) Z(\mathrm{i}s) \hat{D}^\dagger(\alpha) = \mathrm{e}^{-s^2}\mathrm{e}^{2s\alpha} X(s) Z(\mathrm{i}s) , \tag{2.86}$$

using Eq. (2.84) with $r = 0$, we obtain the following general stabilizer for a single-qumode Gaussian pure state,

$$\begin{aligned}
&\hat{D}(\alpha) g^{(\theta)}_{p=0}(s,r) \hat{D}^\dagger(\alpha) \\
&= \mathrm{e}^{+2s\cos\theta\left(\mathrm{e}^{-2r}x_\alpha + \mathrm{i}p_\alpha\right) - 2\mathrm{i}s\sin\theta\left(x_\alpha + \mathrm{i}\mathrm{e}^{-2r}p_\alpha\right)} g^{(\theta)}_{p=0}(s,r) ,
\end{aligned} \tag{2.87}$$

using Eq. (2.85). This is the stabilizer for an arbitrary displaced squeezed vacuum state, $\hat{D}(\alpha)\hat{S}(\zeta)|0\rangle$, depending on four real parameters, x_α, p_α, r, and θ, with $\alpha = x_\alpha + \mathrm{i}p_\alpha$. In Section 3.2, we shall utilize stabilizers for Gaussian multi-mode pure states in order to define and represent multipartite entangled qumode cluster and graph states.

2.2.8.2 Gaussian States

Consider the Wigner function of a displaced position-squeezed vacuum state for a single qumode in Eq. (2.59). It may be rewritten in the following way,

$$W(x,p) = \frac{2}{\pi} \exp\left[-\frac{1}{2}(x-x_\alpha, p-p_\alpha) \begin{pmatrix} 4\mathrm{e}^{+2r} & 0 \\ 0 & 4\mathrm{e}^{-2r} \end{pmatrix} \begin{pmatrix} x-x_\alpha \\ p-p_\alpha \end{pmatrix}\right], \tag{2.88}$$

or, using a more compact notation,

$$W(\xi) = \frac{1}{(2\pi)^N \sqrt{\det V^{(N)}}} \exp\left\{-\frac{1}{2}(\xi-\xi_0)\left[V^{(N)}\right]^{-1}(\xi-\xi_0)^{\mathrm{T}}\right\} , \tag{2.89}$$

with $N = 1$, the 2-dimensional vectors $\xi = (x, p)$, $\xi_0 = (x_\alpha, p_\alpha)$, and the 2×2 matrix

$$V^{(1)} = \frac{1}{4} \begin{pmatrix} \mathrm{e}^{-2r} & 0 \\ 0 & \mathrm{e}^{+2r} \end{pmatrix} . \tag{2.90}$$

This matrix contains the (co-)variances of the displaced position-squeezed vacuum state, namely, $\langle (\Delta \hat{x})^2 \rangle = \langle \hat{x}^2 \rangle - x_\alpha^2 = \mathrm{e}^{-2r}/4$, $\langle (\Delta \hat{p})^2 \rangle = \langle \hat{p}^2 \rangle - p_\alpha^2 = \mathrm{e}^{+2r}/4$, using Eq. (1.40), and $\langle (\hat{x}\,\hat{p} + \hat{p}\,\hat{x}) \rangle /2 - x_\alpha\, p_\alpha = 0$.

More generally, Eq. (2.89) for $N = 1$, with a real, symmetric 2×2 covariance matrix $V^{(1)}$, represents an arbitrary displaced squeezed thermal state and therefore an arbitrary single-qumode Gaussian state. Such a state is determined through five parameters; three for the displaced position-squeezed state, x_α, p_α, and r; an extra phase rotation θ and a thermal excitation number (see below). Compared to the stabilizer states presented in the preceding section, here, a general Gaussian state for a single qumode can be pure or mixed.[10] The Wigner function for a general multi-mode Gaussian state is also expressed by Eq. (2.89), in this general case with a $2N$-dimensional vector ξ having the quadrature pairs of all N modes as its components,

$$\xi = (x_1, p_1, x_2, p_2, \ldots, x_N, p_N) , \quad \hat{\xi} = (\hat{x}_1, \hat{p}_1, \hat{x}_2, \hat{p}_2, \ldots, \hat{x}_N, \hat{p}_N) , \tag{2.91}$$

and similarly for the first moments, $\xi_0 = (\langle \hat{x}_1 \rangle, \langle \hat{p}_1 \rangle, \langle \hat{x}_2 \rangle, \langle \hat{p}_2 \rangle, \ldots, \langle \hat{x}_N \rangle, \langle \hat{p}_N \rangle)$. In general, the covariance matrix is then given by $V_{ij}^{(N)} = \langle (\hat{\xi}_i \hat{\xi}_j + \hat{\xi}_j \hat{\xi}_i)/2 \rangle - \langle \hat{\xi}_i \rangle \langle \hat{\xi}_j \rangle$. However, many important properties in the multi-mode case, such as entanglement, are independent of the first moments, as these can always be locally adjusted through phase-space displacements. We may therefore assume zero first moments and define the $2N \times 2N$ correlation matrix $V^{(N)}$, having as its elements the second moments symmetrized according to the Weyl correspondence in Eq. (2.71),

$$\begin{aligned} \mathrm{Tr}\left[\hat{\rho} \left(\Delta\hat{\xi}_i \Delta\hat{\xi}_j + \Delta\hat{\xi}_j \Delta\hat{\xi}_i\right)/2\right] &= \left\langle \left(\hat{\xi}_i \hat{\xi}_j + \hat{\xi}_j \hat{\xi}_i\right)/2 \right\rangle \\ &= \int W(\xi) \xi_i \xi_j \mathrm{d}^{2N}\xi \equiv V_{ij}^{(N)} , \end{aligned} \tag{2.92}$$

where $\Delta\hat{\xi}_i = \hat{\xi}_i - \langle \hat{\xi}_i \rangle = \hat{\xi}_i$ for zero first moments. For (zero-mean) Gaussian states of the form in Eq. (2.89), the Wigner function is completely determined by the second-moment correlation matrix. In order to represent a physical state (Gaussian or non-Gaussian), the correlation matrix must be real, symmetric, and positive; in addition, it must be consistent with the commutation relation from Eq. (1.39) [116, 117],

$$[\hat{\xi}_k, \hat{\xi}_l] = \frac{i}{2} \Lambda_{kl} , \qquad k, l = 1, 2, 3, \ldots, 2N . \tag{2.93}$$

10) As discussed in Section 1.9, stabilizer states can be generalized in terms of stabilizer codes, which gives an interesting recipe for extending the qumode stabilizer formalism from Gaussian pure to Gaussian mixed states.

Here, the $2N \times 2N$ "symplectic matrix" Λ is block diagonal and contains the 2×2 matrix J as the diagonal entries for each quadrature pair,

$$\Lambda = \bigoplus_{k=1}^{N} J \,, \qquad J = \begin{pmatrix} 0 & 1 \\ -1 & 0 \end{pmatrix}. \tag{2.94}$$

A direct consequence of this commutation relation and the non-negativity of the density operator $\hat{\rho}$ is then the following N-mode uncertainty relation,

$$V^{(N)} + \frac{\mathrm{i}}{4}\Lambda \geq 0 \,. \tag{2.95}$$

This matrix equation means that the matrix sum on the left-hand side only has non-negative eigenvalues. The N-mode uncertainty relation is a necessary condition on any physical state. For Gaussian states, however, it is also a sufficient condition that guarantees the positivity of $\hat{\rho}$ [117]. In the simplest case of a single qumode, $N = 1$, Eq. (2.95) is reduced to the statement $\langle \hat{x}^2 \rangle \langle \hat{p}^2 \rangle - 1/4 \langle \hat{x}\,\hat{p} + \hat{p}\,\hat{x} \rangle^2 = \det V^{(1)} \geq 1/16$, which is a stronger version of the Heisenberg uncertainty relation in Eq. (1.43).[11] For any N, (2.95) becomes exactly the Heisenberg uncertainty relation of Eq. (1.43) for each individual mode, if $V^{(N)}$ is diagonal.

Gaussian states

one qumode: pure state is displaced squeezed vacuum state:

$$\hat{D}(\alpha)\hat{S}(\zeta)|0\rangle \;\; (2 \text{ parameters } \alpha, \zeta \in \mathbb{C} \sim 4 \text{ parameters } x_\alpha, p_\alpha, r, \theta \in \mathbb{R})$$

pure state is stabilized by $\mathrm{e}^{+2s\cos\theta(\mathrm{e}^{-2r}x_\alpha + \mathrm{i}p_\alpha) - 2\mathrm{i}s\sin\theta(x_\alpha + \mathrm{i}\mathrm{e}^{-2r}p_\alpha)} g^{(\theta)}_{p=0}(s, r)$

mixed state is displaced squeezed thermal state:

$$\frac{1}{1+\bar{n}}\,\hat{D}(\alpha)\hat{S}(\zeta)\left(\frac{\bar{n}}{1+\bar{n}}\right)^{\hat{a}^\dagger\hat{a}}\hat{S}^\dagger(\zeta)\hat{D}^\dagger(\alpha) \;\; (5 \text{ parameters } x_\alpha, p_\alpha, r, \theta, \bar{n})$$

N qumodes: zero-mean Gaussian-state Wigner function:

$$W(\xi) = \frac{1}{(2\pi)^N\sqrt{\det V^{(N)}}} \exp\left\{-\frac{1}{2}\xi\left[V^{(N)}\right]^{-1}\xi^{\mathrm{T}}\right\}$$

real, symmetric, positive correlation matrix:

$$V^{(N)}_{ij} = \left\langle \left(\hat{\xi}_i\hat{\xi}_j + \hat{\xi}_j\hat{\xi}_i\right)/2 \right\rangle = \int W(\xi)\xi_i\xi_j \mathrm{d}^{2N}\xi \,, \quad V^{(N)} + \frac{\mathrm{i}}{4}\Lambda \geq 0$$

$$\Lambda = \bigoplus_{k=1}^{N} J \,, \;\; J = \begin{pmatrix} 0 & 1 \\ -1 & 0 \end{pmatrix}, \;\; \left[\hat{\xi}_k, \hat{\xi}_l\right] = \frac{\mathrm{i}}{2}\Lambda_{kl} \,, \;\; k, l = 1, 2, 3, \ldots, 2N$$

11) That is, $\det V^{(1)} \geq 1/16$ implies $\langle \hat{x}^2 \rangle \langle \hat{p}^2 \rangle \geq 1/16$, but the converse is not generally true.

N real, positive, symplectic eigenvalues:

$$\left|\text{eigenvalues of } \mathrm{i}\Lambda V^{(N)}\right|$$

uncertainty relation:

$$\nu_k \geq \frac{1}{4}\,, \quad \forall k = 1, 2, \ldots, N \quad \Leftrightarrow \quad V^{(N)} + \frac{\mathrm{i}}{4}\Lambda \geq 0$$

pure states:

$$\nu_k = \frac{1}{4}\,, \quad \forall k = 1, 2, \ldots, N$$

mixed states:

$$\exists k \in \{1, 2, \ldots, N\} \quad \text{such that} \quad \nu_k > \frac{1}{4}$$

We should also mention here that there is an equivalent representation of the uncertainty relation in Eq. (2.95) using the so-called *symplectic eigenvalues*. There are N real, positive, symplectic eigenvalues and these are obtained for any N-mode Gaussian state through *Williamson diagonalization* [118] of its correlation matrix into normal modes,

$$V^{(N)} = S^{\mathrm{T}} \bar{V}^{(N)} S\,, \tag{2.96}$$

where the matrix $S \in \mathrm{Sp}(2N, \mathbb{R})$ describes a global symplectic transformation.[12] The resulting diagonal matrix $\bar{V}^{(N)}$ contains the N symplectic eigenvalues ν_k,

$$\bar{V}^{(N)} = \bigoplus_{k=1}^{N} \begin{pmatrix} \nu_k & 0 \\ 0 & \nu_k \end{pmatrix}. \tag{2.97}$$

The uncertainty relation in Eq. (2.95) can then be recast as $(S^{-1})^{\mathrm{T}} V^{(N)} S^{-1} + \mathrm{i}/4 (S^{-1})^{\mathrm{T}} \Lambda S^{-1} = \bar{V}^{(N)} + \mathrm{i}/4 \Lambda \geq 0$, which corresponds to

$$\nu_k \geq \frac{1}{4}\,, \quad \forall k = 1, 2, \ldots, N\,. \tag{2.98}$$

The effect of the Williamson diagonalization is that any correlations between the quadratures and between the modes are eliminated such that the resulting correlation matrix represents an N-mode product state with every qumode in a thermal state,

$$\bar{V}^{(N)} = \bigoplus_{k=1}^{N} V_k^{(1)}\,, \quad V_k^{(1)} = \frac{1}{4} \begin{pmatrix} 1 + 2\bar{n}_k & 0 \\ 0 & 1 + 2\bar{n}_k \end{pmatrix}. \tag{2.99}$$

12) The linear, symplectic transformations S on the $2N$-dimensional phase space form the symplectic group $\mathrm{Sp}(2N, \mathbb{R})$, where $S^{\mathrm{T}} \Lambda S = \Lambda$ and hence $\det S = 1$, $\forall S \in \mathrm{Sp}(2N, \mathbb{R})$. The symplectic transformations correspond to the Gaussian unitaries up to displacements (see Section 2.4).

The parameters $\bar{n}_k = (4\nu_k - 1)/2$ are the mean thermal excitation numbers for every one of the N qumodes after diagonalization. The corresponding density operator is a tensor product state of thermal states for qumode k,[13)]

$$\hat{\rho}_k = \frac{2}{4\nu_k + 1} \sum_{n=0}^{\infty} \left(\frac{4\nu_k - 1}{4\nu_k + 1} \right)^n |n\rangle\langle n| = \frac{1}{1 + \bar{n}_k} \sum_{n=0}^{\infty} \left(\frac{\bar{n}_k}{1 + \bar{n}_k} \right)^n |n\rangle\langle n|. \tag{2.100}$$

As a result, the symplectic eigenvalues contain the entire information about the physicality, purity, and mixedness of the N-mode Gaussian state. Any physical state must satisfy Eq. (2.98). The structure and the size of the thermal noise that makes the state a mixed state is determined by the number of symplectic eigenvalues with $\nu_k > 1/4$ and by the extent to which the minimum-uncertainty vacuum bound $\nu_k = 1/4$ is exceeded, respectively.[14)]

Compared to the position-squeezed vacuum state in Eq. (2.90), the position-squeezed thermal state for a single qumode has the following correlation matrix,

$$V^{(1)} = \frac{1}{4} \begin{pmatrix} \mathrm{e}^{-2r}(1 + 2\bar{n}) & 0 \\ 0 & \mathrm{e}^{+2r}(1 + 2\bar{n}) \end{pmatrix}. \tag{2.101}$$

Compared with the mean photon number as given in Eq. (2.60), we obtain for the displaced squeezed thermal state,

$$\langle \hat{n} \rangle = \langle \hat{x}^2 \rangle + \langle \hat{p}^2 \rangle - \frac{1}{2} = |\alpha|^2 + \sinh^2 r + \bar{n} \cosh 2r \,, \tag{2.102}$$

using Eq. (2.37). This is the mean photon number for an arbitrary single-qumode Gaussian state. It depends on three parameters: the size of the coherent amplitude $|\alpha|$, the amount of squeezing r, and the mean thermal number $\bar{n}$. This photon number is independent of the phases in α and ζ for a general displaced squeezed thermal state. Further, the purity for an N-mode Gaussian state depends on[15)]

$$\mathrm{Tr}\hat{\rho}^2 = \frac{1/4^N}{\sqrt{\det V^{(N)}}} = \frac{1/4^N}{\prod_{k=1}^{N} \nu_k} \,, \tag{2.103}$$

13) Where the mean excitation numbers can be associated with a temperature according to $\bar{n} = 1/(\mathrm{e}^{\beta} - 1)$ with the usual parameter $\beta = \frac{\hbar\omega}{k_B T}$. Note that, while the uncertainty relation bound and the symplectic eigenvalues are convention-dependent (in our case with $\hbar = 1/2$), the mean thermal number, of course, is not.

14) One may define the number of symplectic eigenvalues different from 1/4, i.e., the number of non-vacuum normal modes as the symplectic rank [119], in analogy to the standard rank R of a finite-dimensional density operator corresponding to the number of its nonzero eigenvalues. For example, a d-dimensional state has $R = 1$ when it is pure and $R = d$ when it corresponds to an incoherent mixture with d terms. However, a full rank $R = d$-state, though having a complex noise structure, may still have low noise with most eigenvalues almost vanishing. In the Gaussian case, a pure state has zero symplectic rank, whereas a mixed state has a noise structure given by a symplectic rank between one and N, and a size of the noises given by the respective values of the symplectic eigenvalues between 1/4 and infinity.

15) Which can be derived using $\mathrm{Tr}\hat{\rho}^2 = \pi^N \int \mathrm{d}^{2N}\xi \, W^2(\xi)$ for Gaussian Wigner functions $W(\xi)$ from Eq. (2.89).

according to Eq. (1.21). A pure state has $\det V^{(N)} = 1/16^N$, for instance, $\det V^{(1)} = 1/16$ for one qumode, which is the minimal bound of the one-mode uncertainty relation, as mentioned before.

Finally, let us mention that there is an easy way to compute the symplectic eigenvalues directly from the correlation matrix. First, one has to calculate the ordinary eigenvalues of the Hermitian matrix $\mathrm{i}\Lambda V^{(N)}$. The modulus of each of the resulting $2N$ real eigenvalues then gives the N real and positive values ν_k, $k = 1, 2, \ldots, N$.

In this section, we defined multi-mode Gaussian states using Wigner functions and correlation matrices. A general Gaussian state of a single qumode is a displaced squeezed thermal state; a Gaussian pure state of a single qumode is a displaced squeezed vacuum state as well as a physical, properly normalized qumode stabilizer state. Physical stabilizer states for many qumodes, corresponding to (entangled) multi-mode Gaussian pure states, will be discussed in Section 3.2.

2.2.9 Experiment: Broadband Qumodes

In quantum optical CV experiments, we have to define the qumodes as some physical modes of light, for example, temporal, frequency, spatial, or polarization modes. In any case, they will represent wavepackets of the electromagnetic field with various time duration. One extreme is infinite time duration as shown in Figure 2.10a – a continuous wave or a frequency single mode. Usually, a frequency single mode is realized as a sideband of the fundamental carrier light. In this case, each sideband corresponds to a qumode. Two sidebands i, j have no overlap in frequency domain and satisfy the commutators $[\hat{a}_i, \hat{a}_j^\dagger] = \delta_{ij}$ and $[\hat{a}_i, \hat{a}_j] = 0$. Another extreme is very short time duration as shown in Figure 2.10b – pulsed light. In this case, each pulse corresponds to a qumode. Two pulses i, j do not have any overlap and would then also satisfy the commutators $[\hat{a}_i, \hat{a}_j^\dagger] = \delta_{ij}$ and $[\hat{a}_i, \hat{a}_j] = 0$.

However, the mode operators for pulsed light represent temporal modes at times t_i of which each mode contains a finite bandwidth of frequency modes, $\hat{a}_{t_i} = \int \mathrm{d}\omega g(\omega)\hat{a}_\omega$, with some spectral function $g(\omega)$ that is almost flat in this limit. The other limit of a frequency single mode is then approached for $g(\omega) \to \delta(\omega_i)$. In the experiment, the realistic situation will be between these two extremes.

As mentioned above, a frequency sideband of a carrier light beam is often used for a frequency single mode. The bandwidth Δf is usually very narrow compared to the sideband frequency f ($\Delta f \ll f$). So the wavepacket of the qumode has time duration of $1/\Delta f$ which is extremely long, and thus the spatial size of the wavepacket is very long ($c/\Delta f$, c: speed of light). From this point of view, the wavepacket exhibits *wave nature*. For example, in the case of $f = 1\,\mathrm{MHz}$ and $\Delta f = 1\,\mathrm{kHz}$, the time duration is 1 ms and the spatial length is 300 km! This is a very long *wave*! However, this frequency mode may even contain only a single

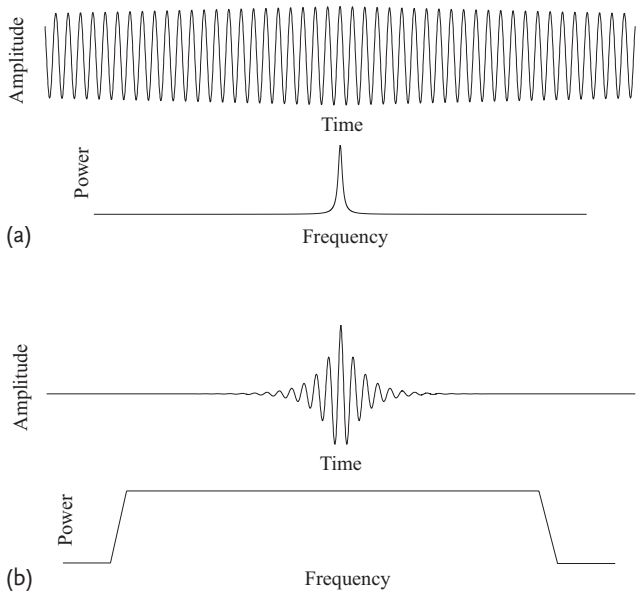

Figure 2.10 Two extremes of wavepackets, (a) a frequency single mode and (b) pulsed light.

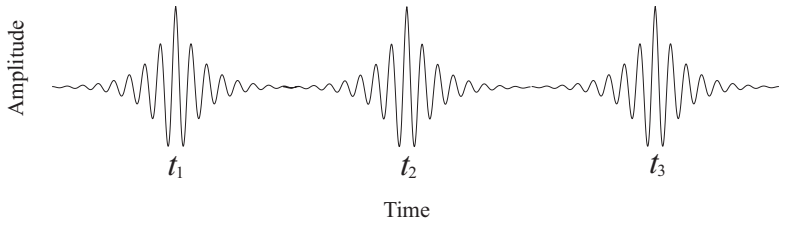

Figure 2.11 A temporal mode i with the temporal function of $\exp(-\gamma|t-t_i|)$ can be extracted from broadband continuous-wave light and defined as a qumode when the continuous light is very weak.

photon – usually associated with a *particle* – which then corresponds to a 300 km long single photon.[16)]

Nonetheless, pulsed light shows *particle nature* of the wavepacket which is intuitively understandable. However, in the real situation, this is not always the case. Pulsed light or, more precisely, a pulsed qumode can be defined even in terms of broadband (frequency-multimode) continuous-wave light. For example, a temporal mode i with the temporal function of $\exp(-\gamma|t-t_i|)$ can be extracted from broadband continuous-wave light and defined as a qumode, as shown in Figure 2.11, when the continuous light is very weak (see Section 8.2).

16) Recall the discussion at the beginning of this chapter, where the occupation number of a qumode, i.e., its photon number, and hence the photons themselves are a mathematical construct (to represent the energy levels of a qumode) rather than a physical entity.

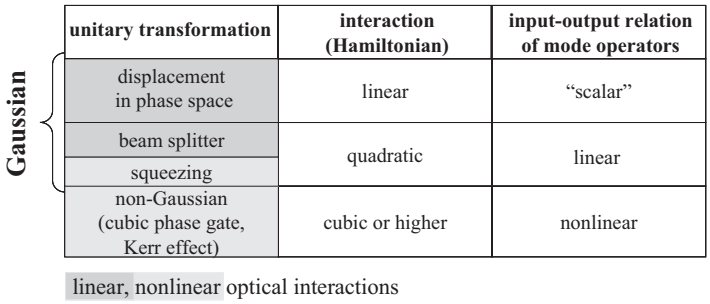

Figure 2.12 Optical interactions and transformations in terms of the annihilation and creation operators representing a discrete set of qumodes for the optical field.

2.3 Quantum Optical Unitaries

We shall now turn to unitary, linear and nonlinear optical manipulations of quantum optical states. The discussion in this section is a continuation of the more abstract introduction to unitaries and quantum computation in Sections 1.3 and 1.8, though here, it is applied to optical systems.

In Figure 2.12, a table is shown summarizing possible optical interactions and transformations for state preparation and manipulation. The most accessible and practical interactions are those described by linear and quadratic Hamiltonians, where as before, quadratic refers to the order of a polynomial of the qumode operators $\hat{a}_k$.

In Section 2.2.8.2, we learned that an arbitrary single-qumode Gaussian pure state is a displaced squeezed vacuum state, $\hat{D}(\alpha)\hat{S}(\zeta)|0\rangle$. Similarly, an arbitrary single-qumode Gaussian unitary that transforms a Gaussian state into a Gaussian state is given by Eq. (1.126), supplemented by a complex phase-space displacement $\hat{D}(\alpha)$. When Eq. (1.126) is applied upon a single-mode vacuum state, the first phase rotation $\hat{R}(\phi')$ has no effect. The remaining position-squeezing $\hat{S}(r)$ can be combined with the second phase rotation $\hat{R}(\phi)$ into the general, complex squeezing operation $\hat{S}(\zeta)$. Therefore, an arbitrary, single-qumode Gaussian pure state is obtained through an arbitrary single-qumode Gaussian unitary acting on the vacuum state. However, a single-qumode Gaussian unitary may as well act upon an arbitrary single-qumode state. In this case, the exact decomposition from Eq. (1.126) should be used, including the first phase rotation $\hat{R}(\phi')$, together with $\hat{D}(\alpha)$.

We will shortly see that the decomposition of Eq. (1.126) corresponds to the single-qumode case of a more general decomposition for any multi-qumode Gaussian unitary. These unitary multi-mode transformations are linear and generated from quadratic Hamiltonians. An arbitrary quadratic Hamiltonian then transforms the optical mode operators as

$$\hat{a}'_k = \sum_l A_{kl}\hat{a}_l + B_{kl}\hat{a}_l^\dagger + \gamma_k \ . \tag{2.104}$$

Here, the matrices A and B satisfy the conditions $AB^{\mathrm{T}} = (AB^{\mathrm{T}})^{\mathrm{T}}$ and $AA^{\dagger} = BB^{\dagger} + \mathbb{1}$ according to the bosonic commutation relations. This transformation is also referred to as the linear unitary Bogoliubov (LUBO) transformation [120]. It combines passive (photon-number preserving) and active elements, that is, *beam splitters* and *squeezers*, respectively; the γ_k's in Eq. (2.104) describe the phase-space displacements.

As an example, for a single-mode position squeezer, we have $\hat{a}' = \hat{a}\cosh r - \hat{a}^{\dagger}\sinh r$ such that the x-quadrature would become $\hat{x}' = \mathrm{e}^{-r}\hat{x}$, and the p-quadrature $\hat{p}' = \mathrm{e}^{+r}\hat{p}$, similar to Eqs. (2.53) and (2.56).

By comparing the LUBO transformation to a purely passive, linear transformation,

$$\hat{a}'_k = \sum_l U_{kl}\hat{a}_l \ , \tag{2.105}$$

with an arbitrary unitary matrix U, we observe that there is no mixing between the annihilation and creation operators in the passive transformation. Despite this difference, also the active, more general LUBO transformation is only linear in the mode operators. Therefore, general *linear optical transformations* are referred to here as LUBO transformations, including squeezers. As squeezing, however, typically involves a nonlinear optical interaction (see Section 2.2.4), it may as well be excluded from the "linear-optics" toolbox (see Figure 2.12). Our more mathematical than physical definition of linear optical transformations is motivated by the special character of the Clifford and symplectic transformations (see Section 1.8 and next section) with regard to quantum information processing.

As an example for Eq. (2.105), consider a general two-mode beam splitter transformation in the Heisenberg picture,

$$(\hat{a}'_1\hat{a}'_2)^{\mathrm{T}} = U(2)(\hat{a}_1\hat{a}_2)^{\mathrm{T}} \ , \tag{2.106}$$

with a unitary matrix

$$U(2) = \begin{pmatrix} \mathrm{e}^{-\mathrm{i}(\phi+\delta)}\sin\theta & \mathrm{e}^{-\mathrm{i}\delta}\cos\theta \\ \mathrm{e}^{-\mathrm{i}(\phi+\delta')}\cos\theta & -\mathrm{e}^{-\mathrm{i}\delta'}\sin\theta \end{pmatrix} . \tag{2.107}$$

An ideal phase-free beam splitter operation is then simply given by the linear transformation

$$\begin{pmatrix} \hat{a}'_1 \\ \hat{a}'_2 \end{pmatrix} = \begin{pmatrix} \sin\theta & \cos\theta \\ \cos\theta & -\sin\theta \end{pmatrix} \begin{pmatrix} \hat{a}_1 \\ \hat{a}_2 \end{pmatrix} \ , \tag{2.108}$$

with the transmittance and reflectivity parameters $\sin\theta$ and $\cos\theta$. Thus, the general unitary matrix $U(2)$ corresponds to two phase shifts and one phase-free beam splitter,

$$U(2) = \begin{pmatrix} \mathrm{e}^{-\mathrm{i}\delta} & 0 \\ 0 & \mathrm{e}^{-\mathrm{i}\delta'} \end{pmatrix} \begin{pmatrix} \sin\theta & \cos\theta \\ \cos\theta & -\sin\theta \end{pmatrix} \begin{pmatrix} \mathrm{e}^{-\mathrm{i}\phi} & 0 \\ 0 & 1 \end{pmatrix} . \tag{2.109}$$

The link between elementary quantum optical devices such as phase shifters, beam splitters, and single-mode squeezers on one side and an arbitrary LUBO transformation as in Eq. (2.104) on the other side is provided through two important results:

- any active, multi-mode LUBO transformation as in Eq. (2.104) can be decomposed into a three-step circuit consisting of a passive, linear optical multi-mode transformation as in Eq. (2.105), single-mode squeezers, and another passive, linear optical multi-mode transformation [89], and
- any passive, linear optical multi-mode transformation described by an arbitrary unitary matrix as in Eq. (2.105) can be realized through a sequence of two-mode beam splitters and single-mode phase shifters [121].

The former result is on the so-called *Bloch–Messiah reduction*. It can be derived through singular value decomposition with $A = UA_{\mathrm{D}}V^{\dagger}$ and $B = UB_{\mathrm{D}}V^{\mathrm{T}}$, a unitary matrix U that simultaneously diagonalizes the two commuting Hermitian operators $AA^{\dagger}$ and $BB^{\dagger}$ such that $U^{\dagger}(AA^{\dagger})U = A_{\mathrm{D}}^2$ and $U^{\dagger}(BB^{\dagger})U = B_{\mathrm{D}}^2$, a unitary matrix V that simultaneously diagonalizes the two commuting Hermitian operators $A^{\dagger}A$ and $(B^{\dagger}B)^{\mathrm{T}}$ such that $V^{\dagger}(A^{\dagger}A)V = A_{\mathrm{D}}^2$ and $V^{\dagger}(B^{\dagger}B)^{\mathrm{T}}V = B_{\mathrm{D}}^2$, and non-negative, real, diagonal matrices A_{D} and B_{D}, $A_{\mathrm{D}}^2 = B_{\mathrm{D}}^2 + \mathbb{1}$ [89]. Then, Eq. (2.104) becomes ($\gamma_k \equiv 0$)

$$\begin{aligned}\hat{a}'_k &= \sum_l A_{kl}\hat{a}_l + B_{kl}\hat{a}_l^{\dagger} \\ &= \sum_{l,j}\left[U_{kj}(A_{\mathrm{D}})_{jj}(V^{\dagger})_{jl}\hat{a}_l + U_{kj}(B_{\mathrm{D}})_{jj}(V^{\mathrm{T}})_{jl}\hat{a}_l^{\dagger}\right] \\ &= \sum_j U_{kj}\left[(A_{\mathrm{D}})_{jj}\hat{b}_j + (B_{\mathrm{D}})_{jj}\hat{b}_j^{\dagger}\right] = \sum_j U_{kj}\hat{c}_j \ . \end{aligned} \tag{2.110}$$

Here, $\hat{b}_j = \sum_l (V^{\dagger})_{jl}\hat{a}_l$ are the mode operators after the first passive transformation according to Eq. (2.105) and $\hat{c}_j = (A_{\mathrm{D}})_{jj}\hat{b}_j + (B_{\mathrm{D}})_{jj}\hat{b}_j^{\dagger}$ are the squeezed mode operators after the N single-mode squeezing transformations on every output mode j of the first circuit. The final step is another passive transformation, this time with matrix U.

The above two results together imply that any multi-mode LUBO transformation, that is, any linear multi-mode transformation as in Eq. (2.104), can be implemented with single-mode phase shifters, single-mode squeezers, and two-mode beam splitters. The displacements in Eq. (2.104) (the γ_k's) can be also realized using highly reflective beam splitters. An example for a three-mode LUBO transformation is shown in Figure 2.13.

The decomposability of the passive parts in the LUBO transformation follows from the fact that any $N \times N$ unitary matrix may be expressed as [121],

$$\begin{aligned}U(N) = &(B_{N-1N}B_{N-2N}\cdots B_{1N} \\ &\times B_{N-2N-1}B_{N-3N-1}\cdots B_{12}D)^{-1} \ . \end{aligned} \tag{2.111}$$

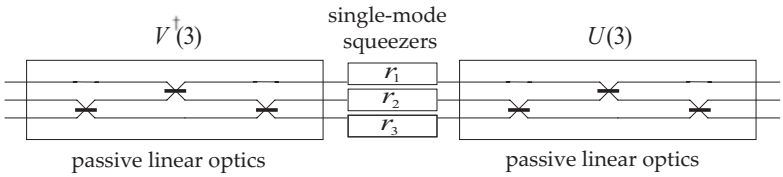

Figure 2.13 Bloch–Messiah reduction and "tree structure" for a general three-mode LUBO transformation (without phase-space displacements). Bloch–Messiah leads to a decomposition into three blocks: a middle-block with three single-mode squeezers (parameterized by three real squeezing parameters $\{r_1, r_2, r_3\}$) and two passive linear-optics blocks, one at the beginning and one at the end of the circuit. The tree structure for each passive block consists of three beam splitters with one reflectivity parameter and one phase per beam splitter. Three extra phases in each passive block (omitted in the figure) give nine parameters for each passive circuit and, together with the three squeezers, a total of 21 parameters for the entire LUBO circuit. Note that this decomposition is independent of the input state.

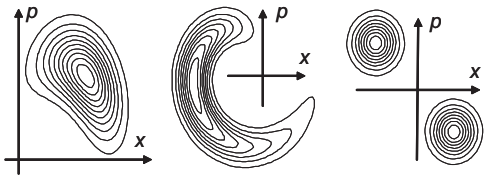

Figure 2.14 Examples of single-mode states generated through highly nonlinear interactions. Shown is the Q function $Q(x, p)$ for a Gaussian coherent state evolving into various non-Gaussian states subject to a quartic self-Kerr interaction with $\hat{H} \propto \hat{a}^{\dagger}\hat{a}(\hat{a}^{\dagger}\hat{a} - 1)$.

Here, the $N(N-1)/2$ beam splitter operations each depend on two parameters, the reflectivity/transmittance parameter and one phase, $B_{kl} \equiv B_{kl}(\theta_{kl}, \phi_{kl})$. The B_{kl} do not represent matrix elements, but N-dimensional identity matrices with the entries I_{kk}, I_{kl}, I_{lk}, and I_{ll} replaced by

$$\mathrm{e}^{\mathrm{i}\phi_{kl}} \sin\theta_{kl}\,, \qquad \mathrm{e}^{\mathrm{i}\phi_{kl}} \cos\theta_{kl}\,, \qquad \cos\theta_{kl}\,, \quad \text{and} \quad -\sin\theta_{kl}\,, \tag{2.112}$$

respectively. Extra phase shifts are included through the diagonal matrix D with elements $\mathrm{e}^{\mathrm{i}\delta_1}, \mathrm{e}^{\mathrm{i}\delta_2}, \ldots, \mathrm{e}^{\mathrm{i}\delta_N}$. For example, the unitary 2×2 matrix in Eq. (2.107) corresponds to $U(2) = (B_{12}D)^{-1}$, with $\phi \equiv \phi_{12}$, $\theta \equiv \theta_{12}$, $\delta \equiv \delta_1$, and $\delta' \equiv \delta_2$.

A general LUBO transformation on N qumodes is then parameterized by $2N^2$ real parameters for the two passive networks and N real squeezing parameters, apart from the phase-space displacements. When acting upon an N-mode vacuum state, the first passive network has no effect, and hence $N^2 + N$ parameters suffice to represent any (zero-mean) N-mode Gaussian pure state.

As shown in Figure 2.12, going beyond the regime of linear resources and operations means to include *cubic or higher-order interactions* leading to *nonlinear transformations*. Such a nonlinear interaction would normally map a Gaussian state onto a non-Gaussian state described by non-Gaussian Q and Wigner functions, see Figure 2.14. These interactions are typically very weak; an example would be the

extremely weak Kerr effect in an optical fiber. Therefore, for sufficiently long interaction times, unwanted photon losses will normally dominate over the desired nonlinear transformation.

In the following section on Gaussian unitaries in form of phase-space displacements and symplectic transformations, we shall see that the transformation rules for the Wigner function are particularly simple for Gaussian unitaries.

2.4 Gaussian Unitaries

In the preceding section, we showed that a multi-qumode LUBO transformation is a linear transformation of the mode operators, as described by Eq. (2.104), decomposable into phase-shift, beam-splitter, and squeezing transformations supplemented by phase-space displacements. Such Gaussian unitaries, omitting the local shifts of the first quadrature moments, can be most conveniently expressed on the level of the correlation matrices. In this case, they correspond to the *symplectic transformations*,

$$V^{(N)} \longrightarrow V^{(N)'} = S\,V^{(N)}\,S^{\mathrm{T}}\,, \tag{2.113}$$

with the $2N\times 2N$ real matrices $S \in \mathrm{Sp}(2N,\mathbb{R})$. For unitarity and in order to preserve the commutators, we have the condition $S\Lambda S^{\mathrm{T}} = \Lambda$, as

$$\begin{aligned}\left[\hat{\xi}'_k, \hat{\xi}'_l\right] &= \left[\sum_i S_{ki}\hat{\xi}_i, \sum_j S_{lj}\hat{\xi}_j\right] = \sum_{i,j} S_{ki}S_{lj}\left[\hat{\xi}_i, \hat{\xi}_j\right] \\ &= \sum_{i,j} S_{ki}S_{lj}\frac{\mathrm{i}}{2}\Lambda_{ij} = \frac{\mathrm{i}}{2}\left(S\Lambda S^{\mathrm{T}}\right)_{kl} = \frac{\mathrm{i}}{2}\Lambda_{kl}\,,\end{aligned} \tag{2.114}$$

using the linear transformation of the phase-space operators, $\hat{\xi}^{\mathrm{T}'} = S\hat{\xi}^{\mathrm{T}}$ with $\hat{\xi}$ from Eq. (2.91). Similar to the LUBO transformations, the symplectic transformations depend on $2N^2 + N$ real parameters. Those transformations which are both symplectic, $O\Lambda O^{\mathrm{T}} = \Lambda$, and orthogonal, $OO^{\mathrm{T}} = \mathbb{1}$, belong to the class of passive transformations,[17] as described by Eq. (2.105) in terms of the evolution of the mode operator. Recall that these transformations, realizable through beam splitters and phase shifters alone, are photon-number preserving, leaving $\mathrm{Tr}\,V^{(N)}$ invariant.

Important examples of symplectic transformations are the passive 50/50 two-qumode beam splitter,

$$O_{\mathrm{BS}} = \frac{1}{\sqrt{2}}\begin{pmatrix} 1 & 0 & 1 & 0 \\ 0 & 1 & 0 & 1 \\ 1 & 0 & -1 & 0 \\ 0 & 1 & 0 & -1 \end{pmatrix}, \tag{2.115}$$

17) They form a compact subgroup of $\mathrm{Sp}(2N,\mathbb{R})$ with elements $O \in \mathrm{Sp}(2N,\mathbb{R}) \cap O(2N)$.

and the active single-qumode x and p squeezers,

$$S_{\mathrm{XSQ}} = \begin{pmatrix} \mathrm{e}^{-r} & 0 \\ 0 & \mathrm{e}^{+r} \end{pmatrix}, \qquad S_{\mathrm{PSQ}} = \begin{pmatrix} \mathrm{e}^{+r} & 0 \\ 0 & \mathrm{e}^{-r} \end{pmatrix}, \tag{2.116}$$

respectively. Similar to the Bloch–Messiah reduction of arbitrary LUBO transformations, as derived in Eq. (2.110), an arbitrary $S \in \mathrm{Sp}(2N, \mathbb{R})$ can be decomposed as

$$S = O \bigoplus_{k=1}^{N} \begin{pmatrix} \mathrm{e}^{-r_k} & 0 \\ 0 & \mathrm{e}^{+r_k} \end{pmatrix} O' , \tag{2.117}$$

with orthogonal N-mode transformations O, O' and single-mode position squeezing r_k for every qumode. This is sometimes referred to as *Euler decomposition* of symplectic transformations. Next, we shall now turn to quantum optical non-unitaries, that is, channels and measurements in the quantum optical setting.

2.5 Quantum Optical Non-unitaries

We are now in a position to apply the general irreversible quantum operations as introduced in Section 1.4 to quantum optical systems. We shall first consider CPTP maps, that is, quantum optical channels, and then quantum optical measurements (CPTD maps). Finally, we will discuss the important Gaussian channels and measurements.

2.5.1 Channels

Consider again the scenario illustrated in Figure 1.5. The signal and ancilla systems are now supposed to be represented by some quantum optical states, and the global unitary $\hat{U}_{\mathrm{AB}}$ will be a certain optical interaction generated by some Hamiltonian polynomial of the qumode operators. The trace over the ancilla then gives the signal state subject to the corresponding reduced dynamics.

For example, a one-photon signal state $|1\rangle_{\mathrm{A}} = \hat{a}_{\mathrm{A}}^{\dagger}|0\rangle_{\mathrm{A}}$ would partially leak into a vacuum ancilla mode ($\hat{\rho}_{\mathrm{B}} = |0\rangle_{\mathrm{B}}\langle 0|$) through a beam splitter unitary, $\hat{a}_{\mathrm{A}}^{\dagger}|0\rangle_{\mathrm{A}} \otimes |0\rangle_{\mathrm{B}} \to \sqrt{\eta}|10\rangle_{\mathrm{AB}} + \sqrt{1-\eta}|01\rangle_{\mathrm{AB}}$, using the definitions $\cos^2\theta \equiv \eta$ and $\sin^2\theta \equiv 1-\eta$, similar to Eq. (2.108). Tracing over the ancilla mode leads to the final signal state $\eta|1\rangle_{\mathrm{A}}\langle 1| + (1-\eta)|0\rangle_{\mathrm{A}}\langle 0|$. This simple model describes, for instance, the transmission of a single photon through a lossy channel with transmission parameter $\eta = \exp(-L/L_{\mathrm{att}})$ and the channel attenuation length L_{att}.

A general photonic single-rail qubit together with a vacuum ancilla, $(\alpha + \beta\hat{a}_{\mathrm{A}}^{\dagger})|0\rangle_{\mathrm{A}} \otimes |0\rangle_{\mathrm{B}}$, is transformed into $\alpha|00\rangle_{\mathrm{AB}} + \beta\sqrt{\eta}|10\rangle_{\mathrm{AB}} + \beta\sqrt{1-\eta}|01\rangle_{\mathrm{AB}}$.

This can be recast in terms of Kraus operators as

$$\begin{aligned}\hat{\rho}_{\mathrm{A}} \to \hat{\rho}'_{\mathrm{A}} &= \sum_{k=0}^{1} \hat{A}_k \hat{\rho}_{\mathrm{A}} \hat{A}_k^\dagger \\ &= \hat{A}_0 \begin{pmatrix} |\alpha|^2 & \alpha\beta^* \\ \alpha^*\beta & |\beta|^2 \end{pmatrix} \hat{A}_0^\dagger + \hat{A}_1 \begin{pmatrix} |\alpha|^2 & \alpha\beta^* \\ \alpha^*\beta & |\beta|^2 \end{pmatrix} \hat{A}_1^\dagger \\ &= \begin{pmatrix} |\alpha|^2 & \sqrt{1-\gamma}\,\alpha\beta^* \\ \sqrt{1-\gamma}\,\alpha^*\beta & (1-\gamma)|\beta|^2 \end{pmatrix} + \begin{pmatrix} \gamma|\beta|^2 & 0 \\ 0 & 0 \end{pmatrix} \\ &= \left(\alpha|0\rangle_{\mathrm{A}} + \beta\sqrt{\eta}|1\rangle_{\mathrm{A}}\right)\left(\alpha^*_{\mathrm{A}}\langle 0| + \beta^*\sqrt{\eta}_{\mathrm{A}}\langle 1|\right) \\ &\quad + |\beta|^2(1-\eta)|0\rangle_{\mathrm{A}}\langle 0| \,, \end{aligned} \tag{2.118}$$

with

$$\hat{A}_0 = \begin{pmatrix} 1 & 0 \\ 0 & \sqrt{1-\gamma} \end{pmatrix}, \quad \hat{A}_1 = \begin{pmatrix} 0 & \sqrt{\gamma} \\ 0 & 0 \end{pmatrix}, \tag{2.119}$$

using $\hat{A}_k \equiv {}_{\mathrm{B}}\langle k|\hat{U}_{\mathrm{AB}}|0\rangle_{\mathrm{B}}$ in the Fock basis, $\gamma \equiv \sin^2\theta = 1-\eta$, and the beam splitter unitary $\hat{U}_{\mathrm{AB}} = \mathrm{e}^{\theta(\hat{a}_{\mathrm{A}}^\dagger \hat{a}_{\mathrm{B}} - \hat{a}_{\mathrm{A}}\hat{a}_{\mathrm{B}}^\dagger)}$. The amplitude of the one-photon component is always attenuated and as the photon can be absorbed by the ancilla, we obtain for the signal output state an incoherent mixture of the attenuated input state and a vacuum noise term.

Consider now for the signal system a single qumode in an initial coherent state $|\alpha\rangle_{\mathrm{A}}$. Importantly, as the only optical state, the coherent state remains a pure coherent state after the action of the generalized amplitude damping channel, $\sum_{k=0}^{\infty} \hat{A}_k \hat{\rho}_{\mathrm{A}} \hat{A}_k^\dagger$, with Kraus operators

$$\hat{A}_k = \sum_{n=k}^{\infty} \sqrt{\binom{n}{k}} \sqrt{\eta^{n-k}(1-\eta)^k}\,|n-k\rangle\langle n| \,, \tag{2.120}$$

for which we obtain

$$\hat{A}_k|\alpha\rangle_{\mathrm{A}} = \frac{\alpha^k}{\sqrt{k!}}\sqrt{1-\eta}^{\,k}\,\mathrm{e}^{-(1-\eta)|\alpha|^2/2}|\sqrt{\eta}\alpha\rangle_{\mathrm{A}} \,, \tag{2.121}$$

using Eq. (2.43). Eventually, we have

$$\sum_{k=0}^{\infty} \hat{A}_k|\alpha\rangle_{\mathrm{A}}\langle\alpha|\hat{A}_k^\dagger = |\sqrt{\eta}\alpha\rangle_{\mathrm{A}}\langle\sqrt{\eta}\alpha| \,. \tag{2.122}$$

This is the expected result according to the beam splitter transformation $|\alpha\rangle_{\mathrm{A}} \otimes |0\rangle_{\mathrm{B}} \to |\sqrt{\eta}\alpha\rangle_{\mathrm{A}} \otimes |\sqrt{1-\eta}\alpha\rangle_{\mathrm{B}}$, corresponding to the signal map $|\alpha\rangle_{\mathrm{A}} \to |\sqrt{\eta}\alpha\rangle_{\mathrm{A}}$. Although the coherent state remains pure, its amplitude gets attenuated exponentially with $\eta = \exp(-L/L_{\mathrm{att}})$ in the case of a channel transmission.

The lossy beam splitter channel discussed so far, describing the effect of photon losses in a very simple way, is certainly the most important imperfection in optical

quantum information processing. As it corresponds to a quadratic interaction (the beam splitter) together with a Gaussian ancilla state (the vacuum, or, more generally, any Gaussian ancilla state), it will always map Gaussian signal states to Gaussian signal states – it is a Gaussian channel (see Section 2.6).

In the Heisenberg picture, the reduced dynamics may be calculated using the dual, CPUP map, as introduced in Section 1.4.1 in Eq. (1.76), with the Kraus operators depending on the global unitary and the initial ancilla state. For the above example of the beam splitter model, we obtain

$$\begin{aligned}\mathcal{E}^*(\hat{a}_\mathrm{A}) &= \sum_k \hat{A}_k^\dagger \hat{a}_\mathrm{A} \hat{A}_k = \sum_k {}_\mathrm{B}\langle 0|\, \hat{U}_\mathrm{AB}^\dagger |k\rangle_\mathrm{B}\, \hat{a}_\mathrm{A}\, {}_\mathrm{B}\langle k|\, \hat{U}_\mathrm{AB}|0\rangle_\mathrm{B} \\ &= {}_\mathrm{B}\langle 0|\, \hat{U}_\mathrm{AB}^\dagger \hat{a}_\mathrm{A}\, \hat{U}_\mathrm{AB}|0\rangle_\mathrm{B} = {}_\mathrm{B}\langle 0|\left(\sqrt{\eta}\,\hat{a}_\mathrm{A} + \sqrt{1-\eta}\,\hat{a}_\mathrm{B}\right)|0\rangle_\mathrm{B} \\ &= \sqrt{\eta}\,\hat{a}_\mathrm{A}\,, \end{aligned} \tag{2.123}$$

using $\hat{a}_\mathrm{B}|0\rangle_\mathrm{B} = 0$. Note that now $[\mathcal{E}^*(\hat{a}_\mathrm{A}), \mathcal{E}^*(\hat{a}_\mathrm{A}^\dagger)] = \eta$, indicating the non-unitarity of the evolution. The reduced dynamics here, corresponding to a Gaussian channel, map the generators $\hat{x}$ and $\hat{p}$, and linear combinations of them such as $\hat{a}$, into another linear combination of $\hat{x}$ and $\hat{p}$. In Section 2.6, we will see how to recast this using the covariance formalism. Channels with global unitaries generated by Hamiltonians with an order higher than quadratic or those with non-Gaussian ancilla states will, in general, lead to nonlinear evolution equations.

2.5.2 Measurements

Now, for the case of CPTD maps in form of photon measurements on optical states, we shall again first consider a photonic qubit (qudit) and later a photonic qumode. The photon measurements will either project onto the Fock basis $|n\rangle\langle n|$ (using photon-number resolving detectors) or, more realistically, they will only discriminate between the vacuum and the non-vacuum state which is described by the binary POVM $\hat{E}_1 = |0\rangle\langle 0|$ and $\hat{E}_2 = \mathbb{1} - |0\rangle\langle 0|$.

Let us consider the very general case of all those POVMs where the signal states only contain *one photon*. In this case, any unitary operation (gate) can be accomplished with linear optics [121]. This statement applies to arbitrary qudit states where each basis vector of the qudit is described by one photon occupying one of d modes, $\hat{a}_i^\dagger|\mathbf{0}\rangle$, $i = 1 \ldots d$ (so-called "multiple-rail encoding"). It can be understood by looking at the corresponding Naimark extension of the POVM introduced in Section 1.4.2. The POVM is then described by a von Neumann measurement onto the orthogonal set

$$|w_\mu\rangle = |u_\mu\rangle + |N_\mu\rangle\,, \tag{2.124}$$

in a Hilbert space larger than the original signal space.

In the multiple-rail encoding, this leads to an orthogonal set of vectors

$$|w_\mu\rangle = \sum_{j=1}^{N} U_{\mu j}\, \hat{a}_j^\dagger |\mathbf{0}\rangle \ , \tag{2.125}$$

with a unitary $N \times N$ matrix U having elements $U_{\mu j}$. The application of a linear-optics transformation V to this set (in order to project onto it) can be written as

$$|w_\mu\rangle \longrightarrow |w'_\mu\rangle = \sum_{j,k=1}^{N} U_{\mu j}\, V^*_{kj}\, \hat{a}_k^\dagger |\mathbf{0}\rangle = \sum_{k=1}^{N} \delta_{\mu k}\, \hat{a}_k^\dagger |\mathbf{0}\rangle = \hat{a}_\mu^\dagger |\mathbf{0}\rangle \ , \tag{2.126}$$

choosing $V \equiv U$. As a result, when detecting the outgoing state, for every one-photon click in mode μ, one can unambiguously identify the input state $|w_\mu\rangle$.

As an example, the linear-optics implementation of the POVM for the optimal USD of the non-orthogonal states in Eq. (1.87), using one-photon signal states and multiple-rail encoding, $|\bar{0}\rangle \equiv |100\rangle$, $|\bar{1}\rangle \equiv |010\rangle$, $|\bar{2}\rangle \equiv |001\rangle$, can be directly obtained. In this case, the output states after the linear-optics circuit, $|100\rangle$, $|010\rangle$, and $|001\rangle$, uniquely refer to one of the three orthogonal states $|w_\mu\rangle$, and hence identify the signal states $|\chi_+\rangle$ and $|\chi_-\rangle$ with the best possible probability.

For states other than one-photon states, it is generally not obvious whether a given POVM can be implemented with linear optics. There are important examples for which the exact POVM cannot be implemented by linear optics such as the Bell measurement on two dual-rail encoded photonic qubits [122].

Now, considering a single qumode, remarkably, there is also a very simple linear optical scheme for the USD of two arbitrary coherent states such as $\{|\pm\alpha\rangle\}$ (see Figure 2.9 at the beginning of Section 2.2.8) that achieves the quantum mechanically optimal USD for two pure non-orthogonal states $\{|\psi_1\rangle, |\psi_2\rangle\}$ [123]. In this case, the success probability for a conclusive result equals $1 - |\langle\psi_1|\psi_2\rangle| = 1 - |\langle\alpha| - \alpha\rangle| = 1 - \exp(-2\alpha^2)$ (assuming α real) [30–32]. The detectors only have to discriminate between the vacuum and non-vacuum components at the output ports of the beam splitter, where the two possible states are either $|\sqrt{2}\alpha, 0\rangle$ or $|0, -\sqrt{2}\alpha\rangle$, and only the term $|0, 0\rangle$ is ambiguous. This scheme can also be formulated using the Naimark extension, however, in this case, the signal and Naimark vectors must be expressed in terms of more complicated superpositions of coherent states (see Chapter 8).

2.6
Gaussian Non-unitaries

Gaussian channels (Gaussian CPTP maps) may be most conveniently expressed in terms of covariance (correlation) matrices. One can show that a general multi-qumode Gaussian channel acts on the level of the covariance matrices as [124]

$$V^{(N)'} = F\, V^{(N)} F^{\mathrm{T}} + G \ , \tag{2.127}$$

where for the channel to be physical, the $2N \times 2N$ matrices F and G must satisfy the condition

$$16 \det G \geq (\det F - 1)^2 \,. \tag{2.128}$$

The special case of reversible, unitary, symplectic transformations is again obtained when $G = 0$ (the zero matrix) and $F = S \in \mathrm{Sp}(2N, \mathbb{R})$ with $\det S = 1$.

Let us again consider the effect of a lossy channel, as described by the beam splitter model in Section 2.5.1. Since the signal mode operator transforms as $\hat{a}_\mathrm{A} \to \sqrt{\eta}\,\hat{a}_\mathrm{A} + \sqrt{1-\eta}\,\hat{a}_\mathrm{B}$ through the beam splitter and, similarly, $\hat{x}_\mathrm{A} \to \sqrt{\eta}\,\hat{x}_\mathrm{A} + \sqrt{1-\eta}\,\hat{x}_\mathrm{B}$ and $\hat{p}_\mathrm{A} \to \sqrt{\eta}\,\hat{p}_\mathrm{A} + \sqrt{1-\eta}\,\hat{p}_\mathrm{B}$, we obtain

$$\begin{aligned} V_\mathrm{A}^{(1)} \to V_\mathrm{A}^{(1)'} &= \eta\, V_\mathrm{A}^{(1)} + (1-\eta)\frac{1}{4}\mathbb{1} \\ &= \begin{pmatrix} \sqrt{\eta} & 0 \\ 0 & \sqrt{\eta} \end{pmatrix} V_A^{(1)} \begin{pmatrix} \sqrt{\eta} & 0 \\ 0 & \sqrt{\eta} \end{pmatrix} + (1-\eta)\frac{1}{4}\mathbb{1} \,, \end{aligned} \tag{2.129}$$

assuming that the ancilla mode started in the vacuum state. Note that, in general, the excess noise matrix G depends on the initial ancilla state. We can read off the F and G matrices and obtain $\det G = (1-\eta)^2/16$ and $\det F = \eta$, such that $16 \det G = (1-\eta)^2 = (\det F - 1)^2$. We finally note that in the covariance formalism, the reduced dynamics are expressed simply by the corresponding signal submatrix of the globally transformed signal-ancilla covariance matrix after discarding the ancilla submatrix. The signal submatrix is a valid covariance matrix since the global transformation such as, for instance, $\hat{x}_\mathrm{A} \to \sqrt{\eta}\,\hat{x}_\mathrm{A} + \sqrt{1-\eta}\,\hat{x}_\mathrm{B}$, is unitary and hence preserves the commutators. This is different from the non-unitary, dual map $\hat{x}_\mathrm{A} \to \mathcal{E}^*(\hat{x}_\mathrm{A}) = \sqrt{\eta}\,\hat{x}_\mathrm{A}$.

Let us now briefly discuss the important linear, Gaussian measurements which are well approximated by means of so-called *homodyne detectors*. In this case, instead of the discrete photon numbers, the rotated quadrature observables are measured. A photodetector measuring an electromagnetic mode converts the photons into electrons and hence into an electric current called the "photocurrent" $\hat{i}$. We may then assume $\hat{i} \propto \hat{n} = \hat{a}^\dagger \hat{a}$ or $\hat{i} = q\,\hat{a}^\dagger \hat{a}$ with q a constant. In order to detect a quadrature of the mode $\hat{a}$, the mode must be combined with an intense "local oscillator" at a 50/50 beam splitter. The local oscillator is assumed to be in a coherent state with large photon number, $|\alpha_\mathrm{LO}\rangle$. It is therefore reasonable to describe this oscillator by a classical complex amplitude α_LO rather than by an annihilation operator $\hat{a}_\mathrm{LO}$. The two output modes of the beam splitter, $(\hat{a}_\mathrm{LO} + \hat{a})/\sqrt{2}$ and $(\hat{a}_\mathrm{LO} - \hat{a})/\sqrt{2}$, may then be approximated by

$$\hat{a}_1 = (\alpha_\mathrm{LO} + \hat{a})/\sqrt{2} \,, \qquad \hat{a}_2 = (\alpha_\mathrm{LO} - \hat{a})/\sqrt{2} \,. \tag{2.130}$$

This yields the photocurrents

$$\begin{aligned} \hat{i}_1 &= q\hat{a}_1^\dagger \hat{a}_1 = q\left(\alpha_\mathrm{LO}^* + \hat{a}^\dagger\right)(\alpha_\mathrm{LO} + \hat{a})/2 \,, \\ \hat{i}_2 &= q\hat{a}_2^\dagger \hat{a}_2 = q\left(\alpha_\mathrm{LO}^* - \hat{a}^\dagger\right)(\alpha_\mathrm{LO} - \hat{a})/2 \,. \end{aligned} \tag{2.131}$$

The actual quantity to be measured is the difference photocurrent

$$\delta\hat{\imath} \equiv \hat{\imath}_1 - \hat{\imath}_2 = q\left(\alpha_{\mathrm{LO}}^{*}\hat{a} + \alpha_{\mathrm{LO}}\hat{a}^{\dagger}\right) . \tag{2.132}$$

By introducing the phase Θ of the local oscillator, $\alpha_{\mathrm{LO}} = |\alpha_{\mathrm{LO}}| \exp(\mathrm{i}\Theta)$, we can see that any quadrature $\hat{x}^{(\Theta)}$ from Eq. (2.35) can be measured when the local oscillator's phase $\Theta \in [0, \pi]$ is adjusted accordingly. A possible way to realize quantum tomography [113] by reconstructing the Wigner function relies on this measurement.

Gaussian operations

Gaussian *channels*:

$$V^{(N)\prime} = F V^{(N)} F^{\mathrm{T}} + G , \quad 16 \det G \geq (\det F - 1)^2$$

Gaussian *unitaries*:

$$\text{LUBO transformation:} \quad \hat{a}'_k = \sum_l A_{kl}\hat{a}_l + B_{kl}\hat{a}_l^{\dagger} (+\gamma_k)$$

Bloch–Messiah reduction:

$$A = U A_{\mathrm{D}} V^{\dagger} , \quad B = U B_{\mathrm{D}} V^{\mathrm{T}} , \quad U^{\dagger}U = \mathbb{1} , \quad V^{\dagger}V = \mathbb{1}$$
$$\hat{a}'_k = \sum_{l,j} \left[U_{kj} (A_{\mathrm{D}})_{jj} (V^{\dagger})_{jl} \hat{a}_l + U_{kj} (B_{\mathrm{D}})_{jj} (V^{\mathrm{T}})_{jl} \hat{a}_l^{\dagger} \right] (+\gamma_k)$$

passive linear transformation:

$$A \to U , \quad U^{\dagger}U = \mathbb{1} , \quad B \to 0 :$$
$$\hat{a}'_k = \sum_l U_{kl}\hat{a}_l$$

symplectic transformation:

$$F \to S , \quad G \to 0 :$$
$$V^{(N)\prime} = S V^{(N)} S^{\mathrm{T}} , \quad S \Lambda S^{\mathrm{T}} = \Lambda , \quad \det S = 1 , \quad \forall S \in \mathrm{Sp}(2N, \mathbb{R})$$

Euler decomposition:

$$S = O \left(\bigoplus_{k=1}^{N} S_{\mathrm{XSQ}} \right) O'$$

passive, orthogonal, symplectic transformation:

$$O \Lambda O^{\mathrm{T}} = \Lambda , \quad O O^{\mathrm{T}} = \mathbb{1}$$

2.7 Linear Optics: Possibilities and Impossibilities

CV Gaussian resources can be unconditionally prepared in the laboratory and Gaussian operations are deterministic and experimentally efficient. Nonetheless, there are various, highly advanced tasks in quantum information which would require a non-Gaussian element:

- quantum error detection and correction for qumodes are impossible in the Gaussian regime [93, 125–127],
- universal quantum computation on qumodes and quantum computational speed-up through it are impossible in the Gaussian regime [86, 90].

The former of these two important results can be understood by realizing that Gaussian channels (e.g., the lossy channel described in the preceding sections) typically lack the stochastic nature of those channels for which the standard quantum error correction codes are designed (recall Section 1.9). Amplitude damping is an error that will occur in every optical transmission line of an encoded state. In this case, although for photonic qubits, stabilizer codes help, for photonic qumodes encoded into Gaussian states, the CV stabilizer codes have no effect.[18] The latter result above is related with the Gottesmann–Knill theorem for CV qumode systems. It fully applies to physical, Gaussian stabilizer states (see Sections 1.8, 2.2.8.1, and 3.2.2) and their manipulation through Gaussian operations.

The necessary non-Gaussian element may be provided in form of a DV measurement such as photon counting. There are also a few simpler tasks which can be performed better with some non-Gaussian element compared to a fully Gaussian approach, for instance, quantum teleportation [128] or optimal cloning [129, 130] of coherent states.

Similarly, in the DV regime, (efficient) universal quantum computation on photonic qubits would depend on some nonlinear element, either directly implemented through nonlinear optics or induced by photon measurements (see next section and Chapters 7 and 8). In addition, there are even supposedly simpler tasks which are impossible, using only quadratic interactions (linear transformations) and standard DV measurements such as photon counting. The prime example for this is a complete photonic Bell measurement (see Sections 1.5 and 1.6) on two photonic dual-rail qubits [122, 131].

In contrast, in the CV regime, a photonic Bell measurement onto the CV Bell basis of two qumodes as given by Eq. (1.95) is very simple: measuring the two stabilizer eigenvalues $u = \hat{x}_1 - \hat{x}_2$ and $v = \hat{p}_1 + \hat{p}_2$ only requires a 50/50 beam splitter and two homodyne detectors. Now, recall that any POVM is effectively a von Neumann, projection measurement in a higher-dimensional Hilbert space (compared to the signal space, see Section 1.4.2). The CV Bell measurement turns out

18) Nonetheless, in Chapter 5, an experiment will be described in which a nine-qumode stabilizer code was realized; this code can still be useful for protecting a qumode against non-Gaussian error channels different from the Gaussian amplitude-damping photon-loss channel.

to be a two-qumode projection measurement that corresponds to a single-qumode POVM, namely, $\hat{E}_\alpha = (1/\pi)|\alpha\rangle\langle\alpha|$ with $\alpha = u + \mathrm{i}v$. This is also the POVM for the optimal coherent-state estimation, equivalent to a so-called Arthurs–Kelly measurement [132]. An Arthurs–Kelly measurement is effectively an attempt to simultaneously detect position and momentum; and optically this can be realized by splitting the mode of interest at a 50/50 beam splitter and detecting the position at one output and the momentum at the other output. The input mode of the "unused port" of the beam splitter, playing the role of an ancilla, would (ideally) start in a vacuum state. The signal POVM $\hat{E}_\alpha$ is then equivalent to the signal-ancilla projectors $|\Psi(u,v)\rangle\langle\Psi(u,v)|$ with the CV Bell states of Eq. (1.95) [133].

It is worth pointing out that the above restrictions and no-go results apply even when linear elements and photon detectors are available that operate with 100% efficiency (i.e., every photon is counted) and 100% reliability (i.e., every photon is counted correctly). In other words, the imposed constraints are of fundamental nature and cannot be circumvented by improving the experimental performance of the linear elements, for example, by further increasing the squeezing levels.

2.8 Optical Quantum Computation

A necessary criterion for a quantum computer to give a true advantage over classical computers is that its realization does not require exponential resources. In other words, the exponential "speed-up" quantum computation it is usually associated with must not be at the expense of an exponential increase of physical resources (see Section 1.8). The exponentially large dimension of the Hilbert space of N logical qubits, 2^N, should be exploited with a number of physical resources scaling as $\sim N$ (or a polynomial of N) rather than $\sim 2^N$.

Both for qubit and qumode computations, there is always at least one universal gate of those gates discussed in Section 1.8 which is not realizable through linear transformations alone. In single-photon single-rail encoding, even a single-qubit Hadamard gate, transforming a Gaussian vacuum state into a non-Gaussian superposition of vacuum and one-photon Fock state would be highly nonlinear. The hardest part of universally processing dual-rail encoded qubits would be the entangling gate which has to act upon at least two photons. Ultimately, the universal processing of even a single qumode requires some form of nonlinearity.

The most obvious approach now to optically implement an entire set of universal quantum gates would be directly through *nonlinear interactions*. The two-qubit C_Z gate from Section 1.8 is accomplished by applying a quartic cross-Kerr interaction on two photonic occupation number qubits,

$$\exp\left(\mathrm{i}\pi\hat{a}_1^\dagger\hat{a}_1 \otimes \hat{a}_2^\dagger\hat{a}_2\right)|k\rangle \otimes |l\rangle = (-1)^{kl}|k\rangle \otimes |l\rangle \,. \tag{2.133}$$

The same interaction leads to a C_Z gate for two photonic dual-rail qubits, with the cross-Kerr interaction acting on the second rail (mode) of each qubit such that only

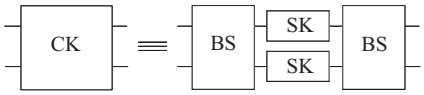

Figure 2.15 Implementing a controlled sign gate (C_Z) on two single-rail qubits using cross-Kerr (CK) or self-Kerr (SK) nonlinearities. The first beam splitter (BS) transforms the term $|11\rangle$ into $(|20\rangle - |02\rangle)/\sqrt{2}$, while the other terms stay in the vacuum and one-photon space. As the SK interactions affect sign flips only for the two-photon components, only the term $|11\rangle$ acquires a sign flip.

the term $|01\rangle \otimes |01\rangle$ acquires a sign flip. This is the conceptually simplest and, in theory, most efficient method to complete the set of universal gates in dual-rail encoding. In the low-photon number subspace here, we may even decompose the cross-Kerr two-mode unitary into a beam splitter, two self-Kerr one-mode unitaries,

$$\exp\left[\mathrm{i}\frac{\pi}{2}\hat{a}_1^\dagger\hat{a}_1\left(\hat{a}_1^\dagger\hat{a}_1-1\right)\right]\otimes\exp\left[\mathrm{i}\frac{\pi}{2}\hat{a}_2^\dagger\hat{a}_2\left(\hat{a}_2^\dagger\hat{a}_2-1\right)\right], \tag{2.134}$$

and another beam splitter (see Figure 2.15). Thus, a sufficiently strong one-mode self-Kerr interaction would be enough to fulfill the criteria for DV universality on the finite-dimensional multi-qubit subspace of the infinite-dimensional, multi-mode optical Fock space. At the same time, the quartic one-mode self-Kerr interaction together with Gaussian, linear transformations (LUBO transformations) would also be sufficient for the strong notion of full (asymptotically arbitrarily precise) CV universality, as expressed by Eq. (1.119).

The problem of this approach, however, is that an effective coupling strength of $\sim \pi$ for the self/cross-Kerr interactions is totally infeasible on the level of single photons. Therefore, it is worth examining carefully if there is a way to implement universal quantum gates through linear optical elements, ideally just using beam splitters and phase shifters. A very early proposal for *linear-optics-based quantum computation* indeed does work with only linear elements [134]. It is based upon multiple-rail encoding, as introduced earlier in the context of optical POVMs. The multiple-rail scheme encodes a d-level system into a single photon and d optical modes, with the basis states $\hat{a}_k^\dagger|00\cdots0\rangle$, $k = 1, 2, \ldots, d$. Any unitary operator can be realized in the space spanned by this basis as we only need

$$\hat{U}\hat{a}_k^\dagger|00\cdots0\rangle = \sum_{l=1}^{d} U_{kl}\hat{a}_l^\dagger|00\cdots0\rangle\ , \quad \forall k = 1, 2, \ldots, d\ . \tag{2.135}$$

This linear transformation, as in Eq. (2.105), is easily achieved through a sequence of beam splitters and phase shifters [121]. The realizability of any POVM is then an obvious consequence of the implementability of any unitary operator on one-photon states.

As a result, universal quantum computation is, in principle, possible using a single photon and linear optics. This kind of realization would be clearly efficient from an experimental point of view. In fact, implementing a universal two-qubit gate in a $d = 2^2 = 4$-dimensional Hilbert space would only require the modest set of resources of an optical "ququart", in "quad-rail" encoding corresponding to

a single photon and four optical modes. In fact, for small quantum applications, by adding to the polarization of the photons (their spin angular momenta) extra degrees of freedom such as orbital angular momenta, this kind of approach can be useful [135].

Nonetheless, the drawback of the multiple-rail-based linear-optics quantum computer [134] is its bad scaling. Even in theory, this type of quantum computer is inefficient. Scaling it up to computations involving N qubits, we need 2^N basis states and hence 2^N optical modes. All these modes have to be controlled and processed in a linear optical circuit with an exponentially increasing number of optical elements. For example, a 10-qubit circuit would only require 10 photons and 20 modes in dual-rail encoding, while it consumes $2^{10} = 1024$ modes (for just a single photon), and at least as many optical elements in multiple-rail encoding.

More recently, there are now conceptually very different approaches to obtain the necessary nonlinear elements. One such approach uses measurement-induced nonlinearities and can be incorporated into quantum information protocols through gate teleportation (see Chapter 6) or, ultimately, in the form of one-way cluster computations (see Chapter 7). Another important and promising concept is that of using weak nonlinear interactions which are experimentally accessible and still, in principle, sufficient for universal quantum information processing (see Chapter 8).

Part Two Fundamental Resources and Protocols

3
Entanglement

Entanglement is an essential resource for quantum information processing. In quantum optics, typically, nonlinear optical interactions such as parametric down conversion (PDC) are employed to create photonic entangled states. In the parametric approximation, the signal-idler twin beam generation is described by a quadratic Hamiltonian, which, according to our definition, corresponds to a linear transformation.

Hence, linear transformations, though insufficient for universal quantum information processing on qubits or qumodes, are enough to prepare entangled states of light. Then, typically, the creation of photonic qubit entanglement relies upon some heralding mechanism, that is, the entangled states can be prepared only conditionally. In contrast, the Gaussian entangled states of optical qumodes can emerge unconditionally from linear optical transformations. In this case, the PDC interaction can be used to directly obtain entangled two-mode squeezed states. Alternatively, individually squeezed qumodes may be entangled through beam splitter transformations.

From a theoretical point of view, it turns out that there is a link between the stabilizers (Section 1.9) that uniquely determine an entangled state and the witnesses (Section 1.5) that may be used to unambiguously verify the presence of entanglement in that state. This link can be established both for qubits and qumodes.

In this chapter, we shall first focus on qubit entanglement (Section 3.1), including an overview of various types of entanglement such as bipartite and multipartite entanglement, and some explicit entanglement witnesses for qubit entangled states (Section 3.1.1). Further, we will define qubit cluster states and qubit graph states as a rather general notion of multi-party entanglement (Section 3.1.2). In Section 3.1.3, we will then describe a selection of experiments in which qubit EPR, GHZ, and cluster states were realized.

The CV qumode counterparts of the qubit entangled states will be discussed in Section 3.2, including a few distinct features of graph states in the CV regime; in particular, the connection between complex-valued stabilizers/nullifiers for qumodes, complex-weighted qumode graph states, and multi-mode Gaussian pure states (Section 3.2.2). A selection of experiments is presented in Section 3.2.3.

Quantum Teleportation and Entanglement. Akira Furusawa, Peter van Loock
Copyright © 2011 WILEY-VCH Verlag GmbH & Co. KGaA, Weinheim
ISBN: 978-3-527-40930-3

3.1 Qubit Entanglement

3.1.1 Characterization and Witnesses

In a realistic experiment, the entangled states will be always imperfect, corresponding to noisy, mixed entangled states. In this case, it is useful to measure entanglement witnesses which may still be able to detect entanglement for not too noisy states. There are various references, for instance, [136–138], which provide good reviews on general entanglement theory, including the bipartite (two-party) and multipartite (N-party with $N > 2$) cases, and covering important notions such as inseparability, witnesses, and distillability, with a focus on finite-dimensional DV systems and qubit states.

3.1.1.1 Two Parties

In Section 1.5, we introduced the maximally entangled Bell basis for two qubits as well as for two qumodes, general pure and mixed entangled states, inseparability criteria, entanglement witnesses, and some examples of entanglement measures. The discussion there was restricted to the bipartite case of two entangled subsystems.

Let us now continue the discussion on entanglement witnesses for two-qubit density operators. Recall that the partial transpose criterion (Section 1.5) is necessary and sufficient for detecting the entanglement of two-qubit states. Therefore, *any* inseparable state $\hat{\rho}_{\rm AB}$ of two qubits A and B has at least one negative eigenvalue λ_- such that $\mathrm{Tr}(\hat{\rho}_{\rm AB}^{T_{\rm B}}|\phi\rangle\langle\phi|) = \lambda_- < 0$, where the superscript $T_{\rm B}$ denotes partial transposition on qubit B and $|\phi\rangle$ is the corresponding eigenvector with eigenvalue λ_-. Then, since for any pair of matrices C and D, $\mathrm{Tr}(C^{T_{\rm B}} D) = \mathrm{Tr}(C D^{T_{\rm B}})$, we also have $\mathrm{Tr}(\hat{\rho}_{\rm AB}|\phi\rangle\langle\phi|^{T_{\rm B}}) = \lambda_- < 0$. Thus, by defining

$$W \equiv |\phi\rangle\langle\phi|^{T_{\rm B}} , \tag{3.1}$$

we immediately obtain a valid entanglement witness W that detects the inseparability of $\hat{\rho}_{\rm AB}$, $\mathrm{Tr}(\hat{\rho}_{\rm AB} W) = \lambda_- < 0$ and correctly gives $\mathrm{Tr}(\hat{\sigma}_{\rm AB} W) \geq 0$ for any separable state $\hat{\sigma}_{\rm AB}$ since $\hat{\sigma}_{\rm AB}$ must have positive partial transposition and hence $\mathrm{Tr}(\hat{\sigma}_{\rm AB} W) = \langle\phi|\hat{\sigma}_{\rm AB}^{T_{\rm B}}|\phi\rangle \geq 0$. The witness W detects every entangled state of two qubits as partial transposition is necessary and sufficient in this case.

An example for the witness in Eq. (3.1) is given by

$$W = \frac{1}{2}\begin{pmatrix} 0 & 0 & 0 & -1 \\ 0 & 1 & 0 & 0 \\ 0 & 0 & 1 & 0 \\ -1 & 0 & 0 & 0 \end{pmatrix}, \quad W^{T_{\rm B}} = \frac{1}{2}\begin{pmatrix} 0 & 0 & 0 & 0 \\ 0 & 1 & -1 & 0 \\ 0 & -1 & 1 & 0 \\ 0 & 0 & 0 & 0 \end{pmatrix}, \tag{3.2}$$

where $|\phi\rangle = (|10\rangle - |01\rangle)/\sqrt{2}$ is the eigenvector for the partially transposed Bell state $|\Phi^+\rangle$ from Eq. (1.93) with $\mathrm{Tr}(|\Phi^+\rangle\langle\Phi^+|^{T_{\rm B}}|\phi\rangle\langle\phi|) = \langle\phi|(|\Phi^+\rangle\langle\Phi^+|^{T_{\rm B}})|\phi\rangle$

$= -1/2 < 0$ and hence also $\mathrm{Tr}(|\Phi^+\rangle\langle\Phi^+||\phi\rangle\langle\phi|^{T_B}) = -1/2 < 0$. This witness clearly detects the entanglement of the Bell state $|\Phi^+\rangle$. An alternative way to write the witness W in Eq. (3.2) is $W = \mathbb{1}/2 - |\Phi^+\rangle\langle\Phi^+|$, from which one can see that W also detects the presence of entanglement for states that deviate from $|\Phi^+\rangle$ such as $\hat{\rho} = (1-p)|\Phi^+\rangle\langle\Phi^+| + p\mathbb{1}/4$. The term $\mathbb{1}/2$ in W comes from the maximal squared overlap between $|\Phi^+\rangle$ and all pure separable states.

For our discussion here, it is useful to understand the connection of the entanglement witnesses with the stabilizers of an entangled state. Now, the projector of any N-qubit stabilizer state $|\psi\rangle$ can be written as [5]

$$|\psi\rangle\langle\psi| = \frac{1}{2^N}\sum_{g\in S} g = \prod_{k=1}^{N}(\mathbb{1} + g_k)/2\,, \tag{3.3}$$

where the sum goes over all the 2^N elements of the state's stabilizer group S, while the product only goes over all of its N generators. Thus, for $N = 2$, the witness $W = \mathbb{1}/2 - |\Phi^+\rangle\langle\Phi^+|$ can be expressed in terms of local Pauli operators, that is, the stabilizers of $|\Phi^+\rangle$, $S = \langle XX, ZZ\rangle$ (see Section 1.5). For $N = 2$, this is fine, but for larger N (see next section), the number of terms in the sum in Eq. (3.3) grows exponentially; and the product may also be an unnecessarily complicated function of the stabilizer generators.

However, there are simpler ways to write an entanglement witness in terms of stabilizers [139]. For instance, the following witness,

$$W = \mathbb{1} - X\otimes X - Z\otimes Z\,, \tag{3.4}$$

detects entangled states in the vicinity of $|\Phi^+\rangle$ because we have

$$\mathrm{Tr}\left[\left|\Phi^+\right\rangle\left\langle\Phi^+\right|(XX+ZZ)\right] = \left\langle\Phi^+\right|XX\left|\Phi^+\right\rangle + \left\langle\Phi^+\right|ZZ\left|\Phi^+\right\rangle = 2\,, \tag{3.5}$$

such that $\mathrm{Tr}(|\Phi^+\rangle\langle\Phi^+|\,W) = -1$. This is the simplest linear witness, and nonlinear refinements (i.e., additional nonlinear correction terms) may lead to even better witnesses [40] (see Figure 1.6). Note that the stabilizers that uniquely define the entangled Bell state can also be used to detect its entanglement as their expectation values indicate the quantum correlations for two non-commuting Pauli operators inherent in that state. Next, we shall now consider multipartite entangled states of more than two qubits.

3.1.1.2 Three or More Parties

First, we must consider pure states. In general, there is no Schmidt decomposition for the case of more than two parties directly obtainable as for the two-party case. Nonetheless, there is one important representative of multipartite entanglement which is reminiscent of a Schmidt decomposition, namely, the Greenberger–Horne–Zeilinger (GHZ) state [140]

$$|\mathrm{GHZ}\rangle = \frac{1}{\sqrt{2}}(|000\rangle + |111\rangle)\,, \tag{3.6}$$

here written as a three-qubit state. Although there is no rigorous definition of maximally entangled multi-party states, the form of the GHZ state with identical Schmidt coefficients suggests that it exhibits maximum multipartite entanglement.[1] In fact, the N-qubit GHZ states, $(|000\cdots000\rangle + |111\cdots111\rangle)/\sqrt{2}$, yield maximum violations of multi-party inequalities imposed by local realistic theories [143]. Further, their entanglement relies on all qubits as they become separable states when one qubit is traced out, for example, for $N = 3$,

$$\mathrm{Tr}_1|\mathrm{GHZ}\rangle\langle\mathrm{GHZ}| = \frac{1}{2}\left(|0\rangle\langle 0| \otimes |0\rangle\langle 0| + |1\rangle\langle 1| \otimes |1\rangle\langle 1|\right) . \tag{3.7}$$

Turning now to multi-qubit mixed states, there are, for instance, five classes of three-qubit states of which the extreme cases are the fully separable states, $\sum_i \eta_i \hat{\rho}_{i,1} \otimes \hat{\rho}_{i,2} \otimes \hat{\rho}_{i,3}$, and the genuinely tripartite inseparable states [144]. The entanglement witnesses introduced in the preceding section can be, to some extent, straightforwardly generalized to the multi-qubit case. For example, the canonical witness for states close to the three-qubit GHZ state is

$$W = \mathbb{1}/2 - |\mathrm{GHZ}\rangle\langle\mathrm{GHZ}| , \tag{3.8}$$

where the first term again corresponds to the maximal squared overlap between the GHZ state and all pure biseparable states (being separable with respect to a certain bipartite splitting). This ensures that states with only a pair of qubits being entangled and with the remaining qubit factoring out will not be detected as multipartite entangled states. In this sense, this witness detects genuine multipartite entanglement. Now, notice that for three qubits, the linear witness

$$W = \mathbb{1} - X \otimes X \otimes X - Z \otimes Z \otimes \mathbb{1} , \tag{3.9}$$

though sufficient to rule out fully separable states, is not enough to negate certain biseparable states [139]. Therefore, in order to faithfully detect genuine tripartite entanglement around the three-qubit GHZ state, we must incorporate the full set of stabilizer generators for the GHZ state

$$S = \langle ZZI, XXX, IZZ\rangle , \tag{3.10}$$

1) For the case of three qubits, any pure and fully entangled state can be transformed to either the GHZ state or the so-called $\mathcal{W}$ state [141], $|\mathcal{W}\rangle = 1/\sqrt{3}\,(|100\rangle + |010\rangle + |001\rangle)$, via stochastic local operations and classical communication. In this sense, there are two inequivalent classes of genuine tripartite entanglement represented by the GHZ and the $\mathcal{W}$ state. Genuinely or fully tripartite entangled means that the entanglement of the three-qubit state is not just present between two parties while the remaining party can be separated by a tensor product. The $\mathcal{W}$ state is fully tripartite inseparable and, in contrast to the GHZ state, after tracing out one qubit, $\mathrm{Tr}_1|\mathcal{W}\rangle\langle\mathcal{W}| = 1/3(|00\rangle\langle 00| + |10\rangle\langle 10| + |01\rangle\langle 01| + |01\rangle\langle 10| + |10\rangle\langle 01|)$, the $\mathcal{W}$ state remains inseparable which can be verified by taking the partial transpose [the eigenvalues are $1/3$, $1/3$, $(1 \pm \sqrt{5})/6$]. More quantitatively, there is no "residual entanglement" in the $\mathcal{W}$ state which solely stems from tripartite correlations; the total entanglement of one qubit with the rest is composed of pairwise bipartite entanglement. In contrast, the GHZ state has zero pairwise entanglement and maximal residual entanglement [142].

into the witness [139],

$$W = 2\mathbb{1} - X \otimes X \otimes X - Z \otimes Z \otimes \mathbb{1} - \mathbb{1} \otimes Z \otimes Z \,. \tag{3.11}$$

Hence, similar to the two-qubit case, for three qubits (and also for more qubits), the stabilizer generators that define the entangled state in question can also be used to detect the presence of genuine multipartite entanglement around that state. This method also works for qubit cluster and graph states which we will introduce next.

3.1.2 Cluster and Graph States

Let us consider again the two-qubit Bell state $|\Phi^+\rangle$ from Eq. (1.93) and its stabilizer $\langle X \otimes X, Z \otimes Z\rangle$. By applying a local Hadamard gate upon either qubit, we obtain the state with stabilizer $\langle X \otimes HXH, Z \otimes HZH\rangle = \langle X \otimes Z, Z \otimes X\rangle$. This is the stabilizer of the simplest cluster or graph state, namely, that of just two qubits. It is equivalent to the Bell state $|\Phi^+\rangle$ up to a local Hadamard gate.

Operationally, the two-mode cluster state is obtained by applying the C_Z gate (see Section 1.8) upon two qubits each initially in the state $|+\rangle$,

$$\begin{aligned} C_Z\left(|+\rangle \otimes |+\rangle\right) &= \left(|0\rangle|+\rangle + |1\rangle|-\rangle\right)/\sqrt{2} = \left(|+\rangle|0\rangle + |-\rangle|1\rangle\right)/\sqrt{2}\,; \\ \left\langle C_Z\,(X \otimes \mathbb{1})\,C_Z^\dagger,\, C_Z\,(\mathbb{1} \otimes X)\,C_Z^\dagger \right\rangle &= \langle X \otimes Z, Z \otimes X\rangle\,, \end{aligned} \tag{3.12}$$

with the stabilizer of the initial product state $\langle X \otimes \mathbb{1}, \mathbb{1} \otimes X\rangle$.

This operational definition can be generalized to graph states of N qubits, most conveniently expressed in terms of the evolution of the stabilizer generators,

$$\begin{aligned} \hat{U}\left(X_k \otimes \mathbb{1}^{N-1}\right)\hat{U}^\dagger &= X_k \prod_{l \in N(k)} Z_l = X_k \prod_{l \neq k} Z_l^{A_{kl}} \\ &\equiv K_k\,, \quad \forall k \in G\,, \end{aligned} \tag{3.13}$$

where $\hat{U}$ describes all the C_Z gates pairwise acting upon all qubits of the graph G according to the adjacency matrix elements $A_{kl} = A_{lk}$ which are one when the qubits become connected and zero otherwise. The product above is a tensor product and whenever there are less than N Pauli operators in this product, the remaining operators are the unity operators.

Important examples of graph states (see Figure 3.1) are the N-qubit GHZ state, corresponding to a star graph (up to local Hadamards), and the 2D lattice graph, which is known to be a universal resource for quantum computation [1] (see Section 1.8 and Chapter 7). For example, the three-qubit GHZ state with the stabilizer in Eq. (3.10) corresponds to a linear three-qubit cluster/graph state, $(|+\rangle|0\rangle|+\rangle + |-\rangle|1\rangle|-\rangle)/\sqrt{2}$, with stabilizer $\langle XZI, ZXZ, IZX\rangle$, up to Hadamard gates on the first and third qubit. Note that the linear four-qubit cluster state is no more a GHZ-type state.

Graph states are a subset of the set of stabilizer states (with every stabilizer state locally unitarily transformable into a graph state) and the strength (weight) of each

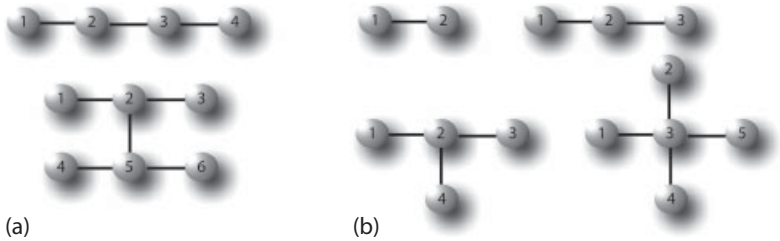

Figure 3.1 Examples of graph states; (a) linear four-qubit cluster state, nonlinear six-qubit cluster state; (b) "Bell/GHZ-type" graphs: linear two- and three-mode clusters, star graphs.

C_Z-type gate, expressed by the elements of the adjacency matrix of the graph, must be zero or one. Otherwise, a so-called weighted graph state is no longer a stabilizer state. This will turn out to be dramatically different for the case of qumode graph states (see Section 3.2.2), for which weighted C_Z interactions still belong to the CV Clifford group describing Gaussian transformations.

Finally, we give the corresponding entanglement witness for qubit graph states expressed in terms of the stabilizer generators [139],

$$W = (N-1)\mathbb{1} - \sum_{k\in G} K_k \,, \tag{3.14}$$

with the definition of Eq. (3.13). This witness would detect genuine N-qubit multipartite entanglement by verifying the quantum correlations in *all* stabilizer generators that define the corresponding graph state.

3.1.3 Experiment: Entangled Photonic Qubits

3.1.3.1 EPR/Bell State

Entanglement between two qubits is one of the most important resources for quantum information processing. There are various ways to create such two-qubit entanglement experimentally.

One of the simplest ways might be to employ a single-photon Fock state $|1\rangle$ and a symmetric beam splitter, as shown in Figure 3.2, in order to obtain a single-photon state which is path-entangled between two single-rail encoded qubits. Let us now discuss how this state can be used for the creation of a polarization-entangled state of two photons (i.e., a polarization-entangled state between two dual-rail encoded qubits),

$$\left|\Psi^{(+)}\right\rangle = \frac{1}{\sqrt{2}}\left(|\leftrightarrow\rangle_A \otimes |\updownarrow\rangle_B + |\updownarrow\rangle_A \otimes |\leftrightarrow\rangle_B\right), \tag{3.15}$$

where $|\leftrightarrow\rangle$ and $|\updownarrow\rangle$ denote horizontally and vertically polarized photons, respectively.

A neat way to create this type of two-photon polarization entanglement was invented by Kwiat *et al.* [145]. A schematic is shown in Figure 3.3. First, a pump

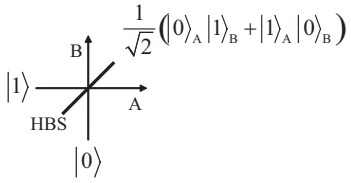

Figure 3.2 Quantum entanglement generated from a single-photon state $|1\rangle$ using a half beam splitter (HBS). The vacuum state $|0\rangle$ "enters" the unused port of the beam splitter.

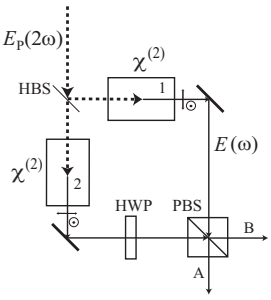

Figure 3.3 Quantum entanglement created through parametric down conversion (PDC) [145]. The parameter $\chi^{(2)}$ denotes the second order nonlinear process of PDC; $E_p(2\omega)$: pump light, HBS: half beam splitter, HWP: half wave plate, PBS: polarization beam splitter.

photon of angular frequency 2ω hits a half beam splitter (HBS). The output state is then the same as the one shown in Figure 3.2, corresponding to a superposition state of one pump photon arriving at either one of two second order nonlinear crystals 1,2 ($\chi^{(2)}$),

$$\frac{1}{\sqrt{2}}\left(|0\rangle_{2\omega,1}\otimes|1\rangle_{2\omega,2}+|1\rangle_{2\omega,1}\otimes|0\rangle_{2\omega,2}\right). \tag{3.16}$$

In that nonlinear crystal that does interact with a pump photon, parametric down conversion will occur, and a photon pair $|\leftrightarrow\rangle|\updownarrow\rangle$ is created. Thus, the state before the polarization beam splitter (PBS) in Figure 3.3 can be written as:

$$\frac{1}{\sqrt{2}}\left(|0\rangle_{2\omega,1}\otimes|\leftrightarrow\rangle_{\omega,2}|\updownarrow\rangle_{\omega,2}+|\leftrightarrow\rangle_{\omega,1}|\updownarrow\rangle_{\omega,1}\otimes|0\rangle_{2\omega,2}\right). \tag{3.17}$$

Now, for the case when the half wave plate (HWP) before the PBS has no effect on the beam, the output state of the PBS becomes,

$$\frac{1}{\sqrt{2}}\left(|\leftrightarrow\rangle_{\omega,A}\otimes|\updownarrow\rangle_{\omega,B}+|\updownarrow\rangle_{\omega,A}\otimes|\leftrightarrow\rangle_{\omega,B}\right), \tag{3.18}$$

where the pump light 2ω is omitted. This state is equivalent to that in Eq. (3.15).

Moreover, by suitably rotating the HWP, one can create any one of the four Bell states using this scheme,

$$\begin{aligned}\left|\Psi^{(\pm)}\right\rangle &= \frac{1}{\sqrt{2}}\left(|\leftrightarrow\rangle_A\otimes|\updownarrow\rangle_B\pm|\updownarrow\rangle_A\otimes|\leftrightarrow\rangle_B\right),\\ \left|\Phi^{(\pm)}\right\rangle &= \frac{1}{\sqrt{2}}\left(|\leftrightarrow\rangle_A\otimes|\leftrightarrow\rangle_B\pm|\updownarrow\rangle_A\otimes|\updownarrow\rangle_B\right),\end{aligned} \tag{3.19}$$

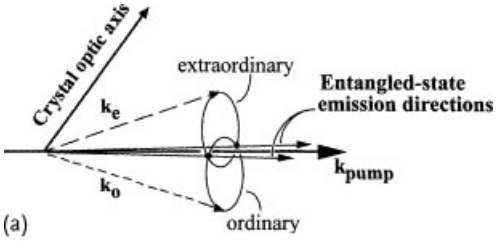

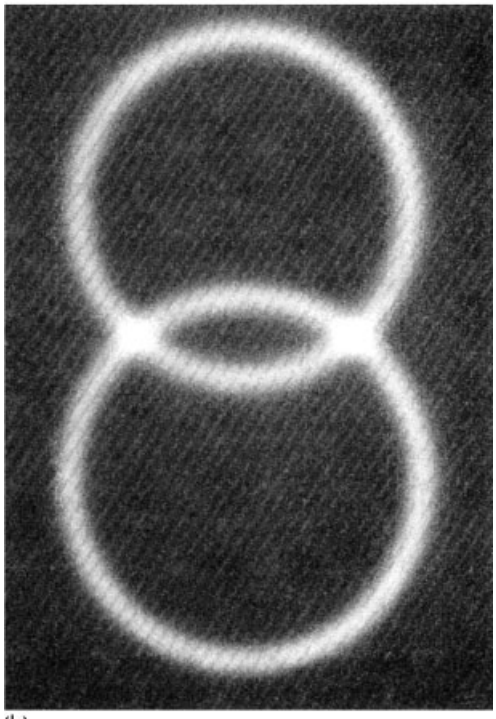

Figure 3.4 Experimental results of Kwiat *et al.* for the creation of polarization entangled photons [146]. Those photons emitted at the intersection of the two rings are entangled in polarization. (a) Spontaneous down-conversion cones present with type-II phase matching; (b) a photograph of the down-conversion photons.

where these are realization of Eq. (1.93) with polarized single photons. So this scheme is very versatile. However, a disadvantage of this scheme is its very low probability for successful entangled-photon pair creation, because the parametric down conversion of a single pump photon occurs very rarely and most of the time nothing will happen. Therefore, the present scheme has to rely upon "postselecting" successful creation events. Thus, the whole protocol becomes highly conditional and must be heralded by photon detection.

A modification of the scheme exploits certain crystal angle and phase-matching conditions, as it was realized by Kwiat *et al.* [146]. Figure 3.4 shows the experimental

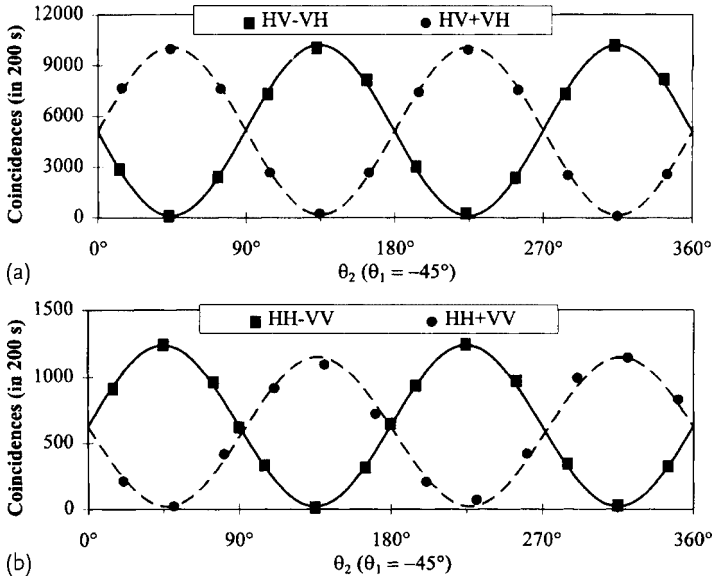

Figure 3.5 Coincidence fringes for verifying photonic Bell states (Eq. (3.19)) [146]. The photons emitted at the intersection of the two rings are detected by means of polarizers and the coincidences are plotted as a function of relative angle. (a) $|\leftrightarrow\rangle_A|\updownarrow\rangle_B \pm |\updownarrow\rangle_A|\leftrightarrow\rangle_B$(HV $\pm$ VH); (b) $|\leftrightarrow\rangle_A|\leftrightarrow\rangle_B \pm |\updownarrow\rangle_A|\updownarrow\rangle_B$(HH $\pm$ VV).

results for the creation of polarization entangled photons. Those photons emitted at the intersection of the two rings are entangled in polarization.

By using the HWP trick explained above, Kwiat *et al.* demonstrated the generation of all four Bell pairs experimentally verified through coincidence fringes of the photons, as shown in Figure 3.5.

3.1.3.2 GHZ State

A three-qubit GHZ state as in Eq. (3.6) can also be created through postselection for polarization qubits. The corresponding experimental scheme was proposed by Zeilinger *et al.* [147] and eventually implemented by Pan *et al.* [148]. Let us now discuss this scheme in detail.

Figure 3.6 shows the experimental scheme for the creation of a GHZ state using two pairs of polarization entangled photons [147]. A and B in Figure 3.6 denote photon-pair sources, as described in the preceding section, generating states like $(1/\sqrt{2})(|\leftrightarrow\rangle|\updownarrow\rangle + |\updownarrow\rangle|\leftrightarrow\rangle)$. In total, four photons will be emitted from the sources A and B. For the case that photons are simultaneously detected in modes 1, 2, 3, and D_T, the photons in modes 1, 2, and 3 are in the state $|\leftrightarrow\rangle_1|\leftrightarrow\rangle_2|\updownarrow\rangle_3$ or $|\updownarrow\rangle_1|\updownarrow\rangle_2|\leftrightarrow\rangle_3$. The reason for this is as follows. A polarization beam splitter (PBS) always reflects $\leftrightarrow$-photons and transmits $\updownarrow$-photons. If photons are simultaneously detected in modes 1, 2, 3, and D_T, only one $\leftrightarrow$-photon has arrived at D_T. However, we do not know from which PBS the $\leftrightarrow$-photon comes. If the $\leftrightarrow$-photon comes from the left PBS, the polarization of a photon in mode 1 as well as that of a photon in

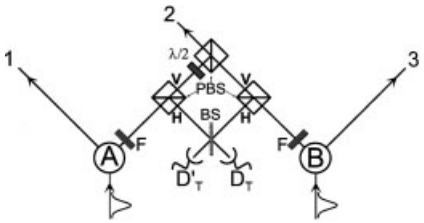

Figure 3.6 Scheme for the creation of a GHZ state using two pairs of polarization entangled photons [147]. BS: half beam splitter, PBS: polarization beam splitter, H: horizontal polarization ↔, V: vertical polarization ↕, F: narrow bandwidth filter, $\lambda/2$: half wave plate. The half wave plate switches V to H.

mode 2 must be ↕. Then, it follows from the entanglement of the photons that the polarization of a photon in mode 3 must be ↔. Similarly, for the case that the ↔-photon comes from the right PBS, the polarization of a photon in mode 1 must be ↔ and that of a photon in mode 2 as well. As a consequence, the polarization of a photon in mode 3 has to be ↕.

From the above discussion, we can conclude that whenever the photons are simultaneously detected in modes 1, 2, 3, and D_T, the photons in modes 1, 2, and 3 are in a superposition state of $|{\leftrightarrow}\rangle_1|{\leftrightarrow}\rangle_2|{\updownarrow}\rangle_3$ and $|{\updownarrow}\rangle_1|{\updownarrow}\rangle_2|{\leftrightarrow}\rangle_3$, namely,

$$|\mathrm{GHZ}'\rangle = \frac{1}{\sqrt{2}}\left(|{\leftrightarrow}\rangle_1|{\leftrightarrow}\rangle_2|{\updownarrow}\rangle_3 + |{\updownarrow}\rangle_1|{\updownarrow}\rangle_2|{\leftrightarrow}\rangle_3\right). \tag{3.20}$$

Now, by putting a half wave plate in the path of mode 3 in order to switch ↔ to ↕ and ↕ to ↔, we can convert $|\mathrm{GHZ}'\rangle$ into $|\mathrm{GHZ}\rangle$,

$$|\mathrm{GHZ}\rangle = \frac{1}{\sqrt{2}}\left(|{\leftrightarrow}\rangle_1|{\leftrightarrow}\rangle_2|{\leftrightarrow}\rangle_3 + |{\updownarrow}\rangle_1|{\updownarrow}\rangle_2|{\updownarrow}\rangle_3\right). \tag{3.21}$$

Figure 3.7 shows the experimental realization of Figure 3.6, as done by Pan *et al.* [148]. For the case of simultaneous photon detection events at detectors T, D_1, D_2, and D_3 in Figure 3.7, the state $|\mathrm{GHZ}'\rangle$ of Eq. (3.20) is obtained. The main difference between Figures 3.6 and 3.7 appears to be that two sources are present in Figure 3.6, whereas only one source (BBO) is used in the scheme of Figure 3.7. However, since the source of Figure 3.7 actually creates two pairs of polarization entangled photons simultaneously, the two supposedly different schemes are essentially the same.

Pan *et al.* checked for nonclassical correlations of polarization measurement results between two of the three modes (D_1, D_2, and D_3) and the remaining one. For example, if one performs polarization measurements on modes 1 and 2 and obtains a click in both detectors, one can automatically determine the polarization of mode 3 owing to the GHZ entanglement. In particular, Pan *et al.* made polarization measurements using the following two bases,

$$\begin{aligned} |H'\rangle &= \frac{1}{\sqrt{2}}\left(|{\leftrightarrow}\rangle + |{\updownarrow}\rangle\right), \qquad |V'\rangle = \frac{1}{\sqrt{2}}\left(|{\leftrightarrow}\rangle - |{\updownarrow}\rangle\right), \\ |R\rangle &= \frac{1}{\sqrt{2}}\left(|{\leftrightarrow}\rangle + \mathrm{i}|{\updownarrow}\rangle\right), \qquad |L\rangle = \frac{1}{\sqrt{2}}\left(|{\leftrightarrow}\rangle - \mathrm{i}|{\updownarrow}\rangle\right), \end{aligned} \tag{3.22}$$

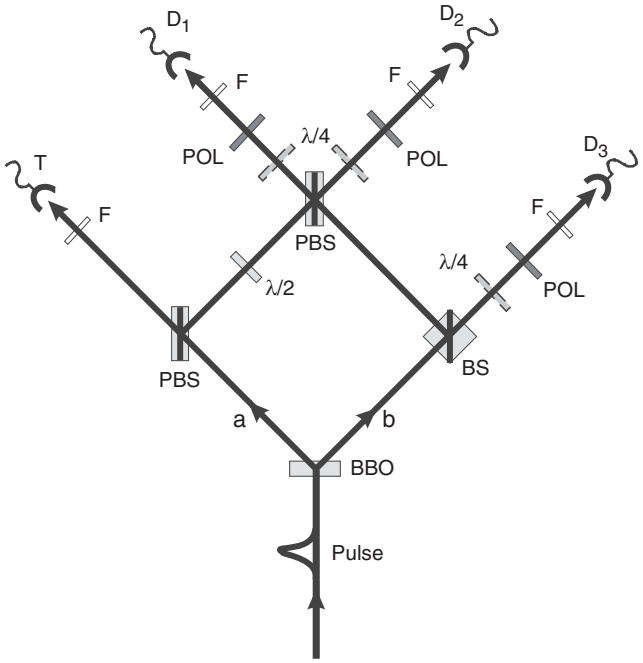

Figure 3.7 Experimental setup for the creation of a GHZ state using two pairs of polarization entangled photons [148]. BBO: second-order nonlinear crystal, BS: half beam splitter, PBS: polarization beam splitter, POL: polarizer, $\lambda/4$: quarter wave plate, F: narrow bandwidth filter, $\lambda/2$: half wave plate. The half wave plate switches $|\updownarrow\rangle$ to $(1/\sqrt{2})\,(|\leftrightarrow\rangle + |\updownarrow\rangle)$. Quarter wave plates and polarizers just before the detectors are used for correlation measurements.

corresponding to $\pm 45°$ rotated linear polarizations and right/left circular polarizations, respectively (representing the $\pm X$ and $\pm Y$ one-qubit stabilizer states of Section 1.2, respectively).

With the bases of Eq. (3.22), $|\mathrm{GHZ}\rangle$ of Eq. (3.21) can be rearranged as follows,

$$|\mathrm{GHZ}\rangle = \frac{1}{2}\left(|R\rangle_1|L\rangle_2|H'\rangle_3 + |L\rangle_1|R\rangle_2|H'\rangle_3 + |R\rangle_1|R\rangle_2|V'\rangle_3 + |L\rangle_1|L\rangle_2|V'\rangle_3\right). \tag{3.23}$$

Now, for polarization measurements in the L/R basis, the photons in modes 1 and 2 have equal probability for the combinations RL, LR, RR, and LL. If RR is obtained, the photon in mode 3 has to be in the state V' according to Eq. (3.23). Figure 3.8 shows the experimental results for this correlation measurement [148]. Quarter wave plates and polarizers just before detectors D_1, D_2, and D_3 in Figure 3.7 are set to RRV' or RRH'. The results clearly confirm the strong correlations of RRV' in comparison to RRH'.

Pan *et al.* also checked the other tripartite correlations according to Eq. (3.23) illustrated in Figure 3.9. In this case, polarization measurements are performed

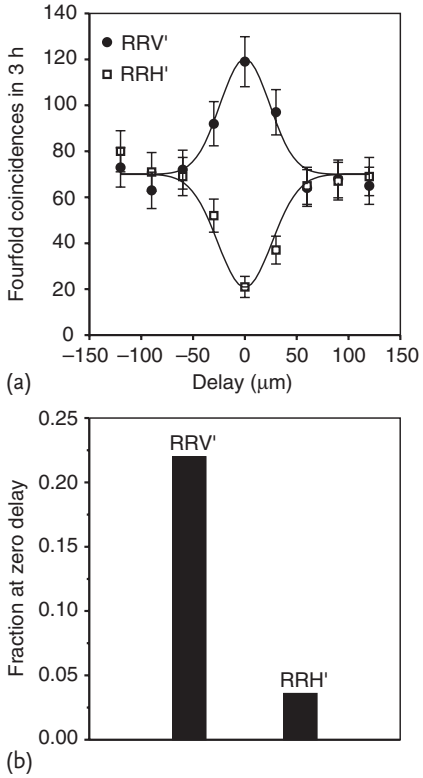

Figure 3.8 A typical result of correlation measurements for GHZ entanglement [148]. RRV' correlation signals are clearly bigger than those of RRH'.

in the L/R basis with two photons in modes 1 and 2 (a), modes 1 and 3 (b), and modes 2 and 3 (c). The polarization of the photon in the remaining mode was then checked in order to verify GHZ entanglement.

3.1.3.3 **Cluster States**

Cluster states of polarization qubits can be also created through postselection. The first experimental demonstration for this was reported by Walther *et al.* [149]. They created linear four-qubit and square cluster states using the setup shown in Figure 3.10. In this setup, two pairs of polarization entangled photons are generated by parametric down conversion as explained in the previous section. These polarization entangled photons pass through half wave plates (HWPs) and polarization beam splitters (PBSs), and are then converted into cluster states when all photodetectors detect photons for the right quarter wave plate (QWP) and polarizer (Pol) settings.

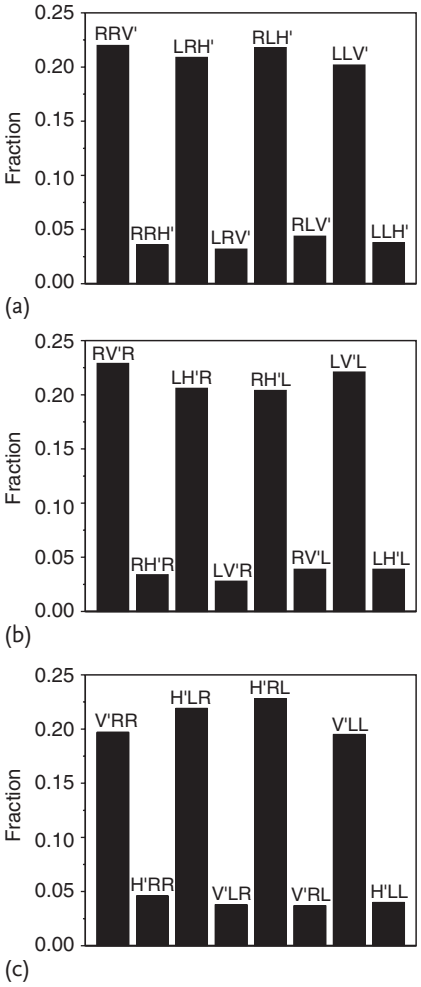

Figure 3.9 Correlation measurement results for GHZ entanglement according to Eq. (3.23) [148]. Polarization measurements in the L/R basis with two photons in (a); modes 1 and 2, (b); modes 1 and 3, (c); modes 2 and 3. The polarization of the photon in the remaining mode was checked to confirm the GHZ entanglement.

The cluster state $|\Phi_{\text{cluster}}\rangle$ obtained after the two polarization beam splitters (PBSs) in Figure 3.10 is

$$|\Phi_{\text{cluster}}\rangle = \frac{1}{2}\left(|\leftrightarrow\rangle_1|\leftrightarrow\rangle_2|\leftrightarrow\rangle_3|\leftrightarrow\rangle_4 + |\leftrightarrow\rangle_1|\leftrightarrow\rangle_2|\updownarrow\rangle_3|\updownarrow\rangle_4 + |\updownarrow\rangle_1|\updownarrow\rangle_2|\leftrightarrow\rangle_3|\leftrightarrow\rangle_4 - |\updownarrow\rangle_1|\updownarrow\rangle_2|\updownarrow\rangle_3|\updownarrow\rangle_4\right), \tag{3.24}$$

where subscripts 1–4 label the mode numbers of the PBS outputs.

When the polarizers before the detectors in modes 1 and 4 in Figure 3.10 are rotated by 45°, then in these modes, $|\leftrightarrow\rangle$ is transformed into $|+\rangle = (1/\sqrt{2})(|\leftrightarrow\rangle +$

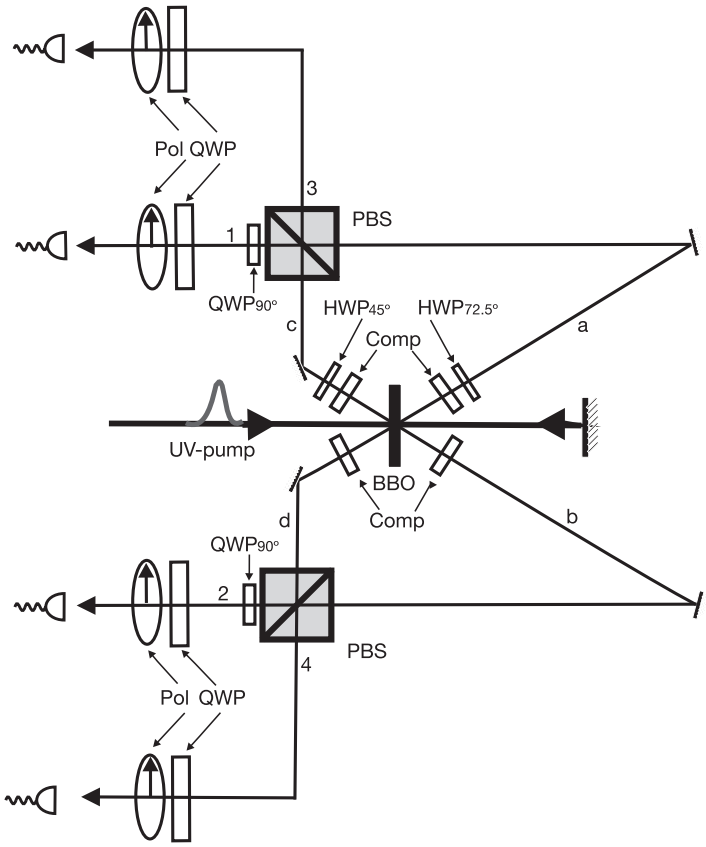

Figure 3.10 Experimental setup for the creation of four-qubit linear and square cluster states [149]. Comp: birefringence compensator, PBS: polarization beam splitter, HWP: half wave plate, QWP: quarter wave plate, and Pol: polarizer.

$|\updownarrow\rangle$), while $|\updownarrow\rangle$ is converted to $|-\rangle = (1/\sqrt{2})(|\leftrightarrow\rangle - |\updownarrow\rangle)$. This corresponds to local Hadamard transformations on the polarization qubits in modes 1 and 4. The postselected state becomes a linear four-qubit cluster state $|\Phi_{\text{lin-cluster}}\rangle$ as expressed by

$$|\Phi_{\text{lin-cluster}}\rangle = \frac{1}{2}\left(|+\rangle_1|\leftrightarrow\rangle_2|\leftrightarrow\rangle_3|+\rangle_4 + |+\rangle_1|\leftrightarrow\rangle_2|\updownarrow\rangle_3|-\rangle_4 + |-\rangle_1|\updownarrow\rangle_2|\leftrightarrow\rangle_3|+\rangle_4 - |-\rangle_1|\updownarrow\rangle_2|\updownarrow\rangle_3|-\rangle_4\right). \tag{3.25}$$

This state is equivalent to the following state when we replace $|\leftrightarrow\rangle$ by $|0\rangle$ and $|\updownarrow\rangle$ by $|1\rangle$ and rearrange the terms,

$$|\Phi_{\text{lin-cluster}}\rangle = \frac{1}{2}\left(|0\rangle_1|+\rangle_2|0\rangle_3|+\rangle_4 + |0\rangle_1|-\rangle_2|1\rangle_3|-\rangle_4 + |1\rangle_1|-\rangle_2|0\rangle_3|+\rangle_4 + |1\rangle_1|+\rangle_2|1\rangle_3|-\rangle_4\right). \tag{3.26}$$

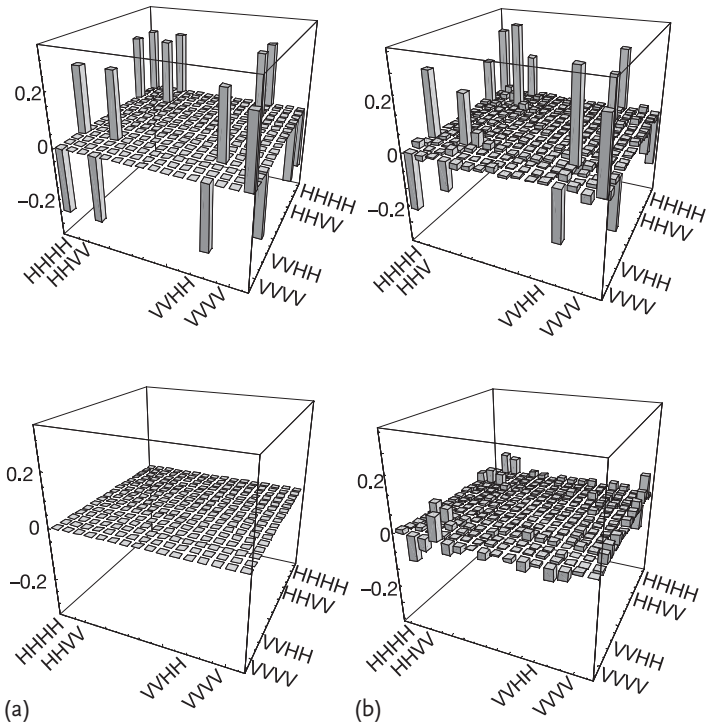

Figure 3.11 Experimental results of quantum-state tomography for a four-qubit cluster state $|\Phi_{\text{cluster}}\rangle$ [149]. "H" corresponds to $|\leftrightarrow\rangle$ and "V" corresponds to $|\updownarrow\rangle$. (a) ideal case; (b) experimental density matrices, where the top and the bottom represent the real and imaginary parts, respectively.

Similarly, when the polarizers before the detectors in modes 1–4 are all rotated by 45° and modes 2 and 3 are swapped, the postselected state becomes a square four-qubit cluster state $|\Phi_{\text{squ-cluster}}\rangle$. This state can be written as

$$|\Phi_{\text{squ-cluster}}\rangle = \frac{1}{2}\left(|0\rangle_1|+\rangle_2|0\rangle_3|+\rangle_4 + |0\rangle_1|-\rangle_2|1\rangle_3|-\rangle_4 + |1\rangle_1|-\rangle_2|0\rangle_3|-\rangle_4 + |1\rangle_1|+\rangle_2|1\rangle_3|+\rangle_4\right). \tag{3.27}$$

Walther *et al.* characterized the output state using quantum-state tomography [149] achievable by tuning the quarter wave plates (QWPs) and polarizers (Pols) in front of the photodetectors. The results are shown in Figure 3.11. From these results, a fidelity of $F = \langle\Phi_{\text{cluster}}|\hat{\rho}|\Phi_{\text{cluster}}\rangle = 0.63 \pm 0.02$ was obtained. This value is greater than the maximum overlap of 0.5 between any bi-separable four-qubit state and the target cluster state $|\Phi_{\text{cluster}}\rangle$.

Similar to the simpler case of bipartite polarization-entangled photon pairs, those experimental generalizations to more complex, multipartite states such as cluster states always rely upon postselection. Therefore, the scaling of the efficiency in building polarization-entangled graph states depends to a large extent on the post-

selection efficiency at which the elementary polarization-entangled pairs are produced. Moreover, once a sufficiently large supply of such pairs is available, further conditional fusion operations are needed in order to grow clusters and graphs of a desirable size [104, 150, 151]. Even though there are theoretical proposals for optimizing these fusions of subclusters and hence minimizing the temporal costs in building single-photon-based graph states [152, 153], the creation of polarization-entangled cluster states will remain highly conditional.

In the next section, we shall discuss a complementary way of building complicated, multipartite entangled states. In this alternative approach, the whole Hilbert space of photonic qumodes is exploited, and infinite-dimensional, CV graph states can be prepared in an unconditional, though intrinsically imperfect fashion.

3.2 Qumode Entanglement

3.2.1 Characterization and Witnesses

Optical CV entangled states on qumodes rely upon resources of squeezed light (see Section 2.2.4). This type of entanglement is therefore intrinsically and fundamentally imperfect since energies are always bounded and hence squeezing is always finite. However, CV Gaussian entangled states can be unconditionally prepared with extremely high efficiencies. Entanglement witnesses (see Section 1.5.3) in this case are typically based on variance measurements of certain multi-mode quadrature linear combinations, confirming the corresponding quantum correlations. These combinations will turn out to be related with the qumode stabilizers (see Section 1.9) that define the corresponding Gaussian entangled state. Reviews on the theory of Gaussian entangled states can be found in various articles, in particular, in [119, 154].

3.2.1.1 Two Parties

Recall the unphysical, maximally entangled CV Bell states introduced in Section 1.5.1. These CV stabilizer states are defined through their relative-position ($x_1 - x_2 = u$) and total-momentum ($p_1 + p_2 = v$) eigenvalues. The CV Bell state with $u = v = 0$ is the famous EPR state [23]. Although the EPR state is unnormalizable and unphysical, it can be thought of as the limiting case of a regularized version where the positions and momenta are correlated only to some finite extent given by a Gaussian width. A regularized EPR state is, for example, given by a two-mode squeezed state. The position and momentum wave functions for the *two-mode squeezed vacuum state* are

$$\psi_{\mathrm{TMSS}}(x_1, x_2) = \sqrt{\frac{2}{\pi}} \exp\left[-\mathrm{e}^{-2r}(x_1 + x_2)^2/2 - \mathrm{e}^{+2r}(x_1 - x_2)^2/2\right],$$
$$\tilde{\psi}_{\mathrm{TMSS}}(p_1, p_2) = \sqrt{\frac{2}{\pi}} \exp\left[-\mathrm{e}^{-2r}(p_1 - p_2)^2/2 - \mathrm{e}^{+2r}(p_1 + p_2)^2/2\right], \quad (3.28)$$

approaching $\propto \delta(x_1 - x_2)$ and $\propto \delta(p_1 + p_2)$, respectively, in the limit of infinite squeezing $r \to \infty$.

Instead of the position or momentum basis, the two-mode squeezed vacuum state may also be written in the Fock basis,

$$|\mathrm{TMSS}\rangle = \sqrt{1-\lambda^2} \sum_{n=0}^{\infty} \lambda^n |n\rangle|n\rangle \,, \tag{3.29}$$

where $\lambda = \tanh r$. The form in Eq. (3.29) reveals that the two modes of the two-mode squeezed vacuum state are also quantum correlated in photon number and phase. The form in Eq. (3.29) is the Schmidt decomposition (see Section 1.5.1) for the two-mode squeezed vacuum state. Since $\tanh r \to 1$ for $r \to \infty$, and hence $c_{n+1}/c_n \to 1$ in this limit, we can see that the state $|\mathrm{TMSS}\rangle$ in Eq. (3.29) approaches a maximally entangled state for infinite squeezing.

In this Schmidt form, we can quantify the entanglement of the two-mode squeezed vacuum state via the partial von Neumann entropy (recall the discussion in Section 1.5.1),

$$\begin{aligned} E\left(|\mathrm{TMSS}\rangle\right) &= -\log(1-\lambda) - \lambda \log \lambda/(1-\lambda) \\ &= \cosh^2 r \log(\cosh^2 r) - \sinh^2 r \log(\sinh^2 r) \,. \end{aligned} \tag{3.30}$$

Note that any pure two-mode Gaussian state can be transformed into the canonical two-mode squeezed state form through local LUBO transformations and hence its entanglement can be quantified as in Eq. (3.30). More generally, any bipartite pure multi-mode Gaussian state corresponds to a product of two-mode squeezed states up to local LUBO transformations [155].

The two-mode squeezed vacuum state is represented by a Gaussian Wigner function,

$$\begin{aligned} W_{\mathrm{TMSS}}(\xi) = \frac{4}{\pi^2} \exp\big\{ &-\mathrm{e}^{-2r}\left[(x_1+x_2)^2 + (p_1-p_2)^2\right] \\ &-\mathrm{e}^{+2r}\left[(x_1-x_2)^2 + (p_1+p_2)^2\right]\big\} \,. \end{aligned} \tag{3.31}$$

This Wigner function approaches $\propto \delta(x_1 - x_2)\delta(p_1 + p_2)$ in the limit of infinite squeezing $r \to \infty$, corresponding to the original EPR-state Wigner function.

Upon tracing (integrating) out either mode of the Wigner function in Eq. (3.31), we obtain the (undisplaced) *thermal state*

$$\int_{-\infty}^{\infty} W_{\mathrm{TMSS}}(\xi) \mathrm{d}x_1 \mathrm{d}p_1 = \frac{2}{\pi(1+2\bar{n})} \exp\left[-\frac{2\left(x_2^2+p_2^2\right)}{1+2\bar{n}}\right], \tag{3.32}$$

with mean photon number $\bar{n} = \sinh^2 r$. As the two-mode squeezed state is the maximally entangled state at a given energy, the thermal state corresponds to the maximally mixed state at this energy. This is analogous to the finite-dimensional discrete case, where tracing out one party of a maximally entangled state yields the

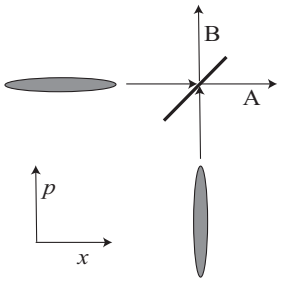

Figure 3.12 Creation of an EPR-type state using squeezed vacua and a beam splitter; ellipses represent squeezed vacua.

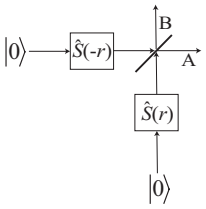

Figure 3.13 Operator description of Figure 3.12; $|0\rangle$ represents vacuum states and $\hat{S}(r)$ is the single-mode x-squeezing operator.

maximally mixed state. The correlation matrix of the two-mode squeezed state is given by

$$V_{\mathrm{TMSS}}^{(2)} = \frac{1}{4}\begin{pmatrix} \cosh 2r & 0 & \sinh 2r & 0 \\ 0 & \cosh 2r & 0 & -\sinh 2r \\ \sinh 2r & 0 & \cosh 2r & 0 \\ 0 & -\sinh 2r & 0 & \cosh 2r \end{pmatrix}, \tag{3.33}$$

according to Eqs. (3.31) and (2.89). By extracting the second moments from the correlation matrix in Eq. (3.33), we can verify that the individual quadratures become very noisy for large squeezing r, whereas the relative position and the total momentum become very quiet,

$$\begin{aligned} \langle(\hat{x}_1 - \hat{x}_2)^2\rangle &= \langle\hat{x}_1^2\rangle + \langle\hat{x}_2^2\rangle - 2\langle\hat{x}_1\hat{x}_2\rangle = \mathrm{e}^{-2r}/2\,, \\ \langle(\hat{p}_1 + \hat{p}_2)^2\rangle &= \langle\hat{p}_1^2\rangle + \langle\hat{p}_2^2\rangle + 2\langle\hat{p}_1\hat{p}_2\rangle = \mathrm{e}^{-2r}/2\,. \end{aligned} \tag{3.34}$$

The two-mode squeezed vacuum state can be directly obtained from a so-called nondegenerate optical parametric amplifier or oscillator (NOPO) in a single quadratic interaction [156]. However, towards scaling up qumode bipartite entanglement to qumode multipartite entanglement (see the following sections), it is very instructive to see that an entangled two-mode squeezed vacuum state is created equivalently by combining two independent single-mode squeezed vacuum states (each obtainable from a degenerate OPO [156, 157]) at a symmetric beam splitter, see Figures 3.12 and 3.13.

Let us see how this works. A single-mode vacuum state squeezed in p, as described by Eq. (2.53) with $\Theta = \pi$,

$$\hat{a}_1 = \hat{a}_1^{(0)}\cosh r + \hat{a}_1^{(0)\dagger}\sinh r\,, \tag{3.35}$$

and another one squeezed in x, as given by Eq. (2.53) with $\Theta = 0$,

$$\hat{a}_2 = \hat{a}_2^{(0)} \cosh r - \hat{a}_2^{(0)\dagger} \sinh r \,, \tag{3.36}$$

are combined at a 50 : 50 beam splitter,

$$\begin{aligned} \hat{b}_1 &= (\hat{a}_1 + \hat{a}_2)/\sqrt{2} = \hat{b}_1^{(0)} \cosh r + \hat{b}_2^{(0)\dagger} \sinh r \,, \\ \hat{b}_2 &= (\hat{a}_1 - \hat{a}_2)/\sqrt{2} = \hat{b}_2^{(0)} \cosh r + \hat{b}_1^{(0)\dagger} \sinh r \,, \end{aligned} \tag{3.37}$$

where $\hat{b}_1^{(0)} = (\hat{a}_1^{(0)} + \hat{a}_2^{(0)})/\sqrt{2}$ and $b_2^{(0)} = (\hat{a}_1^{(0)} - \hat{a}_2^{(0)})/\sqrt{2}$ are again two vacuum modes. The resulting state is a two-mode squeezed vacuum state with quadrature operators given by

$$\begin{aligned} \hat{x}_1 &= \left(\mathrm{e}^{+r}\hat{x}_1^{(0)} + \mathrm{e}^{-r}\hat{x}_2^{(0)}\right)\Big/\sqrt{2} \,, \\ \hat{p}_1 &= \left(\mathrm{e}^{-r}\hat{p}_1^{(0)} + \mathrm{e}^{+r}\hat{p}_2^{(0)}\right)\Big/\sqrt{2} \,, \\ \hat{x}_2 &= \left(\mathrm{e}^{+r}\hat{x}_1^{(0)} - \mathrm{e}^{-r}\hat{x}_2^{(0)}\right)\Big/\sqrt{2} \,, \\ \hat{p}_2 &= \left(\mathrm{e}^{-r}\hat{p}_1^{(0)} - \mathrm{e}^{+r}\hat{p}_2^{(0)}\right)\Big/\sqrt{2} \,, \end{aligned} \tag{3.38}$$

where $\hat{b}_k = \hat{x}_k + \mathrm{i}\hat{p}_k$ and $\hat{a}_k^{(0)} = \hat{x}_k^{(0)} + \mathrm{i}\hat{p}_k^{(0)}$. While the individual quadratures $\hat{x}_k$ and $\hat{p}_k$ become very noisy for large squeezing r, the relative position and the total momentum,

$$\begin{aligned} \hat{x}_1 - \hat{x}_2 &= \sqrt{2}\mathrm{e}^{-r}\hat{x}_2^{(0)} \,, \\ \hat{p}_1 + \hat{p}_2 &= \sqrt{2}\mathrm{e}^{-r}\hat{p}_1^{(0)} \,, \end{aligned} \tag{3.39}$$

become quiet, $\langle(\hat{x}_1 - \hat{x}_2)^2\rangle = \mathrm{e}^{-2r}/2$ and $\langle(\hat{p}_1 + \hat{p}_2)^2\rangle = \mathrm{e}^{-2r}/2$, as in Eq. (3.34).

The creation of two-mode squeezing and entanglement from single-mode squeezing through beam splitter interference can also be described in the language of correlation matrices. In this case, the correlation matrix of the two-mode input state to the beam splitter, a product state of two single-mode squeezed states with the first one squeezed in p and the second one squeezed in x, is given by $V^{(2)} = V_{-r}^{(1)} \oplus V_r^{(1)}$, using $V_r^{(1)} \equiv V^{(1)}$ from Eq. (2.90). Now, applying the beam splitter operation of Eq. (2.115) to $V^{(2)}$ leads to the following transformation,

$$V^{(2)} \longrightarrow V^{(2)\prime} = O_{\mathrm{BS}}\, V^{(2)}\, O_{\mathrm{BS}}^{\mathrm{T}} = V_{\mathrm{TMSS}}^{(2)} \,, \tag{3.40}$$

with the correlation matrix of a two-mode squeezed state in Eq. (3.33).

Besides the direct way of quantifying the entanglement of a two-mode squeezed state written in the Schmidt–Fock basis through the partial von Neumann entropy [Eq. (3.30)], one may also calculate the entropy with the help of the symplectic eigenvalues, as introduced in Section 2.2.8.2. As mentioned there, in general, these eigenvalues contain complete information about the structure and size of thermal noise in Gaussian mixed states. More explicitly, the von Neumann entropy $S(\hat{\rho})$ from Eq. (1.22) for the case of an N-mode Gaussian state is a function of its N

symplectic eigenvalues,

$$S(\hat{\rho}) = \sum_{k=1}^{N} \left(\frac{4\nu_k + 1}{2} \log \frac{4\nu_k + 1}{2} - \frac{4\nu_k - 1}{2} \log \frac{4\nu_k - 1}{2} \right). \tag{3.41}$$

Hence, for any *pure* bipartite Gaussian state of $N + M$ modes, the N symplectic eigenvalues of the reduced N-mode state immediately give the entanglement with respect to the splitting between the N and M modes. Correspondingly, the reduced entropy of a two-mode squeezed state is determined by a single symplectic eigenvalue for the reduced thermal state, with $\nu = (2\bar{n} + 1)/4 = (2\sinh^2 r + 1)/4$, reproducing the entanglement calculated in Eq. (3.30).

For bipartite entangled Gaussian *mixed* states, the entanglement is no longer given by the reduced entropy. In this more general case, one has to consider alternate measures, as discussed in Section 1.5. In particular, the logarithmic negativity turns out to be very useful in this case. Similar to the reduced entropy, for pure two-mode states, the logarithmic negativity can be computed directly from the Schmidt–Fock coefficients. For example, using $|| \, (|\mathrm{TMSS}\rangle_{12}\langle\mathrm{TMSS}|)^{\mathrm{T}_2} \, || = (1-\lambda^2)(\sum_{n=0}^{\infty} \lambda^n)^2$, we obtain $E_N(|\mathrm{TMSS}\rangle_{12}\langle\mathrm{TMSS}|) = \log_2[||(|\mathrm{TMSS}\rangle_{12}\langle\mathrm{TMSS}|)^{\mathrm{T}_2}||] = \log_2 \frac{1+\lambda}{1-\lambda}$. Though this approach would work for any pure two-mode state in Schmidt–Fock form (including non-Gaussian ones), for mixed states, an analytic expression independent of the assumption of Gaussian states is rather hard to obtain [158].

If one does have Gaussian states, one may once again employ the symplectic eigenvalues. Entanglement can then be quantified by checking to what extent the symplectic eigenvalues indicate unphysicality of the partially transposed state, $\tilde{\nu}_k < 1/4$ (recall Section 2.2.8.2), where $\tilde{\nu}_1, \tilde{\nu}_2, \ldots, \tilde{\nu}_N$ are the symplectic eigenvalues of the partially transposed correlation matrix.[2] In fact, in this case, we obtain

$$E_N = -\sum_{k=1}^{N} \log_2 \left[\min\left(1, 4\tilde{\nu}_k\right) \right]. \tag{3.42}$$

For two-mode Gaussian states with only two (partially transposed) symplectic eigenvalues $\tilde{\nu}_1$ and $\tilde{\nu}_2$, E_N only depends on the smallest symplectic eigenvalue $\equiv \tilde{\nu}_-$, $E_N = \max[0, -\ln(4\tilde{\nu}_-)]$. For example, for the two-mode squeezed state, we have $E_N = \max[0, -\ln(\mathrm{e}^{-2r})] = 2r$.[3]

The mixed-state case corresponds to the realistic scenario encountered in an experiment. When the full correlation matrix of the bipartite, quantum optical state in question is available, inseparability criteria such as the CV version of the partial transpose criterion (Section 1.5.2) may be applied; and even be used for quantification when the state is Gaussian, as described above. Otherwise, a sufficient, small number of suitable observables, the so-called entanglement witnesses, may be utilized as entanglement qualifiers (Section 1.5.3).

2) What partial transposition (see Section 1.5.2) actually means in the CV case and in terms of correlation matrices shall be discussed shortly.

3) In order to obtain this simple expression, one has to use suitable units which depend on the base of the logarithm, $\log_2 \to \ln$.

Let us discuss an important class of CV entanglement witnesses. For verifying the inseparability of a given two-mode CV state, Duan *et al.* derived an inequality in terms of the variances of position and momentum linear combinations [159], similar to those in Eq. (3.34). This inequality is satisfied by any separable state and is only violated by inseparable states. Thus, its violation is a sufficient (but, in general, not a necessary) condition for the inseparability of arbitrary states, including non-Gaussian states.

Duan *et al.* proved that, for example, the sum of the variances of $\hat{u} \equiv \hat{x}_1 - \hat{x}_2$ and $\hat{v} \equiv \hat{p}_1 + \hat{p}_2$ can never drop below some nonzero bound for any separable state $\hat{\rho}_{12}$. However, for an inseparable state, this total variance may drop to zero. This is possible, because the observables $\hat{u}$ and $\hat{v}$ have a vanishing commutator,

$$[\hat{x}_1 - \hat{x}_2, \hat{p}_1 + \hat{p}_2] = 0 \,, \tag{3.43}$$

and hence they may simultaneously take on arbitrarily well defined values; ultimately, they have a common eigenbasis, namely, the CV Bell basis (see Section 1.5.1). Recalling the discussions in Sections 1.5.1 and 1.9, we see that there is a link between the CV Bell-state stabilizers and the entanglement witnesses proposed by Duan *et al.*

The proof of Duan's criterion works as follows. Assume that a given state $\hat{\rho}_{12}$ is separable and hence can be written as in Eq. (1.99). Now, calculating the total variance of the operators $\hat{u} \equiv \hat{x}_1 - \hat{x}_2$ and $\hat{v} \equiv \hat{p}_1 + \hat{p}_2$ for this state (labeled by ρ) gives

$$\begin{aligned}
&\langle(\Delta\hat{u})^2\rangle_\rho + \langle(\Delta\hat{v})^2\rangle_\rho = \sum_i \eta_i \left(\langle\hat{u}^2\rangle_i + \langle\hat{v}^2\rangle_i\right) - \langle\hat{u}\rangle_\rho^2 - \langle\hat{v}\rangle_\rho^2 \\
&= \sum_i \eta_i \left(\langle\hat{x}_1^2\rangle_i + \langle\hat{x}_2^2\rangle_i - 2\langle\hat{x}_1\rangle_i\langle\hat{x}_2\rangle_i + \langle\hat{p}_1^2\rangle_i + \langle\hat{p}_2^2\rangle_i + 2\langle\hat{p}_1\rangle_i\langle\hat{p}_2\rangle_i\right) \\
&\quad - \langle\hat{u}\rangle_\rho^2 - \langle\hat{v}\rangle_\rho^2 \\
&= \sum_i \eta_i \left(\left\langle(\Delta\hat{x}_1)^2\right\rangle_i + \left\langle(\Delta\hat{x}_2)^2\right\rangle_i + \left\langle(\Delta\hat{p}_1)^2\right\rangle_i + \left\langle(\Delta\hat{p}_2)^2\right\rangle_i\right) \\
&\quad + \sum_i \eta_i \langle\hat{u}\rangle_i^2 - \left(\sum_i \eta_i \langle\hat{u}\rangle_i\right)^2 + \sum_i \eta_i \langle\hat{v}\rangle_i^2 - \left(\sum_i \eta_i \langle\hat{v}\rangle_i\right)^2 ,
\end{aligned} \tag{3.44}$$

where $\langle\cdots\rangle_i$ represents the expectation value in the product state $\hat{\rho}_{i,1} \otimes \hat{\rho}_{i,2}$. Using the Cauchy–Schwarz inequality $\sum_i \eta_i \langle\hat{u}\rangle_i^2 \geq \left(\sum_i \eta_i |\langle\hat{u}\rangle_i|\right)^2$, one can see that the last line in Eq. (3.44) is bounded below by zero. By also considering the sum uncertainty relation $\langle(\Delta\hat{x}_j)^2\rangle_i + \langle(\Delta\hat{p}_j)^2\rangle_i \geq |[\hat{x}_j, \hat{p}_j]| = 1/2$ ($j = 1, 2, \forall i$), we find that the total variance itself is bounded below by one. Thus, the inequality

$$\left\langle[\Delta(\hat{x}_1 - \hat{x}_2)]^2\right\rangle + \left\langle[\Delta(\hat{p}_1 + \hat{p}_2)]^2\right\rangle \geq 1 \,, \tag{3.45}$$

is a *necessary* condition for any separable state. A violation of it proves inseparability of the state in question. For example, the position and momentum correlations of

Eq. (3.34) confirm that the two-mode squeezed vacuum state is entangled for any nonzero squeezing $r > 0$.

A generalization of the above condition may be based upon the general linear combinations

$$\hat{u} \equiv h_1 \hat{x}_1 + h_2 \hat{x}_2 \,, \qquad \hat{v} \equiv g_1 \hat{p}_1 + g_2 \hat{p}_2 \,. \tag{3.46}$$

For any separable state, we have

$$\langle (\Delta \hat{u})^2 \rangle_\rho + \langle (\Delta \hat{v})^2 \rangle_\rho \geq (|h_1 g_1| + |h_2 g_2|)/2 \,, \tag{3.47}$$

whereas for a potentially entangled state, this bound is changed to

$$\langle (\Delta \hat{u})^2 \rangle_\rho + \langle (\Delta \hat{v})^2 \rangle_\rho \geq (|h_1 g_1 + h_2 g_2|)/2 \,. \tag{3.48}$$

The h_l and g_l are arbitrary real parameters. When choosing, for instance, $h_1 = -h_2 = g_1 = g_2 = 1$, the bound for a separable state becomes one, whereas that for an entangled state drops to zero.

The derivation of Eq. (3.45) does not depend on the assumption of Gaussian states. However, for two-mode Gaussian states in a particular standard form, a condition similar to that in Eq. (3.45) turns out to be necessary and sufficient for separability [159]. This standard form can be obtained for any two-mode Gaussian state via local Gaussian unitary transformations. As opposed to those qubit entanglement witnesses introduced in Section 3.1.1, the second-moment-based, CV Duan witness is a nonlinear entanglement witness (see Section 1.5.3). Even though it appears to be independent of partial transposition (which we did not use for its derivation), it can be shown to be a special case from the family of partial-transpose-based criteria (see Section 8.3). We shall now briefly discuss a particular manifestation [116] of the CV partial transpose criterion.

As discussed in detail in Section 1.5.2, transposition is a positive, but not completely positive map, which means its application to a subsystem may yield an unphysical state when the subsystem is entangled to other subsystems. The class of $(1 \times N)$-mode Gaussian states belongs to those states for which negative partial transpose (npt) is necessary and sufficient for inseparability [116, 117].

Recall that due to the Hermiticity of a density operator, transposition corresponds to complex conjugation. Moreover, for the time evolution of a quantum system described by the Schrödinger equation, complex conjugation is equivalent to time reversal, $\mathrm{i}\hbar\partial/\partial t \rightarrow -\mathrm{i}\hbar\partial/\partial t$. Hence, intuitively, transposition of a density operator means time reversal, or, expressed in terms of continuous variables, sign change of the momenta. Thus, in phase space, transposition is described by $\xi^{\mathrm{T}} \longrightarrow \Gamma \xi^{\mathrm{T}} = (x_1, -p_1, x_2, -p_2, \ldots, x_N, -p_N)^{\mathrm{T}}$, that is, by transforming the Wigner function as [116]

$$W(x_1, p_1, x_2, p_2, \ldots, x_N, p_N) \longrightarrow W(x_1, -p_1, x_2, -p_2, \ldots, x_N, -p_N) \,. \tag{3.49}$$

This general transposition rule is, in the case of N-mode Gaussian states, reduced to the transformation

$$V^{(N)} \longrightarrow V^{(N)'} = \Gamma V^{(N)} \Gamma \tag{3.50}$$

for the second-moment correlation matrix (where, again, the first moments do not affect the entanglement). Now, the partial transposition of a bipartite Gaussian system can be expressed by $\Gamma_{\mathrm{a}} \equiv \Gamma \oplus \mathbb{1}$. Here, again, $A \oplus B$ means the block-diagonal matrix with the matrices A and B as diagonal entries, and A and B are respectively $2N \times 2N$ and $2M \times 2M$ square matrices for N modes at a's side and M modes at b's side. According to Eq. (2.95), the condition that the partially transposed Gaussian state described by $\Gamma_{\mathrm{a}} V^{(N+M)} \Gamma_{\mathrm{a}}$ is unphysical,

$$\Gamma_{\mathrm{a}} V^{(N+M)} \Gamma_a \ngeq \frac{\mathrm{i}}{4} \Lambda \ , \tag{3.51}$$

is sufficient for the inseparability between a and b [116, 117]. For Gaussian states with $N = M = 1$ [116] and for those with $N = 1$ and arbitrary M [117], this condition is necessary and sufficient. For two-mode Gaussian states, it can be compactly expressed in terms of the blocks of any given correlation matrix [116]. By considering other, operational inseparability criteria independent of the NPT criterion, in principle, the separability problem for bipartite Gaussian states with arbitrarily many modes at each side is completely solved [160]. Recent efforts are therefore aiming at extending the theory of CV entanglement criteria and witnesses to the realm of non-Gaussian states (see Section 8.3).

3.2.1.2 Three or More Parties

Consider the unphysical, infinitely correlated, entangled states of N qumodes,

$$\begin{aligned} |\Psi(v, u_1, u_2, \ldots, u_{N-1})\rangle = \frac{1}{\sqrt{\pi}} \int_{-\infty}^{\infty} \mathrm{d}x \mathrm{e}^{2\mathrm{i}vx} |x\rangle \otimes |x - u_1\rangle \otimes |x - u_1 - u_2\rangle \\ \otimes \cdots \otimes |x - u_1 - u_2 - \cdots - u_{N-1}\rangle \ . \end{aligned} \tag{3.52}$$

Since $\int_{-\infty}^{\infty} \mathrm{d}x |x\rangle\langle x| = \mathbb{1}$ and $\langle x|x'\rangle = \delta(x - x')$, they form a complete,

$$\begin{aligned} \int_{-\infty}^{\infty} \mathrm{d}v \mathrm{d}u_1 \mathrm{d}u_2 \cdots \mathrm{d}u_{N-1} \\ \times |\Psi(v, u_1, u_2, \ldots, u_{N-1})\rangle\langle\Psi(v, u_1, u_2, \ldots, u_{N-1})| = \mathbb{1}^{\otimes N} \ , \end{aligned} \tag{3.53}$$

and orthogonal,

$$\begin{aligned} \left\langle \Psi\left(v, u_1, u_2, \ldots, u_{N-1}\right) \middle| \Psi\left(v', u_1', u_2', \ldots, u_{N-1}'\right) \right\rangle \\ = \delta\left(v - v'\right) \delta\left(u_1 - u_1'\right) \delta\left(u_2 - u_2'\right) \cdots \delta\left(u_{N-1} - u_{N-1}'\right) \ , \end{aligned} \tag{3.54}$$

set of basis states for N qumodes. Note that for two qumodes, $N = 2$, this basis is just the CV Bell basis of Eq. (1.95). For the case with $N = 3$ qumodes, $v \equiv p_1 + p_2 + p_3 = 0$, $u_1 \equiv x_1 - x_2 = 0$, and $u_2 \equiv x_2 - x_3 = 0$, we obtain the state

$$|\Psi(0,0,0)\rangle = \frac{1}{\sqrt{\pi}} \int_{-\infty}^{\infty} \mathrm{d}x |x\rangle \otimes |x\rangle \otimes |x\rangle \ . \tag{3.55}$$

This is the CV version of the three-qubit GHZ state in Eq. (3.6) with stabilizer generators given by Eq. (3.10). Correspondingly, the CV stabilizer for this state, expressed in terms of WH operators, is

$$S = \left\langle Z(s) \otimes Z^{\dagger}(s) \otimes \mathbb{1} \ , \ \ X(s) \otimes X(s) \otimes X(s) \ , \ \ \mathbb{1} \otimes Z(s) \otimes Z^{\dagger}(s) \right\rangle \ . \tag{3.56}$$

Generalizing the two-mode CV Bell-basis stabilizer derived in Section 1.5.1.2 to a three-mode CV GHZ-basis stabilizer gives the nonlocal stabilizer generators

$$\begin{aligned} &\left\langle \mathrm{e}^{-2\mathrm{i}su_1} Z(s) \otimes Z^{\dagger}(s) \otimes \mathbb{1} \ , \quad \mathrm{e}^{+2\mathrm{i}sv} X(s) \otimes X(s) \otimes X(s) \ , \right. \\ &\left. \mathrm{e}^{-2\mathrm{i}su_2} \mathbb{1} \otimes Z(s) \otimes Z^{\dagger}(s) \right\rangle . \end{aligned} \tag{3.57}$$

Because this constitutes a full set of stabilizer generators for three qumodes (recall Section 1.9), the eigenvalues v, u_1, and u_2 completely and uniquely determine a particular GHZ basis state. Instead of the WH stabilizers, again, the qumode states are more conveniently expressed in terms of x and p linear combinations.

In an N-qumode "CV GHZ-state analyzer", determining the stabilizer eigenvalues $v \equiv p_1 + p_2 + \cdots + p_N$, $u_1 \equiv x_1 - x_2$, $u_2 \equiv x_2 - x_3, \ldots$, and $u_{N-1} \equiv x_{N-1} - x_N$ means projecting onto the CV GHZ basis $\{|\Psi(v, u_1, u_2, \ldots, u_{N-1})\rangle\}$. Similar to the two-party two-mode case from the preceding section, these stabilizers correspond to a set of observables that can be used as a multi-party multi-mode entanglement witness. Before discussing such a witness in more detail, let us first explain how to actually generate an approximate version of a CV GHZ state using squeezed light and beam splitters [161].

The simplest way to generate a tripartite entangled state of three qumodes is to split a single-mode squeezed vacuum state $|x \approx 0\rangle$ (idealized by an x zero-eigenstate) subsequently at two beam splitters, as shown in Figure 3.14 [161]. In this case, the inputs of the two unused ports of the beam splitters are vacuum states. This is practically easy to implement, but when applied to a quantum protocol, the performance would be of only limited quality due to the vacuum input states. For example, in the qumode teleportation network described in Chapter 4, the maximum fidelity between any pair will be only $1/\sqrt{2}$, even in the limit of infinite squeezing.[4)]

However, the CV GHZ state in Eq. (3.55) can be generated by sending a momentum-squeezed vacuum state, $|p \approx 0\rangle_1$, and two position-squeezed vacuum states, $|x \approx 0\rangle_2$ and $|x \approx 0\rangle_3$, into a "tritter", consisting of two beam splitters with transmissivity/reflectivity of 1/2 and 1/1, as shown in Figure 3.15. Applying first

4) Excluding additional local squeezers [162] by means of which the one-squeezer GHZ-type state can be locally converted into a three-squeezer GHZ-type state.

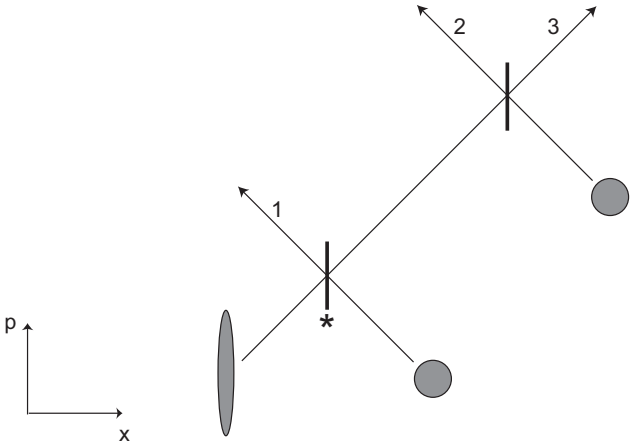

Figure 3.14 Creation of a CV tripartite entangled state with a single-mode squeezed vacuum state, $|x \approx 0\rangle$. The ellipse represents the squeezed vacuum and the circles correspond to the vacua. The beam splitter labeled by * is a 1/2 beam splitter and the other one is a half (1/1) beam splitter.

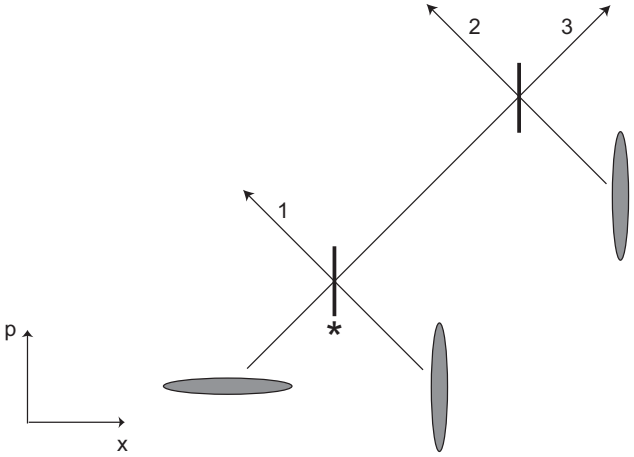

Figure 3.15 Creation of a CV GHZ-type state by combining a momentum-squeezed vacuum state $|p \approx 0\rangle_1$ and two position-squeezed vacuum states $|x \approx 0\rangle_2$ and $|x \approx 0\rangle_3$ at two beam splitters with transmissivity/reflectivity of 1/2 and 1/1. The ellipses represent the squeezed vacua. The beam splitter labeled by * is a 1/2 beam splitter and the other one is a half (1/1) beam splitter.

$\hat{B}_{12}(\cos^{-1} 1/\sqrt{3})$ and then $\hat{B}_{23}(\pi/4)$ to the input state $|p = 0\rangle_1|x = 0\rangle_2|x = 0\rangle_3$ yields the state in Eq. (3.55), using phase-free beam splitting operators $\hat{B}_{kl}(\theta)$ corresponding to the linear transformations in Eq. (2.108). The realistic finite-squeezing case will be described in Section 3.2.3.3.

Let us now see how one can find entanglement witnesses for states with three parties and three qumodes [165]. The goal is to extend the simple two-party two-

mode entanglement check of the preceding section to a simple test for genuine three-party three-mode entanglement. The criteria are to be expressed in terms of variances of quadrature linear combinations for those qumodes involved. Defining

$$\hat{u} \equiv h_1\hat{x}_1 + h_2\hat{x}_2 + h_3\hat{x}_3 \,, \quad \hat{v} \equiv g_1\hat{p}_1 + g_2\hat{p}_2 + g_3\hat{p}_3 \,, \tag{3.58}$$

a fairly general ansatz is

$$\langle(\Delta\hat{u})^2\rangle_\rho + \langle(\Delta\hat{v})^2\rangle_\rho \geq f(h_1, h_2, h_3, g_1, g_2, g_3) \,, \tag{3.59}$$

as a potential necessary condition for an at least partially separable state. The position and momentum variables $\hat{x}_l$ and $\hat{p}_l$ are the quadratures of the three qumodes. The h_l and g_l are arbitrary real parameters. We will prove the following statement(s) for (at least partially) separable states,

$$\hat{\rho} = \sum_i \eta_i \hat{\rho}_{i,km} \otimes \hat{\rho}_{i,n}$$
$$\Rightarrow f(h_1, h_2, h_3, g_1, g_2, g_3) \tag{3.60}$$
$$= (|h_n g_n| + |h_k g_k + h_m g_m|)/2 \,. \tag{3.61}$$

Here, $\hat{\rho}_{i,km} \otimes \hat{\rho}_{i,n}$ indicates that the three-party density operator is a mixture of states i where parties (qumodes) k and m may be entangled or not, but party n is not entangled with the rest, and where (k, m, n) is any triple of $(1, 2, 3)$. Hence, also the fully separable state is included in the above statements. In fact, for the fully separable state, we have

$$\hat{\rho} = \sum_i \eta_i \hat{\rho}_{i,1} \otimes \hat{\rho}_{i,2} \otimes \hat{\rho}_{i,3}$$
$$\Rightarrow f(h_1, h_2, h_3, g_1, g_2, g_3) \tag{3.62}$$
$$= (|h_1 g_1| + |h_2 g_2| + |h_3 g_3|)/2 \,, \tag{3.63}$$

which is always greater or equal than any of the boundaries in Eq. (3.61). For the proof, let us assume that the relevant state can be written as in Eq. (3.60). For the combinations in Eq. (3.58), we find

$$\begin{aligned}
&\left\langle(\Delta\hat{u})^2\right\rangle_\rho + \left\langle(\Delta\hat{v})^2\right\rangle_\rho \\
&= \sum_i \eta_i \left(\left\langle\hat{u}^2\right\rangle_i + \left\langle\hat{v}^2\right\rangle_i\right) - \langle\hat{u}\rangle_\rho^2 - \langle\hat{v}\rangle_\rho^2 \\
&= \sum_i \eta_i \left[h_k^2 \left\langle\hat{x}_k^2\right\rangle_i + h_m^2 \left\langle\hat{x}_m^2\right\rangle_i + h_n^2 \left\langle\hat{x}_n^2\right\rangle_i \right. \\
&\quad + g_k^2 \left\langle\hat{p}_k^2\right\rangle_i + g_m^2 \left\langle\hat{p}_m^2\right\rangle_i + g_n^2 \left\langle\hat{p}_n^2\right\rangle_i \\
&\quad + 2\left(h_k h_m \left\langle\hat{x}_k\hat{x}_m\right\rangle_i + h_k h_n \left\langle\hat{x}_k\hat{x}_n\right\rangle_i + h_m h_n \left\langle\hat{x}_m\hat{x}_n\right\rangle_i\right) \\
&\quad \left. +2\left(g_k g_m \left\langle\hat{p}_k\hat{p}_m\right\rangle_i + g_k g_n \left\langle\hat{p}_k\hat{p}_n\right\rangle_i + g_m g_n \left\langle\hat{p}_m\hat{p}_n\right\rangle_i\right)\right] \\
&\quad - \langle\hat{u}\rangle_\rho^2 - \langle\hat{v}\rangle_\rho^2
\end{aligned}$$

$$
\begin{aligned}
&= \sum_i \eta_i \left[h_k^2 \left\langle (\Delta \hat{x}_k)^2 \right\rangle_i + h_m^2 \left\langle (\Delta \hat{x}_m)^2 \right\rangle_i + h_n^2 \left\langle (\Delta \hat{x}_n)^2 \right\rangle_i \right. \\
&\quad + g_k^2 \left\langle (\Delta \hat{p}_k)^2 \right\rangle_i + g_m^2 \left\langle (\Delta \hat{p}_m)^2 \right\rangle_i + g_n^2 \left\langle (\Delta \hat{p}_n)^2 \right\rangle_i \\
&\quad + 2h_k h_m \left(\langle \hat{x}_k \hat{x}_m \rangle_i - \langle \hat{x}_k \rangle_i \langle \hat{x}_m \rangle_i \right) + 2h_k h_n \left(\langle \hat{x}_k \hat{x}_n \rangle_i - \langle \hat{x}_k \rangle_i \langle \hat{x}_n \rangle_i \right) \\
&\quad + 2h_m h_n \left(\langle \hat{x}_m \hat{x}_n \rangle_i - \langle \hat{x}_m \rangle_i \langle \hat{x}_n \rangle_i \right) + 2g_k g_m \left(\langle \hat{p}_k \hat{p}_m \rangle_i - \langle \hat{p}_k \rangle_i \langle \hat{p}_m \rangle_i \right) \\
&\quad \left. + 2g_k g_n \left(\langle \hat{p}_k \hat{p}_m \rangle_i - \langle \hat{p}_k \rangle_i \langle \hat{p}_m \rangle_i \right) + 2g_m g_n \left(\langle \hat{p}_m \hat{p}_n \rangle_i - \langle \hat{p}_m \rangle_i \langle \hat{p}_n \rangle_i \right) \right] \\
&\quad + \sum_i \eta_i \langle \hat{u} \rangle_i^2 - \left(\sum_i \eta_i \langle \hat{u} \rangle_i \right)^2 \\
&\quad + \sum_i \eta_i \langle \hat{v} \rangle_i^2 - \left(\sum_i \eta_i \langle \hat{v} \rangle_i \right)^2 ,
\end{aligned}
\tag{3.64}
$$

where $\langle \cdots \rangle_i$ represents the expectation value in the state $\hat{\rho}_{i,km} \otimes \hat{\rho}_{i,n}$. Note that in the derivation so far, we have not used the particular form in Eq. (3.60) yet. Exploiting this form of the state, we obtain $\langle \hat{x}_k \hat{x}_n \rangle_i = \langle \hat{x}_k \rangle_i \langle \hat{x}_n \rangle_i$, $\langle \hat{x}_m \hat{x}_n \rangle_i = \langle \hat{x}_m \rangle_i \langle \hat{x}_n \rangle_i$, and similarly for the terms involving p. Because modes k and m may be entangled in the states i, we cannot replace $\langle \hat{x}_k \hat{x}_m \rangle_i$ by $\langle \hat{x}_k \rangle_i \langle \hat{x}_m \rangle_i$, and so on. By applying the Cauchy–Schwarz inequality as in the two-party derivation of [159], $\sum_i P_i \langle \hat{u} \rangle_i^2 \geq (\sum_i P_i |\langle \hat{u} \rangle_i|)^2$, we see that the last two lines in Eq. (3.64) are bounded below by zero. Hence, in order to prove $\langle (\Delta \hat{u})^2 \rangle_\rho + \langle (\Delta \hat{v})^2 \rangle_\rho \geq (|h_n g_n| + |h_k g_k + h_m g_m|)/2$, it remains to be shown that for any i [recall that the mixture in Eq. (3.60) is a convex sum with $\sum_i \eta_i = 1$],

$$
\begin{aligned}
&h_k^2 \left\langle (\Delta \hat{x}_k)^2 \right\rangle_i + h_m^2 \left\langle (\Delta \hat{x}_m)^2 \right\rangle_i + h_n^2 \left\langle (\Delta \hat{x}_n)^2 \right\rangle_i \\
&\quad + g_k^2 \left\langle (\Delta \hat{p}_k)^2 \right\rangle_i + g_m^2 \left\langle (\Delta \hat{p}_m)^2 \right\rangle_i + g_n^2 \left\langle (\Delta \hat{p}_n)^2 \right\rangle_i \\
&\quad + 2h_k h_m \left(\langle \hat{x}_k \hat{x}_m \rangle_i - \langle \hat{x}_k \rangle_i \langle \hat{x}_m \rangle_i \right) \\
&\quad + 2g_k g_m \left(\langle \hat{p}_k \hat{p}_m \rangle_i - \langle \hat{p}_k \rangle_i \langle \hat{p}_m \rangle_i \right) \\
&\geq (|h_n g_n| + |h_k g_k + h_m g_m|)/2 .
\end{aligned}
\tag{3.65}
$$

By rewriting the left-hand side of Eq. (3.65) in terms of variances only, indeed we find

$$
\begin{aligned}
&h_n^2 \langle (\Delta \hat{x}_n)^2 \rangle_i + g_n^2 \langle (\Delta \hat{p}_n)^2 \rangle_i \\
&\quad + \left\langle \left[\Delta \left(h_k \hat{x}_k + h_m \hat{x}_m \right) \right]^2 \right\rangle_i + \left\langle \left[\Delta \left(g_k \hat{p}_k + g_m \hat{p}_m \right) \right]^2 \right\rangle_i \\
&\geq \left| \langle \left[h_n \hat{x}_n, g_n \hat{p}_n \right] \rangle \right| + \left| \langle \left[h_k \hat{x}_k + h_m \hat{x}_m, g_k \hat{p}_k + g_m \hat{p}_m \right] \rangle \right| \\
&= (|h_n g_n| + |h_k g_k + h_m g_m|)/2 ,
\end{aligned}
\tag{3.66}
$$

using the sum uncertainty relation $\langle (\Delta \hat{A})^2 \rangle + \langle (\Delta \hat{B})^2 \rangle \geq |\langle [\hat{A}, \hat{B}] \rangle|$ and $[\hat{x}_l, \hat{p}_j] = i\delta_{lj}/2$. Hence, the statements in Eq. (3.61) with Eq. (3.60) are proven for all permutations of $(k, m, n) = (1, 2, 3)$. The inequalities Eq. (3.59) with Eqs. (3.61) and (3.60) represent necessary conditions for all kinds of (partial) separability in a tripartite three-mode state. One may then prove the presence of genuine tripartite

entanglement through violations of these inequalities, thus ruling out any (partially) separable form.

A particularly useful example for these conditions is the GHZ-type witness [165] as expressed by the inequalities in Eq. (3.86), directly related with the CV GHZ stabilizers discussed above. Since the three-mode GHZ state is determined by three stabilizer combinations, the witness also only requires three such combinations and hence it is sufficient (as well as it is necessary) to consider only (at least) two of the three inequalities in Eq. (3.86).

Besides the above entanglement witnesses, the CV partial transpose criterion can be utilized to decide on the separability properties of three-party three-mode Gaussian states [166], provided the correlation matrix of the state in question is available. For three-party three-mode Gaussian states, the only partially separable forms are those with a bipartite splitting of 1×2 modes. In this case, the NPT criterion is necessary and sufficient.

In Section 3.2.3.3, we shall describe an experiment in which tripartite CV entanglement was created and verified. Moreover, in another recent experiment, tripartite Gaussian states with entanglement between three qumodes of three different frequencies (colors) was demonstrated [167]. In other more recent experiments, as we will also discuss below, entanglement between more than three parties was produced and detected in multi-mode CV graph and cluster states. In the next section, we shall define and discuss such CV qumode graph states.

3.2.2
Cluster and Graph States

Similar to the operational definition of qubit graph states in terms of C_Z-gate edges pairwise acting upon $|+\rangle$-state nodes (Section 3.1.2), we may define CV graph states on qumodes (see Figure 3.16). For this purpose, we use the CV analogues for the basis states, stabilizers, and gates as presented in Chapter 1, especially, in Sections 1.8 and 1.9.

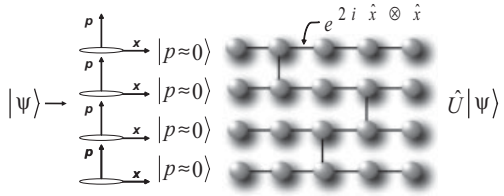

Figure 3.16 An approximate, Gaussian CV cluster state built from momentum-squeezed states of light and Gaussian, CV versions of the C_Z gate, $e^{2i\hat{x}\otimes\hat{x}}$. In Chapter 7, we shall see that such a cluster state becomes a resource for universal quantum computing on qumodes in the limit of infinite squeezing. In this case, an arbitrary multi-mode state $|\psi\rangle$ attached from the left can be universally transformed into the output state $\hat{U}|\psi\rangle$ appearing on the most right column when all the remaining qumodes are measured out in suitable bases.

Let us start with every qumode representing a single node of the graph in an infinitely squeezed zero-momentum eigenstate $|p = 0\rangle$. The initial N-qumode product state, $|p = 0\rangle^{\otimes N}$, is stabilized by $\langle X_k(s)\rangle$, with the WH operators $X_k(s)$ for qumode $k = 1, \ldots, N$ and $s \in \mathbb{R}$. The canonical generation of CV cluster states in terms of CV C_Z gates, $\mathrm{e}^{2\mathrm{i}\hat{x}\otimes\hat{x}}$, pairwise acting upon the input qumodes in state $|p = 0\rangle$, leads to the following evolution of the stabilizer generators,

$$\begin{aligned}\hat{U}\left(X_k(s)\otimes\mathbb{1}^{N-1}\right)\hat{U}^\dagger &= X_k(s)\prod_{l\in N(k)} Z_l(s) = X_k(s)\prod_{l\neq k} Z_l^{A_{kl}}(s)\\ &\equiv K_k(s)\,, \quad \forall k\in G\,, \quad \forall s\in\mathbb{R}\,,\end{aligned} \tag{3.67}$$

where $\hat{U}$ describes all the C_Z gates pairwise acting upon all qumodes of the graph G according to the adjacency matrix elements $A_{kl} = A_{lk}$ which are one when the qumodes become connected and zero otherwise. This set of stabilizer generators can be rewritten as

$$\begin{aligned}X_k(s)\prod_{l\in N(k)} Z_l(s) &= \mathrm{e}^{-2\mathrm{i}s\hat{p}_k}\prod_{l\in N(k)}\mathrm{e}^{2\mathrm{i}s\hat{x}_l}\\ &= \mathrm{e}^{-2\mathrm{i}s\left[\hat{p}_k-\sum_{l\in N(k)}\hat{x}_l\right]}\,.\end{aligned} \tag{3.68}$$

Now, applying the stabilizer conditions to a given graph state $|G\rangle$,

$$\mathrm{e}^{-2\mathrm{i}s\left[\hat{p}_k-\sum_{l\in N(k)}\hat{x}_l\right]}|G\rangle = |G\rangle\,, \quad \forall s\in\mathbb{R}\,, \quad \forall k\in G\,, \tag{3.69}$$

immediately leads to the definition

$$\left[\hat{p}_k - \sum_{l\in N(k)}\hat{x}_l\right]\to 0\,, \quad \forall k\in G\,. \tag{3.70}$$

Hence, we define cluster-type (graph-type) states as those multi-mode Gaussian states for which certain quadrature correlations, as expressed by Eq. (3.70), become perfect in the limit of infinite squeezing. More precisely, in this limit, the N-mode graph state becomes a simultaneous zero-eigenstate of the N linear combinations in Eq. (3.70). We therefore name these combinations *nullifiers*, uniquely defining the corresponding CV graph state.

This definition covers all Gaussian states which, in the infinite-squeezing limit, become zero-eigenstates of all those quadrature combinations that generate the stabilizer group of the corresponding graph. Here, the zero-eigenstates are the representatives for a given graph. More generally, one may define CV graph states as common eigenstates of the corresponding quadrature combinations. However, eigenvalues other than zero correspond to simple phase-space displacements which have no effect on the entanglement properties of the graph states. This definition then still means that the variance of the quadrature combinations vanishes in the limit of infinite squeezing, $\mathrm{Var}[\hat{p}_k - \sum_{l\in N(k)}\hat{x}_l]\to 0$, $\forall k\in G$.

A simple example for a CV graph state is the tripartite GHZ-type state defined in the preceding section corresponding to a linear three-mode graph up to local Fourier transforms. The graph stabilizer in this case is

$$S = \langle X(s) \otimes Z(s) \otimes \mathbb{1} \,, \quad Z(s) \otimes X(s) \otimes Z(s) \,, \quad \mathbb{1} \otimes Z(s) \otimes X(s) \rangle \,, \quad (3.71)$$

differing from that in Eq. (3.56) only by local Fourier rotations on qumodes 1 and 3. More generally, GHZ-type graph states correspond to star graphs, as illustrated in Figure 3.1b, differing from standard GHZ-type states only by local Fourier rotations acting upon all nodes except the central one.

The CV graph states discussed so far are only defined in the unphysical limit of infinite squeezing as expressed by Eq. (3.70), which we may rewrite as

$$\hat{\boldsymbol{p}} - \boldsymbol{A}\hat{\boldsymbol{x}} \to \boldsymbol{0} \,. \quad (3.72)$$

Here, $\hat{\boldsymbol{p}} \equiv (\hat{p}_1, \hat{p}_2, \ldots, \hat{p}_N)^{\mathrm{T}}$ and $\hat{\boldsymbol{x}} \equiv (\hat{x}_1, \hat{x}_2, \ldots, \hat{x}_N)^{\mathrm{T}}$ are the vectors of position and momentum operators, and $\boldsymbol{A}$ is the corresponding adjacency matrix of the graph. Thus, Eq. (3.72) represents the entire set of N stabilizer/nullifier conditions from Eq. (3.70). Any multi-mode Gaussian state satisfying this set of nullifier relations in the limit of infinite squeezing belongs to the same class of CV graph states with matrix $\boldsymbol{A}$. This matrix is symmetric (so the graph is "undirected"), has all diagonal entries zero (so the graph has no "self-loops"), and whenever the graph has an edge, the corresponding element of $\boldsymbol{A}$ is one, otherwise it is zero.

There is now one straightforward and conceptually distinct generalization of the notion of CV graph states as defined above. First, we may consider arbitrary real elements in $\boldsymbol{A}$ instead of only zeros and ones. This gives rise to the notion of *weighted* CV graph states. In this case, one can think of a network of "weighted" CV C_Z gates, $\mathrm{e}^{2\mathrm{i}g_{kl}\hat{x}_k \otimes \hat{x}_l}$, again, pairwise acting upon the input qumodes in state $|p = 0\rangle$ with real-valued "gains" $A_{kl} \equiv g_{kl} \in \mathbb{R}$ for each quadratic interaction. This leads to a set of more general nullifiers which still satisfy Eq. (3.72) in the unphysical limit of infinite squeezing. Thus, these weighted graph states remain stabilizer states which are defined through idealized stabilizer conditions. We note that for qubits, weighted graph states are no longer stabilizer states. While the additional coefficients in the CV nullifier conditions still give quadrature linear combinations, an extra weight in the qubit C_Z gates would result in non-stabilizer states.

The most general manifestation of a CV graph state, however, allows for *complex-weighted* edges of the graph and correspondingly complex nullifier conditions [168]. In this case, the complex adjacency matrix shall be denoted by $\boldsymbol{Z}$, this time with nonzero diagonal entries including self-loops in the graph. We define the complex nullifier conditions

$$\hat{\boldsymbol{p}} - \boldsymbol{Z}\hat{\boldsymbol{x}} = \boldsymbol{0} \,, \quad (3.73)$$

now representing a set of *exact* eigenvalue equations satisfied by the corresponding complex-weighted graph state $|G\rangle$, $(\hat{\boldsymbol{p}} - \boldsymbol{Z}\hat{\boldsymbol{x}})|G\rangle = \boldsymbol{0}$. What are these generalized graph states? One can show that every N-mode Gaussian pure state can be uniquely

represented as a graph state with complex adjacency matrix $\boldsymbol{Z}$, up to phase-space displacements. In this case, finite squeezing and phase rotations such as Fourier transforms are incorporated into $\boldsymbol{Z}$. In other words, the complex-weighted graph states are the physical, properly normalized versions of CV graph states.

In Section 1.8, we implicitly used the fact that all Gaussian pure states are stabilizer states in order to show that their manipulation through Gaussian operations can be efficiently classically simulated. For this CV Gottesman–Knill theorem to hold in the regime of physical states, we needed to keep track of complex eigenvalues of non-Hermitian operators. Similarly, in Section 2.2.8.1, we used complex-valued stabilizers (nullifiers) to uniquely represent arbitrary single-qumode Gaussian pure states. Here, in the context of CV graph states, we may generalize these results to the multi-mode case (for which we shall omit representing phase-space displacements).

Let us see how the canonical CV cluster states, operationally defined and created by pairwise applying the controlled Z gates, C_{kl} (where we define $C_Z \equiv C$ here), are represented when the stabilizers for physical squeezed states are used from the beginning (see Section 2.2.8.1). The N stabilizers of the initial N momentum-squeezed modes as derived in Eq. (2.84), $\mathrm{e}^{-\mathrm{e}^{-2r_k}s^2} X_k(s) Z_k(\mathrm{ie}^{-2r_k}s)$, $k = 1, 2, \ldots, N$, are then transformed for each interaction with neighbor l as

$$\begin{aligned} &\mathrm{e}^{-\mathrm{e}^{-2r_k}s^2} C_{kl} X_k(s) C_{kl}^\dagger C_{kl} Z_k(\mathrm{ie}^{-2r_k}s) C_{kl}^\dagger \\ &= \mathrm{e}^{-\mathrm{e}^{-2r_k}s^2} X_k(s) Z_l(s) Z_k(\mathrm{ie}^{-2r_k}s) \,. \end{aligned} \tag{3.74}$$

Eventually, by collecting all these interactions, we obtain the N new stabilizers

$$\mathrm{e}^{-\mathrm{e}^{-2r_k}s^2} X_k(s) Z_k(\mathrm{ie}^{-2r_k}s) \prod_{l \in N(k)} Z_l(s) \,. \tag{3.75}$$

In the limit of infinite squeezing $r_k \to \infty$, we get back the ideal CV cluster stabilizers from Eq. (3.68). However, this time, the above stabilizers also do the job for finite squeezing and uniquely represent the corresponding approximate cluster state. The nullifiers can be derived from

$$\begin{aligned} &\mathrm{e}^{-\mathrm{e}^{-2r_k}s^2} X_k(s) Z_k(\mathrm{ie}^{-2r_k}s) \prod_{l \in N(k)} Z_l(s) \\ &= \mathrm{e}^{-\mathrm{e}^{-2r_k}s^2} \mathrm{e}^{-2\mathrm{i}s\left(\hat{p}_k - \mathrm{ie}^{-2r_k}\hat{x}_k\right)} \mathrm{e}^{+\mathrm{e}^{-2r_k}s^2} \prod_{l \in N(k)} \mathrm{e}^{2\mathrm{i}s\hat{x}_l} \\ &= \mathrm{e}^{-2\mathrm{i}s\left(\hat{p}_k - \mathrm{ie}^{-2r_k}\hat{x}_k - \sum_l \hat{x}_l\right)} \,, \\ &\forall k = 1, 2, \ldots, N \,, \quad \forall s \in \mathbb{R} \,, \end{aligned} \tag{3.76}$$

and become

$$\hat{p}_k - \mathrm{ie}^{-2r_k}\hat{x}_k - \sum_{l \in N(k)} \hat{x}_l = 0 \,, \forall k \,. \tag{3.77}$$

This result corresponds to the complex nullifier conditions in Eq. (3.73), with a complex adjacency matrix $\boldsymbol{Z}$ having imaginary diagonal entries ie^{-2r_k} and the re-

maining entries being either zero or one depending on the particular graph state with unweighted edges.

Now, we also know that any pure N-mode Gaussian state can be built from N squeezed vacua through passive linear optics (modulo phase-space displacements, see Chapter 2). In terms of stabilizers, this means that without loss of generality, the stabilizers of N momentum-squeezed states are transformed as

$$\mathrm{e}^{-\mathrm{e}^{-2r_k}s^2}\, U X_k(s)\, U^\dagger\, U Z_k(\mathrm{i}\mathrm{e}^{-2r_k}s)\, U^\dagger = \mathrm{e}^{-2\mathrm{i}s\left(\hat{p}'_k - \mathrm{i}\mathrm{e}^{-2r_k}\hat{x}'_k\right)} \,. \tag{3.78}$$

Here, the $\hat{p}'_k$ and $\hat{q}'_k$ are the linearly transformed momentum and position operators after the corresponding (inverse) unitary transformation U. Provided this U represents a Gaussian (Clifford) transformation, we will always obtain linear combinations in terms of the generators on the right-hand side of Eq. (3.78). This would include the canonical C_Z interactions, as discussed before. However, now we shall restrict ourselves to only passive, number-preserving unitaries U, without loss of generality (recall the Bloch–Messiah decomposition discussed in Chapter 2). The canonical case would then require that the squeezing parts of the C_Z gates be absorbed into the offline momentum squeezers corresponding to Bloch–Messiah reduction [169].

For the case of a passive linear transformation, we can write $\hat{a}'_k = \sum_l U_{kl}\hat{a}_l$, and so $\hat{x}'_k = \sum_l (\mathrm{Re}\, U_{kl}\hat{x}_l - \mathrm{Im}\, U_{kl}\hat{p}_l)$ and $\hat{p}'_k = \sum_l (\mathrm{Im}\, U_{kl}\hat{x}_l - \mathrm{Re}\, U_{kl}\hat{p}_l)$, with some unitary $N \times N$ matrix $\boldsymbol{U}$, $(\boldsymbol{U})_{kl} \equiv U_{kl}$. Finally, through Eq. (3.78), we arrive at the new stabilizers

$$\mathrm{e}^{-2\mathrm{i}s\sum_l \left[\left(\mathrm{Im}\, U_{kl} - \mathrm{i}\mathrm{e}^{-2r_k}\mathrm{Re}\, U_{kl}\right)\hat{x}_l + \left(\mathrm{Re}\, U_{kl} + \mathrm{i}\mathrm{e}^{-2r_k}\mathrm{Im}\, U_{kl}\right)\hat{p}_l\right]} \,. \tag{3.79}$$

For the nullifiers, we then obtain

$$(\boldsymbol{A}\hat{\boldsymbol{p}} + \boldsymbol{B}\hat{\boldsymbol{x}})\,|G\rangle = \boldsymbol{0} \,, \tag{3.80}$$

which we may rewrite as

$$\left(\boldsymbol{A}^{-1}\boldsymbol{A}\hat{\boldsymbol{p}} + \boldsymbol{A}^{-1}\boldsymbol{B}\hat{\boldsymbol{x}}\right)|G\rangle = (\hat{\boldsymbol{p}} - \boldsymbol{Z}\hat{\boldsymbol{x}})\,|G\rangle = \boldsymbol{0} \,, \tag{3.81}$$

with $\boldsymbol{Z} \equiv -\boldsymbol{A}^{-1}\boldsymbol{B}$, $(\boldsymbol{A})_{kl} \equiv \mathrm{Re}\, U_{kl} + \mathrm{i}\mathrm{e}^{-2r_k}\mathrm{Im}\, U_{kl}$, and $(\boldsymbol{B})_{kl} \equiv \mathrm{Im}\, U_{kl} - \mathrm{i}\mathrm{e}^{-2r_k}\mathrm{Re}\, U_{kl}$. This gives us the complex adjacency matrix for an arbitrary pure Gaussian N-mode state. We note that there are at most $4N^2$ parameters to determine the stabilizer/nullifier (see Section 1.8). These, however, are not independent, as $\boldsymbol{U}$ must be unitary and $\boldsymbol{B}$ follows from $\boldsymbol{A}$. A general LUBO transformation has $2N^2 + N$ free parameters without displacements, which is the same number for representing a symplectic transformation from $\mathrm{Sp}(2N, \mathbb{R})$. For representing pure Gaussian N-mode states (modulo displacements), it is enough to apply a general LUBO transformation to an N-mode vacuum state where after Bloch–Messiah reduction, the first passive transformation has no effect on the vacuum [169]. Thus, N real squeezing parameters r_k and N^2 parameters for the remaining passive transformation $\boldsymbol{U}$ suffice to uniquely determine the matrices $\boldsymbol{A}$ and $\boldsymbol{B}$, and hence the state through $\boldsymbol{Z}$.

Stabilizer and graph states

⊙ **Qubits**
unweighted graph state ∼ any stabilizer state: (up to local Cliffords)

$$X_k \prod_{l\in N(k)} Z_l|G\rangle = X_k \prod_{l\neq k} Z_l^{A_{kl}}|G\rangle = |G\rangle\,, \quad \forall k \in G\,, \quad A_{kl} = 0,1$$

∼∼∼∼ **Qumodes**
real-weighted graph state ∼ any unphysical ∞-squeezing stabilizer state: (up to local Gaussian unitaries)

$$\hat{\boldsymbol{p}} - \boldsymbol{A}\hat{\boldsymbol{x}} \to \boldsymbol{0}\,, \qquad \left[\hat{p}_k - \sum_{l\in N(k)} g_{kl}\hat{x}_l\right] \to 0\,, \quad \forall k \in G$$

complex-weighted graph state ∼ any Gaussian pure state:
(up to local WH unitaries)

$$\hat{\boldsymbol{p}} - \boldsymbol{Z}\hat{\boldsymbol{x}} = \boldsymbol{0}\,,$$

canonical graph:

$$\hat{p}_k - \mathrm{i}\mathrm{e}^{-2r_k}\hat{x}_k - \sum_{l\in N(k)} \hat{x}_l = 0\,, \quad \forall k \in G$$

Even though every Gaussian pure state is effectively a graph state, these would include trivial graphs such as products of vacuum states with an imaginary, diagonal $\boldsymbol{Z}$ matrix only describing self-loops. Note that, for universal quantum information processing, not even GHZ-type star graphs would suffice as a resource. Other nontrivial, highly entangled, two-dimensional CV graphs would be needed.

Before we start describing various experiments in which optical qumode entanglement was generated, including various CV Gaussian graph states, let us mention that there are currently five distinct proposals for preparing CV graph states optically. The canonical generation method [171] is in one-to-one correspondence with the operational definition of CV cluster states and uses CV C_Z gates for every link of the cluster. These gates are rather hard to achieve online, that is, upon non-vacuum states such as the initial squeezed-state cluster nodes. A second, more practical scheme would shift every squeezer to the very beginning of the cluster generation circuit such that only offline, single-mode vacuum squeezing is required and the rest is just interferometry with a suitable network of beam splitters [169]. This works for arbitrary graph states and hence is the chosen technique for all those experiments conducted so far, including those described below.

A conceptually different method for creating CV graph states is based upon a single, quadratic OPO interaction [172]. This very compact approach is a multimode extension of the method for creating a two-mode squeezed state from a single NOPO instead of using two single-mode squeezed states from two OPOs. The sufficient degree of nondegeneracy in order to obtain many qumodes for the desired graph state can be achieved within a so-called frequency comb. Finally, there are two more, very recent proposals for making arbitrarily large CV cluster states. The first one would employ just a single squeezer and a single C_Z gate which is achieved through a temporal encoding where the OPO-squeezer and the C_Z gate can be reused after each measurement step [173]. A drawback of this scheme is that the C_Z gate again requires online squeezing and the need for sufficient delay lines. The former complication, however, was eliminated very recently in a variation that uses only four offline squeezers and six beam splitters [174].

3.2.3 Experiment: Entangled Photonic Qumodes

3.2.3.1 Frequency-Domain EPR-Type State

Nonclassical, so-called Einstein–Podolsky–Rosen (EPR) correlations were originally associated with two canonically conjugate, continuous quantum variables such as particle position and momentum, as described in the seminal paper from 1935 [23]. Ou *et al.* were the first to realize these EPR correlations experimentally in the optical setting by employing a two-mode squeezed state [156, 157]. Here, the two-mode squeezed state can be built from two squeezed vacua using a half beam splitter, as mentioned before. It is equivalent to the state obtainable from type-II phase matching of a second order nonlinear crystal ($\chi^{(2)}$) for two orthogonally polarized (signal and idler) modes, as shown in Figure 3.17. Figure 3.18 shows the results of the experiment in Figure 3.17.

Note that frequency sidebands at $\pm\Omega$ were used for the quadrature field amplitudes in this experiment. More precisely, in accordance to the discussion on broadband qumodes in Section 2.2.9, the relevant state corresponds to the electromagnetic field at frequency offset $\pm\Omega \equiv \pm 2\pi f$ within a finite bandwidth $\Delta\Omega \equiv 2\pi\Delta f$ about the carrier ω_L (laser frequency); in other words, we have AM and FM sidebands (recall the discussion in Section 2.1 and see Figure 2.10a).

In Figure 3.18, we have $\Delta^2_{\text{inf}} X \equiv \langle(\bar{X}_s - g_x \bar{X}_i)^2\rangle$ and $\Delta^2_{\text{inf}} Y \equiv \langle(\bar{Y}_s - g_y \bar{Y}_i)^2\rangle$ with $\bar{A} \equiv A - \langle A\rangle$, and these values were obtained from the measurement of the photocurrent difference Φ in Figure 3.17 [156]. Here, X and Y represent the amplitude and phase quadratures.[5] In Figure 3.18, the noise in Φ is plotted in dB, and so Ψ_{0s} corresponds to unity noise (with $1 = \Delta^2 X_{\Psi_{0s}} \Delta^2 Y_{\Psi_{0s}}$). Then, the results show that $\Delta^2_{\text{inf}} X \Delta^2_{\text{inf}} Y < 1$, which is a sufficient condition for entanglement.

5) More precisely, these are rescaled position and momentum variables, $X \equiv \sqrt{2}\hat{x}$ and $Y \equiv \sqrt{2}\hat{p}$, using our convention as introduced in Section 1.2.

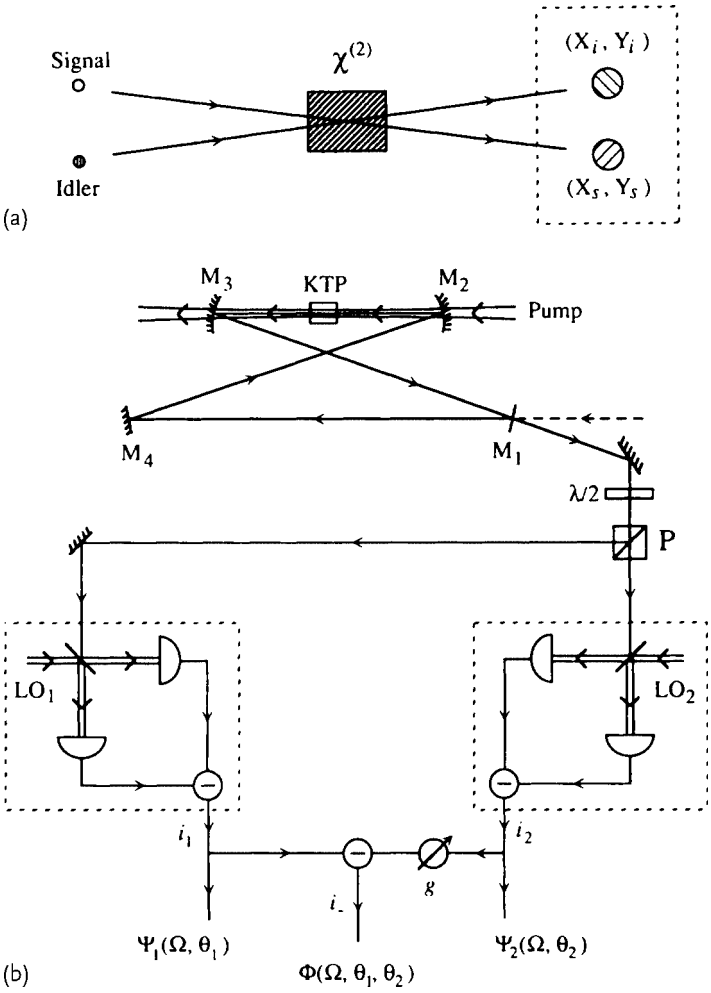

Figure 3.17 Scheme for creating an EPR-type entangled state [156]. (a) Parametric coupling through a second order nonlinear crystal ($\chi^{(2)}$) between two orthogonally polarized modes (Signal and Idler), (b) the experimental setup. KTP: $KTiOPO_4$, LO: local oscillator for homodyne detection, *i*: photocurrent, *g*: gain, Ψ and Φ: variances of photocurrents.

Since this significant milestone, there have been further experimental demonstrations of this type of EPR correlations [175–181].

3.2.3.2 Time-Domain EPR-Type State

Complementary to those experiments demonstrating EPR correlations in the frequency domain, a more recent approach considers this type of CV entanglement in the time domain. In order to incorporate those DV encodings and techniques inherited from single-photon-based quantum protocols into a CV scheme and to

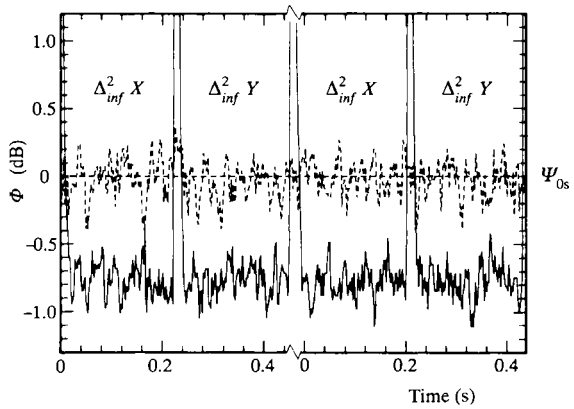

Figure 3.18 Results of the experiment in Figure 3.17 [156]; $\Delta^2_{\text{inf}}X \equiv \langle(\bar{X}_s - g_x \bar{X}_i)^2\rangle$ and $\Delta^2_{\text{inf}}Y \equiv \langle(\bar{Y}_s - g_y \bar{Y}_i)^2\rangle$ with $\bar{A} \equiv A - \langle A\rangle$. Subscripts *s* and *i* denote Signal and Idler. Ψ_{0s} corresponds to the variance without quantum correlations (entanglement).

obtain those hybrid protocols discussed in detail later, it will actually be necessary to switch from the frequency to the time domain.

As a result, quantum correlations will no longer become manifest only in statistical form. Instead, the entanglement will be resolved, in principle, down to the level of single shots. This corresponds to a new generation of experiments that come along with a paradigm shift from *frequency to time* and from *statistics to single shots*. For example, as a crucial step towards CV quantum teleportation of non-Gaussian states such as a superposition of coherent states, a time-domain two-mode squeezed vacuum state must be employed. The shift from frequency to time therefore starts with the entanglement resources. These will then correspond to a kind of "fast entanglement" as opposed to the "slow entanglement" in the frequency domain and would, in principle, allow for detecting true causal EPR correlations.

In this section, the generation and characterization of a two-mode squeezed vacuum state in the time domain will be explained in detail according to the experiment of Takei *et al*. [182]. The EPR resource is created using two squeezed vacuum states of continuous-wave (CW) light beams from two independent subthreshold optical parametric oscillators (OPOs). Hence, the resource state to start with is the same as before for the creation of frequency-domain entanglement. The two squeezed vacuum states have well-defined frequency and spatial modes, and almost the whole frequency bandwidth of the OPO cavities is used in order to define a quantum state in a temporal mode. So this time, using the *broad bandwidth* allows one to make *time-resolved* measurements such as photon counting, as described below.

The time-domain experiment is rather different from the schemes in the frequency domain [156, 175–180], including the experiment of Ou *et al*. which we had discussed in the preceding section [156]. As those frequency-domain experiments only deal with frequency sidebands a few MHz apart from the optical carrier frequency, they are simply not compatible with photon counting measurements.

The two-mode squeezed vacuum generated by subthreshold OPOs has EPR correlations within the variance spectra $S_x(\Omega)$, $S_p(\Omega)$, as usually measured in the frequency-domain experiments.[6] In this case, Ω is a sideband frequency around the fundamental wavelength (laser frequency). Now, for measuring the CW beams through time-gated detection, we need to specify two temporal modes for which the entangled quantum state is defined. Because of the broadband correlations of the CW beams, there is a large degree of freedom for choosing these modes. For instance, in a teleportation experiment, the temporal modes should be chosen such that they match the temporal mode of the input state.

A simple choice of temporal mode is a square filter of duration T. Let us define the filtered quadrature operators,

$$\hat{x}^f = \frac{1}{\sqrt{T}} \int_0^T \hat{x}(t) \mathrm{d}t \ , \tag{3.82}$$

and similarly for $\hat{p}^f$, still satisfying the usual commutation relation, $[\hat{x}^f, \hat{p}^f] = \mathrm{i}/2$. The EPR variances for two such wavepackets corresponding to two temporal modes will be given by [183],

$$\left\langle \left[\Delta \left(\hat{x}_{\mathrm{A}}^f - \hat{x}_{\mathrm{B}}^f \right) \right]^2 \right\rangle = \frac{T}{2\pi} \int_{-\infty}^{+\infty} S_x(\Omega) \frac{\sin^2\left(\frac{\Omega T}{2}\right)}{\left(\frac{\Omega T}{2}\right)^2} \mathrm{d}\Omega \ , \tag{3.83}$$

$$\left\langle \left[\Delta \left(\hat{p}_{\mathrm{A}}^f + \hat{p}_{\mathrm{B}}^f \right) \right]^2 \right\rangle = \frac{T}{2\pi} \int_{-\infty}^{+\infty} S_p(\Omega) \frac{\sin^2\left(\frac{\Omega T}{2}\right)}{\left(\frac{\Omega T}{2}\right)^2} \mathrm{d}\Omega \ . \tag{3.84}$$

The variances are thus filtered by a sinc function, and by adjusting the integration time T, the frequency range that contributes to the integrated correlations can be selected. The square temporal filter is simple, but not necessarily the most suitable choice for a given application of time-domain entanglement. Theoretical investigations concerning the shape of the filter combined with photon counting experiments can be found in [183, 184].

A schematic diagram of the experiment is shown in Figure 3.19 [182]. The primary source of the experiment is a CW Ti:sapphire laser at 860 nm. About 90% of this laser light is frequency doubled in an external cavity. The output beam at 430 nm is divided into two beams in order to pump two OPOs.

A two-mode squeezed vacuum is produced by combining two squeezed vacua at a half beam splitter (HBS). Each squeezed vacuum is generated from a subthreshold OPO with a 10 mm long $KNbO_3$ crystal. The crystal is temperature-tuned for type-I noncritical phase matching. Each OPO cavity is a bow-tie-type ring cavity consisting of two spherical mirrors (radius of curvature 50 mm) and two flat mirrors. The round trip length is about 500 mm and the waist size in the crystal is 20 μm. An output coupler has transmissivity of 12.7%, while the other mirrors

6) $S_x(\Omega)$ and $S_p(\Omega)$ correspond to $\Delta^2_{\mathrm{inf}} X$ and $\Delta^2_{\mathrm{inf}} Y$ of Ou *et al.* [156], respectively.

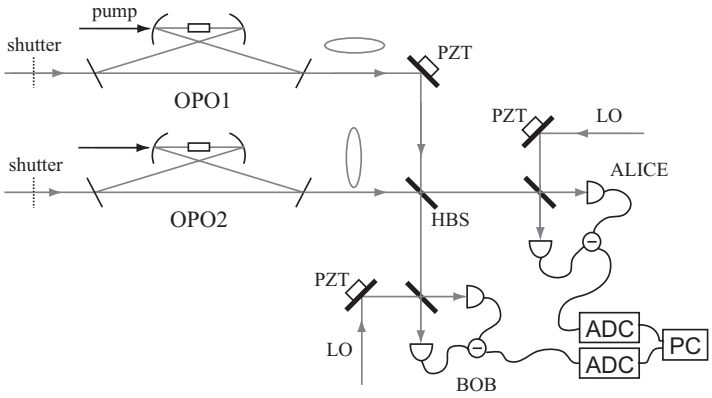

Figure 3.19 Setup of the *time-domain* EPR experiment [182]. OPOs: sub-threshold optical parametric oscillators, HBS: a half beam-splitter, PZTs: piezo-electric transducers, LOs: local oscillators, ADC: an analogue-to-digital converter. The ADC is an ingredient specific to the time-domain experiment and would not be used in a frequency-domain experiment. The measured quantities here are amplitudes and no more intensities, as they would be measured in a spectrum analyzer of a frequency-domain experiment.

have a coating with extremely high reflectivity at 860 nm. They also have a high transmittivity for 430 nm so that the pump beam passes the crystal only once. The pump power is about 70 mW for each OPO. The total intracavity losses are around 2%, giving a cavity bandwidth of 7 MHz HWHM. The resonant frequency of the OPO is locked via the FM sideband locking method [185] by introducing a lock beam which counterpropagates against the squeezed vacuum beam in order to avoid any interference between the two beams.

The two output beams A and B from the HBS are measured using homodyne detectors with a bandwidth of 8.4 MHz. The relative phases between the EPR beams and the local oscillators (LOs), that is, the x and p quadratures are locked in the following way. First, weak coherent beams that propagate along the same paths as the squeezed states are injected into the OPOs from one of the flat mirrors. These are then used for the conventional dither and lock method. The relative phases between the weak coherent beams and the squeezed vacua at the HBS are actively controlled by applying feedback voltages to piezo-actuators (PZTs). The quadratures to be detected by the homodyne detectors are also adjusted by locking the phases between the LOs and the injected coherent beams. However, the weak beams and the modulation on them will contaminate the EPR correlations in some frequency ranges. Therefore, eventually we need to remove these beams and achieve the phase locking without them.

For this purpose, an electronic circuit is introduced that holds the feedback voltage and keeps the phase relation for some time. Within 2 ms, the beams are blocked using mechanical shutters before the OPOs and the EPR beams are measured by the homodyne detectors. Each output from the detectors is sampled with an analogue-to-digital converter (ADC) at a rate of 5×10^7 samples per second and

is then filtered on a computer to yield a certain number of measured quadrature values.

Before observing the EPR correlations through time-gated measurements, the frequency bandwidth of the OPOs was estimated in order to determine the effective time interval of a temporal mode. Figure 3.20 shows the frequency spectra $S_x(\Omega)$ and $S_p(\Omega)$ for the measured EPR beams calculated by digital Fourier analysis on the 50 M-sampled raw data. The EPR correlations are observed over the full bandwidth of the OPOs. In particular, they are present at frequencies as low as 5 kHz (a high pass filter with a cut-off of 5 kHz is used to eliminate noise at frequencies close to DC). Such correlations at sufficiently low frequencies are essential for the non-Gaussian photon subtraction experiments discussed later.[7] From these results, one can determine a quantum state within the time interval that corresponds to the inverse of the cavity bandwidth (7 MHz). Since the EPR correlations degrade at higher frequencies, the temporal filter of Eq. (3.82) with an integration time of $T = 0.2$ μs was used, yielding 10 000 points in every measurement round. It follows from the frequency filters expressed by the sinc functions in Eqs. (3.83) and (3.84) that we mainly select a frequency range below 5 MHz.

Now, one can explicitly compare the time-resolved quadrature values measured for the beams A and B in every 0.2 μs time interval instead of measuring the variances $\langle[\Delta(\hat{x}_{\mathrm{A}}^{f} - \hat{x}_{\mathrm{B}}^{f})]^2\rangle$ and $\langle[\Delta(\hat{p}_{\mathrm{A}}^{f} + \hat{p}_{\mathrm{B}}^{f})]^2\rangle$, as done in the frequency-domain experiments [156, 175–177]. This approach also differs from the pulsed scheme

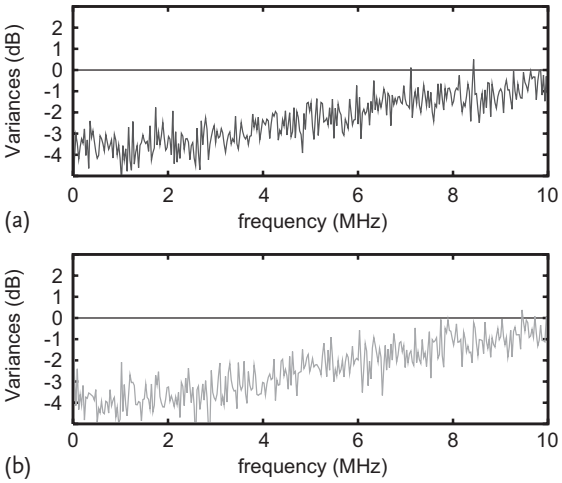

Figure 3.20 Fourier analysis of the 50M-sampled raw data without averaging. (a) $S_x(\Omega)$ for $\langle[\Delta(\hat{x}_{\mathrm{A}}^{f} - \hat{x}_{\mathrm{B}}^{f})]^2\rangle$. (b) $S_p(\Omega)$ for $\langle[\Delta(\hat{p}_{\mathrm{A}}^{f} + \hat{p}_{\mathrm{B}}^{f})]^2\rangle$. Each trace is normalized to the corresponding vacuum level.

7) In principle, it would be better to have access to even lower frequencies near zero Hz. In practice, however, those very low frequency components below 5 kHz are often neglected, for instance, in non-Gaussian state creation through photon subtraction [186]. Therefore, for practical purposes, very low frequency components are not required in the EPR source, for example, when teleporting such non-Gaussian states.

of [181] where the EPR beams are recombined at a beam splitter, yielding two unentangled squeezed vacua of which one is measured by homodyne detection.

Figure 3.21 shows a typical example for the measured quadrature values within a time interval of $T = 0.2\,\mu s$. In this example, only 50 points are picked up. As mentioned above, the measured values behave in such a way that the x and p quadratures are correlated ($x_A^f \simeq x_B^f$) and anticorrelated ($p_A^f \simeq -p_B^f$), respectively. Hence, EPR-type correlations are verified in the time domain.

The quality of the EPR correlations can be estimated by using correlation diagrams like those with 10 000 points shown in Figure 3.22. When repeating the same measurement ten times, correlations, compared to the vacuum level, corresponding to $\langle[\Delta(\hat{x}_A^f - \hat{x}_B^f)]^2\rangle = -3.30 \pm 0.28\,\mathrm{dB}$ and $\langle[\Delta(\hat{p}_A^f + \hat{p}_B^f)]^2\rangle = -3.74 \pm 0.32\,\mathrm{dB}$ are obtained. Accordingly, the sufficient entanglement criteria of Duan *et al.* are satisfied: $\langle[\Delta(\hat{x}_A^f - \hat{x}_B^f)]^2\rangle + \langle[\Delta(\hat{p}_A^f + \hat{p}_B^f)]^2\rangle = 0.45 \pm 0.02 < 1$.

As a result, the generated state is entangled for two temporal modes defined over the time interval $T = 0.2\,\mu s$. While it is, in principle, possible to further reduce the integration time T for faster data acquisition and hence potentially faster (quantum) information processing, the EPR correlations would degrade in this case due to the contribution of higher frequencies. Alternatively, it is also possible to obtain correlations over a broader bandwidth by using OPOs of smaller size corresponding to shorter round-trip length, or by employing waveguide crystals, for example, periodically poled lithium niobate waveguides [187].

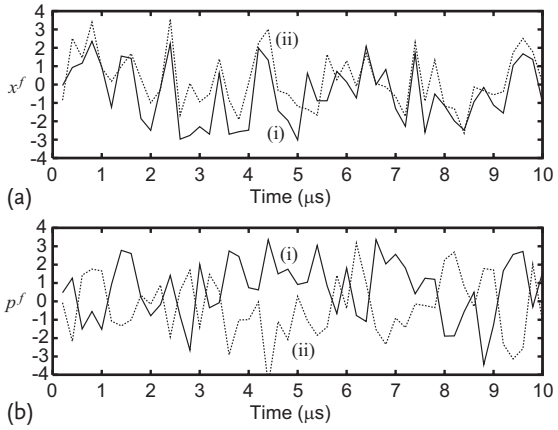

Figure 3.21 Typical measured correlations. Only 50 points are used to generate this plot. (a) and (b) are measured quadrature values within a time interval of $T = 0.2\,\mu s$ for the x and p quadratures, respectively. In each figure, trace (i) is for beam A, while (ii) is for beam B. In the frequency-domain experiments, none of these single-shot points would be actually recorded; in order to reveal the frequency EPR correlations, the Fourier-transformed power spectrum is directly detected. In contrast, here the EPR correlations are much "faster" and can be resolved by recording a small number of points. In principle, true causal EPR correlations would even be present for every single shot.

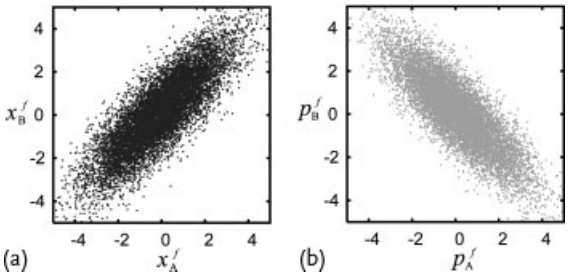

Figure 3.22 Correlation diagrams of 10 000 measured values for (a) x and (b) p quadratures.

3.2.3.3 GHZ-Type State

We shall describe the experiment of Aoki *et al.* [188] in detail. In the real experiment, only finite squeezing is available. Thus, the output state is no longer the ideal CV GHZ state – it is rather GHZ-type. Accordingly, total momentum and relative positions have finite variances: $\langle[\Delta(\hat{p}_1 + \hat{p}_2 + \hat{p}_3)]^2\rangle > 0$ and $\langle[\Delta(\hat{x}_i - \hat{x}_j)]^2\rangle > 0$. This becomes clear when we express the operators for the output mode i in the Heisenberg picture [161]:

$$
\begin{aligned}
\hat{x}_1 &= \frac{1}{\sqrt{3}}\mathrm{e}^{+r_1}\hat{x}_1^{(0)} + \sqrt{\frac{2}{3}}\mathrm{e}^{-r_2}\hat{x}_2^{(0)}\,,\\
\hat{p}_1 &= \frac{1}{\sqrt{3}}\mathrm{e}^{-r_1}\hat{p}_1^{(0)} + \sqrt{\frac{2}{3}}\mathrm{e}^{+r_2}\hat{p}_2^{(0)}\,,\\
\hat{x}_2 &= \frac{1}{\sqrt{3}}\mathrm{e}^{+r_1}\hat{x}_1^{(0)} - \frac{1}{\sqrt{6}}\mathrm{e}^{-r_2}\hat{x}_2^{(0)} + \frac{1}{\sqrt{2}}\mathrm{e}^{-r_3}\hat{x}_3^{(0)}\,,\\
\hat{p}_2 &= \frac{1}{\sqrt{3}}\mathrm{e}^{-r_1}\hat{p}_1^{(0)} - \frac{1}{\sqrt{6}}\mathrm{e}^{+r_2}\hat{p}_2^{(0)} + \frac{1}{\sqrt{2}}\mathrm{e}^{+r_3}\hat{p}_3^{(0)}\,,\\
\hat{x}_3 &= \frac{1}{\sqrt{3}}\mathrm{e}^{+r_1}\hat{x}_1^{(0)} - \frac{1}{\sqrt{6}}\mathrm{e}^{-r_2}\hat{x}_2^{(0)} - \frac{1}{\sqrt{2}}\mathrm{e}^{-r_3}\hat{x}_3^{(0)}\,,\\
\hat{p}_3 &= \frac{1}{\sqrt{3}}\mathrm{e}^{-r_1}\hat{p}_1^{(0)} - \frac{1}{\sqrt{6}}\mathrm{e}^{+r_2}\hat{p}_2^{(0)} - \frac{1}{\sqrt{2}}\mathrm{e}^{+r_3}\hat{p}_3^{(0)}\,.
\end{aligned}
\tag{3.85}
$$

Here, a superscript (0) denotes initial vacuum modes, and r_1, r_2, and r_3 are the squeezing parameters. In addition to the finite squeezing, the inevitable losses in the experiment further degrade the entanglement. It is important to stabilize the relative phase of the three input modes in order to properly adjust the squeezing directions. The phase fluctuations in this stabilization lead to an extra degradation of the entanglement. As a result, the output state does not necessarily exhibit genuine tripartite entanglement: it may be fully or partially separable. Therefore, we need to experimentally verify the full inseparability of the state.

A feasible scheme for this purpose is to check the following set of inequalities [165] (see Section 3.2.1.2):

$$\begin{aligned}
&\text{I.} \quad \left\langle \left[\Delta(\hat{x}_1 - \hat{x}_2)\right]^2 \right\rangle + \left\langle \left[\Delta(\hat{p}_1 + \hat{p}_2 + g_3\hat{p}_3)\right]^2 \right\rangle \geq 1 \,, \\
&\text{II.} \quad \left\langle \left[\Delta(\hat{x}_2 - \hat{x}_3)\right]^2 \right\rangle + \left\langle \left[\Delta(g_1\hat{p}_1 + \hat{p}_2 + \hat{p}_3)\right]^2 \right\rangle \geq 1 \,, \\
&\text{III.} \quad \left\langle \left[\Delta(\hat{x}_3 - \hat{x}_1)\right]^2 \right\rangle + \left\langle \left[\Delta(\hat{p}_1 + g_2\hat{p}_2 + \hat{p}_3)\right]^2 \right\rangle \geq 1 \,.
\end{aligned} \tag{3.86}$$

Here, the g_i are arbitrary real parameters. Note that the variances of the vacuum state are $\langle(\Delta\hat{x}_i^{(0)})^2\rangle = \langle(\Delta\hat{p}_i^{(0)})^2\rangle = 1/4$.

The violation of inequality I. is a sufficient condition for the inseparability of modes 1 and 2, and is a criterion for the success of a quantum protocol between parties 1 and 2. Note that inequality I. alone does not impose any restriction on the separability of mode 3 from the others. In other words, the success of a quantum protocol between parties 1 and 2 with the help of party 3 (by conveying classical information about a measurement of $\hat{p}_3$ [161]) does not prove the inseparability of the third party from the rest. Thus, we need to check the violation of at least two of the three inequalities Eq. (3.86) to verify the full inseparability of the tripartite entangled state.

From Eq. (3.85), we find that the optimum gain g_i^{opt} to minimize the l.h.s. of the inequalities in Eq. (3.86) depends on the squeezing parameters, namely,

$$g_i^{\text{opt}} = \frac{\mathrm{e}^{+2r_2} - \mathrm{e}^{-2r_1}}{\mathrm{e}^{+2r_2} + \frac{1}{2}\mathrm{e}^{-2r_1}} \,, \tag{3.87}$$

where $r_2 = r_3$ (which makes the three-mode state totally symmetric and hence g_i^{opt} independent of i). In the case of infinite squeezing (CV GHZ state), the optimum gain g_i^{opt} is one, while it is less than one for finite squeezing. Although the smallest values of the l.h.s. of the inequalities in Eq. (3.86) are observed when we experimentally adjust g_i^{opt}, Aoki *et al.* employed $g_i = 1$ for all i [188]. This makes the experimental verification simpler. Moreover, the measured variances then directly correspond to those of the eigenvalues of the ideal CV GHZ state. Figure 3.23 shows the schematic of the experimental setup to generate three independent squeezed vacuum states [188].

Figure 3.24 shows the noise-power measurement results on output mode 1 as an example of noise-power measurements on each output mode. The minimum noise of 1.14 ± 0.25 dB compared to the corresponding vacuum noise level is observed for the x quadrature, while the maximum noise of 4.69 ± 0.26 dB is observed for the p quadrature. Similarly, the minimum noise of 0.75 ± 0.27 and 1.21 ± 0.29 dB for the x quadrature and the maximum noise of 4.12 ± 0.27 and 4.69 ± 0.21 dB for p are observed for output modes 2 and 3, respectively.

The variances of the relative positions and the total momentum are measured to check the inequalities in Eq. (3.86). Figure 3.25a shows the schematic of the

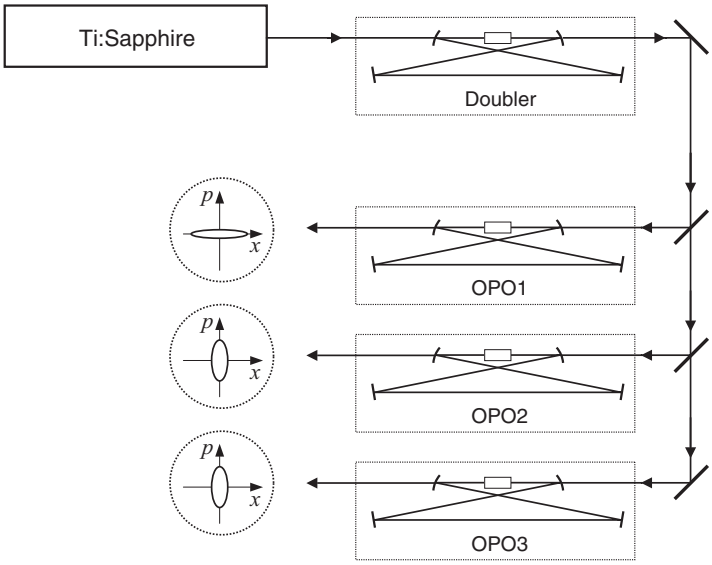

Figure 3.23 Schematic of the generation of three independent squeezed vacuum states [188].

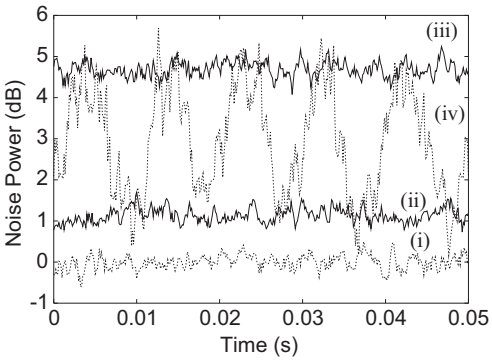

Figure 3.24 Noise measurement results on output mode 1 alone [188]. (i) represents the corresponding vacuum noise $\langle(\Delta\hat{x}_1^{(0)})^2\rangle = 1/4$; (ii) the noise of the x quadrature $\langle(\Delta\hat{x}_1)^2\rangle$; (iii) the noise of the p quadrature $\langle(\Delta\hat{p}_1)^2\rangle$; (iv) the noise of the scanned phase. The measurement frequency is centered at 900 kHz, resolution bandwidth is 30 kHz, video bandwidth is 300 Hz. Except for (iv) traces are averaged ten times.

measurement of the variances $\langle[\Delta(\hat{x}_1 - \hat{x}_2)]^2\rangle$ and $\langle[\Delta(\hat{x}_2 - \hat{x}_3)]^2\rangle$. The outputs of the homodyne detection are electronically subtracted, and the noise power is measured by spectrum analyzers. The variance $\langle[\Delta(\hat{x}_3 - \hat{x}_1)]^2\rangle$ is measured in a similar manner. In the case of the variance $\langle[\Delta(\hat{p}_1 + \hat{p}_2 + \hat{p}_3)]^2\rangle$, the noise power of the electronical sum of the homodyne detection outputs is measured as shown in Figure 3.25b.

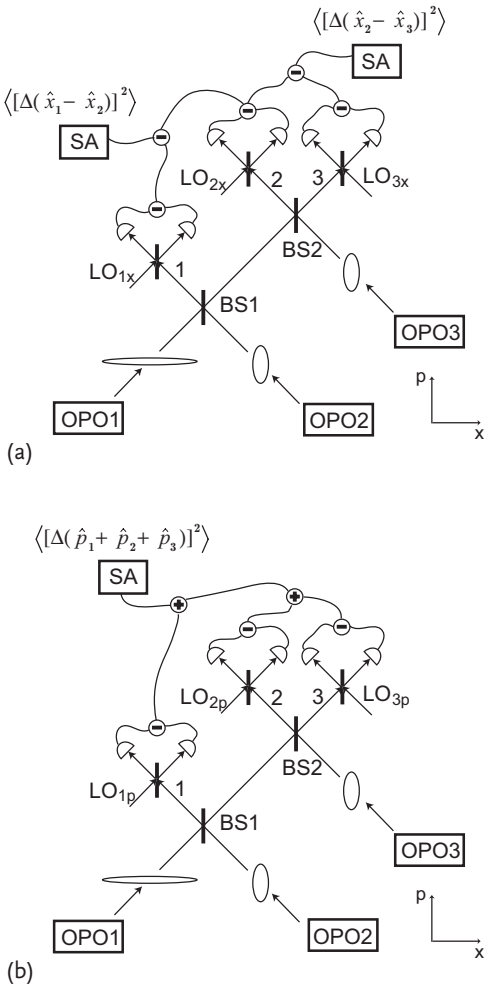

Figure 3.25 Schematic of the measurements of the variances (a) $\langle[\Delta(\hat{x}_1 - \hat{x}_2)]^2\rangle$ and $\langle[\Delta(\hat{x}_2 - \hat{x}_3)]^2\rangle$ and (b) $\langle[\Delta(\hat{p}_1 + \hat{p}_2 + \hat{p}_3)]^2\rangle$. BS1 and BS2 are beam splitters with t/r ratios of 1/2 and 1/1, respectively [188]. The ellipses illustrate the squeezed quadrature of each beam. $LO_{ix,p}$ denote local oscillator beams for homodyne detector i with their phases locked at the x and p quadratures, respectively.

Figure 3.26 shows a series of measurement results of (a) $\langle[\Delta(\hat{x}_1 - \hat{x}_2)]^2\rangle$, (b) $\langle[\Delta(\hat{x}_2 - \hat{x}_3)]^2\rangle$, (c) $\langle[\Delta(\hat{x}_3 - \hat{x}_1)]^2\rangle$, and (d) $\langle[\Delta(\hat{p}_1 + \hat{p}_2 + \hat{p}_3)]^2\rangle$, which have the average noise power of −1.95, −2.04, −1.78, and −1.75 dB, respectively, compared to the corresponding vacuum noise level. These results clearly show the nonclassical correlations among the three modes. After repeating the measurement series

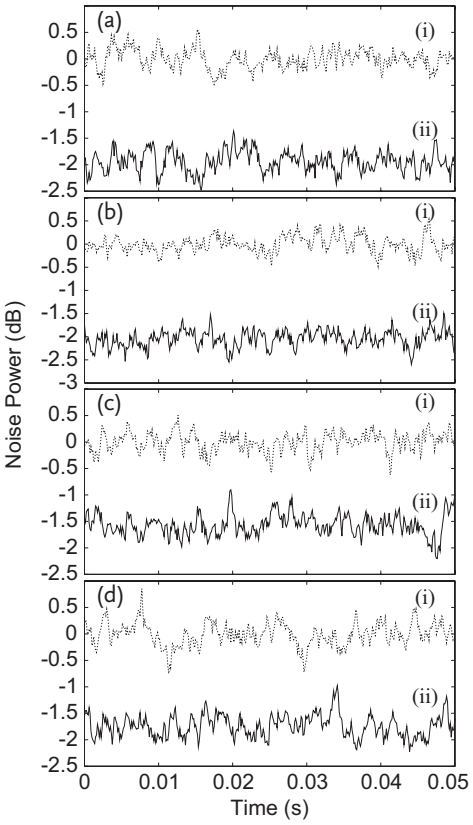

Figure 3.26 Noise measurement results corresponding to the variances of the l.h.s. of Eq. (3.86) [188]. (a) (i) is $\langle[\Delta(\hat{x}_1^{(0)} - \hat{x}_2^{(0)})]^2\rangle = 1/2$ and (ii) is $\langle[\Delta(\hat{x}_1 - \hat{x}_2)]^2\rangle$; (b) (i) $\langle[\Delta(\hat{x}_2^{(0)} - \hat{x}_3^{(0)})]^2\rangle = 1/2$ and (ii) $\langle[\Delta(\hat{x}_2 - \hat{x}_3)]^2\rangle$; (c) (i) $\langle[\Delta(\hat{x}_3^{(0)} - \hat{x}_1^{(0)})]^2\rangle = 1/2$ and (ii) $\langle[\Delta(\hat{x}_3 - \hat{x}_1)]^2\rangle$; (d) (i) $\langle[\Delta(\hat{p}_1^{(0)} + \hat{p}_2^{(0)} + \hat{p}_3^{(0)})]^2\rangle = 3/4$ and (ii) $\langle[\Delta(\hat{p}_1 + \hat{p}_2 + \hat{p}_3)]^2\rangle$. The measurement conditions are the same as for Figure 3.24 with ten times averages.

ten times, the following values are measured for the l.h.s. of Eq. (3.86),

$$\begin{aligned}
&\text{I.} \quad \left\langle\left[\Delta(\hat{x}_1 - \hat{x}_2)\right]^2\right\rangle + \left\langle\left[\Delta(\hat{p}_1 + \hat{p}_2 + \hat{p}_3)\right]^2\right\rangle \\
&\qquad = 0.851 \pm 0.062 < 1\,, \\
&\text{II.} \quad \left\langle\left[\Delta(\hat{x}_2 - \hat{x}_3)\right]^2\right\rangle + \left\langle\left[\Delta(\hat{p}_1 + \hat{p}_2 + \hat{p}_3)\right]^2\right\rangle \\
&\qquad = 0.840 \pm 0.065 < 1\,, \\
&\text{III.} \quad \left\langle\left[\Delta(\hat{x}_3 - \hat{x}_1)\right]^2\right\rangle + \left\langle\left[\Delta(\hat{p}_1 + \hat{p}_2 + \hat{p}_3)\right]^2\right\rangle \\
&\qquad = 0.867 \pm 0.062 < 1\,.
\end{aligned} \tag{3.88}$$

Since violations of all the inequalities are shown, the full inseparability of the generated tripartite entangled state is proved.

3.2.3.4 Cluster-Type States

Similar to GHZ states, one can create CV cluster states with squeezed vacua and beam splitters. In this section, we explain the creation of four-mode cluster states in detail according to the experiment of Yukawa *et al.* [189].

The quadrature correlations of cluster-type states are such that in the limit of infinite squeezing, the states become zero eigenstates of a set of quadrature combinations,

$$\left(\hat{p}_a - \sum_{b\in N_a} \hat{x}_b\right) \to 0 \,, \quad \forall a \in G \,, \tag{3.89}$$

as explained in Section 3.2.2.

A possible way to obtain CV cluster states is to entangle a corresponding number of optical modes, each initially in a squeezed state through quantum nondemolition, in analogy to the creation of qubit cluster states via controlled sign gates. We may refer to this specific type of cluster states as canonical cluster states [169]. Experimentally, the optical CV QND gates for every single link of the cluster state can be realized with two beam splitters and two on-line squeezers [89] for each link. Alternatively, the initial squeezing transformations can be absorbed into the entire QND network; after Bloch–Messiah reduction [89], only off-line squeezed states and linear optics are effectively needed to produce a canonical cluster state [169].

In another approach for building CV cluster-type states from squeezed light using linear optics [169], the beam splitter network is carefully chosen such that, by construction, all antisqueezing components are completely eliminated in the output operator combinations, $\hat{p}_a - \Sigma_{b\in N_a}\hat{x}_b$; hence, these combinations, being proportional to the squeezing factor, $\hat{p}_a - \Sigma_{b\in N_a}\hat{x}_b \propto \mathrm{e}^{-r}$, automatically satisfy the conditions of Eq. (3.89) in the limit of infinite squeezing $r \to \infty$. Moreover, generating cluster-type states in this way requires smaller degrees of input squeezing than needed for making the canonical states with the same quality of correlations [169].

The complete removal of antisqueezing components is particularly beneficial, as in the actual experiment, the antisqueezing levels are typically greater than the squeezing levels due to experimental imperfections such as losses and fluctuations in the phase locking. By employing the above-mentioned method for eliminating the antisqueezing components in the experiment being explained here, we can observe that the single-mode squeezing levels of the input states before the generation of the cluster states are effectively reproduced in the multi-mode squeezing levels of the resulting cluster states. This is in contrast to the experiments of [190, 191], where the antisqueezing components are not completely suppressed. Another advantage of the approach here is that the resulting quadrature correlations are precisely those occurring in the excess noise terms when quantum information propagates through a CV Gaussian cluster state [171]. Suppressing this excess noise efficiently means reducing the errors in cluster-based quantum computations.

According to the efficient method proposed in [169], Yukawa *et al.* created three kinds of four-mode CV cluster states in this experiment, including a linear cluster state, a square cluster state, and a T-shape cluster state (see Figure 3.27) [189].

In general, four-mode CV graph states can be built from four off-line squeezed states using up to six beam splitters [121, 169]. For the linear four-mode cluster state, three beam splitters have been shown to be sufficient [169]. Similarly, only three beam splitters are needed to produce the square and the T-shape cluster states. The optical setups are illustrated in detail below.

In order to create these cluster states, four p-squeezed states with mode operators $\hat{a}_i = \mathrm{e}^{+r_i}\hat{x}_i^{(0)} + \mathrm{i}\mathrm{e}^{-r_i}\hat{p}_i^{(0)} (i = 1,\ldots,4)$ are prepared first. A superscript (0) denotes initial vacuum modes and r_i is the squeezing parameter of the ith mode. For a unitary matrix U representing a sequence of beam splitters, the output mode operators $\hat{a}'_i$ can be obtained according to $\hat{a}'_i = \Sigma_j U_{ij}\hat{a}_j$.

A possible solution for the matrix U_L giving the linear cluster state is [169]

$$U_\mathrm{L} = \begin{pmatrix} \frac{1}{\sqrt{2}} & \frac{1}{\sqrt{10}} & \frac{2\mathrm{i}}{\sqrt{10}} & 0 \\ \frac{\mathrm{i}}{\sqrt{2}} & -\frac{\mathrm{i}}{\sqrt{10}} & \frac{2}{\sqrt{10}} & 0 \\ 0 & -\frac{2}{\sqrt{10}} & \frac{\mathrm{i}}{\sqrt{10}} & \frac{\mathrm{i}}{\sqrt{2}} \\ 0 & -\frac{2\mathrm{i}}{\sqrt{10}} & -\frac{1}{\sqrt{10}} & \frac{1}{\sqrt{2}} \end{pmatrix}. \tag{3.90}$$

With this matrix, the quadrature quantum correlations of the output state become

$$\begin{aligned} \hat{p}_{\mathrm{L}1} - \hat{x}_{\mathrm{L}2} &= \sqrt{2}\mathrm{e}^{-r_1}\hat{p}_1^{(0)}, \\ \hat{p}_{\mathrm{L}2} - \hat{x}_{\mathrm{L}1} - \hat{x}_{\mathrm{L}3} &= \sqrt{\frac{5}{2}}\mathrm{e}^{-r_3}\hat{p}_3^{(0)} + \frac{1}{\sqrt{2}}\mathrm{e}^{-r_4}\hat{p}_4^{(0)}, \\ \hat{p}_{\mathrm{L}3} - \hat{x}_{\mathrm{L}2} - \hat{x}_{\mathrm{L}4} &= \frac{1}{\sqrt{2}}\mathrm{e}^{-r_1}\hat{p}_1^{(0)} - \sqrt{\frac{5}{2}}\mathrm{e}^{-r_2}\hat{p}_2^{(0)}, \\ \hat{p}_{\mathrm{L}4} - \hat{x}_{\mathrm{L}3} &= \sqrt{2}\mathrm{e}^{-r_4}\hat{p}_4^{(0)}. \end{aligned} \tag{3.91}$$

All these linear combinations are proportional to the squeezing factors approaching zero in the limit of infinite squeezing. Hence, the output state is a linear four-mode cluster state in agreement with Eq. (3.89).

The matrix U_L can be decomposed into $U_\mathrm{L} = F_4 S_{12} F_1^\dagger B_{34}^+(1/\sqrt{2}) B_{21}^+(1/\sqrt{2}) \times B_{23}^-(1/\sqrt{5}) F_3 F_4$. Here, F_k denotes the Fourier transform (90° rotation in phase space) of mode k, $\hat{a}_k \to \mathrm{i}\hat{a}_k$. $B_{ij}^\pm(t)$ corresponds to a beam splitter transformation of modes i and j with transmittance parameter t; it is equivalent to the four-mode

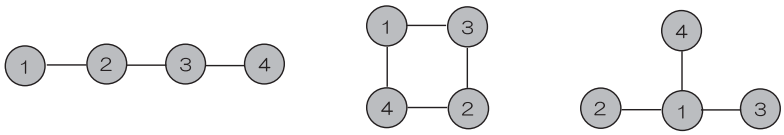

Figure 3.27 The created four-mode cluster states. Each cluster node, corresponding to an optical mode, is represented by a circle. Neighboring nodes are connected by lines.

identity matrix except for $(B_{ij}^{\pm})_{ii} = t$, $(B_{ij}^{\pm})_{ij} = \sqrt{1-t^2}$, $(B_{ij}^{\pm})_{ji} = \pm\sqrt{1-t^2}$ and $(B_{ij}^{\pm})_{jj} = \mp t$. S_{ij} is the swapping operation of modes i and j. As a result, two symmetric beam splitters and one 1 : 4 beam splitter can be used.

Let us now consider the square cluster state. A possible solution for the unitary matrix U_S is

$$U_S = \begin{pmatrix} -\frac{1}{\sqrt{2}} & -\frac{1}{\sqrt{10}} & -\frac{2i}{\sqrt{10}} & 0 \\ \frac{1}{\sqrt{2}} & -\frac{1}{\sqrt{10}} & -\frac{2i}{\sqrt{10}} & 0 \\ 0 & -\frac{2i}{\sqrt{10}} & -\frac{1}{\sqrt{10}} & -\frac{1}{\sqrt{2}} \\ 0 & -\frac{2i}{\sqrt{10}} & -\frac{1}{\sqrt{10}} & \frac{1}{\sqrt{2}} \end{pmatrix}. \tag{3.92}$$

The correlations of the output state are

$$\begin{aligned} \hat{p}_{S1} - \hat{x}_{S3} - \hat{x}_{S4} &= -\frac{1}{\sqrt{2}} e^{-r_1} \hat{p}_1^{(0)} - \sqrt{\frac{5}{2}} e^{-r_2} \hat{p}_2^{(0)}, \\ \hat{p}_{S2} - \hat{x}_{S3} - \hat{x}_{S4} &= \frac{1}{\sqrt{2}} e^{-r_1} \hat{p}_1^{(0)} - \sqrt{\frac{5}{2}} e^{-r_2} \hat{p}_2^{(0)}, \\ \hat{p}_{S3} - \hat{x}_{S1} - \hat{x}_{S2} &= -\sqrt{\frac{5}{2}} e^{-r_3} \hat{p}_3^{(0)} - \frac{1}{\sqrt{2}} e^{-r_4} \hat{p}_4^{(0)}, \\ \hat{p}_{S4} - \hat{x}_{S1} - \hat{x}_{S2} &= -\sqrt{\frac{5}{2}} e^{-r_3} \hat{p}_3^{(0)} + \frac{1}{\sqrt{2}} e^{-r_4} \hat{p}_4^{(0)}, \end{aligned} \tag{3.93}$$

all of which approach zero in the limit of infinite squeezing.

We find that the matrix U_S is equal to $U_{add} U_L$, with $U_{add} = \mathrm{diag}(-1, -i, i, 1)$. Thus, the square cluster state can be obtained from the linear cluster state via local Fourier transforms. In the experiment, the local Fourier transforms can be easily achieved by changing the locking phase of the local oscillator beams. Therefore, the optical setup for the square cluster state is more or less identical to that for the linear cluster state. Using the identities, $\hat{p}_{S1} - \hat{x}_{S3} - \hat{x}_{S4} = -\hat{p}_{L1} + \hat{p}_{L3} - \hat{x}_{L4}$, $\hat{p}_{S2} - \hat{x}_{S3} - \hat{x}_{S4} = -\hat{x}_{L2} + \hat{p}_{L3} - \hat{x}_{L4}$, $\hat{p}_{S3} - \hat{x}_{S1} - \hat{x}_{S2} = \hat{x}_{L1} - \hat{p}_{L2} + \hat{x}_{L3}$, $\hat{p}_{S4} - \hat{x}_{S1} - \hat{x}_{S2} = \hat{x}_{L1} - \hat{p}_{L2} + \hat{p}_{L4}$, the measurement of the correlations of the linear cluster state and the square cluster state can be performed in a single experiment.

Finally, the T-shape cluster state can be obtained from four p-squeezed states followed by a unitary transform,

$$U_T = \begin{pmatrix} \frac{i}{\sqrt{2}} & \frac{1}{2} & \frac{i}{2} & 0 \\ \frac{1}{\sqrt{2}} & \frac{i}{2} & -\frac{1}{2} & 0 \\ 0 & \frac{i}{2} & \frac{1}{2} & \frac{1}{\sqrt{2}} \\ 0 & \frac{i}{2} & \frac{1}{2} & -\frac{1}{\sqrt{2}} \end{pmatrix}. \tag{3.94}$$

This can also be decomposed into $U_T = F_1^{\dagger} B_{34}^{+}(1/\sqrt{2}) B_{21}^{+}(1/\sqrt{2}) B_{32}^{-}(1/\sqrt{2}) F_2$. Thus, this time, the optical setup has to be modified, but three beam splitters are

still sufficient. The quantum correlations of the output state are

$$\begin{aligned}
\hat{p}_{\mathrm{T}1} - \hat{x}_{\mathrm{T}2} - \hat{x}_{\mathrm{T}3} - \hat{x}_{\mathrm{T}4} &= 2\mathrm{e}^{-r_2}\hat{p}_2^{(0)}\,, \\
\hat{p}_{\mathrm{T}2} - \hat{x}_{\mathrm{T}1} &= \sqrt{2}\mathrm{e}^{-r_1}\hat{p}_1^{(0)}\,, \\
\hat{p}_{\mathrm{T}3} - \hat{x}_{\mathrm{T}1} &= \frac{1}{\sqrt{2}}\mathrm{e}^{-r_2}\hat{p}_2^{(0)} + \mathrm{e}^{-r_3}\hat{p}_3^{(0)} + \frac{1}{\sqrt{2}}\mathrm{e}^{-r_4}\hat{p}_4^{(0)}\,, \\
\hat{p}_{\mathrm{T}4} - \hat{x}_{\mathrm{T}1} &= \frac{1}{\sqrt{2}}\mathrm{e}^{-r_2}\hat{p}_2^{(0)} + \mathrm{e}^{-r_3}\hat{p}_3^{(0)} - \frac{1}{\sqrt{2}}\mathrm{e}^{-r_4}\hat{p}_4^{(0)}\,.
\end{aligned} \tag{3.95}$$

They all approach zero in the limit of infinite squeezing. Hence, the output state is a T-shape cluster state according to Eq. (3.89). Note that up to local Fourier transforms, the T-shape cluster state is equivalent to a four-mode GHZ-type state [161].

From here, we explain the experimental implementation in detail. The schematic of the optical setups is shown in Figure 3.28 [189]. They used a continuous-wave Ti:sapphire laser (Coherent MBR110, $\lambda = 860\,\mathrm{nm}$) as a light source. In order to

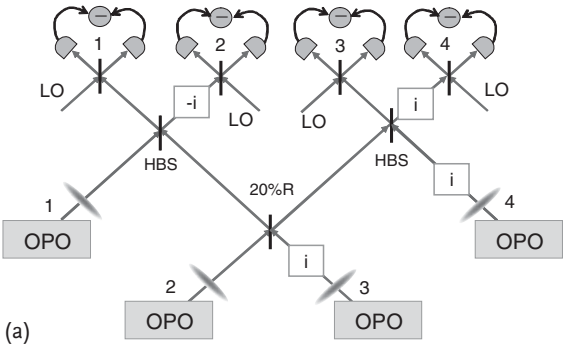

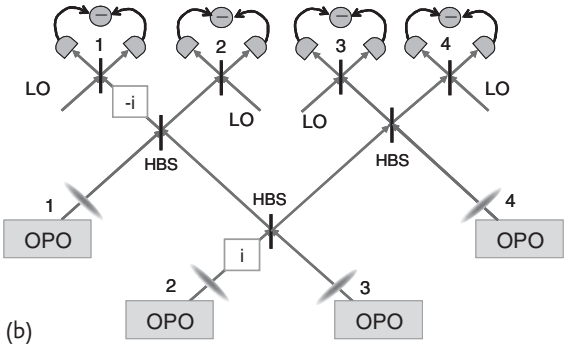

Figure 3.28 The schematic of the optical setups to create the linear cluster state (a) and T-shape cluster state (b) [189]. Four squeezed states are generated by OPOs (optical parametric oscillators). HBS is half beam splitter and 20% is 1 : 4 beam splitter. Boxes including i are Fourier transforms (90° rotations in phase space), and −i is a −90° rotation. LO is local oscillator for homodyne detection of the output states.

generate squeezed states, optical parametric oscillators (OPOs) were used via optical degenerate parametric downconversion. Periodically poled $KTiOPO_4$ (PPKTP) crystals were employed as nonlinear optical media. Each OPO is pumped by a second harmonic beam obtained from a cavity which contains a potassium niobate ($KNbO_3$) crystal for second harmonic generation. The pump powers ranged from 76 to 96 mW.

Weak coherent beams are also injected into the OPOs and the emitted beams are set to 2 μW. On each beam, phase modulations are applied for locking, with 140 kHz for OPO2, 210 kHz for OPO3, and 98 kHz for OPO1 and OPO4. In this experiment, a 1 MHz sideband is chosen for the measurements so the phase modulations do not affect these measurements.

An output state is measured via homodyne detection with a strong beam around 5mW used as a local oscillator. The homodyne detector gives a voltage signal of the measurement result. After electronically combining the outputs of the homodyne detectors, the signals of the correlations can be obtained. The signals are sent to a spectrum analyzer in order to get the measurement data.

Figures 3.29 and 3.30 show the results of the measurements. Theoretically, the correlations should be proportional to the squeezing levels. Every graph shows the results with squeezing and without squeezing. For the linear cluster state and the square cluster state, $\langle[\Delta(\hat{p}_{L1} - \hat{x}_{L2})]^2\rangle = -5.4 \pm 0.2$ dB, $\langle[\Delta(\hat{p}_{L2} - \hat{x}_{L1} - \hat{x}_{L3})]^2\rangle = \langle[\Delta(\hat{p}_{S3} - \hat{x}_{S1} - \hat{x}_{S2})]^2\rangle = -5.8 \pm 0.2$ dB, $\langle[\Delta(\hat{p}_{L3} - \hat{x}_{L2} - \hat{x}_{L4})]^2\rangle = \langle[\Delta(\hat{p}_{S2} - \hat{x}_{S3} - \hat{x}_{S4})]^2\rangle = -5.3 \pm 0.2$ dB, $\langle[\Delta(\hat{p}_{L4} - \hat{x}_{L3})]^2\rangle = -5.8 \pm 0.2$ dB, $\langle[\Delta(\hat{p}_{S1} - \hat{x}_{S3} - \hat{x}_{S4})]^2\rangle = -5.2 \pm 0.2$ dB, $\langle[\Delta(\hat{p}_{S4} - \hat{x}_{S1} - \hat{x}_{S2})]^2\rangle = -5.9 \pm 0.2$ dB are obtained. We point out again that only six measurements are sufficient to detect the eight correlations of these two states.

For the T-shape cluster state, the results of the measurements are $\langle[\Delta(\hat{p}_{T1} - \hat{x}_{T2} - \hat{x}_{T3} - \hat{x}_{T4})]^2\rangle = -6.0 \pm 0.2$ dB, $\langle[\Delta(\hat{p}_{T2} - \hat{x}_{T1})]^2\rangle = -5.2 \pm 0.2$ dB, $\langle[\Delta(\hat{p}_{T3} - \hat{x}_{T1})]^2\rangle = -4.9 \pm 0.2$ dB and $\langle[\Delta(\hat{p}_{T4} - \hat{x}_{T1})]^2\rangle = -5.2 \pm 0.2$ dB.

Various ways for constructing multi-party entanglement witnesses (i.e., observables for detecting the presence of multi-party entanglement) are known in the regime of CV multi-mode states [165, 192]. We employ the method of [165] using a set of sufficient conditions for the full inseparability of a multi-mode state which can be easily tested with our experimental results. The corresponding inequalities to be satisfied are shown below. Recall that if the linear cluster state is confirmed to be fully inseparable, the full inseparability of the square cluster state is verified at the same time as the square and linear cluster states are locally equivalent up to local Fourier transforms. For the linear cluster state, we obtain

$$\begin{aligned}
\left\langle\left[\Delta(\hat{p}_{L1} - \hat{x}_{L2})\right]^2\right\rangle + \left\langle\left[\Delta(\hat{p}_{L2} - \hat{x}_{L1} - \hat{x}_{L3})\right]^2\right\rangle < 1\,, \\
\left\langle\left[\Delta(\hat{p}_{L3} - \hat{x}_{L2} - \hat{x}_{L4})\right]^2\right\rangle + \left\langle\left[\Delta(\hat{p}_{L2} - \hat{x}_{L1} - \hat{x}_{L3})\right]^2\right\rangle < 1\,, \\
\left\langle\left[\Delta(\hat{p}_{L3} - \hat{x}_{L2} - \hat{x}_{L4})\right]^2\right\rangle + \left\langle\left[\Delta(\hat{p}_{L4} - \hat{x}_{L3})\right]^2\right\rangle < 1\,.
\end{aligned} \tag{3.96}$$

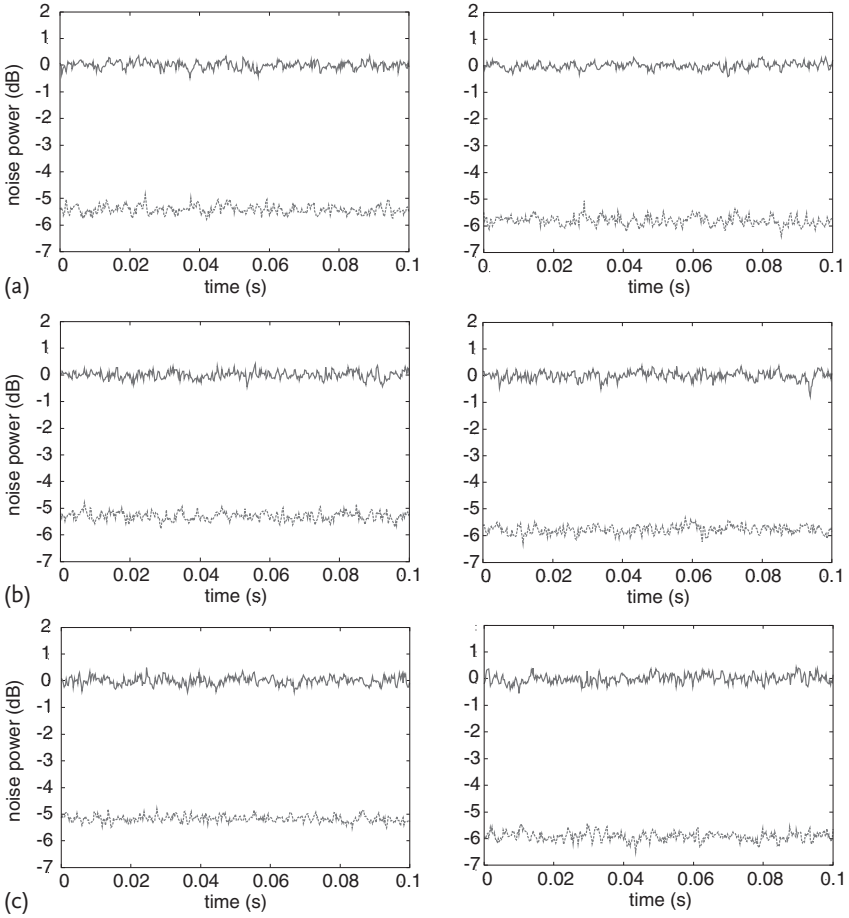

Figure 3.29 In all graphs, the measurement variances without squeezing (a) and with squeezing (c) are shown [189]. The graphs in (a) are the results of $\langle[\Delta(\hat{p}_{L1} - \hat{x}_{L2})]^2\rangle$ and $\langle[\Delta(\hat{p}_{L2} - \hat{x}_{L1} - \hat{x}_{L3})]^2\rangle = \langle[\Delta(\hat{p}_{S3} - \hat{x}_{S1} - \hat{x}_{S2})]^2\rangle$. The ones in (b) are for $\langle[\Delta(\hat{p}_{L3} - \hat{x}_{L2} - \hat{x}_{L4})]^2\rangle = \langle[\Delta(\hat{p}_{S2} - \hat{x}_{S3} - \hat{x}_{S4})]^2\rangle$ and $\langle[\Delta(\hat{p}_{L4} - \hat{x}_{L3})]^2\rangle$. The ones in (c) are for $\langle[\Delta(\hat{p}_{S1} - \hat{x}_{S3} - \hat{x}_{S4})]^2\rangle$ and $\langle[\Delta(\hat{p}_{S4} - \hat{x}_{S1} - \hat{x}_{S2})]^2\rangle$. The measurement frequency is 1 MHz, resolution bandwidth is 30 kHz, and video bandwidth is 300 Hz. All results are obtained with 20 times averaging.

For the T-shape cluster state, we have

$$\begin{aligned}
&\left\langle\left[\Delta(\hat{p}_{T2} - \hat{x}_{T1})\right]^2\right\rangle + \left\langle\left[\Delta(\hat{p}_{T1} - \hat{x}_{T2} - \hat{x}_{T3} - \hat{x}_{T4})\right]^2\right\rangle < 1\,, \\
&\left\langle\left[\Delta(\hat{p}_{T3} - \hat{x}_{T1})\right]^2\right\rangle + \left\langle\left[\Delta(\hat{p}_{T1} - \hat{x}_{T2} - \hat{x}_{T3} - \hat{x}_{T4})\right]^2\right\rangle < 1\,, \\
&\left\langle\left[\Delta(\hat{p}_{T4} - \hat{x}_{T1})\right]^2\right\rangle + \left\langle\left[\Delta(\hat{p}_{T1} - \hat{x}_{T2} - \hat{x}_{T3} - \hat{x}_{T4})\right]^2\right\rangle < 1\,.
\end{aligned} \tag{3.97}$$

Note that the variances of a vacuum state are $\langle[\Delta\hat{x}_{vac}]^2\rangle = \langle[\Delta\hat{p}_{vac}]^2\rangle = 1/4$.

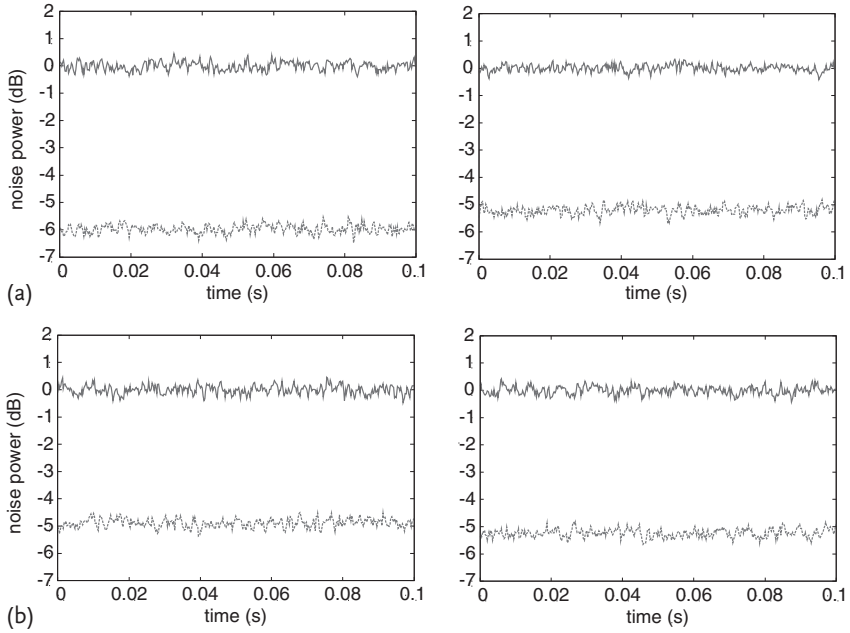

Figure 3.30 The graphs in (a) $\langle[\Delta(\hat{p}_{T1} - \hat{x}_{T2} - \hat{x}_{T3} - \hat{x}_{T4})]^2\rangle$ and $\langle[\Delta(\hat{p}_{T2} - \hat{x}_{T1})]^2\rangle$. The graphs in (b) $\langle[\Delta(\hat{p}_{T3} - \hat{x}_{T1})]^2\rangle$ and $\langle[\Delta(\hat{p}_{T4} - \hat{x}_{T1})]^2\rangle$. The conditions of the measurements are the same as in Figure 3.29.

The values of the left-hand sides of the inequalities are 0.34 ± 0.02, 0.42 ± 0.02, and 0.35 ± 0.02 for Eq. (3.96), respectively, and 0.42 ± 0.02, 0.43 ± 0.02, and 0.42 ± 0.02 for Eq. (3.97), respectively. Thus, all inequalities are simultaneously satisfied and hence the full inseparability of the created cluster states is verified [165].

Besides confirming the inseparability of the cluster states, Yukawa *et al.* also verified that the measured correlations correspond to the squeezing levels of the input states [189]. It is possible to detect the squeezing levels by removing the beam splitters. The measured squeezing levels range from -5.5 to -6.3 dB and the antisqueezing levels are between $+9.1$ and $+11.9$ dB. After removing the beam splitters needed for generating the cluster states, the signal at this stage of the experiment is free of fluctuations in phase locking. Therefore, the squeezing levels are slightly better than the measured correlations. Nonetheless, these results demonstrate the efficient generation of the desired quadrature quantum correlations through cancellation of all antisqueezing components of the light fields involved.

4
Quantum Teleportation

In this chapter, we will describe various experiments in detail in which photonic quantum states encoded into qubits or qumodes were teleported using optical resources of entanglement. In Section 1.6, we introduced the concept of quantum teleportation and specific protocols for it in the DV and CV regime. In this case, ideally, the input states will be transferred from the sender to the receiver with unit fidelity. Quantum state manipulation is not wanted in standard quantum teleportation, only quantum state transfer as faithfully as possible.

The teleportation experiments described here include, respectively for qubits and qumodes, quantum teleportation of a qubit and a coherent state from one sender to one receiver (Sections 4.1.1 and 4.2.1) and from one sender to two receivers involving an approximate form of quantum state cloning (Sections 4.1.2 and 4.2.2); quantum teleportation of halves of entangled states, so-called entanglement swapping (Sections 4.1.3 and 4.2.4); and for qumodes, in Section 4.2.3, we will describe an experiment of a quantum teleportation network which achieves the nonclassical transfer of coherent states between any two parties in a small network of three nodes and participants.

In these experiments, all or at least one or two of the following three criteria were fulfilled:

1. An "unknown" quantum state enters the sending station for teleportation.
2. A teleported state emerges from the receiving station for subsequent evaluation or exploitation.
3. The degree of overlap between the input and the teleported states is higher than that which could be achieved if the sending and the receiving stations were linked only by a classical channel.

Especially, the third criterion becomes important in a realistic experimental situation when the entangled resource and the quantum operations are not ideal as it is the case, for instance, in CV quantum teleportation using imperfect squeezed-light resources. In contrast, in the DV quantum teleportation experiments, most subtle are the first two criteria. In this case, since typically some form of postselection is employed, the physical occurrence of actual input and output states to the teleporter is not automatically guaranteed.

Quantum Teleportation and Entanglement. Akira Furusawa, Peter van Loock
Copyright © 2011 WILEY-VCH Verlag GmbH & Co. KGaA, Weinheim
ISBN: 978-3-527-40930-3

4.1 Qubit Quantum Teleportation

As we explained in Section 1.6, through DV quantum teleportation, an arbitrary, unknown qubit state can be transferred using shared entanglement and classical communication. If instead, without using shared entanglement, Alice and Bob attempted to transfer the qubit state, Alice would have to measure the state in order to gain as much information as possible and to convey this classical information to Bob who would eventually prepare a quantum state according to that information. This classical teleportation of an unknown qubit state achieves a fidelity of $F = 2/3$ at most. This value represents the boundary between classical and quantum teleportation when unknown qubit states are to be transmitted [193]. Let us now discuss various qubit teleportation experiments.

4.1.1 Experiment: Qubit Quantum Teleportation

One of the most famous experiments of qubit teleportation was performed by Bouwmeester *et al.* [194]. In this section, we shall explain it in detail.

Figure 4.1 shows the scheme of qubit teleportation as done by Bouwmeester *et al.* [194]. First, Alice and Bob share a polarization entangled photon pair,

$$|\Psi^{(-)}\rangle = \frac{1}{\sqrt{2}}\left(|\leftrightarrow\rangle_{\mathrm{A}} \otimes |\updownarrow\rangle_{\mathrm{B}} - |\updownarrow\rangle_{\mathrm{A}} \otimes |\leftrightarrow\rangle_{\mathrm{B}}\right), \tag{4.1}$$

which can be created by the method shown in Section 3.1.3.1.

Alice now performs a Bell measurement on the input $c_0|\leftrightarrow\rangle_{\mathrm{in}} + c_1|\updownarrow\rangle_{\mathrm{in}}$ and her entangled photon. This Bell measurement can be understood from the following decomposition (recall Section 1.6),

$$\begin{aligned}
&(c_0|\leftrightarrow\rangle_{\mathrm{in}} + c_1|\updownarrow\rangle_{\mathrm{in}}) \otimes \left|\Psi^{(-)}\right\rangle_{\mathrm{AB}} \\
&= \frac{1}{2}\Big[\left|\Psi^{(-)}\right\rangle_{\mathrm{inA}} \otimes (-c_0\,|\leftrightarrow\rangle_{\mathrm{B}} - c_1\,|\updownarrow\rangle_{\mathrm{B}}) \\
&\quad + \left|\Psi^{(+)}\right\rangle_{\mathrm{inA}} \otimes (-c_0\,|\leftrightarrow\rangle_{\mathrm{B}} + c_1\,|\updownarrow\rangle_{\mathrm{B}}) \\
&\quad + \left|\Phi^{(-)}\right\rangle_{\mathrm{inA}} \otimes (c_0\,|\updownarrow\rangle_{\mathrm{B}} + c_1\,|\leftrightarrow\rangle_{\mathrm{B}}) \\
&\quad + \left|\Phi^{(+)}\right\rangle_{\mathrm{inA}} \otimes (c_0\,|\updownarrow\rangle_{\mathrm{B}} - c_1\,|\leftrightarrow\rangle_{\mathrm{B}})\Big],
\end{aligned} \tag{4.2}$$

where $|\Psi^{(\pm)}\rangle$ and $|\Phi^{(\pm)}\rangle$ are the Bell states defined in Eq. (3.19).

In the experiment of Bouwmeester *et al.*, only the case of $|\Psi^{(-)}\rangle_{\mathrm{inA}}$ can be detected. This is because their scheme of Bell measurement corresponds to simultaneous detection of photons at detectors f1 and f2 as follows.

Simultaneous detection of photons at detectors f1 and f2 may be represented by $\langle 0|\hat{a}^{j}_{\mathrm{f1}}\hat{a}^{k}_{\mathrm{f2}}$ [195], where $j, k = \leftrightarrow, \updownarrow$ and,

$$\hat{a}^{j}_{\mathrm{f1}} = \frac{1}{\sqrt{2}}\left(\hat{a}^{j}_{\mathrm{in}} + \hat{a}^{j}_{\mathrm{A}}\right), \quad \hat{a}^{j}_{\mathrm{f2}} = \frac{1}{\sqrt{2}}\left(\hat{a}^{j}_{\mathrm{in}} - \hat{a}^{j}_{\mathrm{A}}\right). \tag{4.3}$$

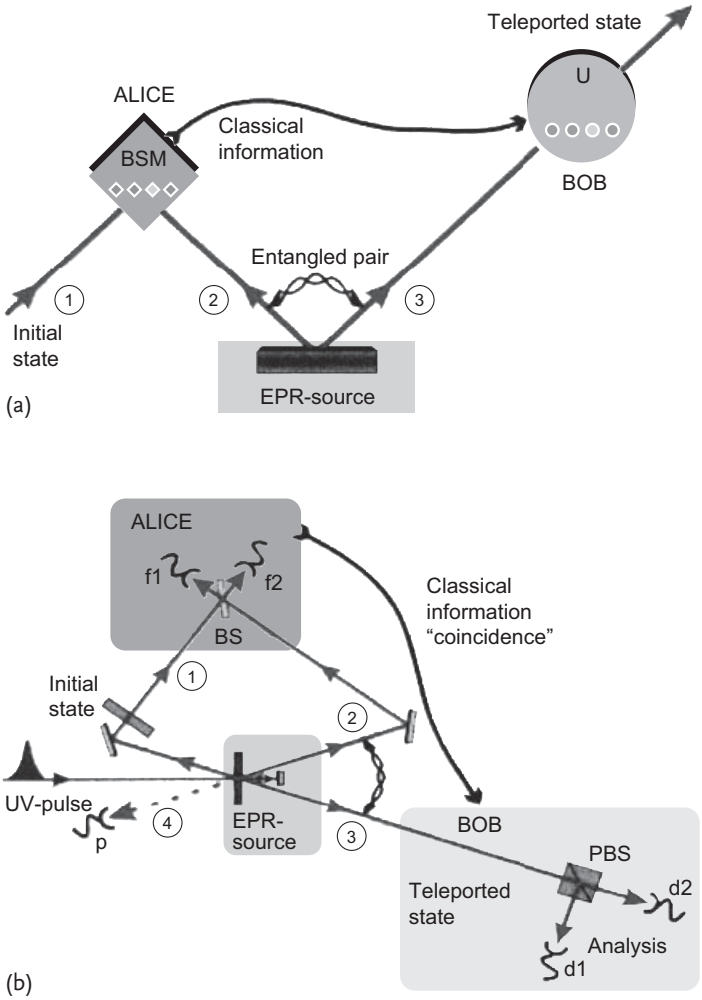

Figure 4.1 Scheme of qubit quantum teleportation demonstrated by Bouwmeester *et al.* [194]. (a) the concept, (b) the experimental setup.

Here, the relations of Eq. (4.3) come from a half beam splitter at Alice. Therefore, $\langle 0|\hat{a}_{\mathrm{f1}}^{j}\hat{a}_{\mathrm{f2}}^{k}$ becomes

$$\langle 0|\hat{a}_{\mathrm{f1}}^{j}\hat{a}_{\mathrm{f2}}^{k} = \frac{1}{2}\langle 0|\left(\hat{a}_{\mathrm{in}}^{j}\hat{a}_{\mathrm{in}}^{k} + \hat{a}_{\mathrm{A}}^{j}\hat{a}_{\mathrm{in}}^{k} - \hat{a}_{\mathrm{in}}^{j}\hat{a}_{\mathrm{A}}^{k} - \hat{a}_{\mathrm{A}}^{j}\hat{a}_{\mathrm{A}}^{k}\right) . \tag{4.4}$$

If we neglect the probability of two photons in the input and Alice's mode, we can omit $\hat{a}_{\mathrm{in}}^{j}\hat{a}_{\mathrm{in}}^{k}$ and $\hat{a}_{\mathrm{A}}^{j}\hat{a}_{\mathrm{A}}^{k}$ in Eq. (4.4). Thus, the final expression of $\langle 0|\hat{a}_{\mathrm{f1}}^{j}\hat{a}_{\mathrm{f2}}^{k}$ becomes

$$\langle 0|\,\hat{a}_{\mathrm{f1}}^{j}\hat{a}_{\mathrm{f2}}^{k} = \begin{cases} \pm\frac{1}{\sqrt{2}}\,{}_{\mathrm{inA}}\langle\Psi^{(-)}| & j \neq k \\ 0 & j = k\,. \end{cases} \tag{4.5}$$

From this consideration, simultaneous detection of photons at detectors f1 and f2 is physically equivalent to projection onto $|\Psi^{(-)}\rangle_{\mathrm{inA}}$.

With the scheme of Bell measurement, one can detect the case of $|\Psi^{(-)}\rangle_{\mathrm{inA}}$ in Eq. (4.2). So when detectors f1 and f2 have simultaneous "clicks", the overall state of the input and an entangled photon pair of Alice and Bob in Eq. (4.2) shrinks into

$$\begin{aligned} &|\Psi^{(-)}\rangle_{\mathrm{inA}} \otimes (-c_0|\leftrightarrow\rangle_{\mathrm{B}} - c_1|\updownarrow\rangle_{\mathrm{B}}) \\ &= -|\Psi^{(-)}\rangle_{\mathrm{inA}} \otimes (c_0|\leftrightarrow\rangle_{\mathrm{B}} + c_1|\updownarrow\rangle_{\mathrm{B}}) . \end{aligned} \tag{4.6}$$

Since we can neglect overall phase, Bob can recover the input state at his place (mode).

Note that this scheme depends on post-selection and only the case of $|\Psi^{(-)}\rangle_{\mathrm{inA}}$ can be determined from the four Bell states $|\Psi^{(\pm)}\rangle_{\mathrm{inA}}$ and $|\Phi^{(\pm)}\rangle_{\mathrm{inA}}$. This means that 3/4 of events are discarded and so the success probability is 1/4.[1)]

Figure 4.2 shows the experimental results for teleportation of $(|\leftrightarrow\rangle_{\mathrm{in}} + |\updownarrow\rangle_{\mathrm{in}})/\sqrt{2}$ and $|\updownarrow\rangle_{\mathrm{in}}$ demonstrated by Bouwmeester *et al.* [194]. It was checked with four-fold coincidence of detection of photons at detector p, f1, f2, and d1 (d2), where "click" at detector p shows the existence of input photon, simultaneous "clicks" at detectors f1 and f2 correspond to projection onto $|\Psi^{(-)}\rangle_{\mathrm{inA}}$, and "click" at detector d1

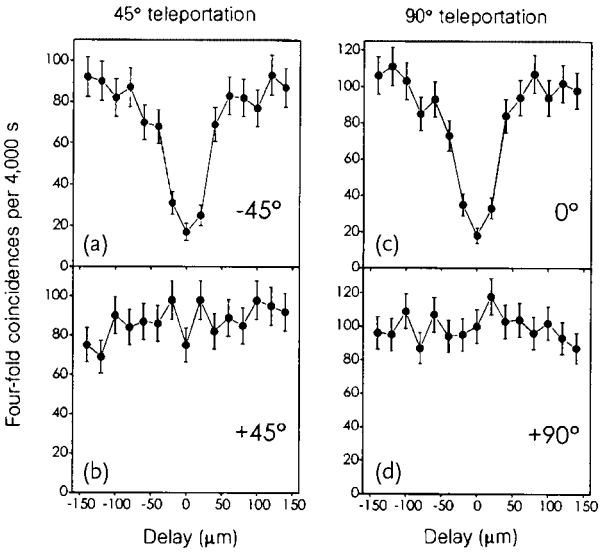

Figure 4.2 Experimental results of qubit quantum teleportation demonstrated by Bouwmeester *et al.* [194]. They checked four-fold coincidence of detection of photons at detector p, f1, f2, and d1 (d2). (a) and (b) reflect the case of 45° input $((1/\sqrt{2})(|\leftrightarrow\rangle_{\mathrm{in}}+|\updownarrow\rangle_{\mathrm{in}}))$, (c) and (d) reflect the case of 90° input $(|\updownarrow\rangle_{\mathrm{in}})$. (a) and (c) are the reference experiments.

1) Which is only half as big as the maximal success probability of 1/2 for a Bell measurement using linear optics without ancilla photons and feedforward [196] (see Chapter 2).

(d2) shows the proper output. Thus, four-fold coincidences around zero delay in Figure 4.2 mean the success of teleportation (Figure 4.2a and c are references).

Braunstein and Kimble pointed out the disadvantage of this scheme [197]. It comes from the indistinguishability between a single photon and two photons in the input using an on-off detector without resolving photon numbers. In the case of two photons in the input, simultaneous detection of photons at detectors p, f1 and f2 occurs as the case of success of teleportation without entangled photons of Alice and Bob. It is because we cannot neglect $\hat{a}_{\mathrm{in}}^{j}\hat{a}_{\mathrm{in}}^{k}$ in Eq. (4.4) and then simultaneous detection of photons at detectors f1 and f2 no longer means projection onto $|\Psi^{(-)}\rangle_{\mathrm{inA}}$. Therefore, one must detect a photon at the output (detector d1 or d2) to verify the success of teleportation. In other words, four-fold coincidence is a necessary condition here for the success of teleportation. However, in the teleportation scheme described here, a survival and a potentially further exploitation of the teleported state by avoiding post-selection is possible when photon-number resolving detectors are used.

4.1.2 Experiment: Qubit Telecloning

Telecloning is a generalized version of teleportation where n senders send the same quantum information to m receivers (n-to-m telecloning) [198]. Since the no-cloning theorem [14, 15] prohibits the receivers to have perfect clones of the input state, the clones are approximate ones which have higher fidelities to the original than the classical limit [25]. Although complete telecloning for qubits is not realized so far, "partial" telecloning is proposed by Filip [199] and demonstrated by Zhao *et al.* [200]. In this section, we will explain the experiment in detail. Again, this is also a post-selection experiment with polarization qubits (single photons).

Figure 4.3 shows the proposed scheme of "partial" telecloning by Filip [199] which was actually proposed as "partial teleportation". Zhao *et al.* used an anticlone in Figure 4.3 as a trigger, and demonstrated the "partial" telecloning with the scheme shown in Figure 4.4 [200]. In these schemes, an input is cloned to two, one is a local clone and the other is distant one (teleclone). In any case, the scheme is very similar to the one for qubit teleportation explained in the previous section. The only difference is that a half beam splitter for Alice's Bell measurement in Figure 4.1 is replaced by an asymmetrical (unbalanced) beam splitter as shown in Figures 4.3 and 4.4.

Figure 4.5 shows the experimental setup of "partial" telecloning demonstrated by Zhao *et al.* [200]. In Figure 4.5, an asymmetric beam splitter is realized by a Mach–Zehnder interferometer [201].

The asymmetric beam splitter transforms modes b and c to modes e and f as follows,[2)]

$$b \to t \cdot e + \mathrm{i}r \cdot f\,, \quad c \to \mathrm{i}r \cdot e + t \cdot f\,, \tag{4.7}$$

2) Here, we drop the hats on annihilation operators and use "mode" and "mode operator" synonymously.

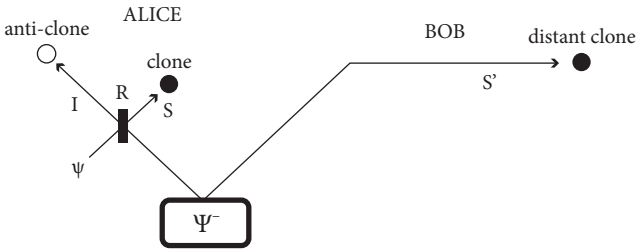

Figure 4.3 Proposed scheme of "partial" telecloning as partial teleportation by Filip [199]. S, S' are clones, I is an anti-clone. R: reflectivity of beam splitter.

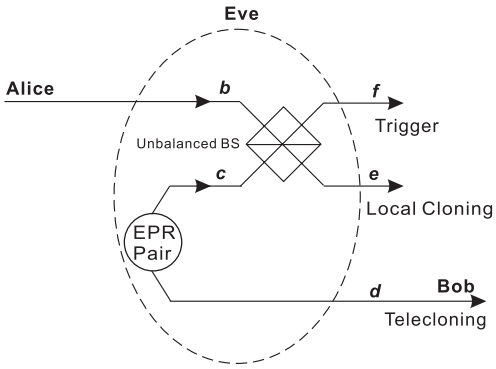

Figure 4.4 Experimental scheme of "partial" telecloning demonstrated by Zhao *et al.* [200].

where $R = r^2$, $1-R = t^2$, and R is the reflectivity of the asymmetric beam splitter. If an input to the cloner is in the state $|\psi\rangle = \alpha|\updownarrow\rangle + \beta|\leftrightarrow\rangle$ and the outputs from the asymmetric beam are single photons in modes e and f, the overall state $|\Psi\rangle_{\rm all}$ can be written as follows [199],

$$\begin{aligned}|\Psi\rangle_{\rm all} = {} & \alpha(1-2R)|\updownarrow\rangle_e|\updownarrow\rangle_f|\leftrightarrow\rangle_d - \beta(1-2R)|\leftrightarrow\rangle_e|\leftrightarrow\rangle_f|\updownarrow\rangle_d \\ & - \alpha(1-R)|\updownarrow\rangle_e|\leftrightarrow\rangle_f|\updownarrow\rangle_d + \alpha R|\leftrightarrow\rangle_e|\updownarrow\rangle_f|\updownarrow\rangle_d \\ & + \beta(1-R)|\leftrightarrow\rangle_e|\updownarrow\rangle_f|\leftrightarrow\rangle_d - \beta R|\updownarrow\rangle_e|\leftrightarrow\rangle_f|\leftrightarrow\rangle_d\,, \end{aligned} \tag{4.8}$$

where modes c and d are originally in the entangled state $|\Psi^{(-)}\rangle_{cd}$ defined in Eq. (3.19).

When detectors D_2 and D_4 detect photons as $|\leftrightarrow\rangle_f|\updownarrow\rangle_d$, the state of mode e becomes $\alpha(1-R)|\updownarrow\rangle_e + \beta(1-2R)|\leftrightarrow\rangle_e$, whose fidelity to the input $|\psi\rangle = \alpha|\updownarrow\rangle + \beta|\leftrightarrow\rangle$ is [199],

$$F_{\rm local\ clone} = \frac{1}{2P(R)}\left[(1-2R)^2 + (1-R)^2\right], \tag{4.9}$$

where $P(R) = 1-3R+3R^2$. Similarly, when detectors D_2 and D_4 detect photons as $|\updownarrow\rangle_f|\leftrightarrow\rangle_d$, the state of mode e (local clone) becomes $\alpha(1-2R)|\updownarrow\rangle_e + \beta(1-R)|\leftrightarrow\rangle_e$, whose fidelity is the same as Eq. (4.9).

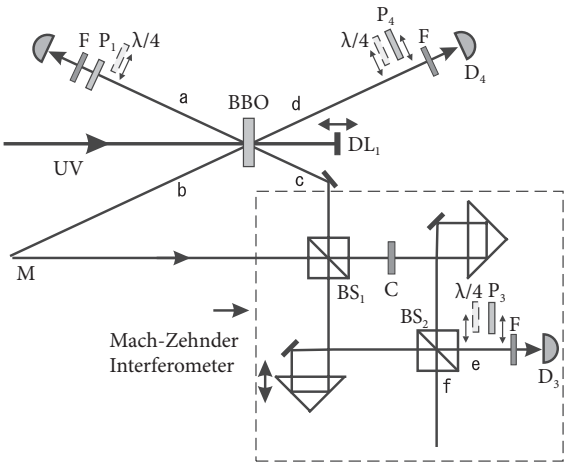

Figure 4.5 Experimental setup of "partial" telecloning demonstrated by Zhao *et al.* [200]. P: polarizer, F: bandpath filter, DL: delay line, BBO: second-order nonlinear crystal (beta-barium borate), BS: beam splitter, D: photon detector, $\lambda/4$: quarter wave plate. The Mach–Zehnder interferometer acts as a variable beam splitter. C is compensator to equalize the path length of orthogonal polarizations.

When detectors D_2 and D_3 detect photons as $|\updownarrow\rangle_e|\leftrightarrow\rangle_f$, the state of mode d (distant clone or teleclone) becomes $\alpha(1-R)|\updownarrow\rangle_d - \beta R|\leftrightarrow\rangle_d$, whose fidelity to the input $|\psi\rangle = \alpha|\updownarrow\rangle + \beta|\leftrightarrow\rangle$ is [199]

$$F_{\text{teleclone}} = \frac{1}{2P(R)}\left[R^2 + (1-R)^2\right]. \tag{4.10}$$

Similarly, when detectors D_2 and D_3 detect photons as $|\leftrightarrow\rangle_e|\updownarrow\rangle_f$, the state of mode d (distant clone or teleclone) becomes $\alpha R|\updownarrow\rangle_d + \beta(1-R)|\leftrightarrow\rangle_d$, whose fidelity is the same as in Eq. (4.10).

Here, classical limit of the fidelity for one-to-two cloning is 2/3. From Eqs. (4.9) and (4.10), one can obtain the fidelity of 5/6 for both clones with $R = 1/3$, which is higher than the classical limit and thus shows the success of "partial" telecloning.

Zhao *et al.* checked the fidelities as a function of reflectivity R of the asymmetric beam splitter as shown in Figure 4.6. Theoretical curves are calculated by Eqs. (4.9) and (4.10). The experimental results agree well with the theoretical prediction and show the higher fidelities than the classical limit of 2/3 with $R = 1/3$. Thus "partial" telecloning is successfully demonstrated.

4.1.3
Experiment: Qubit Entanglement Swapping

With post-selection illustrated in the previous sections, entanglement swapping – teleportation of entanglement – can be performed for polarization qubits. Pan *et al.* implemented this for the first time [202]. Here, we will explain their experiment in detail.

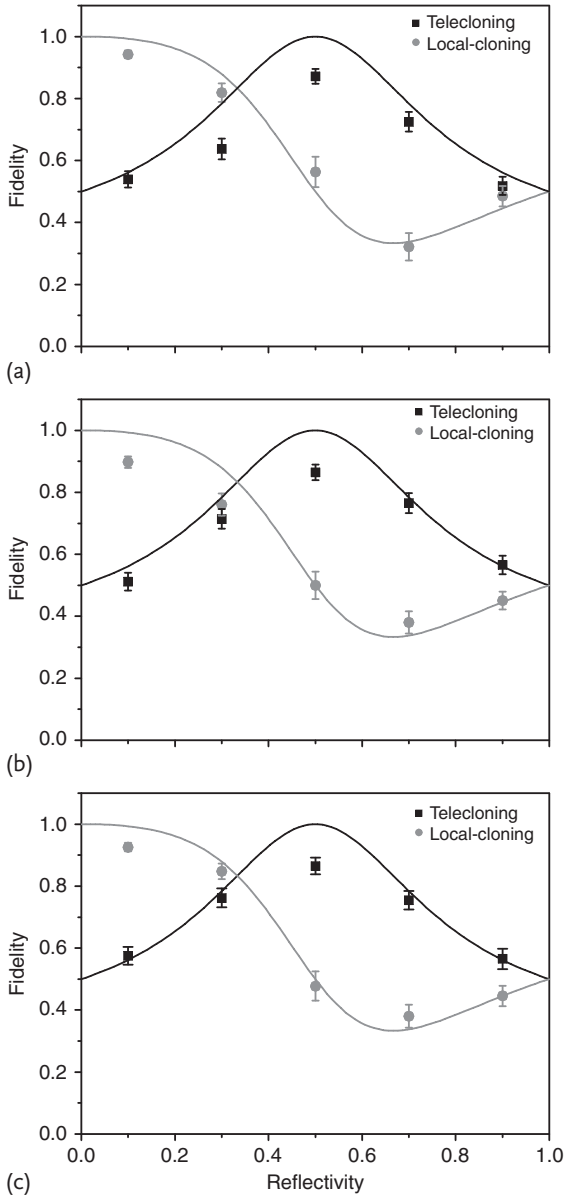

Figure 4.6 Experimental fidelities of local and telecloning as a function of the reflectivity R of the asymmetric beam splitter [200]. Polarization angle of polarizers P_1, P_3, and P_4 are 0° (a), $+45^\circ$ (b), and circularly polarized with a quarter wave plate (c). Theoretical curves are calculated by Eqs. (4.9) and (4.10).

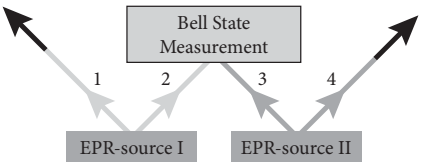

Figure 4.7 Principle of entanglement swapping [202]. Two EPR sources produce two pairs of entangled photons, pair 1–2 and pair 3–4. One photon from each pair (photons 2 and 3) is subjected to a Bell measurement. This results in projecting the other two outgoing photons 1 and 4 onto an entangled state.

Figure 4.7 shows the principle of entanglement swapping [202]. First, two EPR sources each simultaneously emit a pair of entangled photons, pair 1–2 and pair 3–4. The overall state of photons 1–4 $|\Psi\rangle_{1234}$ is represented as follows:

$$\begin{aligned} |\Psi\rangle_{1234} &= \left|\Psi^{(-)}\right\rangle_{12} \otimes \left|\Psi^{(-)}\right\rangle_{34} \\ &= \frac{1}{2}\left(|\leftrightarrow\rangle_1|\updownarrow\rangle_2 - |\updownarrow\rangle_1|\leftrightarrow\rangle_2\right) \otimes \left(|\leftrightarrow\rangle_3|\updownarrow\rangle_4 - |\updownarrow\rangle_3|\leftrightarrow\rangle_4\right), \end{aligned} \tag{4.11}$$

with $|\Psi^{(-)}\rangle$ from Eq. (3.19). Next, a Bell measurement is performed on photons 2 and 3. After the Bell measurement, photons 2 and 3 are projected onto one of the four Bell states $|\Psi^{(\pm)}\rangle$ and $|\Phi^{(\pm)}\rangle$ described in Eq. (3.19), and the overall state $|\Psi\rangle_{1234}$ gets "rearranged" to

$$\begin{aligned} |\Psi\rangle_{1234} = \frac{1}{2}\Big(&\left|\Psi^{(+)}\right\rangle_{14}\left|\Psi^{(+)}\right\rangle_{23} + \left|\Psi^{(-)}\right\rangle_{14}\left|\Psi^{(-)}\right\rangle_{23} \\ &+ \left|\Phi^{(+)}\right\rangle_{14}\left|\Phi^{(+)}\right\rangle_{23} + \left|\Phi^{(-)}\right\rangle_{14}\left|\Phi^{(-)}\right\rangle_{23}\Big). \end{aligned} \tag{4.12}$$

When we know the result of Bell measurement, the overall state shrinks to one of the four cases as shown in Eq. (4.12). For example, in the case of $|\Psi^{(-)}\rangle_{23}$ obtained in the Bell measurement, the overall state shrinks to $|\Psi^{(-)}\rangle_{14}|\Psi^{(-)}\rangle_{23}$. In this state, photons 1 and 4 are entangled and photons 2 and 3 are entangled. The situation is similar for the other results of the Bell measurement, that means photons 1 and 4 are entangled and photons 2 and 3 are entangled in all cases. Thus, entanglements in 1–2 and 3–4 are swapped, and 1–4 and 2–3 become entangled.

Figure 4.8 shows the experimental setup of entanglement swapping demonstrated by Pan *et al.* [202], which is very similar to the one shown in Figure 4.1 [194]. EPR sources are the same ones illustrated in Section 3.1.3.1. The trick for the Bell measurement is the same as the one in teleportation, which is explained in Section 4.1.1. With this trick, one can detect only $|\Psi^{(-)}\rangle_{23}$ with simultaneous detection of photons at detectors D_2 and D_3. Moreover, as the case of the teleportation experiment by Bouwmeester *et al.* [194], simultaneous detection of four photons at detectors D_1–D_4 is the necessary condition for success of the experiment. To check the entanglement between photons 1 and 4, correlation measurement was performed by changing the polarizer angle Θ before detector D_4 in Figure 4.1.

Figure 4.9 shows the experimental results. Counting rates of four-fold coincidence are shown as a function of polarizer angle Θ before detector D_4. Since the

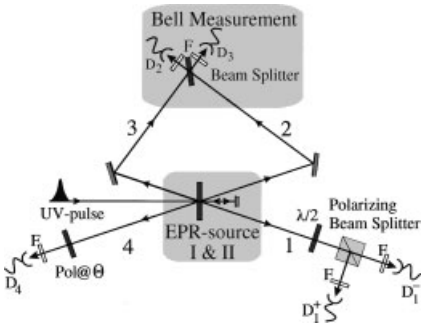

Figure 4.8 Experimental setup of entanglement swapping demonstrated by Pan *et al.* [202]. The half wave plate ($\lambda/2$) just before a polarization beam splitter was set at 22.5°. The polarizer angle before detector D_4 was scanned.

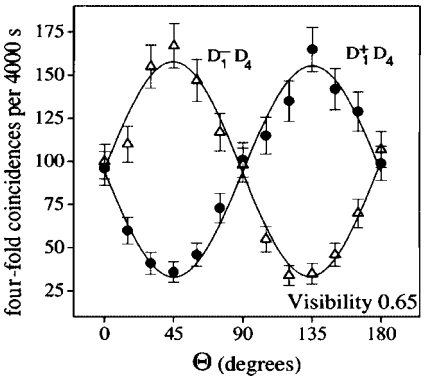

Figure 4.9 Results of the correlation measurement to check the entanglement between photons 1 and 4 [202].

angle of the half wave plate before the polarization beam splitter was set at 22.5°, detector D_1^+ detects a +45°-polarized photon and detector D_1^- detects a −45°-polarized photon. From Figure 4.9, we can clearly see the correlation between detectors D_1^+ and D_4 and between detectors D_1^- and D_4, which are the proof of $|\Psi^{(-)}\rangle$-type entanglement between photons 1 and 4. Since four-fold coincidence also guarantees $|\Psi^{(-)}\rangle_{23}$, we can conclude that the overall state is $|\Psi^{(-)}\rangle_{14}|\Psi^{(-)}\rangle_{23}$, meaning success of entanglement swapping.

4.2 Qumode Quantum Teleportation

By using an optical field, qumode quantum teleportation has been experimentally realized for Gaussian input states – a coherent state [177, 203–205], a squeezed state [206], and an EPR state, for so-called entanglement swapping [205, 207]. All

these experiments are based on the well-developed techniques of optical Gaussian operations consisting of beam splitter, phase shifting, and squeezing transformations as well as phase-space displacements and homodyne detection. Those CV quantum protocols implemented so far operated only with Gaussian states and operations. However, non-Gaussian states or non-Gaussian operations are needed to potentially achieve universal CV quantum information processing (see Chapters 6 and 7). Quantum teleportation of a non-Gaussian state would become the next important challenge (see Chapter 8).

In Section 1.6, we presented an idealized version of CV quantum teleportation using unphysical, infinitely squeezed states. In the following reports on experimental implementations of CV quantum teleportation, of course, a realistic, physical description must be employed. For this purpose, it is most convenient to use the Heisenberg representation for the quadrature operators. Alternative formalisms for CV quantum teleportation include using the Wigner [163] and the Fock representations [208, 209]. These are also both useful to describe quantum teleportation of non-Gaussian states (see Chapter 8).

Note that unlike the discussion in Section 1.6 on idealized CV quantum teleportation, Alice does gain partial information about the input state through her Bell measurement on the input state and one half of the finitely squeezed EPR state, and as a consequence, perfect state transfer is no longer achievable. Criteria in order to assess the nonclassicality of CV quantum teleportation were derived in [210–212].

4.2.1
Experiment: Qumode Quantum Teleportation

In this section, we first explain the CV teleportation experiment demonstrated by Furusawa *et al.* [203] in detail.

Figure 4.10 shows the experimental setup of CV teleportation demonstrated by Furusawa *et al.* [203]. First, Alice and Bob share the EPR beams that are created with the technique explained in Section 3.2.3.1 where two squeezed vacua with squeezing parameter r are combined at a half beam splitter. The state of the electromagnetic field to be teleported $(\hat{x}_{\text{in}}, \hat{p}_{\text{in}})$ is created by Victor, which for the experiment here, is more precisely a particular set of modulation sidebands (coherent state). The beam to be teleported is combined with Alice's EPR beam $(\hat{x}_{\text{A}}, \hat{p}_{\text{A}})$ by using a half beam splitter. This process creates states described by the quadrature amplitudes $(\hat{x}_u, \hat{p}_u)$ and $(\hat{x}_v, \hat{p}_v)$ where[3)]

$$\begin{aligned} \hat{x}_u &= \frac{1}{\sqrt{2}}\hat{x}_{\text{in}} - \frac{1}{\sqrt{2}}\hat{x}_{\text{A}}\,, \quad \hat{p}_u = \frac{1}{\sqrt{2}}\hat{p}_{\text{in}} - \frac{1}{\sqrt{2}}\hat{p}_{\text{A}}\,, \\ \hat{x}_v &= \frac{1}{\sqrt{2}}\hat{x}_{\text{in}} + \frac{1}{\sqrt{2}}\hat{x}_{\text{A}}\,, \quad \hat{p}_v = \frac{1}{\sqrt{2}}\hat{p}_{\text{in}} + \frac{1}{\sqrt{2}}\hat{p}_{\text{A}}\,. \end{aligned} \tag{4.13}$$

Alice measures both quadratures $\hat{x}_u$ and $\hat{p}_v$ using two homodyne detectors and obtains the classical results x_u and p_v. This measurement corresponds to a CV

3) Compared to Eq. (3.38), the number subscripts for the two EPR modes are replaced by "A" and "B", indicating that those beams are in Alice's and Bob's possession, respectively.

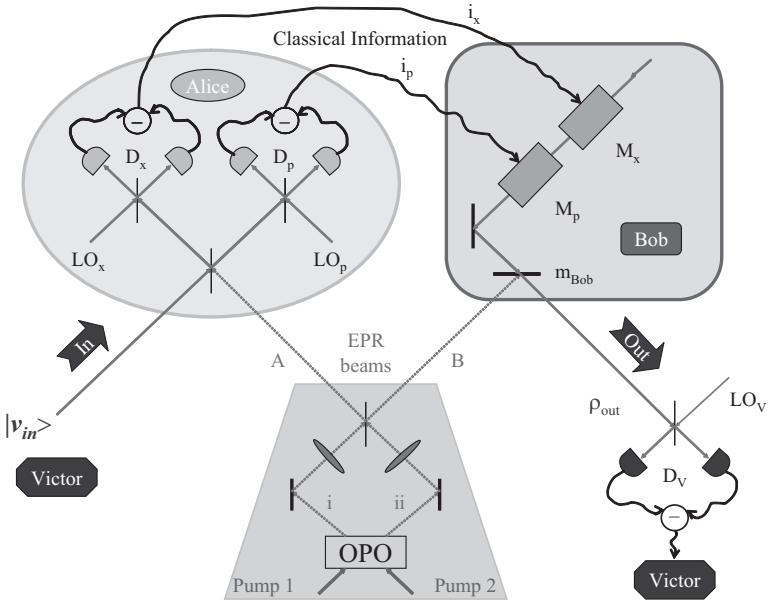

Figure 4.10 Experimental setup for continuous-variable quantum teleportation [203].

Bell-state measurement. In the ideal case ($r \to \infty$), Alice cannot gain any information on the input state because the amount of quantum noise $\sim e^{+2r}$ in $(\hat{x}_A, \hat{p}_A)$ will render the amplitude information of the state to be teleported inaccessible. If, by contrast, she attempted to directly measure both quadrature-phase amplitudes of the state to be teleported simultaneously without using shared entanglement, she may indeed gain partial information [213], and in this process, demolish the state.

Figure 4.11 shows the outputs of one of Alice's homodyne detectors. The horizontal axis corresponds to the phase of Alice's local oscillator θ_{Ax} which is being swept in time. The vertical axis $\Psi(\Omega)_x^{\text{Alice}}$ corresponds to spectral density of photocurrent fluctuations associated with the quadrature amplitude $\hat{x}_u(\Omega, \theta_{Ax})$ where the maxima in $\Psi(\Omega)_x^{\text{Alice}}$ give the power (relative to the vacuum state) for the amplitude $\hat{x}_u(\Omega, \theta_{Ax} = 0) \equiv \hat{x}_u(\Omega)$. In this experiment, Victor generates a coherent state which consists of a classical phase-space displacement and one unit of vacuum noise. The peak value in the periodic modulation of $\Psi(\Omega)_x^{\text{Alice}}$ in the figure corresponds to the power associated with $1/\sqrt{2}$ of the coherent displacement (-3 dB) which is 22 dB higher than the vacuum noise level in this particular case. The reduction by 3 dB arises because the intensity of the unknown state is reduced by half by the beam splitter for mixing the unknown state and Alice's EPR beam. The minima in the periodic variation of $\Psi(\Omega)_x^{\text{Alice}}$ are equivalent to the level of the corresponding flat trace Λ_x^{Alice} which is the quantum noise level with Alice's EPR beam present. The associated level without Alice's EPR beam is $\Phi_{0,x}^{\text{Alice}}$ (with a vacuum-state input). The figure shows the quantum noise level with her EPR

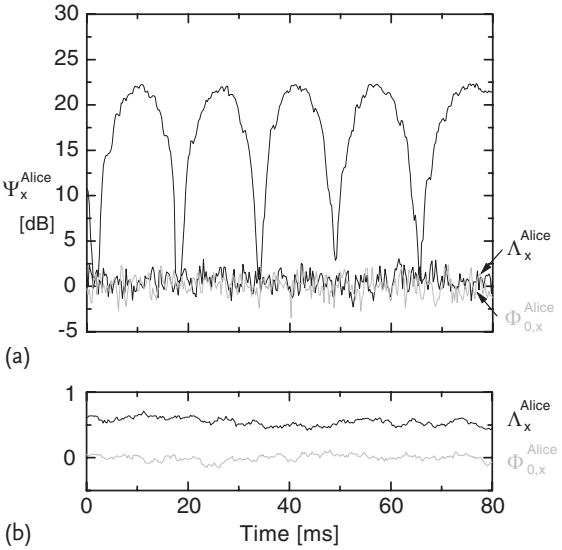

Figure 4.11 (a) Output of one of Alice's homodyne detectors (D_x). $\Omega/2\pi = 2.9$ MHz and $\Delta\Omega/2\pi = 30$ kHz. The part (b) is the expanded view with a ten-trace average for the input state which has no displacements, namely, vacuum state [203].

beam is higher than the level without her EPR beam, namely, $\Lambda_x^{\text{Alice}} > \Phi_{0,x}^{\text{Alice}}$, in correspondence to a loss of information by Alice for quantum teleportation. Note that the quantum noise level with her EPR beam would diverge in the ideal case ($r \to \infty$).

With Eqs. (4.13) and (3.38), for subscripts 1 $\to$ A and 2 $\to$ B, Bob's beam has [161],

$$\begin{aligned} \hat{x}_{\text{B}} &= \hat{x}_{\text{in}} - \sqrt{2}\text{e}^{-r}\hat{x}_{\text{B}}^{(0)} - \sqrt{2}\hat{x}_u \,, \\ \hat{p}_{\text{B}} &= \hat{p}_{\text{in}} + \sqrt{2}\text{e}^{-r}\hat{p}_{\text{A}}^{(0)} - \sqrt{2}\hat{p}_v \,. \end{aligned} \tag{4.14}$$

Alice's generalized Bell-state measurement results effectively in the quantum variables $\hat{x}_u$ and $\hat{p}_v$ being transformed into the classical variables x_u and p_v in the Eq. (4.14). When the quantum efficiency of the homodyne detectors (η) is less than unity, the x_u and p_v fluctuate under the influence of the invasion of vacuum noise. In this case, $\hat{x}_u$ and $\hat{p}_v$ in the Eq. (4.14) are replaced by $\eta\hat{x}_u + \sqrt{1-\eta^2}\hat{x}_u^{(0)}$ and $\eta\hat{p}_v + \sqrt{1-\eta^2}\hat{p}_v^{(0)}$, respectively, where $\hat{x}_u^{(0)}$ and $\hat{p}_v^{(0)}$ are the quadrature amplitudes of the respective invading vacua.

Alice sends the measurement results x_u and p_v to Bob. He uses this information to modulate a (coherent) light beam in both amplitude and phase, with some overall gain g [203]. This modulated beam is then combined coherently at the highly reflecting mirror m_{Bob} shown in Figure 4.10 to interfere with his component of the entangled EPR beam ($\hat{x}_{\text{B}}$, $\hat{p}_{\text{B}}$), thereby creating the teleported output state ($\hat{x}_{\text{tel}}$, $\hat{p}_{\text{tel}}$). This procedure corresponds to a simple phase-space displacement of

Bob's EPR beam as follows:

$$\hat{x}_{\text{tel}} = \hat{x}_{\text{B}} + g\sqrt{2}x_u \ ,$$
$$\hat{p}_{\text{tel}} = \hat{p}_{\text{B}} + g\sqrt{2}p_v \ . \tag{4.15}$$

In the absence of losses ($\eta = 1$) and for unity gain ($g = 1$), the quadrature operators associated with the teleported state become

$$\hat{x}_{\text{tel}} = \hat{x}_{\text{in}} - \sqrt{2}\text{e}^{-r}\hat{x}_{\text{B}}^{(0)} \ ,$$
$$\hat{p}_{\text{tel}} = \hat{p}_{\text{in}} + \sqrt{2}\text{e}^{-r}\hat{p}_{\text{A}}^{(0)} \ . \tag{4.16}$$

For $r \to \infty$, $\hat{x}_{\text{tel}} \to \hat{x}_{\text{in}}$, $\hat{p}_{\text{tel}} \to \hat{p}_{\text{in}}$, corresponding to perfect teleportation.

Of course, in an actual experiment, the gain g must be determined operationally. For the particular case of Figure 4.11, the displacement of the input coherent state determined by Alice's homodyne detectors (22 dB above the vacuum-state limit) corresponds to half of the input signal power. If Bob's output (as verified by Victor) carries twice the power specified by Alice's output (namely, 25 dB in the case at hand), the gain g is then determined to be unity, namely, 0 dB. Precisely speaking, the g should be corrected by the detection efficiency ζ associated with Alice's homodyne detection (propagation, homodyne efficiency, and detector quantum efficiency). However, since $\zeta \approx 0.97$ is almost unity in the experiment, the aforementioned procedure for fixing $g = 1$ (0 dB) can be used with small error.

In somewhat more global terms, the actual procedure for determining $g = 1$ (0 dB) is illustrated by Figure 4.12. This figure gives the variation of the coherent amplitude and of the variance with power gain g^2 without EPR beams. Since these two dependences are different and both agree with theory without adjustable parameters, we can conclude that the setup functions are in agreement with our simple model. When A_{out} is equal to A_{in} (here, $A_{\text{in}} = A_{\text{out}} = 21$ dB), we can determine $g = 1$. From the Figure 4.12, we can see $\sigma_{\text{W}} = 4.8$ dB for $g = 1$, whose meaning will be presented later.

Moving then to the case of teleportation in the presence of entangled EPR beams, Bob combines his modulated beam with his EPR beam and reconstructs the state to be teleported. In this process, the "noise" arising from the EPR beam is effectively "subtracted" from Bob's modulated beam by destructive interference at m_{Bob}.

Experimental results from this protocol are shown in Figure 4.13. The horizontal axis corresponds to the phase of Victor's local oscillator, which is being swept in time. The vertical axis Ψ^{Victor} corresponds to the spectral density of photocurrent fluctuations associated with the quadrature amplitudes $\hat{x}_{\text{tel}}(\Omega)$ and $\hat{p}_{\text{tel}}(\Omega)$ measured by Victor for a fixed (but arbitrary) phase for the input state. The maximum value of the periodic curve corresponds to a coherent amplitude for the output state approximately 25 dB above the vacuum-state level Φ_0^{Victor}; here, the gain has been set to be $g \approx 1$ as in the previous discussion. This result shows the classical phase-space displacement is successfully reconstructed.

The minima of the trace for Ψ^{Victor} correspond to the variance of the output state for the quadrature orthogonal to that of the coherent amplitude, and are

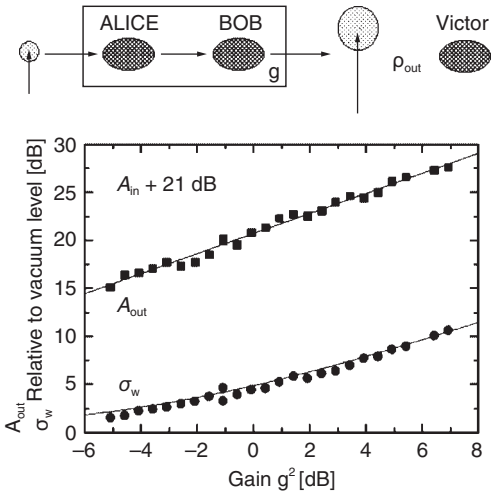

Figure 4.12 The variation of the coherent amplitude A_{out} and of the variance σ_W with gain g^2 without EPR beams. The input amplitude A_{in} is +21 dB above the vacuum-state limit in this particular case. The solid lines are the theoretical curves for $\zeta = 1$.

equivalent to the level Λ^{Victor} shown by the labeled flat trace. The various phase-independent traces in the figure correspond to the quantum noise levels with the EPR beams present for Alice and Bob (Λ^{Victor}), without these EPR beams at both locations (Υ_0^{Victor}), and with a vacuum-state input to Victor's homodyne detector (Φ_0^{Victor}). Of course, "without the EPR beams" means that vacuum noise ($r = 0$) invades Alice and Bob's stations, leading to a degradation of the "quality" of teleportation.

Indeed, for teleportation of coherent states in the absence of shared entanglement between Alice and Bob (no EPR beams), Eq. (4.16) shows that the quantum noise for Bob's output becomes three units of vacuum noise (in either quadrature, $\langle \Delta \hat{x}_{tel}^2 \rangle$, $\langle \Delta \hat{p}_{tel}^2 \rangle$). One unit comes from the original quantum noise of the input coherent state, and the other two units correspond to successive "quantum duties", the first being to cross the boundary from the quantum to classical world (Alice's attempt to detect both quadrature amplitudes) and the second from the classical to quantum (Bob's generation of a coherent displacement) [163]. The experimental result $\Upsilon_0^{Victor} \approx 4.8$ dB in correspondence to a factor of three above the vacuum-state limit in Figures 4.12 and 4.13 indicates almost perfect performance of the "classical" teleportation with near unity detection efficiency (recall $\zeta = 0.97$). As discussed in more detail in [210, 211], Υ_0^{Victor} is the limit of "classical" teleportation, where we explicitly mean teleportation without shared entanglement.

From Figure 4.13 and similar measurements, we determine that Λ^{Victor} lies 1.1 dB-lower than Υ_0^{Victor}. This means that quantum teleportation is successfully performed beyond the classical limit, as clarified by the following discussion. To quantify the "quality" of the teleportation for a pure state $|\psi_{in}\rangle$, we calculate the teleportation fidelity $F \equiv \langle \psi_{in} | \hat{\rho}_{out} | \psi_{in} \rangle$ [210, 211]. For the case of teleportation

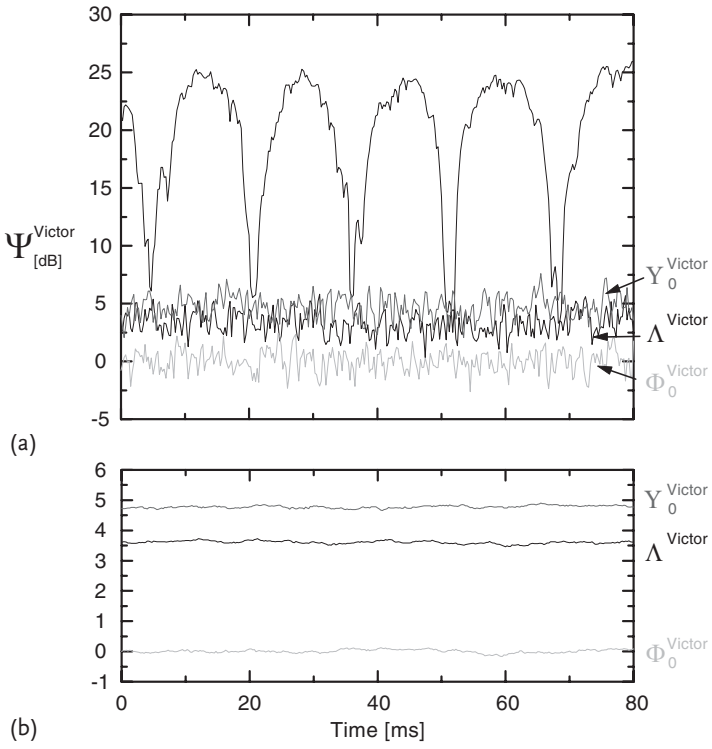

Figure 4.13 (a) Bob's output verified by Victor. The part (b) is the expanded view with a ten-trace average for the vacuum input for Alice [203].

of coherent states, the boundary between classical and quantum teleportation has been shown to be fidelity $F = 0.50$ [210–212]. We stress that this limit applies to the specific case of coherent states and to the distinction between what Alice and Bob can accomplish with and without shared entanglement. Teleportation to accomplish other tasks in quantum information science requires yet higher values for the fidelity.

Nonetheless, when the input state is a coherent state, the fidelity F of the teleported output can be represented as follows [214]:

$$F = \frac{1}{2\sqrt{\sigma_{\text{Q}}^{x}\sigma_{\text{Q}}^{p}}} \exp\left[-(1-g)^2\left(\frac{x_{\text{in}}^2}{2\sigma_{\text{Q}}^{x}} + \frac{p_{\text{in}}^2}{2\sigma_{\text{Q}}^{p}}\right)\right], \tag{4.17}$$

where σ_{Q}^{x} and σ_{Q}^{p} are the variances of the Q function of the teleported field for the corresponding quadratures. The relevant variances σ_{Q}^{x} and σ_{Q}^{p} can be determined from the measured efficiency factors in the experiment and are given by the

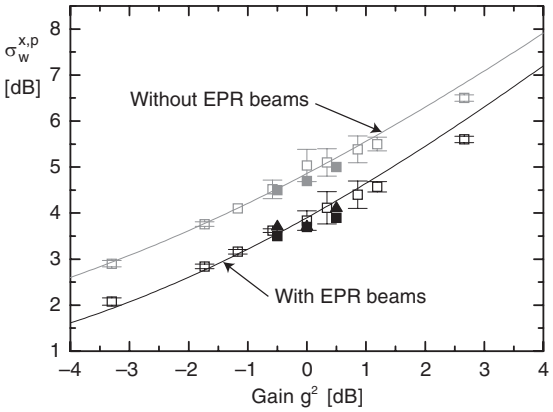

Figure 4.14 Variances $\sigma_{\mathrm{W}}^{x,p}$ of the teleported field measured by Victor [203]. Open and filled symbols in the figure are experimental results. The open squares represent the results for the case with the slight imbalance of amount of squeezing in the two-mode squeezed vacuum. The filled squares and triangles represent the results for the case of the balanced amount of squeezing. The solid lines represent the theoretical predictions of Eq. (4.18).

following equation [203]:

$$\sigma_{\mathrm{Q}}^{x,p} = \frac{1}{4}\left(1+g^2\right) + \frac{\mathrm{e}^{2r_{x,p}}}{8}(g\xi_{\mathrm{A}} - \xi_{\mathrm{B}})^2 + \frac{\mathrm{e}^{-2r_{x,p}}}{8}(g\xi_{\mathrm{A}} + \xi_{\mathrm{B}})^2 + \frac{1}{4}\left(1-\xi_{\mathrm{A}}^2\right)g^2 + \frac{1}{4}\left(1-\xi_{\mathrm{B}}^2\right) + \frac{g^2}{2}\left(\frac{1}{\eta^2}-1\right), \tag{4.18}$$

where $r_{x,p}$ are the squeezing parameters for the respective quadrature components, $\xi_{\mathrm{A,B}}$ characterize the (amplitude) efficiency with which the EPR beams are propagated and detected along paths (A,B), and η gives the (amplitude) efficiency for detection of the unknown input state by Alice. We stress that all of these quantities can be directly measured so that the comparison of theory as in the above equation and the experimentally recorded variances can be made with no adjustable parameters.

Following such a procedure, we show in Figure 4.14 the experimental results for the variances $\sigma_{\mathrm{W}}^{x,p}$ as well as the theoretical prediction of Eq. (4.18), again with no adjustable parameters. By using these measured values of σ_{Q}^{x} and σ_{Q}^{p} together with the independently measured values for the gain g, we can use Eq. (4.17) to arrive at an experimental estimate of the fidelity F_{exp} with the results shown by the points in Figure 4.14 for the cases with and without the EPR beams present. We can also calculate F_{theory} by way of Eqs. (4.17) and (4.18), with this theoretical prediction shown by the curves in Figure 4.15. The agreement between theory and experiment is evidently quite good.

From Figure 4.15, we see that the fidelity F_{exp} for the case with EPR beams exceeds the classical limit $F_0 = 0.50$ for $g = 1$ (0 dB), with the maximum value $F_{\mathrm{exp}} = 0.58 \pm 0.02$ obtained. $F_{\mathrm{exp}} > F_0$ is an unambiguous demonstration of the quantum character of the teleportation protocol.

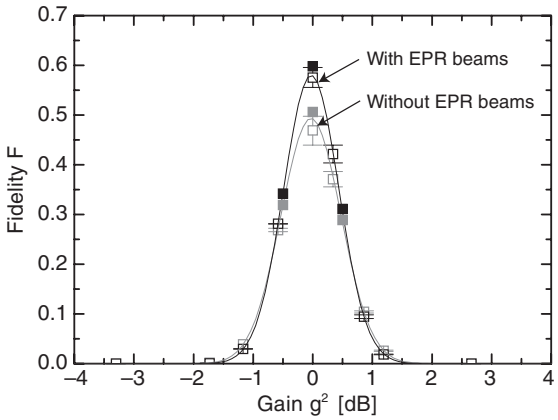

Figure 4.15 Fidelity F inferred from the measurement of Victor [203]. Open and filled squares in the figure are experimental estimates of the fidelity F_{exp}. The open squares represent the F_{exp} for the case with the slight imbalance of amount of squeezing in the two-mode squeezed vacuum. The filled squares represent the F_{exp} for the case of the balanced amount of squeezing. The solid lines represent the theoretical predictions F_{theory}.

After this achievement, qumode or CV teleportation has often been demonstrated [177, 204, 205, 215, 216]. The fidelity of teleportation is getting better and better, now reaching $F = 0.83$ [216], which is much higher than the no-cloning limit of $F = 2/3$ [217]. It is owing to the high level of experimentally available squeezing where -9 dB [218] and -10 dB [219] of squeezing are demonstrated. Theoretically, it should be possible to have the fidelity of $F = 0.9$ with current technology.

4.2.2 Experiment: Qumode Telecloning

CV quantum telecloning was demonstrated by Koike *et al.* for a coherent-state input [220]. In this section, we will explain the experiment in detail.

Quantum telecloning can be regarded as generalized quantum teleportation with multiple receivers as mentioned in Section 4.1.2 [198]. In quantum teleportation, bipartite entanglement shared by two parties (Alice and Bob) enables them to teleport an unknown quantum state from Alice to Bob only by communicating through classical channels [17]. If three parties (Alice, Bob, and Claire) share an appropriate type of tripartite entanglement, Alice is now able to teleport an unknown quantum state to Bob and Claire simultaneously. This is called "$1 \rightarrow 2$ quantum telecloning". Since the no-cloning theorem [14, 15] prohibits the receivers to have perfect clones of the input state, the clones are approximate ones [25]. However, the tripartite entanglement makes the quality of the clones better than that attainable with any classical method. In a similar way, quantum telecloning to an arbitrary number of receivers ($1 \rightarrow n$ quantum telecloning) can be performed by using multipartite entanglement.

The heart of quantum telecloning is the multipartite entanglement shared among the sender and the receivers. Even without multipartite entanglement, it is still possible to perform an equivalent protocol: first the sender makes clones locally, and then sends them to each receiver with bipartite quantum teleportation. In quantum telecloning, these two steps are processed simultaneously. In other words, the use of multipartite entanglement reduces the number of steps in this protocol. Moreover, in the case of coherent state telecloning, the optimum requires only finite entanglement [221], while the local cloning followed by teleportation requires maximal bipartite entanglement.

Let us concentrate on $1 \rightarrow 2$ quantum telecloning of a coherent state input [221]. This process requires tripartite entanglement, which is the minimum unit of multipartite entanglement. Tripartite entanglement for CV can be generated by using squeezed vacua and two beam splitters [161]. Even when the level of squeezing is infinitesimal, we obtain a fully inseparable tripartite state [165], which means any of the three parties cannot be separated. The generated state can be classified by the separability of the reduced bipartite state after tracing out one of the three subsystems. In the qubit regime, this classification is well established. For example, the Greenberger–Horne–Zeilinger (GHZ) state [140] does not have bipartite entanglement after the trace-out, while the $\mathcal{W}$ state [141] does. In the CV regime, it is possible to generate various types of tripartite entanglement by choosing proper transmittances/reflectivities of beam splitters and the levels of squeezing. For example, in the quantum teleportation network, which is one of the successful examples of manipulations of tripartite entanglement [161, 222] and will be explained in the next section, we use the CV analogue of the GHZ state. The CV GHZ state can be created by combining three squeezed vacua with a high level of squeezing on two beam splitters, and is a tripartite maximally entangled state in the limit of infinite squeezing as shown in Section 3.2.3.3. In this case, there is no bipartite entanglement between any pairs of three parties and the quantum teleportation does not work between a sender and a receiver without the help of the third member.

On the other hand, the tripartite entanglement required for quantum telecloning has a nature of both bipartite and tripartite entanglement like the $\mathcal{W}$ state, although it is not a maximally entangled state. This type of tripartite entanglement can be generated by using two squeezed vacua with a modest level of squeezing and two half beam splitters. In the case of telecloning of a coherent state, the level of squeezing required to perform the optimal quantum telecloning [221] is finite and within reach of current technology [218, 219]. This is in contrast to the quantum teleportation which requires an infinite level of squeezing for perfect teleportation. Experimental quantum telecloning will provide us with another method of manipulation of multipartite entanglement which plays an essential role in quantum computation and multipartite quantum communication.

The scheme for creating the tripartite entanglement for quantum telecloning is shown in the center of Figure 4.16 [221]. Two optical parametric oscillators ($\mathrm{OPO}_i, \mathrm{OPO}_{ii}$) pumped below oscillation threshold create two individual squeezed vacuum modes ($\hat{x}_i$, $\hat{p}_i$) and ($\hat{x}_{ii}$, $\hat{p}_{ii}$). These beams are first combined with a half beam splitter with a $\pi/2$ phase shift and then one of the output beams is divided

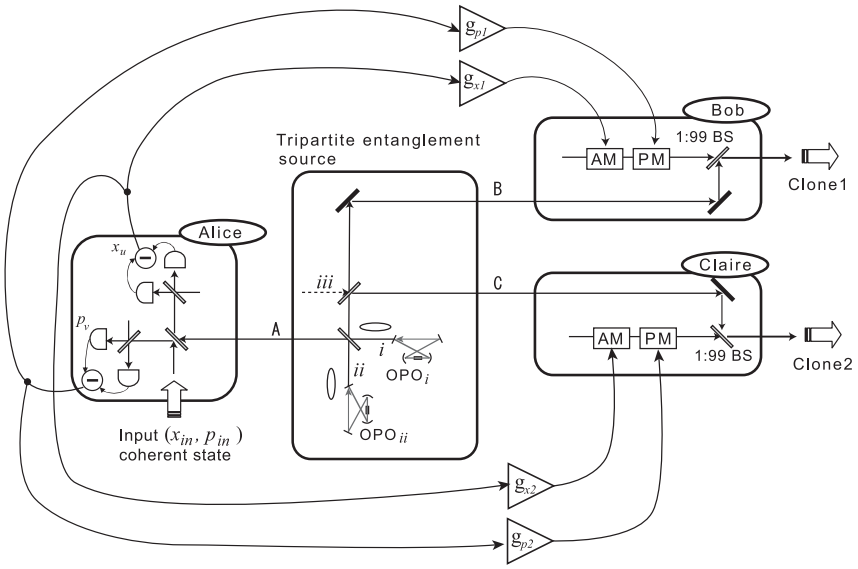

Figure 4.16 The experimental set-up for quantum telecloning from Alice to Bob and Claire to produce Clones 1 and 2 [220].

into two beams (B, C) with another half beam splitter. The three output modes $(\hat{x}_j, \hat{p}_j)$ $(j = \mathrm{A}, \mathrm{B}, \mathrm{C})$ (abbreviated as $(\hat{x}_{\mathrm{A,B,C}}, \hat{p}_{\mathrm{A,B,C}})$ hereafter) are entangled with arbitrary levels of squeezing. Here, modes A and B, and modes A and C are bipartitely entangled and modes A, B, and C are tripartitely entangled while each mode alone is in a thermal state and show excess noises. This can be verified by applying the sufficient inseparability criteria for a bipartite case [116, 159] and a tripartite case [165]. In the present situation, the criteria are

$$\begin{aligned}
&\left\langle \left[\Delta(\hat{x}_{\mathrm{A}} - \hat{x}_{\mathrm{B,C}})\right]^2 \right\rangle + \left\langle \left[\Delta(\hat{p}_{\mathrm{A}} + \hat{p}_{\mathrm{B,C}})\right]^2 \right\rangle \\
&= \left(\frac{1-\sqrt{2}}{2}\right)^2 \left[\left\langle (\Delta \hat{x}_i)^2 \right\rangle + \left\langle (\Delta \hat{p}_{ii})^2 \right\rangle\right] \\
&\quad + \left(\frac{1+\sqrt{2}}{2}\right)^2 \left[\left\langle (\Delta \hat{x}_{ii})^2 \right\rangle + \left\langle (\Delta \hat{p}_i)^2 \right\rangle\right] + \frac{1}{4} < 1 \,, \qquad (4.19)
\end{aligned}$$

where $\langle (\Delta \hat{x}^{(0)})^2 \rangle = \langle (\Delta \hat{p}^{(0)})^2 \rangle = 1/4$ and superscript (0) denotes a vacuum. The left-hand side of the inequality can be minimized when $(\hat{x}_i, \hat{p}_i) = (\mathrm{e}^r \hat{x}_i^{(0)}, \mathrm{e}^{-r} \hat{p}_i^{(0)})$, $(\hat{x}_{ii}, \hat{p}_{ii}) = (\mathrm{e}^{-r} \hat{x}_{ii}^{(0)}, \mathrm{e}^r \hat{p}_{ii}^{(0)})$, and $\mathrm{e}^{-2r} = (\sqrt{2}-1)/(\sqrt{2}+1)$ (7.7 dB squeezing). By using these tripartitely entangled modes, sender Alice can perform quantum telecloning of a coherent state input to two receivers Bob and Claire to produce Clone 1 and 2 at their sites. In other words, success of quantum telecloning is a sufficient condition for the existence of this type of entanglement.

For quantum telecloning, Alice first performs a joint measurement or a so-called "Bell measurement" on her entangled mode $(\hat{x}_{\mathrm{A}}, \hat{p}_{\mathrm{A}})$ and an unknown input mode

$(\hat{x}_{\text{in}}, \hat{p}_{\text{in}})$. In the experiment presented here, the input state is a coherent state and a sideband of continuous wave 860 nm carrier light. The Bell measurement instrument consists of a half beam splitter and two homodyne detectors as shown in Figure 4.16, which is the same as the one shown in Section 4.2.1. Two outputs of the input half beam splitter are labeled as $\hat{x}_u = (\hat{x}_{\text{in}} - \hat{x}_{\text{A}})/\sqrt{2}$ and $\hat{p}_v = (\hat{p}_{\text{in}} + \hat{p}_{\text{A}})/\sqrt{2}$ for the relevant quadratures. Before Alice's measurement, the initial modes of Bob and Claire are, respectively,

$$\begin{aligned}\hat{x}_{\text{B,C}} &= \hat{x}_{\text{in}} - (\hat{x}_{\text{A}} - \hat{x}_{\text{B,C}}) - \sqrt{2}\hat{x}_u \ , \\ \hat{p}_{\text{B,C}} &= \hat{p}_{\text{in}} + (\hat{p}_{\text{A}} + \hat{p}_{\text{B,C}}) - \sqrt{2}\hat{p}_v \ . \end{aligned} \tag{4.20}$$

Note that in this step, Bob's and Claire's modes remain unchanged. After Alice's measurement on $\hat{x}_u$ and $\hat{p}_v$, these operators collapse and reduce to certain values. Receiving these measurement results from Alice, Bob and Claire displace their modes as $\hat{x}_{\text{B,C}} \to \hat{x}_{1,2} = \hat{x}_{\text{B,C}} + \sqrt{2}x_u$, $\hat{p}_{\text{B,C}} \to \hat{p}_{1,2} = \hat{p}_{\text{B,C}} + \sqrt{2}p_v$ and accomplish the telecloning. Note that the values of x_u and p_v are classical information and can be duplicated. In our experiment, displacement is performed by applying electro-optical modulations. Bob and Claire modulate beams by using amplitude and phase modulators (AM and PM in Figure 4.16). The amplitude and phase modulations correspond to the displacement of p and x quadratures, respectively. The modulated beams are combined with Bob's and Claire's initial modes $(\hat{x}_{\text{B,C}}, \hat{p}_{\text{B,C}})$ at 1/99 beam splitters.

The output modes produced by the telecloning process are represented as [221]

$$\begin{aligned}\hat{x}_{1,2} &= \hat{x}_{\text{in}} - (\hat{x}_{\text{A}} - \hat{x}_{\text{B,C}}) \\ &= \hat{x}_{\text{in}} + \frac{1-\sqrt{2}}{2}\hat{x}_i - \frac{1+\sqrt{2}}{2}\hat{x}_{ii} \pm \frac{1}{\sqrt{2}}\hat{x}^{(0)}_{iii} \ , \end{aligned} \tag{4.21}$$

$$\begin{aligned}\hat{p}_{1,2} &= \hat{p}_{\text{in}} + (\hat{p}_{\text{A}} + \hat{p}_{\text{B,C}}) \\ &= \hat{p}_{\text{in}} + \frac{1+\sqrt{2}}{2}\hat{p}_i - \frac{1-\sqrt{2}}{2}\hat{p}_{ii} \pm \frac{1}{\sqrt{2}}\hat{p}^{(0)}_{iii} \ , \end{aligned} \tag{4.22}$$

where subscript iii denotes a vacuum input to the second beam splitter in the tripartite entanglement source, and $+$ of $\pm$ for Clone 1 and $-$ for Clone 2. From these equations, we can see that the telecloned states have additional noise terms to the input mode $(\hat{x}_{\text{in}}, \hat{p}_{\text{in}})$. The additional noise can be minimized by tuning the squeezing levels of the two output modes of OPOs. This corresponds to the minimization of the left-hand of the inequalities in Eq. (4.19). In the ideal case with 7.7 dB squeezing, the additional noise is minimized and we obtain $\hat{x}_{1,2} = \hat{x}_{\text{in}} - 1/2(\hat{x}^{(0)}_i + \hat{x}^{(0)}_{ii}) \pm 1/\sqrt{2}\hat{x}^{(0)}_{iii}$ and $\hat{p}_{1,2} = \hat{p}_{\text{in}} + 1/2(\hat{p}^{(0)}_i + \hat{p}^{(0)}_{ii}) \pm 1/\sqrt{2}\hat{p}^{(0)}_{iii}$. These are the optimal clones of coherent state inputs [221]. In contrast to quantum teleportation, these optimal clones are degraded from the original input by one unit of vacuum noise. In the classical case, where no quantum entanglement is used, two units of vacuum noise will be added. This is called quduty and has to be paid for crossing the boarder between quantum and classical domains [163].

In the real experiment, however, the OPO output modes suffer from inevitable losses and hence deviate from the ideal case. In particular, the mixedness of the states renders the experimental procedure more complicated than for the above discussion based on pure states. Now, the states are no longer minimum uncertainty states, having the uncertainty product $\langle(\Delta\hat{x}_{i,ii})^2\rangle \cdot \langle(\Delta\hat{p}_{i,ii})^2\rangle > 1/16$. This gives rise to the asymmetry between squeezing and antisqueezing and leads us to optimize two parameters of squeezing and antisqueezing for minimization of the additional noise. This is again in contrast to quantum teleportation: in principle, the antisqueezing terms are canceled out and the asymmetry never affects the performance of teleportation.

To evaluate the performance of telecloning, we use a fidelity which is defined as $F = \langle\psi_{\rm in}|\hat{\rho}_{\rm out}|\psi_{\rm in}\rangle$ [210, 211]. The classical limit for the case of coherent state inputs is derived by averaging the fidelity for a randomly chosen coherent input; the classical limit of the averaged fidelity $F_{\rm av}$ is 1/2 [210, 212]. In a real experiment, it is impossible to take an average over the entire phase space. However, if the gains of the classical channels that are defined as $g_{x1,x2} = \langle\hat{x}_{1,2}\rangle/\langle\hat{x}_{\rm in}\rangle$ and $g_{p1,p2} = \langle\hat{p}_{1,2}\rangle/\langle\hat{p}_{\rm in}\rangle$ are unity $g_{x1,x2} = g_{p1,p2} = 1$, the averaged fidelity is identical to the fidelity for a particular coherent state input ($F_{\rm av} = F$). This is because the fidelity with unity gains can be determined by only the variances of the telecloned states, which is independent of the amplitude of the coherent state input. Experimental adjustments of $g_x = g_p = 1$ is performed in the manner of [204]. The fidelity for a coherent state input and $g_x = g_p = 1$ can be written as [203]

$$F = 2\Big/\sqrt{\left[1 + 4\left\langle(\Delta\hat{x}_{1,2})^2\right\rangle\right]\left[1 + 4\left\langle(\Delta\hat{p}_{1,2})^2\right\rangle\right]}\,. \tag{4.23}$$

From the above discussion, if we measure $\langle(\Delta\hat{x}_{1,2})^2\rangle$ and $\langle(\Delta\hat{p}_{1,2})^2\rangle$ of the outputs for a coherent state input and get $F > 1/2$, then we can declare the success of telecloning of coherent state inputs. Note that the fidelity of the optimal telecloning of coherent state inputs is 2/3 [221], which can be calculated from the parameters of the ideal case mentioned above.

By using Eq. (4.23) and experimental results of squeezing/antisqueezing, we can calculate the expected fidelities of the telecloning experiments. Figure 4.17a shows the typical pump power dependence of squeezing and antisqueezing of the output of the OPOs. Here, the OPO cavities contain potassium niobate crystals inside as nonlinear mediums and are pumped with frequency doubled outputs of continuous wave Ti:sapphire laser at 860 nm. In order to minimize the asymmetry of squeezing without sacrificing the level of squeezing, Koike *et al.* selected mirrors with a reflectivity of 12% for the output couplers of the OPOs [220]. With Eqs. (4.21)–(4.23) and these experimental results, the expected fidelities of the telecloning experiments were calculated and are plotted in Figure 4.17b. From these calculations, Koike *et al.* set the pump power at 60 mW, at which they expected the best fidelity to be around 0.6.

Figure 4.18 shows the results of quantum telecloning from Alice to Bob and Claire. The experiments for two types of input states were performed. One is a vacuum and the other is a coherent state that is created by applying electro-optic mod-

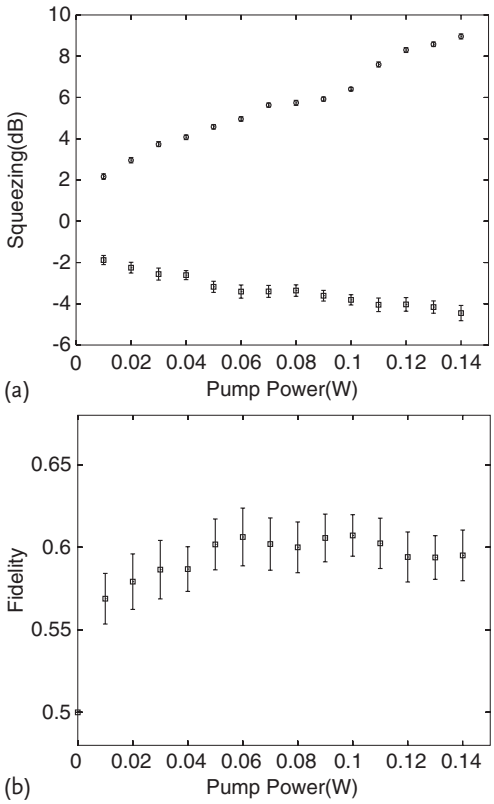

Figure 4.17 (a) Pump power dependence of squeezing and antisqueezing of the output of OPO_i [220]. The squeezing and antisqueezing are measured at 1 MHz. Visibility at a half beam splitter for homodyne measurement is about 0.95 and quantum efficiency of the detector is more than 99%. (b) Calculated fidelities from the squeezing and antisqueezing [220].

ulation to a very weak carrier beam. In Figure 4.18a, trace ii shows the result of Alice's p-quadrature measurement for a vacuum input which corresponds to $\langle(\hat{p}'_\nu)^2\rangle$ where $\hat{p}'_\nu = (\hat{p}^{(0)}_{\rm in} + \hat{p}_{\rm A})/\sqrt{2}$. Note that $\langle\hat{p}^{(0)}_{\rm in}\rangle = \langle\hat{p}_{\rm A}\rangle = 0$; thus $\langle(\hat{p}'_\nu)^2\rangle = \langle(\Delta\hat{p}'_\nu)^2\rangle$, and the variance of a coherent state input $\langle(\Delta\hat{p}_\nu)^2\rangle$ is equivalent to $\langle(\hat{p}'_\nu)^2\rangle$ because a vacuum state is a coherent state with zero amplitude. The noise level is 2.1 dB higher compared to the vacuum noise level $\langle(\Delta\hat{p}^{(0)})^2\rangle = 1/4$. This additional noise comes from "entangled noise" $\hat{p}_{\rm A}$. The noise will be canceled to some extent with the entanglement between Alice and Bob, and between Alice and Claire. Trace iii in Figure 4.18a shows the case for a coherent state input with the phase scanned. The bottom of the trace shows the same level as that of trace ii within the experimental accuracy. This fact is consistent with the above discussion on the variance of a coherent state input. The top of trace iii corresponds to the amplitude of the measured state and is 3 dB lower than that of the input state because of the input half beam splitter. Figure 4.18b,c shows the measurement results of the telecloned

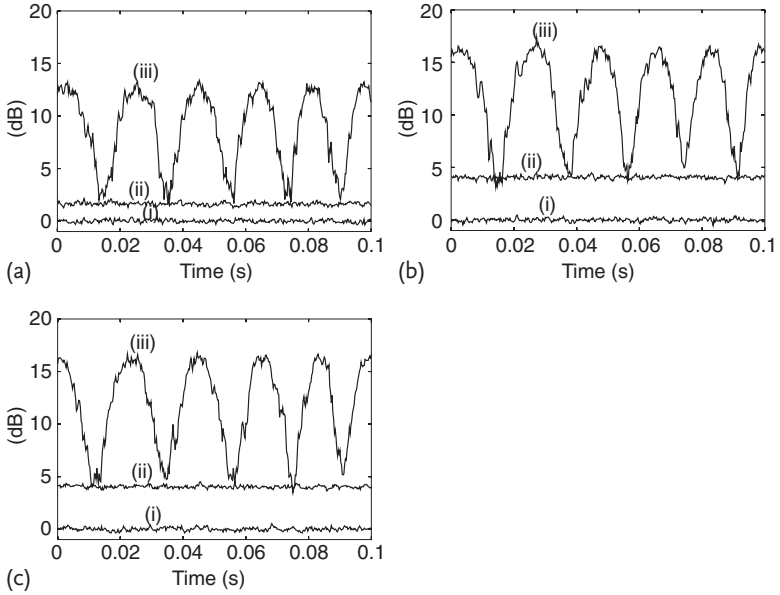

Figure 4.18 Quantum telecloning from Alice to Bob and Claire [220]. All traces are normalized to the corresponding vacuum noise levels. (a) Alice's measurement results for p quadrature (x quadrature is not shown). Trace i, the corresponding vacuum noise level $\langle(\Delta\hat{p}^{(0)})^2\rangle = 1/4$. Trace ii, the measurement result of a vacuum input $\langle(\hat{p}'_\nu)^2\rangle$ where $\hat{p}'_\nu = (\hat{p}^{(0)}_{\rm in} + \hat{p}_{\rm A})/\sqrt{2}$. Trace iii, the measurement result of a coherent state input $\langle(\hat{p}_\nu)^2\rangle$ with the phase scanned. (b, c) The measurement results of the telecloned states at Bob (b) and Claire (c) for p quadratures (x quadratures are not shown). Trace i, the corresponding vacuum noise levels. Trace ii, the telecloned states for a vacuum input $\langle(\Delta\hat{p}_{1,2})^2\rangle$. Trace iii, the telecloned states for a coherent state input. The measurement frequency is centered at 1 MHz, and the resolution and video bandwidths are 30 kHz and 300 Hz, respectively. All traces except for trace iii are averaged twenty times.

states. Traces ii in the figures show the results for a vacuum input which correspond to $\langle(\Delta\hat{p}_{1,2})^2\rangle$. The noise level for Clone 1 is 4.06 ± 0.17 dB and that for Clone 2 is 4.03 ± 0.15 dB. The x quadratures were also measured, which correspond to $\langle(\Delta\hat{x}_{1,2})^2\rangle$ and were 3.74 ± 0.15 dB for Clone 1 and 3.79 ± 0.15 dB for Clone 2 (not shown in the figures). Note that the telecloned states have the same mean amplitude as that of the input inferred from Alice's measurement, which is consistent with the unity gains of classical channels.

By using the measurement results of $\langle(\Delta\hat{x}_{1,2})^2\rangle$ and $\langle(\Delta\hat{p}_{1,2})^2\rangle$, the fidelity of Eq. (4.23) was calculated. Both of the values were 0.58 ± 0.01 and greater than the classical limit of 0.5. Thus, one can declare the success of $1 \rightarrow 2$ telecloning of coherent states. Moreover, these results are operational evidences of the existence of the tripartite entanglement. The slight discrepancies from the expected fidelities are attributed to the fluctuation of phase locking of the system.

4.2.3 Experiment: Qumode Teleportation Network

Quantum teleportation [17] is one of the remarkable manifestations of quantum physics as mentioned before. In the scheme of quantum teleportation, one can transport an unknown quantum state from one location to another without sending the quantum state itself. So far, several experiments of quantum teleportation have been demonstrated [177, 194, 203, 204, 215, 223–225]. Quantum teleportation is, of course, a bipartite quantum protocol, but the scheme of quantum teleportation is extendable to a multipartite quantum protocol which is called a quantum teleportation network [161]. In the quantum teleportation network, more than two parties are connected on the network, and a member in the network can transport a quantum state to the other members. Multipartite quantum protocols like this will be fundamental components for larger-scale quantum communication and quantum computation.

In this section, we will illustrate an experiment of a tripartite quantum teleportation network for continuous variables demonstrated by Yonezawa *et al*. [222]. Quantum entanglement shared by three parties enables teleportation between any two of the three parties with the help of the other. In the experiment, Yonezawa *et al*. demonstrated teleportation of a coherent state between three different pairs in the tripartite network.

A quantum teleportation network is a quantum communication network linked by quantum teleportation. For example, in a tripartite network, three parties (we call Alice, Bob and Claire) are connected on the network in which they are spatially separated and previously share GHZ-type tripartite entanglement. They can only use local operations and classical channels to communicate with each other. In principle, they need not even know where the others are as long as they can communicate through the classical channels. On these conditions, they exchange a quantum state. Here, the quantum state to be teleported is that of an electromagnetic field mode. We use the Heisenberg picture to describe an evolution of the quantum state in this section as well.

In some respects, a quantum teleportation network is similar to bipartite quantum teleportation. In both schemes, the parties share quantum entanglement, and send a quantum state using local operations and the classical channels. However, the properties of tripartite entanglement make it different from the bipartite teleportation in other respects.

If Alice sends a quantum state to Bob, what role does Claire play? Recall that the three parties are in the tripartite entangled state. The third party Claire also has a quantum correlation with the other parties. Thus, Alice and Bob need Claire's information to succeed in teleportation. In other words, Claire can control the transfer of the quantum state from Alice to Bob by restricting their access to her information. This is a clear manifestation of GHZ-type tripartite entanglement.

GHZ-type tripartite entanglement for continuous variables can be generated by using three squeezed vacuum states and two beam splitters as shown in Section 3.2.3.3 [161, 188]. In the limit of infinite squeezing, the state is the CV ana-

logue [161, 188] of Greenberger–Horne–Zeilinger (GHZ) state [140]. The CV GHZ state is a maximally entangled state and a simultaneous eigenstate of zero total momentum ($p_1+p_2+p_3=0$) and zero relative positions ($x_i-x_j=0 \quad i,j=1,2,3$). The entanglement properties of the GHZ state are very fragile under partial losses of a state. For example, if one of the three subsystems is traced out, the remaining state ($\hat{\rho}_{AB}$, $\hat{\rho}_{AC}$, $\hat{\rho}_{BC}$) is completely unentangled [141]. Thus, without Claire's information, the quantum entanglement between Alice and Bob vanishes, and quantum teleportation is no longer possible.

In a real experiment, a maximally entangled state is not available because of finite squeezing and inevitable losses. We can still obtain, however, a fully inseparable tripartite entangled state (a state none of whose subsystems can be separated) as shown in Section 3.2.3.3 [188]. An entangled state generated by three *highly*-squeezed vacuum states still behaves like the GHZ state. The properties of the state are fragile under partial losses of the state. In this case, Claire can completely determine success or failure of quantum teleportation between Alice and Bob.

In contrast, even if three *weakly*-squeezed vacuum states are used, the state is a fully inseparable tripartite entangled state, but the remaining bipartite state after tracing out one of the three subsystems is still entangled [165], which is similar to the case of telecloning in the previous section. In this case, after tracing out one subsystem (e.g., mode 3), the variance $\langle[\Delta(\hat{x}_1-\hat{x}_2)]^2\rangle+\langle[\Delta(\hat{p}_1+\hat{p}_2)]^2\rangle$ is still below unity [165] and shows the presence of bipartite entanglement between modes 1 and 2. If we use such a state, we will succeed in teleportation even without Claire's information, although teleportation fidelity is lower than the case with her information which is again similar to the case of telecloning. In order to control success or failure of teleportation, we need to use three highly-squeezed vacuum states.

There is another important point to be made when we develop bipartite quantum teleportation into a tripartite quantum teleportation network. Only if we use a fully inseparable tripartite entangled state, can we succeed in teleportation between an arbitrary pair in the network. Namely, each party can play any of the three roles: a sender, a receiver and a controller. Note that if we use a partially entangled state, we may succeed in teleportation for a particular combination of the sender, the receiver and the controller, but may fail for other combinations. From this point of view, a *truly* tripartite quantum protocol is defined as a protocol that succeeds only if a fully inseparable (GHZ-type) tripartite entanglement is used. In order to verify success of a truly tripartite quantum protocol, we need to succeed in teleportation for at least two different combinations [165, 188]. For example, the experiment by Jing *et al.* [226], a controlled dense coding for a particular combination, only shows partial success and is not sufficient for the demonstration of a truly tripartite quantum protocol. In the experiment presented here, quantum teleportation for three different combinations are demonstrated.

Here, we illustrate the procedure of our quantum teleportation network experiment. Figure 4.19 shows the schematic of the experimental setup. Tripartite entangled states [188] are distributed to Alice, Bob and Claire. We represent the operators for each mode as ($\hat{x}_i$, $\hat{p}_i$) ($i=\mathrm{A,B,C}$) in the Heisenberg representation. We first

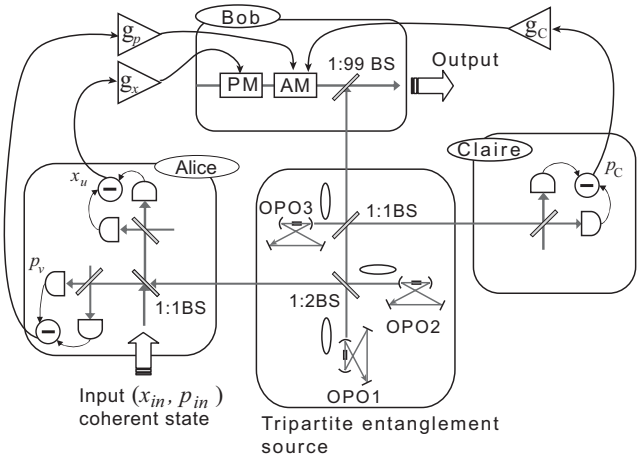

Figure 4.19 The experimental setup for the quantum teleportation from Alice to Bob under the control of Claire [222]. In order to generate quadrature squeezed vacuum states, we use subthreshold optical parametric oscillators (OPOs) with a potassium niobate crystal. An output of CW Ti:sapphire laser at 860 nm is frequency doubled in an external cavity. The output beam at 430 nm is divided into three beams to pump three OPOs. The pump powers are about 50 mW. Three squeezed vacuum states are combined at two beam splitters with relative phases locked. Three outputs of the two beam splitters are in a tripartite entangled state and sent to three parties, Alice, Bob and Claire. The input state is a coherent state and an optical sideband at 1 MHz.

consider the teleportation with the combination of sender Alice, receiver Bob, and controller Claire.

First, Alice performs a joint measurement or so-called "Bell measurement" on her entangled mode $(\hat{x}_{\rm A}, \hat{p}_{\rm A})$ and an unknown input mode $(\hat{x}_{\rm in}, \hat{p}_{\rm in})$. In the experiment, the input state is a coherent state and an optical sideband of CW 860 nm carrier light. The Bell measurement instrument consists of a half beam splitter and two optical homodyne detectors, which is the same as the case of teleportation. Two outputs of the half beam splitter are labeled as $\hat{x}_u = (\hat{x}_{\rm in} - \hat{x}_{\rm A})/\sqrt{2}$ and $\hat{p}_v = (\hat{p}_{\rm in} + \hat{p}_{\rm A})/\sqrt{2}$ for relevant quadratures. The output powers of homodyne detectors are measured with a spectrum analyzer.

Figure 4.20a shows the measurement result of $\langle(\hat{p}_v)^2\rangle$ at Alice ($\langle(\hat{x}_u)^2\rangle$ is not shown). The visibility between the input modes and the local oscillators of Alice's homodyne detectors are both 0.99. The visibilities between the other modes are about 0.97. The quantum efficiency of the photodiode is 0.998 at 860 nm. In Figure 4.20a, the noise level of a vacuum input $\langle(\Delta\hat{p}_v)^2\rangle$ (the variance of $\hat{p}_v$) is 3.7 dB compared to the corresponding vacuum noise level $\langle(\Delta\hat{p}^{(0)})^2\rangle$ while the noise level for x quadrature is 2.1 dB (not shown). The measured noise levels for x and p quadratures are asymmetric. This is because tripartite entanglement is generated by two x and one p quadrature squeezed vacuum states. For example, the variances of the mode A are described $\langle(\Delta\hat{x}_{\rm A})^2\rangle = (2e^{-2r} + e^{2r})/12$, $\langle(\Delta\hat{p}_{\rm A})^2\rangle = (e^{-2r} + 2e^{2r})/12$, respectively [188] (here, r is a squeezing parameter for the same

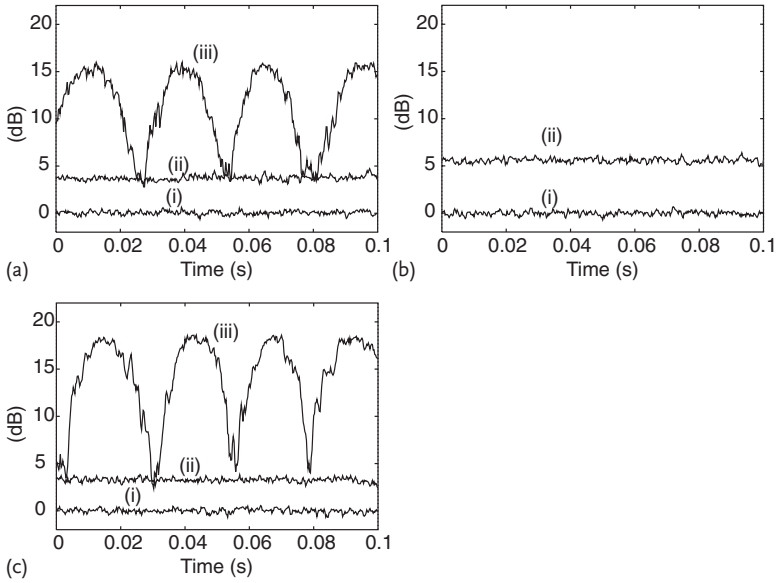

Figure 4.20 Quantum teleportation from Alice to Bob under the control of Claire [222]. All traces are normalized to the corresponding vacuum noise levels. (a) Alice's measurement results for p quadrature (x quadrature is not shown). (i) The corresponding vacuum noise level $\langle(\Delta\hat{p}^{(0)})^2\rangle = 1/4$. (ii) The measurement result of a vacuum input $\langle(\hat{p}'_\nu)^2\rangle$ where $\hat{p}'_\nu = (\hat{p}^{(0)}_{\rm in} + \hat{p}_{\rm A})/\sqrt{2}$. Note that $\langle\hat{p}^{(0)}_{\rm in}\rangle = \langle\hat{p}_{\rm A}\rangle = 0$ thus $\langle(\hat{p}'_\nu)^2\rangle = \langle(\Delta\hat{p}'_\nu)^2\rangle$, and the variance of a coherent state input $\langle(\Delta\hat{p}_\nu)^2\rangle$ is equivalent to $\langle(\Delta\hat{p}'_\nu)^2\rangle$ because a vacuum state is a coherent state with zero amplitude. The noise level is 3.7 dB, while the noise level for x quadrature is 2.1 dB (not shown). (iii) The measurement result of a coherent state input $\langle(\hat{p}_\nu)^2\rangle$ with the phase scanned. The measured amplitude of the input beam is about 15 dB which is 3 dB lower than the actual input because of the input half beam splitter. (b) Claire's measurement results for p quadrature. (i) The corresponding vacuum noise level. (ii) The measurement result of $\langle(\hat{p}_{\rm C})^2\rangle = \langle(\Delta\hat{p}_{\rm C})^2\rangle$. The noise level is 5.7 dB. (c) The measurement results of the teleported states for p quadrature (x quadrature is not shown). (i) The corresponding vacuum noise level. (ii) The teleported state for a vacuum input $\langle(\Delta\hat{p}_{\rm tel})^2\rangle$. Note that the variance of the teleported state for a vacuum input corresponds to that for a coherent state input. The noise level is 3.3 dB for p quadrature, while the noise level for x quadrature is 3.5 dB (not shown). (iii) The teleported state for a coherent state input. The measured amplitude of the teleported state is about 18 dB which is 3 dB higher than that of the input at Alice. It assures that the classical channel's gains are almost unity. The measurement frequency is centered at 1 MHz, the resolution and video bandwidths are 30 kHz, 300 Hz, respectively. All traces except for trace (iii) are averaged ten times.

degree of three squeezing $r = r_1 = r_2 = r_3$). Thus, the measured noise levels at Alice ($\langle(\Delta\hat{p}_\nu)^2\rangle$ and $\langle(\Delta\hat{x}_u)^2\rangle$) are asymmetric.

The measured values x_u and p_ν for $\hat{x}_u$ and $\hat{p}_\nu$ are sent through the classical channels with gain g_x and g_p, respectively. The third party Claire measures $\hat{p}_{\rm C}$ of her entangled mode. Note that Claire does not measure the x quadrature. Figure 4.20b

shows her measurement result $\langle(\Delta\hat{p}_{\rm C})^2\rangle$. Claire also observes a noise and sends it to Bob through the classical channel with gain $g_{\rm C}$.

The classical channel's gains are adjusted as in the manner of [204]. The normalized gains of Alice's classical channels $g_x = \langle\hat{x}_{\rm out}\rangle/\langle\hat{x}_{\rm in}\rangle$, $g_p = \langle\hat{p}_{\rm out}\rangle/\langle\hat{p}_{\rm in}\rangle$ are adjusted to $g_x = 0.99 \pm 0.04$ and $g_p = 1.00 \pm 0.03$, respectively. For simplicity, these gains are fixed through the experiment and treated as unity.

Let us write Bob's initial mode before the measurement of Alice and Claire as

$$\begin{aligned}\hat{x}_{\rm B} &= \hat{x}_{\rm in} - (\hat{x}_{\rm A} - \hat{x}_{\rm B}) - \sqrt{2}\hat{x}_u \ , \\ \hat{p}_{\rm B} &= \hat{p}_{\rm in} + (\hat{p}_{\rm A} + \hat{p}_{\rm B} + g_{\rm C}\hat{p}_{\rm C}) - \sqrt{2}\hat{p}_v - g_{\rm C}\hat{p}_{\rm C} \ . \end{aligned} \tag{4.24}$$

Note that in this step, Bob's mode remains unchanged. After measuring $\hat{x}_u$, $\hat{p}_v$ and $\hat{p}_{\rm C}$, these operators collapse and reduce to certain values. Receiving these measurement results, Bob displaces his mode as $\hat{x}_{\rm B} \to \hat{x}_{\rm tel} = \hat{x}_{\rm B} + \sqrt{2}x_u$, $\hat{p}_{\rm B} \to \hat{p}_{\rm tel} = \hat{p}_{\rm B} + \sqrt{2}p_v + g_{\rm C}p_{\rm C}$ and accomplishes the teleportation. In our experiment, displacement is performed by applying electro-optical modulations. Bob modulates a beam by using amplitude and phase modulators (AM and PM in Figure 4.19). The amplitude and phase modulations correspond to the displacement of p and x quadratures, respectively. The modulated beam is combined with Bob's mode $(\hat{x}_{\rm B}, \hat{p}_{\rm B})$ at a 1/99 beam splitter, which is also the same procedure as in the teleportation experiment.

The teleported mode becomes

$$\begin{aligned}\hat{x}_{\rm tel} &= \hat{x}_{\rm in} - (\hat{x}_{\rm A} - \hat{x}_{\rm B}) \ , \\ \hat{p}_{\rm tel} &= \hat{p}_{\rm in} + (\hat{p}_{\rm A} + \hat{p}_{\rm B} + g_{\rm C}\hat{p}_{\rm C}) \ . \end{aligned} \tag{4.25}$$

In the ideal case, total momentum $\hat{p}_{\rm A} + \hat{p}_{\rm B} + \hat{p}_{\rm C}$ and relative position $\hat{x}_{\rm A} - \hat{x}_{\rm B}$ have zero-eigenvalues $p_{\rm A} + p_{\rm B} + p_{\rm C} = 0$ and $x_{\rm A} - x_{\rm B} = 0$ simultaneously, and the teleported state is identical to the input state ($g_{\rm C} = 1$). In a real experiment, however, the teleported state has additional fluctuations. Without entanglement, at least two units of a vacuum fluctuation are added ($g_{\rm C} = 0$). These additional vacuum fluctuations are called two quduties [163] which must be paid for crossing the boundary between classical and quantum domains, as mentioned before.

Figure 4.20c shows the measurement result of the teleported mode for p quadrature with the gain $g_{\rm C} = 1.02 \pm 0.03$.

The noise level of a vacuum input $\langle(\Delta\hat{p}_{\rm tel})^2\rangle$ is 3.3 dB compared to the corresponding vacuum noise level for p quadrature, while the noise level for x quadrature is 3.5 dB (not shown). In the classical limit, the teleported state has three units of a vacuum fluctuation (one unit for the input state, the other two for quduties), and the variances of the teleported state become 4.77 dB compared to the corresponding vacuum noise level. The observed noise reduction from the classical limit shows success of teleportation.

To evaluate the performance of teleportation, we use a fidelity which is defined as $F = \langle\psi_{\rm in}|\rho_{\rm out}|\psi_{\rm in}\rangle$ [210, 211]. Although the classical limit of teleportation is derived for the case of two parties in [212] and previous sections, it can be applied to the case of three parties [161]. In a classical case, three parties have no

quantum correlation with each other. Thus, the third party can not improve the performance of teleportation beyond the classical limit. The classical limit of teleportation is derived by averaging the fidelity for randomly chosen coherent state input [212]. The classical limit of the averaged fidelity $F_{\rm av}$ is 1/2. In a real experiment, however, it is impossible to take an average upon the entire phase space. However, if the gains of the classical channels are unity $g_x = g_p = 1$ (not included $g_{\rm C}$), the averaged fidelity is identical to the fidelity for a particular coherent state input ($F_{\rm av} = F$) as shown in the previous section. The fidelity for a coherent state input can be written as $F = 2/\sqrt{1+4\sigma_x}\sqrt{1+4\sigma_p}$ where $\sigma_x = \langle(\Delta\hat{x}_{\rm tel})^2\rangle$ and $\sigma_p = \langle(\Delta\hat{p}_{\rm tel})^2\rangle$ [161]. Note that a coherent state is a minimum uncertain state whose variances are $\langle(\Delta\hat{x}^{(0)})^2\rangle = \langle(\Delta\hat{p}^{(0)})^2\rangle = 1/4$. In the experiment presented here, the gains were set as $g_x = g_p = 1$, and the teleportation apparatus was examined for a particular coherent state input.

Although the gains were set as $g_x = g_p = 1$ to estimate fidelity, the third party's gain $g_{\rm C}$ was changed. The best fidelity should be obtained at the optimum gain $g_{\rm C}$ is determined by the degree of the squeezing [161]. Here, the fidelity is measured, and the gain $g_{\rm C}$ dependence of the fidelity is examined.

The fidelity calculated from the variances of the teleported state is plotted as a function of $g_{\rm C}$ in Figure 4.21a.

Without entanglement, the fidelity is lower than 1/2. Quantum teleportation fails and optimum $g_{\rm C}$ is zero because Claire has no correlation with the other parties. With tripartite entanglement, $F = 0.63 \pm 0.02$ ($g_{\rm C} \simeq 0.9$) is obtained, which clearly shows success of quantum teleportation between Alice and Bob. At $g_{\rm C} = 0$, however, quantum teleportation fails. This is because the tripartite entanglement used in this experiment behaves like the GHZ state. To succeed in teleportation, Alice and Bob need Claire's information. If Claire does not send her information to them, the fidelity becomes even lower than that without entanglement. This clearly shows that Claire controls success or failure of the teleportation.

Thus far, we have illustrated the experiment for the particular combination, sender Alice, receiver Bob, and controller Claire. Note that again, one needs to perform experiments for at least two different combinations to verify success of a truly tripartite quantum protocol. Teleportation experiments were performed for the other two combinations. The one combination is sender Alice, receiver Claire, and controller Bob. The other is sender Claire, receiver Bob, and controller Alice. The configuration of the experimental setup was changed only locally while the global configuration remains unchanged. Namely, the paths distributing the tripartite entangled states remain unchanged throughout the experiment. On the other hand, each party changes his or her setup locally according to their roles.

The gain dependence of the teleportation fidelity from Alice to Claire and from Claire to Bob are shown in Figure 4.21b and c, respectively. Both figure parts show almost the same dependence as Figure 4.21a. This ensures that the tripartite entanglement source have the same capability to perform teleportation for different combinations. The best fidelities are 0.63 ± 0.02 and 0.64 ± 0.02 ($g_{\rm B} \simeq g_{\rm A} \simeq 0.9$), respectively, which are greater than the classical limit $F = 1/2$ and show success of teleportation for these two combinations. In total, three different combinations

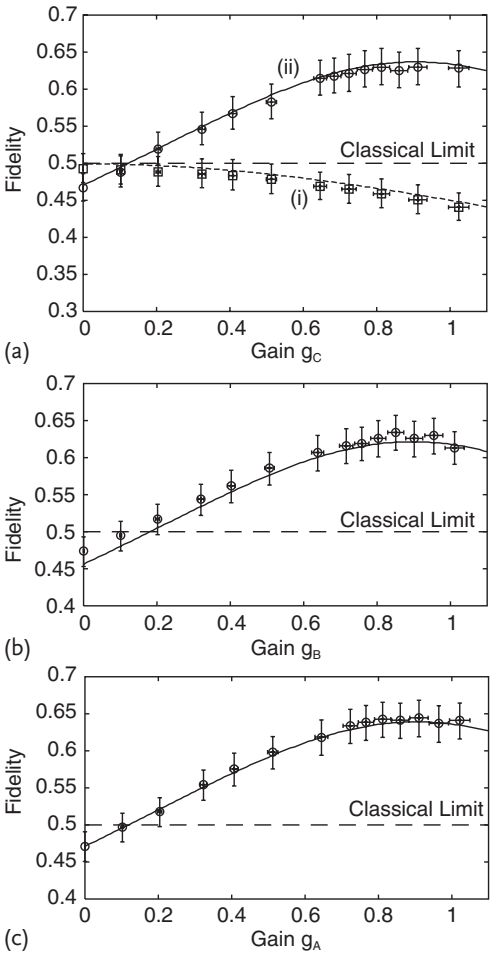

Figure 4.21 The controller's gain dependences of the fidelities [222]. (a) The fidelity of the teleportation from Alice to Bob under the control of Claire. (i) The teleportation without entanglement. (ii) The teleportation with tripartite entanglement. The best fidelity 0.63 ± 0.02 is obtained at $g_C \simeq 0.9$ and the fidelity is better than 1/2 in the broad range of g_C. The solid lines represent the theoretical curves calculated from the experimental conditions. (b) The fidelity of the teleportation from Alice to Claire under the control of Bob. The best fidelity 0.63 ± 0.02 is obtained at $g_B \simeq 0.9$. (c) The fidelity of the teleportation from Claire to Bob under the control of Alice. The best fidelity 0.64 ± 0.02 is obtained at $g_A \simeq 0.9$. In Figure 2, each trace contains 401 measurement points, and the measurement series are repeated 3 times. The error bars are derived by the 1 sigma which are calculated by 401 measurement points and averaged over three times measurements.

were demonstrated. These results show success of a quantum teleportation network, that is, a truly tripartite quantum protocol.

4.2.4 Experiment: Qumode Entanglement Swapping

Quantum teleportation can also be combined with other operations to construct advanced quantum circuits in quantum information processing. The teleported state will be manipulated in subsequent operations, some of which may rely on the nonclassicality contained in the state. Therefore, it is desirable to realize a high-quality teleporter which preserves the nonclassicality throughout the process.

In a continuous-variable (CV) system [161, 163], a required quality to accomplish the transfer of nonclassicality is as follows: the fidelity F_c of a coherent state input exceeds 2/3 at unity gains of classical channels [228]. Here, the fidelity is a measure that quantifies the overlap between the input and the output states: $F = \langle\psi_{in}|\hat{\rho}_{out}|\psi_{in}\rangle$ [210]. Quantum teleportation succeeds when the fidelity exceeds the classical limit ($F_c = 1/2$ for a coherent state input) which is the best achievable value without the use of entanglement. The value of 2/3 is referred to as the no-cloning limit because surpassing this limit warrants that the teleported state is the best remaining copy of the input state [217]. As mentioned in previous sections, the essence of teleportation is the transfer of an arbitrary quantum state. To achieve it, the gains of classical channels must be set to unity. Otherwise, the displacement of the teleported state does not match that of the input state, and the fidelity drops to zero when it is averaged over the whole phase space [214]. Note that the concept of gain is peculiar to a CV system and there is no counterpart in a qubit system.

A teleporter surpassing the no-cloning limit enables the transfer of the following nonclassicality in an input quantum state. It is possible to transfer a negative part of the Wigner function of a quantum state like the Schrödinger-cat state $\propto |\alpha\rangle \pm |-\alpha\rangle$ and a single photon state [228] (see Chapter 8). The negative part is the signature of the nonclassicality [113]. Moreover, two resources of quantum entanglement for teleporters surpassing the no-cloning limit allows one to perform entanglement swapping [202, 229]: one resource of entanglement can be teleported by the use of the other, which is the title of this section. Here, the teleported entanglement is still capable of bipartite quantum protocols (e.g., quantum teleportation).

In terms of the transfer of nonclassicality, entanglement swapping was demonstrated by Jia *et al*. [207]. However, the gains of classical channels were tuned to optimal values (non-unity) for the transfer of the particular entanglement. At such non-unity gains, one would fail in teleportation of other input states such as a coherent state.

In this section, we will illustrate unity-gain entanglement swapping demonstrated by Takei *et al*. [205] in detail. The reason why we stick to unity gain is that it is very important for quantum information processing as mentioned above. First, we will show high-fidelity teleportation beyond the no-cloning limit of 2/3, and then will show unity-gain entanglement swapping with the high-fidelity teleporter.

The fidelity F_c is mainly limited by the degree of correlation of shared quantum entanglement between sender Alice and receiver Bob. For CVs such as quadrature-phase amplitudes, the ideal EPR (Einstein–Podolsky–Rosen) entangled state shows

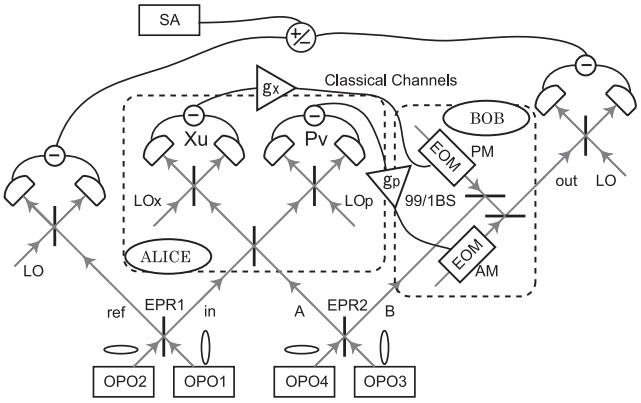

Figure 4.22 The experimental set-up for teleportation of quantum entanglement [205]. OPOs are optical parametric oscillators. All beam splitters except 99/1 BSs are 50/50 beam splitters. LOs are local oscillators for homodyne detection. SA is a spectrum analyzer. The ellipses illustrate the squeezed quadrature of each beam. Symbols and abbreviations are defined in the text.

entanglement of $\hat{x}_i - \hat{x}_j \to 0$ and $\hat{p}_i + \hat{p}_j \to 0$, where subscripts i and j denote two relevant modes of the state. The existence of entanglement between the relevant modes can be checked by the inseparability criterion [116, 159] as mentioned before: $\Delta_{i,j} \equiv \langle[\Delta(\hat{x}_i - \hat{x}_j)]^2\rangle + \langle[\Delta(\hat{p}_i + \hat{p}_j)]^2\rangle < 1$, where the variances of a vacuum state are $\langle(\Delta\hat{x}^{(0)})^2\rangle = \langle(\Delta\hat{p}^{(0)})^2\rangle = 1/4$ and a superscript (0) denotes the vacuum state. If this inequality holds, the relevant modes are entangled. In the case in which Alice (mode A) and Bob (mode B) share entanglement of $\langle[\Delta(\hat{x}_\mathrm{A} - \hat{x}_\mathrm{B})]^2\rangle \simeq \langle[\Delta(\hat{p}_\mathrm{A} + \hat{p}_\mathrm{B})]^2\rangle$, the inseparability criterion $\Delta_{\mathrm{A,B}} < 1$ corresponds to the fidelity $F_\mathrm{c} > 1/2$ for a teleporter without losses [211]. Furthermore, $\Delta_{\mathrm{A,B}} < 1/2$ corresponds to the fidelity $F_\mathrm{c} > 2/3$. Therefore, in order to achieve $F_\mathrm{c} > 2/3$, we need quantum entanglement with at least $\Delta_{\mathrm{A,B}} < 1/2$.

When $F_\mathrm{c} > 2/3$ is achieved, it is possible to perform entanglement swapping with the teleporter and an entanglement resource with $\Delta_{\mathrm{ref,in}} < 1/2$, where we assume that the entangled state consists of two sub-systems: "reference" and "input". While the reference is kept during a teleportation process, the input is teleported to an output station. After the process, the success of this protocol is verified by examining quantum entanglement between the reference and the output: $\Delta_{\mathrm{ref,out}} < 1$. Note that to accomplish this protocol, we need two pairs of entangled states with $\Delta_{i,j} < 1/2$.

The scheme for entanglement swapping is illustrated in Figure 4.22. Two pairs of entangled beams denoted by EPR1 and EPR2 are generated by combining squeezed vacuum states at half beam splitters. One of the EPR1 beams is used as a reference. The other is used as an input and teleported to the output mode. The EPR2 beams consist of mode A and B, and they are utilized as a resource of teleportation. In the case of a coherent state input, a modulated beam is put into the input mode instead of the EPR1 beam.

Each squeezed vacuum state is generated from a subthreshold optical parametric oscillator (OPO) with a potassium niobate crystal (length 10 mm). The crystal is temperature-tuned for type-I noncritical phase matching. Each OPO cavity is a bow-tie-type ring cavity which consists of two spherical mirrors (radius of curvature 50 mm) and two flat mirrors. The round trip length is 500 mm and the waist size in the crystal is 20 μm. The output of a continuous wave Ti:sapphire laser at 860 nm is frequency doubled in an external cavity with the same configuration as the OPOs. The output beam at 430 nm is divided into four beams to pump four OPOs. The pump power is about 80 mW for each OPO.

Here, we will describe a teleportation process in the Heisenberg picture as similar to previous sections. First Alice and Bob share entangled EPR2 beams of mode A and B. Alice performs a "Bell measurement" on her entangled mode $(\hat{x}_A, \hat{p}_A)$ and an unknown input mode $(\hat{x}_{in}, \hat{p}_{in})$. She combines these modes at a half beam splitter and measures $\hat{x}_u = (\hat{x}_{in} - \hat{x}_A)/\sqrt{2}$ and $\hat{p}_v = (\hat{p}_{in} + \hat{p}_A)/\sqrt{2}$ with two optical homodyne detectors. These measured values x_u and p_v for $\hat{x}_u$ and $\hat{p}_v$ are sent to Bob through classical channels with gains g_x and g_p, respectively.

The gains are adjusted in the manner of [204] as similar to previous sections. The normalized gains are defined as $g_x = \langle \hat{x}_{out} \rangle / \langle \hat{x}_{in} \rangle$ and $g_p = \langle \hat{p}_{out} \rangle / \langle \hat{p}_{in} \rangle$. We obtain the measured gains of $g_x = 1.00 \pm 0.02$ and $g_p = 0.99 \pm 0.02$, respectively. For simplicity, these gains are fixed throughout the experiment and treated as unity.

Let us write Bob's initial mode before the measurement of Alice as: $\hat{x}_B = \hat{x}_{in} - (\hat{x}_A - \hat{x}_B) - \sqrt{2}\hat{x}_u$ and $\hat{p}_B = \hat{p}_{in} + (\hat{p}_A + \hat{p}_B) - \sqrt{2}\hat{p}_v$. Note that in this step, Bob's mode remains unchanged. After measuring $\hat{x}_u$ and $\hat{p}_v$ at Alice, these operators collapse and reduce to certain values. Receiving her measurement results, Bob displaces his mode as $\hat{x}_B \to \hat{x}_{out} = \hat{x}_B + \sqrt{2} g_x x_u$, $\hat{p}_B \to \hat{p}_{out} = \hat{p}_B + \sqrt{2} g_p p_v$ and accomplishes the teleportation. Here, we explicitly write the gains g_x and g_p to show the meaning of them, but they are treated as unity as mentioned before. In the experiment, displacement operation is performed by using electro-optical modulators (EOMs) and highly reflecting mirrors (99/1 beam splitters) as shown in the previous sections. Bob modulates two beams by using amplitude and phase modulators (AM and PM in Figure 4.22). Two beams are used to avoid the mixing of amplitude and phase modulations. The amplitude and phase modulations correspond to the displacement of p and x quadratures, respectively. The modulated beams are combined with Bob's mode $(\hat{x}_B, \hat{p}_B)$ at 99/1 beam splitters.

The teleported mode becomes

$$\begin{aligned} \hat{x}_{out} &= \hat{x}_{in} - (\hat{x}_A - \hat{x}_B) \,, \\ \hat{p}_{out} &= \hat{p}_{in} + (\hat{p}_A + \hat{p}_B) \,. \end{aligned} \tag{4.26}$$

In the ideal case, the EPR2 state is the state for which $\hat{x}_A - \hat{x}_B \to 0$ and $\hat{p}_A + \hat{p}_B \to 0$. Then the teleported state is identical to the input state. In real experiments, however, the teleported state has additional fluctuations. Without entanglement, at least two units of vacuum noise are added [163] as similar to previous sections. In other words, the noise $\langle [\Delta(\hat{x}_A - \hat{x}_B)]^2 \rangle \geq 2 \times 1/4$ is added in x quadrature (similarly

in p quadrature). These variances correspond to $\Delta_{A,B} \geq 1$, resulting in the fidelity $F_c \leq 1/2$. On the other hand, with entanglement, added noise is less than two units of vacuum noise. In the case with entanglement of $\Delta_{A,B} < 1/2$ which is necessary to accomplish $F_c > 2/3$, the added noise is less than a unit of vacuum noise.

We first explain a coherent-state teleportation experiment to quantify the quality of the teleporter with the fidelity F_c. In the experiment, frequency sidebands at ± 1 MHz of an optical carrier beam is used as a quantum state, which is the same as the experiment illustrated in the previous sections. Thus, a coherent state can be generated by applying phase modulation with EOM to the carrier beam. This modulated beam is put into the input mode instead of the EPR1 beam.

Figure 4.23 shows measurement results of the teleported mode. The measured amplitude of the coherent state is 20.7 ± 0.2 dB compared to the corresponding vacuum noise level. The measured values of the variances are $\langle(\Delta \hat{x}_{out})^2\rangle = 2.82 \pm 0.09$ dB and $\langle(\Delta \hat{p}_{out})^2\rangle = 2.64 \pm 0.08$ dB (not shown). The fidelity for a coherent state input can be written as $F_c = 2/\sqrt{(1+4\sigma_x)(1+4\sigma_p)}$, where $\sigma_x = \langle(\Delta \hat{x}_{out})^2\rangle$ and $\sigma_p = \langle(\Delta \hat{p}_{out})^2\rangle$ [203, 211]. The fidelity obtained from the measured variances is $F_c = 0.70 \pm 0.02$. This result clearly shows the success of teleportation of a coherent state beyond the no-cloning limit. Moreover, the correlation of the EPR2 beams is examined and the entanglement of $\Delta_{A,B} = 0.42 \pm 0.01$ is obtained, from which the expected fidelity of $F_c = 0.70 \pm 0.01$ is calculated. The experimental result is in good agreement with the calculation. Such good agreement indicates that the phase-locking system is very stable and that the fidelity is mainly limited by the degree of entanglement of the resource. As discussed in [204], residual phase

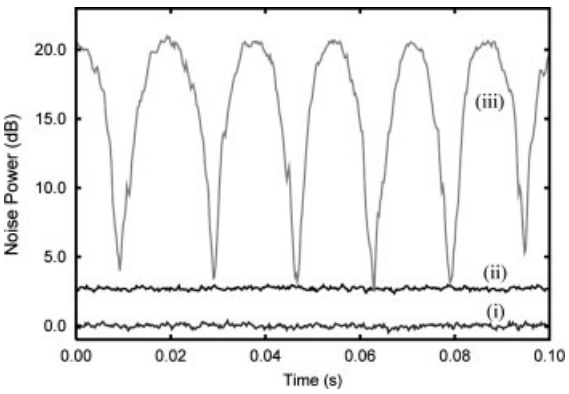

Figure 4.23 The measurement results of the teleported state for a coherent state input in x quadrature [205]. Each trace is normalized to the corresponding vacuum noise level. Trace i shows the corresponding vacuum noise level $\langle(\Delta \hat{x}^{(0)}_{out})^2\rangle = 1/4$. Traces ii shows the teleported state for a vacuum input. Note that the variance of the teleported state for a vacuum input corresponds to that for a coherent state input. Trace iii shows the teleported state for a coherent state input with the phase scanned. At the top (bottom) of the trace, the relative phase between the input and the LO is 0 or π ($\pi/2$ or $3\pi/2$). The measurement frequency is centered at 1 MHz, and the resolution and video bandwidths are 30 kHz and 300 Hz, respectively. Traces i and ii are averaged 20 times.

fluctuation in a locking system affects an achievable fidelity, and probably has prevented previous works from surpassing the no-cloning limit. A highly stabilized phase-locking system (both mechanically and electronically) allows one to achieve the fidelity of 0.70.

Next, we illustrate the entanglement swapping experiment. For the reference, the noise power of each mode for EPR1 beams and the initial correlation between the modes are measured with homodyne detection before the experiment. The noise levels of 5.23 ± 0.14 dB and 4.44 ± 0.14 dB are obtained for x and p quadratures for the reference mode, respectively (Figure 4.24a). Similarly, the noise levels of 5.19 ± 0.13 dB and 4.37 ± 0.14 dB are obtained for x and p quadratures for the input mode (not shown). By making electrical subtraction or summation of the homodyne detection outputs, the noise levels of -3.19 ± 0.13 dB for x quadrature and -4.19 ± 0.14 dB for p quadrature are observed (Figure 4.24b). From these values, one obtains the measured variances of $\Delta_{\mathrm{ref,in}} = 0.43 \pm 0.01 < 1$. This result shows the existence of the quantum entanglement between the input and the reference, and also indicates that we can transfer this entanglement with the teleporter.

We then proceed to illustrate the experiment of entanglement swapping and the measurement of the correlation between the output and the reference in a similar way. The state in the reference mode does not change in the process. For the output mode, the noise levels of 6.06 ± 0.12 dB and 5.47 ± 0.14 dB are obtained for x and p quadratures, respectively, as shown in Figure 4.25a. Because of the imperfect teleportation, some noises are added to the teleported state, resulting in the larger variances than that of the reference. Figure 4.25b shows the results of the correlation measurement. The noise levels of -0.25 ± 0.13 dB and -0.60 ± 0.13 dB are observed for x and p quadratures, respectively, yielding $\Delta_{\mathrm{ref,out}} = 0.91 \pm 0.02 < 1$. This result

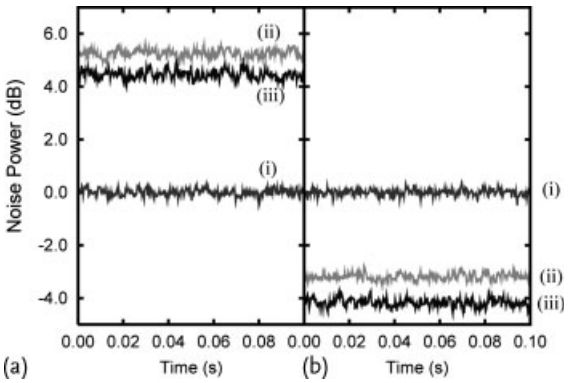

Figure 4.24 Correlation measurement for EPR1 beams [205]. (a) The measurement result of the reference mode alone. Trace i shows the corresponding vacuum noise level $\langle(\Delta \hat{x}_{\mathrm{ref}}^{(0)})^2\rangle = \langle(\Delta \hat{p}_{\mathrm{ref}}^{(0)})^2\rangle = 1/4$. Traces ii and iii are the measurement results of $\langle(\Delta \hat{x}_{\mathrm{ref}})^2\rangle$ and $\langle(\Delta \hat{p}_{\mathrm{ref}})^2\rangle$, respectively. (b) The measurement result of the correlation between the input mode and the reference mode. Trace i shows the corresponding vacuum noise level $\langle[\Delta(\hat{x}_{\mathrm{ref}}^{(0)} - \hat{x}_{\mathrm{in}}^{(0)})]^2\rangle = \langle[\Delta(\hat{p}_{\mathrm{ref}}^{(0)} + \hat{p}_{\mathrm{in}}^{(0)})]^2\rangle = 1/2$. Traces ii and iii are the measurement results of $\langle[\Delta(\hat{x}_{\mathrm{ref}} - \hat{x}_{\mathrm{in}})]^2\rangle$ and $\langle[\Delta(\hat{p}_{\mathrm{ref}} + \hat{p}_{\mathrm{in}})]^2\rangle$, respectively. The measurement condition is the same as that of Figure 4.23.

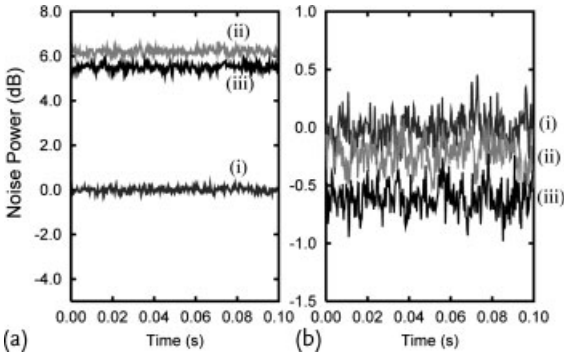

Figure 4.25 Correlation measurement results of the teleportation of quantum entanglement. (a) The measurement result of the output mode alone. Trace i shows the corresponding vacuum noise level $\langle(\Delta\hat{x}_{\text{out}}^{(0)})^2\rangle = \langle(\Delta\hat{p}_{\text{out}}^{(0)})^2\rangle = 1/4$. Traces ii and iii are the measurement results of $\langle(\Delta\hat{x}_{\text{out}})^2\rangle$ and $\langle(\Delta\hat{p}_{\text{out}})^2\rangle$, respectively. (b) The measurement result of the correlation between the output mode and the reference mode. Trace i shows the corresponding vacuum noise level $\langle[\Delta(\hat{x}_{\text{ref}}^{(0)} - \hat{x}_{\text{out}}^{(0)})]^2\rangle = \langle[\Delta(\hat{p}_{\text{ref}}^{(0)} + \hat{p}_{\text{out}}^{(0)})]^2\rangle = 1/2$. Traces ii and iii are the measurement results of $\langle[\Delta(\hat{x}_{\text{ref}} - \hat{x}_{\text{out}})]^2\rangle$ and $\langle[\Delta(\hat{p}_{\text{ref}} + \hat{p}_{\text{out}})]^2\rangle$, respectively. The measurement condition is the same as that of Figure 4.23.

clearly shows the existence of quantum entanglement between the output and the reference. Thus unity-gain entanglement swapping is successfully demonstrated.

5
Quantum Error Correction

In Section 1.9, we gave a brief introduction to the general concept of quantum error correction (QEC) and its specific application to DV qubit and CV qumode systems. Though being one of the most important elements for the implementation of any advanced quantum information protocol, QEC has been demonstrated so far only in a few experiments. Full QEC codes that provide universal protection against all types of errors are, in general, fairly hard to implement. However, depending on the system used for quantum information processing, it is often not necessary to achieve such a universal QEC. For example, in the optical context, photon loss is the primary source of errors and other kinds of errors such as depolarizing noise channels as usually modeled in quantum information theory (see Section 1.4.1) would only occur in very specific optical protocols.

As discussed in Section 1.7, also for quantum communication, especially over long distances, there is a need to deal with transmission errors/noises and photon losses. However, as opposed to quantum computation, in the communication scenario, quantum protocols for detecting and avoiding errors can be probabilistic. In particular, in a quantum repeater (Section 1.7), usually entanglement distillation protocols are used. Nonetheless, in any such probabilistic scheme, quantum information has to be stored reliably and hence the qubits or qumodes are again subject to errors due to realistically imperfect memories. Therefore, some form of QEC will always be required in any quantum protocol that is intended to achieve a true advantage over any classical approach. A full-scale implementation would then be based on a fully fault-tolerant protocol [5]. This may use concatenations of standard QEC codes or, as envisaged in more recent approaches, some form of topological protection against errors [230]. This latter technique may even be combined with the more recent, measurement-based approaches to quantum computation [231–236] (see Section 1.8 and Chapter 7).

There are just a few experiments on optical QEC, and in this chapter, we shall describe one such experiment for qubits (Section 5.3.1) and one for qumodes (Section 5.3.2); after a brief theoretical discussion on the simplest and oldest, full QEC codes for protecting a qubit (Section 5.1) and a qumode (Section 5.2) against arbitrary single-qubit and single-qumode errors, respectively. This brief discussion will especially provide the link with the stabilizer formalism introduced in Section 1.9. Finally, we will talk about an optical approach to entanglement distillation in Sec-

Quantum Teleportation and Entanglement. Akira Furusawa, Peter van Loock
Copyright © 2011 WILEY-VCH Verlag GmbH & Co. KGaA, Weinheim
ISBN: 978-3-527-40930-3

tion 5.4 and a few optical experiments of entanglement distillation, both for qubits (Section 5.5.1) and for qumodes (Section 5.5.2).

5.1 The Nine-Qubit Code

Shor [21] proposed a concatenated quantum code to protect an arbitrary single-qubit state, $|\psi\rangle = \alpha|0\rangle + \beta|1\rangle$, against arbitrary single-qubit errors by encoding the logical qubit state into nine physical qubits,

$$|\psi_{\text{encode}}\rangle = \alpha|+++\rangle + \beta|---\rangle \,, \tag{5.1}$$

with $|\pm\rangle = (|000\rangle \pm |111\rangle)/\sqrt{2}$. This code is basically a concatenation of the three-qubit bit-flip repetition code, as discussed in Section 1.9, with the analogous three-qubit phase-flip repetition code. While the former protects against X errors, that is, flips in the computational basis, the latter allows one to suppress the effect of Z errors corresponding to flips in the conjugate, Hadamard-transformed basis. Accordingly, the phase-flip code is based on a codesubspace spanned by the Hadamard-transformed bit-flip codespace, $\{|+++\rangle, |---\rangle\}$. Since Shor's concatenated version can correct both Z and X errors, it can also correct arbitrary superpositions of Z and X errors, and thus any error that occurs on a single physical qubit (Section 1.9).

Though again reminiscent of the redundant encoding in classical error correction, the full quantum code exhibits some highly nonclassical features of which the most significant is the presence of multi-party entanglement. It is the concatenation of the three-party entangled states $|\pm\rangle$ into nine-party states that enables one to correct both bit-flip and phase-flip errors. Moreover, the phase-flip errors on their own only occur in the quantum regime and do not exist classically.

As described in Section 1.9 for a three-qubit code, suitable error syndrome measurements would collapse an arbitrary error including coherent superpositions of bit-flip and phase-flip errors into the discrete set of only bit-flip and/or phase-flip errors. These discrete Pauli errors can then be easily reversed to recover the original state. Note that even though Shor's code was the first full QEC code and its concatenated structure appears particularly instructive, there are cheaper QEC codes which are nonetheless universal, protecting a given logical subspace against arbitrary errors on one or even more of the physical subsystems. The minimal number of physical qubits in a full QEC code is five. For certain restricted sets of errors, there are channel-adapted codes which require even less physical resources. For example, a four-qubit QEC code is known to correct amplitude damping errors.

In the stabilizer formalism, the Shor code corresponds to a $[N = 9, k = 1]$ stabilizer code, encoding one logical qubit into nine physical qubits. Its $N - k = 8$ stabilizer generators are

$$\begin{aligned} S = \langle & Z_1 \otimes Z_2, Z_2 \otimes Z_3, Z_4 \otimes Z_5, Z_5 \otimes Z_6, Z_7 \otimes Z_8, Z_8 \otimes Z_9, \\ & X_1 \otimes X_2 \otimes X_3 \otimes X_4 \otimes X_5 \otimes X_6, X_4 \otimes X_5 \otimes X_6 \otimes X_7 \otimes X_8 \otimes X_9 \rangle \,. \end{aligned} \tag{5.2}$$

Again, the codespace is spanned by the set of simultaneous $+1$ eigenvectors of S. Measuring the eight stabilizer generators, yielding 2^8 classical syndrome bit values, reveals which orthogonal error subspace an encoded input state is mapped. As before, signal recovery is then achieved by mapping the state back into the codespace with stabilizer eigenvalues $+1$.

5.2 The Nine-Qumode Code

The CV qumode version [237, 238] of Shor's nine-qubit code is based on the following encoded nine-qumode state,

$$|\psi_{\text{encode}}\rangle = \int \mathrm{d}P\, \psi(P)|P, P, P\rangle \,, \tag{5.3}$$

with $|P\rangle = 1/\sqrt{\pi}\int \mathrm{d}x \mathrm{e}^{2\mathrm{i}xP}|x, x, x\rangle$. Through this code, an arbitrary single-qumode state, $|\psi\rangle = \int \mathrm{d}x\, \psi(x)|x\rangle$, is encoded into nine optical modes. Similar to its qubit counterpart, the qumode version corrects both WH $X(s)$ and $Z(s)$ shift errors in phase space as well as any superpositions of such shift errors. As a consequence, an arbitrary single-qumode error can be corrected. Note that compared with the incomplete three-mode code against arbitrary $\mathrm{e}^{\mathrm{i}f(\hat{p})}$-errors discussed in Section 1.9, the full CV Shor code is really capable of correcting arbitrary errors including those on non-commuting variables. The stabilizer of the CV nine-mode code is

$$\begin{aligned} S = \Big\langle & Z_1 \otimes Z_2^\dagger, Z_2 \otimes Z_3^\dagger, Z_4 \otimes Z_5^\dagger, Z_5 \otimes Z_6^\dagger, Z_7 \otimes Z_8^\dagger, Z_8 \otimes Z_9^\dagger \,, \\ & X_1 \otimes X_2 \otimes X_3 \otimes X_4^\dagger \otimes X_5^\dagger \otimes X_6^\dagger, X_4 \otimes X_5 \otimes X_6 \otimes X_7^\dagger \otimes X_8^\dagger \otimes X_9^\dagger \Big\rangle \,, \end{aligned} \tag{5.4}$$

corresponding to the following nullifier conditions,

$$\begin{aligned} \hat{x}_1 - \hat{x}_2 = 0 \,, \quad \hat{x}_2 - \hat{x}_3 = 0 \,, \quad \hat{x}_4 - \hat{x}_5 = 0 \,, \\ \hat{x}_5 - \hat{x}_6 = 0 \,, \quad \hat{x}_7 - \hat{x}_8 = 0 \,, \quad \hat{x}_8 - \hat{x}_9 = 0 \,, \\ \hat{p}_1 + \hat{p}_2 + \hat{p}_3 - \hat{p}_4 - \hat{p}_5 - \hat{p}_6 = 0 \,, \\ \hat{p}_4 + \hat{p}_5 + \hat{p}_6 - \hat{p}_7 - \hat{p}_8 - \hat{p}_9 = 0 \,. \end{aligned} \tag{5.5}$$

Note that these quantum correlations hold for *any* signal-qumode input state, as the stabilizer code encodes the full, infinite-dimensional Hilbert space of a single qumode. In order to obtain a sufficient set of entanglement witnesses for verifying a fully inseparable nine-party state, recall that we need a full set of stabilizer generators (see Chapter 3). Hence, in this case, we need nine generators for nine qumodes, uniquely defining an unphysical nine-qumode stabilizer state (a one-dimensional subspace of the nine-qumode Hilbert space) instead of defining a one-qumode subspace of the nine-qumode Hilbert space (see Section 1.9).

Therefore, additional quadrature correlations must be considered and these extra correlations are expressed in terms of the "logical" quadratures in the codespace which also depend on the signal state. The missing correlations depend on the combinations $\hat{X} \equiv \hat{x}_1 + \hat{x}_4 + \hat{x}_7$ and $\hat{P} \equiv \hat{p}_1 + \hat{p}_2 + \hat{p}_3$. These linear combinations correspond to the logical quadratures in the codespace and are given by the quadratures of the signal input state, $\hat{X} = \hat{x}_{\rm in}$ and $\hat{P} = \hat{p}_{\rm in}$. For a finitely squeezed, imperfect encoded state (see Section 5.3.2), there will be excess noises in all these correlations and the variance-based entanglement witnesses of Section 3.2 can be used to verify inseparabilities (see supplemental material of [239]).

5.3 Experiment: Quantum Error Correction

5.3.1 Qubits

There are several demonstrations of qubit quantum error correction in NMR [240, 241, 243, 244],[1] ion-trap [245], and single-photons [246–248]. In this section, we concentrate on optical approaches especially on the demonstration of Pittman *et al.* [248]. This is because one of the most important essences of error corrections is feedforward, and Pittman *et al.* demonstrated error correction with feedforward.

Figure 5.1 shows the quantum circuit of qubit error correction demonstrated by Pittman *et al.* [248]. First, the input qubit $|\psi\rangle = \alpha|0\rangle + \beta|1\rangle$ is encoded in the circuit as follows:

$$\alpha|0\rangle + \beta|1\rangle \rightarrow \alpha\frac{|00\rangle + |11\rangle}{\sqrt{2}} + \beta\frac{|01\rangle + |10\rangle}{\sqrt{2}}\,. \tag{5.6}$$

Then, one of the two qubits is measured on $\{|0\rangle, |1\rangle\}$ basis, which corresponds to an error to be corrected in the experiment. To recover the input state, one makes

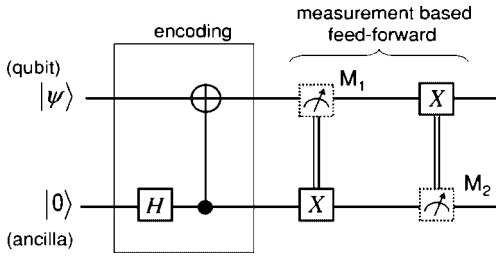

Figure 5.1 Quantum circuit of qubit error correction demonstrated by Pittman *et al.* [248]. *X* denotes σ_x operation (bit flip).

1) Input coherent states should be selected randomly from the entire phase space. In the real experiments, however, we cannot do so. We usually measure averaged fidelity in real experiments, which is only determined by variances for Gaussian states..

a feedforward of the measurement result to the other untouched qubit and makes a σ_x operation (bit flip) on it. For example, if one makes the measurement on the first qubit and gets $|0\rangle$, the second qubit becomes $\alpha|0\rangle + \beta|1\rangle$. In this case, there is no need for feedforward. On the other hand, if one gets $|1\rangle$, then the second qubit becomes $\alpha|1\rangle + \beta|0\rangle$. In this case, one has to make a feedforward (bit flip) to recover the input.

Figure 5.2 shows the experimental setup of the qubit error correction demonstrated by Pittman *et al.* [248]. A pair of photons in the state $|\leftrightarrow\rangle \otimes |\leftrightarrow\rangle$ is prepared by parametric down conversion. One of the pair photons passes through a half wave plate (HWP1) to create an input state. Here, the input qubit $|\psi\rangle = \alpha|0\rangle + \beta|1\rangle$ is described by a logical qubit as follow:

$$|0_L\rangle = \frac{|\leftrightarrow\rangle + |\updownarrow\rangle}{\sqrt{2}} ,$$
$$|1_L\rangle = \frac{|\leftrightarrow\rangle - |\updownarrow\rangle}{\sqrt{2}} , \tag{5.7}$$

where they correspond to $\pm 45°$-linear polarization, respectively. Thus, the input state is

$$|\psi\rangle = \alpha \frac{|\leftrightarrow\rangle + |\updownarrow\rangle}{\sqrt{2}} + \beta \frac{|\leftrightarrow\rangle - |\updownarrow\rangle}{\sqrt{2}} . \tag{5.8}$$

The other photon of the pair passes through another half wave plate (HWP2) to prepare $|0_L\rangle = (|\leftrightarrow\rangle + |\updownarrow\rangle)/\sqrt{2}$. After the half wave plates, these two photons are combined by a polarization beam splitter (PBS). The PBS acts as a Hadamard gate and controlled NOT gate in which the trick is following. At a PBS, each photon goes to different directions (both photons are reflected or transmitted) for the case of same polarization, and each photon goes to the same direction for the case of orthogonal polarization. By post-selection, the former case will be selected in the experiment. Therefore, the state after combining these two photons by a polariza-

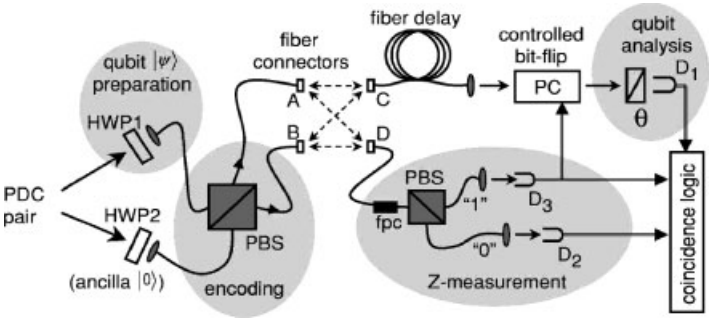

Figure 5.2 Experimental setup for qubit error correction demonstrated by Pittman *et al.* [248]. PDC: parametric down conversion, HWP: half wave plate, PBS: polarization beam splitter, fpc: fiber polarization controller, PC: Pockels cell, Z-measurement: measurement on the basis of $\{|0_L\rangle, |1_L\rangle\}$.

tion beam splitter can be described as

$$
\begin{aligned}
|\psi_{\text{encode}}\rangle &= \alpha\frac{|\leftrightarrow\rangle\otimes|\leftrightarrow\rangle+|\updownarrow\rangle\otimes|\updownarrow\rangle}{\sqrt{2}}+\beta\frac{|\leftrightarrow\rangle\otimes|\leftrightarrow\rangle-|\updownarrow\rangle\otimes|\updownarrow\rangle}{\sqrt{2}}\\
&=\sqrt{2}\Bigg[\alpha\left(\frac{|\leftrightarrow\rangle+|\updownarrow\rangle}{\sqrt{2}}\otimes\frac{|\leftrightarrow\rangle+|\updownarrow\rangle}{\sqrt{2}}+\frac{|\leftrightarrow\rangle-|\updownarrow\rangle}{\sqrt{2}}\otimes\frac{|\leftrightarrow\rangle-|\updownarrow\rangle}{\sqrt{2}}\right)\\
&\quad+\beta\left(\frac{|\leftrightarrow\rangle+|\updownarrow\rangle}{\sqrt{2}}\otimes\frac{|\leftrightarrow\rangle-|\updownarrow\rangle}{\sqrt{2}}+\frac{|\leftrightarrow\rangle-|\updownarrow\rangle}{\sqrt{2}}\otimes\frac{|\leftrightarrow\rangle+|\updownarrow\rangle}{\sqrt{2}}\right)\Bigg]\\
&=\sqrt{2}\left(\alpha\frac{|0_L0_L\rangle+|1_L1_L\rangle}{\sqrt{2}}+\beta\frac{|0_L1_L\rangle+|1_L0_L\rangle}{\sqrt{2}}\right),
\end{aligned}
\tag{5.9}
$$

where the factor $\sqrt{2}$ in front of the right-hand side means that the success probability of post-selection is 50%. Thus, the input state is encoded.

As an error, a measurement on the basis of $\{|0_L\rangle, |1_L\rangle\}$, physically it can be realized by photon detection in $\pm 45°$-linearly polarization with a fiber polarization controller and a PBS. In the case of $|1_L\rangle$ obtained, polarization of the photon is rotated with a Pockels cell to make a bit-flip, where a fiber delay is used to compensate the time delay of measurement and feedforward. Finally, the output is analyzed. For eliminating the false events at the encoding stage described above, coincidence logic for detectors 1–3 is used. Of course, this also works as usual post-selection.

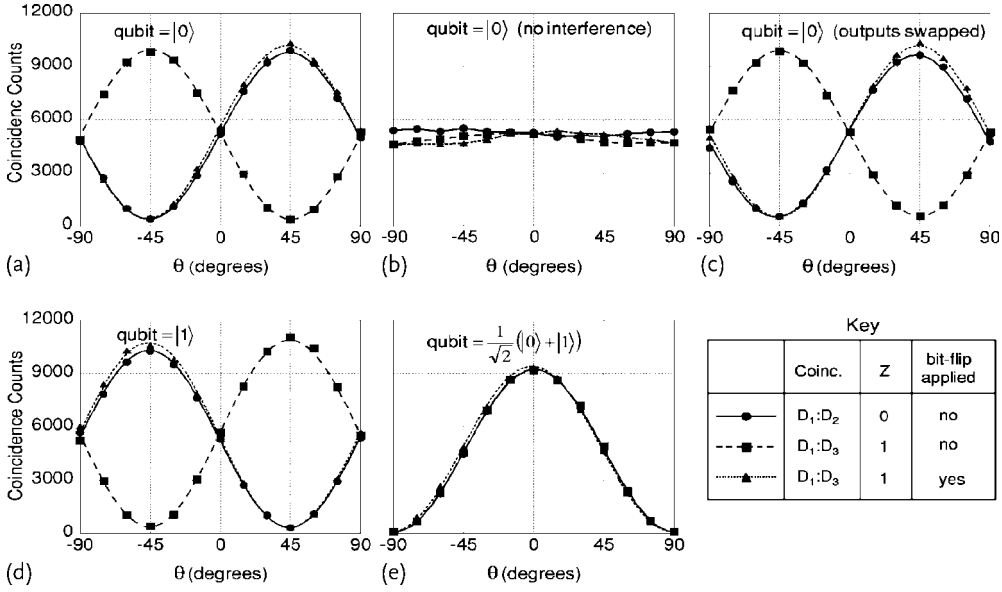

Figure 5.3 Experimental results of qubit error correction demonstrated by Pittman *et al.* [248]. Input is (a)–(c) $|0_L\rangle$, (d) $|1_L\rangle$ (e) $(|0_L\rangle + |1_L\rangle)/\sqrt{2}$. Only in the case of (b), the input photon was delayed compared to ancilla photon by roughly twice its coherence length. Z: measurement result.

Figure 5.3 shows results of the experiments. The quantum error correction was successful for various inputs. Note that Figure 5.3b shows the results for the case of the input photon delayed compared to ancilla photon by roughly twice its coherence length. The disappearance of interference in Figure 5.3b shows nonclassical nature of the encoding operation.

5.3.2 Qumodes

In this section, we will describe the experimental implementation of a CV QEC code based upon an entangled state of nine optical beams [164]. This experiment was performed by Aoki *et al*. [239]. It is the nine-wavepacket adaptation of Shor's original nine-qubit scheme [21], as introduced in Section 5.2. In principle, this scheme allows for full quantum error correction against an arbitrary single-beam (single-party) error.

The CV version of Shor's nine-qubit code [21, 164] is the only code to date which can be deterministically (unconditionally) implemented using only linear optics and sources of entanglement. Like the discrete Shor code, it can correct arbitrary errors on single channels; however, more sophisticated codes would be required to correct some important forms of error such as loss on all channels simultaneously [93, 249]. The experiment explained here is the first implementation of a Shor-type code, as the preparation of nine-party entanglement is still beyond the scope of existing non-optical approaches and single-photon-based, optical schemes. Indeed, previous implementations of QEC were based on qubit codes, either in liquid-state NMR (using up to five qubits) [240, 241, 243, 244], linear ion trap hardware configurations (using up to three qubits) [245], or single-photon linear optics (using up to four qubits) [246, 247]. Here, continuous-variable QEC [237, 238] utilizes squeezed states of light and networks of beam splitters [164] which are extensively explained in the previous sections. Even this optical approach requires an optical network three times the size as that used in teleportation network experiments explained in Section 4.2.3 to achieve the large-scale multi-partite entanglement for a nine-wavepacket code.

In the scheme presented here, as for the simplest QEC codes (whether for qubits or for continuous variables), a single, arbitrary error can be corrected. Such schemes typically assume errors occur stochastically and therefore rely on the low frequency of multiple errors. Stochastic error models may describe, for example, stochastic, depolarizing channels for qubits, or in the CV regime [94], free-space channels with atmospheric fluctuations causing beam jitter, as considered recently for various nondeterministic distillation protocols [250–253] (see Figure 5.4 for a three-mode QEC scheme with such a stochastic error model).

The overall performance of this family of QEC codes is only limited by the accuracy with which ancilla state preparation, encoding and decoding circuits, and syndrome extraction and recovery operations can be achieved. In the continuous-variable scheme, all these ingredients can be efficiently implemented. In the absence of squeezing, the fidelity is limited by the vacuum noise. We dub this case

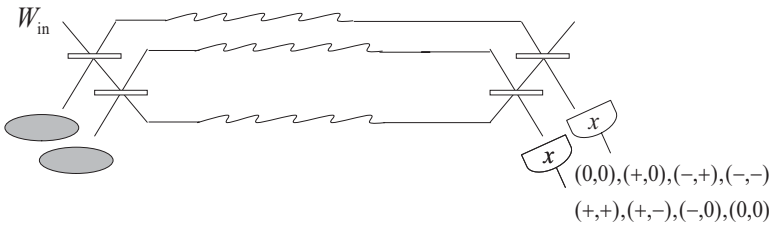

Figure 5.4 Protecting an arbitrary input state W_{in} against stochastic position shift errors using two squeezed ancilla modes and two beam splitters for encoding, two beam splitters for decoding, and two homodyne detectors for syndrome identification [94]. The final correction step is accomplished through phase-space displacements of the signal mode conditioned upon the syndrome results for the ancilla modes. The syndromes are position shifts of the ancilla modes in either + or − direction.

quantum-limited error correction. Squeezing of the auxiliary modes is linked with the presence of entanglement and thus determines whether the transfer fidelities exceed those of the quantum-limited error correction.

In the limit of infinite ancilla squeezing, the encoded state would be given by Eq. (5.3). Figure 5.5 shows a schematic of our linear-optics realization of the nine-wavepacket code using finite-squeezing resources. In the encoding stage, an input state is entangled with eight squeezed ancillae, each corresponding to an approximate "0" ("blank") state. After an error is introduced, the states are decoded simply

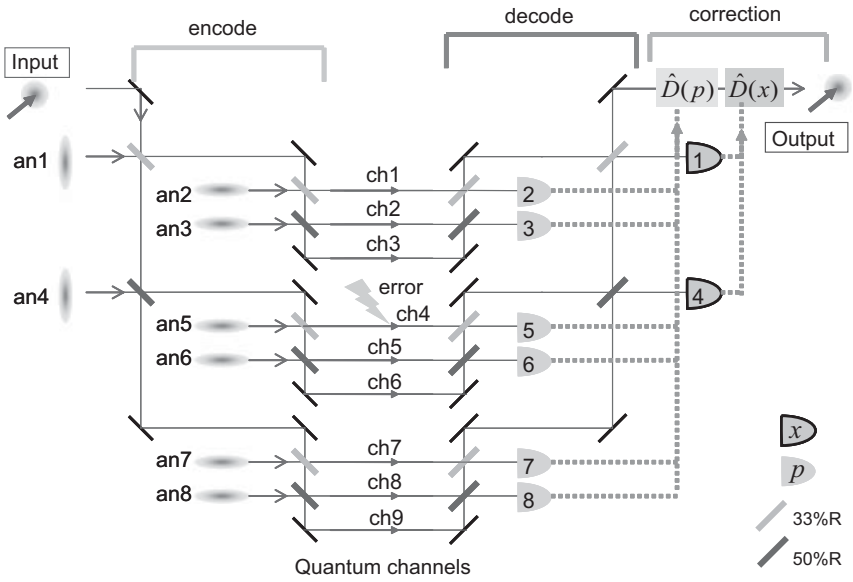

Figure 5.5 Schematic for nine-wavepacket quantum error correction code [164] operation; for correcting an arbitrary error occurring in any one of the nine channels [239]. The dotted lines represent the classical information that is used to compute the necessary syndrome recovery operations.

by inverting the encoding. The eight ancilla modes are then measured (with x-quadrature measurements performed in detectors 1 and 4 and p-quadrature measurements in six other detectors), and the results of the measurements are used for error syndrome recognition. More precisely, these are the results of homodyne detection applied to the ancilla modes along their initial squeezing direction.

The encoding stage consists of two steps in order to realize the concatenation of position and momentum codes [164]. First, position-encoding is achieved via a *tritter* $T_{\text{in,an1,an4}}$ that is two beam splitters (33%R and 50%R in Figure 5.5) acting upon the input mode and two x-squeezed ancilla modes (an1 and an4 in Figure 5.5). The second step provides the momentum-encoding via three more tritters, with six additional p-squeezed ancilla modes (an2, an3, an5, an6, an7 and an8 in Figure 5.5). The overall encoding circuit becomes

$$T_{\text{an4,an7,an8}}\, T_{\text{an1,an5,an6}}\, T_{\text{in,an2,an3}}\, T_{\text{in,an1,an4}}\ . \tag{5.10}$$

In the experiment, a code state was generated with position x and momentum p interchanged. This alternate encoding (and the corresponding QEC protocol) only involves a change of basis with no drop in performance. Quantum optically, this change corresponds to a 90-degree rotation of the quadrature amplitudes, requiring local oscillator phases to be shifted by 90 degrees for homodyne detection.

The finitely squeezed, encoded state exhibits the following quadrature quantum correlations,

$$\begin{aligned}
\hat{x}_1 + \hat{x}_2 + \hat{x}_3 - (\hat{x}_4 + \hat{x}_5 + \hat{x}_6) &= \frac{3}{\sqrt{2}}\hat{x}^{(0)}_{\text{an1}}\mathrm{e}^{-r_1} - \sqrt{\frac{3}{2}}\hat{x}^{(0)}_{\text{an4}}\mathrm{e}^{-r_4}\ ,\\
\hat{x}_4 + \hat{x}_5 + \hat{x}_6 - (\hat{x}_7 + \hat{x}_8 + \hat{x}_9) &= \sqrt{6}\hat{x}^{(0)}_{\text{an4}}\mathrm{e}^{-r_4}\ ,\\
\hat{p}_1 - \hat{p}_2 &= \sqrt{\frac{3}{2}}\hat{p}^{(0)}_{\text{an2}}\mathrm{e}^{-r_2} - \frac{1}{\sqrt{2}}\hat{p}^{(0)}_{\text{an3}}\mathrm{e}^{-r_3}\ ,\\
\hat{p}_2 - \hat{p}_3 &= \sqrt{2}\hat{p}^{(0)}_{\text{an3}}\mathrm{e}^{-r_3}\ ,\\
\hat{p}_4 - \hat{p}_5 &= \sqrt{\frac{3}{2}}\hat{p}^{(0)}_{\text{an5}}\mathrm{e}^{-r_5} - \frac{1}{\sqrt{2}}\hat{p}^{(0)}_{\text{an6}}\mathrm{e}^{-r_6}\ ,\\
\hat{p}_5 - \hat{p}_6 &= \sqrt{2}\hat{p}^{(0)}_{\text{an6}}\mathrm{e}^{-r_6}\ ,\\
\hat{p}_7 - \hat{p}_8 &= \sqrt{\frac{3}{2}}\hat{p}^{(0)}_{\text{an7}}\mathrm{e}^{-r_7} - \frac{1}{\sqrt{2}}\hat{p}^{(0)}_{\text{an8}}\mathrm{e}^{-r_8}\ ,\\
\hat{p}_8 - \hat{p}_9 &= \sqrt{2}\hat{p}^{(0)}_{\text{an8}}\mathrm{e}^{-r_8}\ .
\end{aligned} \tag{5.11}$$

In the limit $r_{1-8} \to \infty$, the quadrature operators become perfectly correlated and we obtain the ideal stabilizer/nullifier conditions of Eq. (5.5) (with $\hat{x}$ and $\hat{p}$ interchanged throughout).

As the decoding stage merely inverts the encoding, the eight ancilla modes will remain all "0" in the absence of errors. In the presence of an error in any one of the nine channels, the measurement results of the decoded ancillae will lead to nonzero components containing a sufficient amount of information for identifying and

Table 5.1 Error syndrome measurements [239]. LO phase: quadrature at which the local oscillator phase of the homodyne detector is locked, ES: equal signs, DS: different signs.

Channel with an error	Detectors with nonzero outputs	LO phase
1	1	x
	2	p
2	1	x
	2,3 (DS)	p
3	1	x
	2,3 (ES)	p
4	1,4 (DS)	x
	5	p
5	1,4 (DS)	x
	5,6 (DS)	p
6	1,4 (DS)	x
	5,6 (ES)	p
7	1,4 (ES)	x
	7	p
8	1,4 (ES)	x
	7,8 (DS)	p
9	1,4 (ES)	x
	7,8 (ES)	p

hence correcting the error (see Table 5.1 for an error-syndrome map). Similar to the qubit QEC scheme where the conditional state after the syndrome measurements becomes the original input state up to some discrete Pauli errors, the conditional state of the present scheme coincides with the input state up to some simple phase-space displacements. Thus, it only remains to apply the appropriate (inverse) displacement operations in order to correct the errors.

The detailed experimental setup for the nine-wavepacket QEC scheme is shown in Figure 5.6. Eight squeezed vacua are created by four optical parametric oscillators (OPOs) which have two counter-propagating modes; thus, every OPO creates two individual squeezed vacua. The squeezing level of each single-mode squeezed vacuum state corresponds to roughly 1 dB below shot noise. For pumping the OPOs, the second harmonic of a cw Ti:sapphire laser output is used. The syndrome measurements are performed via homodyne detection with near-unit efficiency.

To apply a single error, a coherent modulation is first generated in a so-called error beam using an electro-optic modulator (EOM) ("modulated mode"). This beam is then superimposed onto the selected mode or channel ("target mode") through a high-reflectivity beam splitter [203] with independently swept phase, resulting in a quasi-random displacement error. The error-correcting displacement operations (as determined by decoding and measurement) are then similarly performed via

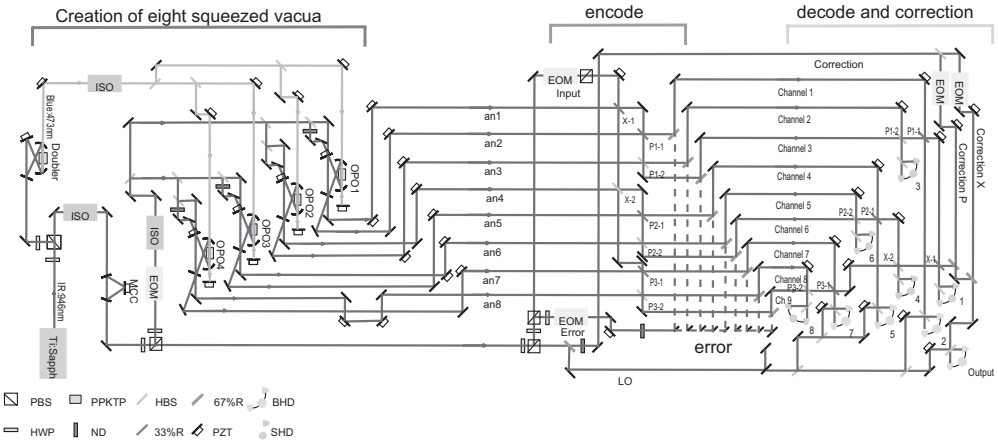

Figure 5.6 Experimental setup of the nine-wavepacket quantum error correction [239]; PBS: polarization beam splitter, PPKTP: periodically poled $KTiOPO_4$, HBS: half (symmetric) beam splitter, HWP: half wave plate, ND: neutral density filter, PZT: piezoelectric transducer, BHD: balanced homodyning, SHD: self-homodyning, OPO: optical parametric oscillator, MCC: mode-cleaning cavity, LO: local oscillator, ISO: optical isolator, EOM: electro-optic modulator.

an EOM and a high-reflectivity beam splitter, but now with phase locking between the modulated and target modes along either the x or p axis as appropriate.

Figure 5.7 shows some examples for error syndrome measurement results. Here, the input state is chosen to be a vacuum state. A random displacement error in phase space is imposed on channel 1 (Figure 5.7(I)) and on channel 9 (Figure 5.7(II)). A two-channel oscilloscope is used to measure the outputs of pairs of detectors
(1, 4), (2, 3), (5, 6), and (7, 8). Comparing the results of Figure 5.7(I) with Table 5.1, one can identify an error occurring in channel 1 since only detectors 1 and 2 have nonzero outputs. The outputs from detectors 1 and 2 correspond to the desired x and p displacements, respectively. Similarly, from Figure 5.7(II), we can recognize that an error has occurred in channel 9. Here, detectors 1, 4, 7, and 8 have nonzero outputs and the outputs of detectors 1 and 4, as well as 7 and 8 have equal signs (distinguishing it from the case of an error in channel 8, for which outcomes 7 and 8 have different signs).

Figure 5.8 shows two examples of QEC results, comparing output states with and without error correction, and with and without squeezing of the ancilla modes. In Figure 5.8(I), an error was introduced in channel 1. The local oscillator (LO) phase of the homodyne detector was tuned to detect the x quadrature of channel 1. Similarly, in Figure 5.8(II), the error was introduced in channel 9 and the LO phase is locked to the p quadrature. For ease of experimental implementation, only the measurement outcomes of detectors 4 and 8 were fed forward to the error correction step. In principle, using the combined outputs of detectors 1 and 4 for x and detectors 7 and 8 for p would yield even higher fidelities.

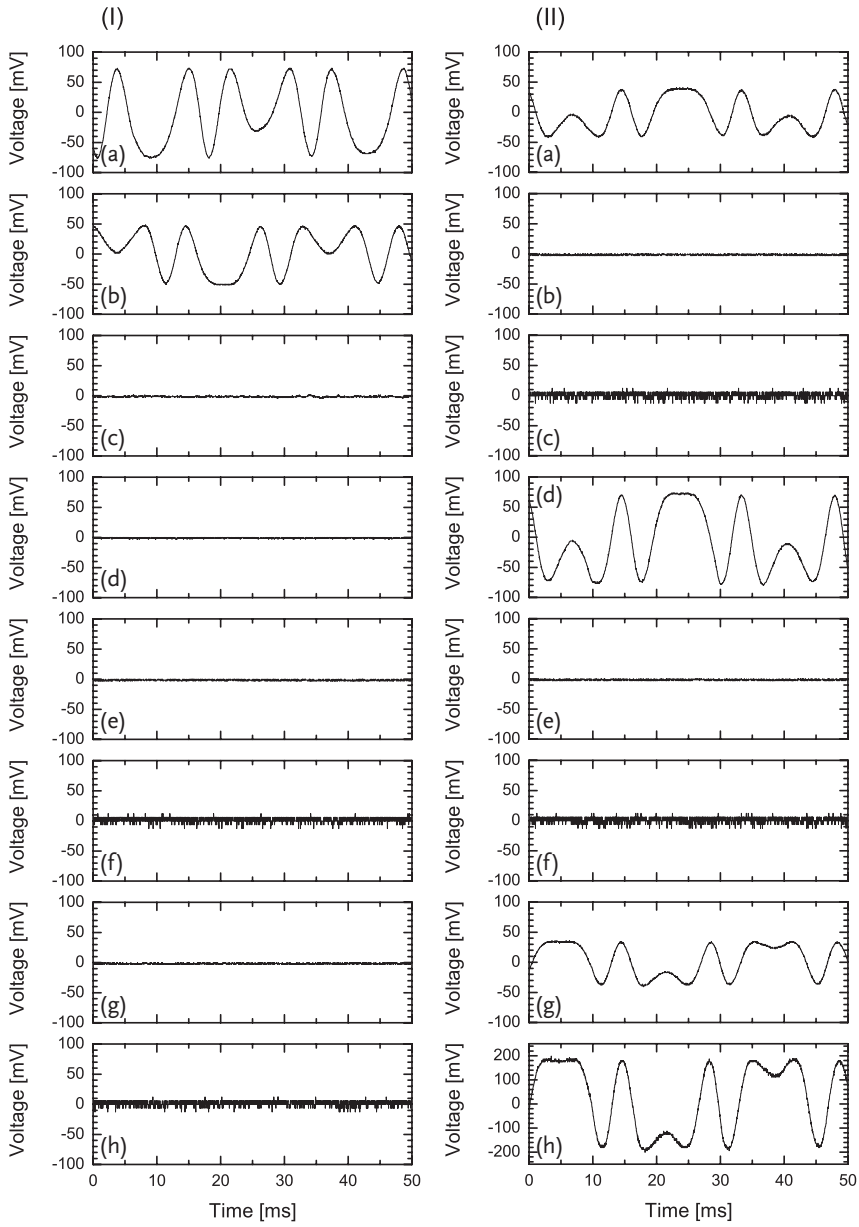

Figure 5.7 Error syndrome measurement results [239]. (I) A random displacement error is imposed on channel 1. (II) A random displacement error is imposed on channel 9. A two-channel oscilloscope is used measuring the outputs of detectors 1 and 4, 2 and 3, 5 and 6 and 7 and 8. (a) output signal of detector 1, (b) detector 2, (c) detector 3, (d) detector 4, (e) detector 5, (f) detector 6, (g) detector 7, (h) detector 8.

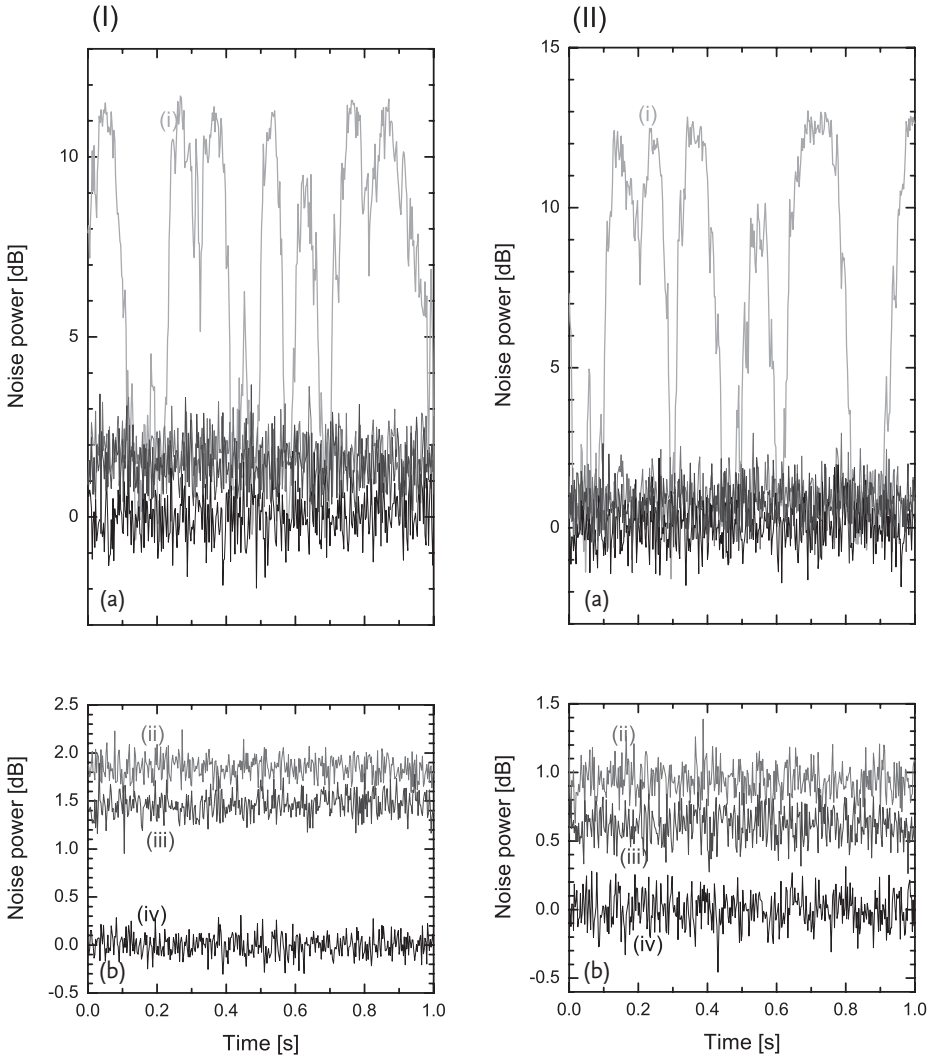

Figure 5.8 Results of quantum error correction [239]. (I) A random phase-space displacement error is imposed on channel 1. The LO phase of the homodyne detector is locked to the *x* quadrature. (II) A random displacement error is imposed on channel 9. The LO phase of the homodyne detector is locked to the *p* quadrature. In each case, four traces are compared: (i) Homodyne detector output without error correction (no feed forward step). (ii) Error correction output without squeezing. (iii) Error correction output with squeezing. (iv) Shot noise level. (a) Single scan of a spectrum analyzer with zero span mode. 2 MHz center frequency, 30 kHz resolution band width and 300 Hz video band width. (b) 30 times average of traces (ii–iv) above.

The quality of the error correction can be assessed via the fidelity $F = \langle\psi_{\text{in}}|\hat{\rho}_{\text{out}}|\psi_{\text{in}}\rangle$, where $|\psi_{\text{in}}\rangle$ represents the input state and $\hat{\rho}_{\text{out}}$ corresponds to the output state of the error correction circuit [203, 211, 212]. Here, the fidelity is calculated as

$$F = \frac{2}{\sqrt{\left(1 + 4\left\langle(\Delta\hat{x}_{\text{out}})^2\right\rangle\right)\left(1 + 4\left\langle(\Delta\hat{p}_{\text{out}})^2\right\rangle\right)}}\,, \tag{5.12}$$

where $\hat{x}_{\text{out}}$ and $\hat{p}_{\text{out}}$ are quadrature operators of the output field. For example, in the case of an error in channel 1, the output quadrature operators become

$$\begin{aligned}\hat{x}_{\text{out}} &= \hat{x}_{\text{in}} - \frac{1}{\sqrt{2}}\hat{x}^{(0)}_{\text{an1}}\mathrm{e}^{-r_1}\\ \hat{p}_{\text{out}} &= \hat{p}_{\text{in}} - \frac{1}{\sqrt{6}}\hat{p}^{(0)}_{\text{an2}}\mathrm{e}^{-r_2}\,,\end{aligned} \tag{5.13}$$

where $\hat{x}_{\text{in}}$, $\hat{p}_{\text{in}}$, $\hat{x}^{(0)}_{\text{an1}}$, and $\hat{p}^{(0)}_{\text{an2}}$ are quadrature operators of the input field and the ancilla vacuum modes, and r_i are squeezing parameters for ancilla i. In the ideal case of $r_i \to \infty$, unit fidelity is obtained with output states approaching the input states. For zero squeezing, Eq. (5.13) yields an excess noise of 1/2 and 1/6 for the x and p quadratures corresponding to 1.76 and 0.67 dB of output powers, respectively (see Table 5.2 and all the experimental results are summarized in the table).

Equation (5.12) can be used to translate the measured noise level values from Table 5.2 into fidelity values. Indeed, for every possible error introduced (in any of the channels), the fidelity after error correction exceeds the maximum values achievable for the scheme in the absence of ancilla squeezing. For example, for an error in mode 1, a fidelity of 0.88 ± 0.01 was achieved (exceeding the "classical" cutoff of 0.86). Similarly, for an error in channel 9, we obtain a fidelity of 0.86 ± 0.01, exceeding a cutoff of 0.82 (The lower cutoff takes into consideration that only two of the four nonzero components are used.). The improvement over quantum-limited fidelities for errors in *any* one of the nine channels is the key demonstration of this experiment, providing indirect evidence of entanglement-enhanced error correction. By comparison, in complete absence of any error correction, that is, without reversing displacement errors (including the zero-squeezing case; for an application of such quantum-limited error correction), fidelity values under 0.007 ± 0.001 were obtained. Nonetheless, instead of this absolute improvement, it is the extent to which the classical cutoff is exceeded which quantifies the effectiveness of the nonclassical resources.

In the experiment of [239], evidence is obtained for an entanglement-enhanced correction of displacement errors; a further increase of the small enhancement of that implementation would only require higher squeezing levels of the resource states. The scheme could be useful for applications where stochastic errors occur such as free-space communication with fluctuating losses and beam pointing errors [250–253].

Table 5.2 Output noise power of QEC circuit in dB, relative to the shot noise level. Perfect error correction therefore corresponds to 0 dB. SQ: squeezing.

Error on mode	Quadrature of output	Output power without SQ (theory)	Output power without SQ (experiment)	Output power with SQ (experiment)
1	x	1.76	1.84 ± 0.12	1.46 ± 0.13
	p	0.67	0.68 ± 0.12	0.57 ± 0.12
2	x	1.76	1.75 ± 0.12	1.42 ± 0.13
	p	0.87	0.97 ± 0.12	0.72 ± 0.12
3	x	1.76	1.83 ± 0.12	1.41 ± 0.12
	p	0.87	0.92 ± 0.12	0.70 ± 0.12
4	x	2.22	2.26 ± 0.12	1.67 ± 0.12
	p	0.67	0.73 ± 0.12	0.50 ± 0.12
5	x	2.22	2.33 ± 0.12	1.79 ± 0.12
	p	0.87	0.88 ± 0.12	0.73 ± 0.13
6	x	2.22	2.34 ± 0.12	1.77 ± 0.12
	p	0.87	0.87 ± 0.13	0.73 ± 0.13
7	x	2.22	2.30 ± 0.13	1.72 ± 0.12
	p	0.67	0.69 ± 0.12	0.57 ± 0.12
8	x	2.22	2.18 ± 0.13	1.79 ± 0.13
	p	0.87	0.84 ± 0.12	0.65 ± 0.12
9	x	2.22	2.18 ± 0.14	1.82 ± 0.13
	p	0.87	0.94 ± 0.12	0.61 ± 0.12

5.4 Entanglement Distillation

The entanglement of a composite quantum state is distillable if a sufficiently large number of copies of that state can be converted into a pure maximally entangled state (or arbitrarily close to it) through local operations and classical communication. This entanglement distillation is typically (but not necessarily) probabilistic.[2)]

Although various experiments for distilling pure and even mixed entangled qubit states have been performed [255–258], the situation for CV entangled states is quite different. The need for a non-Gaussian element in CV distillation[3)] led to a few distinct approaches. One such approach is to induce non-Gaussian noise such that the resulting mixed entangled state is no longer a Gaussian state [250–252, 259, 260], in which case distillation is possible with Gaussian operations. Along these

2) In general, the overall entanglement cannot be increased deterministically through local operations and classical communication. However, this still allows, for instance, to transform two equally entangled copies into one more and one less entangled copy in a deterministic fashion [254].

3) Recall that Gaussian entangled states cannot be distilled through Gaussian operations alone (see Chapter 2).

lines, channels with random phase fluctuations [252] and random attenuation [251] have been experimentally demonstrated.

An example of probabilistic entanglement distillation (concentration) of a single copy of a *pure* Gaussian two-mode squeezed state (TMSS) into a higher entangled non-Gaussian (but still infinite-dimensional) state through non-Gaussian operations, namely, by subtracting photons, was presented in [261]. The original version of this protocol required photon number resolving (PNR) detectors. Nonetheless, simple on/off detectors work as well [262]. The entanglement before and after the distillation can be generally quantified in a numerical fashion [263] as well as analytically to some extent [158].

More important and more realistic, however, is the distillation of *mixed* Gaussian TMSSs because a TMSS will be subject to losses and noise in a channel when used for communication, and in most experiments, the TMSS is not entirely pure when the antisqueezing exceeds the squeezing level (see below). An extended theoretical analysis of photon-subtraction-based distillation techniques including Gaussian mixed states as resources can be found in [158]. This type of distillation was recently demonstrated experimentally [264].

In order to understand single-copy distillation through photon subtraction, consider a TMSS in the Fock basis (see Chapter 3),

$$|\Psi\rangle = \sum_{n=0}^{\infty} \sqrt{1-\lambda^2}\lambda^n |n,n\rangle \ , \tag{5.14}$$

giving at the same time the Schmidt decomposition (see Section 1.5) with Schmidt coefficient $\sqrt{1-\lambda^2}\lambda^n$. These decrease exponentially with photon number n. Intuitively, the photon subtraction can be described by applying the photon annihilation operator $\hat{a}$ upon the TMSS, corresponding to the asymptotic case of a beam splitter with transmittance $T \to 1$. After photon subtraction, $(\hat{a}\otimes\hat{a})|n,n\rangle = n|n-1,n-1\rangle$, the renormalized state is

$$|\Psi'\rangle = \sum_{n=0}^{\infty} \frac{(1-\lambda^2)^{3/2}}{\lambda\sqrt{1+\lambda^2}}(n+1)\lambda^{n+1}|n,n\rangle \ , \tag{5.15}$$

whose Schmidt coefficients now decrease more slowly with increasing photon number n. Quantifying the entanglement of the states in Eqs. (5.14) and (5.15) using the logarithmic negativity (see Section 1.5) gives

$$E_N(|\Psi\rangle) = \log_2 \frac{1+\lambda}{1-\lambda} \ , \tag{5.16}$$

$$E_N(|\Psi'\rangle) = \log_2 \frac{(1+\lambda)^3}{(1-\lambda)(1+\lambda^2)} \ . \tag{5.17}$$

For any squeezing $0 < \lambda < 1$, the entanglement of the TMSS state can be enhanced through a perfect photon annihilation operation. However, this is no longer so straightforward, though similar conclusions can still be drawn when we replace the pure TMSS by a mixed state corresponding to the realistic situation in the experiment described below or after a lossy-channel transmission for communication;

or when we use a beam splitter and photon detectors instead of the ideal photon annihilation operator (see [158] for more details).

5.5 Experiment: Entanglement Distillation

5.5.1 Qubits

Although there are several experimental demonstrations of qubit entanglement distillation [255, 257, 265], we will explain the experiment of Pan *et al.* [265] in detail in this section. This is because the error model used in this experiment is rather general and instructive. The original proposal for this type of entanglement distillation was made by Bennett *et al.* [22] and a scheme realizable with linear optics was proposed by Pan *et al.* [256]. Based on that scheme, Pan *et al.* demonstrated qubit entanglement distillation [265].

Figure 5.9 shows qubit entanglement distillation as proposed and demonstrated by Pan *et al.* [256, 265]. In this experiment, the polarization entangled state $|\Phi^{(+)}\rangle$ [see Eq. (3.19)] is distilled. First, Alice and Bob share two mixed entangled pairs a1–b1 and a2–b2 whose density operators are

$$\hat{\rho}_{aibi} = F \left|\Phi^{(+)}\right\rangle_{aibi}\left\langle\Phi^{(+)}\right| + (1-F)\left|\Psi^{(-)}\right\rangle_{aibi}\left\langle\Psi^{(-)}\right|, \tag{5.18}$$

where $i = 1, 2$ denotes pair 1 or 2, $|\Psi^{(-)}\rangle$ is defined in Eq. (3.19), and $F = \langle\Phi^{(+)}|\hat{\rho}_{aibi}|\Phi^{(+)}\rangle$ is the fidelity to the desired state $|\Phi^{(+)}\rangle$. Then, Alice combines photons a1 and a2 with a polarization beam splitter (PBS) and gets photons a3 and a4. Similarly, Bob combines photons b1 and b2 with a PBS and gets photons b3 and b4. Here, only the case with photons simultaneously at a3, a4, b3, and b4 is post-selected.

From the nature of PBS shown in Figure 5.10, photons a3 and a4 and photons b3 and b4 have to have the same polarization in the case of photons being

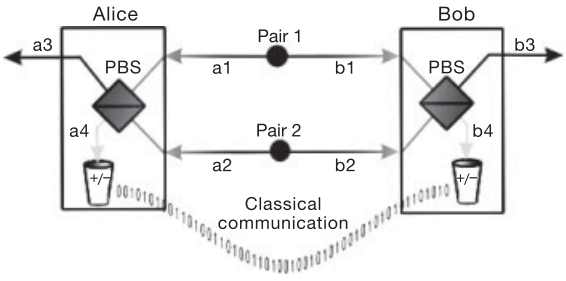

Figure 5.9 Scheme for qubit entanglement distillation proposed and demonstrated by Pan *et al.* [256, 265]. Photons a4 and b4 are measured with $\{|+\rangle, |-\rangle\}$ basis, where $|\pm\rangle = (|\leftrightarrow\rangle \pm |\updownarrow\rangle)/\sqrt{2}$.

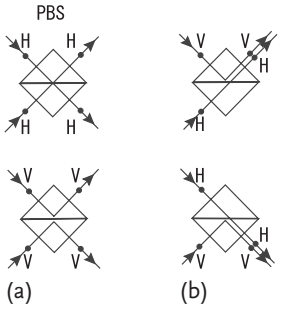

Figure 5.10 Nature of a PBS used in the experiment [256, 265]. Two photons with horizontal (H) or vertical (V) polarization are combined by a PBS. (a) Two photons have the same polarization and (b) different polarization.

simultaneously present at a3, a4, b3, and b4. From the constraint, only the cases of $|\Phi^{(+)}\rangle_{a1b1} \otimes |\Phi^{(+)}\rangle_{a2b2}$ and $|\Psi^{(-)}\rangle_{a1b1} \otimes |\Psi^{(-)}\rangle_{a2b2}$ can survive with the probability $F^2/2$ and $(1-F)^2/2$, respectively. More explicitly,

$$\begin{aligned}
\left|\Phi^{(+)}\right\rangle_{a1b1} \otimes \left|\Phi^{(+)}\right\rangle_{a2b2} &= \frac{1}{\sqrt{2}}\left(|\leftrightarrow\rangle_{a1} \otimes |\leftrightarrow\rangle_{b1} + |\updownarrow\rangle_{a1} \otimes |\updownarrow\rangle_{b1}\right) \\
&\quad \otimes \left(|\leftrightarrow\rangle_{a2} \otimes |\leftrightarrow\rangle_{b2} + |\updownarrow\rangle_{a2} \otimes |\updownarrow\rangle_{b2}\right) \\
&= \frac{1}{2}\left(|\leftrightarrow\rangle_{a1} \otimes |\leftrightarrow\rangle_{a2} \otimes |\leftrightarrow\rangle_{b1} \otimes |\leftrightarrow\rangle_{b2}\right. \\
&\quad + |\leftrightarrow\rangle_{a1} \otimes |\updownarrow\rangle_{a2} \otimes |\leftrightarrow\rangle_{b1} \otimes |\updownarrow\rangle_{b2} \\
&\quad + |\updownarrow\rangle_{a1} \otimes |\leftrightarrow\rangle_{a2} \otimes |\updownarrow\rangle_{b1} \otimes |\leftrightarrow\rangle_{b2} \\
&\quad \left. + |\updownarrow\rangle_{a1} \otimes |\updownarrow\rangle_{a2} \otimes |\updownarrow\rangle_{b1} \otimes |\updownarrow\rangle_{b2}\right) \\
&\rightarrow \frac{1}{2}\left(|\leftrightarrow\rangle_{a3} \otimes |\leftrightarrow\rangle_{a4} \otimes |\leftrightarrow\rangle_{b3} \otimes |\leftrightarrow\rangle_{b4}\right. \\
&\quad \left. + |\updownarrow\rangle_{a3} \otimes |\updownarrow\rangle_{a4} \otimes |\updownarrow\rangle_{b3} \otimes |\updownarrow\rangle_{b4}\right), \qquad (5.19)
\end{aligned}$$

and

$$\begin{aligned}
\left|\Psi^{(-)}\right\rangle_{a1b1} \otimes \left|\Psi^{(-)}\right\rangle_{a2b2} &= \frac{1}{\sqrt{2}}\left(|\leftrightarrow\rangle_{a1} \otimes |\updownarrow\rangle_{b1} - |\updownarrow\rangle_{a1} \otimes |\leftrightarrow\rangle_{b1}\right) \\
&\quad \otimes \left(|\leftrightarrow\rangle_{a2} \otimes |\updownarrow\rangle_{b2} - |\updownarrow\rangle_{a2} \otimes |\leftrightarrow\rangle_{b2}\right) \\
&= \frac{1}{2}\left(|\leftrightarrow\rangle_{a1} \otimes |\leftrightarrow\rangle_{a2} \otimes |\updownarrow\rangle_{b1} \otimes |\updownarrow\rangle_{b2}\right. \\
&\quad - |\leftrightarrow\rangle_{a1} \otimes |\updownarrow\rangle_{a2} \otimes |\updownarrow\rangle_{b1} \otimes |\leftrightarrow\rangle_{b2} \\
&\quad - |\updownarrow\rangle_{a1} \otimes |\leftrightarrow\rangle_{a2} \otimes |\leftrightarrow\rangle_{b1} \otimes |\updownarrow\rangle_{b2} \\
&\quad \left. + |\updownarrow\rangle_{a1} \otimes |\updownarrow\rangle_{a2} \otimes |\leftrightarrow\rangle_{b1} \otimes |\leftrightarrow\rangle_{b2}\right) \\
&\rightarrow \frac{1}{2}\left(|\leftrightarrow\rangle_{a3} \otimes |\leftrightarrow\rangle_{a4} \otimes |\updownarrow\rangle_{b3} \otimes |\updownarrow\rangle_{b4}\right. \\
&\quad \left. + |\updownarrow\rangle_{a3} \otimes |\updownarrow\rangle_{a4} \otimes |\leftrightarrow\rangle_{b3} \otimes |\leftrightarrow\rangle_{b4}\right). \qquad (5.20)
\end{aligned}$$

As a final step, Alice and Bob make a polarization measurement with $\{|+\rangle, |-\rangle\}$ basis for photons a4 and b4 where $|+\rangle = (|\leftrightarrow\rangle + |\updownarrow\rangle)/\sqrt{2}$ and $|-\rangle = (|\leftrightarrow\rangle - |\updownarrow\rangle)/\sqrt{2}$. Then, Alice and Bob make a classical communication to compare the measurement

results and finish the distillation. Here, they use the following relations:

$$
\begin{aligned}
&|\leftrightarrow\rangle_{a3}\otimes|\leftrightarrow\rangle_{a4}\otimes|\leftrightarrow\rangle_{b3}\otimes|\leftrightarrow\rangle_{b4}\\
&=|\leftrightarrow\rangle_{a3}\otimes\frac{|+\rangle_{a4}+|-\rangle_{a4}}{\sqrt{2}}\otimes|\leftrightarrow\rangle_{b3}\otimes\frac{|+\rangle_{b4}+|-\rangle_{b4}}{\sqrt{2}}\,,\\
&|\leftrightarrow\rangle_{a3}\otimes|\leftrightarrow\rangle_{a4}\otimes|\updownarrow\rangle_{b3}\otimes|\updownarrow\rangle_{b4}\\
&=|\leftrightarrow\rangle_{a3}\otimes\frac{|+\rangle_{a4}+|-\rangle_{a4}}{\sqrt{2}}\otimes|\updownarrow\rangle_{b3}\otimes\frac{|+\rangle_{b4}-|-\rangle_{b4}}{\sqrt{2}}\,,\\
&|\updownarrow\rangle_{a3}\otimes|\updownarrow\rangle_{a4}\otimes|\leftrightarrow\rangle_{b3}\otimes|\leftrightarrow\rangle_{b4}\\
&=|\updownarrow\rangle_{a3}\otimes\frac{|+\rangle_{a4}-|-\rangle_{a4}}{\sqrt{2}}\otimes|\leftrightarrow\rangle_{b3}\otimes\frac{|+\rangle_{b4}+|-\rangle_{b4}}{\sqrt{2}}\,,\\
&|\updownarrow\rangle_{a3}\otimes|\updownarrow\rangle_{a4}\otimes|\updownarrow\rangle_{b3}\otimes|\updownarrow\rangle_{b4}\\
&=|\updownarrow\rangle_{a3}\otimes\frac{|+\rangle_{a4}-|-\rangle_{a4}}{\sqrt{2}}\otimes|\updownarrow\rangle_{b3}\otimes\frac{|+\rangle_{b4}-|-\rangle_{b4}}{\sqrt{2}}\,.
\end{aligned}
\tag{5.21}
$$

For example, if both Alice and Bob get $+$ and make it sure with classical communication, the state of photons a3 and a4 becomes the mixed state of $|\Phi^{(+)}\rangle_{a3b3}$ and $|\Psi^{(+)}\rangle_{a3b3}$ with the density operator

$$
\hat{\rho}_{a3b4}=F'\left|\Phi^{(+)}\right\rangle_{aibi}\left\langle\Phi^{(+)}\right|+\left(1-F'\right)\left|\Psi^{(+)}\right\rangle_{aibi}\left\langle\Psi^{(+)}\right|\,, \tag{5.22}
$$

where $F'=F^2/(F^2+(1-F)^2)$. In the case of $F>0.5$, which means the fidelity to $|\Phi^{(+)}\rangle$ is not bad at the very beginning, $F'>F$ and the distillation is accomplished.

For the case of the other measurement results like $--$, $-+$, and $+-$, Alice and Bob can make a distillation in principle, but they have to make a feedforward like teleportation and quantum error correction [22, 256]. In the experiment of Pan *et al.*, they just post-selected the case of $++$ for eliminating feedforward [265].

Figure 5.11 shows the experimental setup for qubit entanglement distillation demonstrated by Pan *et al.* [265]. By using the method explained in Section 3.1.3.1, they created two pairs of polarization entangled photons a1–b1 and a2–b2 in the state $|\Phi^{(+)}\rangle$. Both pairs suffer from decoherence or error which is imposed with half wave plates shown in Figure 5.11.

Figure 5.12 shows the experimental results. In the cases of Figure 5.12a,b, the half-wave-plate axis was oriented at 14° which corresponds to the initial fidelity $F=0.75$, and the results were consistent with the theory explained above. Here, we can check it with the following relations:

$$
\begin{aligned}
\left|\Phi^{(+)}\right\rangle&=\frac{1}{\sqrt{2}}\left(|\leftrightarrow\rangle_A\otimes|\leftrightarrow\rangle_B+|\updownarrow\rangle_A\otimes|\updownarrow\rangle_B\right)\\
&=\frac{1}{\sqrt{2}}\left(|+\rangle_A\otimes|+\rangle_B+|-\rangle_A\otimes|-\rangle_B\right),
\end{aligned}
\tag{5.23}
$$

$$
\begin{aligned}
\left|\Psi^{(-)}\right\rangle&=\frac{1}{\sqrt{2}}\left(|\leftrightarrow\rangle_A\otimes|\updownarrow\rangle_B-|\updownarrow\rangle_A\otimes|\leftrightarrow\rangle_B\right)\\
&=\frac{1}{\sqrt{2}}\left(|+\rangle_A\otimes|-\rangle_B-|-\rangle_A\otimes|+\rangle_B\right).
\end{aligned}
\tag{5.24}
$$

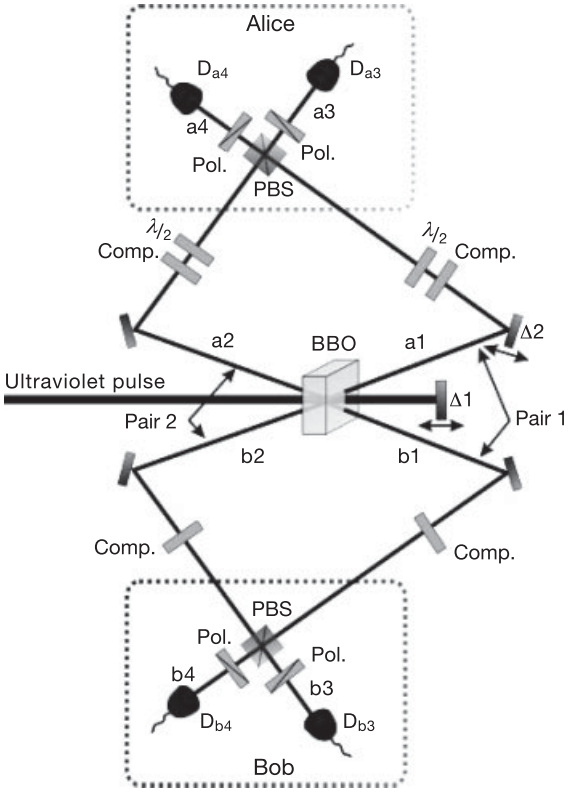

Figure 5.11 Experimental setup for qubit entanglement distillation demonstrated by Pan *et al.* [265]. $\lambda/2$: half wave plate for imposing an error.

Figure 5.12c,d shows the results of entanglement distillation (integration time was about 0.5 h). We can check the success of distillation with Eqs. (5.23) and (5.24) again.

5.5.2 Qumodes

Although there are several experimental demonstrations of CV entanglement distillation [250–252, 259], we will explain the experiment performed by Hage *et al.* [252] in detail. This is because this CV experiment is very similar to qubit entanglement distillation explained in Section 5.5.1.

As shown in Section 3.2.3.1, a CV (two-party) entangled state can be created with two squeezed vacua and a half beam splitter. More precisely, one can create a CV entangled state with only one squeezed vacuum and a half beam splitter which can be regarded as an asymmetric state with squeezing parameters with $r_1 > 0$ and $r_2 = 0$. In the experiment of Hage *et al.*, this type of entangled state is distilled when phase noise is present in each beam.

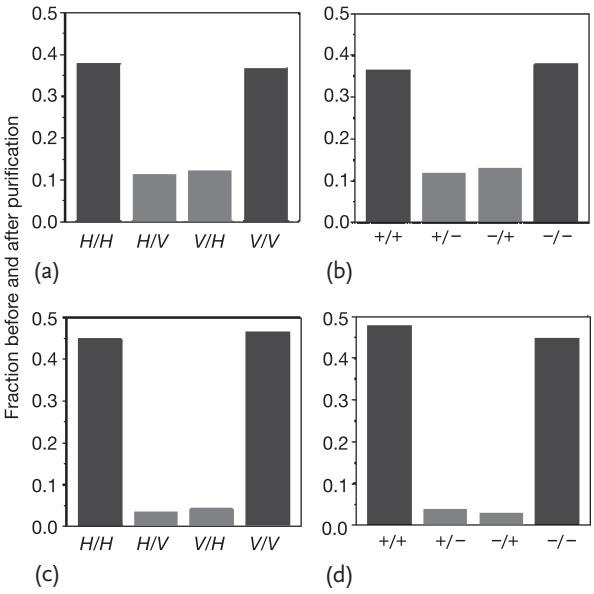

Figure 5.12 Experimental results for qubit entanglement distillation demonstrated by Pan *et al.* [265]. H: ↔, V: ↕. (a, b) before distillation (a) $\{|\leftrightarrow\rangle, |\updownarrow\rangle\}$ basis measurement, (b) $\{|+\rangle, |-\rangle\}$ basis measurement. (c, d) after distillation (c) $\{|\leftrightarrow\rangle, |\updownarrow\rangle\}$ basis measurement, (d) $\{|+\rangle, |-\rangle\}$ basis measurement.

Figure 5.13 shows the experimental setup for CV entanglement distillation demonstrated by Hage *et al.* [252]. Two optical parametric amplifiers (subthreshold optical parametric oscillators) create two independent squeezed light beams. These two beams are divided into two beams by half beam splitters $\mathrm{BS}_{\mathrm{E},1}$ and $\mathrm{BS}_{\mathrm{E},2}$, respectively, and two pairs of entangled light beams are created. The two pairs of entangled light beams are shared by Alice and Bob. Phase noises are imposed on the entangled light beams as decoherence.

For distillation, first, Alice and Bob locally combine their parts of entangled pairs with half beam splitters $\mathrm{BS}_{\mathrm{D,A}}$ and $\mathrm{BS}_{\mathrm{D,B}}$. Then, they make local measurements on amplitude quadratures $X_{\mathrm{T,A}}$ and $X_{\mathrm{T,B}}$ respectively for one of the output of the beam splitters with balanced homodyne detectors $\mathrm{BHD}_{\mathrm{T,A}}$ and $\mathrm{BHD}_{\mathrm{T,B}}$. Alice and Bob make a classical communication to chose trigger condition for distillation which satisfies

$$|X_{\mathrm{T,A}} + X_{\mathrm{T,B}}| < Q\,, \tag{5.25}$$

where Q is a certain threshold selected in the experiment. Here, we should recall that a sufficient condition for entanglement is

$$\left\langle \left[\Delta\left(\hat{x}_{\mathrm{A}} + \hat{x}_{\mathrm{B}}\right)\right]^2 \right\rangle + \left\langle \left[\Delta\left(\hat{p}_{\mathrm{A}} - \hat{p}_{\mathrm{B}}\right)\right]^2 \right\rangle < 1\,. \tag{5.26}$$

This condition would be satisfied with a certain value of Q in Eq. (5.25) [266]. Note that this procedure is very similar to the qubit distillation protocol explained in

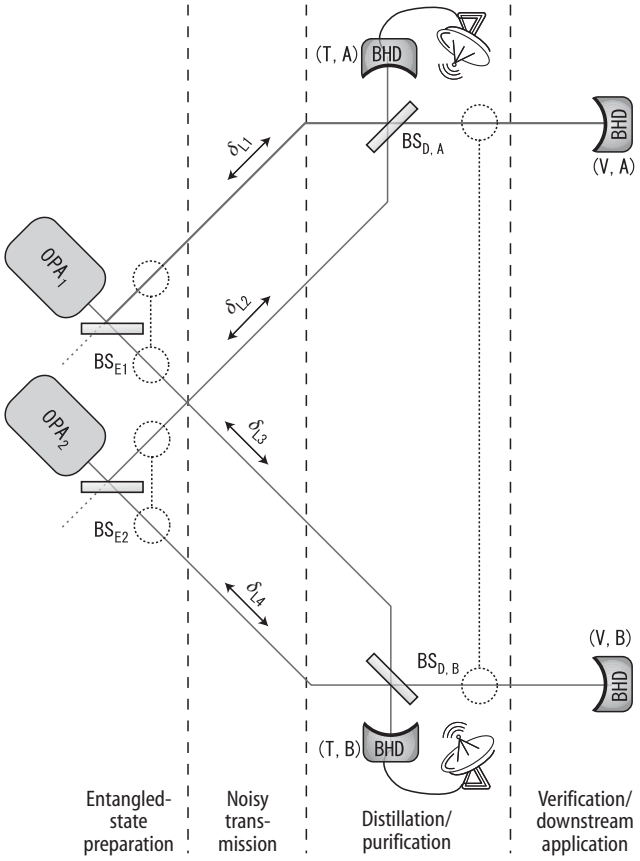

Figure 5.13 Experimental setup for CV entanglement distillation demonstrated by Hage *et al.* [252]. δ_{Li}: fluctuation of path length, BHD: balanced homodyne detector, OPA: optical parametric oscillator (squeezer), BS: half beam splitter.

Section 5.5.1 where Alice and Bob make local measurement and classical communication.

As a final step of distillation, Alice and Bob select those times when Eq. (5.25) is satisfied and so the other outputs of the half beam splitters $BS_{D,A}$ and $BS_{D,B}$ become a distilled pair. The outputs are measured with balanced homodyne detectors $BHD_{V,A}$ and $BHD_{V,B}$ to verify distillation.

Figure 5.14 shows the results of distillation [252]. The results show the success of entanglement distillation with a certain threshold value Q when the phase fluctuation is up to $\sigma = 0.545$. Here, total variance of $(X_{V,A} + X_{V,B})$ and $(P_{V,A} - P_{V,B})$ below unity means the existence of entanglement according to the inequality in Eq. (5.26).

In the remainder of this section, we will describe another example of a CV entanglement distillation experiment which was performed by Takahashi *et al.* [264]. In this experiment, Gaussian entangled states are distilled through non-Gaussian

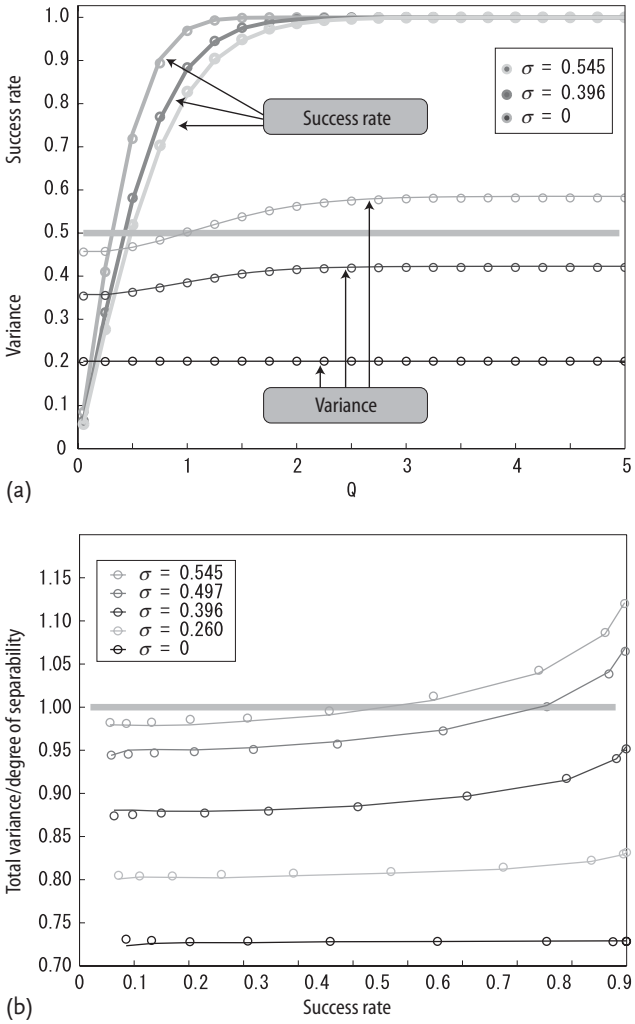

Figure 5.14 Experimental results for CV entanglement distillation demonstrated by Hage *et al.* [252]. (a) Variance of $(X_{V,A} + X_{V,B})$ and corresponding success rates versus threshold value Q for different strengths of the phase fluctuation σ. (b) The total variance of $(X_{V,A} + X_{V,B})$ and $(P_{V,A} - P_{V,B})$ plotted against the success rate. The total variance below one means the existence of entanglement.

operations. Therefore, we have the converse situation compared with Hage's experiment described above, where non-Gaussian entangled states were distilled by means of Gaussian operations.

In order to apply an appropriate non-Gaussian measurement such as photon counting upon a Gaussian state, we need to be able to perform the whole experiment in the time domain. This is different from the more traditional CV experiments which were mainly conducted in the frequency domain; recall our discus-

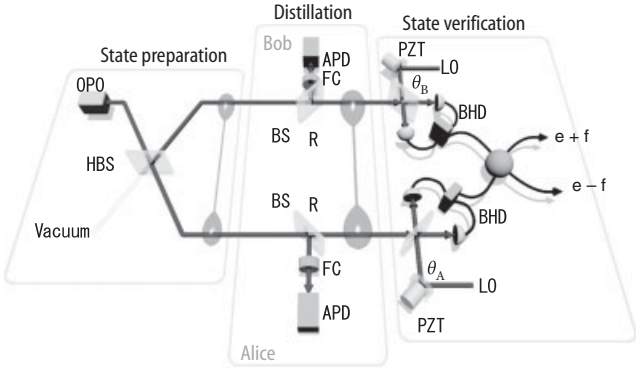

Figure 5.15 Experimental setup for for CV entanglement distillation demonstrated by Takahashi *et al.* [264]. OPO: optical parametric oscillator for creation of squeezed vacuum, HBS: half beam splitter, BS: beam splitter, R: Reflectivity of beam splitter, BHD: balanced homodyne detector, LO: local oscillator, θ: local oscillator phase, FC: filtering cavity, APD: avalanche photodiode, PZT: piezo electric transducer.

sion on the necessary paradigm shift from frequency to time in Section 3.2.3. The DV-type photon-subtraction-based distillation of CV entanglement represents an important example of a protocol whose realization relies upon such a new generation of experiments. According to our definition, it is an example of a hybrid protocol, exploiting at the same time unconditionally producible, Gaussian resource states and DV measurements. In this sense, the experiment described below could as well be listed among those hybrid schemes that we shall discuss in Chapter 8.

Figure 5.15 shows the experimental setup for CV entanglement distillation demonstrated by Takahashi *et al.* [264]. The scheme itself was proposed by Opatrný for improvement of CV teleportation fidelities [261]. In this scheme, two-mode EPR-like state created by two squeezed vacua and a beam splitter is distilled by using "photon subtraction" technique which is also used for creation of a "Schrödinger kitten" and will be explained in more detail in Section 8.2.

In Figure 5.15, first, two entangled light beams are created with a squeezed vacuum and a half beam splitter. Then, a single photon is subtracted from one of the beams, or single photons are subtracted from both beams with avalanche photodiodes (APDs). More precisely, the outputs of the balanced homodyne detectors (BHDs) are recorded by a digital oscilloscope triggered by either logical OR or AND of the click signals from the two APDs. Here, filtering cavities (FCs) before the APDs correspond to frequency-mode filters which only select the same frequency-mode as local oscillators (LOs) for BHDs. For the state verification, a set of the homodyne outcomes are numerically converted into the "+/−" basis which correspond to two outputs from a *virtual* half beam splitter. If the experiment succeeds, the outputs from the *virtual* half beam splitter should be an "odd" Schrödinger kitten ($|\alpha\rangle - |-\alpha\rangle$, $|\alpha| \sim 1$) and a vacuum for single photon subtraction from one of the beams or OR case of the click signals from APDs, and should be an "even" Schrödinger kitten ($|\alpha\rangle + |-\alpha\rangle$, $|\alpha| \sim 1$) and a vacuum for single photon subtrac-

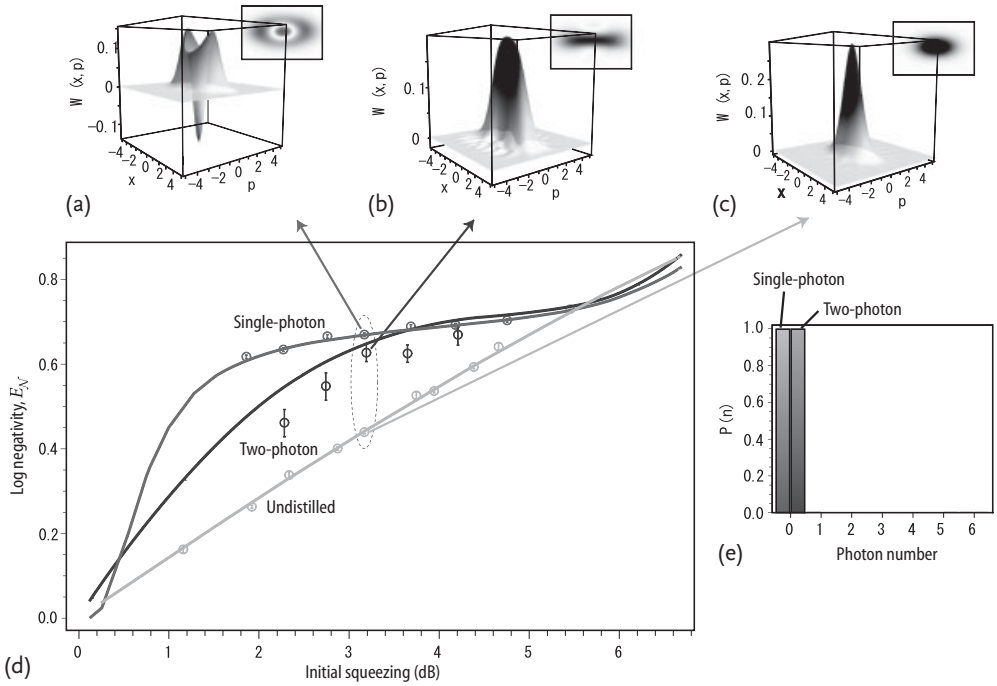

Figure 5.16 Experimental results for for CV entanglement distillation demonstrated by Takahashi *et al.* [264]. Experimentally reconstructed Wigner functions and contour plots of the "−" mode states for the distilled state via single photon subtraction with $R = 5\%$ (a), distilled state via two-photon subtraction with $R = 10\%$ (b), and the undistilled initial state (squeezed vacuum with $R = 0\%$) (c), all with initial squeezing of −3.2 dB. (d) Experimental logarithmic negativities as functions of the initial squeezing. Single-photon: single-photon subtracted states, Two-photon: two-photon subtracted state. (e) Photon number distributions of the experimentally reconstructed "+" mode states corresponding to (a) and (b).

tion from both beams or AND case of the click signals from APDs. Here, the "odd" Schrödinger kitten will be explained in Section 8.2 and the "even" Schrödinger kitten is just the extension of single photon subtraction for "odd" kitten creation to two photon subtraction [267].

Figure 5.16 shows the experimental results for the CV entanglement distillation demonstrated by Takahashi *et al.* [264]. From Figure 5.16, we can see the Wigner function of an "odd" Schrödinger kitten for single photon subtraction and the one of an "even" Schrödinger kitten for single photon subtraction from both beams or two photon subtraction. It is clear from the results that the distillation is successfully performed for both single photon subtraction from one of the beams and single photon subtractions from both beams. Moreover, the values of the logarithmic negativity show that the entanglement increases through distillation.

Part Three Measurement-Based and Hybrid Approaches

6
Quantum Teleportation of Gates

In Section 1.6, we introduced quantum teleportation as a protocol to reliably transfer arbitrary, "unknown" quantum states using shared entanglement and classical communication. In the ideal case, an unknown qubit state can be perfectly restored at the receiving station while the ideal scenario for a perfect transfer of an infinite-dimensional qumode state is unphysical and corresponds to the limiting case of quantum teleportation using two-mode squeezed states (see Section 3.2) with infinite squeezing and energy. Real experiments in which optical qubit or qumode states were teleported using physical resources, such as polarization-entangled photon pairs or finitely squeezed two-mode squeezed states, were discussed in Chapter 4.

In this chapter, we shall now explain various experiments in which the true power of quantum teleportation was revealed, namely, as a primitive for quantum information processing and computing. The initial quantum states in such teleportation-based approaches are to be manipulated and processed through teleportation, and not simply transferred from a sender to a receiver – entanglement-assisted communication becomes entanglement-assisted computation. This generalization of quantum teleportation may be referred to as *gate* teleportation extending the original notion of *state* teleportation.

This gate teleportation [84] is the simplest manifestation of *measurement-based* quantum information processing: as opposed to standard quantum teleportation, a suitably modified entangled-state resource is employed with the corresponding gate applied upon that resource state *offline* prior to the actual computation. The computation itself is then conducted in the same manner as in state teleportation by performing a Bell measurement *jointly* on the input state for the desired gate and one half of the entangled resource state. This joint measurement contains an entangling element as it projects onto an entangled-state basis. For a different gate, the entangled resource state has an accordingly different gate applied on it and hence must *vary* depending on the algorithm to be computed. In contrast, in an ultimate manifestation of measurement-based quantum information processing, the offline resource state would always remain *fixed* during the entire computation and the measurements on it would be *local* single-party projections whose orthogonal measurement bases can be adjusted depending on the individual gates of the algorithm to be computed. All entangling gates would be performed offline in this

Quantum Teleportation and Entanglement. Akira Furusawa, Peter van Loock
Copyright © 2011 WILEY-VCH Verlag GmbH & Co. KGaA, Weinheim
ISBN: 978-3-527-40930-3

case. This so-called cluster-state computation (recall also Section 1.8) and the corresponding experiments will be discussed in Chapter 7.

It turned out that the offline-resource-based and measurement-based approaches offer a distinct advantage over those schemes with every single gate performed directly and unitarily online: the offline gates may be implemented in a probabilistic fashion until they succeed; only for these successful events are the offline states delivered for consumption during the online computation. This feature is particularly useful for DV qubit processing with single photons where entangling gates (or the essential elements of it) cannot be achieved with near-unit, but with a reasonable, nonzero success probability. In this approach, the measurement itself is used to induce the required nonlinearity to achieve the universal gate (see Section 1.8). The seminal theoretical work by Knill, Laflamme, and Milburn ("KLM") [242], which initiated linear-optics measurement-based quantum information processing, and experiments related with this proposal will be discussed in Sections 6.1.1 and 6.1.2, respectively.

In the CV qumode case, experimentally inefficient interactions such as non-Gaussian operations can be implemented offline. Moreover, even Gaussian squeezing gates, otherwise hard to apply upon arbitrary quantum optical states, that is, states other than the vacuum, can be enacted in an offline fashion. Experiments along these lines will be described in Section 6.2.1, including a universal squeezer (Section 6.2.1.1) and a Quantum Non-Demolition (QND) gate (Section 6.2.1.2). Finally, in Section 6.2.2, we briefly discuss alternate protocols for realizing universal quantum gates including a kind of CV version of KLM, namely, the CV gate teleporter by Bartlett and Munro [268].

6.1 Teleporting Qubit Gates

6.1.1 KLM

In Section 2.8, we explained that, besides a direct implementation of universal gates through nonlinear optical interactions (which are hard to obtain efficiently), one may use the so-called multiple-rail encoding for which arbitrary quantum gates are realizable through linear optics alone [134]. However, this very first linear-optics quantum computer proposal is not scalable. A breakthrough towards an in-principle efficient, scalable quantum computer based upon linear optics came with the KLM proposal [242].

The KLM scheme is a fully DV-based protocol, demonstrating that, in principle, passive linear optics and DV photonic auxiliary states are sufficient for (theoretically) efficient, universal DV quantum computation. Inducing nonlinearity through photon counting measurements renders the KLM scheme nondeterministic. However, the probabilistic quantum gates can be made asymptotically near-deterministic by adding to the toolbox feedforward and complicated, multi-photon

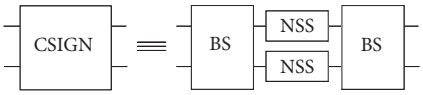

Figure 6.1 Implementing a probabilistic controlled sign gate (CSIGN $\equiv C_Z$) on two single-rail qubits using two nondeterministic NSS gates. The resulting two-qubit gate works in a similar way to the deterministic implementation described in Figure 2.15 using Kerr nonlinearities.

entangled auxiliary states with sufficiently high photon numbers, and by employing quantum teleportation [84]. KLM is "in-principle efficient", as the number of the ancillary photons grows only polynomially with the success rate. Fidelities are always, in principle, perfect in the KLM approach.

The essential ingredient for the nondeterministic realization of a two-photon two-qubit entangling gate (in dual-rail encoding) is the one-mode nonlinear sign shift (NSS) gate. It acts on the qutrit subspace $\{|0\rangle, |1\rangle, |2\rangle\}$ of the optical Fock space as $|k\rangle \rightarrow (-1)^{k(k-1)/2}|k\rangle$. Placing two such NSS gates in the middle between two beam splitters will then act as a controlled sign gate, $|k\rangle \otimes |l\rangle \rightarrow (-1)^{kl}|k\rangle \otimes |l\rangle$, on two single-rail as well as two dual-rail qubits. In fact, we may replace the deterministic Kerr-based circuit of Figure 2.15 by the equivalent circuit depicted in Figure 6.1. The latter, however, becomes nondeterministic with NSS gates operating only probabilistically.

In the original KLM proposal, the NSS gate can be realized with 1/4 success probability, corresponding to a success probability of 1/16 for the full controlled sign gate as shown in Figure 6.1. In subsequent works, this efficiency was slightly improved [269]. There are also various, more general treatments of these nondeterministic linear-optics gates deriving bounds on their efficiencies [270–272].

Probabilistic quantum gates cannot be used directly for quantum computation. The essence of KLM (see Figure 6.2) is that near-unit success probabilities are attainable by combining nondeterministic gates on offline entangled states with the concept of quantum gate teleportation [84]. As the necessary Bell measurements for quantum teleportation succeed at most with 1/2 probability, if only fixed arrays

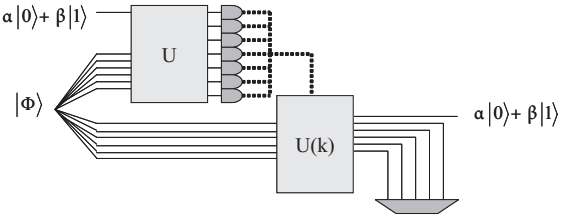

Figure 6.2 Making nondeterministic gates near-deterministic through single-rail quantum teleportation. The Bell measurement is performed by means of the linear-optics circuit U plus photon counting. For an entangled two-mode state $|\Phi\rangle \propto |10\rangle + |01\rangle$ with one ancilla photon, teleportation only succeeds in one half of the cases. For larger ancillae with sufficiently many photons, teleportation can be made almost perfect. In order to teleport a gate near-deterministically onto an input state, the corresponding gate must be first applied offline and probabilistically to the multi-photon entangled ancilla state.

of beam splitters are used [196], entangled ancilla states and feedforward must be added to boost efficiencies beyond 1/2 to near 1.

To sum up, the efficiency of KLM comes from mainly two facts: (1) they use dual-rail encoding (instead of multiple-rail encoding which scales exponentially) using only one photon per qubit; (2) they achieve near-unit gate efficiencies (near-deterministic gate operations) with auxiliary photons scaling only polynomially with any desired efficiency.

Even though KLM is "in-principle efficient", it is still highly impractical as near-deterministic operations would require ancilla states too complicated to engineer with current experimental capabilities. It is therefore extremely important to further enhance the efficiencies of linear-optics quantum computation with regard to the resource scaling. Steps into this direction have been made already by merging the teleportation-based KLM approach with the fairly recent concept of one-way (cluster) computation [1] (see Chapter 7).

6.1.2 Experiment: Qubit Gates

As shown in the previous section and in Figure 6.3, the essence of the KLM scheme is that the CPhase gate is reduced to state preparation and teleportation. Although there is no report of full implementation of the KLM scheme at the moment, there is some reports for conditional CPhase or CNOT gate for the state prepa-

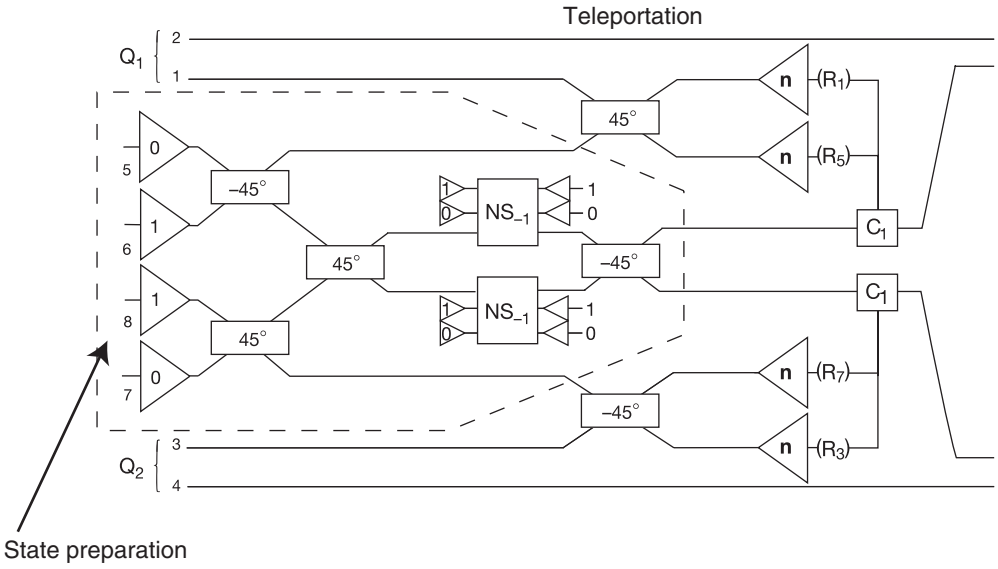

Figure 6.3 Conditional CPhase gate with success probability 1/4 proposed by Knill *et al.* [242]. The essence of this protocol is that the CPhase gate is reduced to state preparation and teleportation.

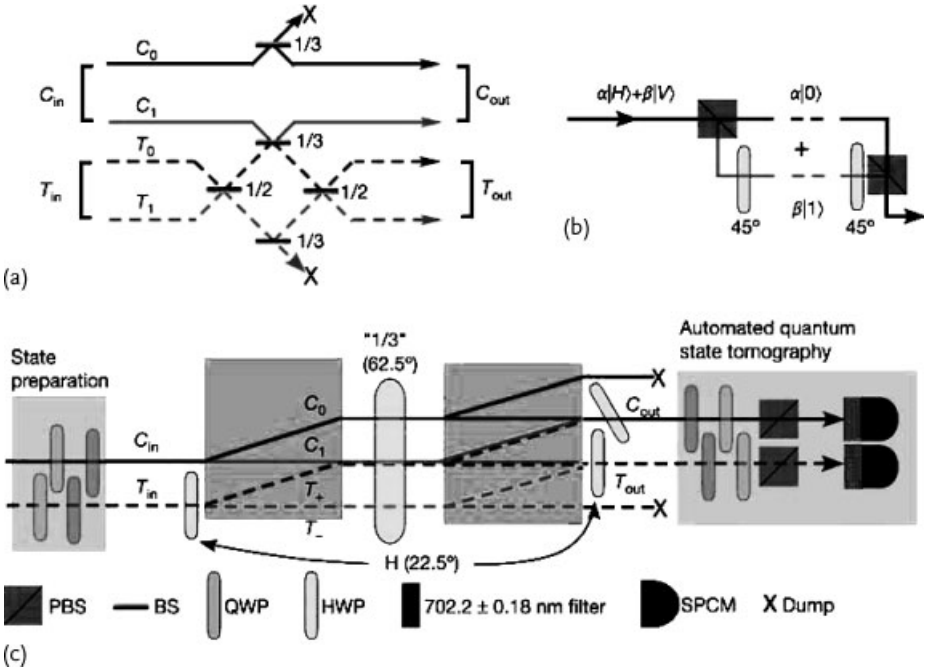

Figure 6.4 A schematic of the CNOT gate realized by O'Brien *et al.* [273]. The theoretical success probability is 1/9. (a) A conceptual description of the gate. (b) A polarization encoded photonic qubit can be converted into a spatially encoded qubit suitable for the gate shown in (a) using a polarization beam splitter (PBS) and a half wave plate (HWP) set to rotate the polarization of one of the outputs by 90°. The reverse process converts the spatial encoding back to polarization encoding. (c) A schematic of the experimental CNOT gate.

ration [273]. In this section, we will explain the experiment performed by O'Brien *et al.* [273] in detail as a typical example.

Figure 6.4 shows a schematic of conditional CNOT gate with linear optics and post-selection demonstrated by O'Brien *et al.* [273]. This conditional CNOT gate can be used for the state preparation for the KLM scheme as mentioned above.

The main trick is shown in Figure 6.4a. This trick was proposed by Ralph *et al.* [274], which is illustrated in Figure 6.5. We first use the Heisenberg picture and will derivate the operator input–output relation of the beam splitter network shown in Figure 6.5.

A beam splitter input–output relation is (see Chapter 2)

$$\begin{aligned} \hat{a}_{1\,\mathrm{out}} &= \sqrt{\eta}\,\hat{a}_{1\,\mathrm{in}} + \sqrt{1-\eta}\,\hat{a}_{2\,\mathrm{in}}\,, \\ \hat{a}_{2\,\mathrm{out}} &= \sqrt{1-\eta}\,\hat{a}_{1\,\mathrm{in}} - \sqrt{\eta}\,\hat{a}_{2\,\mathrm{in}}\,, \end{aligned} \tag{6.1}$$

where η is the reflectivity of the beam splitter. By using this beam-splitter relation, we can get the input–output relation of the beam splitter network in Figure 6.5 as

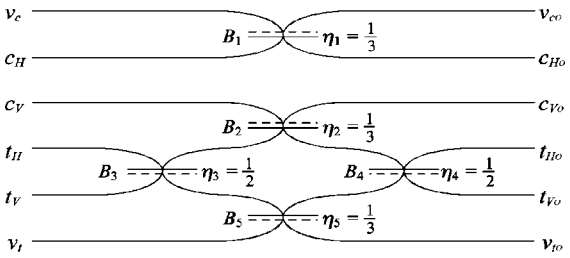

Figure 6.5 A schematic of conditional CNOT gate proposed by Ralph *et al.* [274]. B_i is a beam splitter whose reflectivity is η_i. The control qubit is represented by modes C_H and C_V with the dual-rail fashion, and the target qubit is represented by modes t_H and t_V. The modes ν_c and ν_t are ancillary vacuum inputs.

follows [274],

$$
\begin{aligned}
\hat{a}_{C_H\text{out}} &= \frac{1}{\sqrt{3}}\left(\sqrt{2}\hat{a}_{\nu_c\text{in}} + \hat{a}_{C_H\text{in}}\right), \\
\hat{a}_{C_V\text{out}} &= \frac{1}{\sqrt{3}}\left(-\hat{a}_{C_V\text{in}} + \hat{a}_{t_H\text{in}} + \hat{a}_{t_V\text{in}}\right), \\
\hat{a}_{t_H\text{out}} &= \frac{1}{\sqrt{3}}\left(\hat{a}_{C_V\text{in}} + \hat{a}_{t_H\text{in}} + \hat{a}_{\nu_t\text{in}}\right), \\
\hat{a}_{t_V\text{out}} &= \frac{1}{\sqrt{3}}\left(\hat{a}_{C_V\text{in}} + \hat{a}_{t_V\text{in}} - \hat{a}_{\nu_t\text{in}}\right), \\
\hat{a}_{\nu_c\text{out}} &= \frac{1}{\sqrt{3}}\left(-\hat{a}_{\nu_c\text{in}} + \sqrt{2}\hat{a}_{C_H\text{in}}\right), \\
\hat{a}_{\nu_t\text{out}} &= \frac{1}{\sqrt{3}}\left(\hat{a}_{t_H\text{in}} - \hat{a}_{t_V\text{in}} - \hat{a}_{\nu_t\text{in}}\right),
\end{aligned}
\tag{6.2}
$$

where the control qubit is represented by modes C_H and C_V with the dual-rail fashion, and the target qubit is represented by modes t_H and t_V. The modes ν_c and ν_t are ancillary vacuum inputs.

The general input state to the gate (the control and target qubits) can be described in the Schrödinger picture as

$$
\begin{aligned}
|\psi\rangle_{\text{in}} &= (\alpha|HH\rangle + \beta|HV\rangle + \gamma|VH\rangle + \delta|VV\rangle)\,|00\rangle \\
&= \left(\alpha\hat{a}^{\dagger}_{C_H\text{in}}\hat{a}^{\dagger}_{t_H\text{in}} + \beta\hat{a}^{\dagger}_{C_H\text{in}}\hat{a}^{\dagger}_{t_V\text{in}} + \gamma\hat{a}^{\dagger}_{C_V\text{in}}\hat{a}^{\dagger}_{t_H\text{in}}\right. \\
&\quad \left. + \delta\hat{a}^{\dagger}_{C_V\text{in}}\hat{a}^{\dagger}_{t_V\text{in}}\right)|0000\rangle|00\rangle\,,
\end{aligned}
\tag{6.3}
$$

where the ordering in the kets is $|n_{C_H\text{in}}\ n_{C_V\text{in}}\ n_{t_H\text{in}}\ n_{t_V\text{in}}\rangle|n_{\nu_c\text{in}}\ n_{\nu_t\text{in}}\rangle$ with $\hat{n}_{C_H\text{in}} = \hat{a}^{\dagger}_{C_H\text{in}}\hat{a}_{C_H\text{in}}$, and so on, and we use $|1010\rangle = |HH\rangle$, and so on, where appropriate.

Thus, we can derive the output state of the beam splitter network by using Eqs. (6.2) and (6.3),

$$
\begin{aligned}
|\psi\rangle_{\text{out}} = & \Big(\alpha\,\hat{a}^{\dagger}_{C_{\text{H}}\text{out}}\hat{a}^{\dagger}_{t_{\text{H}}\text{out}} + \beta\,\hat{a}^{\dagger}_{C_{\text{H}}\text{out}}\hat{a}^{\dagger}_{t_{\text{V}}\text{out}} + \gamma\,\hat{a}^{\dagger}_{C_{\text{V}}\text{out}}\hat{a}^{\dagger}_{t_{\text{H}}\text{out}} \\
& + \delta\,\hat{a}^{\dagger}_{C_{\text{V}}\text{out}}\hat{a}^{\dagger}_{t_{\text{V}}\text{out}}\Big)\,|0000\rangle|00\rangle \\
= & \frac{1}{3}\Big\{[\alpha|HH\rangle + \beta|HV\rangle + \gamma|VV\rangle + \delta|VH\rangle]\,|00\rangle \\
& + \sqrt{2}(\alpha+\beta)|0100\rangle|10\rangle + \sqrt{2}(\alpha-\beta)|0000\rangle|11\rangle \\
& + (\alpha+\beta)|1100\rangle|00\rangle + (\alpha-\beta)|1000\rangle|01\rangle \\
& + \sqrt{2}\alpha|0010\rangle|10\rangle + \sqrt{2}\beta|0001\rangle|10\rangle \\
& - \sqrt{2}(\gamma+\delta)|0200\rangle|00\rangle - (\gamma-\delta)|0100\rangle|01\rangle \\
& + \sqrt{2}\gamma|0020\rangle|00\rangle + (\gamma-\delta)|0010\rangle|01\rangle \\
& + (\gamma+\delta)|0011\rangle|00\rangle + (\gamma-\delta)|0001\rangle|01\rangle \\
& + \sqrt{2}\delta|0002\rangle|00\rangle\Big\}\,. \qquad (6.4)
\end{aligned}
$$

From this result, we obtain (after renormalization)

$$
|\psi\rangle_{\text{post-select}} = \alpha|HH\rangle + \beta|HV\rangle + \gamma|VV\rangle + \delta|VH\rangle\,, \qquad (6.5)
$$

by measuring $|n_{v_{\text{c}}\text{out}}\; n_{v_{\text{t}}\text{out}}\rangle = |00\rangle$, exactly one photon in total for $\{n_{C_{\text{H}}\text{out}}, n_{C_{\text{V}}\text{out}}\}$, and the same for $\{n_{t_{\text{H}}\text{out}}, n_{t_{\text{V}}\text{out}}\}$. These patterns can be postselected in the experiment and they occur with a success probability of 1/9. The state of Eq. (6.5) is the CNOT output for the input of Eq. (6.3); the target qubit only flips when the control qubit is V.

O'Brien *et al.* realized this postselected gate as shown in Figure 6.4c. The two input polarization qubits are converted to spatial dual-rail qubits using the trick shown in Figure 6.4b. Then, the dual-rail qubits enter a beam splitter network, as depicted in Figure 6.4a (Figure 6.5), which is implemented with half wave plates (HWPs) and polarization beam splitters (PBSs). Especially, a 1/2-beam splitter is realized through a polarization rotation by 45° (HWP rotation by 22.5°) and a 1/3-beam splitter is realized by means of a polarization rotation by 125° (HWP rotation by 62.5°), where $-\sqrt{1/3} \simeq \cos 125°$.

Figure 6.6 shows the experimental results for the CNOT gate operation as it was demonstrated by O'Brien *et al.* [273]. The results agree well with the ideal operation of the gate. Note that postselection was a crucial part of this experiment. In particular, the protocol for this gate implementation (achieving a gate efficiency of 1/9) relies upon a final step that includes destroying the two-qubit output state of the gate. More precisely, it is absolutely necessary to detect (and hence destroy) the photon number states of *all* six modes in Eq. (6.4) in order to accomplish the gate operation; including postselection in the gate output ports themselves.

In this sense, the current CNOT gate is a destructive gate, conceptually different from, for example, those gates obtainable in the KLM scheme. There, the output

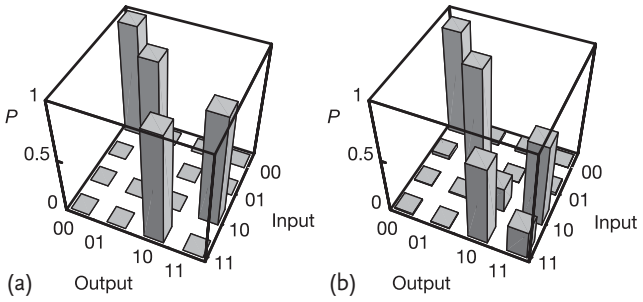

Figure 6.6 Experimental results for the CNOT gate operation demonstrated by O'Brien *et al.* [273]. (a) Ideal logical basis operation of a CNOT gate. (b) Measured operation of the gate.

ports need not be detected and the two-qubit output state of the gate can be further exploited in subsequent quantum circuits, potentially leading to a fully scalable quantum computation.

However, the KLM two-qubit entangling gate is much harder to implement experimentally; and, again from a conceptual point of view, the KLM gates representing non-destructive gates are fundamentally limited in their efficiencies depending on the resources employed. Here, the bounds on the nondestructive gates are naturally lower than those on the destructive gates. For instance, the nondeterministic implementation of a non-destructive CNOT gate according to KLM achieves an efficiency of 1/16, and this value is near 2/27, which is conjectured to be the theoretical optimum when no feedforward operations are permitted (like in the destructive gate protocol described above).

6.2
Teleporting Qumode Gates

6.2.1
Experiment: Gaussian Qumode Gates

6.2.1.1 Universal Squeezer

In this section, we will describe a universal squeezer as an example for off-line Gaussian quantum information processing on qumodes, focusing on the experiment demonstrated by Yoshikawa *et al.* [275] based upon the theoretical proposal by Filip *et al.* [276].

The implementation of a direct nonlinear quantum operation is often hampered by decoherence due to inevitable practical imperfections in physical systems. Because of the necessity of invoking such unitary transformations in a fault-tolerant quantum information processor, the future of developing such units was not too bright. However, new optimism arose from the introduction of the so-called off-line schemes where a nonlinear transformation is executed on a quantum state through simple linear interference with some off-line prepared ancillas followed by detec-

tion and feedforward [84, 170, 242, 249, 268]. The significance of that approach is that the nonlinear transformation need not be performed directly onto the fragile quantum state, but is accomplished by tailoring the off-line resource states that can be prepared at anytime.

The first simple example of such an off-line scheme is teleportation which demonstrates the implementation of the most trivial unitary quantum operation [17, 163, 277], namely, the identity operation: The off-line resource is a bipartite entangled state which is detected jointly with the fragile quantum information in a Bell measurement and the classical outcomes are fed forward to achieve the identity (or teleportation) operation. Remarkably, it was found that by manipulating the off-line entangled state in the teleporter, it is possible to implement any unitary transformation through teleportation. This was first realized for qubits [84] and subsequently used in the linear optical quantum computer [242], and later extended to continuous variables (CVs) which benefit from the practical CV Bell measurement [268].

Such a teleportation-based off-line scheme can, for example, be used for the implementation of a squeezing operation. It was however proposed in [276] that a

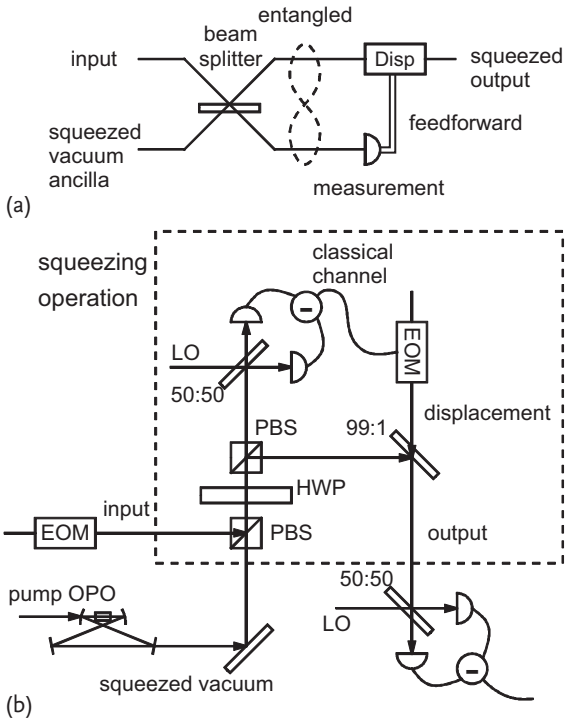

Figure 6.7 (a) Schematic of high-fidelity squeezing [275]. (b) Experimental setup for high-fidelity squeezing [275]. A variable beam splitter is realized by a half-wave plate (HWP) and two polarizing beam splitters (PBS). EOM: electro-optic modulator, LO: local oscillator, OPO: optical parametric oscillator.

much simpler off-line scheme relying only on a single vacuum squeezed ancilla suffices to implement the squeezing operation (see Figure 6.7a). In essence, this simple setup allows for the experimentally feasible and noise-resistant squeezing transformation of optical quantum states, and it can be seen as the CV analog to the one-qubit teleportation approach in [278].

The single-mode squeezer is ideally described by a single-mode LUBO transformation (see Chapter 2) which maps the input Wigner function $W(x, p)$ onto $W'(x, p) = W(xe^{r}, pe^{-r})$ where x and p represent the amplitude and phase quadrature of the field and r is the squeezing factor. Although this simple transformation is standard in any text book on quantum optics, its experimental realization for arbitrary inputs (that is quantum information) remained extremely challenging. Previously demonstrated squeezing transformations either were suffering from large decoherence (as is the case for fiber or cavity implementations), thus corrupting the fragile quantum information of a quantum state, or were using an input dependent nondeterministic approach [279]. In contrast to previous implementations, the squeezing transformation explained here is deterministic and it processes quantum information with very high fidelity.

The scheme is illustrated in Figure 6.7 and goes as follows. The input state under interrogation is combined with a squeezed vacuum at a beam splitter. A quadrature to be anti-squeezed is measured using homodyne detection, and after appropriate rescaling of the outcomes the remaining field is displaced accordingly. Mathematically, the transformation can be easily derived in the Heisenberg picture. First, we consider the input–output relations for the beam splitter:

$$\hat{x}_{\mathrm{i}}' = \sqrt{T}\hat{x}_{\mathrm{i}} + \sqrt{1-T}\hat{x}_{\mathrm{a}} , \tag{6.6}$$

$$\hat{p}_{\mathrm{i}}' = \sqrt{T}\hat{p}_{\mathrm{i}} + \sqrt{1-T}\hat{p}_{\mathrm{a}} , \tag{6.7}$$

$$\hat{x}_{\mathrm{a}}' = \sqrt{T}\hat{x}_{\mathrm{a}} - \sqrt{1-T}\hat{x}_{\mathrm{i}} , \tag{6.8}$$

$$\hat{p}_{\mathrm{a}}' = \sqrt{T}\hat{p}_{\mathrm{a}} - \sqrt{1-T}\hat{p}_{\mathrm{i}} , \tag{6.9}$$

where $\hat{x}$ and $\hat{p}$ represent the quadratures to be squeezed and anti-squeezed, the indices "i" and "a" refer to the input and ancillary mode, respectively, and T is the transmittance of the beam splitter. The quadratures of the ancilla are written as $(\hat{x}_{\mathrm{a}}, \hat{p}_{\mathrm{a}}) = (\hat{x}_{\mathrm{a}}^{(0)}e^{-r_{\mathrm{a}}}, \hat{p}_{\mathrm{a}}^{(0)}e^{r_{\mathrm{a}}})$ where r_{a} is the squeezing parameter and $\hat{x}_{\mathrm{a}}^{(0)}$ and $\hat{p}_{\mathrm{a}}^{(0)}$ represent vacuum fluctuations. In the reflected part, the quadrature $\hat{p}_{\mathrm{a}}'$ is measured using homodyne detection. The measurement outcomes are subsequently rescaled by a factor denoted by g and finally used to displace the remaining part of the system which is equivalent to the transformation $\hat{x}_{\mathrm{i}}' \to \hat{x}_{\mathrm{i}}'' = \hat{x}_{\mathrm{i}}'$ and $\hat{p}_{\mathrm{i}}' \to \hat{p}_{\mathrm{i}}'' = \hat{p}_{\mathrm{i}}' + g\hat{p}_{\mathrm{a}}'$. By choosing $g = -\sqrt{(1-T)/T}$, we arrive at the following input–output relations

$$\hat{x}_{\mathrm{i}}'' = \sqrt{T}\hat{x}_{\mathrm{i}} + \sqrt{1-T}\hat{x}_{\mathrm{a}}^{(0)}e^{-r_{\mathrm{a}}} , \tag{6.10}$$

$$\hat{p}_{\mathrm{i}}'' = \frac{1}{\sqrt{T}}\hat{p}_{\mathrm{i}} . \tag{6.11}$$

In the limit of the infinitely squeezed ancilla corresponding to $r_a \to \infty$, the transformation coincides with perfect unitary squeezing operation with the actual squeezing parameter $r = -\ln\sqrt{T}$ which is directly controlled by the transmittance of the beam splitter. Furthermore, the quadrature being squeezed can also be easily controlled through adjustment of the relative phase between the signal and the squeezed ancilla and correspondingly the measured quadrature in the feedforward loop [276]. Therefore, full control of the squeezing process is accessed through simple operations on linear passive devices. Let us note that by changing some of the settings of the setup (such as the local oscillator phase, the feedforward gain and the ancilla state), the setup can function as a non-unitary noiseless amplifier [280], a non-unitary quantum nondemolition measurement device [281] or as a squeezed state purifier [282].

In a realistic situation, the ancilla state is not infinitely squeezed and some extra quantum noise will inevitably be added to the squeezed quadrature as indicated by the second term in Eq. (6.10). Note that the noise suppression performance never goes further than that of the ancilla. In contrast, the imperfections of the ancilla state do not degrade the quality of the transformation of the anti-squeezed quadrature as well as the mean values: The excess noise of the ancilla is not coupled into the mode nor does it disturb the mean value transformation.

The operation described above is universal and thus squeezes all input states. In the following experimental investigation, however, the squeezing of particular states is considered, namely, coherent states. To ensure that the coherent states are truly pure, they are defined as a sideband at a radio-frequency relative to the carrier of a laser beam. This beam as well as other auxiliary beams are delivered by a Ti:sapphire laser operating at 860 nm. The experiment is divided in three parts; preparation, processing and verification which will now be discussed.

Preparation: In the preparation stage, the input coherent state and the squeezed ancilla state are generated. The coherent state is prepared by traversing a part of the laser beam through an electro-optic modulator operating at 1 MHz and set to modulate the amplitude and phase simultaneously. As a result, a true coherent state is generated at a 1 MHz sideband and the bandwidth is assumed to be 30 kHz. The power of the optical carrier is about 3 μW, whereas the power of the sideband is about 15 dB above the corresponding shot noise level. The ancillary squeezed state is produced in an optical parametric oscillator (OPO). It is a 500 mm long bow-tie shaped cavity consisting of two plane mirrors and two mirrors with a 50 mm radius of curvature. The nonlinear crystal is a 10 mm periodically-poled $KTiOPO_4$ (PPKTP) crystal (see [283] for details). The OPO is pumped with light at 430 nm, stemming from a second harmonic generator with the same configuration as the OPO cavity but with a $KNbO_3$ crystal. The second harmonic generator is pumped with the light from the Ti:sapphire laser. To monitor and lock the squeezing phase, we inject a weak coherent beam to the OPO. The output from the OPO and the coherent state are then directed to the processing part. They have 97 and 143 kHz modulation sidebands for phase locking.

Processing: At this stage the actual squeezing transformation is implemented. First, the two states from the preparation stage merge at a variable beam splitter

composed of a half wave plate (HWP) sandwiched between two polarizing beam splitters (PBS). The beam splitting ratio is thus easily controlled via a wave plate rotation. One output of the beam splitter is directed to a homodyne detector which measures the p quadrature. The visibility between the output and a local oscillator is 96% and the quantum efficiency of the detectors is more than 99%. The measurement outcomes are amplified electrically in a low-noise amplifier and subsequently used to drive a phase modulator which displaces an auxiliary beam in phase space. Finally, the displacement of the signal is achieved by combining it with the displaced auxiliary field using a highly asymmetric beam splitter (99/1).

Verification: In the final stage of the experiment, the protocol is verified by measuring the input states as well as the squeezed output states. The states are fully characterized by balanced homodyne detection. The visibility between the squeezed output beam and a local oscillator is 96% and the total propagation efficiency is 96%. The electronic noise is always 19 dB smaller than the optical noise. After detection, the photocurrents are used to reconstruct the quantum states: The 1 MHz component of the measured output signal is extracted by means of a lock-in detection scheme. The signal is mixed with a 1 MHz sine-wave signal from a function generator, low pass filtered (30 kHz) and finally digitized and fed into a computer with the sampling rate of 300 kHz.

Figure 6.8 shows the raw data of the time resolved measurements of the input states and the output states. The time series for the input coherent states (Figure 6.8a) and the vacuum squeezed states (Figure 6.8e) are measured by adjusting the beam splitter transmittance to unity and zero, respectively (and blocking the displacement beam). Then, the squeezing transformation is activated and the time series for three different transmittances, namely, 0.75, 0.50, and 0.25, are measured, the results of which are shown in Figure 6.8b–d respectively. It is evident from the plots that the input coherent states become more and more deformed as the transmittance decreases (and thus the squeezing degree increases). In Figure 6.8f, the reconstructed Wigner function of the transformed states with $T = 0.25$ is presented.

As indicated by the reconstructed Wigner function, the involved states are Gaussian. With this a priori information, the states are completely characterized by the first two moments. Due to the symmetry of the states (squeezed in x and antisqueezed in p), it suffices to evaluate the mean values and variances of x and p. Results of such evaluations are shown in Figures 6.9 and 6.10.

In Figure 6.9, the phase space diagrams of the input coherent states as well as the output states are shown by ellipses which correspond to the cross sections of their respective Wigner functions. When a coherent state is unitarily squeezed, the amplitude is transformed along a hyperbolic curve, as shown by the dotted line. The four ellipses correspond to (from the right) the input coherent states, the squeezed outputs with $T = 0.75$, $T = 0.50$, $T = 0.25$, respectively, and their centers, marked by dots, represent the measured averages. The circles represent the data obtained without the feedforward. The lengths of the major and minor axes of the ellipses are the measured standard deviations of x and p. Obviously, the mean values are transformed almost ideally.

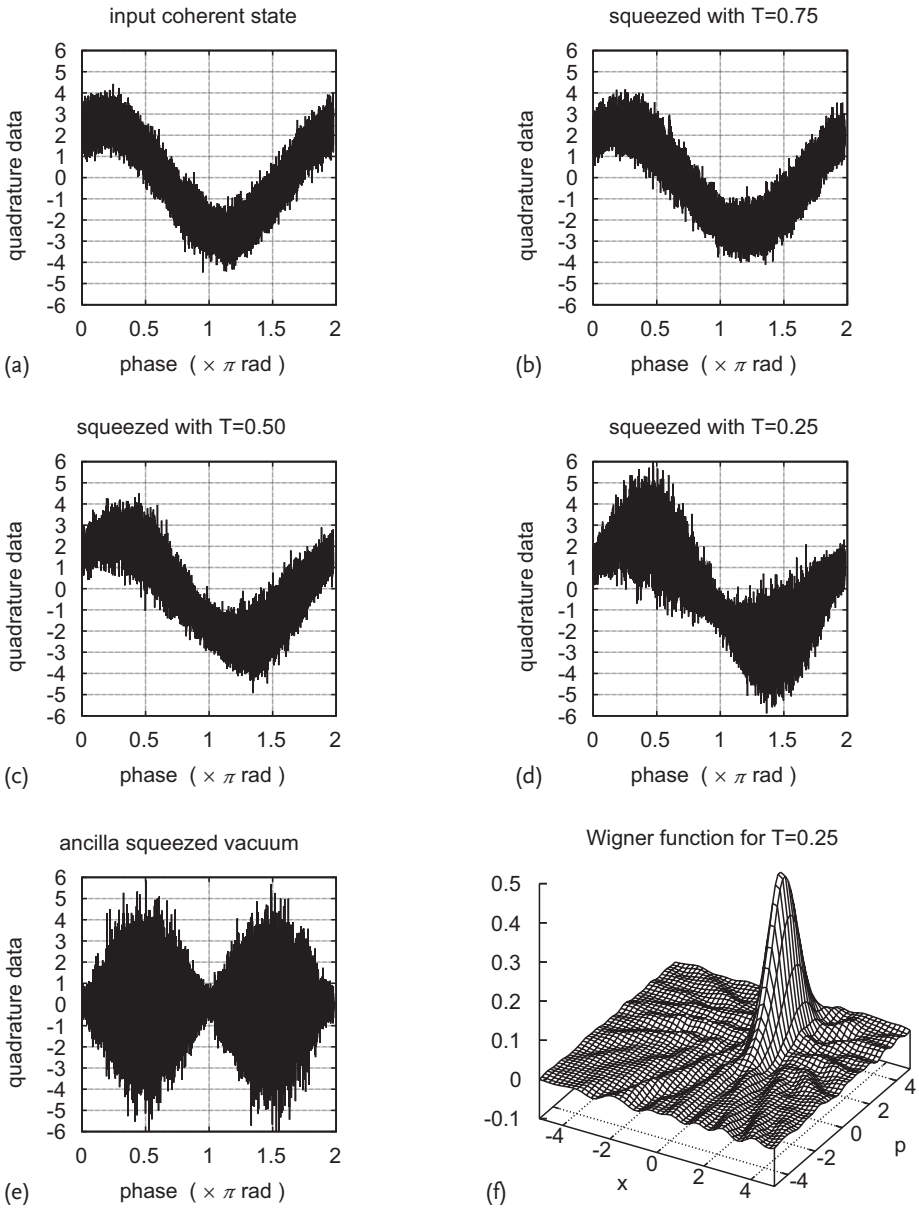

Figure 6.8 Results of the homodyne measurements [275]. (a)–(e) are the raw quadrature data as a function of the phase of the local oscillator and (f) is the reconstructed Wigner function (using inverse radon transformation [113]) for one realization of the experiment.

In Figure 6.10, the noise powers of the squeezed and anti-squeezed quadratures are plotted as a function of the transmittance. The three curves represent theoretical predictions for the noise power of the anti-squeezed quadrature (curve i),

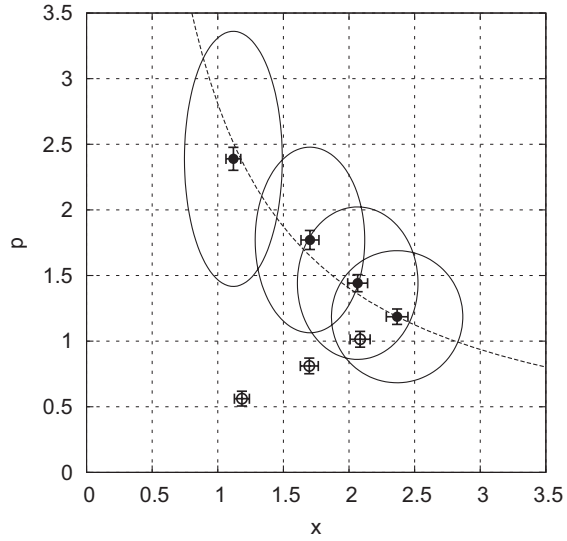

Figure 6.9 Phase space representation of the experimental results [275]. The phase space is normalized so that the standard deviation of the vacuum fluctuation is 1/2 ($\hbar = 1/2$). Note that the measured results are directly plotted without accounting for detection and propagation losses.

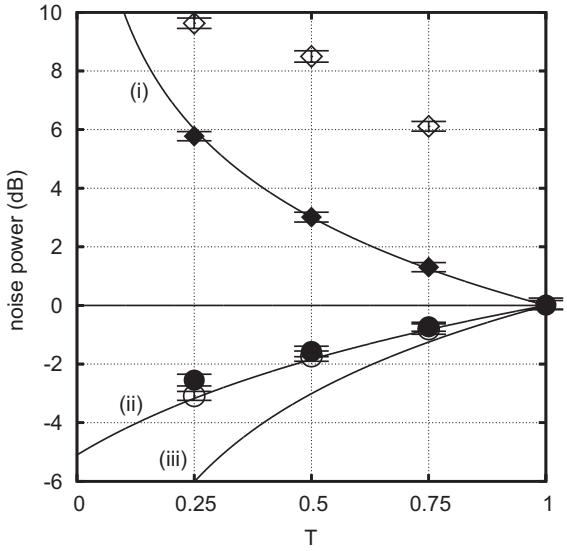

Figure 6.10 The noise powers of the squeezer outputs relative to the shot noise limit [275]. We measure 0.7, 1.6 and 2.5 dB for the squeezed quadrature and 1.3, 3.0 and 5.8 dB for the anti-squeezed quadrature. The two quadrature variances of the input coherent states are equal to those of vacuum within ± 0.1 dB.

the squeezed quadrature with the ancilla 5.1 dB squeezed (curve ii) and infinitely squeezed (curve iii). Note again that the anti-squeezed noise does not depend on the ancilla. Experimental data taken with and without the feedforward in place are also shown in Figure 6.10: The noise powers of $x(p)$ with feedforward are indicated by dots (filled diamonds), and without feedforward by circles (open diamonds). We see that the anti-squeezed noise of the ancilla is canceled and the transformation in p becomes almost ideal after the feedforward. The noise powers of the squeezed quadrature, however, deviate from the ideal operation due to the finite squeezing in the ancilla states. Furthermore we observe a small degradation of the noise suppression due to some imperfections of the feedforward, such as phase fluctuation.

Now, the fidelities [68] of these transformations are calculated. For the case of Gaussian states, the fidelity between the ideal squeezed state, $|\psi_{\mathrm{id}}\rangle$, and the actual obtained mixed state, $\hat{\rho}_{\mathrm{out}}$, is given by (in the unit of $\hbar = 1/2$)

$$\begin{aligned} F &= \langle\psi_{\mathrm{id}}|\hat{\rho}_{\mathrm{out}}|\psi_{\mathrm{id}}\rangle \\ &= \frac{1}{2\sqrt{\left(V^x_{\mathrm{out}} + V^x_{\mathrm{id}}\right)\left(V^p_{\mathrm{out}} + V^p_{\mathrm{id}}\right)}} \\ &\quad \times \exp\left[-\frac{\left(\langle x_{\mathrm{out}}\rangle - \langle x_{\mathrm{id}}\rangle\right)^2}{2\left(V^x_{\mathrm{out}} + V^x_{\mathrm{id}}\right)} - \frac{\left(\langle p_{\mathrm{out}}\rangle - \langle p_{\mathrm{id}}\rangle\right)^2}{2\left(V^p_{\mathrm{out}} + V^p_{\mathrm{id}}\right)}\right], \end{aligned} \tag{6.12}$$

where the subscripts "id" and "out" denote the ideal squeezing and the experimental output, respectively, and V denotes the variance. Actually, due to small propagation and detection losses in the experiment, the fidelity ultimately depends on the input state. We therefore quantify the individual single shot fidelities for the inputs considered in the experiment, though the average fidelity will be found by integrating the fidelity in Eq. (6.12) over all possible input states. From the measured means and variances, the fidelities between the ideally squeezed states of the inferred inputs (accounting for losses) and the directly measured squeezed states are computed, and $94\% \pm 1\%$ for $T = 0.75$ (1.2 dB squeezing), $89\% \pm 1\%$ for $T = 0.50$ (3.0 dB squeezing), and $78\% \pm 2\%$ for $T = 0.25$ (6.0 dB squeezing) are found. Note that the fidelity between the measured input states and the inferred ones is found to be $97\% \pm 1\%$. For comparison, the theoretically calculated fidelities with vacuum ancilla states (which correspond to the classical limits) are 93, 82, 63%, for the transformations corresponding to 1.2, 3.0, 6.0 dB squeezing, respectively.

6.2.1.2 Quantum Non-demolition (QND) Sum Gate

In this section, we explain the demonstration of quantum non-demolition (QND) sum gate by Yoshikawa *et al.* [284] by using two universal squeezers explained in the previous section. Here, the proposal was made by Filip *et al.* [276] in the same paper as the universal squeezer.

The analogue of a two-qubit C-NOT gate when continuous quantum variables are considered is the so-called sum gate. It represents the canonical version of a two-mode entangling gate for universal quantum computation in the regime of continuous variables [90] (see Section 1.8). When applied to two optical, bosonic

modes, as opposed to a simple beam splitter transformation, the sum gate is even capable of entangling two modes each initially in a coherent state, that is, a close-to-classical state.

Apart from representing a universal two-mode gate, the sum gate also describes a quantum nondemolition (QND) interaction. The concept of a QND measurement has been known for almost 30 years. Initially, it was proposed to allow for better accuracies in the detection of gravitational waves [285, 286]. A QND measurement is a projection measurement onto the basis of a QND observable which is basically a constant of motion. The QND measurement should preserve the measured observable, but still gain sufficient information about its value; the back action is confined to the conjugate observable.

Various demonstrations of QND or back-action evading measurements have been reported [287]. The interest in the realization of a full QND *gate* only grew recently, mainly in the context of continuous-variable (CV) quantum information processing [105]. In particular, the QND sum gate is (up to local phase rotations) the canonical entangling gate for building up Gaussian cluster states [288], a sufficient resource for universal quantum computation [171]. Other applications of the sum gate are CV quantum error correction [237, 238] and CV coherent communication [289].

In this section, the experimental demonstration of a full QND sum gate by Yoshikawa *et al.* [284] is extensively explained. The gate leads to quantum correlations in *both* conjugate variables consistent with an entangled state and allowing for a QND measurement of either variable with signal and probe interchanged. While previous works focused on fulfilling the criteria for a QND measurement [290] of one fixed variable, here, the experiment of Yoshikawa *et al.* satisfies the QND criteria for two non-commuting observables, verifying entanglement at the same time. As the implementation is very efficient and controllable, the scheme can be used to process arbitrary optical quantum states, including fragile non-Gaussian states. Similar to the measurement-based implementation of single-mode squeezing gates [275, 276] explained in the previous section, realization of the QND gate only requires two offline squeezed ancilla modes [89, 276].

Let us write the QND-gate Hamiltonian as $\hat{H}_{\mathrm{QND}} = \hat{x}_1 \hat{p}_2$ with a suitable choice of the absolute phase for each mode. Here, $\hat{x}/2$ and $\hat{p}/2$ are the real and imaginary parts of each mode's annihilation operator, $\hat{a} = (\hat{x} + \mathrm{i}\hat{p})/2$, and the subscripts "1" and "2" denote two independent modes. Note that we use $\hbar = 2$ in this section. The ideal QND input–output relations then become

$$\begin{aligned}
\hat{x}_1^{\mathrm{out}} &= \hat{x}_1^{\mathrm{in}} \,, \\
\hat{x}_2^{\mathrm{out}} &= \hat{x}_2^{\mathrm{in}} + G\,\hat{x}_1^{\mathrm{in}} \,, \\
\hat{p}_1^{\mathrm{out}} &= \hat{p}_1^{\mathrm{in}} - G\,\hat{p}_2^{\mathrm{in}} \,, \\
\hat{p}_2^{\mathrm{out}} &= \hat{p}_2^{\mathrm{in}} \,,
\end{aligned} \tag{6.13}$$

where G is the gain of the interaction.

Through this ideal QND interaction, the "signal" QND variable $\hat{x}_1$ ($\hat{p}_2$) is preserved in the output state and its value is added to the "probe" variable $\hat{x}_2$ ($\hat{p}_1$).

This allows for a QND measurement of either $\hat{x}_1$ or $\hat{p}_2$, with a back action confined to the conjugate variable. The usual criteria for QND measurements (in the linearized, Gaussian regime) are [290],

$$\begin{aligned} 1 < T_S + T_P \leq 2 \, , \\ V_{S|P} < 1 \, , \end{aligned} \tag{6.14}$$

where T_S and T_P are the transfer coefficients from signal input to signal output ("signal preservation") and from signal input to probe output ("information gain"), respectively; $V_{S|P}$ is the conditional variance of the signal output when the probe output is measured ("quantum state preparation").

The implementation of the QND gate based on offline resources is shown in Figure 6.11. The interaction gain G in Eq. (6.13) is related to the reflectivities of the four beam splitters via one free parameter R, with $G = (1/\sqrt{R}) - \sqrt{R}$, taking arbitrary values for $0 < R \leq 1$. The full scheme is described by the input–output relations [276],

$$\hat{x}_1^{\text{out}} = \hat{x}_1^{\text{in}} - \sqrt{\frac{1-R}{1+R}}\,\hat{x}_A^{(0)} e^{-r_A} \, , \tag{6.15}$$

$$\hat{x}_2^{\text{out}} = \hat{x}_2^{\text{in}} + \frac{1-R}{\sqrt{R}}\,\hat{x}_1^{\text{in}} + \sqrt{R\frac{1-R}{1+R}}\,\hat{x}_A^{(0)} e^{-r_A} \, , \tag{6.16}$$

$$\hat{p}_1^{\text{out}} = \hat{p}_1^{\text{in}} - \frac{1-R}{\sqrt{R}}\,\hat{p}_2^{\text{in}} + \sqrt{R\,\frac{1-R}{1+R}}\,\hat{p}_B^{(0)} e^{-r_B} \, , \tag{6.17}$$

$$\hat{p}_2^{\text{out}} = \hat{p}_2^{\text{in}} + \sqrt{\frac{1-R}{1+R}}\,\hat{p}_B^{(0)} e^{-r_B} \, , \tag{6.18}$$

where $\hat{x}_A^{(0)} e^{-r_A}$ and $\hat{p}_B^{(0)} e^{-r_B}$ are the squeezed quadratures of the ancillas (the subscripts "A" and "B" denote two independent ancilla modes), leading to some excess noise for finite squeezing. The gate operation becomes ideal in the limit of infinite squeezing ($r_A, r_B \to \infty$). Note that here precise control of active squeezing arising from an unstable process of parametric down conversion is not needed; instead, the gate is completely controlled via passive optical devices. For sufficiently large squeezing of the ancilla modes, this transformation also allows for QND measurements. Using variable beam splitters, two interaction gains, $G = 1.0$ and 1.5, were experimentally realized. In particular, the unit gain interaction is significant for quantum information processing. Nonetheless, a better performance in the QND measurements using higher gain could be observed. Note that a non-unitary and single quadrature QND measurement based on squeezed vacuum and feedforward has been demonstrated in [281].

Experimental setup. A schematic of the experimental setup is illustrated in Figure 6.11. It basically consists of a Mach–Zehnder interferometer with a single-mode squeezing gate in each arm. To implement fine-tunable and lossless squeezing operations, the measurement-induced squeezing approach or off-line squeezing explained in the previous section is used which is illustrated inside the dashed boxes of Figure 6.11.

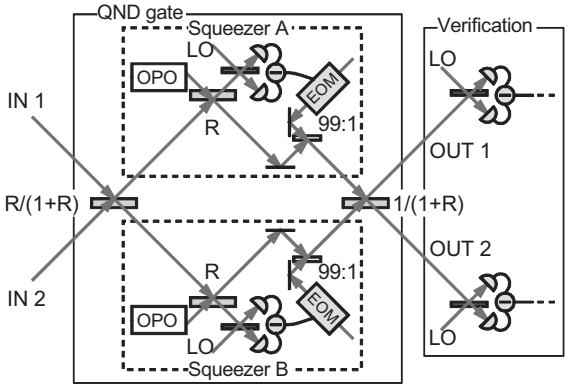

Figure 6.11 Schematic of the experimental setup [284]. The parameter R determines the reflectivities of the four beam splitters which are $R/(1+R)$, R, R, and $1/(1+R)$. We employ optical parametric oscillators (OPO) to produce squeezed vacuum modes, local oscillators (LO) for homodyne detection, and electro-optic modulators (EOM) combined with beam splitters (99 : 1) for signal displacement.

The quantum information is encoded at frequency sidebands of 1.25 MHz relative to the optical carrier of the bright continuous wave light beam at a wavelength of 860 nm from a Ti:sapphire laser. The powers in each of the two input modes and the squeezed modes are 10 and 2 μW, respectively. These powers are considerably smaller than the powers (3 mW) of the local oscillators (LOs) used for homodyne detection. All the interferences at the beam splitters are actively phase locked using modulation sidebands of 77, 106 kHz, and their beat in 29 kHz. Subthreshold optical parametric oscillators (OPOs) generate the squeezed vacuum ancillas. To control the beam splitting ratios of the four beam splitters in the squeezing operations and the Mach–Zehnder interferometer, they are composed of two polarizing beam splitters and a half wave plate [275] which are the same as the ones explained in the previous section.

The OPOs are bow-tie shaped cavities of 500 mm in length, containing a periodically-poled $KTiOPO_4$ (PPKTP) crystal of 10 mm in length. The pump beams for the OPOs (with wavelengths of 430 nm and powers of about 100 mW) are the second harmonic of the output of the Ti:sapphire laser. The frequency doubling cavity (not shown in the figure) has the same configuration as the OPOs, but contains a $KNbO_3$ crystal. For details of a squeezed vacuum generation, see [283]. Each OPO enables a squeezing degree of about −5 dB relative to the shot noise level.

The outcomes of the homodyne detection in the QND gate are fed forward to the remaining part. After low-noise electric amplification, they drive an electro-optical modulator (EOM) traversed by an auxiliary beam with the power of 150 μW, which is subsequently mixed with the signal beam by an asymmetric beam splitter (99 : 1).

The QND scheme is characterized by measuring the two input modes as well as the two output modes using homodyne detection. The detector's quantum efficiencies are higher than 99%, the interference visibilities to the LOs are on average 98%, and the dark noise of each homodyne detector is about 17 dB below the opti-

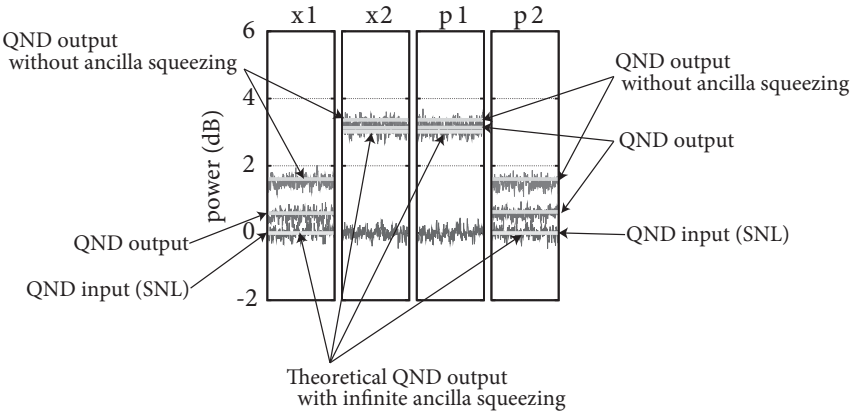

Figure 6.12 Variances of the quadrature components corresponding to vacuum inputs and $G = 1.0$ [284]. Shown are the experimental QND output variances with their theoretical values (lines) compared to the results with vacuum-state ancillas (without ancilla squeezing) and their theoretical values (lines).

cal shot noise level produced by the local oscillator. The propagation losses in each of the two main modes through the QND apparatus were about 7%.

Experimental results. The three measures in Eq. (6.14) are used to quantify the performance of our QND system. To estimate them, measurements of second moments of the input fields and the output fields are performed, employing a spectrum analyzer with a center frequency of 1.25 MHz, resolution and video bandwidths of 30 kHz and 300 Hz, respectively, a sweep time set to 0.1 s and further averaging of 20 traces. In Figures 6.12–6.14, the results for $G = 1.0$ are shown; in Table 6.1, the performance of the QND device is listed for both $G = 1.0$ and $G = 1.5$.

In the first series of measurements, we determine the variances of conjugate quadratures of the output states when the input states are pure vacua. The results corresponding to $G = 1.0$ are presented in Figure 6.12. The variances of the two input states are at the vacuum noise level as illustrated in the figure. As a result of the QND interaction, in the ideal case (infinite ancilla squeezing), the noise of the signal variables ($\hat{x}_1$ and $\hat{p}_2$) is added to the probe variables ($\hat{x}_2$ and $\hat{p}_1$) while the signal variables are preserved. The deviation from the ideal performance is due to the finite amount of squeezing for the ancillas. For comparison, the variances of the output states are also measured when no squeezing is used. The expected variances for finite squeezing or without squeezing are calculated and marked by lines.

In the second series of measurements, in order to test the universality of the QND gate, the input vacuum states are replaced by a pair of coherent states. The coherent amplitude in each quadrature of the two input modes is generated by modulating the amplitude or phase of their carriers using an EOM operating at 1.25 MHz. Four different input states, each corresponding to a coherent excitation in, respectively, (a) x_1^{in}, (b) x_2^{in}, (c) p_1^{in} and (d) p_2^{in}, are investigated. The mea-

Table 6.1 Evaluation of the QND interaction [284]. Shown are the quadrature transfer coefficients T_S and T_P and the conditional variance $V_{S|P}$ for two different gains G.

G	1.0		1.5	
Quadrature	***x***	***p***	***x***	***p***
T_S	0.79 ± 0.03	0.71 ± 0.03	0.80 ± 0.03	0.71 ± 0.03
T_P	0.41 ± 0.02	0.39 ± 0.02	0.62 ± 0.03	0.56 ± 0.02
$T_S + T_P$	1.20 ± 0.05	1.10 ± 0.05	1.42 ± 0.06	1.27 ± 0.05
$V_{S\|P}$	0.75 ± 0.01	0.78 ± 0.01	0.61 ± 0.01	0.63 ± 0.01

surement results of the second moments of the input and output quadratures for $G = 1.0$ are shown in Figure 6.13. The excitations of the input states are measured by setting the reflectivities of the four beam splitters to unity and blocking the auxiliary displacement beams in the feedforward construction. We observe that the amplitude of the input states is preserved in the same quadrature with almost unity gain. Furthermore, it is clearly seen that the expected feature that the information in a signal variable, $\hat{x}_1^{\text{in}}$ or $\hat{p}_2^{\text{in}}$, is coupled into the probe variable $\hat{x}_2^{\text{out}}$ or $\hat{p}_1^{\text{out}}$ (see Figure 6.13a,d), whereas the amplitude in the probe variables $\hat{x}_2^{\text{in}}$ and $\hat{p}_1^{\text{in}}$ does not couple to any of the other quadratures (see Figure 6.13b,c). These results verify the interaction in Eq. (6.13). From these measurements, we determine the transfer coefficients T_S and T_P using the method outlined in [291]. The results are summarized in Table 6.1. Note that the experimentally determined values of T_S and T_P are degraded by propagation and detection losses compared to the ideal scheme described by Eqs. (6.15)–(6.18).

Finally, the conditional variance using the setup shown in Figure 6.14a is measured. The outcomes from one of the homodyne detectors are rescaled by a gain g, subtracted from (or added to) the outcomes of the other homodyne detector and subsequently directed to a spectrum analyzer. The resulting normalized noise powers are shown in Figure 6.14b,c as a function of the rescaling gain g. The minima of these plots correspond to the conditional variances for the various realizations: curves (i) represent ideal performance, curves (ii) are associated with our system with finitely squeezed ancillas, and curves (iii) are the performance of the system without squeezing of ancilla states. The parabolic curves are theoretical calculations, and the dots with vertical error bars along the curves (ii) and (iii) are the experimental results. The experimental results for $V_{S|P}$ are shown in Table 6.1. No compensation of losses is carried out for these results.

The experiment presented here demonstrates the canonical two-mode entangling gate. From the noise correlations in Figure 6.14, we verify entanglement between the two output modes. According to Duan and Simon [116, 159], a sufficient condition for an entangled state is (see also Chapter 3)

$$\left\langle \left(\hat{x}_1^{\text{out}} - g\hat{x}_2^{\text{out}}\right)^2 \right\rangle + \left\langle \left(\hat{p}_2^{\text{out}} + g\hat{p}_1^{\text{out}}\right)^2 \right\rangle < 4|g| \,, \tag{6.19}$$

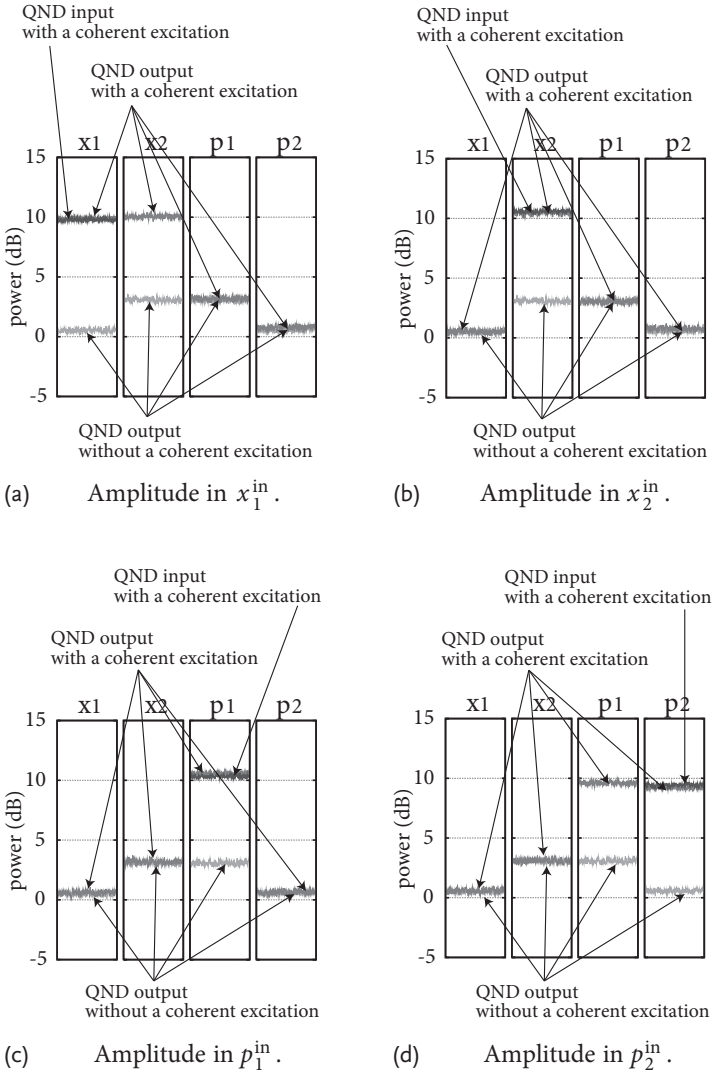

Figure 6.13 Second moments of the quadrature components of the input and output states with respect to four different input states for $G = 1.0$ [284]. One of the input quadratures is excited (with amplitude). We add traces without excitation for references.

where g is the rescaling gain. Thus, if the parabolic curves in Figure 6.14b,c go below the lines (iv) *simultaneously* for both quadratures, the two output modes are entangled, which is the case for curves (ii) with squeezed ancillas.[1)] Note that the

1) We can standardize Eq. (6.19) and eliminate dependence on g by considering fictive local squeezings. The standard form of the inseparability criterion is $\langle(\hat{x}_1^{\text{out}} - \hat{x}_2^{\text{out}})^2\rangle + \langle(\hat{p}_1^{\text{out}} + \hat{p}_2^{\text{out}})^2\rangle < 4$. Experimentally obtained values are 2.57 ± 0.03 for $G = 1.0$ and 2.33 ± 0.03 for $G = 1.5$, which are smaller than 4.

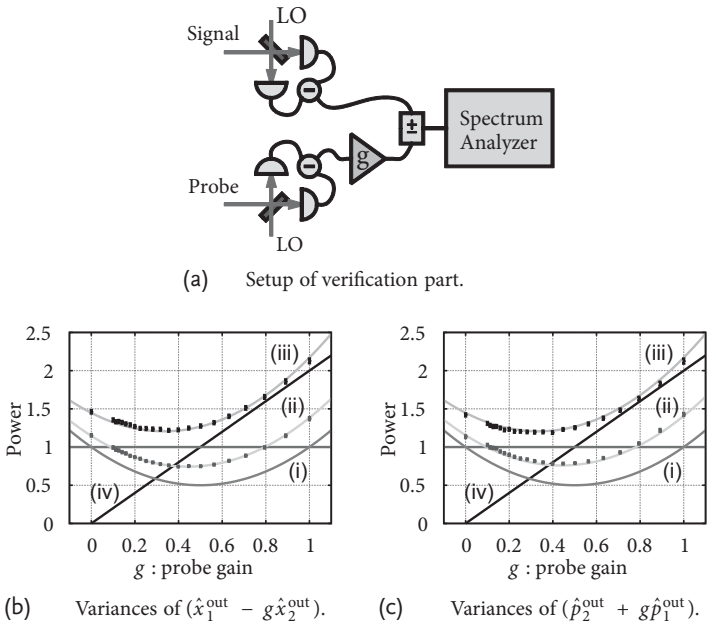

(a) Setup of verification part.

(b) Variances of $(\hat{x}_1^{\text{out}} - g\hat{x}_2^{\text{out}})$. (c) Variances of $(\hat{p}_2^{\text{out}} + g\hat{p}_1^{\text{out}})$.

Figure 6.14 Noise Correlations between output quadratures determining the conditional variances and verifying entanglement [284]. (a) Experimental setup. The measured probe quadrature is rescaled with a variable gain g, added (subtracted) ($\pm$) to (from) the signal quadrature detector output, and analyzed with an electronic spectrum analyzer (S.A.). Variances of $\hat{x}_1^{\text{out}} - g\hat{x}_2^{\text{out}}$ and of $\hat{p}_2^{\text{out}} + g\hat{p}_1^{\text{out}}$ are shown in (b) and (c), respectively: theoretical prediction for an ideal QND interaction (i), a QND interaction with finite degrees of squeezing of the ancilla modes (ii), and with vacuum ancilla modes (iii). By entering the areas below the lines (iv) entanglement is verified. The vertical axes are variances normalized to the shot noise power of the signal variable.

two-mode gate here has been applied to two coherent input states which, without the squeezed ancillas, would not become entangled via *any* linear optical transformation alone (see, e.g., curve (iii)).

From the above description, we see that a close-to-unitary quantum nondemolition sum gate can be created by using only linear optics and offline squeezed vacuum states. The gate operates in the quantum regime since even two input coherent states become entangled through it.

6.2.2
Universal Qumode Gates

There is a CV scheme which could be interpreted as the analogue of KLM because it is also teleportation-based and uses CV Bell measurements on non-Gaussian resource states [268]. Consider the quantum circuit in Figure 6.15 and assume that the entangling C_Z gate acting on the second and third rails of the circuit is performed offline prior to the C_Z that acts on the first and second rails. In this way, the C_Z on the upper two rails together with the two homodyne detections can be

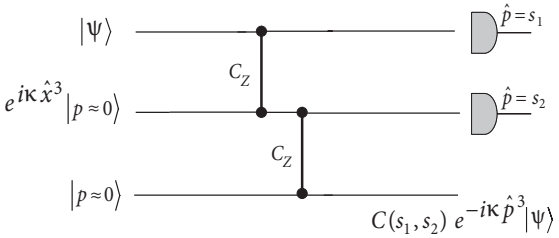

Figure 6.15 Teleporting the cubic phase gate $e^{-i\kappa\hat{p}^3}$ onto an arbitrary input state $|\psi\rangle$ by first applying it offline upon an effective two-mode squeezed EPR state and then doing standard CV quantum teleportation using a CV Bell measurement. The advantage of this realization is that only linear, Gaussian operations are performed online and the offline cubic gate could be implemented by any scheme, even in a probabilistic fashion. The final, Gaussian correction step to undo the operator $C(s_1, s_2)$ depending on the homodyne results s_1 and s_2 involves displacements, rotations, and squeezers because of the commuting properties of the cubic gate which is non-Gaussian/non-Clifford (see Section 1.8) and so does not preserve the WH group under conjugation [268].

interpreted as a collective, homodyne-based CV two-mode Bell measurement on an input state $|\psi\rangle$ and one half of a non-Gaussian entangled resource state which is the so-called cubic phase state (see Chapter 8) coupled to a momentum-squeezed state through a CV C_Z gate. This resource then is actually equivalent to a two-mode squeezed state with one mode subject to a cubic phase gate (see Section 1.8) up to a local Fourier transform as the C_Z gate and the cubic gate $D_3(\kappa)$ commute.

Eventually, we may describe the protocol in terms of standard CV quantum teleportation (compare with Figure 1.8) where a nonlinearly transformed offline two-mode squeezed state is used as an EPR channel for CV quantum teleportation. In the case of a cubic offline resource, the online correction operations during the teleportation process will be quadratic containing squeezers and displacements; a quartic offline resource such as a self-Kerr transformed two-mode squeezed state leads to cubic corrections [268].

However, there are various ways how to incorporate a desired gate operation into a CV quantum teleportation scheme (see Figure 6.16). As long as only linear (but collective two-mode), homodyne-based measurements on an input mode and one mode of a nonlinear, non-Gaussian resource state are permitted, the degree of the correction operations is always one order less than the order of the desired gate. As a result, only the cubic gate can realized using cubic resources and Gaussian measurements and corrections; a quartic gate requires linear measurements, but cubic corrections which, of course, may also be implemented using cubic offline resources.

Once a quartic self-Kerr-type gate can be implemented using CV quantum teleportation (e.g., as in Figure 6.16b or c), such a scheme could be applied to two qubits, as shown in Figure 2.15. Together with the two beam splitters (and taking into account the finiteness of the resource squeezing for teleportation), this results in an *approximate, unconditional, and thus deterministic* realization of a two-qubit C_Z gate as opposed to the perfect, nondeterministic implementation of KLM [242].

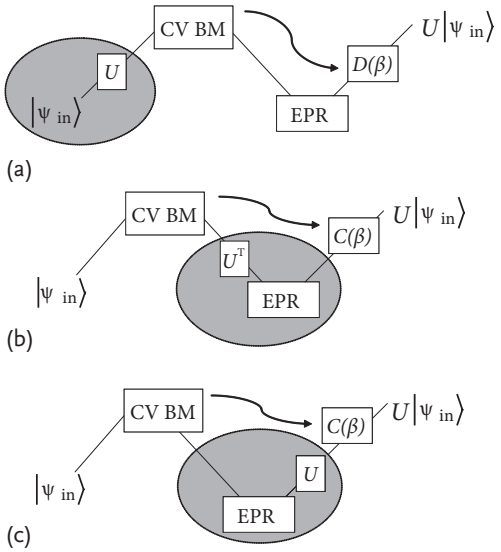

Figure 6.16 Teleportation-based implementation of a nonlinear, unitary gate U such as the cubic phase gate or a quartic Kerr-type gate. In all schemes, the online operations are: a two-mode, homodyne-based CV Bell measurement "CV BM" and the measurement-dependent corrections using displacements $D(\beta)$ or displacements and additional operations $C(\beta)$ with a Hamiltonian degree of one order lower that the nonlinearity order of U; the offline resource state is a nonlinearly transformed, Gaussian two-mode squeezed "EPR" state, except in the trivial, teleportation-based scheme (a) where the input state $|\psi_{\text{in}}\rangle$ is first transformed according to the desired gate U and then teleported; as $|\psi_{\text{in}}\rangle$ may be arbitrary and unknown, the scheme (a) is not a valid offline-scheme and would require an online gate U acting upon $|\psi_{\text{in}}\rangle$. The schemes (b) and (c) are similar, only differing in the particular EPR-mode to which the nonlinear gate U is applied offline. The nonlinear resources are always indicated by a gray circle; only for the case of a cubic gate U are all online operations Gaussian. Up to local Fourier transforms and squeezers, the scheme of Figure 6.15 is a special example of that in (b). Of course, we may also consider combinations of (a), (b), and (c).

However, note that the correction operations before the second beam splitter are still cubic and so would require further nonlinear processing.

The scheme of Figure 6.15 is a special example of Figure 6.16b. In the general case of Figure 6.16b, the gate U to be implemented can be arbitrary and need not be diagonal in the x-basis. For the cluster-type circuit (see Chapter 7) in Figure 6.15, however, it is useful that the entangling gates C_Z and the desired cubic gate operation D_3 are all diagonal in x and hence commute.[2)] Start-

2) In the scheme of Figure 6.16c, an arbitrary gate U, instead of applying it at the very end of CV quantum teleportation, can just be commuted through the final teleportation displacement operation, $U\,D(\beta) = C(\beta)\,U$, with $C(\beta)$ a correction operation of one order lower than the order of U and U applied offline to the EPR state [268]. Similarly, the scheme of Figure 6.16b may be understood by rewriting the offline transformed, maximally entangled EPR state of (c), $(\mathbb{1} \otimes U)|\text{EPR}\rangle = (U^{\text{T}} \otimes \mathbb{1})|\text{EPR}\rangle$, in the limit of infinite squeezing; for the finite-squeezing case, see main text.

ing with a two-mode squeezed state $\sum_{n=0}^{\infty} c_n |n, n\rangle_{1,2}$ with $c_n \equiv \tanh^n r/\cosh r$ for a squeezing parameter r, we may apply the transfer formalism for standard CV quantum teleportation [208] and extend it to the present case of gate teleportation. Then, we obtain the conditional state after the Bell projection of the input qumode and qumode 1 onto $\hat{\Pi}(\beta) \equiv |\Phi(\beta)\rangle\langle\Phi(\beta)|$ for the CV Bell basis $|\Phi(\beta)\rangle \equiv [\hat{D}(\beta) \otimes \mathbb{1}] \sum_{m=0}^{\infty} |m, m\rangle/\sqrt{\pi}$,

$$\hat{\Pi}_{\mathrm{in},1}(\beta) \left\{ |\psi_{\mathrm{in}}\rangle \otimes \left[\left(U_1^{\mathrm{T}} \otimes \mathbb{1}_2 \right) \sum_{n=0}^{\infty} c_n |n, n\rangle_{1,2} \right] \right\}, \tag{6.20}$$

corresponding to a conditional state of qumode 2 alone,

$$\sum_n \frac{c_n}{\sqrt{\pi}} |n\rangle \sum_m U_{mn}^{\mathrm{T}} \langle m| \hat{D}^{\dagger}(\beta) |\psi_{\mathrm{in}}\rangle = \mathcal{D}\, U\, \hat{D}^{\dagger}(\beta) |\psi_{\mathrm{in}}\rangle \,, \tag{6.21}$$

with the "distortion operator" $\mathcal{D} \equiv \sum_n c_n |n\rangle\langle n|/\sqrt{\pi}$ and the matrix elements $U_{mn}^{\mathrm{T}} \equiv \langle m|U^{\mathrm{T}}|n\rangle = \langle n|U|m\rangle$. After a suitable correction operation $C(\beta)$, the input state is "transferred" onto the output state $\hat{T}_{\mathrm{U}}(\beta)|\psi_{\mathrm{in}}\rangle$ with

$$C(\beta)\mathcal{D}\, U\, \hat{D}^{\dagger}(\beta) \equiv C(\beta)\mathcal{D} C^{\dagger}(\beta)\, U \equiv \hat{T}_{\mathrm{U}}(\beta) \,, \tag{6.22}$$

where the first equality defines the right correction operation $C(\beta)$ depending on the gate U and its commuting properties with the displacement operator, $U\hat{D}^{\dagger}(\beta) = C^{\dagger}(\beta)\, U$. The degree of $C^{\dagger}(\beta)$ will always be one order lower than the order of U [268]. In the limit of infinite squeezing, we obtain the desired gate teleportation. For finite squeezing r, there will be a distortion resulting in a non-unit-fidelity gate, $F = \int \mathrm{d}^2\beta |\langle\psi_{\mathrm{in}}| U^{\dagger} \hat{T}_{\mathrm{U}}(\beta)|\psi_{\mathrm{in}}\rangle|^2 < 1$.

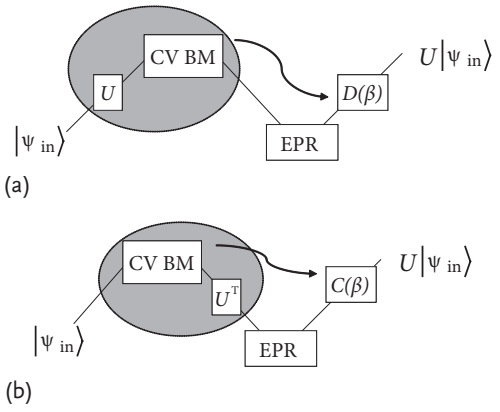

Figure 6.17 Gate teleportation using collective nonlinear projection measurements on an input state $|\psi_{\mathrm{in}}\rangle$ and one half of a Gaussian two-mode squeezed state that serves as an EPR source; (a) compared to Figure 6.16a, the nonlinear gate U is absorbed into the Bell measurement; similarly, (b) compared to Figure 6.16b, the nonlinear gate U^{T} is absorbed into the Bell measurement. The nonlinear elements are again indicated by the gray circles, this time corresponding to suitable projective measurements.

Formally, we may also interpret some of the schemes in Figure 6.16 as gate teleportations for arbitrary qumode gates U using nonlinear operations on linear resources, where a Gaussian two-mode squeezed state is used as an EPR source and a nonlinearly modified, two-mode Bell measurement is employed (see Figure 6.17). For example, the scheme in Figure 6.17a can be formally described as

$$\hat{\Pi}^{(U)}_{\mathrm{in},1}(\beta)\left(|\psi_{\mathrm{in}}\rangle \otimes \sum_{n=0}^{\infty} c_n |n,n\rangle_{1,2}\right) = \mathcal{D}D^{\dagger}(\beta)\,U|\psi_{\mathrm{in}}\rangle\ , \tag{6.23}$$

using the definitions given earlier in this section and $\hat{\Pi}^{(U)}(\beta) \equiv (U^{\dagger}\otimes\mathbb{1})\hat{\Pi}(\beta)(U\otimes\mathbb{1})$, describing a projection onto the basis $\{(U^{\dagger}\otimes\mathbb{1})|\Phi(\beta)\rangle\}$ for a fixed U. As such collective nonlinear measurements are not known to be experimentally available, there seems to be no advantage of the schemes in Figure 6.17 besides the conceptual insights they provide. The scheme in Figure 6.17a does not require any correction operations other than displacements because it is equivalent to that in Figure 6.16a where the gate U is trivially applied through teleportation by first performing U on $|\psi_{\mathrm{in}}\rangle$ and then teleporting $U|\psi_{\mathrm{in}}\rangle$ using standard CV quantum teleportation.

7
Cluster-Based Quantum Information Processing

In the preceding chapter, we introduced the concept of gate teleportation as an extension of state teleportation, and we presented various experiments that realized gates through teleportation on qubits or qumodes. Similar to these gate teleportations, the cluster-based schemes and experiments described in this chapter are again manifestations of the paradigm of measurement-based quantum computation where the unitary gates of the standard circuit model [5] are replaced by irreversible sequences of measurements [1] on an offline prepared resource state (see Section 1.8 and Figure 1.11).

However, as mentioned before in the introduction to Chapter 6, cluster-based quantum computing represents the ultimate form of measurement-based quantum information processing: measurements are performed locally on the smallest subsystems of the cluster resource state, that is, the individual qubits or qumodes that form the cluster; the cluster itself embodies the maximal offline resource needed because once it has been prepared, it remains fixed during the computation with measurements on it still offering sufficient freedom to realize universal and hence arbitrary quantum gates.

The locality of the measurements means that every entangling gate required for a multi-qubit or multi-qumode computation is already embedded in the cluster state. This is particularly useful when such entangling gates can only be probabilistically implemented as in the single-photon-based approaches.

In this chapter, we will first explain cluster computation on qubits (Section 7.1), including the elementary teleportation steps needed (Section 7.1.1), their use for Clifford and for universal quantum computing, and an experimental demonstration of a small cluster computation (Section 7.1.2). The analogous qumode schemes are presented in Section 7.2, similarly divided into Section 7.2.1 on elementary qumode teleportations, Section 7.2.2 on Gaussian computations, and Section 7.2.3 describing various experiments in the CV Gaussian regime of cluster-based quantum information processing. Gaussian regime here means that all these experiments so far have demonstrated only Gaussian transformations using cluster states.

An experiment that incorporates a *non-Gaussian* measurement into the cluster computation and thereby leaves the regime of Gaussian gates as required for universal quantum computation is yet to be performed. Nonetheless, the experiment

Quantum Teleportation and Entanglement. Akira Furusawa, Peter van Loock
Copyright © 2011 WILEY-VCH Verlag GmbH & Co. KGaA, Weinheim
ISBN: 978-3-527-40930-3

presented in Section 7.2.3.2 can be seen as an almost ultimate demonstration of single-mode Gaussian cluster computation as it implements Fourier and squeezing gates on independent, single-qumode optical states through a linear four-mode cluster state which is universal for arbitrary single-qumode LUBO transformations.

7.1 Qubits

A multi-qubit cluster state is illustrated in Figure 1.11. Let us see how an elementary teleportation step between two adjacent qubits works.

7.1.1 Elementary Qubit Teleportations

Consider the qubit circuit in Figure 7.1. The output state of that circuit is

$$X^m H Z_\theta |\psi\rangle \tag{7.1}$$

for an arbitrary input state $|\psi\rangle$. In other words, up to a Pauli correction operation depending on the measurement result m for the measurement on the upper qubit and up to a Hadamard gate, the resulting state is $Z_\theta|\psi\rangle$. For arbitrary angles θ, arbitrary Z rotations are applied upon the input state.

Now the crucial point is that, instead of the unitary circuit shown in Figure 7.1a, the unitary operator that describes the desired Z-rotation gate can be absorbed into the measurement apparatus as shown in Figure 7.1b. This way any Z rotation can be enacted by choosing a suitably rotated measurement basis. By concatenat-

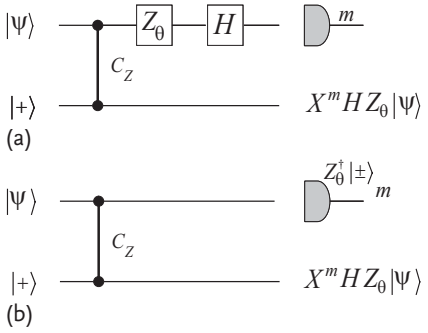

Figure 7.1 Elementary "one-bit" teleportation circuit for qubit cluster computation. (b) the C_Z gate represents a horizontal edge connecting two nodes of the cluster state. An input state $|\psi\rangle$ is teleported into the left node, and a subsequent, local single-qubit measurement in the binary basis $\{Z_\theta^\dagger|\pm\rangle\}$ leaves the second node, up to a Hadamard gate H and a Pauli correction X depending on result $m = 0, 1$, in the unitarily evolved state $Z_\theta|\psi\rangle$, with the rotation angle θ for a Z-rotation $\exp(-i\theta Z/2)$ controlled by the actual choice θ for the measurement basis. (a) shows the equivalent circuit in which the measurement is decomposed into unitary gates and a computational basis measurement.

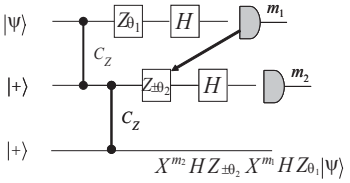

Figure 7.2 Two cascading elementary qubit teleportations.

ing these elementary teleportation steps, one can apply sequences of single-qubit rotations such as for two steps (see Figure 7.2)

$$X^{m_2} H Z_{\theta_2} X^{m_1} H Z_{\theta_1} |\psi\rangle \ . \tag{7.2}$$

Now, it depends on the commuting properties of the rotation gate (if it is Clifford or not, see Section 1.8) as to whether and how the Pauli corrections can be applied.

Assume the first measurement result is $m_1 = 1$. In this case, we have

$$Z_{-\theta_2} X = X Z_{\theta_2} \tag{7.3}$$

such that the desired gate Z_{θ_2} ends up in front of the state vector $|\psi\rangle$ only provided the actual measurement basis was chosen different from Z_{θ_2}, namely, according to a rotated basis with $Z_{-\theta_2}$. Whether or not this basis change is necessary in the second teleportation step depends on the measurement outcome of the first step. Therefore, in general, feedforward is required, where the later measurement bases must be adjusted according to the earlier measurement outcomes. However, there is an exception. Whenever the rotations are Clifford rotations, they would simply commute through the Pauli correction operators; in which case only the required Pauli correction would change and no more the subsequent measurement bases (see Chapter 1). In this case, no feedforward is needed, and all measurements can be performed at any time and in any order, even in parallel – a notion known as *Clifford parallelism*.

7.1.2
Experiment: Qubit Cluster Computation

One of the most famous experiments of qubit cluster computation would be the one performed by Walther *et al.* [149] which uses the cluster states explained in Section 3.1.3.3. Since the cluster states are created by post-selection, this experiment also works with post-selection. Moreover, there is no feedforward in the experiment. Only those events with no need for feedforward are post-selected as shown later. In this sense, it is a partial demonstration of cluster computation because feedfoward is one of the most important features of cluster computation. In this section, we will first explain this experiment in detail.

Walther *et al.* performed two types of experiments which are cascaded single-qubit operations and two-qubit quantum logic gates [149]. For the cascaded operation experiment, they performed two or three cascaded operations with a four-mode

linear cluster state. These states are given in Eq. (3.25) in polarization qubit representation and in Eq. (3.26) in the computational basis.

For two cascaded operations, they first made a polarization measurement of the photon in mode 1 in the $\{|+\rangle_1,\ |-\rangle_1\}$ basis ($\pm 45^\circ$-linearly polarization) to prepare a three-mode linear cluster state of modes 2–4. Of course, one should make a measurement in the $\{|0\rangle, |1\rangle\}$ basis (computational basis) to make the first qubit of the linear four-mode cluster state disentangled and the rest intact. However, in this particular experiment, they used "lab basis" which needs an extra Hadamard transformation ($|+\rangle \rightleftharpoons |\leftrightarrow\rangle = |H\rangle, |-\rangle \rightleftharpoons |\updownarrow\rangle = |V\rangle$) with quarter wave plates. Thus, the measurement on $\{|+\rangle_1, |-\rangle_1\}$ basis here corresponds to a measurement on the computational basis. They only took the case of $|+\rangle_1$ and discarded the case of $|-\rangle_1$. This action eliminates the need for feedforward.

To make two cascaded operations, polarization measurements on $B_j(\alpha)$ basis are made in modes 2 and 3 where $B_j(\alpha) = \{|\alpha_+\rangle_j,\ |\alpha_-\rangle_j\}$ and $|\alpha_\pm\rangle_j = (e^{i\alpha/2}|0\rangle_j \pm e^{-i\alpha/2}|1\rangle_j)/\sqrt{2}$.[1] Here, only the cases of $|+\alpha\rangle_j$ were post-selected in the experiment to obtain the input $|+\rangle_2$ and to eliminate the feedforwards. The $B_j(\alpha)$-basis measurement corresponds to single-qubit rotation around z-axis ($|0\rangle$–$|1\rangle$ axis) $R_z(\alpha) = \exp(-i\alpha\sigma_z/2)$ followed by a Hadamard operation $H = (\sigma_x + \sigma_z)/\sqrt{2}$, where $\{\sigma_x, \sigma_y, \sigma_z\}$ are the Pauli matrices.[2] Thus, the post-selected state of mode 4 (qubit 4) $|\psi_{\text{out}}\rangle_4$ after the measurements becomes

$$\begin{aligned} |\psi_{\text{out}}\rangle_4 &= H R_z(\alpha_3) H R_z(\alpha_2)|+\rangle \\ &= R_x(\alpha_3) R_z(\alpha_2)|+\rangle\ , \end{aligned} \tag{7.4}$$

where $R_x(\alpha) = H R_z(\alpha) H = \exp(-i\alpha\sigma_x/2)$. This sequence of two elementary teleportations is an example of the general concatenation shown in Figure 7.2. Again, in the experimental scenario, feedforward was not needed because those cases without feedforward were post-selected.

Walther *et al.* performed the experiment with $\alpha_2 = \pi/2, \pi/4, 0$ and $\alpha_3 = \pi/2$, which was realized by tuning of quarter wave plates and polarization angles of polarizers just before the detectors in modes 1–4 (Figure 3.10). The results are shown in Figure 7.3. The fidelity of operations with the ideal cases were 0.86 ± 0.03, 0.85 ± 0.04, and 0.83 ± 0.03 for $\alpha_2 = \pi/2$, π, and $/4, 0$, respectively [149].

Two-qubit-gate experiments were performed as follows. As explained in Section 3.1.3.3, a four-qubit square cluster state can be created using post-selection. Walther *et al.* performed a two-qubit gate operation with the four-mode square cluster state where the gate operation is shown in Figure 7.4.

In this experiment, the input state is $|+\rangle_1 \otimes |+\rangle_4$ which is automatically post-selected in the experiment. The two-qubit gate operation performed by polarization measurements of photons (qubits) in modes 1 and 4 of the square cluster state is

1) In [149], the definitions of $B_j(\alpha)$ and $|\pm\alpha\rangle_j$ are $B_j(\alpha) = \{|+\alpha\rangle_j, |-\alpha\rangle_j\}$ and $|\pm\alpha\rangle_j = (|0\rangle_j \pm e^{i\alpha}|1\rangle_j)/\sqrt{2}$.

2) Identical to $\{X, Y, Z\}$ according to the alternate notation used throughout this book. Similarly, $R_z(\alpha) \equiv Z_\alpha$, etc. because here we choose to use the same notation as in [149].

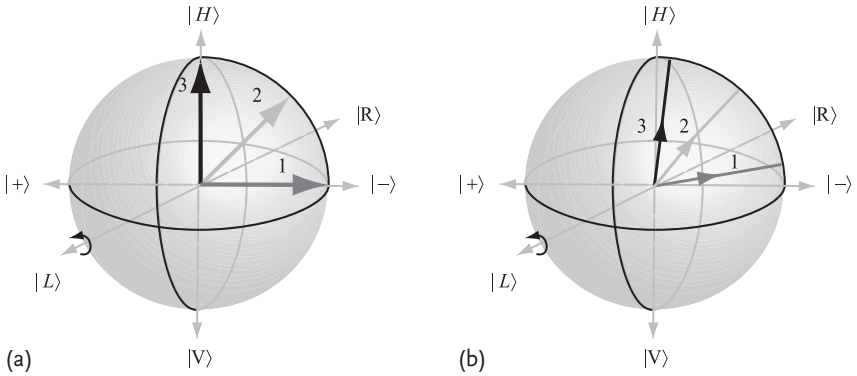

Figure 7.3 The state of qubit 4 after the measurements of qubits in modes 1–3 [149]. Here, "lab basis" is used for mode 4, which makes additional Hadamard operation on the state of Eq. (7.4). The states of qubit 4 with $\alpha_2 = \pi/2, \pi/4, 0$ are labeled 1, 2, and 3 in this figure, respectively, and $\alpha_3 = \pi/2$. (a) depicts the ideal case, and (b) depicts the experimental results.

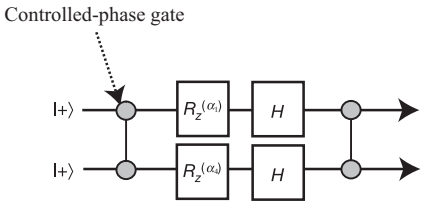

Figure 7.4 Scheme of two-qubit gate operation with a four-mode square cluster state demonstrated by Walther *et al.* [149]. Polarization measurements were performed in modes 1 and 4.

the following:

$$|\psi_{\text{out}}\rangle_{23} = \text{CPhase}(H \otimes H)[R_z(\alpha_1) \otimes R_z(\alpha_4)]\text{CPhase}|+\rangle \otimes |+\rangle \,, \tag{7.5}$$

where CPhase is the controlled-phase-gate operation (identical to C_Z, see Section 1.8),

$$\text{CPhase}|x\rangle \otimes |y\rangle = (-1)^{xy}|x\rangle \otimes |y\rangle \,, \quad (x, y = 0, 1) \,. \tag{7.6}$$

Note that the CPhase acts as an entangling gate in the first operation for separable inputs, but it acts as a disentangling gate in the second operation as in Figure 7.4 and Eq. (7.5). Experimentally, the case of $\alpha_1 = \pi$ and $\alpha_4 = 0$ should result in the operation $|+\rangle_1 \otimes |+\rangle_4 \rightarrow |+\rangle_2 \otimes |-\rangle_3$. The corresponding results are shown in Figure 7.5a. Note the "lab basis" was used and $|+\rangle_2 \otimes |-\rangle_3$ corresponds to $|V\rangle_2 \otimes |H\rangle_3$ where $|V\rangle = |\updownarrow\rangle$ and $|H\rangle = |\leftrightarrow\rangle$ because modes 2 and 3 are switched in the "lab basis" of this experiment. In Figure 7.5a, only the diagonal element of VH appears, consistent with the theoretical predictions and showing that the experiment is successful depending on postselection.

Similar to the case of the square cluster state, a two-qubit gate operation can be performed with a four-mode linear cluster state. In this case, we make measure-

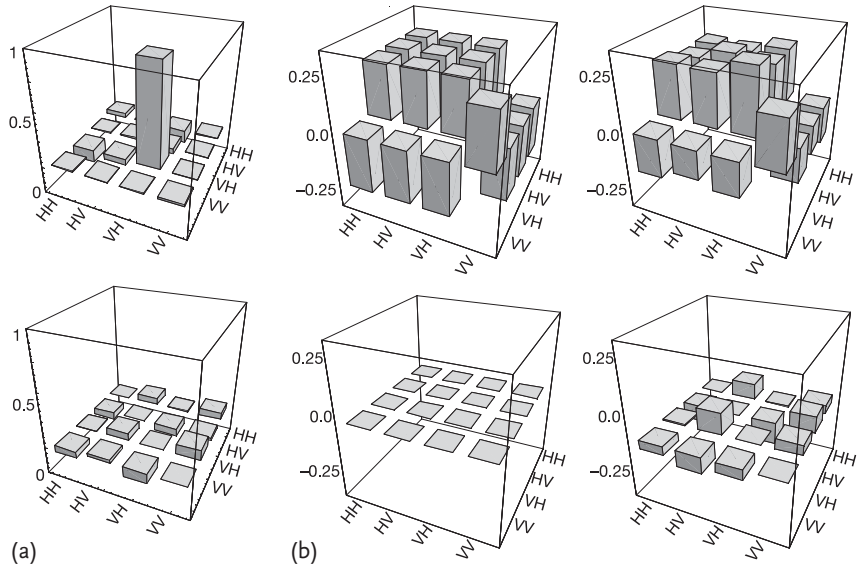

Figure 7.5 Experimental density matrices of two-qubit gate operation with four-mode square and horseshoe cluster states demonstrated by Walther *et al.* [149]. The "lab basis" is used. (a) results for the four-mode square cluster state, (b) for the four-mode horseshoe cluster state. Upper charts are for the real parts of density matrices and lower charts are for imaginary parts. The outputs for (a) and (b) are a separable and entangled states, respectively, and it is consistent with the theory.

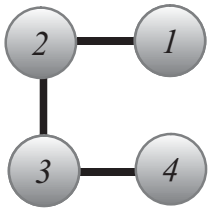

Figure 7.6 Graph representation of a four-qubit horseshoe cluster state.

ments of qubits 2 and 3 and the four-mode linear cluster state is regarded as a horseshoe cluster state shown in Figure 7.6. Here, the expression of the operation with this state is

$$|\psi_{\text{out}}\rangle_{14} = (H \otimes H)[R_z(\alpha_2) \otimes R_z(\alpha_3)]\text{CPhase}|+\rangle \otimes |+\rangle \,, \tag{7.7}$$

as shown in Figure 7.7.

The important thing here is that the output state $|\psi\rangle_{14}$ is an entangled state while the output state $|\psi\rangle_{23}$ from the operation in Eq. (7.5) is not an entangled state. Experimentally, they tried the case of $\alpha_2 = \alpha_3 = 0$ (both measurement results are $|+\rangle = +45^\circ$ linear polarization) which should make the operation $|+\rangle_2 \otimes |+\rangle_3 \rightarrow (|\leftrightarrow\rangle_1 \otimes |+\rangle_4 + |\updownarrow\rangle_1 \otimes |-\rangle_4)/\sqrt{2} = (|0\rangle_1 \otimes |+\rangle_4 + |1\rangle_1 \otimes |-\rangle_4)/\sqrt{2}$. The experimental results are shown in Figure 7.5b. Note again that the "lab basis" was employed, requiring extra Hadamard operations in modes 1 and 4. The exper-

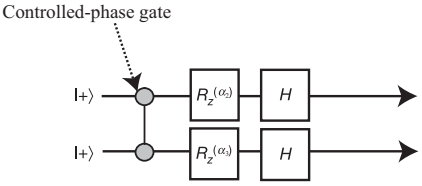

Figure 7.7 Scheme of two-qubit gate operation with a four-mode horseshoe cluster state demonstrated by Walther *et al.* [149]. Polarization measurements were performed in modes 2 and 3.

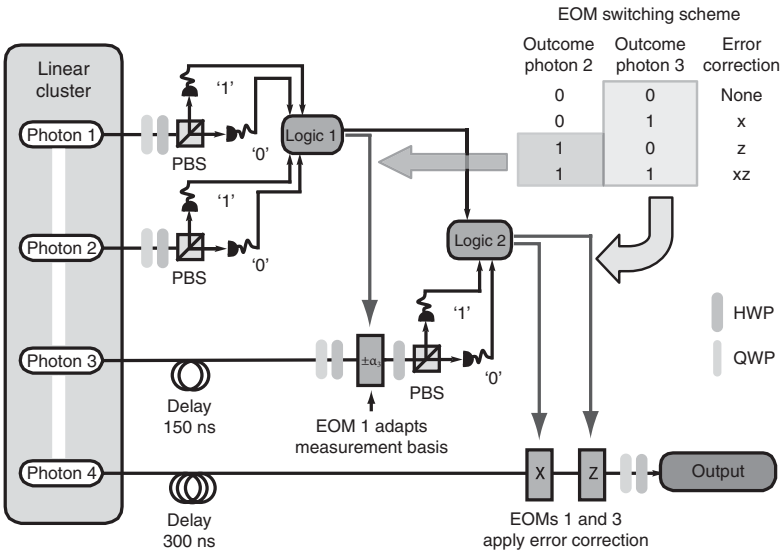

Figure 7.8 Experimental setup for cluster computation with feedforward [292].

imental results are again consistent with the theoretical predictions and confirm that the experiment is successful based on postselection.

Thus far, we have described an experiment for qubit cluster computation without the use of feedforward because such an experimental situation is much easier. However, since feedforward is a crucial ingredient of universal cluster computation, we shall now discuss an example for this kind of advanced cluster experiment *including feedforward*. The corresponding experiment of cluster computation with feedforward was performed by Prevedel *et al.* [292].

Figure 7.8 shows the experimental setup where the cluster state used in this experiment is the same as the ones used in Walther's experiment explained up to here (post-selection). In this sense, this experiment corresponds to Walther's experiment with feedforward.

First, Prevedel *et al.* performed the operation described in Eq. (7.4) with a four-mode linear cluster state. This is very similar to the experiment explained above. They first made a polarization measurement of the photon in mode 1 on

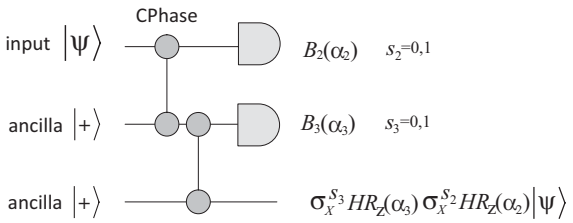

Figure 7.9 Elementary-teleportation picture for the experiment of Prevedel *et al.* similar to Figure 7.2 (in the figure here and in the main text of this section we use the same notation as in the article of Prevedel *et al.* differing from the notation used mostly throughout this book); $s_j = 0, 1$ correspond to the measurement results $|\alpha_+\rangle_j$, $|\alpha_-\rangle_j$, respectively.

$\{|+\rangle_1, |-\rangle_1\}$ basis ($\pm 45°$-linearly polarization) and took the case of $|+\rangle_1$ to prepare a three-mode linear cluster state of modes 2–4. Then, they made consecutive polarization measurements of the photons in modes 2 and 3 with α_2 and α_3 to make consecutive operations.

Figure 7.9 illustrates the operations according to the elementary-teleportation picture. The output state of the photon in mode 4 can be written as

$$|\psi_{\text{out}}\rangle_4 = \sigma_x^{s_3} H R_z(\alpha_3) \sigma_x^{s_2} H R_z(\alpha_2) |\psi\rangle \,, \tag{7.8}$$

corresponding to two cascaded elementary teleportations (see Figure 7.2). Here, $s_j = 0, 1$ correspond to the measurement results $|\alpha_+\rangle_j, |\alpha_-\rangle_j$, respectively. In this experiment, they wanted to have the output of $H R_z(\alpha_3) H R_z(\alpha_2)|\psi\rangle = R_x(\alpha_3) R_z(\alpha_2)|\psi\rangle$ irrespective of the measurement results. Therefore, they used feedforward.

In the case of $s_2 = s_3 = 0$, the output state of mode 4 is $R_x(\alpha_3) R_z(\alpha_2)|\psi\rangle$ and thus feedforwad is not needed. In the case of $s_2 = 1$ and $s_3 = 0$, the output state of mode 4 becomes

$$\begin{aligned} |\psi_{\text{out}}\rangle_4 &= H R_z(\alpha_3) \sigma_x H R_z(\alpha_2) |\psi\rangle \\ &= H R_z(\alpha_3) H H \sigma_x H R_z(\alpha_2) |\psi\rangle \\ &= R_x(\alpha_3) \sigma_z R_z(\alpha_2) |\psi\rangle \\ &= \sigma_z \sigma_z R_x(\alpha_3) \sigma_z R_z(\alpha_2) |\psi\rangle \\ &= \sigma_z R_x(-\alpha_3) R_z(\alpha_2) |\psi\rangle \,. \end{aligned} \tag{7.9}$$

From the equation, one needs to switch the measurement basis of mode 3 from $B_3(\alpha_3)$ to $B_3(-\alpha_3)$ and make σ_z operation for the output state $|\psi_{\text{out}}\rangle_4$ to get $R_x(\alpha_3) R_z(\alpha_2)|\psi\rangle$. In the case of $s_2 = 0$ and $s_3 = 1$, the output state of mode 4 becomes

$$\begin{aligned} |\psi_{\text{out}}\rangle_4 &= \sigma_x H R_z(\alpha_3) H R_z(\alpha_2) |\psi\rangle \\ &= \sigma_x R_x(\alpha_3) R_z(\alpha_2) |\psi\rangle \,. \end{aligned} \tag{7.10}$$

Therefore, one needs to make a σ_x operation for the output state $|\psi_{\text{out}}\rangle_4$ to get $R_x(\alpha_3) R_z(\alpha_2)|\psi\rangle$. In the case of $s_2 = s_3 = 1$, one needs to switch the measurement basis of mode 3 from $B_3(\alpha_3)$ to $B_3(-\alpha_3)$ and make a σ_z and σ_x operation.

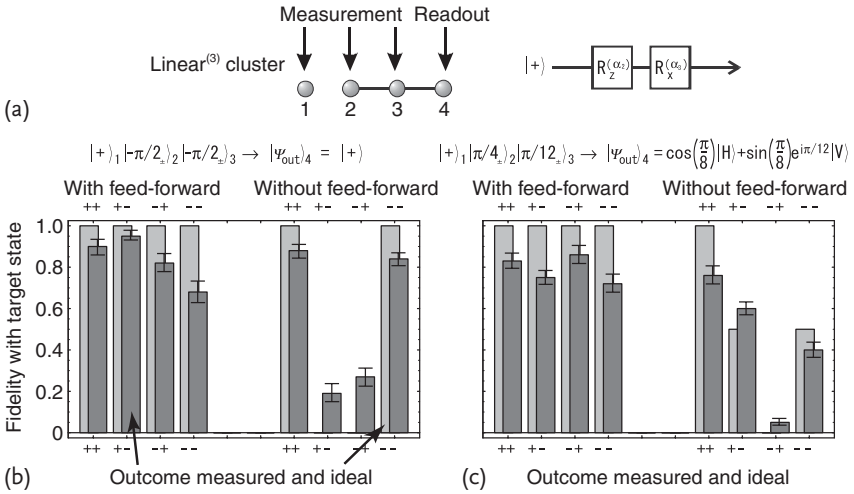

Figure 7.10 Experimental results of one-way quantum computation with three-mode linear cluster with and without feedforward [292]. "+", "−" denote $S_j = 0, 1$, respectively. The linear qubit cluster state and the circuit it implements; (b) $\alpha_2 = \alpha_3 = -\pi/2$, (c) $\alpha_2 = \pi/4$ and $\alpha_3 = \pi/12$.

Thus, the output state including feedforward can be described as

$$|\psi_{\text{out}}\rangle_4 = \sigma_x^{s_3}\sigma_z^{s_2} R_x((-1)^{s_2}\alpha_3) R_z(\alpha_2)|\psi\rangle \,, \tag{7.11}$$

where the switching table of feedforward is shown in Figure 7.8 as an inset.

The experiment was realized as shown in Figure 7.8. The most important thing here is that there are delay lines to compensate the time delay of photodetectors and logic circuits. By using the delay lines, the consecutive measurements and feedforwards were performed.

Experimental results of one-way quantum computation with three-mode linear cluster with feedforward are shown in Figure 7.10. Here, the input state is $|+\rangle_2$. The results are consistent with theory, confirming success of the experiments dependence on post-selection.

Prevedel *et al.* also tried to perform a two-qubit-gate operation with feedforward with the same experimental setup shown in Figure 7.8. They used a four-mode linear cluster as a horseshoe cluster state. Similar to the single-qubit-gate operations of Eq. (7.11), the performed two-qubit-gate operation can be described as

$$|\psi_{\text{out}}\rangle_{14} = (\sigma_x^{s_2} \otimes \sigma_x^{s_3})(H \otimes H)[R_z(\alpha_2) \otimes R_z(\alpha_3)]\text{CPhase}|\psi_2\rangle \otimes |\psi_3\rangle \,. \tag{7.12}$$

Figure 7.11 shows the experimental results. In this figure, the results for $S_2 = S_3 = 1$ and the input $|+\rangle_2 \otimes |+\rangle_3$ are shown. In the case with feedforward, the output should be $(|\leftrightarrow\rangle_1 \otimes |+\rangle_4 + |\updownarrow\rangle_1 \otimes |-\rangle_4/\sqrt{2}$, which is of course the same as the one of Walther's experiment mentioned before. On the other hand, in the case without feedforward, the output should become $(|+\rangle_1 \otimes |\updownarrow\rangle_4 + |-\rangle_1 \otimes |\leftrightarrow\rangle_4/\sqrt{2}$ in the case of $S_2 = S_3 = 1$. The experimental results presented in Figure 7.11 agree well with the theoretical prediction. However, we note again that a crucial ingredi-

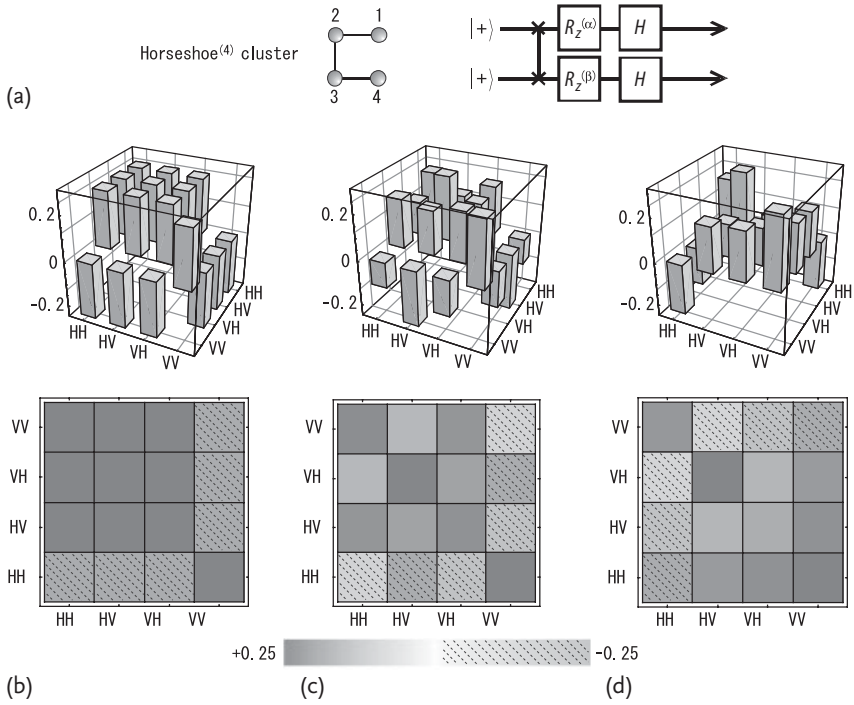

Figure 7.11 (a) Experimental results of one-way quantum computation with a four-mode linear cluster (horseshoe) with and without feedforward [292]. Two-qubit-gate operation of Figure 7.7 ($\alpha_2 = \alpha_3 = 0$) for the input state of $|+\rangle_2 \otimes |+\rangle_3$ was performed with and without feedforward. Only the case of $S_2 = S_3 = 1$ is shown in this figure. (b) The ideal case, (c) with feedforward and (d) without feedforward. $|H\rangle = |\leftrightarrow\rangle$, $|V\rangle = |\updownarrow\rangle$.

ent of the experiment is postselection. The readout in Figure 7.10a is part of the cluster computation protocol. Thus, the output state must be destroyed and is not directly available for further exploitation. Nevertheless, the principal mechanism of cluster computation with qubits was clearly demonstrated in this experiment.

7.2 Qumodes

A canonical version of a Gaussian (approximate) CV cluster state is shown in Figure 3.16. The cluster computation proceeds from left to right through measurements on the individual qumodes of the cluster state. Similar to the qubit case, quantum information propagates along the horizontal wires with single-qumode gates depending on the measurement bases. Two-qumode couplings are achieved because the cluster is two-dimensional such that the information effectively propagates along the whole lattice. Let us again consider an elementary teleportation circuit, this time on two qumodes.

7.2.1
Elementary Qumode Teleportations

Consider just one horizontal link between two adjacent qumodes in the cluster. The corresponding elementary qumode teleportation is shown in Figure 7.12.

Similar to the elementary qubit circuit, the gates in front of the computational x-homodyne detector in the circuit of Figure 7.12 can be absorbed into the measurement apparatus such that instead of measuring the observable $\hat{x}$, the projection is onto the rotated p-basis $\{D^\dagger|p\rangle\}$ measuring the observable $D^\dagger \hat{p} D$.

The output state of the elementary CV circuit is

$$X(s)FD|\psi\rangle \tag{7.13}$$

for an arbitrary input state $|\psi\rangle$. This time, up to a WH correction operation depending on the measurement result s for the measurement on the upper qumode and up to a Fourier transform, the resulting state is $D|\psi\rangle$. This way we can apply any gate $D = e^{if(\hat{x})}$ to an arbitrary input state teleported into the upper rail, that is, into one or, in the multi-mode case, several qumodes of the far left column in Figure 3.16. Further application of such elementary steps by measuring out the other qumodes in the CV cluster state beginning from the left in Figure 3.16 may lead to, in principle, universal quantum computation on multi-qumode states in the approximate, asymptotic sense [171]. This can be understood by concatenating the elementary teleportation steps such that for two steps (see Figure 7.13), we obtain the state

$$X(s_2)FD_2'(s_1)X(s_1)FD_1|\psi\rangle\ . \tag{7.14}$$

Now, again it depends on the commuting properties of the D gate (if it is Clifford or not, see Section 1.8) whether and how the WH corrections can be applied. In case

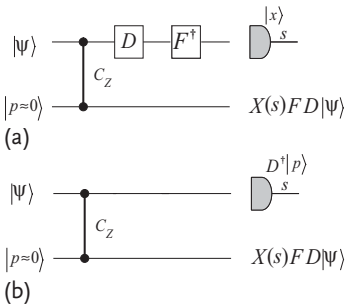

Figure 7.12 Elementary teleportation of a CV cluster computation. (b) the desired gate operation $D = e^{if(\hat{x})}$ and the inverse Fourier transform $F^\dagger$ can be absorbed into the measurement apparatus such that a projection of the upper qumode onto the basis $\{D^\dagger|p\rangle\}$ with result s leaves the lower qumode in the desired output state up to a Fourier transform and a WH correction $X(s)$. (a) shows the equivalent circuit in which the measurement is decomposed into unitary gates and a computational basis measurement. Compare this with the analogous qubit circuit in Figure 7.1.

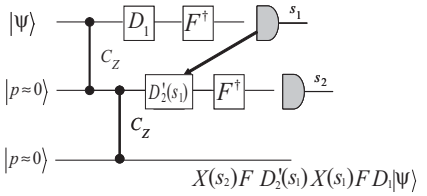

Figure 7.13 Two cascading elementary qumode teleportations.

D is a non-Gaussian unitary, one has to choose the second measurement basis such that

$$D_2'(s_1)X(s_1) = X(s_1)D_2 \tag{7.15}$$

with the desired gate operation D_2 in front of the state vector. Therefore, for general qumode gates, feedforward is required where the later measurement bases must be adjusted according to the earlier measurement outcomes. However, when the gates are Gaussian, they would simply commute through the WH correction operators; in which case only the required WH correction would change and not the subsequent measurement bases (see Chapter 1). In this case, no feedforward is needed and all measurements can be performed at any time and in any order (see next section). The particular observables to be measured at each step, $D^\dagger \hat{p}\, D$, can be chosen to be, for example, linear for D quadratic and quadratic for D cubic, see the universal qumode gates introduced in Section 1.8.

The Fourier transform is performed through the cluster at any step in order to switch between $\hat{x}$ and $\hat{p}$ gates. To complete the universal set in Eq. (1.127), the two-qumode gate C_Z is obtainable through the vertical wires in Figure 3.16 so the cluster must be at least two-dimensional. The total evolution of the input is completely controlled by the measurements with the cluster state prepared offline prior to the computation.

It is important to understand that in the realistic case of finitely squeezed cluster states, there will be errors accumulating during the cluster computation. In fact, it appears that there is no simple way (for instance, via a clever way of encoding quantum information that propagates through the cluster) to suppress these errors [293]. As a consequence, quantum error correction and fault tolerance have to be taken into account from the start, and this will require complicated nonlinear, non-Gaussian approaches (see Chapters 2 and 5).

7.2.2
Gaussian Computation

Any multi-mode LUBO as described by Eq. (2.104) can be performed on an arbitrary multi-mode state through homodyne detections alone. An additional nonlinear measurement such as photon counting is needed in order to be able to realize gates of cubic or higher order. In this case, the basis choice of a measurement in one step would typically depend on the outcomes of the measurements in the pre-

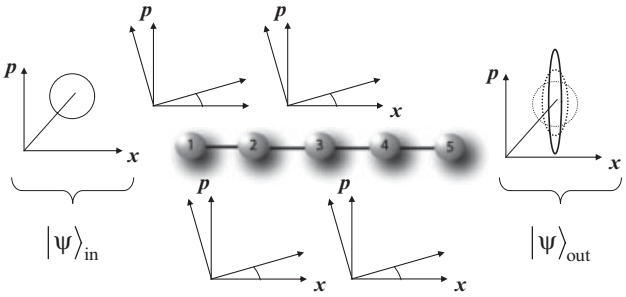

Figure 7.14 Universal single-mode LUBO. After attaching an arbitrary single-qumode input state to a linear four-mode cluster state (qumodes 2–5) appearing in qumode 1, four elementary steps involving four quadrature homodyne detections on qumodes 1–4 with suitably chosen local-oscillator quadrature angles are sufficient to obtain approximately any LUBO-transformed output state in qumode 5, provided the squeezing in the linear cluster state is sufficiently large. The C_Z-attachment of the input state and the two homodyne detections on qumodes 1 and 2 can be replaced by a CV Bell measurement on the input mode and the far left mode, qumode 2, of the cluster [294]. The input state is depicted as a Gaussian coherent state only for illustration. Most significantly, the CV Bell measurement can also be used to teleport non-Gaussian input states into the four-mode cluster for universal, linear processing.

vious steps. In contrast, in the all-homodyne-based scenario for LUBOs, no such feedforward is required and all measurements may be conducted in parallel – this is the CV qumode version of Clifford parallelism.

It has been proven that a linear four-mode cluster state is sufficient to achieve an arbitrary single-mode LUBO (see Figure 7.14); an arbitrary N-mode LUBO is possible using a finite, two-dimensional CV cluster state of $\sim N^2$ qumodes [294]. In this case, no more asymptotic evolutions with infinitesimal, elementary steps must be considered, but rather combinations of beam splitter and single-mode squeezing gates of appropriate strength. Such cluster-based LUBOs circumvent the complication of online squeezing of, especially, fragile non-Gaussian states since all squeezing gates are performed offline on the Gaussian cluster state. Provided enough squeezing is available to create the cluster states [169, 295–297], this approach may also be used to realize the necessary squeezing corrections for nonlinear gate implementations as discussed in the preceding section. The single-mode LUBO scheme was recently implemented experimentally [298, 299] (see the following sections on experimental schemes).

7.2.3
Experiment: Gaussian Qumode Cluster Computation

7.2.3.1 Quadratic Phase Gate

In this section, we will explain a quadratic phase gate demonstrated by Miwa *et al.* [299] in detail. It was realized by using a QND sum gate explained in Section 6.2.1.2, which is an example of off-line quantum information processing.

Measurement-based one-way quantum computation [1] using an off-line prepared, multi-party entangled cluster state is a conceptually interesting alternative to the standard unitary circuit model of quantum computation [5]. In the cluster-model, universality is achieved through different choices of measurement bases, while the cluster state remains fixed. Unitary gates are effectively applied at each measurement step corresponding to elementary teleportations [278, 300] for propagating and manipulating a quantum state through the cluster. The cluster model also turned out to provide new, potentially more efficient approaches to the experimental realization of quantum logical gates, especially in the quantum optical setting [150, 151].

A translation of the circuit model for quantum computation over continuous variables (CV) [86] to universal cluster computation with CV was given in [171]. The canonical, universal gate set for CV is $\{\hat{U}_3(\lambda), C\}$, where $C = \{\hat{Z}(s), \hat{U}_2(\kappa), \hat{F}, C_Z\}$ with the momentum shift operator $\hat{Z}(s) = \exp(2is\hat{x})$, the phase gates $\hat{U}_l(\kappa_l) = \exp(i\kappa_l \hat{x}^l)$, the Fourier transform operator $\hat{F}$, and the controlled-Z gate $C_Z = \exp(2i\hat{x} \otimes \hat{x})$ [170]. Through concatenation, the full set enables one to simulate any Hamiltonian in terms of arbitrary polynomials of the position $\hat{x}$ and the momentum $\hat{p}$ to any precision [86].[3)]

The same set without the cubic gate $\hat{U}_3$, that is, the set C, is still universal for realizing any quadratic Hamiltonian, that is, the whole group of Gaussian unitary transformations, the analogue to the Clifford group for discrete variables (DV). In the case of DV, for example, single-qubit Clifford transformations are fully covered by the Hadamard gate $\hat{H}$ and the "$\pi/4$"-phase gate $\hat{U}_{\pi/4}$ acting upon the qubit Pauli operators as $\hat{U}^\dagger_{\pi/4} Z \hat{U}_{\pi/4} = Z$ and $\hat{U}^\dagger_{\pi/4} X \hat{U}_{\pi/4} = -iXZ = -Y$; full universality for single-qubit transformations would then require, in addition, the well-known "$\pi/8$"-phase gate [5], the analogue to the cubic phase gate $\hat{U}_3$ for CV (see Section 1.8). Focusing on CV, the quadratic gate from the universal set C for all Gaussian transformations maps the Weyl–Heisenberg displacement operators $\hat{Z}(s)$ and $\hat{X}(s) = \exp(-2is\hat{p})$ into

$$\begin{aligned} \hat{U}_2^\dagger(\kappa)\hat{Z}(s)\hat{U}_2(\kappa) &= \hat{Z}(s) \\ \hat{U}_2^\dagger(\kappa)\hat{X}(s)\hat{U}_2(\kappa) &= e^{-i\kappa s^2}\hat{X}(s)\hat{Z}(-\kappa s)\,, \end{aligned} \tag{7.16}$$

in analogy to the qubit "$\pi/4$"-phase gate $\hat{U}_{\pi/4}$. The effect of the phase gate may be more conveniently expressed in terms of the generators of the Weyl–Heisenberg group, $\hat{U}_2^\dagger(\kappa)\hat{x}\hat{U}_2(\kappa) = \hat{x}$, $\hat{U}_2^\dagger(\kappa)\hat{p}\hat{U}_2(\kappa) = \hat{p} + \kappa\hat{x}$.

From Section 2.3 we know that there is an exact, finite decomposition of any quadratic unitary into single-mode squeezers and beam splitters [89, 121]. In this quantum optical language, the quadratic phase gate being explained in this section $\hat{U}_2$ together with the Fourier transform $\hat{F}$ provides single-mode squeezing, and the two-mode gate C_Z involves beam splitting modulo single-mode squeezing.

In the cluster-based one-way model, the quadratic gate can be fully controlled through the local oscillator phase of the homodyne detector [171]. Here, we will

3) Compared to Section 1.8, we are using a slightly modified notation in this section, consistent with [299]

explain the experimental demonstration of this controllability by Miwa *et al.* [299], with a fixed, off-line two-mode cluster state. In the demonstration, a large set of squeezing transformations was achieved by means of this one-way phase gate; sequential application of the gate would lead to universal single-mode Gaussian transformations (where changes of the first moments in phase space require, in addition, p-displacements $\hat{Z}(s)$, trivially realizable through a cluster state for CV [171]).

The output states of the elementary cluster computations exhibit sub-shot-noise quadrature variance; thus, nonclassical states are created deterministically through cluster computation with the degree of nonclassicality fully controlled by the measurement apparatus. Therefore, the demonstration differs from previous implementations of universal offline squeezing [275, 276] explained in Section 6.2.1.1 in which different squeezing transformations require different beam splitter transformations to achieve universality.

The elementary teleportation step for the case of CV [171] is described as follows. First, in the ideal scheme (Figure 7.15a), an arbitrary input state is coupled to a single-mode, infinitely squeezed state (a position eigenstate $|x = 0\rangle$), $\hat{U}_{\mathrm{QND}}|\psi\rangle_{\mathrm{in}}|x = 0\rangle_{\mathrm{A}}$. This results in $\mathrm{e}^{-2\mathrm{i}\hat{x}_{\mathrm{in}}\hat{p}_{\mathrm{A}}}\int \mathrm{d}x\,\psi(x)|x\rangle_{\mathrm{in}}\int \mathrm{d}p\,|p\rangle_{\mathrm{A}}/\sqrt{\pi} = \int \mathrm{d}x\,\psi(x)|x\rangle_{\mathrm{in}}|x\rangle_{\mathrm{A}}$, where the subscripts "in" and "A" denote the input and ancilla modes, respectively. Up to local Fourier rotations, the resulting state corresponds to a perfect two-mode cluster state already carrying the quantum information to be processed through the cluster (i.e., the quantum state $|\psi\rangle_{\mathrm{in}}$).

Next, we measure the observable $\hat{U}^{\dagger}(\hat{x})\hat{p}\,\hat{U}(\hat{x})$ of mode 1 where $\hat{U}(\hat{x}) \equiv \exp[\mathrm{i}\,f(\hat{x})]$ is diagonal in the position basis and $\hat{p}$ is the conjugate momentum to $\hat{x}$ ($[\hat{x}, \hat{p}] = \mathrm{i}/2$). The quantum state after the measurement with outcome p_0 is

$$\begin{aligned}\sqrt{\pi}\,{}_{\mathrm{in}}\langle p_0|\hat{U}(\hat{x}_{\mathrm{in}})\int \psi(x)|x\rangle_{\mathrm{in}}|x\rangle_{\mathrm{A}}\mathrm{d}x &= \sqrt{\pi}\int {}_{\mathrm{in}}\langle p_0|x\rangle_{\mathrm{in}}\,U(x)\psi(x)|x\rangle_{\mathrm{A}}\mathrm{d}x \\ &= \hat{Z}(-p_0)\,\hat{U}(\hat{x}_{\mathrm{A}})|\psi\rangle_{\mathrm{A}}\,. \end{aligned} \tag{7.17}$$

After correcting the displacement $\hat{Z}(-p_0)$, we obtain the desired state $\hat{U}(\hat{x})|\psi\rangle$ in the ancilla mode. Through this scheme, in principle, we can apply an arbitrary unitary operator $\hat{U}(\hat{x})$ to $|\psi\rangle_{\mathrm{in}}$; for nonlinear gates such as the cubic gate $\hat{U}_3$, however, this would require measuring a nonlinear observable. Here, we consider detection of the whole range of rotated quadratures (all linear combinations of $\hat{x}$ and $\hat{p}$), effectively applying the quadratic phase gate $\hat{U}_2(\kappa) = \exp\left(\mathrm{i}\kappa\hat{x}^2\right)$ to $|\psi\rangle_{\mathrm{in}}$, up to a phase-space displacement depending on the measurement result p_0.

In the optical realization, $\hat{x}$ and $\hat{p}$ are quadrature operators for the mode operator $\hat{a} = \hat{x} + \mathrm{i}\hat{p}$. The quadratic gate $\hat{U}_2(\kappa)$ corresponds to a sequence of rotation, squeezing, and rotation [89] with (see Section 1.8)

$$\begin{aligned}\hat{x}_{\mathrm{out}} &= \hat{x}_{\mathrm{in}} \\ \hat{p}_{\mathrm{out}} &= \hat{p}_{\mathrm{in}} + \kappa\,\hat{x}_{\mathrm{in}}\,. \end{aligned} \tag{7.18}$$

Thus, the required measurement corresponds to measuring [171]

$$\hat{p} + \kappa\hat{x} = \sqrt{1 + \tan^2\theta}\,\left(\hat{p}\cos\theta + \hat{x}\sin\theta\right)\,, \tag{7.19}$$

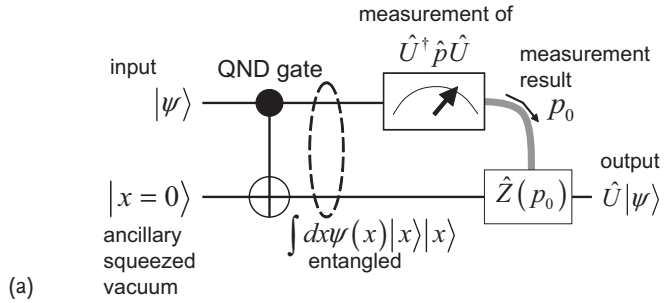

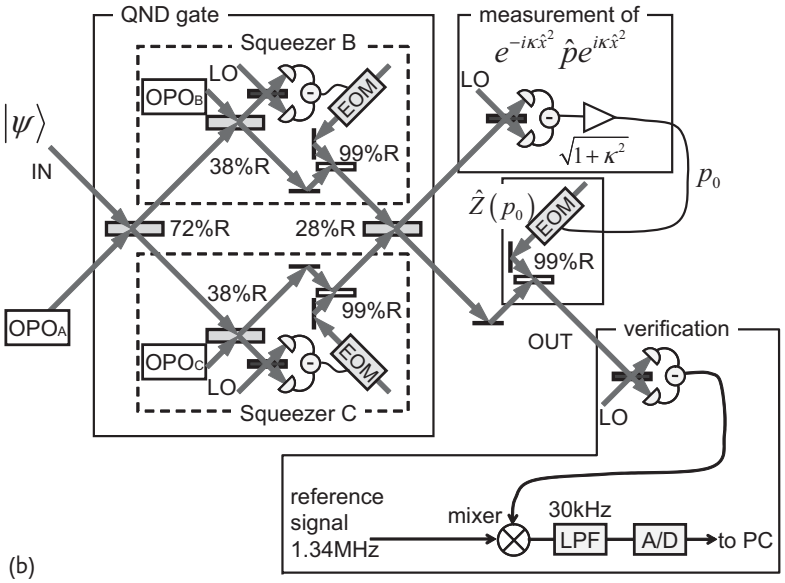

Figure 7.15 Schematic of a one-way quantum gate (a) and the experimental setup (b) [299]. OPO: optical parametric oscillator, LO: optical local oscillator, and EOM: electro-optic modulator.

with $\kappa = \tan\theta$. Using homodyne detection and setting the phase of the local oscillator (LO) to θ, we can measure $(\hat{p}\cos\theta + \hat{x}\sin\theta)$. Appropriate electric amplification of the homodyne results with gain $(1 + \tan^2\theta)^{1/2}$ leads to the desired measurement of $\hat{U}^\dagger \hat{p} \hat{U}$. Miwa *et al.* showed this for several values of κ: 0, ± 1.0, ± 1.5, ± 2.0, with coherent-state inputs [299]. The corresponding LO phases are $0°$, $\pm 45°$, $\pm 56.3°$, and $\pm 63.4°$, respectively.

In this optical demonstration, three squeezed-vacuum ancillae are used. One ancilla is coupled to the input via a QND gate (denoted by subscript A). The QND gate itself requires two additional squeezed vacuum states (denoted by subscripts B, C) as explained in Section 6.2.1.2. The full input-output relations of the scheme

including finite-squeezing resources are

$$\hat{x}_{\text{out}} = \hat{x}_{\text{in}} + \hat{x}_{\text{A}}^{(0)} e^{-r_{\text{A}}} - \frac{\sqrt{5}-1}{2\sqrt[4]{5}} \hat{x}_{\text{B}}^{(0)} e^{-r_{\text{B}}} ,$$
$$\hat{p}_{\text{out}} = \hat{p}_{\text{in}} + \kappa \hat{x}_{\text{in}} + \frac{1}{\sqrt[4]{5}} \kappa \hat{x}_{\text{B}}^{(0)} e^{-r_{\text{B}}} + \frac{\sqrt{5}+1}{2\sqrt[4]{5}} \hat{p}_{\text{C}}^{(0)} e^{-r_{\text{C}}} . \tag{7.20}$$

Even with the excess noise from the finite squeezing of the ancillae, we are able to observe sub-shot-noise quadrature squeezing for sufficiently large κ.

Experimental setup. – A schematic of the experimental setup is illustrated in Figure 7.15b. The original source of light is a continuous wave (CW) Ti:sapphire laser whose output is 860 nm in wavelength and 1.5 W in power. Quantum states at the 1.34 MHz sideband are used in our demonstration.

The experimental setup consists of the following parts: preparation of the input and ancilla states, the QND coupling gate, measurement, feedforward, and, finally, the verification measurement.

The input state, a coherent state at the 1.34 MHz sideband, is generated by modulating a weak laser beam of about 10 μW using electro-optic modulators (EOMs). Three types of coherent states $|\alpha\rangle$ are prepared: $\alpha = x_{\text{in}}$, $\alpha = \mathrm{i}p_{\text{in}}$, and $\alpha = 0$ corresponding to phase modulation, amplitude modulation, and no modulation of the laser beam, respectively.

In order to prepare the ancilla states, there are three sub-threshold optical parametric oscillators (OPOs), each generating a single-mode squeezed state, whose squeezing level is −4.3, −4.9, and −5.2 dB. An OPO is a bow-tie shaped cavity of 500 mm in length containing a PPKTP crystal [283]. The second harmonic (430 nm in wavelength) of Ti:sapphire output is divided into three beams in order to pump the OPOs.

The QND gate basically consists of a Mach–Zehnder interferometer with a single-mode squeezing gate in each arm [284]. Each single-mode squeezing gate contains a squeezed vacuum ancilla, homodyne detection, and feedforward [275, 276]. The variable beam splitters in the QND gate are composed of two polarizing beam splitters and a half-wave plate as explained in Section 6.2.1.1. One can eliminate the QND gate and just measure the input states by setting the transmittances of the variable beam splitters to unity. At each beam splitter, the relative phase of the two input beams is locked by means of active feedback to a piezoelectric transducer. For this purpose, two modulation sidebands of 154 and 107 kHz are used as phase references. For the homodyne detection, the LO phase is adjusted in accordance to the desired κ value; the feedforward displacement is carried out with the right gain depending on κ.

To verify the output state, another homodyne detection is employed. As is well known from optical homodyne tomography, we can reconstruct the quantum state from the marginal distributions for various phases [301]. The LO phase is slowly scanned and a series of homodyne measurements are performed. The 1.34 MHz component of the homodyne signal is extracted by means of lock-in detection: it is mixed with a reference signal and then sent through a 30 kHz low pass filter.

Finally, it is analog-to-digital converted where the sampling rate is 300 000 samples per second.

The powers of the LOs are about 3 mW. The detector's quantum efficiencies are greater than 99%, the interference visibilities to the LOs are on average 98%, and the dark noise of each homodyne detector is about 17 dB below the optical shot noise level produced by the LO. Propagation losses of our whole setup are about 7%.

Experimental results. – As mentioned earlier, Miwa *et al.* carried out the experiment with three types of input coherent states $|\alpha\rangle$: $\alpha = x_{\text{in}}$ ($x_{\text{in}} = 1.4$), $\alpha = \mathrm{i}p_{\text{in}}$ ($p_{\text{in}} = 1.3$), and $\alpha = 0$. For each input state, the gate for seven different κ values: 0, ± 1.0, ± 1.5, and ± 2.0 were demonstrated.

Figure 7.16 shows the raw data of marginal distributions and the Wigner functions reconstructed via the maximum-likelihood method [302]. We show the results for the input state with the amplitude in x as an example. Each scan contains about 80 000 data points which are uniformly distributed in phase from 0 to 2π, and every 20 points are plotted in the figure (about 4000 data points). For $\kappa = 0$ (Figure 7.16b), the input state is regenerated at the output except for some excess noise. For nonzero κ (Figure 7.16c,d), we can see that the distribution of the p variable is shifted proportional to x with a proportionality factor κ. As a result, the output states are squeezed and rotated.

In Figure 7.17, the elliptic output Wigner functions for $\kappa = 0, \pm 1.0, \pm 2.0$ are shown where the position, size, and shape of each ellipse correspond to the averaged amplitudes and variances. Figure 7.17a,b are for the case of $\alpha = x_{\text{in}}$: (a) experimental results and (b) theoretical, ideal operation. They agree well in positions and inclinations of ellipses, although the ellipses in Figure 7.17a are thermalized because of the finite squeezing of the ancilla states. Experimentally estimated κ is obtained via $\kappa_{\text{act}} = \langle \hat{p}_{\text{out}} \rangle / \langle \hat{x}_{\text{in}} \rangle$, and the values obtained are $\kappa_{\text{act}} = 0.00$, 0.95, -1.04, 1.94, and -2.02 for theoretical values $\kappa_{\text{th}} = 0$, ± 1.0, and ± 2.0, respectively. The differences in inclinations between experimental and ideal Wigner functions are less than 3°. The experimental results for the other input states are shown in Figure 7.17c,d. The change of the amplitude in the input states only affects the positions of the ellipses; the shapes and inclinations of the ellipses remain the same. We can see in Fig 7.17d that the input amplitude in the p quadrature (p_{in}) is simply reproduced at the output and is otherwise not affected for any κ. All of these results are in good agreement with the theoretical input–output relations.

In Figure 7.18a, the fidelities of the experimental output states compared to the ideal pure output states (i.e., without excess noise) are plotted. The fidelity quantifies the overlap between two quantum states and it can be calculated as ${}_{\text{in}}\langle \psi | \hat{U}^{\dagger} \hat{\rho}_{\text{out}} \hat{U} | \psi \rangle_{\text{in}}$. In the case of infinitely squeezed ancillae, unit fidelity is achieved. In the experiment, excess noises due to finitely squeezed ancillae lead to non-unit fidelities. Without quantum resources (i.e., using vacuum states for ancillary inputs), the experimental fidelity is 0.62 ± 0.01 for $\kappa = 0$, which agrees with the theoretical result 0.63 derived from Eq. (7.20). With squeezed-vacuum ancillae, the experimental fidelity is 0.81 ± 0.01 for $\kappa = 0$, which is much better than the case without nonclassical resources. For nonzero κ, the fidelities decrease as $|\kappa|$

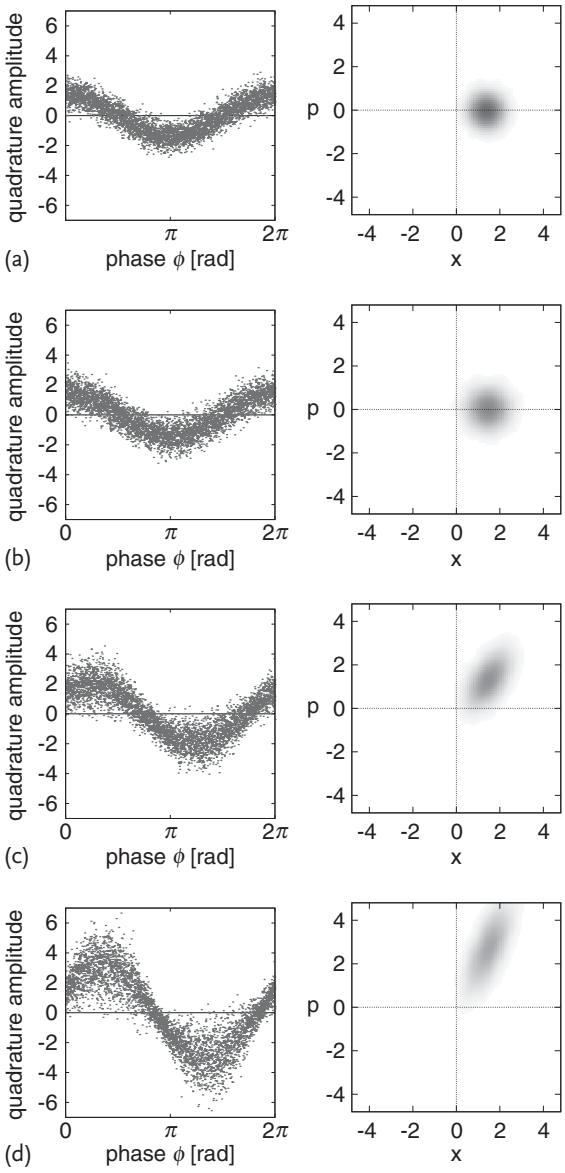

Figure 7.16 Input and output states with several κ [299]. Left figures show raw data of marginal distributions and right ones show the Wigner functions reconstructed via maximum-likelihood method [302]. (a) Input coherent state; (b) output for $\kappa = 0$; (c) output for $\kappa = 1.0$; (d) output for $\kappa = 2.0$.

increases because the squeezing of the ideal output state grows compared to that used in the ancillary states. Experimental results are very close to the theoretical

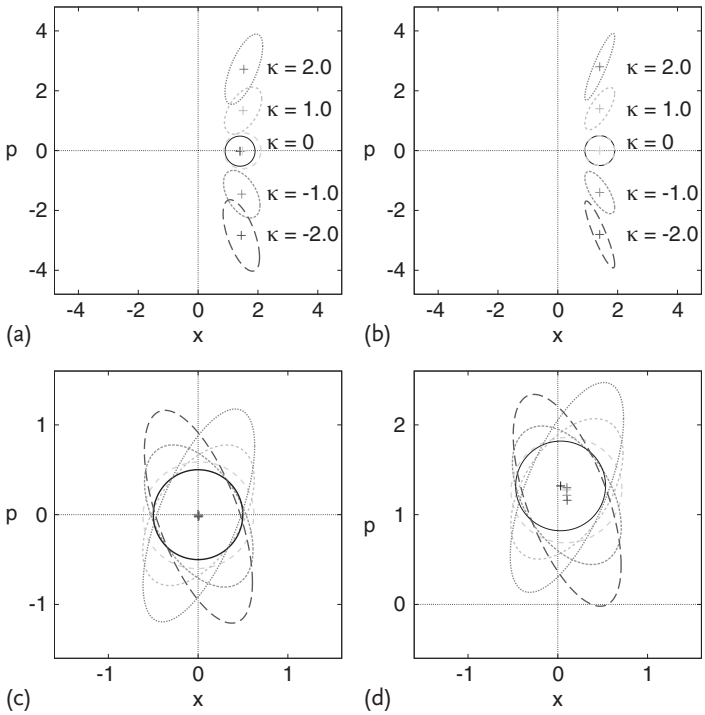

Figure 7.17 Input coherent state (center circle) and output states for several κ [299]. Gaussian distributions are assumed and averaged amplitudes variances are shown. (a, c, d) Experimental results for three types of input coherent state $|\alpha\rangle$, where α is the complex amplitude ($\hat{a} = \hat{a}^{(0)} + \alpha$). (b) Theoretical prediction with infinite squeezed ancillae for the same input state as (a).

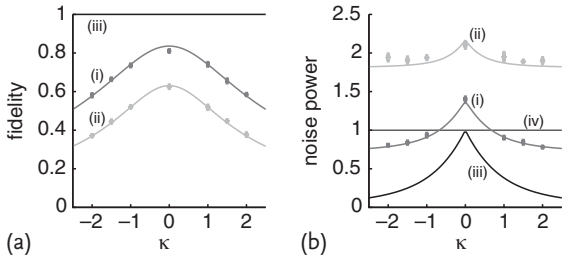

Figure 7.18 (a) Fidelities of output states and variances of squeezed quadrature [299]. (i) experimental results with squeezed ancillae and their theoretical curves derived from Eq. (7.20). (ii) experimental results with vacuum-state ancillae and their theoretical curves. (iii) theoretical results with infinite squeezing ancillae. (iv) shot-noise limit. The vertical axis in (b) is normalized to the shot-noise limit.

curves which are calculated from the experimentally obtained squeezing levels of the ancillae.

In Figure 7.18b, the quadrature squeezing of our setup is plotted. Note that the squeezed quadratures are fragile and easily degraded by excess noise. In the case of infinitely squeezed ancillae, squeezing is obtained for any nonzero κ; for $\kappa = 0$, on the other hand, the variance of the input coherent state is preserved. With finitely squeezed ancillae, the excess noises are added to the variances of the ideal outputs. Without nonclassical resources, squeezing below the SNL is, of course, not obtained for any κ. In the case of a squeezing level of the ancillae below -2.9 dB relative to the SNL, the output state is squeezed for sufficiently large $|\kappa|$. We can observe a noise suppression below the SNL by 0.3 ± 0.1 dB for $\kappa = \pm 1.0$, 0.8 ± 0.1 dB for $\kappa = \pm 1.5$, and 1.0 ± 0.1 dB for $\kappa = \pm 2.0$.

7.2.3.2 Fourier and Squeezing Gates

In this section, we will explain an experiment of CV cluster computation performed by Ukai *et al.* where the Fourier transformation and squeezing operation were demonstrated with a linear four-mode cluster state [298].

All demonstrations of qubit cluster computation so far work in a probabilistic way since the resource cluster is generated only when the photons that compose the cluster are produced and, at the same time, detected. In other words, creation of the cluster state and consumption of the cluster photons for computation must go hand in hand, rendering the cluster computation highly probabilistic. Moreover, the probabilities of success decrease exponentially with respect to the number of photons and so scalability is unattainable. Another typical feature of the single-photon-based cluster computation experiments is that the usual input states, $|+\rangle$, are prepared as part of the initial cluster states. Although this approach is sufficient for proof-of-principle demonstrations of cluster state computation, it would pose severe limitations when unitary gates are to be deterministically applied online to an unknown input state which is prepared independently of the cluster state, for instance, as the output of a preceding computation. In contrast, Ukai *et al.* reported on *unconditional* CV cluster computation experiments conducted on *independently prepared* input states [294, 298].

Ukai *et al.* demonstrated unconditional realizations of linear gates, necessary for universal processing of an optical mode, utilizing a continuous-variable (CV) four-mode cluster state [169, 189, 190] as a resource independent of the input state to be processed. This scheme represents a module for arbitrary linear, Clifford or Gaussian, or linear unitary Bogoliubov (LUBO) transformations which can be directly incorporated into a full, universal cluster-based QC together with photon counting measurements [297]. Though it requires no postselection, a realistic extension of our scheme would increasingly suffer from errors induced by the finite squeezing of the cluster state. Nonetheless, for a given accuracy of the cluster state, the squeezing required per node of the cluster would not grow with the size of the cluster [297].

Ukai *et al.* used the following CV four-mode linear cluster state [294] defined as

$$\frac{1}{\pi}\int \mathrm{d}a\mathrm{d}b\mathrm{e}^{2\mathrm{i}ab}|p_1 = a\rangle|x_2 = a\rangle|x_3 = b\rangle|p_4 = b\rangle \ , \tag{7.21}$$

where $|x = c\rangle$ and $|p = c\rangle = \hat{F}|x = c\rangle$ (with the Fourier transformation $\hat{F} = e^{(i\pi)/2(\hat{x}^2+\hat{p}^2)}$) are eigenstates of the canonical conjugate position and momentum operators, respectively $\hat{x}$ and $\hat{p}$, with eigenvalues $c \in \mathbf{R}$; the subscripts label the corresponding modes. Here, $|x\rangle$ is the computational basis for our CV system. An approximate version of this cluster state can be obtained deterministically by combining four squeezed vacuum states on an 80%-transmissivity beam splitter and two half beam splitters (HBSs) [169, 189, 190]. In the limit of infinite squeezing, we obtain the state in Eq. (7.21).

Recently, it was shown that the complete set of one-mode LUBO transformations can be implemented using a four-mode linear cluster state as a resource [294]. In this case, a one-mode LUBO transformation can be expressed by an operator $\hat{U}_2 = e^{i\hat{H}_2}$ with Hamiltonian $\hat{H}_2$ quadratic in $\hat{x}$ and $\hat{p}$. It can then be decomposed into three steps, a ϕ-rotation, squeezing, and a φ-rotation in phase space: $\hat{R}(\varphi)\hat{S}(r)\hat{R}(\phi)$ ($\hat{R}(\theta) = e^{i\theta(\hat{x}^2+\hat{p}^2)}$, $\hat{S}(r) = e^{ir(\hat{x}\hat{p}+\hat{p}\hat{x})}$) [89] (see Section 1.8). The measurements required to achieve these operations are efficient homodyne detections with quadrature angles θ_i which are easily controllable by adjusting the local oscillator phases in the homodyne detectors, as shown in the previous section. Now, an unknown input state can be coupled with the cluster state using a half beam splitter, effectively employing CV quantum teleportation [163, 203, 277]. The total procedure then consists of the teleportation-based coupling $\hat{M}_{\text{tele}}(\theta_{\text{in}}, \theta_1)$ with two degrees of freedom, followed by two elementary, measurement-based, one-mode operations $\hat{M}(\theta_i)$ with one degree of freedom for each [297, 299, 304]. As a result, the output state becomes

$$|\psi_{\text{out}}\rangle = \hat{M}(\theta_3)\hat{M}(\theta_2)\hat{M}_{\text{tele}}(\theta_{\text{in}}, \theta_1)|\psi_{\text{in}}\rangle. \tag{7.22}$$

Note that $\hat{M}_{\text{tele}}(\theta_{\text{in}}, \theta_1)$ cannot be decomposed into $\hat{M}_1(\theta_1)\hat{M}_{\text{in}}(\theta_{\text{in}})$ because the measurements on modes *in* and 1 are nonlocal measurements. We have $\hat{M}_{\text{tele}}(\theta_{\text{in}}, \theta_1) = \hat{R}(-\theta_+/2)\hat{S}(r)\hat{R}(-\theta_+/2)$ with $r = \log\tan(\theta_-/2)$ and $\theta_\pm = \theta_{\text{in}} \pm \theta_1$, while $\hat{M}(\theta_i) = \hat{R}(\phi_i)\hat{S}(r_i)\hat{R}(\phi_i)$ with $r_i = \log(\sqrt{k_i^2+4} + k_i)/2$, $\phi_i = \pi/2 - \tan^{-1}(\sqrt{k_i^2+4} - k_i)/2$, and $k_i = 1/\tan\theta_i$. The operations $\hat{M}_{\text{tele}}(\theta_{\text{in}}, \theta_1)$ and $\hat{M}(\theta_i)$ are each elements of the one-mode LUBO transformations.

In Ukai's experiment, they demonstrated four types of LUBO transformations: the Fourier transformation $\hat{F} = \hat{R}(\pi/2)$ (90° rotation); and three different x-squeezing operations $\hat{S}(r)$ with $r = \ln 10^{x/20}$, $x = 3, 6, 10$ [dB]; all realized through the same four-mode linear cluster state. Together with phase-space displacements and rotations such as the Fourier transformation, the set of x-squeezing operations gives us, in principle, access to any kind of single-mode LUBO transformation. Realizability of the entire set of linear gates with the same, fixed cluster state shows that the application of any linear gate to an arbitrary input state can be fully controlled by the (homodyne) detectors, the essential feature of one-way quantum computation.

Figure 7.19a illustrates how to perform one-mode LUBO transformations using a four-mode linear cluster state as a resource. The experimental setup is shown in Figure 7.19c. Following the above discussion, regarding the experimental pro-

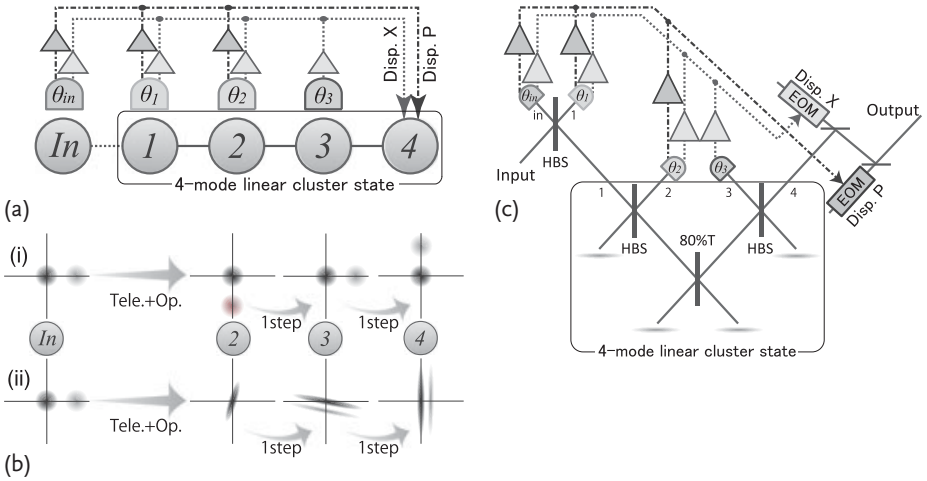

Figure 7.19 (a) Abstract illustration and (c) experimental setup of one-mode LUBO transformations using a four-mode linear cluster state [298]. There is a 1-to-1 correspondence between (a) and (c). Squeezed vacuum states are generated by subthreshold optical parametric oscillators containing periodically poled $KTiOPO_4$ crystals as nonlinear media. (b) phase space representations of quantum states in each step of the Fourier transformation (b-i) and the 10dB *x*-squeezing operation (b-ii), starting with a vacuum state input (dark gray) and a *x*-coherent state input (light gray). Tele.: teleportation, Op: operation.

cedure, the scheme is divided into four parts: (1) generation of a four-mode linear cluster state and an input state; (2) coupling of these two states; (3) measurements on modes *in*, 1–3 and feed-forward; (4) verification of the output state in mode 4. None of these processes are probabilistic; no postselection is required and the whole experiment is deterministic.

The Fourier transformation is achieved by choosing for step (3) measurement quadrature angles $(\theta_{\text{in}}, \theta_1, \theta_2, \theta_3)$ as $(90°, 0°, 90°, 90°)$. The quality of the implemented Fourier transformation can be evaluated in a similar way to standard quantum teleportation (corresponding to a 0° phase-space rotation); the Fourier transformation is then just a 90° rotation in phase space.

The measurement results for the Fourier transformation of a coherent state input are shown in Figure 7.20. As clearly shown in Figure 7.20a, the input is a coherent state with amplitude 17.7 ± 0.2 dB. The output state is shown in Figure 7.20b. The peak level of trace Figure 7.20b(ii) is 17.5 ± 0.2 dB higher than the shot noise level (SNL), which is the same level as the input within the error bar, confirming successful implementation of the desired quantum operation.

The quality of the operation can be quantified by using the fidelity defined as $F = \langle \Psi_{\text{ideal}} | \hat{\rho}_{\text{out}} | \Psi_{\text{ideal}} \rangle$. Theoretically, the expected fidelity of our experiment can be derived as $F = 1/(1 + 3/2e^{-2r})$, where r is the squeezing parameter of the squeezing resources for the cluster state. The four squeezed vacuum states used as resources have an average squeezing level of -5.5 dB; this gives a theoretical fidelity of $F = 0.71$.

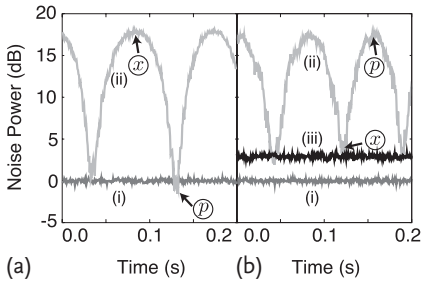

Figure 7.20 Fourier transformation operation [298]; (a) Measurement results of the input state. Trace (a-i) shows the shot noise level (SNL) and (a-ii) shows the phase scan of the input state. (b) Measurement results of the output state. Trace (b-i) shows the SNL, (B-ii) shows the phase scan of the output state, and (b-iii) shows the measurement result of the x quadrature with a vacuum input. The measurement frequency is 1 MHz and the resolution and video bandwidths are 30 kHz and 300 Hz, respectively. Traces (a-i), (b-i), and (b-iii) are averaged 20 times.

In the specific case of our experiment, the fidelity for a coherent input state as given above is $F = 2/\sqrt{(1+4\sigma^x_{\rm out})(1+4\sigma^p_{\rm out})}$, where $\sigma^x_{\rm out}$ and $\sigma^p_{\rm out}$ are the variances of the position and momentum operators in the output state, respectively as similar to quantum teleportation [211]. The measured variances with a vacuum input are used to determine the fidelity. Ukai *et al.* obtained $\sigma^x_{\rm out} = 2.9 \pm 0.2$ dB (Figure 7.20b(iii)), and $\sigma^p_{\rm out} = 2.8 \pm 0.2$ dB (not shown) above the SNL, corresponding to a fidelity of $F = 0.68 \pm 0.02$. This is in good agreement with the theoretical result.

It is possible to observe the peak of the scanning trace (Figure 7.20a(ii)) by measuring the x quadrature of the input, while the peak can be detected in p quadrature at the output. Therefore, the canonical conjugate variables x and p have swapped at the output, and this swapping corresponds to a 90° rotation in phase space. The measurement results thus confirm that the Fourier transformation is applied to the input coherent state.

Another fundamental element of the LUBO transformations is squeezing. We note that ordinary squeezing without rotations cannot be achieved only through teleportation coupling $\hat{M}_{\rm tele}(\theta_{\rm in}, \theta_1)$; neither can it be performed by an elementary one-mode one-way operation $\hat{M}(\theta_i)$. This is because $\hat{M}_{\rm tele}(\theta_{\rm in}, \theta_1)$ and $\hat{M}(\theta_i)$ are decomposed as $\hat{R}(\varphi_i)\hat{S}(r_i)\hat{R}(\phi_i)$, and $\varphi_i = \phi_i = 0$ are not achievable when $r_i \neq 0$. Therefore, a sequence of these operations is required in order to extract squeezing without rotations (see Figure 7.19b(ii)). Note that the state of mode *in* is transferred to mode 2 through the nonlocal measurement on modes *in* and 1.

Three different squeezing operations are implemented in the experiment corresponding to three different sets of quadrature measurement angles $(\theta_{\rm in}, \theta_1, \theta_2, \theta_3)$:

$$\begin{aligned} &(-42.5^\circ, 62.4^\circ, 63.5^\circ, 76.0^\circ)\,, \\ &(-41.4^\circ, 72.2^\circ, 41.9^\circ, 74.4^\circ)\,, \\ \text{and}\quad &(-47.7^\circ, 79.2^\circ, 25.9^\circ, 78.4^\circ)\,, \end{aligned} \tag{7.23}$$

resulting in 3, 6, and 10 dB x-squeezing operations, respectively [298]. In all these squeezing gates, the inputs are chosen to be coherent states with a nonzero amplitude in x (x-coherent) or in p (p-coherent), and these amplitudes are 14.7 ± 0.2 dB.

Figure 7.21a shows the measurement results of the 10 dB x-squeezing operation on the x-coherent state. In this figure, the extra dotted lines are plotted for comparison in order to show the levels of the input state: x quadrature with the (iii)-line (14.7 dB) and p quadrature with the (iv)-line (SNL). Signal levels of 5.1 ± 0.2 dB and 11.5 ± 0.2 dB above the SNL are obtained for the measurement of the x and p quadratures of the output, respectively. The level of the x quadrature of the output (Figure 7.21a(iii)) is about 10 dB lower than that of the input (the dashed line in Figure 7.21a), while the variance of the p quadrature of the output (Figure 7.21a(iv)) increases by about 10 dB compared to that of the input (the dotted line in Figure 7.21a). These observations are consistent with a 10 dB x-squeezing operation (see Figure 7.21c). Note that the x and p quadratures of the output have additional noises. These are caused by the finite squeezing of the cluster state and would vanish in the limit of infinite cluster squeezing.

It is evident from the traces in Figure 7.21a that the operation experimentally performed consists only of squeezing and does not include any rotations. This is verified by noting that the minimum level (Figure 7.21a(iii)) of the scanning trace (Figure 7.21a(ii)) is obtained by measuring the x quadrature while the maximum level (Figure 7.21a(iv)) is obtained by the p measurement.

In order to show the nonclassical nature of the output state, we also use a vacuum state as the input. The measurement results of the 10 dB x-squeezing operation on a vacuum state are shown in Figure 7.21b. The measured variance of the x quadrature is -0.5 ± 0.2 dB which is below the SNL, thus confirming nonclassicality. Note again that the output has additional noise caused by the finitely squeezed resources which would vanish in the limit of infinite squeezing.

Finally, the controllability of the one-way quantum computations is demonstrated. Both theoretical curves and measured results for the three levels (3, 6, and 10 dB) of x-squeezing are plotted in Figure 7.21d. In theory, the effect of the finitely squeezed resources (-5.5 dB) for the cluster is taken into account. Three kinds of input states are used here: a vacuum state; an x-coherent state; and a p-coherent state. As can be seen in Figure 7.21d, the measurement results agree well with the theoretical curves, and all the operations are indeed controlled by the measurement bases for the four homodyne detections.

In summary, Ukai *et al.* have experimentally demonstrated CV cluster computing. All operations were perfectly controllable through an appropriate choice of measurement bases for the homodyne detections. In the scheme, arbitrary linear one-mode transformations can be applied to arbitrary input states coming independently from the outside. This result means no less than the possibility for extending arbitrary linear transformations including arbitrary squeezing, as obtainable from optical parametric oscillators, beyond the realm of offline optical quantum state engineering towards online universal linear processing of optical states with direct applications for optical quantum information processing, including discrete qubit-type as well as continuous infinite-dimensional encodings. The accuracy of

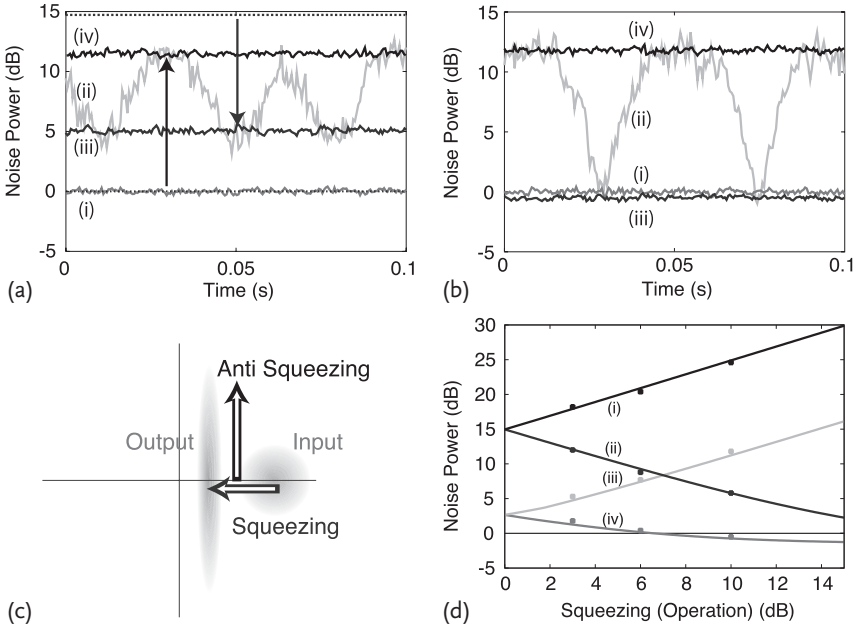

Figure 7.21 Squeezing operations [298]; (a, b) 10 dB *x*-squeezing operation with an *x*-coherent input (a) and a vacuum input (b). (i) shot noise level; (ii) phase scan of the output state; (iii) measurement of *x*; and (iv) measurement of *p*. The dotted lines show the levels of *x* (iii) and *p* (iv) for the input, and the arrows correspond to the squeezing operation. The measurement frequency is 1 MHz and the resolution and video bandwidths are 30 kHz and 300 Hz, respectively. Traces (i), (iii), and (iv) are averaged 20 times. (c) phase space representation of the 10 dB *x*-squeezing operation with an *x*-coherent input (a part of Figure 7.19b(ii)). The light gray circle and ellipse correspond to the input and output, respectively. The *x* component is squeezed while the *p* component is anti-squeezed. The measurement results (a) correspond to the phase representation (c). (d) experimental results (dots) and theoretical calculation (solid curves) of 3, 6, and 10 dB *x*-squeezing operations. Traces (i) and (ii) traces correspond to a *p* measurement with *p*-coherent input, and *x* measurement with *x*-coherent input, respectively; traces (iii) and (iv) traces correspond to a *p* measurement with vacuum input, and *x* measurement with vacuum input, respectively.

our one-way quantum computations only depends on the squeezing levels used to create the resource cluster state. Although in the experiment squeezing levels were sufficient to verify the nonclassical nature of the output states, even higher levels of squeezing, as reported recently [218, 219], may lead to increased accuracies and cluster computations of potentially larger size in the near future. In order to achieve quantum operations other than linear unitary mode transformations, nonlinear measurements besides homodyne detections would be required. However, the demonstration of the experimental capability of implementing an arbitrary linear single-mode transformation through continuous-variable cluster states, as explained here, represents a crucial step toward universal one-way quantum computation.

Concluding this section, we can say that it depends to a large extent on the experimental implementability of nonlinear measurements such as photon number resolving detections whether more advanced or ultimately universal, optical quantum information protocols can be realized in the laboratory. If, similar to the quantum-state tunability between offline Gaussian and non-Gaussian resource states [305], also the online operations for measurement-based approaches, that is, the quantum-state measurements, could be tuned over a sufficient range of linear CV and nonlinear DV POVMs [306], efficient experimental realizations may then be possible in the near future. In this case, the offline resource states may be, for example, Gaussian CV cluster states which can be built unconditionally from squeezed light using beam splitters. However, finite-squeezing-induced imperfections will then require some additional nonlinear element for quantum error correction. Alternatively, instead of attempting to perform full computations over CV cluster states at a precision that decreases linearly with the size of the computation (number of measurement steps) for a given initial squeezing variance [297], one may just use Gaussian ancilla states, nonlinearly measured online or offline, for implementing particularly difficult gates such as the NSS gate on DV photonic states and do the simple gates on dual-rail encoded qubits directly in the standard circuit approach.

8
Hybrid Quantum Information Processing

Inspired by practical as well as fundamental limitations of those optical quantum information schemes which are solely based upon either discrete or continuous degrees of freedom, a hybrid scheme, similar to a classical, digital/analog hybrid computer would simultaneously exploit both DV and CV states, encodings, gates, measurements, and techniques in order to circumvent those limitations.

In the quantum optical setting, this includes, in particular, those approaches that utilize light for communication and employ matter systems for storage (and processing) of quantum information, as the optical qumodes are most naturally represented by their quantized position and momentum (amplitude and phase quadrature) variables, whereas the atomic spins or any two-level structures in a solid-state system provide the natural realization of qubits. An important ingredient of such hybrid schemes may then be a particularly intriguing form of entanglement – hybrid entanglement, that is, an inseparable state of two systems of different dimensionality, for example, between a qubit and a qumode.

However, an effective two-qubit entangled state can also be obtained even when the two individual subsystems are infinite-dimensional, especially, when they are two optical qumodes. We shall encounter such quasi-Bell states in this chapter. These states are qualitatively different from the standard form of photonic two-qubit entanglement expressed in Fock or polarization subspaces.

For our purposes here, the combined DV-CV approach of hybrid schemes falls into two possible categories: those schemes based upon nonlinear resources using linear operations and those based on linear resources using nonlinear operations. In the latter case, for instance, DV photon number measurements may be applied to CV Gaussian resources. The former type of implementations would utilize, for example, CV homodyne measurements and apply them to DV photonic qubit or other non-Gaussian states.

The pioneering "hybrid" work is the experiment of Lvovsky *et al*. in which CV, homodyne-based quantum tomography is performed for the discrete one-photon Fock state [307]. The reconstructed Wigner function in this experiment has a strongly non-Gaussian shape including negative values around the origin in phase space.

It is important to notice that for an experimental implementation of a hybrid scheme in which DV and CV techniques and resources are to be combined (for

Quantum Teleportation and Entanglement. Akira Furusawa, Peter van Loock
Copyright © 2011 WILEY-VCH Verlag GmbH & Co. KGaA, Weinheim
ISBN: 978-3-527-40930-3

example, for CV quantum teleportation of DV states), the standard way of applying such methods has to be generalized. In particular, frequency-resolved homodyne detection, as used, for instance, in CV quantum teleportation of coherent states [203], must be extended to time-resolved homodyning in order to synchronize the CV operations with DV photon counting events. CV operations must act on a faster scale: while the standard CV experiments used single-mode cw light sources with narrow sidebands of $\sim$30 kHz, the new generation of hybrid experiments relies upon bandwidths of at least $\sim$100 MHz, corresponding to time scales of $\sim$100 ns.

For example, in order to teleport a coherent-state superposition (a so-called cat state) using a CV Gaussian EPR resource, the successful photon events that indicate the presence of a cat state at the input of the teleporter must be synchronized with those shots that define successful quantum teleportation events. For this purpose, time-domain EPR correlations are needed (see Section 3.2.3.2). This new generation of experiments is accompanied by a *paradigm shift*, which is necessary in order to combine the complementary wave and particle properties of light. Thus far, experiments have focused either on the particle aspect, using photon counters and postselection, or on the wave aspect, measuring quadratures in phase space. The former type of experiments were always conditional and hence highly inefficient; even worse, in many schemes, there was no way to actually obtain a physical state at the output for further exploitation. The CV quadrature-based experiments were typically performed in the frequency-domain with no time resolution. For those new hybrid approaches to work, the domain must be shifted *from frequency to time*, and measurements *from (power) statistics to (amplitude) single shots*.

In this chapter, we shall first discuss a couple of protocols for the optical engineering of non-Gaussian cat states (Section 8.1). Subsequently, we describe an experiment in which such a cat state was optically generated from squeezed light through photon subtraction techniques (Section 8.2). In Section 8.3, we introduce some examples of hybrid entangled states, and in Section 8.4, we describe two (hybrid) teleportation experiments: one in which a cat state is prepared and then, to some extent, transferred through quantum teleportation (Section 8.4.1); and another one where a DV polarization-encoded photonic qubit is teleported using CV EPR resources and CV Gaussian operations (Section 8.4.2). Finally, we present a few specific hybrid approaches to quantum computing (Section 8.5), including the notion of hybrid Hamiltonians (Section 8.5.1), specific ways to encode qubits into qumodes (Section 8.5.2), and, in Section 8.5.3, the famous proposal by Gottesman, Kitaev, and Preskill (GKP).

8.1
How to Create Non-Gaussian States, Cat States

Coherent states may be used to encode a photonic qubit state in a qualitatively different way compared to the photon number and polarization encodings of

Chapter 2,

$$(a|\alpha\rangle + b|-\alpha\rangle)/\sqrt{N(\alpha)}\,, \tag{8.1}$$

with $N(\alpha) = |a|^2 + |b|^2 + 2\mathrm{e}^{-2|\alpha|^2}\mathrm{Re}(ab^*)$. A proof-of-principle proposal of such cat states for fault-tolerant, universal quantum computation was presented in [308]. This proposal describes an all-optical scheme using photon number resolving detectors. Although in theory, cat states can be produced directly from $\chi^{(3)}$ nonlinear optical interactions, their generation becomes more feasible when conditional state preparation is allowed. A drawback of the cat-type qubit encoding is that these states are fairly sensitive to losses and noise. Below, we shall describe a protocol for cat-state engineering that is not all-optical and uses light-atom interactions.

In the all-optical approaches, there are currently various schemes which often rely upon the resemblance of squeezed Fock states and photon-subtracted, squeezed vacuum states with a cat state,

$$|\alpha\rangle - |-\alpha\rangle \approx \hat{S}(r)|1\rangle \approx \hat{a}\,\hat{S}(r)|0\rangle\,. \tag{8.2}$$

This is the so-called odd cat state that only has odd photon-number terms, as one can easily understand from the Fock expansion of the coherent states. In fact, we may approximately write

$$\hat{S}(r)|1\rangle = \sum_{n=0}^{\infty} \frac{\tanh^n r}{\cosh^{3/2} r} \frac{\sqrt{(2n+1)!}}{2^n n!}|2n+1\rangle\,. \tag{8.3}$$

The above approximation holds with near-unit fidelity for near-unit or smaller amplitudes α. The even cat state is correspondingly $\propto |\alpha\rangle + |-\alpha\rangle$, with only even number terms.

A beautiful example of a typical hybrid scheme according to our definition is the "offline squeezing" protocol from [279] for cat-state engineering, experimentally demonstrated in [309], see Figure 8.1. In this scheme, approximate cat states are built using linear CV measurements with outcomes within a finite postselection window, linear CV squeezed-state, and nonlinear DV Fock-state resources. The protocol works by squeezing the input Fock state, $|1\rangle \to \hat{S}(r)|1\rangle \approx |\alpha\rangle - |-\alpha\rangle$. This squeezing would be hard to achieve "online" directly on the Fock state using the standard squeezing techniques such as optical parametric amplification.[1)]

Let us discuss yet another way to create cat states, this time using light-atom interactions [310]. In Chapter 1, we introduced the qubit Pauli operator basis X, Y, and Z as elementary gates, and rotations along their respective axes, Z_θ, and so on, to describe and realize arbitrary single-qubit unitaries. In analogy, we used a similar notation for the qumode WH operator basis, $X(\tau)$ and $Z(\tau)$. Here, in the hybrid context, we shall exploit interactions and operations involving combinations

1) In the experiment of [309], a two-photon state $|n = 2\rangle$ was simply split at a beam splitter; therefore, the squeezed vacuum in Figure 8.1 was just a vacuum state. Postselection through time-resolved homodyne detection led to an output cat state which was squeezed by 3.5 dB. Theoretically, the fidelity of the cat state would approach unity for input Fock states $|n\rangle$ with $n \to \infty$ [309].

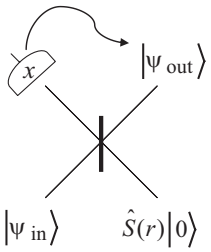

Figure 8.1 Conditional preparation of an odd (even) cat state using DV one-photon (two-photon) Fock states, $|\psi_{\text{in}}\rangle = |1\rangle$ ($|\psi_{\text{in}}\rangle = |2\rangle$) and CV squeezed vacuum resources, $\hat{S}(r)|0\rangle$, together with CV homodyne detection and postselection [279].

of DV qubit and CV qumode operators and therefore we prefer to use unambiguous notations: for qumodes, still $X(\tau) = \exp(-2i\tau\hat{p})$ and $Z(\tau) = \exp(2i\tau\hat{x})$ for the WH group elements, and $\hat{x}$ and $\hat{p}$ for the Lie group generators with $\hat{a} = \hat{x} + i\hat{p}$; for qubits, now $\sigma_x \equiv X$, $\sigma_y \equiv Y$, and $\sigma_z \equiv Z$ for the Pauli basis.

Now, consider the effective interaction obtainable from the fundamental Jaynes–Cummings Hamiltonian, $\hbar g(\hat{a}^\dagger\sigma_- + \hat{a}\sigma_+)$, in the dispersive limit [311],

$$\hat{H}_{\text{int}} = \hbar\chi\sigma_z\hat{a}^\dagger\hat{a}\ . \tag{8.4}$$

Here, $\hat{a}$ ($\hat{a}^\dagger$) refers to the annihilation (creation) operator of the electromagnetic field qumode in a cavity and $\sigma_z = |0\rangle\langle 0| - |1\rangle\langle 1|$ is the corresponding Pauli operator for a two-level atom in the cavity (with ground state $|0\rangle$ and excited state $|1\rangle$). The atomic system may as well be an effective two-level system with an auxiliary level (a so-called Λ-system).

The operators σ_+ and (σ_-) are the raising (lowering) operators of the qubit. The atom-light coupling strength is determined by the parameter $\chi = g^2/\Delta$, where $2g$ is the vacuum Rabi splitting for the dipole transition and Δ is the detuning between the dipole transition and the cavity field. The Hamiltonian in Eq. (8.4) generates a controlled phase-rotation of the field mode depending on the state of the atomic qubit. This can be written as ($\theta = \chi t$)

$$\hat{R}(\theta\sigma_z) = \exp\left(-i\theta\sigma_z\hat{a}^\dagger\hat{a}\right)\ , \tag{8.5}$$

which describes a unitary operator that acts in the combined Hilbert space of a single qubit and a single qumode. We may apply this operator upon a qumode in a coherent state, and may formally write

$$\hat{R}(\theta\sigma_z)|\alpha\rangle = |\alpha\exp(-i\theta\sigma_z)\rangle\ . \tag{8.6}$$

The qumode acquires a phase rotation depending on the state of the qubit, see Figure 8.2. As the eigenvalues of σ_z are ± 1, applying $\hat{R}(\theta\sigma_z)$ to the initial qubit–qumode state $|\alpha\rangle \otimes (|0\rangle + |1\rangle)/\sqrt{2}$ results in

$$\begin{aligned} &|\alpha\exp(-i\theta\sigma_z)\rangle \otimes (|0\rangle + |1\rangle)/\sqrt{2} \\ &\quad = \left(\left|\alpha e^{-i\theta}\right\rangle|0\rangle + \left|\alpha e^{i\theta}\right\rangle|1\rangle\right)/\sqrt{2}\,, \end{aligned} \tag{8.7}$$

a hybrid entangled state between the qubit and the qumode.

The observation that this hybrid entangled state can be used for creating a macroscopic superposition state of a qumode, a cat state, by measuring the microscopic system, the qubit, is about 20 years old [310]. A suitable measurement is a pro-

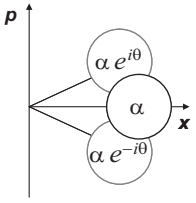

Figure 8.2 Controlled phase rotation of a qumode in a coherent state, α real. Depending on the qubit state, $\sigma_z = \pm 1$, the phase angle of the controlled rotation will be $\mp\theta$. When the qubit starts in a superposition state, $\propto |0\rangle + |1\rangle$, we obtain a hybrid entangled state between the qubit and the qumode.

jection onto the conjugate σ_x qubit basis, $\{|\pm\rangle\}$, equivalent to a Hadamard gate applied to the qubit,

$$\left(\left|\alpha \mathrm{e}^{-\mathrm{i}\theta}\right\rangle|+\rangle + \left|\alpha \mathrm{e}^{\mathrm{i}\theta}\right\rangle|-\rangle\right)/\sqrt{2}\,, \tag{8.8}$$

followed by a qubit computational σ_z measurement. Depending on the result, we obtain $\propto |\alpha \mathrm{e}^{-\mathrm{i}\theta}\rangle \pm |\alpha \mathrm{e}^{\mathrm{i}\theta}\rangle$ for the qumode. The size of this cat state depends on the distance between the rotated states in phase space, see Figure 8.2, scaling as $\sim\alpha\theta$ for typically small θ values. However, sufficiently large initial amplitudes α still lead to arbitrarily "large" cat states (while at the same time increasing their vulnerability against photon losses).

In the next section, we will describe a cat-state engineering experiment using photon subtraction. Let us mention that another method using photon counting, namely, "photon-addition", that is, in the ideal case, applying the photon creation operator, serves a similar role in recent hybrid experiments [312].

8.2
Experiment: Creation of Non-Gaussian States, Cat States

In this section, we shall describe the creation of Schrödinger kitten states as experimentally demonstrated by Wakui *et al.* [313]. This experiment is a hybrid scheme in the sense that an exotic, non-Gaussian CV qumode state is conditionally prepared from an unconditional source of Gaussian squeezed vacuum using DV photon subtraction measurements. Such heralded qumode states are interesting candidates for testing the power of CV processing of DV encoded quantum information, for instance, through CV quantum teleportation using the broadband (time-domain) entangled states presented in Section 3.2.3.2.

As we have encountered throughout this book, with regards to universal processing and so also for conditional state preparation, a sufficiently strong nonlinearity can be induced even on the single-photon level by suitable measurements. Various nonclassical states can be generated, for instance, through photon counting on a subsystem of an entangled state produced by parametric down conversion [314, 315]. States produced this way could be, for example, photon number states or Schrödinger-cat states. The nonclassicality of such states is related with negative regions of a phase-space distribution function such as the Wigner function. This is in contrast to the Wigner function of a squeezed state, which is Gaussian and thus non-negative. Here, for the present discussion of the experiment of

Wakui *et al.* [313], we recall that the Wigner function can be directly reconstructed by optical homodyne tomography [113].

Various nonclassical, non-Gaussian optical quantum states with negative values of $W(x, p)$ have been generated. Those states can be categorized into two families. One family is the Fock states and their variants combined with coherent states [312, 316–319], created in a non-collinear PDC configuration of the signal and idler photons. The other is the photon-subtracted squeezed states, where a small fraction of a squeezed vacuum beam is beam-split and guided into a photon counter as trigger photons, and the remaining beam is conditioned by the detection of the trigger photons [315]. In the ideal case, a squeezed vacuum is a superposition of even photon-number states where the signal and idler photons are collinear, thus, one-photon-subtracted squeezed states must be a particular superposition of odd photon-number states. These states are close to optical Schrödinger-cat states with small coherent amplitudes, and thereby referred to as optical *"Schrödinger kittens"* [186, 320].

In the previous works of Schrödinger kittens, potassium niobate ($KNbO_3$) crystals are used as nonlinear optical media for an optical parametric amplifier (OPA) [320], or in an optical parametric oscillator (OPO) far below threshold [186]. In the case of experiments with $KNbO_3$, however, it is known that there is a big source of loss referred to as pump (blue) light induced infrared absorption (BLIIRA) [321]. The big loss caused by BLIIRA weakens the even-photon nature of a squeezed vacuum, that is, it weakens entanglement between two modes into which the squeezed vacuum is beam-split, and yields uncorrelated trigger photons. They induce false clicks in state preparation and consequently degrade the output conditioned states. The most negative value observed with $KNbO_3$ thus far is -0.026 without any corrections of experimental imperfections [320].

On the other hand, periodically-poled $KTiOPO_4$ (PPKTP) has turned out not to have the BLIIRA effect in continuous-wave squeezing experiments [283, 322]. Therefore, a squeezing level at 860 nm has been significantly improved [283]. Thanks to its almost BLIIRA-free property, one can obtain squeezing with higher purity (even-photon nature) than that in the case of using $KNbO_3$. Purity of squeezing depends on how big the portion of a squeezed vacuum can escape from an OPO cavity. The cavity escape efficiency, which can be calculated by a transmittance of an OPO output coupler and all intracavity losses [323] is $\sim$97% with PPKTP, while that of $KNbO_3$ is $\sim$80% at most.

Let us now explain the generation of a wide range of photon-subtracted squeezed states, including the single-photon state and a Schrödinger kitten state with very deep negative dips of the Wigner functions [313]. A single-photon state can be realized to subtract one photon from a squeezed vacuum with a weakly pumped OPO [184], but it could not be created in photon-subtraction experiments with $KNbO_3$. This is because the squeezed states from $KNbO_3$ are too impure. In contrast, the usage of PPKTP results in low pump-induced losses and hence high squeezing at high purity. This enables one to generate various states from single-photon to Schrödinger kitten states by simply tuning the squeezing level which can be directly controlled by the pump power for the squeezer.

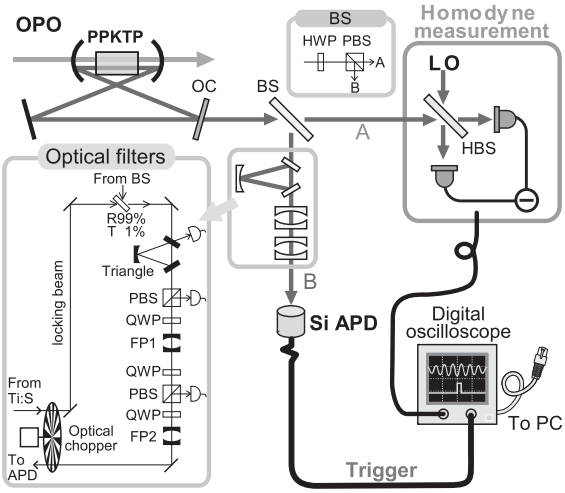

Figure 8.3 Schematic of experimental set-up [313]. OC: output coupler, HWP: half-wave plate, PBS: polarizing beam splitter, BS: beam splitter (consisting of HWP and PBS, variable splitting ratio), Triangle: triangle cavity, QWP: quarter-wave plate, FP1 & FP2: Fabry–Perot cavities, HBS: 50:50 beam-splitter.

A schematic of the experimental setup is shown in Figure 8.3. A continuous-wave Ti:sapphire laser (Coherent MBR-110) is used as a primary source of the fundamental beam at 860 nm, which is mainly used to generate a second harmonic (430 nm) of about 200 mW by a frequency doubler (a bow-tie cavity with $KNbO_3$). It is also used as a local oscillator (LO) for homodyne detection, and as probe beams for various control purposes. The second harmonic beam is used to pump the OPO with a 10 mm long PPKTP crystal (Raicol Crystals) as a nonlinear medium in an optical cavity (a bow-tie configuration with a round-trip length of about 523 mm). The output coupler (OC) of this squeezer cavity has a transmittance of 10.3%. The intracavity loss is about 0.2∼0.3%, which is nearly independent from the pump power and much better than that with $KNbO_3$ in our case (2∼3%). The FWHM of the cavity is about 9.3 MHz.

A small fraction (5%) of the squeezed vacuum beam in path A is split at a beam splitter (BS), guided into a commercial Si-APD (Perkin Elmer SPCM-AQR-16) through three optical filtering cavities in path B, and is used as trigger signals for conditional photon subtraction. The finesses of the filtering cavities are about 60 (Triangle), 600 (FP1), and 1500 (FP2), respectively. All the filtering cavities have 5∼10 times wider bandwidths than that of the OPO. The spectrum of the trigger photons through these filters consists of a single peak around 860 nm at the degenerate mode with a bandwidth of 8.6 MHz (FWHM). Other irrelevant, nondegenerate, modes from the OPO, peaking at every free spectral range of 573 MHz apart from the degenerate frequency, are sufficiently well suppressed. The total transfer efficiency after the BS for the mode of interest is about 30% just in front of the Si-APD. The trigger counting rate varies from less than 1 up to 50 kcps,

changing with the pump power of OPO from 1 up to 160 mW and splitting ratios. These trigger counting rates are mostly much greater than the Si-APD dark counts (100 cps).

Reducing background light is crucial for using an Si-APD because bright background light easily degrades signal-to-noise ratio of trigger photons. Usually, weak coherent beams are used as references to lock optical cavities [283], but they directly yield vast amounts of counts. Therefore, one has to contrive ways to count photons and lock optical cavities in the same experimental setup.

For that purpose, Wakui *et al*. applied a time sharing control of the system by a "sample-and-hold locking" technique which enables us to alternatively switch the system from a "locking time-bin" to a "measurement time-bin" [313]. In the locking time-bin, the resonant frequencies of the filtering cavities are locked in a conventional manner (FM-sideband locking technique [185]). Servo amplifiers keep the filtering cavities in resonance by piezo actuators via demodulating the modulation applied to a "locking beam" (Figure 8.3). In the measurement time-bin, the locking beam is completely blocked for photon counting and servo amplifiers hold the system in the same state as right before the locking beam is blocked. To perform this periodically, the locking beam first passes through an optical chopper (the chopping frequency is 500 Hz), is guided into the filtering cavities, and then returning to the same chopper again after passing them through (Figure 8.3). When the locking beam passes through at one side of the optical chopper, it is blocked at the other side, and vice versa, and thus one realizes the time sharing control. Wakui *et al*. also made the servo amplifiers accept external timing signals in order to be able to be synchronized to the optical chopper's driver. A different experimental approach other than the method presented here can be found in [186].

The generated nonclassical states of light are combined with the LO at a 50 : 50 beam-splitter (HBS) and detected by a balanced homodyne detector with Si photodiodes (Hamamatsu S3759, anti-reflective coated at 860 nm, 99.6% quantum efficiency). In order to improve the homodyne efficiency, the LO beam is spatially filtered by a mode cleaning cavity which yields the same spatial mode as the OPO output. The propagation loss mainly comes from the pickup of a squeezed vacuum itself (5% at BS), and the homodyne efficiency is 98%.

For every trigger signal from the Si-APD, a digital oscilloscope (LeCroy WaveRunner 6050A) samples homodyne signals around the time when trigger photons are detected. Recall the discussion in Section 3.2.3.2; the spectroscope and power measurements of the more conventional frequency-domain CV experiments are here in the time-domain approach replaced by the digital oscilloscope and amplitude measurements. Now, each segment of data contains homodyne signals over a period $\sim$0.5 μs [see Eq. (3.82)]. These are piled one after another until $\sim$10 000 segments fill up the oscilloscope's memory in a single run of the experiment. Each segment of the homodyne signals are sent to a PC, and then time-integrated after being multiplied by a particular temporal mode function $\Psi_0(t)$. Each Wigner function is reconstructed using the iterative maximum-likelihood estimation algorithm [302] from about 50 000 data points of quadrature amplitude.

The temporal mode function $\Psi_0(t)$ should be chosen such that it defines the signal mode which shares the maximal entanglement with the trigger photon mode. The trigger photon mode is well localized in the time domain at least within $T \leq 1\,\mathrm{ns}$. This depends on the single-photon timing resolution of SPCM and is *much shorter than the inverse bandwidth of the squeezed vacua*. The bandwidth of the squeezed vacua are typically $2B \sim 10\,\mathrm{MHz}$ and can be characterized by the bandwidth of the OPO cavity. For such a small BT, a single mode description is valid [183] (see Figure 2.11). In a good approximation, one can consider $\Psi_0(t)$ in a form [184] $\Psi_0(t) = \sqrt{\zeta_0}\mathrm{e}^{-\zeta_0|t|}$, assuming a trigger signal detected at $t = 0$ where $\zeta_0 \equiv (\gamma_\mathrm{T} + \gamma_\mathrm{L})/2$ determines the characteristic bandwidth $\zeta_0/2\pi \sim 4.6\,\mathrm{MHz}$. Here, the leakage rate of the output coupler is $\gamma_\mathrm{T} \sim 57\,\mathrm{MHz}$ and the cavity loss rate is $\gamma_\mathrm{L} \sim 1.2\,\mathrm{MHz}$.

Figure 8.4 shows experimental Wigner functions (top panels) and its contour plots (insets in top panels), raw data of quadrature distributions over half a period (middle panels), and photon-number distributions (bottom panels) of the photon-subtracted squeezed states. First, experimental density matrices in the Fock (photon-number state) basis are obtained from the raw data in the middle

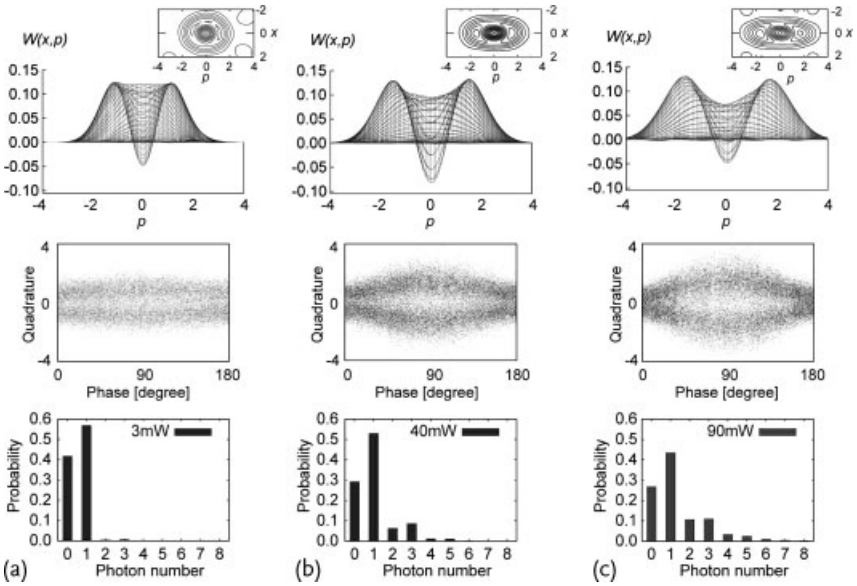

Figure 8.4 Experimental Wigner functions (top panels) constructed from raw data without any correction of measurement imperfections in the case of 5% splitting ratio. (a) The single-photon state generated by −0.7 dB squeezed input. (b) and (c) Schrödinger kittens generated by −2.6 and −3.7 dB squeezed inputs, respectively. The values of the Wigner function at the origin are (a) $W(0,0) = -0.049$, (b) $W(0,0) = -0.083$, and (c) $W(0,0) = -0.048$. The insets in the top panels are the contours of the Wigner functions. The middle panels are quadrature distributions obtained by homodyne detection. The bottom panels are photon-number distributions obtained by the iterative maximum-likelihood estimation. In the calculations in this section, units of $\hbar = 1$ are used.

panels by using the iterative maximum-likelihood estimation. Then, the Wigner functions in the top panels can be directly calculated from the density matrices. Here, any corrections for measurement imperfections are not applied. The bottom panels are diagonal elements of the density matrices in the Fock basis.

The negativity of the photon-subtracted squeezed states tightly depends on a signal-to-noise (S/N) ratio of trigger photons because one cannot distinguish trigger (signal) clicks and false (noise) clicks in state preparation. False clicks just yield vacuum contributions to the generated states. A vacuum state has a Gaussian distribution of the Wigner function and a positive peak at its origin. Therefore, the negative dips of the generated states become shallow when the S/N ratio gets worse and worse, that is, the vacuum contributions increase more and more.

Figure 8.4a corresponds to a single-photon state generated by -0.7 dB squeezed input. In such a low level of squeezing, the counting rate of trigger photons is extremely low (less than 1 kcps) and become comparable to Si-APD's dark-count rate (100 cps). Thus, the negativity in the single-photon state easily disappears even with a small amount of false clicks rather than that in the Schrödinger-kitten states. Therefore, the single-photon state particularly requires a nearly pure squeezed state generated with PPKTP, as mentioned above.

Figure 8.4b and c are for Schrödinger kittens with two kinds of amplitudes generated by -2.6 and -3.7 dB squeezed inputs, respectively. The odd-number enhanced distributions of photon numbers are illustrated in the bottom panels. Furthermore, these two states can be seen as superpositions of mesoscopically distinct components. The large negativity is obtained in a wide range of squeezing levels.

The experimental values of the Wigner functions at their origins are Figure 8.4a: $W(0,0) = -0.049$, Figure 8.4b: $W(0,0) = -0.083$, and Figure 8.4c: $W(0,0) = -0.048$.[2] These values are significantly improved, compared to the values with $KNbO_3$.

By using a similar technology, Neergaard-Nielsen *et al.* succeeded in creating a single photon state [324], which fits CV experiments.

Figure 8.5 shows the setup for creation of a single photon state for CV QIP [324]. This setup is very similar to Figure 8.3, except for frequency shifts to ω_+ and ω_- from the fundamental frequency ω_0 of the laser where $|\omega_0 - \omega_\pm|$ corresponds to the free spectral range (FSR) of the OPO cavity. Since the filtering cavities are all resonant with ω_-, the ω_- component of the output of the OPO passes through the cavities and hits a single-photon detector (APD: avalanche photodiode). On the other hand, the ω_+ component is reflected and goes to a homodyne measurement setup. Here, ω_+ and ω_- components have EPR-type entanglement.

When there is a click at the APD, a single photon state appears at frequency ω_+, which is detected by using the local oscillator of frequency ω_+ of the homodyne measurement. Note that the difference between the previously described single-photon subtraction scheme and the scheme introduced in the preceding paragraph is that single-photon subtraction uses the ω_0 component which has even-photon

2) Note that here, in order to compute the measured negativities, the convention $\hbar = 1$ was used, differing from our usual convention of $\hbar = 1/2$ throughout this book.

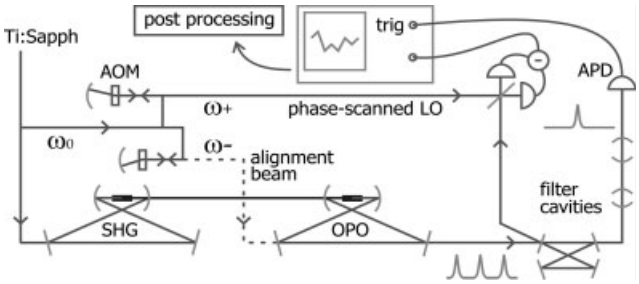

Figure 8.5 Experimental setup for single-photon creation for CV QIP demonstrated by Neergaard-Nielsen *et al.* [324]. SHG: second harmonic generator for pumping the OPO, AOM: acousto optic modulator to shift the fundamental frequency ω_0, LO: local oscillator, APD: avalanche photo diode.

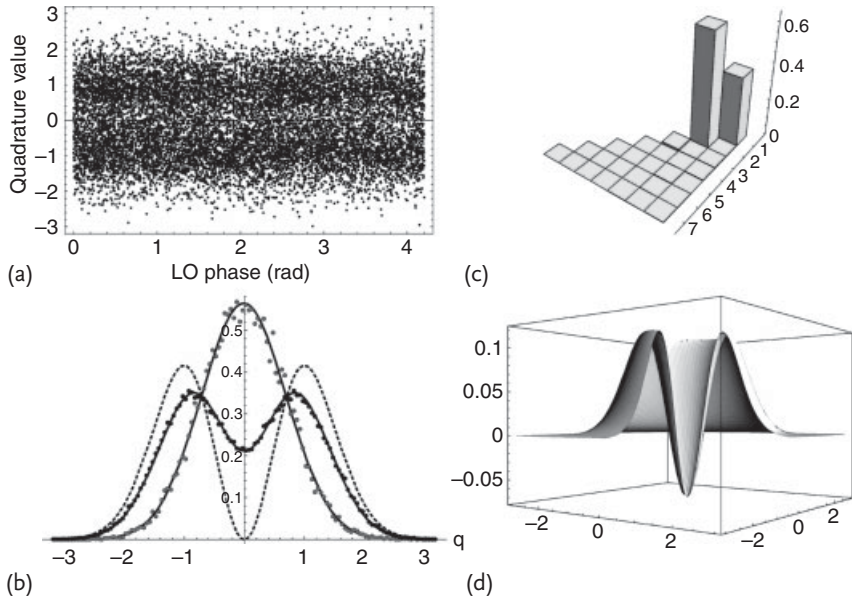

Figure 8.6 Experimental results for single-photon creation for CV QIP demonstrated by Neergaard-Nielsen *et al.* [324]. (a) Part of the recorded quadrature data set with corresponding phases. (b) Histogram of distribution of conditional quadrature points and vacuum points. The dashed curve is the ideal single photon distribution. (c) The density matrix of the state reconstructed via the maximum likelihood method. (d) The corresponding Wigner function.

nature and not EPR-type entanglement. Figure 8.6 shows the experimental results [324].

8.3 Hybrid Entanglement

In the preceding section, we encountered the example of an entangled state between a qubit and a qumode. This state, though defined in a combined qubit–qumode, hence an infinite-dimensional Hilbert space, can be formally written in a two-qubit Hilbert space as we shall explain in this section. One consequence of this is that the entanglement of this state can be conveniently quantified.

Consider the following bipartite state,

$$\left(|\psi_0\rangle|0\rangle + |\psi_1\rangle|1\rangle\right)/\sqrt{2}\,, \tag{8.9}$$

with an orthogonal qubit basis $\{|0\rangle, |1\rangle\}$ and a pair of linearly independent qumode states $|\psi_0\rangle$ and $|\psi_1\rangle$. A specific example of such a state and a possible way to build it was presented in Eq. (8.7) and the preceding discussion.

Clearly, the state in Eq. (8.9) becomes a maximally entangled, effective two-qubit Bell state when $\langle\psi_0|\psi_1\rangle \to 0$. For $0 < |\langle\psi_0|\psi_1\rangle| < 1$, the state is nonmaximally entangled, but still can be expressed effectively as a two-qubit state. This can be seen by writing the two pure, non-orthogonal qumode states in an orthogonal, two-dimensional basis, $\{|u\rangle, |v\rangle\}$,

$$\begin{aligned} |\psi_0\rangle &= \mu|u\rangle + \nu|v\rangle\,, \\ |\psi_1\rangle &= (\mu|u\rangle - \nu|v\rangle)\mathrm{e}^{\mathrm{i}\phi}\,, \end{aligned} \tag{8.10}$$

where $\nu = \sqrt{1-\mu^2}$ with $\mu = [1 + \mathrm{e}^{-\mathrm{i}\phi}\langle\psi_0|\psi_1\rangle]^{1/2}/\sqrt{2}$. Then, using this orthogonal basis,

$$\begin{aligned} |u\rangle &= \left(|\psi_0\rangle + \mathrm{e}^{-\mathrm{i}\phi}|\psi_1\rangle\right)/(2\mu)\,, \\ |v\rangle &= \left(|\psi_0\rangle - \mathrm{e}^{-\mathrm{i}\phi}|\psi_1\rangle\right)/(2\nu)\,, \end{aligned} \tag{8.11}$$

the hybrid entangled state of Eq. (8.9) becomes

$$\mu|u\rangle|0\rangle + \sqrt{1-\mu^2}|v\rangle|1\rangle\,, \tag{8.12}$$

a nonmaximally entangled two-qubit state with Schmidt coefficients μ and $\sqrt{1-\mu^2}$, where 1 ebit is obtained only for $\mu \to 1/\sqrt{2}$ and $\langle\psi_0|\psi_1\rangle \to 0$. Quantifying the entanglement is straightforward, as the entropy of the reduced density matrix is a function of the Schmidt coefficients (see Section 1.5).

It is interesting to compare the state of Eq. (8.9) with a bipartite qumode–qumode entangled state of the form

$$\left(|\psi_0\rangle|\psi_0\rangle \pm |\psi_1\rangle|\psi_1\rangle\right)/\sqrt{N_\pm}\,, \tag{8.13}$$

assuming the overlap $\langle\psi_0|\psi_1\rangle$ is real [325]. First of all, in this case, a normalization constant $N_\pm$ is needed, depending on $\langle\psi_0|\psi_1\rangle$. Secondly, and quite remarkably, such a state may always represent a maximally entangled two-qubit state (in the

subspaces spanned by $|\psi_0\rangle$ and $|\psi_1\rangle$), independent of $\langle\psi_0|\psi_1\rangle$, but depending on the relative phase [325–327], that is, the sign in Eq. (8.13).

The prime example for such qumode–qumode entangled states are two of the so-called *quasi-Bell states*,

$$|\Psi^{\pm}\rangle \equiv (|\alpha\rangle|\alpha\rangle \pm |-\alpha\rangle|-\alpha\rangle)/\sqrt{N_{\pm}}\,, \tag{8.14}$$

with $N_{\pm} \equiv 2 \pm 2e^{-4|\alpha|^2}$. The state $|\Psi^{-}\rangle$ is identical to the two-qubit Bell state $(|u\rangle|v\rangle + |v\rangle|u\rangle)/\sqrt{2}$ when $2\mu = \sqrt{2+2e^{-2|\alpha|^2}}$, $2\nu = \sqrt{2-2e^{-2|\alpha|^2}}$, and $N_{-} = 8\mu^2\nu^2$, which is maximally entangled with exactly 1 ebit of entanglement for *any* $\alpha \neq 0$. In contrast, the state $|\Psi^{+}\rangle$ only equals the one-ebit Bell state $(|u\rangle|u\rangle + |v\rangle|v\rangle)/\sqrt{2}$ in the limit of orthogonal coherent states, $\langle\alpha|-\alpha\rangle \to 0$ for $\alpha \to \infty$.[3)]

The amount of entanglement in the qubit–qumode and qumode–qumode states of Eqs. (8.9) and (8.13), respectively, is bounded above by one ebit, corresponding to a maximally entangled two-qubit Bell state. This is different from a "genuine" CV qumode–qumode entangled state such as a Gaussian two-mode squeezed state which contains an arbitrary amount of entanglement for sufficiently high levels of squeezing.

Let us finally consider entanglement witnesses (see Section 1.5) in the hybrid context. Qumode-qumode entangled states like those in Eq. (8.13) may be identified through the partial transposition criteria (Section 1.5) adapted to the case of arbitrary CV states [328, 329]. As a result, all known CV inseparability criteria, including those especially intended for Gaussian states and expressed in terms of second moments (see Section 3.2.1), can be derived from a hierarchy of conditions for all moments of the mode operators $\hat{a}$ and $\hat{a}^{\dagger}$. Moreover, for non-Gaussian entangled states for which the second-moment criteria may fail to detect entanglement, the higher-moment conditions would work. The concept for these criteria is as follows.

It is known that for any positive operator $\hat{P} \geq 0$, we can write $\hat{P} = \hat{f}^{\dagger}\hat{f}$ such that $\mathrm{Tr}(\rho\hat{f}^{\dagger}\hat{f})$ is non-negative for any operator $\hat{f}$ and any physical state ρ. Then, we may choose the bipartite decomposition $\hat{f} = \sum_{ij} c_{ij}\hat{A}_i \otimes \hat{B}_j$, for which

$$\begin{aligned} 0 &\leq \mathrm{Tr}\left(\rho\hat{f}^{\dagger}\hat{f}\right) \\ &= \sum_{ij,kl} c_{ij}^{*}\mathrm{Tr}\left(\rho\hat{A}_i^{\dagger}\hat{A}_k \otimes \hat{B}_j^{\dagger}\hat{B}_l\right) c_{kl} \\ &\equiv \sum_{ij,kl} c_{ij}^{*}[M(\rho)]_{ij,kl}c_{kl}\,, \end{aligned} \tag{8.15}$$

for any coefficients c_{ij}. Hence, the matrix $M(\rho)$ is positive-semidefinite for any physical state ρ. Now, any separable state ρ remains a physical state after partial transposition of either subsystem such that $M(\rho^{T_A})$ and $M(\rho^{T_B})$ remain positive-semidefinite matrices, where T_A and T_B denote partial transposition for subsys-

3) Similarly, for the other two (quasi-)Bell states, we then have $|\alpha\rangle|-\alpha\rangle - |-\alpha\rangle|\alpha\rangle \propto |u\rangle|v\rangle - |v\rangle|u\rangle$ for *any* value of α, but $|\alpha\rangle|-\alpha\rangle + |-\alpha\rangle|\alpha\rangle \propto |u\rangle|u\rangle - |v\rangle|v\rangle$ only when $\alpha \to \infty$.

tem A and B, respectively. Then, negativity of $M(\rho^{T_A})$ or $M(\rho^{T_B})$, and hence negativity of any subdeterminant of $M(\rho^{T_A})$ or $M(\rho^{T_B})$ is a sufficient criterion for entanglement from which sets of inequalities can be derived with convenient choices for the local operators $\hat{A}_i$ and $\hat{B}_j$ [328].

One such choice for a qumode–qumode state would be each qumode's position and momentum operators, eventually reproducing Simon's criteria in terms of second-moment correlation matrices. Another choice, adapted to a qubit–qumode state of the form in Eq. (8.9), is given by $\{\hat{A}_i\} = \{|\phi\rangle\langle 0|, |\phi\rangle\langle 1|\}$ and $\{\hat{B}_j\} = \{\mathbb{1}, \hat{x}, \hat{p}\}$, with some generic qubit state $|\phi\rangle$ [330]. The resulting expectation value matrix $M(\rho)$ then serves again, using partial transposition, as a tool to detect entanglement, this time for hybrid qubit–qumode states. This can be particularly useful for verifying the presence of effective entanglement in a binary coherent-state-based quantum key distribution protocol [331, 332] as a necessary security requirement (see Section 1.7).

The choices for the local operators $\hat{A}_i$ and $\hat{B}_j$ discussed so far all only lead to second-moment conditions. These are experimentally most accessible, but may fail to detect some form of non-Gaussian entanglement. For qumode–qumode states, a more general choice is the normally ordered form for $\hat{f}$, $\hat{f} = \sum_{nmkl} c_{nmkl} \hat{a}^{\dagger n} \hat{a}^m \hat{b}^{\dagger k} \hat{b}^l$, with mode operators $\hat{a}$ and $\hat{b}$ for the two qumodes A and B, respectively. Inserting this into $\mathrm{Tr}(\rho^{T_A} \hat{f}^\dagger \hat{f}) \geq 0$ or $\mathrm{Tr}(\rho^{T_B} \hat{f}^\dagger \hat{f}) \geq 0$ yields a hierarchy of separability conditions in terms of the moments of the mode operators. For example, the quasi-Bell state $|\Psi^-\rangle$ of Eq. (8.14) leads to a subdeterminant of the matrix of moments with a sufficient order of the moments such as $\langle \hat{a}^\dagger \hat{a} \hat{b}^\dagger \hat{b} \rangle$, which becomes $-\alpha^6(\coth(2\alpha^2))/(\sinh^2(2\alpha^2)) \equiv s$ for real α [328, 329]. This subdeterminant is negative for any nonzero α, proving the entanglement of the state $|\Psi^-\rangle$ for any $\alpha \neq 0$.[4)]

To conclude this section, let us summarize that it is straightforward to quantify the entanglement of hybrid qubit–qumode and non-Gaussian qumode–qumode states, provided these states can be represented in two-dimensional subspaces. Otherwise, in order to detect the inseparability of such states, the partial transposition criteria expressed in terms of matrices of moments can be used. In a recent experiment, employing CV quantum information encoded into the spatial wavefunction of single photons, fourth-order-moment entanglement was detected [333].

8.4 Hybrid Quantum Teleportation

Since photon counting events are defined in the time domain, conventional CV teleportation schemes with a sideband of an optical carrier [203] cannot be used for the teleportation of states conditionally prepared through photon counting. There-

4) Note that $s \to 0$ for $\alpha \to \pm\infty$ and that s is maximally negative, $s \approx -0.125$, for $|\alpha| < 0.4$, even though we know that $|\Psi^-\rangle$ has constant entanglement of one ebit for any nonzero α.

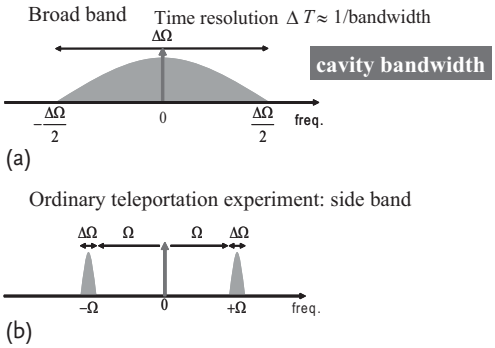

Figure 8.7 (a) Frequency mode of the Schrödinger kitten. (b) Frequency mode for conventional teleportation experiments.

fore, in order to realize CV teleportation of such non-Gaussian states, one needs to generate EPR correlations in the time domain (see Section 3.2).

8.4.1
Experiment: Broadband Qumode Teleportation of a Non-Gaussian Wavepacket

The conditionally prepared, non-Gaussian state of Section 8.2 can be teleported through a time-domain teleporter using a truly broadband entanglement resource as introduced in Section 3.2.3.2. Since conventional teleportation experiments were performed with a frequency sideband of a laser carrier as shown in Section 4.2.1 and Figure 8.7b, this broadband and time-domain teleportation is the next big challenge.

The "Schrödinger kitten" created by photon subtraction only appears when a photon is detected at the APD in Figure 8.3. In this sense, the Schrödinger kitten is defined as a wavepacket in the time domain. Moreover, as is shown in Section 8.2, the frequency mode should be defined by the OPO resonant band which is illustrated in Figure 8.7a. To teleport this type of broadband mode, we can use broadband and time-domain EPR entanglement explained in Section 3.2.3.2 (see Figure 3.20).

Figure 8.8 shows the experimental setup for broadband and time-domain teleportation. The broadband entangled EPR beams are created with the method explained in Section 3.2.3.1 and they are shared between Alice and Bob. Alice makes a Bell measurement for the input kitten and Alice's EPR beam and sends the result to Bob. Since Alice's homodyne detectors for the Bell measurement and Bob's phase modulators for the displacement operations have limited bandwidth, it makes a time delay from the corresponding fraction of Bob's EPR beam. By using an optical delay line in Bob's EPR beam path, Bob can compensate the time delay and can keep the EPR correlation. This is conceptually very different from the necessary phase adjustments in conventional narrow-bandwidth CV teleportation. Bob makes a displacement operation on his EPR beam with high-reflectivity beam splitters ($T = 1\%$) and phase modulators (PM), and restores the input kitten at his

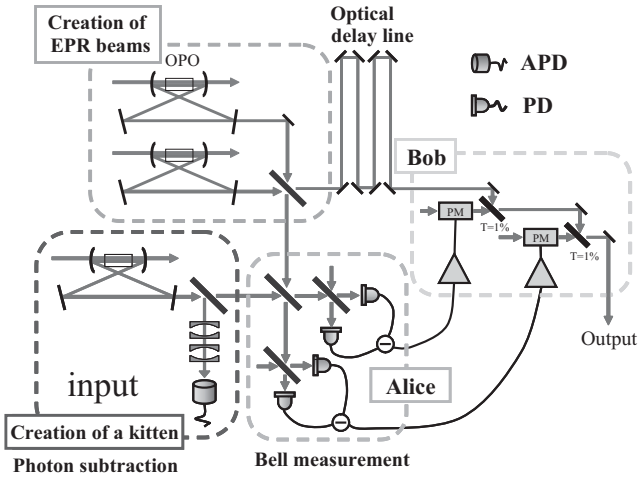

Figure 8.8 Setup for teleportation of a Schrödinger kitten. OPO: optical parametric oscillator for creation of squeezed vacuum, APD: avalanche photodiode, PD: photodiode, PM: phase modulator.

place. Here, the input kitten is created with photon subtraction as explained in Section 8.2, which is conditioned by a click at APD. Therefore, the output is examined only at the click with quantum tomography.

Concluding this section, we should emphasize that the setup described above can be used for teleporting arbitrary wavepackets which can be defined in a broadband fashion. Even though the input state to the teleporter may be conditionally prepared, the whole process of quantum teleportation itself remains deterministic, requiring sufficiently high time resolution and synchronization between the various components (such as Alice's finite-bandwidth Bell measurement and the finite-bandwidth classical communication between Alice and Bob). Such a synchronization was not needed in standard frequency-domain teleportation where just the phases between Alice's and Bob's large wavepackets (each corresponding to a single frequency mode) had to be adjusted.

Another important example for hybrid, broadband quantum teleportation would be the teleportation of a single photon, which then can be extended to the teleportation of a polarization qubit. This shall be discussed in the next section.

8.4.2
Experiment: Broadband Qumode Teleportation of a Polarization Qubit

A polarization qubit $c_0|\leftrightarrow\rangle + c_1|\updownarrow\rangle$ can be teleported with two broadband CV teleporters which are explained in Section 8.4.1. This protocol was proposed by Ide *et al.* [334]. The key is the conversion from a polarization qubit to a dual-rail spatial qubit with the following relation:

$$c_0|\leftrightarrow\rangle + c_1|\updownarrow\rangle \rightarrow c_0|1\rangle_{\leftrightarrow} \otimes |0\rangle_{\updownarrow} + c_1|0\rangle_{\leftrightarrow} \otimes |1\rangle_{\updownarrow} \,, \tag{8.16}$$

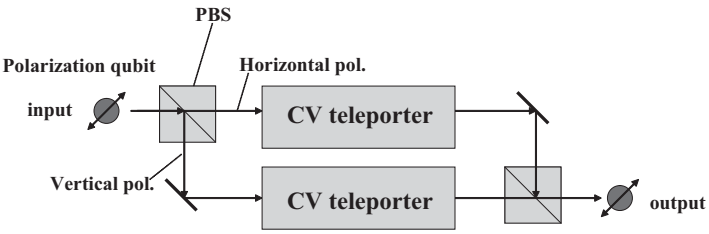

Figure 8.9 Schematic for teleportation of a polarization qubit with two broadband CV teleporters. PBS: polarization beam splitter.

where $|n\rangle_{\leftrightarrow,\updownarrow}$ $(n = 0, 1)$ denotes a vacuum or single photon state in channel $\leftrightarrow$ or $\updownarrow$. This conversion can be realized with a polarization beam splitter (PBS) as shown in Figure 8.9.

The dual-rail spatial qubit can be teleported with two broadband CV teleporters also shown in Figure 8.9. In this process, superpositions of a vacuum and a single photon are teleported in each CV teleporter. As the final step, the teleported dual-rail spatial qubit is converted back to a polarization qubit with another PBS, to obtain the output of teleportation.

Ide *et al*. calculated the teleportation fidelity as a function of the resource squeezing level [334]. From the calculation, it is found that one needs around 10dB of squeezing for the resource of CV teleportation to exceed the classical limit of qubit teleportation of 2/3 [335], which is available with current technology [218, 219].

8.5
Hybrid Quantum Computing

In this section, we shall now discuss a few explicit examples for hybrid quantum processing, the most prominent of which is the GKP scheme [249]. This scheme, in principle, achieves fault-tolerant quantum computing on logical qubits embedded into physical qumodes. We will discuss it in detail in Section 8.5.3 and, in particular, we shall expose its relation with CV cluster computation. Before discussing the GKP proposal, we will introduce the notion of hybrid Hamiltonians in Section 8.5.1 and some natural qubit-into-qumode encodings in Section 8.5.2.

8.5.1
Hybrid Hamiltonians

One particularly interesting hybrid approach is based upon unitary evolutions, that is, Hamiltonians which are hybrid. These Hamiltonians contain DV qubit and CV qumode operator combinations such as, for instance, the controlled rotation in Eq. (8.5) corresponding to a dispersive light-matter interaction Hamiltonian. More generally, we may consider a unitary gate of the form,

$$\hat{U} = \exp\left[\mathrm{i}\lambda\, f(\sigma_x, \sigma_z) \otimes g(\hat{x}, \hat{p})\right], \tag{8.17}$$

acting on the composite system of a qubit and a qumode. In fact, in the context of combining the DV and CV approaches, it has been pointed out [336] that a suitable set of elementary Hamiltonians, including the controlled rotations and additional uncontrolled displacements,

$$\left\{\sigma_x \hat{a}^\dagger \hat{a}, \sigma_z \hat{a}^\dagger \hat{a}, \hat{x}\right\}, \tag{8.18}$$

is, in principle, sufficient for universal quantum computation on qubits.[5] Even earlier, Lloyd considered a universal set containing only controlled displacements [337],

$$\{\pm\sigma_x \hat{x}, \pm\sigma_z \hat{x}, \pm\sigma_z \hat{p}\}\,. \tag{8.19}$$

Typically, in quantum optics, controlled rotations are easier to achieve than controlled displacements. Recall, for instance, the cat engineering scheme of Section 8.1.

There are two ways to understand the universality of the above Hamiltonian sets. One approach is based upon the decomposition of Eq. (1.119). Recall from that decomposition in Section 1.8 that by applying the Hamiltonians H_1 and H_2 for some short time, we can also approximately implement the Hamiltonian $-\mathrm{i}[H_1, H_2]$, provided the interaction times are sufficiently short.[6] Now, first of all, it can be shown that by using Eq. (1.119) and the elementary Hamiltonians of Eq. (8.19), one can generate any single-qubit, any single-qumode as well as any qubit–qumode unitary [337] through commutation. The extra two-qubit and two-qumode entangling gates in order to complete the universal sets for DV and CV universality, respectively, are then achieved through the following commutators,

$$-\mathrm{i}\left[\sigma_z^{(1)}\hat{x}, \sigma_z^{(2)}\hat{p}\right] = \sigma_z^{(1)}\sigma_z^{(2)}/2\,, \tag{8.20}$$

$$-\mathrm{i}\,[\sigma_z \hat{x}_1, \sigma_x \hat{x}_2] = 2\sigma_y \hat{x}_1 \hat{x}_2\,, \tag{8.21}$$

respectively. Here, the superscripts and subscripts denote operators acting upon one of the two qubits or qumodes. In other words, the C_Z-gates of the sets in Eqs. (1.121) and (1.127) can be enacted *approximately* by applying some of the elementary Hamiltonians in Eq. (8.19). However, there is a crucial difference between the above two commutators. The commutator in Eq. (8.20) commutes with the elementary Hamiltonians from which it is built, whereas the commutator in Eq. (8.21) does not. As a consequence, in the latter case, the decomposition formula in Eq. (1.119) is indeed only an approximation that requires infinitesimally small interaction periods. However, since $-\mathrm{i}[\sigma_z^{(1)}\hat{x}, \sigma_z^{(2)}\hat{p}]$ commutes with $\sigma_z^{(1)}\hat{x}$ and $\sigma_z^{(2)}\hat{p}$, and all higher-order commutators vanish as well, the two-qubit C_Z-gate according to Eq. (1.119) with Eq. (8.20) no longer depends on small interaction times.

5) Note that compared to the discussion on universal sets for DV and CV quantum computation in Section 1.8, we are now writing a universal set in terms of elementary Hamiltonians instead of elementary gates.

6) So this is the same asymptotic, approximate model for universal quantum computation as it was used for discrete [85] and continuous [86] variables on their own, see Section 1.8.

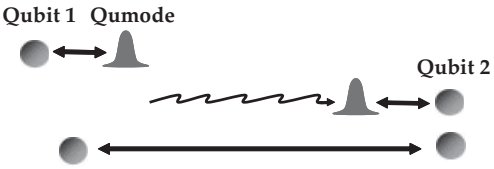

Figure 8.10 A quantum optical illustration of the qubus principle. A CV probe pulse (qumode) subsequently interacts with two matter qubits. After a sequence of interactions, an entangling gate between the two qubits can be mediated through the qubus.

Instead, we obtain the *exact* formula

$$e^{i\sigma_z^{(2)}\hat{p}t}e^{i\sigma_z^{(1)}\hat{x}t}e^{-i\sigma_z^{(2)}\hat{p}t}e^{-i\sigma_z^{(1)}\hat{x}t} = e^{i\sigma_z^{(1)}\sigma_z^{(2)}t^2/2}\,. \tag{8.22}$$

This observation leads us to an alternative way of understanding how the hybrid gates of Eq. (8.19) can be used to achieve universal quantum computation on qubits. In particular, a two-qubit entangling gate of sufficient strength (i.e., $t^2 \sim 2\pi$) is then possible without direct interaction between the two qubits; a single qumode subsequently interacting with each qubit would rather mediate the qubit–qubit coupling – as a kind of *quantum bus* (so-called qubus [338, 339], see Figure 8.10). The sudden exactness of the gate sequence can be explained by interpreting it as a controlled geometric phase gate [336, 340].

Therefore, even though the original hybrid scheme of Lloyd [337] achieves universality using a finite gate set, it appears unrealistic to switch between the elementary Hamiltonians over an arbitrarily short time. Accomplishing the universal gates and hence the Hamiltonian simulation exactly over a finite number of steps, as described by Eq. (8.22), is thus an essential extension of these hybrid approaches.

Let us finally note that the two-qumode C_Z gate, as discussed in Section 1.8, of course, can be implemented directly using beam splitters and squeezers (through Bloch–Messiah reduction, see Chapter 2), independent of a supposed asymptotic scheme based on Eq. (1.119) with Eq. (8.21). Such a simple realization, however, is not available for qubits.

8.5.2 Encoding Qubits into Qumodes

There are various ways to encode a photonic qubit into optical modes such as polarization or spatial modes, as we discussed in Chapter 2. In particular, the photon occupation number in a single-rail, single-mode Fock state may serve as a qubit or a more general DV basis. In dual-rail or, more generally, multiple-rail encoding, a single photon encoded into multi-mode states can even be universally processed through linear optical elements; though, in an unscalable fashion, unless complicated ancilla states and feedforward are employed [242].

Another natural way to encode a logical DV state into a physical, optical multimode state would be based upon at least two qumodes and a constant number of

photons distributed over the physical qumodes such that, for example, a logical, $2J+1$-dimensional spin-J state, $|J, m_j\rangle$, $m_j = -J, -J+1, \ldots, J-1, J$, can be represented by two physical qumodes in the two-mode Fock state,

$$|J \equiv (n_1+n_2)/2, m_j \equiv (n_1-n_2)/2\rangle \ , \tag{8.23}$$

where n_1 and n_2 denote the photon numbers of the two modes.[7] In fact, for $n_1 + n_2 = 1$, we obtain a dual-rail encoded spin-1/2 qubit: $\{|J=1/2, m_j=-1/2\rangle, |J=1/2, m_j=+1/2\rangle\} \equiv \{|n_1=0, n_2=1\rangle, |n_1=1, n_2=0\rangle\}$. Similarly, a spin-1 qutrit, $\{|J=1, m_j=-1\rangle, |J=1, m_j=0\rangle, |J=1, m_j=1\rangle\}$ corresponds to $\{|0,2\rangle, |1,1\rangle, |2,0\rangle\}$ in the Fock basis.

These natural encodings may even automatically provide some resilience against certain errors such as photon losses. For instance, the dual-rail encoding directly serves as an error detection code [5, 242]. However, for the purpose of fault-tolerant, universal quantum information processing, other encodings could be preferable, though they might be much harder to realize. One example is the fault-tolerant quantum computation proposal based upon cat states such as the qubit-type states in Eq. (8.1) [308]. Although some universal DV gates such as the Hadamard gate (possibly using auxiliary hybrid entangled states of the form in Eq. (8.14) for a teleportation-based realization) are hard to implement for this encoding, the effect of photon losses on these cat-type states corresponds to random phase flips in the coherent-state basis such that repetition codes known from DV qubit quantum error correction can be directly applied [341]. Nonetheless, these codes would still require Hadamard gates for encoding and decoding.

8.5.3 GKP

The proposal by Gottesman, Kitaev, and Preskill (GKP) [249] may be referred to as a hybrid scheme for the following reason. It achieves universal quantum computing with logical qubits which are embedded in physical qumodes. This qubit-into-qumode encoding, however, is conceptually different from those that we have considered so far. It is not naturally given in a subspace of the optical Fock space, but would require a rather complicated, highly non-Gaussian encoding step. Nonetheless, physical operations on the qumodes eventually correspond to universal, logical gates on the encoded qubits. Moreover, this can be, in principle, done in a fault-tolerant fashion, as the GKP scheme includes, at the same time, a quantum error correction encoding of the qubit into the qumode.

7) The choice of constant total number $\hat{n}_1 + \hat{n}_2 \equiv \hat{S}_0$ and varying number differences $\hat{n}_1 - \hat{n}_2 \equiv \hat{S}_3$ corresponds to a specific basis in the so-called Schwinger representation. For example, in order to faithfully represent the SU(2) algebra by the Lie algebras of two infinite-dimensional oscillators, i.e., two qumodes $\hat{a}_1$ and $\hat{a}_2$, one may replace the usual Pauli matrices $\sigma_0 \equiv \mathbb{1}$, $\sigma_1 \equiv \sigma_x$, $\sigma_2 \equiv \sigma_y$, and $\sigma_3 \equiv \sigma_z$ by the so-called quantum Stokes operators $\hat{S}_i = (\hat{a}_1^\dagger, \hat{a}_2^\dagger)\sigma_i(\hat{a}_1, \hat{a}_2)^{\mathrm{T}}$, $i = 0, 1, 2, 3$, satisfying the SU(2) Lie algebra commutators $[\hat{S}_1, \hat{S}_2] = 2i\hat{S}_3$, while $[\hat{S}_0, \hat{S}_j] = 0$, for $j = 1, 2, 3$.

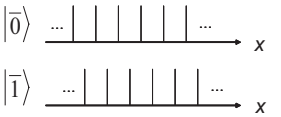

Figure 8.11 Encoding a qubit into a qumode according to GKP [249]. The logical, computational qubit basis states with $\bar{Z}|\bar{k}\rangle = (-1)^k|\bar{k}\rangle$, $k = 0, 1$ are infinite superpositions of delta peaks in position space. This encoding is particularly suited to protect the qubit against small, diffusive shift errors as arising from, for instance, weak amplitude damping of the qumode.

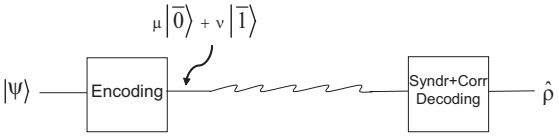

Figure 8.12 The GKP encoding of a logical qubit into a physical qumode to protect the logical qubit against small shift errors on the physical qumode. Such small shift errors would include Gaussian errors such as amplitude damping.

The GKP encoding (see Figure 8.11) is primarily intended to protect a logical qubit against small errors such as small shifts of the physical qumode in phase space (see Figure 8.12). Direct translations of standard qubit quantum error correction codes against rarely occurring Pauli errors into the CV regime, as discussed in Section 1.9 and in Chapter 5, fail to provide any protection against such small, diffusive, typically Gaussian errors [93]. Provided the error shifts are sufficiently small, that is, smaller than $\Delta/4$ with Δ the distance between the delta peaks in Figure 8.11, the encoded states remain sufficiently intact, and suitable syndrome measurements enable one, in principle, to detect the errors and correct the states.

Besides having this special error correction capability, the GKP scheme also includes universal gate operations. The link between logical and physical gate operations can be easily understood from Figure 8.11.[8] A logical Pauli operator $U \in \{\bar{X}, \bar{Y}, \bar{Z}\}$ is transformed under conjugation by a logical qubit Clifford unitary C into a different logical Pauli operator, $C^\dagger U C = U' \in \{\pm\bar{X}, \pm\bar{Y}, \pm\bar{Z}\}$. Thus, as the logical Pauli gates correspond to WH shifts of the physical qumode, any physical Gaussian operation (since it preserves such WH gates under conjugation) can only lead to a logical Clifford operation. Therefore, *a physical non-Gaussian operation is needed in order to achieve logical non-Clifford qubit gates and hence DV qubit universality*. GKP demonstrate two such non-Clifford gates of which one uses a controlled rotation through a dispersive atom-light interaction as in Eq. (8.5), whereas the other one is based upon a cubic phase gate on the physical qumode, $D_3(\kappa_3) = \exp(\mathrm{i}\kappa_3\hat{x}^3)$.

8) In Figure 8.11, we do not show the logical eigenstates of the logical $\bar{X}$ Pauli operator. Similar to the logical eigenstates of the logical $\bar{Z}$ Pauli operator, which are superpositions of delta peaks along the position axis as shown, the $\bar{X}$ eigenstates are delta-peak superpositions along the momentum axis in the physical qumode's phase space. The small shift errors can then be shifts along x and p, and as these WH errors form a basis, *any* sufficiently small error may be corrected. This reasoning is similar to that for the standard CV qumode codes (see Section 1.9 and Chapter 5) against sufficiently large, stochastic shift errors in a single channel.

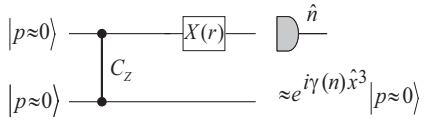

Figure 8.13 The GKP approach for creating a cubic phase state using linear Gaussian resources and DV photon counting measurements. The Gaussian resource state emerging from two momentum-squeezed states and the CV version of the controlled Z gate, $C_Z = \mathrm{e}^{2\mathrm{i}\hat{x}_1\otimes\hat{x}_2}$, is a two-mode squeezed state up to a local Fourier rotation; $X(r) = \mathrm{e}^{-2\mathrm{i}r\hat{p}}$ is a WH operator with fixed and sufficiently large r (much larger than the resource squeezing parameter). The illustrated circuit is reminiscent of an elementary step in a CV cluster computation involving a nonlinear measurement onto the displaced number basis $\{X^\dagger(r)|n\rangle\}$ [297].

Recall that this gate can also be used to complete the universal set for full CV universality in Eq. (1.127), in the spirit of [86].

In optical quantum information processing, it is pretty natural to encode DV quantum information into an appropriate subspace of the full infinite-dimensional qumode space. However, in order to realize the most advanced optical quantum processors which achieve both universality and fault tolerance, the qubit-into-qumode encodings, though conceptually highly interesting, may still be far from being implementable. In this sense, the cat-type encoding [308] and the position/momentum-eigenstate superposition encoding à la GKP [249] are very similar. In both schemes, fault tolerance and universality require complicated non-Gaussian operations or resources. Nonetheless, they do both incorporate the necessary non-Gaussian quantum error correction steps into a DV qubit processor embedded in the physical space of an optical qumode.

In order to obtain the necessary non-Clifford gate on the logical qubit through a non-Gaussian operation on the physical qumode (recall the discussion around Figure 8.11), GKP propose to produce an approximate version of the cubic phase state offline, $D_3(\kappa)|p = 0\rangle = \mathrm{e}^{\mathrm{i}\kappa\hat{x}^3}|p = 0\rangle = \int \mathrm{d}x\mathrm{e}^{\mathrm{i}\kappa x^3}|x\rangle$, using Gaussian two-mode squeezed state resources and photon number measurements (see Figure 8.13). The resulting cubic phase state is then sufficient to accomplish the cubic phase gate $D_3(\kappa)$ and to apply it to an arbitrary input state $|\psi\rangle$ through linear operations including homodyne detections (see Figure 8.14). The circuit in Figure 8.14 with all gates performed offline can be interpreted as a CV cluster computation on a non-Gaussian cluster state, in which case homodyne detections are sufficient for universality [297]. Though the original GKP scheme was not presented as a cluster-based scheme, it can be recast correspondingly [297].

The approximate cubic phase state in Figure 8.13 will depend on the measurement result n, $\mathrm{e}^{\mathrm{i}\gamma(n)\hat{x}^3}|p = 0\rangle$, and so for the desired cubic phase state, phase-free squeezing corrections are needed, $\hat{S}^\dagger[t(n)]\mathrm{e}^{\mathrm{i}\gamma(n)\hat{x}^3}\hat{S}[t(n)] = \mathrm{e}^{\mathrm{i}\kappa\hat{x}^3}$ with $t(n) = [\kappa/\gamma(n)]^{1/3}$ [297].

In the cluster version of GKP, the offline resource state remains Gaussian and thus unconditionally producible, while some of the online operations must then become nonlinear (see Figure 8.14). In order to obtain a desired cubic gate of any given strength κ, as before, additional squeezing corrections are needed. However,

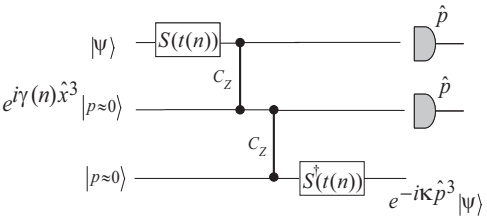

Figure 8.14 Incorporating the GKP scheme into a CV cluster computation. The resource state remains Gaussian, the measurements are CV homodyne detections and DV photon number measurements to teleport the cubic phase state into the middle rail. The initial cubic phase state depends on the measurement outcome n and extra squeezing corrections S are needed to obtain a cubic gate of any desired strength κ. Compared to Figure 6.15, the n-dependent squeezing corrections S are here to be done through the cluster; the additional p-dependent squeezing and WH corrections $C(s_1, s_2)$ can also be incorporated into the cluster computation and are not shown for simplicity.

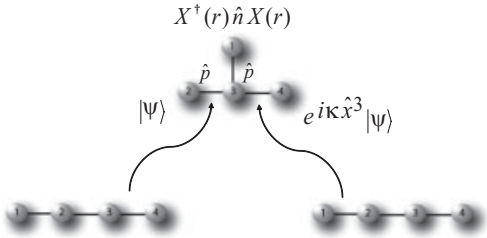

Figure 8.15 Full CV cluster implementation of a cubic phase gate. The extra linear cluster states are needed to realize the necessary squeezing corrections which depend on the photon number measurement result. As the desired cubic gate is non-Gaussian, the order of the measurements matters and the number measurement has to be done first. This implementation using linear and nonlinear measurements on a Gaussian state is conceptually different from that illustrated in Figure 6.15 where the resource state is non-Gaussian and all online operations are linear.

this time, also the squeezing corrections are performed through cluster computation since any squeezing gate is available by propagating the relevant state through a horizontal, linear four-mode wire (see Figure 8.15).

Further refinements and proposals related with GKP can be found in [342, 343]. An alternative approach to implementing a cubic phase gate relies upon potentially more accessible non-Gaussian resources such as Fock-state ancillae [344].

References

1 Raussendorf, R. and Briegel, H.J. (2001) *Phys. Rev. Lett.*, **86**, 5188.
2 Briegel, H.J., Dür, W., Cirac, J.I., and Zoller, P. (1998) *Phys. Rev. Lett.*, **81**, 5932.
3 Dür, W., Briegel, H.J., Cirac, J.I., and Zoller, P. (1999) *Phys. Rev. A*, **59**, 169.
4 Preskill, J. (1998) *Physics 229: Advanced mathematical methods of physics: quantum computation and information*, California Institute of Technology; www.theory.caltech.edu/people/preskill/ph229.
5 Nielsen, M.A. and Chuang, I.L. (2000) *Quantum Computation and Quantum Information*, Cambridge University Press, Cambridge.
6 Bruß, D. and Leuchs, G. (eds) (2007) *Lectures on Quantum Information*, Wiley-VCH Verlag GmbH, Berlin, chapters I.–V.; VII., 26.
7 Bengtsson, I. and Zyczkowski, K. (2006) *Geometry of Quantum States*, Cambridge University Press, Cambridge.
8 Peres, A. (1995) *Quantum Theory: Concepts and Methods*, Kluwer Academic Publishers, Dordrecht.
9 Schumacher, B. (1995) *Phys. Rev. A*, **51**, 2738.
10 Terno, D.R. (2006) Introduction to relativistic quantum information, in *Quantum Information Processing: From Theory to Experiment* (ed. D.G. Angelakis *et al.*), IOP Press p. 61, (2005) arXiv:0508049 [quant-ph].
11 Peres, A. and Terno, D.R. (2004) *Rev. Mod. Phys.*, **76**, 93.
12 Ghernaouti-Hélie, S. *et al.* (2008) SECOQC business white paper, http://www.secoqc.net/, September 2008.
13 Alleaume, R. *et al.* (2007) arXiv:0701168 [quant-ph].
14 Dieks, D. (1982) *Phys, Lett.* **92A**, 271.
15 Wootters, W.K. and Zurek, W.H. (1982) *Nature*, **299**, 802.
16 Herbert, N. (1982) *Found. Phys.*, **12**, 1171.
17 Bennett, C.H. *et al.* (1993) *Phys. Rev. Lett.*, **70**, 1895.
18 Bennett, C.H. and Brassard, G. (1984) in *Proc. IEEE Int. Conference on Computers, Systems and Signal Processing*, IEEE Press, Los Alamitos, Calif., p. 175.
19 Curty, M., Lewenstein, M., and Lütkenhaus, N. (2004) *Phys. Rev. Lett.*, **92**, 217903.
20 Ekert, A.K. (1991) *Phys. Rev. Lett.*, **67**, 661.
21 Shor, P.W. (1995) *Phys. Rev. A*, **52**, R2493.
22 Bennett, C.H., Brassard, G., Popescu, S., Schumacher, B., Smolin, J.A., and Wootters, W.K. (1996) *Phys. Rev. Lett.*, **76**, 722.
23 Einstein, A., Podolsky, B., and Rosen, N. (1935) *Phys. Rev.*, **47**, 777.
24 Werner, R.F. (1998) *Phys. Rev. A*, **58**, 1827.
25 Bužek, V. and Hillery, M. (1996) *Phys. Rev. A*, **54**, 1844.
26 Braunstein, S.L., Bužek, V., and Hillery, M. (2001) *Phys. Rev. A*, **63**, 052313.
27 Cerf, N.J., Ipe, A., and Rottenberg, X. (2000) *Phys. Rev. Lett.*, **85**, 1754.
28 Gottesman, D., Kitaev, A., and Preskill, J. (2001) *Phys. Rev. A*, **64**, 012310.

Quantum Teleportation and Entanglement. Akira Furusawa, Peter van Loock
Copyright © 2011 WILEY-VCH Verlag GmbH & Co. KGaA, Weinheim
ISBN: 978-3-527-40930-3

29 Walls, D.F. and Milburn, G.J. (1994) *Quantum Opics*, Springer, Berlin.
30 Ivanovic, I.D. (1987) *Phys. Lett. A*, **123**, 257.
31 Dieks, D. (1988) *Phys. Lett. A*, **126**, 303.
32 Peres, A. (1988) *Phys. Lett. A*, **128**, 19.
33 Schmidt, E. (1906) *Math. Annal.*, **63**, 433.
34 Bennett, C.H., Bernstein, H.J., Popescu, S., and Schumacher, B. (1996) *Phys. Rev. A*, **53**, 2046.
35 Eisert, J., Simon, C., and Plenio, M.B. (2002) *J. Phys. A*, **35**, 3911.
36 Fattal, D. *et al.* (2004) arXiv:0406168 [quant-ph].
37 Werner, R.F. (1989) *Phys. Rev. A*, **40**, 4277.
38 Peres, A. (1996) *Phys. Rev. Lett.*, **77**, 1413.
39 Horodecki, M., Horodecki, P., and Horodecki, R. (1996) *Phys. Lett. A*, **223**, 1.
40 Gühne, O. and Lütkenhaus, N. (2006) *Phys. Rev. Lett.*, **96**, 170502.
41 Bell, J.S. (1964) *Physics* (N.Y.) **1**, 195.
42 Wootters, W.K. (1998) *Phys. Rev. Lett.*, **80**, 2245.
43 Zyczkowski, K. *et al.* (1998) *Phys. Rev. A*, **58**, 883.
44 Vidal, G. and Werner, R.F. (2002) *Phys. Rev. A*, **65**, 032314.
45 Eisert, J. (2001) PhD thesis, University of Potsdam.
46 Gisin, N. (2007) *Nat. Phys.*, **1**, 165.
47 Gisin, N. *et al.* (2002) *Rev. Mod. Phys.*, **74**, 145.
48 Lütkenhaus, N. and Shields, A.J. (eds) (2009) Focus on Quantum Cryptography: Theory and Practice, *New J. Phys.*, **11**, 045005.
49 Stebila, D., Mosca, M., and Lütkenhaus, N. (2010) Lecture Notes of the Institute for Computer Sciences, Social Informatics and Telecommunications Engineering, **36**, 283–296.
50 Kimble, H.J. (2008) *Nature*, **453**, 1023.
51 Bennett, C.H. (1992) *Phys. Rev. Lett.* **68**, 3121.
52 Grosshans, F., Van Assche, G., Wenger, R.M., Brouri, R., Cerf, N.J., and Grangier, P. (2003) *Nature*, **421**, 238.
53 Maurer, U. and Wolf, S. (1999) *IEEE Trans. Inform. Theory*, **45**, 499.
54 Bennett, C.H., Brassard, G., and Mermin, N.D. (1992) *Phys. Rev. Lett.*, **68**, 557.
55 Shor, P.W. and Preskill, J. (2000) *Phys. Rev. Lett.*, **85**, 441.
56 Gottesman, D. and Preskill, J. (2001) *Phys. Rev. A*, **63**, 022309.
57 Zukowski, M., Zeilinger, A., Horne, M.A., and Ekert, A.K. (1993) *Phys. Rev. Lett.*, **71**, 4287.
58 Jacobs, B.C., Pittman, T.B., and Franson, J.D. (2002) *Phys. Rev. A*, **66**, 052307.
59 de Riedmatten, H. *et al.* (2004) *Phys. Rev. Lett.*, **92**, 047904.
60 Scherer, A. *et al.* (2009) *Phys. Rev. A*, **80**, 062310.
61 Holevo, A.S. (1998) *IEEE Trans. Inform. Theory*, **44**, 269.
62 Caves, C.M. and Drummond, P.D. (1994) *Rev. Mod. Phys.*, **66**, 481.
63 Cover, T.M. and Thomas, J.A. (1991) *Elements of Information theory*, John Wiley & Sons, Inc., New York.
64 Bennett, C.H., Brassard, G., Crepeau, C., and Maurer, U.M. (1995) *IEEE Trans. Inform. Theory*, **41**, 1915.
65 Brassard, G. and Salvail, L. (1994) in *Advances in Cryptology – EUROCRYPT'93*, Lecture Notes in Computer Science **765**, 410, Springer, New York.
66 Ch. Silberhorn, Ralph, T.C., Lütkenhaus, N., and Leuchs, G. (2002) *Phys. Rev. Lett.*, **89**, 167901.
67 Bennett, C.H. and Wiesner, S.J. (1997) *Phys. Rev. Lett.*, **69**, 2881.
68 Schumacher, B. (1995) *Phys. Rev. A*, **51**, 2738.
69 Shannon, C.E. (1948) *Bell Syst. Tech. J.*, **27**, 379–423, 623–656.
70 Ban, M. (1999) *J. Opt. B: Quantum Semiclass. Opt.*, **1**, L9.
71 Braunstein, S.L. and Kimble, H.J. (2000) *Phys. Rev. A*, **61**, 042302.
72 Deutsch, D. (1985) *Proc. R. Soc. Lond. A*, **400**, 97.
73 Feynman, R.P., Hey, A.G.J. (ed.), and Allen, R.W. (ed.) (1999) *Feynman Lectures on Computation*, Penguin Books.
74 Shor, P.W. (1994) *Algorithms for quantum computation: Discrete logarithms and factoring*, in Proc. 35th Annual Symposium on the Foundations of Computer Science, (ed. S. Goldwasser), IEEE

Computer Society Press, Los Alamitos, California, pp. 124–134.
75 Grover, L.K. (1997) *Phys. Rev. Lett.*, **79**, 325.
76 Deutsch, D. and Josza, R. (1992) *Proc. R. Soc. Lond. A*, **439**, 553.
77 Kempe, J. (2007) *Lectures on Quantum Information* (eds D. Bruß and G. Leuchs), Wiley-VCH Verlag GmbH, Berlin, chapter II.6.
78 Lloyd, S. (1999) *Phys. Rev. A*, **61**, 010301(R).
79 Meyer, D.A. (2000) *Phys. Rev. Lett.*, **85**, 2014.
80 van Enk, S.J. (2005) *Phys. Rev. A*, **72**, 064306.
81 van Enk, S.J. (2006) *Phys. Rev. A*, **74**, 026302.
82 Drezet, A. (2006) *Phys. Rev. A*, **74**, 026301.
83 Adcock, M.R.A., Høyer, P., and Sanders, B.C. (2009) *New J. Phys.*, **11**, 103035.
84 Gottesman, D. and Chuang, I. (1999) *Nature*, **402**, 390.
85 Lloyd, S. (1995) *Phys. Rev. Lett.*, **75**, 346.
86 Lloyd, S. and Braunstein, S.L. (1999) *Phys. Rev. Lett.*, **82**, 1784.
87 Bravyi, S. and Kitaev, A. (2005) *Phys. Rev. A*, **71**, 022316.
88 Sefi, S. and van Loock, P. (2010) arXiv:1010.0326 [quant-ph].
89 Braunstein, S.L. (2005) *Phys. Rev. A*, **71**, 055801.
90 Bartlett, S.D., Sanders, B.C., Braunstein, S.L., and Nemoto, K. (2002) *Phys. Rev. Lett.*, **88**, 097904.
91 Steane, A.M. (1996) *Phys. Rev. Lett.*, **77**, 793.
92 Knill, E. and Laflamme, R. (1997) *Phys. Rev. A*, **55**, 900.
93 Niset, J., Fiurášek, J., and Cerf, N.J. (2009) *Phys. Rev. Lett.*, **102**, 120501.
94 van Loock, P. (2010) *J. Mod. Opt.*, **57**, 1965.
95 Gottesmann, D. (1996) *Stabilizer Codes and Quantum Error Correction*, Caltech Ph.D. Thesis.
96 Gottesmann, D. (1996) *Phys. Rev. A*, **54**, 1862.
97 Cirac, J.I. and Zoller, P. (1995) *Phys. Rev. Lett.*, **74**, 4091.
98 Pellizzari, T., Gardiner, S.A., Cirac, J.I., and Zoller, P. (1995) *Phys. Rev. Lett.*, **75**, 3788.
99 Imamoglu, A., Awschalom, D.D., Burkard, G., DiVincenzo, D.P., Loss, D., Sherwin, M., and Small, A. (1999) *Phys. Rev. Lett.*, **83**, 4202.
100 Schmidt-Kaler, F., Häffner, H., Gulde, S., Riebe, M., Lancaster, G.P.T., Deuschle, T., Becher, C., Hänsel, W., Eschner, J., Roos, C.F., and Blatt, R. (2003) *Appl. Phys. B*, **77**, 789.
101 Riebe, M., Häffner, H., Roos, C.F., Hänsel, W., Benhelm, J., Lancaster, G.P.T., Körber, T.W., Becher, C., Schmidt-Kaler, F., James, D.F.V., and Blatt, R. (2004) *Nature*, **429**, 734.
102 Gulde, S., Riebe, M., Lancaster, G.P.T., Becher, C., Eschner, J., Häffner, H., Schmidt-Kaler, F., Chuang, I.L., and Blatt, R. (2003) *Nature*, **421**, 48.
103 Childs, A.M. and Chuang, I.L. (2000) *Phys. Rev. A*, **63**, 012306.
104 Kok, P., Munro, W.J., Nemoto, K., Ralph, T.C., Jonathan Dowling, P., and Milburn, G.J. (2007) *Rev. Mod. Phys.*, **79**, 135.
105 Braunstein, S.L. and van Loock, P. (2005) *Rev. Mod. Phys.*, **77**, 513–577.
106 Glauber, R.J. (1963) *Phys. Rev. Lett.*, **10**, 84.
107 Glauber, R.J. (1963) *Phys. Rev.*, **130**, 2529.
108 Glauber, R.J. (1963) *Phys. Rev.*, **131**, 2766.
109 Caves, C.M. (1980) *Phys. Rev. Lett.*, **45**, 75.
110 Yuen, H.P. (1976) *Phys. Rev. A*, **13**, 2226.
111 Mandel, L. and Wolf, E. (1995) *Optical Coherence and Quantum Optics*, Cambridge University Press, Cambridge.
112 Wigner, E.P. (1932) *Phys. Rev.*, **40**, 749.
113 Leonhardt, U. (1997) *Measuring the Quantum State of Light*, Cambridge University Press, Cambridge.
114 Weyl, H. (1950) *The Theory of Groups and Quantum Mechanics*, Dover Publications, Inc., New York.
115 O'Brien, J.L., Furusawa, A., and Vučkovic, J. (2009) *Nat. Photonics*, **3**, 687.
116 Simon, R. (2000) *Phys. Rev. Lett.*, **84**, 2726.
117 Werner, R.F. and Wolf, M.M. (2001) *Phys. Rev. Lett.*, **86**, 3658.

118 Williamson, J. (1936) *Am. J. Math.*, **58**, 141.

119 Adesso, G. and Illuminati, F. (2007) *J. Phys. A*, **40**, 7821.

120 Bogoliubov, N.N. (1947) *J. Phys.*, **11**, 23.

121 Reck, M., Zeilinger, A., Bernstein, H.J., and Bertani, P. (1994) *Phys. Rev. Lett.*, **73**, 58.

122 Lütkenhaus, N., Calsamiglia, J., and Suominen, K.-A. (1999) *Phys. Rev. A*, **59**, 3295.

123 Banaszek, K. (1999) *Phys. Lett. A*, **253**, 12.

124 Caruso, F., Eisert, J., Giovannetti, V., and Holevo, A.S. (2008) *New J. Phys.*, **10**, 083030.

125 Eisert, J., Scheel, S., and Plenio, M.B. (2002) *Phys. Rev. Lett.*, **89**, 137903.

126 Fiurášek, J. (2002) *Phys. Rev. Lett.*, **89**, 137904.

127 Giedke, G. and Cirac, J.I. (2002) *Phys. Rev. A*, **66**, 032316.

128 Cochrane, P.T., Milburn, G.J., and Munro, W.J. (2000) *Phys. Rev. A*, **62**, 062307.

129 Cerf, N.J. *et al.* (2005) *Phys. Rev. Lett.*, **95**, 070501.

130 Demkowicz-Dobrzański, R., Kuś, M., and Wódkiewicz, K. (2004) *Phys. Rev. A*, **69**, 012301.

131 van Loock, P. and Lütkenhaus, N. (2004) *Phys. Rev. A*, **69**, 012302.

132 Arthurs, E. and Kelly, J.L. Jr. (1965) *Bell. Syst. Tech. J.*, **44**, 725.

133 van Loock, P. (2002) *Fortschr. Phys.*, **50**, 1177.

134 Cerf, N.J., Adami, C., and Kwiat, P.G. (1998) *Phys. Rev. A*, **57**, R1477.

135 Kwiat, P.G. and Weinfurter, H. (1998) *Phys. Rev. A*, **58**, R2623.

136 Horodecki, R. *et al.* (2009) *Rev. Mod. Phys.*, **81**, 865.

137 Bruß, D. and Leuchs, G. (eds) (2007) *Lectures on Quantum Information*, Wiley-VCH Verlag GmbH, Berlin, chapter III.

138 Gühne, O. and Toth, G. (2009) *Phys. Rep.*, **474**, 1.

139 Toth, G. and Gühne, O. (2005) *Phys. Rev. A*, **72**, 022340.

140 Greenberger, D.M., Horne, M.A., Shimony, A., and Zeilinger, A. (1990) *Am. J. Phys.*, **58**, 1131.

141 Dür, W., Vidal, G., and Cirac, J.I. (2000) *Phys. Rev. A*, **62**, 062314.

142 Coffman, V., Kundu, J., and Wootters, W.K. (2000) *Phys. Rev. A*, **61**, 052306.

143 Mermin, N.D. (1990) *Phys. Rev. Lett.*, **65**, 1838.

144 Dür, W., Cirac, J.I., and Tarrach, R. (1999) *Phys. Rev. Lett.*, **83**, 3562.

145 Kwiat, P.G., Eberhard, P.H., Steinberg, A.M., and Chiao, R.Y. (1994) *Phys. Rev. A*, **49**, 3209.

146 Kwiat, P.G., Mattle, K., Weinfurter, H., and Zeilinger, A. (1995) *Phys. Rev. Lett.*, **75**, 4337.

147 Zeilinger, A., Horne, M.A., Weinfurter, H., and Zukowski, M. (1997) *Phys. Rev. Lett.*, **78**, 3031.

148 Pan, J.-W., Bouwmeester, D., Daniell, M., Weinfurter, H., and Zeilinger, A. (2000) *Nature*, **403**, 515.

149 Walther, P., Resch, K.J., Rudolph, T., Schenck, E., Weinfurter, H., Vedral, V., Aspelmeyer, M., Zeilinger, A. (2005) *Nature*, **434**, 169.

150 Nielsen, M.A. (2004) *Phys. Rev. Lett.*, **93**, 040503.

151 Browne, D.E. and Rudolph, T. (2005) *Phys. Rev. Lett.*, **95**, 010501.

152 Gross, D., Kieling, K., and Eisert, J. (2006) *Phys. Rev. A*, **74**, 042343.

153 Kieling, K., Rudolph, T., and Eisert, J. (2007) *Phys. Rev. Lett.*, **99**, 130501.

154 Eisert, J. and Plenio, M.B. (2003) *Int. J. Quant. Inf.*, **1**, 479.

155 Botero, A. and Reznik, B. (2003) *Phys. Rev. A*, **67**, 052311.

156 Ou, Z.Y., Pereira, S.F., Kimble, H.J., and Peng, K.C. (1992) *Phys. Rev. Lett.*, **68**, 3663.

157 Reid, M.D. (1989) *Phys. Rev. A*, **40**, 913.

158 Zhang, S.L. and van Loock, P. (2010) *Phys. Rev. A*. **82**, 062316.

159 Duan, L.-M., Giedke, G., Cirac, J.I., and Zoller, P. (2000) *Phys. Rev. Lett.*, **84**, 2722.

160 Giedke, G., Kraus, B., Lewenstein, M., and Cirac, J.I. (2001) *Phys. Rev. Lett.*, **87**, 167904.

161 van Loock, P. and Braunstein, S.L. (2000) *Phys. Rev. Lett.*, **84**, 3482.

162 Bowen, W.P., Lam, P.K., and Ralph, T.C. (2003) *J. Mod. Opt.*, **50**, 801.

163 Braunstein, S.L. and Kimble, H.J. (1998) *Phys. Rev. Lett.*, **80**, 869.

164 Braunstein, S.L. (1998) *Nature*, **394**, 47.
165 van Loock, P. and Furusawa, A. (2003) *Phys. Rev. A*, **67**, 052315.
166 Giedke, G., Kraus, B., Lewenstein, M., and Cirac, J.I. (2001) *Phys. Rev. A*, **64**, 052303.
167 Coelho, A.S. *et al.* (2009) *Science*, **326**, 823.
168 Menicucci, N.C., Flammia, S.T., and van Loock, P. (2010) arXiv:1007.0725 [quant-ph].
169 van Loock, P. Weedbrook, C., and Gu, M. (2007) *Phys. Rev. A*, **76**, 032321.
170 Bartlett, S.D. and Sanders, B.C. (2002) *Phys. Rev. A*, **65**, 042304.
171 Menicucci, N.C., van Loock, P., Gu, M., Weedbrook, C., Ralph, T.C., and Nielsen, M.A. (2006) *Phys. Rev. Lett.*, **97**, 110501.
172 Menicucci, N.C., Flammia, S.T., and Pfister, O. (2008) *Phys. Rev. Lett.*, **101**, 130501.
173 Menicucci, N.C., Ma, X., and Ralph, T.C. (2010) *Phys. Rev. Lett.*, **104**, 250503.
174 Menicucci, N.C. (2010) arXiv:1007.3434 [quant-ph].
175 Silberhorn, C. *et al.* (2001) *Phys. Rev. Lett.*, **86**, 4267.
176 Schori, C., Sørensen, J.L., and Polzik, E.S. (2002) *Phys. Rev. A*, **66**, 033802.
177 Bowen, W.P., Treps, N., Buchler, B.C., Schnabel, R., Ralph, T.C., Bachor, H.-A., Symul, T., and Lam, P.-K. (2003) *Phys. Rev. A*, **67**, 032302.
178 Villar, A.S. *et al.* (2005) *Phys. Rev. Lett.*, **95**, 243603.
179 Su, X. *et al.* (2006) *Opt. Lett.*, **31**, 1133.
180 Jing, J., Feng, S., Bloomer, R., and Pfister, O. (2006) *Phys. Rev. A*, **74**, 041804(R).
181 Wenger, J. *et al.* (2005) *Euro. Phys. J. D*, **32**, 391.
182 Takei, N., Lee, N., Moriyama, D., Neergaad-Nielsen, J.S., and Furusawa, A. (2006) *Phys. Rev. A*, **74**, 060101(R).
183 Sasaki, M. and Suzuki, S. (2006) *Phys. Rev. A*, **73**, 043807.
184 Mølmer, K. (2006) *Phys. Rev. A*, **73**, 063804.
185 Drever, R.W.P. *et al.* (1983) *Appl. Phys. B*, **31**, 97.
186 Neergaard-Nielsen, J.S., Nielsen, B.M., Hettich, C., Mølmer, K., and Polzik, E.S. (2006) *Phys. Rev. Lett.*, **97**, 083604.
187 Yoshino, K., Aoki, T., and Furusawa, A. (2007) *Appl. Phys. Lett.*, **90**, 041111.
188 Aoki, T., Takei, N., Yonezawa, H., Wakui, K., Hiraoka, T., Furusawa, A. and van Look, P. (2003) *Phys. Rev. Lett.*, **91**, 080404.
189 Yukawa, M. *et al.* (2008) *Phys. Rev. A*, **78**, 012301.
190 Su, X., Tan, A., Jia, X., Zhang, J., Xie, C., and Peng, K. (2007) *Phys. Rev. Lett.*, **98**, 070502.
191 Tan, A., Wang, Y., Jin, X., Su, X., Jia, X., Zhang, J., Xie, C., and Peng, K. (2008) *Phys. Rev. A.*, **78**, 013828.
192 Hyllus, P. and Eisert, J. (2006) *New J. Phys.*, **8**, 51.
193 Massar, S. and Popescu, S. (1995) *Phys. Rev. Lett.*, **74**, 1259.
194 Bouwmeester, D. *et al.* (1997) *Nature*, **390**, 575–579.
195 Braunstein, S.L. and Mann, A. (1995) *Phys. Rev. A*, **51**, R1727.
196 Calsamiglia, J. and Lütkenhaus, N. (2001) *Appl. Phys. B*, **72**, 67.
197 Braunstein, S.L. and Kimble, H.J. (1998) *Nature*, **394**, 840.
198 Murao, M., Jonathan, D., Plenio, M.B., and Vedral, V. (1999) *Phys. Rev. A*, **59**, 156.
199 Filip, R. (2004) *Phys. Rev. A*, **69**, 052301.
200 Zhao, Z., Zhang, A.-N., Zhou, X.-Q., Chen, Y.-A., Lu, C.-Y., Karlsson, A., and Pan, J.-W. (2005) *Phys. Rev. Lett.*, **95**, 030502.
201 Rarity, J.G., Tapster, P.R., Jakeman, E., Larchuk, T., Campos, R.A., Teich, M.C., and Saleh, B.E.A. (1990) *Phys. Rev. Lett.*, **65**, 1348.
202 Pan, J.-W., Bouwmeester, D., Weinfurter, H., and Zeilinger, A. (1998) *Phys. Rev. Lett.*, **80**, 3891.
203 Furusawa, A., Sørensen, J.L., Braunstein, S.L., Fuchs, C.A., Kimble, H.J., and Polzik, E.S. (1998) *Science*, **282**, 706.
204 Zhang, T.C., Goh, K.W., Chou, C.W., Lodahl, P., and Kimble, H.J. (2003) *Phys. Rev. A*, **67**, 033802.
205 Takei, N., Yonezawa, H., Aoki, T., and Furusawa, A. (2005) *Phys. Rev. Lett.*, **94**, 220502.
206 Takei, N., Aoki, T., Koike, S., Yoshino, K., Wakui, K., Yonezawa, H., Hiraoka, T., Mizuno, J., Takeoka, M., Ban, M., and

Furusawa, A. (2005) *Phys. Rev. A*, **72**, 042304.
207 Jia, X. *et al.* (2004) *Phys. Rev. Lett.*, **93**, 250503.
208 Hofmann, H.F., Ide, T., Kobayashi, T., and Furusawa, A. (2000) *Phys. Rev. A*, **62**, 062304.
209 Ide, T., Hofmann, H.F., Kobayashi, T., and Furusawa, A. (2001) *Phys. Rev. A*, **65**, 012313.
210 Braunstein, S.L., Fuchs, C.A., and Kimble, H.J. (2000) *J. Mod. Opt.*, **47**, 267.
211 Braunstein, S.L., Fuchs, C.A., Kimble, H.J., and van Loock, P. (2001) *Phys. Rev. A*, **64**, 022321.
212 Hammerer, K., Wolf, M.M., Polzik, E.S., and Cirac, J.I. (2005) *Phys. Rev. Lett.*, **94**, 150503.
213 Arthurs, E. and Kelly, J.L. Jr. (1965) *Bell. Syst. Tech. J.*, **44**, 725.
214 van Loock, P., Braunstein, S.L., and Kimble, H.J. (2000) *Phys. Rev. A*, **62**, 022309.
215 Yonezawa, H., Braunstein, S.L., and Furusawa, A. (2007) *Phys. Rev. Lett.*, **99**, 110503.
216 Yukawa, M., Benichi, H., and Furusawa, A. (2008) *Phys. Rev. A*, **77**, 022314.
217 Grosshans, F. and Grangier, P. (2001) *Phys. Rev. A*, **64**, 010301(R).
218 Takeno, Y., Yukawa, M., Yonezawa, H., and Furusawa, A. (2007) *Opt. Express*, **15**, 4321.
219 Vahlbruch, H., Mehmet, M., Chelkowski, S., Hage, B., Franzen, A., Lastzka, N., Goßler, S., Danzmann, K., and Schnabel, R. (2008) *Phys. Rev. Lett.*, **100**, 033602.
220 Koike, S., Takahashi, H., Yonezawa, H., Takei, N., Braunstein, S.L., Aoki, T., and Furusawa, A. (2006) *Phys. Rev. Lett.*, **96**, 060504.
221 van Loock, P. and Braunstein, S.L. (2001) *Phys. Rev. Lett.*, **87**, 247901.
222 Yonezawa, H., Aoki, T., and Furusawa, A. (2004) *Nature*, **431**, 430.
223 Boschi, D., Branca, S., Martini, D.F., Hardy, L., and Popescu, S. (1998) *Phys. Rev. Lett.*, **80**, 1121–1125.
224 Nielsen, M. A., Knill, E., and Laflamme, R. (1998) *Nature*, **396**, 52–55
225 Marcikic, I., Riedmatten, D.H., Tittel, W., Zbinden, H., and Gisin, N. (2003) *Nature*, **421** 509–513.
226 Jing, J. *et al.* (2003) *Phys. Rev. Lett.*, **90**, 167903.
227 Barrett, M.D. *et al.* (2004) *Nature*, **429**, 737.
228 Ban, M. (2004) *Phys. Rev. A*, **69**, 054304.
229 Tan, S.M. (1999) *Phys. Rev. A*, **60**, 2752.
230 Kitaev, A. (2003) *Ann. Phys.*, **303**, 2.
231 Raussendorf, R. and Harrington, J. (2007) *Phys. Rev. Lett.*, **98**, 190504.
232 Raussendorf, R., Harrington, J., and Goyal, K. (2007) *New J. Phys.*, **9**, 199.
233 Fowler, A.G., Stephens, A.M., and Groszkowski, P. (2009) *Phys. Rev. A*, **80**, 052312.
234 Fowler, A.G. and Goyal, K. (2009) *Quantum Infom. Comput.*, **9**, 721.
235 Fowler, A.G. *et al.* (2010) *Phys. Rev. Lett.*, **104**, 180503.
236 Devitt, S.J. *et al.* (2009) *New J. Phys.*, **11**, 083032.
237 Braunstein, S.L. (1998) *Phys. Rev. Lett.*, **80**, 4084.
238 Lloyd, S. and Slotine, J.-J.E. (1998) *Phys. Rev. Lett.*, **80**, 4088.
239 Aoki, T., Takahashi, G., Kajiya, T., Yoshikawa, J., Braunstein, S.L., van Loock, P., and Furusawa, A. (2009) *Nat. Phys.*, **5**, 541.
240 Cory, D.G. *et al.* (1998) *Phys. Rev. Lett.*, **81**, 2152–2155.
241 Leung, D. *et al.* (1999) *Phys. Rev. A*, **60**, 1924–1943.
242 Knill, E., Laflamme, R., and Milburn, G.J. (2001) *Nature*, **409**, 46.
243 Knill, E. *et al.* (2001) *Phys. Rev. Lett.*, **86**, 5811–5814.
244 Boulant, N. *et al.* (2005) *Phys. Rev. Lett.*, **94**, 130501.
245 Chiaverini, J. *et al.* (2004) *Nature*, **432**, 602–605.
246 O'Brien, J.L. *et al.* (2005) *Phys. Rev. A*, **71**, 060303.
247 Lu, C.-Y. *et al.* (2008) *Proc. Natl. Acad. Sci. USA*, **105**, 11050–11054.
248 Pittman, T.B., Jacobs, B.C., and Franson, J.D. (2005) *Phys. Rev. A*, **71**, 052332.
249 Gottesman, D., Kitaev, A., and Preskill, J. (2001) *Phys. Rev. A*, **64**, 012310.
250 Heersink, J. *et al.* (2006) *Phys. Rev. Lett.*, **96**, 253601.

251 Dong, R. *et al.* (2008) *Nat. Phys.*, **4**, 919–923.

252 Hage, B. *et al.* (2008) *Nat. Phys.*, **4**, 915–918.

253 Niset, J., Andersen, U. L., and Cerf, N.J. (2008) *Phys. Rev. Lett.*, **101**, 130503.

254 Nielsen, M.A. (1999) *Phys. Rev. Lett.*, **83**, 436.

255 Kwiat, P.G., Barraza-Lopez, S., Stefanov, A., and Gisin, N. (2001) *Nature*, **409**, 1014.

256 Pan, J.-W., Simon, C., Brukner, C., and Zeilinger, A. (2001) *Nature*, **410**, 1067.

257 Yamamoto, T., Koashi, M., Özdemir, S.K., and Imoto, N. (2003) *Nature*, **421**, 343.

258 Reichle, R., Leibfried, D., Knill, E. *et al.* (2006) *Nature*, **443**, 838.

259 Franzen, A., Hage, B., DiGuglielmo, J., Fiurášek, J., and Schnabel, R. (2006) *Phys. Rev. Lett.*, **97**, 150505.

260 Hage, B., Franzen, A., DiGuglielmo, J., Marek, P., Fiurášek, J., and Schnabel, R. (2007) *New J. Phys.*, **9**, 227.

261 Opatrný, T., Kurizki, G., and Welsch, D.-G. (2000) *Phys. Rev. A*, **61**, 032302.

262 Olivares, S., Paris, M.G.A., and Bonifacio, R. (2003) *Phys. Rev. A*, **67**, 032314.

263 Kitagawa, A., Takeoka, M., Sasaki, M., and Chefles, A. (2006) *Phys. Rev. A*, **73**, 042310.

264 Takahashi, H., Neergaard-Nielsen, J.S., Takeuchi, M., Takeoka, M., Hayasaka, K., Furusawa, A., and Sasaki, M. (2010) *Nat. Photonics*, **4**, 178.

265 Pan, J.-W., Gasparoni, S., Ursin, R., Weihs, G., and Zeilinger, A. (2003) *Nature*, **423**, 417.

266 Fiurášek, J., Marek, P., Filip, R., and Schnabel, R. (2007) *Phys. Rev. A*, **75**, 050302(R).

267 Takahashi, H., Wakui, K., Suzuki, S., Takeoka, M., Hayasaka, K., Furusawa, A., and Sasaki, M. (2008) *Phys. Rev. Lett.*, **101**, 233605.

268 Bartlett, S.D. and Munro, W.J. (2003) *Phys. Rev. Lett.*, **90**, 117901.

269 Knill, E. (2003) *Phys. Rev. A*, **68**, 064303.

270 Scheel, S. and Lütkenhaus, N. (2004) *New J. Phys.*, **6**, 51.

271 Eisert, J. (2005) *Phys. Rev. Lett.*, **95**, 040502.

272 Uskov, D.B. *et al.* (2009) *Phys. Rev. A*, **79**, 042326.

273 O'Brien, J.L., Pryde, G.J., White, A.G., Ralph, T.C., and Branning, D. (2003) *Nature*, **426**, 264.

274 Ralph, T.C., Langford, N.K., Bell, T.B., and White, A.G. (2002) *Phys. Rev. A*, **65**, 062324.

275 Yoshikawa, J., Hayashi, T., Akiyama, T., Takei, N., Huck, A., Andersen, U.L., and Furusawa, A. (2007) *Phys. Rev. A*, **76**, 060301(R).

276 Filip, R., Marek, P., and Andersen, U.L. (2005) *Phys. Rev. A*, **71**, 042308.

277 Vaidman, L. (1994) *Phys. Rev. A*, **49**, 1473.

278 Zhou, X., Leung, D.W., and Chuang, I.L. (2000) *Phys. Rev. A*, **62**, 052316.

279 Lance, A.M. *et al.* (2006) *Phys. Rev. A*, **73**, 041801(R).

280 Lam, P.K., Ralph, T.C., Huntington, E.H., and Bachor, H.A. (1997) *Phys. Rev. Lett.*, **79**, 1471.

281 Buchler, B., Lam, P.K., Bachor, H.A., Andersen, U.L., and Ralph, T.C. (2001) *Phys. Rev. A*, **65**, 011803(R).

282 Glöckl, O., Andersen, U.L., Filip, R., Bowen, W.P., and Leuchs, G. (2006) *Phys. Rev. Lett.*, **97**, 053601.

283 Suzuki, S., Yonezawa, H., Kannari, F., Sasaki, M., and Furusawa, A. (2006) *Appl. Phys. Lett.* **89**, 061116.

284 Yoshikawa, J., Miwa, Y., Huck, A., Andersen, U.L., van Loock, P., and Furusawa, A. (2008) *Phys. Rev. Lett.*, **101**, 250501.

285 Caves, C.M., Thorne, K.S., Drever, R.W.P., Sandberg, V.D., and Zimmermann, M. (1980) *Rev. Mod. Phys.*, **52**, 341; Bocko, M.F. and Onofrio, R. (1996) *Rev. Mod. Phys.*, **68**, 755.

286 Bocko, M.F. and Onofrio, R. (1996) *Rev. Mod. Phys.*, **68**, 755.

287 Pereira, S.F., Ou, Z.Y., and Kimble, H.J. (1994) *Phys. Rev. Lett.*, **72**, 214.

288 Zhang, J. and Braunstein, S.L. (2006) *Phys. Rev. A*, **73**, 032318.

289 Wilde, M.M., Krovi, H., and Brun, T.A. (2007) *Phys. Rev. A*, **75**, 060303(R).

290 Holland, M.J., Collet, M.J., and Walls, D.F. (1990) *Phys. Rev. A*, **42**, 2995.

291 Poizat, J.-P., Roch, J.-F., and Grangier, P. (1994) *Ann. Phys.* (Paris) **19**, 265.

292 Prevedel, R., Walther, P., Tiefenbacher, F., Böhi, P., Kaltenbaek, R., Jennewein, T., and Zeilinger, A. (2007) *Nature*, **445**, 65.

293 Ohliger, M., Kieling, K., and Eisert, J. (2010) *Phys. Rev. A.*, **82**, 042336.

294 Ukai, R., Yoshikawa, J., Iwata, N., van Loock, P., and Furusawa, A. (2010) *Phys. Rev. A*, **81**, 032315.

295 Menicucci, N.C., Flammia, S.T., and Pfister, O. (2008) *Phys. Rev. Lett.*, **101**, 130501.

296 Menicucci, N.C. *et al.* (2007) *Phys. Rev. A*, **76**, 010302(R).

297 Gu, M., Weedbrook, C., Menicucci, N.C., Ralph, T.C., and van Loock, P. (2009) *Phys. Rev. A*, **79**, 062318.

298 Ukai, R., Iwata, N., Shimokawa, Y., Armstrong, S.C., Politi, A., Yoshikawa, J., van Loock, P., and Furusawa, A. (2010) arXiv:1001.4860 [quant-ph].

299 Miwa, Y. *et al.* (2009) *Phys. Rev. A*, **80**, 050303(R).

300 Nielsen, M.A. (2006) *Rep. Math. Phys.*, **57**, 147.

301 Lvovsky, A.I. and Raymer, M.G. (2009) *Rev. Mod. Phys.*, **81**, 299.

302 Lvovsky, A.I. (2004) *J. Opt. B*, **6**, S556.

303 Menicucci, N.C., Flammia, S.T., Zaidi, H. and Pfister, O. (2007) *Phys. Rev. A*, **76**, 010302.

304 van Loock, P. (2007) *J. Opt. Soc. Am. B*, **24**, 340.

305 Jain, N. *et al.* (2010) *Opt. Express*, **18**, 18254.

306 Puentes, G. *et al.* (2009) *Phys. Rev. Lett.*, **102**, 080404.

307 Lvovsky, A.I., Hansen, H., Aichele, T., Benson, O., Mlynek, J., and Schiller, S. (2001) *Phys. Rev. Lett.*, **87**, 050402.

308 Lund, A.P. *et al.* (2008) *Phys. Rev. Lett.*, **100**, 030503.

309 Ourjoumtsev, A. *et al.* (2007) *Nature*, **448**, 784.

310 Savage, C.M., Braunstein, S.L., and Walls, D.F. (1990) *Opt. Lett.*, **15**, 628.

311 Schleich, W.P. (2001) *Quantum Optics in Phase Space*, Wiley-VCH Verlag GmbH, Berlin.

312 Zavatta, A., Viciani, S., and Bellini, M. (2004) *Science*, **306**, 660.

313 Wakui, K., Takahashi, H., Furusawa, A., and Sasaki, M. (2007) *Opt. Express*, **15**, 3568.

314 Yurke, B. and Stoler, D. (1987) *Phys. Rev. A*, **36**, 1955–1958.

315 Dakna, M., Anhut, T., Opatrny, T., Knoell, L., and Welsch, D.-G. (1997) *Phys. Rev. A*, **55**, 3184.

316 Lvovsky, A.I., Hansen, H., Aichele, T., Benson, O., Mlynek, J., and Schiller, S. (2001) *Phys. Rev. Lett.*, **87**, 050402.

317 Zavatta, A., Viciani, S., and Bellini, M. (2004) *Phys. Rev. A*, **70**, 053821.

318 Ourjoumtsev, A., Tualle-Brouri, R., and Grangier, P. (2006) *Phys. Rev. Lett.*, **96**, 213601.

319 Lvovsky, A.I. and Babichev, S.A. (2002) *Phys. Rev. A*, **66**, 011801(R).

320 Ourjoumtsev, A., Tualle-Brouri, R., Laurat, J., and Grangier, P. (2006) *Science*, **312**, 83.

321 Mabuchi, H., Polzik, E.S., and Kimble, H.J. (1994) *J. Opt. Soc. Am. B*, **11**, 2023.

322 Aoki, T., Takahashi, G., and Furusawa, A. (2006) *Opt. Express*, **14**, 6930–6935.

323 Polzik, E.S. *et al.* (1992) *Appl. Phys. B*, **55**, 279 .

324 Neergaard-Nielsen, J.S., Melholt Nielsen, B., Takahashi, H., Vistnes, A.I., and Polzik, E.S. (2007) *Opt. Express*, **15**, 7940.

325 Wang, X. (2002) *J. Phys. A: Math. Gen.*, **35**, 165.

326 van Enk, S.J. and Hirota, O. (2001) *Phys Rev. A*, **64**, 022313.

327 Hirota, O. and Sasaki, M. (2001) arXiv: 0101018 [quant-ph].

328 Shchukin, E. and Vogel, W. (2005) *Phys. Rev. Lett.*, **95**, 230502.

329 Miranowicz, A. and Piani, M. (2006) *Phys. Rev. Lett.*, **97**, 058901.

330 Häseler, H., Moroder, T., and Lütkenhaus, N. (2008) *Phys. Rev. A*, **77**, 032303.

331 Rigas, J., Gühne, O., and Lütkenhaus, N. (2006) *Phys. Rev. A*, **73**, 012341.

332 Wittmann, C. *et al.* (2010) *Opt. Express*, **18(5)**, 449.

333 Gomes, R.M. *et al.* (2009) *Proc. Natl. Acad. Sci. USA*, **106**, 21517.

334 Ide, T., Hofmann, H.F., Kobayashi, T., and Furusawa, A. (2001) *Phys. Rev. A*, **65**, 012313.

335 Massar, S. and Popescu, S. (1995) *Phys. Rev. Lett.*, **74**, 1259.
336 Wang, X. and Zanardi, P. (2002) *Phys. Rev. A*, **65**, 032327.
337 Lloyd, S. (2003) *Quantum Information with Continuous Variables* (eds S.L. Braunstein, and A.K. Pati), Kluwer Academic Publisher, part I, chapter 5; arXiv: 0008057 [quant-ph] (2000).
338 Spiller, T.P., Nemoto, K., Braunstein, S.L., Munro, W.J., van Loock, P., and Milburn, G.J. (2006) *New J. Phys.*, **8**, 30.
339 Cirac, J.I. and Zoller, P. (1995) *Phys. Rev. Lett.*, **74**, 4091.
340 Luis, A. (2001) *J. Phys. A*, **34**, 7677.
341 Glancy, S., Vasconcelos, H.M., and Ralph, T.C. (2004) *Phys. Rev. A*, **70**, 022317.
342 Glancy, S. and Knill, E. (2006) *Phys. Rev. A*, **73**, 012325.
343 Pirandola, S. *et al.* (2004) *Europhys. Lett.*, **68**, 323.
344 Ghose, S. and Sanders, B.C. (2007) *J. Mod. Opt.*, **54**, 855.

Index

a

absorption 304
ADC, *see* analogue-to-digital converter
addition modulo 2 56
alphabet 41, 44, 47, 48
amplitude damping channel 26, 115
amplitude quadrature 237
analogue-to-digital converter 164
ancilla system 23, 24, 28, 29, 114
annihilation operator 20, 84, 89, 91, 94, 96, 183, 232, 233, 260
atom 51, 70, 71, 79, 99, 210, 299, 301, 302, 319
atomic system
– dipole transition 302
– two-level system 302
authentication 43
avalanche photodiode 240, 308, 314

b

Baker-Campbell-Hausdorff (BCH) formula 54, 59, 96, 97
basis
– Hermitian 11, 27
– localized 307
– unitary 25, 28, 29, 38, 53, 115, 116, 122, 272, 281, 282
BB84 protocol 42, 43
BCH, *see* Baker-Campbell-Hausdorff
beam splitter
– asymmetric 183–186, 205, 236, 256, 262
– homodyne detection 40, 81, 100, 165, 175, 189, 226, 254, 256, 262, 287, 292, 301, 305
– input-output relation 249, 254, 261
– symmetric 132, 144, 173, 183–186, 205, 227, 236, 256, 262
– transmittance 110, 111, 173, 197, 232, 254–256, 287, 305
Bell basis 36, 75, 76, 120, 128, 147, 150, 269
Bell measurement 39–41, 48, 53, 74, 75, 117, 120, 121, 180, 182, 183, 187, 189, 199, 205, 212, 245, 247, 253, 266–270, 283, 313, 314
Bell state 33, 34, 37, 39–41, 48, 74, 121, 128, 129, 131–133, 135, 142, 180, 182, 187, 299, 310–312
bipartite mixed state 37
bipartite pure state 37
birefringence 140
biseparable state 130
bit-flip 55, 60, 63, 64, 66–68, 218, 220, 221
bit-flip error 63, 64, 66
Bloch
– sphere 12, 13, 19, 21, 63, 99, 100
– vector 12
boson 54, 79, 86, 87, 109, 259
boundary condition
– periodic 85
BS, *see* beam splitter

c

cascade 273, 274, 278
cat state 210, 300–309, 318
cavity 163, 165, 174, 205, 211, 227, 240, 254, 255, 262, 287, 302, 304–308, 313
– Hamiltonian 302
– input-output relation 254
– mode function 306, 307
– quality 211, 255
– Wigner function 254, 304, 306–308
channel 23–26, 114–116
– depolarizing 217, 223
– discrete 3, 4, 64, 66, 218, 223, 225
– noiseless 48
– product 25, 29, 68, 200
characteristic function 95–97

Quantum Teleportation and Entanglement. Akira Furusawa, Peter van Loock
Copyright © 2011 WILEY-VCH Verlag GmbH & Co. KGaA, Weinheim
ISBN: 978-3-527-40930-3

circuit
– quantum 40, 49, 52, 69, 74, 75, 210, 220, 221, 252, 266
CK, *see* cross-Kerr nonlinearity
classical communication 7, 32, 37–41, 45, 47, 50, 130, 180, 210, 231, 234, 235, 237, 238, 245, 314
classical computer 50, 56, 121
classical state 82, 97, 260, 285, 303, 306
classicality 97, 189, 210, 285, 295, 303
classically correlated 34
Clifford group 19, 20, 40, 57, 132, 284
Clifford parallelism 273, 283
cloning 6–8, 10, 30, 40, 42, 45, 62, 63, 120, 179, 183–186, 196–202, 204, 210, 211, 214
cluster state 3, 53, 127, 131, 132, 138–142, 154, 155, 157, 159, 160, 170–178, 260, 271–285, 291–297, 320–322
CNOT gate 40, 55, 56, 60, 63, 70, 72–76, 248–252
code
– quantum 218
– repetition 64, 67, 68, 218, 318
– stabilizer 67–69, 103, 120, 218, 219
coherence 9, 73, 82, 83, 222
coherent state
– mean photon number 90
– nonlinear 112, 120, 200, 255, 293, 301, 304
– P function 192
coherent superposition 9, 11, 218
coincidence 135, 138, 181–183, 187, 188, 221
commutation relation 14, 86–88, 103, 104, 109, 163
– bosonic 109
commutator 14, 25, 54, 59, 87, 107, 113, 118, 147, 316, 318
complete positivity 23
completely positive map 148
– Gaussian 148
completely positive trace-decreasing (CPTD) map 23, 28, 29, 31, 114, 116
completely positive trace-preserving (CPTP) map 9, 23–26, 29, 66, 114, 117
completely positive unity-preserving (CPUP) map 25, 26, 116
completeness relation 90
complexity 50, 69
composability 111
composite system 24, 28, 316
computational basis 13, 16, 52, 56, 71, 100, 218, 272, 274, 281, 292
concurrence 36
conditional probability 48
conditional variance 261, 264, 266
configuration
– space 208, 223
– state 208, 211, 223, 255, 304
connection 37, 41, 46, 101, 127, 129
continuous variables 40, 148, 203, 204, 223, 253, 259, 284
continuous wave 87, 107, 199, 200, 211, 262, 287, 305
control qubit 250, 251
convex sum 34
cooling 76
coordinate
– orthogonal 90
– spherical 12
correlation
– degree of 33, 163, 208, 211, 214
– matrix 103–107, 144–146, 149, 154
Coulomb gauge 84
coupling
– deterministic 292
– effective 122, 280, 292, 302
– mode 122, 280, 287, 292, 294, 302, 317
– strong 122
covariance matrix 103, 118
CPTD, *see* completely positive trace-decreasing
CPTP, *see* completely positive trace-preserving
CPUP, *see* completely positive unity-preserving
creation operator 71, 109, 110, 303
criterion 35, 37, 121, 128, 146–149, 154, 167, 179, 211, 265, 312
– negative partial transpose (npt) 148, 149, 154
– partial transpose 35–37, 128, 146, 148, 149, 154
cross-Kerr nonlinearity 122
cryptography 42, 50
CSIGN 247
current fluctuations 190, 192
CV experiment 107, 236, 239, 300, 306, 308
CV graph state 142, 154–157, 159, 172
CW, *see* continuous wave

d

decoherence 235, 237, 252, 254
– independent 237
decomposition
– orthogonal 11, 114, 311
– polar 86
– spectral 11

degeneracy 160
dense coding 48, 49, 204
density matrix 35, 309, 310
– reduced 310
density operator 7, 9, 11, 18, 23, 24, 26, 27, 29, 32, 34–36, 43, 64, 104, 106, 128, 148, 152, 233, 235
– reduced 24, 32, 36, 43, 64
– thermal 106
depolarizing channel 223
Deutsch-Jozsa algorithm 50, 52
discrete modes 84
dispersion 85
dispersion relation 85
displacement operator 17, 89, 94, 269, 284
distillability 128
distillation 7, 44, 45, 48, 69, 217, 218, 223, 231–233, 235–241
distillation protocol 217, 223, 237
distribution, Gaussian 290, 303, 308, 312
dual-rail encoding 99, 122, 123, 247, 248, 318

e

efficiency 121, 141, 142, 191–195, 201, 205, 226, 247, 248, 251, 252, 256, 304–306
eigenbasis 11, 27, 147
eigenstate 12, 13, 15–17, 33, 52, 59, 89, 94, 100–102, 155, 171, 291, 319
eigenvalue 10, 11, 16, 21, 27, 32–35, 37, 67, 68, 89, 101, 104–107, 120, 128, 130, 142, 145, 146, 150, 155–157, 168, 207, 219, 291, 302
eigenvector 67, 68, 128, 219
Einstein-Podolsky-Rosen (EPR)
– beam 164, 165, 189–193, 195, 196, 313, 314
– correlation 160–162, 164–166, 300, 313
– state 34, 142, 160, 188, 189, 211, 267, 268
Ekert protocol 7
electric field 83, 85–88, 90
electro-optic modulator 213, 226, 227, 253, 255, 262, 263, 277, 286
electromagnetic field 82–87, 89, 90, 107, 160, 189, 203
– Hamiltonian 86
– mode expansion 87
– photon 83, 84, 86, 89, 107, 160
– radiation 82
– wave equation 83
electronic state 71, 73
energy
– resonance 70
– total 80
– vibrational 70
– zero-point 13
entanglement 31–38, 127–178
– bipartite 31, 32, 34, 36, 37, 127, 128, 130, 143, 144, 146, 149, 154, 196–198, 203, 204, 210, 310, 311
– partial transposition 35, 36, 128, 148, 149, 311, 312
– two-party 34, 128, 129, 150, 151, 236
– witness 31, 34–37, 127–130, 132, 142, 146–151, 154, 176, 219, 220, 311
entanglement distillation 7, 44, 45, 69, 217, 218, 231–233, 235–241
entropy
– classical 32
– von Neumann 12, 32, 36, 47, 143, 145
EOM, *see* electro-optic modulator
EPR, *see* Einstein-Podolsky-Rosen
error, bit-flip 63, 64, 66, 67, 218, 221
excitation
– energy 13
– thermal 103, 105, 106

f

Fourier transform
– discrete 15, 284
– quantum 15, 17, 50, 96, 267, 281, 282, 284, 292, 293
function
– balanced 256, 306
– constant 84

g

Gaussian computation 271, 282
Gaussian qumode gates 252
Gaussian unitaries 57, 98, 105, 113, 119, 159
GHZ, *see* Greenberger-Horne-Zeilinger
GKP (Gottesman, Kitaev, and Preskill) 300, 315, 318–321
Gottesmann-Knill theorem 56, 59, 60, 120
graph state 38, 69, 102, 127, 131, 132, 141, 142, 154–157, 159, 172
Greenberger-Horne-Zeilinger (GHZ) state 130, 131, 135–137, 150, 154, 167, 168, 170, 197, 204, 208

h

Hadamard
– beam splitter 40, 66, 99, 100, 221
– gate 15, 40, 55, 98, 99, 121, 131, 221, 272, 284, 303, 318
– transformation 13, 100, 140, 274

half beam splitter 133, 136, 137, 151, 160, 163, 164, 175, 181, 183, 189, 197–199, 201, 202, 205, 206, 211, 212, 227, 236–238, 240, 292, 305, 306
half wave plate 133, 135–138, 140, 188, 220–222, 227, 235, 236, 249, 251, 253, 256, 262, 277, 305
Hamiltonian
– approximate 54, 55, 57, 292, 316
– decomposition 54, 57, 109, 316
– electromagnetic field 86
– Hermitian 13
– hybrid 300, 315
– interaction 54, 91, 109, 315
– light-matter interaction 315
– matrix 54, 55
harmonic oscillator 4, 13, 83, 86, 89
– coherent state 89
– number state 13
– quantum 4, 13, 83, 86, 89
HBS, *see* half beam splitter
homodyne detection
– beam splitter 40, 81, 100, 165, 175, 189, 226, 254, 256, 262, 287, 292, 301, 305
– local oscillator 81, 161, 175, 192, 225, 256, 262, 286, 292, 305
– quadrature 81, 165, 169, 189, 192, 212, 214, 224, 225, 254, 256, 283, 287, 292, 295, 300, 307
– squeezed light 300
horseshoe cluster 276, 277, 279
HWP, *see* half wave plate
hybrid entanglement 32, 44, 299, 310, 311
hybrid Hamiltonian 300, 315
hybrid quantum computing 315–322

i

inequality, Schwarz 147, 153
input-output relation
– beam splitter 249, 254, 261
– cavity 254
interaction Hamiltonian 54, 91, 109, 315
– approximate 54
interaction, two-particle 51
ion
– motional state 76
– phase gate 56–59, 75, 76, 248, 267, 268, 283–285, 317, 319–321
– trap 70, 71, 223
– two-qubit gate 53, 247, 274–277
– wavefunction 312

j

joint measurement 38, 199, 205, 245
joint probability 43

k

Kerr effect 109, 112
Kerr nonlinearities 247
key 3, 6, 7, 30, 41–44, 48, 50, 230, 312, 314
– exchange 43
– transmission 7, 42
Kraus operator 23, 25, 27, 66, 115, 116

l

Langevin equation 25
laser
– control 205, 255, 262, 305
– field 82, 89, 160
– single-mode 226, 287
leakage 307
Lie algebra 57, 318
light
– frequency of 163, 223
– polarization 51, 79, 83, 90, 99, 107, 133, 300
– speed of 7, 40, 46, 83, 107
– wavelength of 262
light source 174, 300
linear ion trap 223
linear optical element 51, 122, 317
linear optics 79, 100, 112, 116, 117, 120, 122, 158, 172, 182, 223, 233, 246, 249, 266
linear unitary Bogoliubov (LUBO) transformation 110–114, 119, 122, 143, 158, 254, 272, 292–294
local measurement 53, 237, 238, 292, 294
local observable 34
local operation 32, 37, 45, 46, 130, 203, 231
local oscillator 80, 81, 118, 119, 161, 164, 170, 174, 175, 190, 192, 205, 212, 225–227, 240, 253, 255–257, 262, 263, 284, 286, 292, 305, 308, 309
logic circuit 279
logic gate 4, 273
lossy channel 114, 118, 120
LUBO, *see* linear unitary Bogoliubov transformation

m

Mach-Zehnder interferometer 183, 185, 261, 262, 287
macroscopic superposition 302
magnetic field 82–87, 89, 90, 107, 160, 189, 203
magnetic resonance 70

magnetization 83
map, completely positive 9, 23–25, 148
Markovian approximation 25
master equation 25
matrix
– density 32, 35, 309, 310
– generator 132, 155, 158
– Pauli 12, 274, 318
– reduced density 32, 310
– rotation 55, 103, 157, 173
Maxwell equation 83, 84, 87
measurement
– exchange 43
– minimal 30, 218
– non-selective 26, 29
– selective 26, 29
measurement-induced nonlinearities 123
measurement outcome 27, 28, 30, 38, 53, 227, 254, 256, 273, 282, 321
message 3, 43, 47
mixing 80, 81, 110, 190, 212
mixture 11, 34, 106, 115, 152, 153
– separable 34, 152
– statistical 11
mode
– bosonic 79, 259
– cavity 163, 174, 211, 227, 254, 255, 262, 287, 302, 304–307
– expansion 87
– function 84, 85, 306, 307
model
– measurement-based 52, 53, 217, 271, 284
momentum
– conjugate 14, 16, 59, 89, 160, 285, 291
– electron 82, 169
multipartite entanglement 127, 129–132, 144, 196, 197
mutual information 47, 48

n

Naimark extension 29, 116, 117
negative-frequency part 84
negativity 36–38, 97, 104, 146, 232, 241, 308, 312
network 6, 45, 112, 150, 156, 159, 172, 179, 197, 203, 204, 209, 223, 249, 251
nine-qubit code 66, 218, 219, 223
no-cloning theorem 6, 8, 30, 62, 196
nonclassical
– characteristic function 97
– entanglement 34, 42, 82, 136, 179, 210, 218, 230, 304
– state 97, 303, 306
nondegenerate optical parametric amplifier or oscillator 144, 160
nonlinear optics 79, 120
nonlocality 34
NOPO, *see* nondegenerate optical parametric amplifier or oscillator
normalization 10, 14, 85, 95, 251, 310
NOT gate 40, 55, 56, 60, 63, 70, 72–74, 76, 221, 248–252, 259
NSS gate 247, 297, 322
nuclear magnetic resonance 70
number operator 13, 87–89
number state 13, 14, 71, 251, 303, 304, 307
– Wigner function 303, 304, 307

o

observable 4, 5, 8, 10–17, 19, 22, 25–27, 34, 35, 82, 88, 118, 146, 147, 150, 176, 260, 281, 282, 285
– classical 4, 5, 8, 15, 82, 118, 260, 285
one-time pad 43
one-way quantum computation 53, 279, 284, 292, 295, 296
OPA, *see* optical parametric amplifier
operator
– annihilation 20, 71, 84, 86, 89, 91, 94, 96, 109, 110, 183, 232, 233, 260, 302
– computation 16, 18, 54, 56, 100, 109, 131, 172, 282, 284
– creation 71, 84, 86, 91, 96, 109, 110, 302, 303
– density 7, 9, 11, 18, 23, 24, 26, 27, 29, 32, 34–36, 43, 64, 104, 106, 128, 148, 152, 192, 233, 235
– expansion 17, 88, 89, 301
– function 17, 95–97, 107, 129, 148, 192, 312
– Hamilton 13, 18, 21, 54, 57, 86, 91, 92, 109, 114, 260, 284, 292, 302, 315, 316
– Hermitian 11, 13, 14, 27, 35, 83, 84, 89, 101, 111, 157
– position 20, 65
– projection 27
– symmetrized 96
– unitary 18, 19, 27, 54, 122, 272, 302
OPO, *see* optical parametric oscillator
optical experiments 218
optical fiber 3, 45, 112, 254
optical parametric amplifier (OPA) 90, 92, 238, 301, 304
optical parametric oscillator (OPO) 144, 159, 160, 162–164, 174, 175, 190, 197, 200, 201, 205, 211, 212, 226, 227, 237, 238, 240, 241,

253, 255, 262, 286, 287, 293, 295, 304–309, 313, 314
optical QEC 217
optical quantum computation 121–123
oscillator, harmonic 4, 13, 83, 86, 89

p
parametric amplifiers 237
parametric down conversion (PDC) 79, 127, 133, 134, 138, 220, 222, 261, 303, 304
partial trace 7
partial transpose 35–37, 128, 146, 148, 149, 154, 311, 312
passive transformation 110, 111, 113, 158
Paul trap 70
Pauli
– channel 26, 64
– group 67
– matrices 12, 274, 318
– operator 13, 17, 19, 22, 33, 40, 55–57, 129, 131, 301, 302, 319
PBS, *see* polarization beam splitter
PDC, *see* parametric down conversion
periodic boundary condition 85
periodically-poled KTiOPO_4 (PPKTP) 174, 227, 255, 262, 287, 304, 305, 308
permittivity 83
phase
– commutation relation 88
– Hermitian 13, 111, 157
– operational 157, 192
– reconstruction 76
– transition 71, 73, 302
– uncertainty 15, 80, 82, 91, 106, 200
phase flip 38, 60, 318
phase gate 56–61, 75, 76, 109, 248, 267, 268, 275, 277, 283–285, 317, 319–321
phase quadrature 160, 254, 299
phase shifter 110, 111, 113, 122
phase space
– displacements 103, 110, 112, 113, 155, 157, 158, 189, 224, 225, 292
– representation 94, 97
– P function 97
– Wigner function 97
– variables 15, 66, 94, 100, 191
phase state 61, 267, 320, 321
phonon 70–74, 76
photoelectric effect 83
photomultiplier tube (PMT) 75
photon
– cavity 163, 165, 304–308
– coherent state 89, 90, 100, 115, 117, 118, 120, 162, 179, 210, 300, 301, 304
– number operator 87, 88
– number state 251, 303
photon number resolving (PNR) detection 232, 296, 301, 321
PMT, *see* photomultiplier tube
PNR, *see* photon number resolving
Pockels cell 221, 222
Poissonian distribution 90
polarization beam splitter 100, 133, 135–140, 188, 221, 227, 233, 251, 315
polarization entanglement 132
polarization qubit 99, 100, 135, 138, 140, 183, 185, 251, 274, 314, 315
positive-frequency part 83
positive map 148
positive operator 23, 27, 311
positive-operator valued measure (POVM) 27–31, 43, 48, 116, 117, 121, 122, 297, 322
– element 27, 28, 30, 121, 122, 297, 322
– measurement 27–31, 43, 48, 116, 117, 121, 297, 322
positive partial transposition 128
postselection 48, 135, 138, 141, 179, 251, 275, 277, 280, 291, 293, 300–302
POVM, *see* positive-operator valued measure
PPKTP, *see* periodically-poled KTiOPO_4
privacy amplification 48
probability
– classical 95–97
– conditional 48
– density 23, 29, 43, 64, 93
projective measurement 73, 269
projector 28, 65, 69, 121, 129
pure quantum state 10
purification 45, 47, 69, 238

q
QEC, *see* quantum error correction
QKD, *see* quantum key distribution
QND, *see* quantum nondemolition
quadratic interactions 120
quadrature
– eigenstate 89, 93, 101, 155, 171, 285
quadrature components 81, 195, 263, 265
quadrature distribution
– measurement 307
– sum 307
quadrature operators 91, 92, 145, 163, 189, 192, 225, 230, 285
quadrature-phase amplitudes 190
quadrupole 71
quantum
– harmonic oscillator 4, 13, 83, 86, 89

quantum algorithm 49, 50, 52
quantum channel 3, 4, 43, 48, 224
quantum circuit 40, 49, 52, 69, 74, 75, 210, 220, 221, 252, 266
quantum cloning 42
quantum code 218
quantum coherence 9
quantum communication 3, 4, 7, 31, 38, 41–49, 62, 69, 197, 203, 210, 217
quantum computation 3, 4, 7, 18, 20, 38, 49–62, 69, 80, 109, 120–123, 131, 172, 197, 203, 217, 246–248, 252, 259, 260, 271, 279–281, 284, 292, 295, 296, 301, 316–318
– Heisenberg picture 203
– linear optical 51, 80, 122, 246, 301
– measurement-based 3, 38, 52, 53, 217, 260, 271, 284
– one-way 18, 53, 54, 248, 279, 284, 292, 295, 296
quantum computer 5, 38, 41, 49–51, 62, 121, 123, 246, 253
quantum correlation 33, 129, 132, 142, 161, 162, 173, 174, 178, 203, 208, 219, 225, 260
quantum cryptography 42, 50
quantum dot 70
quantum efficiency 191, 192, 201, 205, 256, 306
quantum error correction (QEC) 62–69, 217–231
quantum error correction code 120, 224, 319
quantum fluctuations 81, 82, 90
quantum Fourier transform 50
quantum gate 52, 121, 122, 246, 247, 271
– local 271, 286
– universal 52, 121, 122, 246, 271
quantum information theory 3, 4, 6, 82, 86, 217
quantum key distribution (QKD) 6, 7, 30, 41–44, 48, 50, 312
quantum logic 273, 284
– circuit 284
– gate 273, 284
quantum measurement 31
quantum memories 46, 48
quantum noise 190, 191, 193, 255
quantum nondemolition (QND) 246, 259
– interaction 260, 263, 264, 266
– measurement 255
– sum gate 260, 283
quantum objects 13
quantum operation 9, 22, 23, 26, 31, 43, 114, 179, 252, 253, 293, 296
– complete 9, 23, 43
– reversible 22, 26, 31, 114
quantum parallelism 49
quantum repeater 3, 44–47, 217
quantum search algorithm 50
quantum simulation 50
quantum state
– cloning of 10
– coherent 43, 79, 82, 89, 162, 179, 196, 203, 210, 213, 256, 260, 287, 288, 293, 295, 304
– entangled 8, 18, 31, 38, 39, 41, 43, 45, 52, 79, 163, 165, 179, 203, 231, 245, 253, 260, 284
– EPR 4, 8, 43, 79, 82, 89, 94, 95, 162, 165, 180, 213, 254, 256, 260, 288, 293
– number 10, 45, 89, 196, 231, 304
– phase 38, 79, 82, 89, 94, 210, 213, 254, 256, 260, 284, 285, 287, 288, 293
– pure 10
– quadrature 79, 82, 163, 165, 213, 254, 256, 285, 287, 288, 295
– squeezed 52, 82, 162, 165, 245, 254, 256, 260, 285, 287, 288, 295, 304
– thermal 82, 288
quantum system 4, 18, 50, 148
quantum teleportation 38–41, 179–215, 245–270
quarter wave plate (QWP) 137, 138, 140, 141, 185, 186, 274, 277, 305
qubit
– atomic 79, 99, 210, 299, 302
– logical 67, 121, 218, 220, 315, 318–320
– photonic 45, 46, 70, 79, 98, 99, 114, 116, 117, 120–122, 127, 132, 179, 210, 249, 297, 299, 300, 317, 322
– physical 51, 63, 64, 66, 67, 218
qumode 13–17, 20–22, 33, 57–62, 236–241, 280–297
– entanglement swapping 210
– telecloning 196
– teleportation network 150, 203
QWP, *see* quarter wave plate

r

Rabi frequency 71
Radon transformation 257
– inverse 257
read-out 52
receiver 7, 41, 47, 80, 179, 183, 196–198, 204, 205, 208, 211, 245

reduced density operator 32, 43
reduction 27, 57, 90, 111, 112, 114, 119, 158, 172, 190, 207, 317
redundancy 62
relative phase 71, 164, 167, 205, 213, 255, 287, 311
remainder 4, 50, 52, 70, 238
repeater 3, 44–47, 217
repetition code 64, 67, 68, 218, 318
resonance fluorescence 75
reversibility 18
RSA encryption 49, 50

s
sampling 256, 288
scalability 49, 62, 291
Schmidt
– bases 70
– coefficients 32, 130, 146, 232, 310
– decomposition 31, 32, 129, 143, 232
– number 32, 143, 232
– rank 32, 34, 37
Schrödinger equation 148
Schrödinger kitten 240, 241, 303, 304, 307, 308, 313, 314
Schrödinger picture 92, 250
Schwarz inequality 147, 153
self-homodyning 227
self-Kerr nonlinearity 122
separability 24, 31, 34–36, 128, 146–149, 153, 154, 167, 168, 170, 176–178, 197, 198, 211, 239, 265, 311, 312
– criterion 35, 128, 146, 148, 149, 154, 167, 211, 265, 312
separability problem 149
separable 34–37, 43, 44, 128–130, 141, 147, 148, 152, 154, 167, 177, 197, 204, 219, 275, 276, 299, 311
separable state 35, 37, 43, 44, 128–130, 147, 148, 152, 299, 311
Shannon theory 47
sideband cooling 76
sidebands 107, 160, 162, 189, 213, 255, 262, 287, 300
signal state 24, 40, 44, 47–49, 54, 63, 66, 114, 116, 117, 220
signal transfer 80
simulation 50, 57, 58, 317
single-ion 70, 72–74
single-mode squeezer 110–112, 254, 284
single photons 45, 99, 122, 183, 184, 240, 246, 312
single-qubit gate 60
singular value decomposition 111
SK, *see* self-Kerr
spectra 11, 107, 162, 164, 190, 192, 305, 308
– electron 164
– time-resolved 162
spectral function 107
spin 70, 76, 99, 123, 299, 318
– electron 70, 99
– nuclear 70
spin-1/2 318
spontaneous emission 8
squeezed light 82, 142, 150, 172, 237, 297, 300, 322
– condition 142, 237, 297, 300, 322
– homodyne detection 300
– optical parametric oscillator 237
squeezed state
– coherent 91, 100, 164, 174, 188, 255, 256, 287, 304, 311
– minimum uncertainty 91
– quadrature squeezing 287
– quadrature variance 93, 285
– squeeze operator 91
– two-mode 34, 51, 127, 142–146, 159, 160, 232, 245, 267, 269, 270, 285, 311, 320
– two-mode squeezed vacuum 142, 143
– vacuum 51, 90, 91, 93, 102, 103, 142, 143, 159, 164, 172, 223, 256, 259, 287, 303, 304, 308
– Wigner function 103, 143, 256, 303, 304, 307, 308
squeezed vacuum state 92–94, 101, 102, 104, 106, 107, 109, 142–145, 148, 150, 151, 162, 168, 197, 204, 205, 211, 226, 266, 286, 292, 293, 301
squeezing gates 246, 260, 272, 283, 291, 294
stabilizer code 67–69, 103, 120, 218, 219
stabilizer formalism 103, 217, 218
stabilizer group 33, 56, 67, 68, 129, 155
standard deviation 256, 258
standard form 101, 148, 265, 299
state
– cat 210, 300–309, 318
– correlated 34
– estimation 121
– maximally entangled 32, 33, 36, 39, 40, 143, 197, 204, 231
– mixed 11, 12, 17, 18, 29, 31, 32, 34, 36, 37, 103–106, 130, 143–146, 232, 235, 259
– nonclassical 97, 303, 306
– product 32–34, 50, 54, 59, 86, 105, 106, 131, 145, 147, 155
– reduction 27

– separable 34–37, 43, 44, 128–130, 141, 147, 148, 152, 154, 167, 177, 197, 204, 219, 275, 276, 299, 311
– transformation 16, 32
– vector 7, 10, 29, 31, 32, 39, 68, 273, 282
– Werner 9, 34
statistical mixture 11
subsystem 31–33, 36, 63, 66, 67, 128, 148, 197, 204, 218, 271, 299, 303, 311
success probability 46, 117, 182, 221, 246–249, 251
superconducting 70
symplectic matrix 104
system
– closed 18
– composite 24, 28, 71, 76, 316

t

T-shape cluster 172, 174–177
target qubit 250, 251
telecloning 183–186, 196–202, 204
theory
– classical 4–6, 41, 42, 47, 49, 50, 82, 85, 192, 195, 217, 295
– physical 3, 5, 6, 50
thermal state 103–107, 143, 146, 198
Ti:sapphire laser 163, 174, 200, 205, 211, 226, 255, 262, 287, 305
time resolution 300, 313, 314
TMSS, *see* two-mode squeezed state
transformation
– active 110
– Gaussian unitary 80, 109, 148, 284
– orthogonal 67, 113, 114, 119
– passive 58, 110–113
– symplectic 57, 58, 105, 110, 113, 114, 118
– unitary 9, 18, 39–41, 80, 88, 109, 148, 158, 252, 253, 284
transposition 24, 35, 36, 128, 146, 148, 149, 311, 312
trap 70, 71, 73, 220, 223
– configurations 223
trapped atom 70
– Paul trap 70
trapped ion 70, 71, 73
tree 112
tripartite entanglement 130, 167, 196, 197, 199, 203–205, 208, 209
two-level system 3, 51, 71, 302
two-mode squeezed state (TMSS) 34, 51, 127, 142–146, 159, 160, 232, 245, 267, 269, 270, 311, 320
two-mode squeezed vacuum 142–145, 148, 162, 163, 195
two-mode squeezing 145
two-qubit gate 53, 55, 61, 247, 274–277

u

uncertainty relation 6, 15, 80, 82, 104–106, 147, 153
– Heisenberg 6, 15, 82, 104
– N-mode 104, 105
unconditional security 50
unitary operator 18, 19, 27, 54, 122, 272, 302
universal cloning 10
universal gate 22, 121, 122, 246, 284, 317, 319
universal gate set 22, 284
universal quantum gates 121, 122, 246
– criterion 121
universal squeezer 246, 252, 259

v

vacuum
– Rabi splitting 302
variance matrix 103, 118
vibrational
– levels 70, 73
– mode 70, 73
– motion 70, 71
visibility 201, 205, 256
von Neumann entropy 12, 32, 36, 47, 143, 145

w

wave equation 83–85
wave function 17, 92, 93, 142
waveplate 99, 100, 235
Weyl correspondence 96, 97, 103
Weyl-Heisenberg operator 16, 17, 284
Wigner function 92, 94, 95, 97, 98, 102–104, 106, 107, 112, 113, 119, 143, 148, 210, 241, 254, 256, 257, 288, 289, 299, 303, 304, 306–309
witness 31, 34, 35, 37, 127–132, 142, 146–151, 154, 176, 219, 220, 311

z

zero-point energy 13